

DISS. ETH NO. 19889

**Global 3-D imaging of mantle electrical conductivity based
on inversion of observatory *C*-responses.
An approach, data analysis and results.**

A dissertation submitted to

ETH ZÜRICH

for the degree of

Doctor of Sciences

presented by

ALEXEY SEMENOV

Diploma in Mathematics

Lomonosov's Moscow State University (Russian Federation)

born on May 24, 1986

citizen of Russian Federation

accepted on the recommendation of

PD Dr. Alexey Kuvshinov, examiner

Prof. Dr. Andrew Jackson, co-examiner

Prof. Dr. Nils Olsen, co-examiner

Dr. Jakub Velimsky, co-examiner

2011

“You know nothing, Jon Snow.”-Ygritte

George R. R. Martin

A Song of Ice and Fire

To my parents

Abstract

There is a great interest in understanding three-dimensional (3-D) physical properties of the Earth's mantle. Estimates of 3-D variations of Earth's properties come mainly from global seismic tomography. While substantial progress in seismology models have been achieved recently, interpretation of the seismic velocity anomalies in terms of thermodynamical and compositional parameters is often uncertain and needs additional information. The only other means to directly probe the physical properties of the mantle is electromagnetic (EM) induction sounding which recovers the electrical conductivity distribution in the Earth. To separate the effects of composition and temperature, or in illuminating the role of partial melt and fluids (especially water) in the mantle, both techniques are likely to be important.

The objectives of this work are three-fold: a) to develop an efficient global EM inverse solution to recover 3-D conductivity distribution in the mantle. The solution is based on analysis of the experimental *C*-responses from the global net of geomagnetic observatories; b) to obtain a new set of reliable *C*-responses which cover the broadest possible period range from the largest possible number of observatories; c) to invert these new *C*-responses in order to image the 3-D mantle conductivity distribution in the depth range between 400 and 1600 km.

The developed frequency domain 3-D inversion tool exploits a quasi-Newton optimization method. This method requires multiple calculations of the gradient of the data misfit with respect to model parameters. We implemented the adjoint method to allow efficient calculation of the gradient. It is known that the efficiency of 3-D inversions depends critically on the ability to execute the forward problem rapidly. Since our forward solver is based on an integral equation formulation, we take the advantage of this approach and conduct the most time-consuming part of the simulations – calculation of the tensor Green's functions – only once, prior to the inversion. Further improvement in computational time stems from the parallelization of the forward solver.

Our 3-D inverse solution has been applied to real ground-based geomagnetic data. We collected and analyzed very long time series (up to 51 years; 1957-2007) of hourly means of three components of the geomagnetic field from 281 geomagnetic observatories. Special attention was given to data processing in order to obtain unbiased *C*-responses with trustworthy estimates of experimental errors in the period range from 2.9 to 104.2 days. After careful inspection of the obtained *C*-responses we chose the data from 119 observatories for further analysis. Squared coherency was used as a main quality indicator to detect (and then to exclude from consideration) observatories with large noise-to-signal ratios. During this analysis we found that – along with the *C*-responses from high-latitude observatories (geomagnetic latitudes higher than 58°) – the *C*-responses from all low-latitude observatories (geomagnetic latitudes below 11°) also have very low squared coherencies, and thus cannot be used for global induction studies.

We found that the C -responses from the selected 119 mid-latitude observatories show a huge variability both in real and imaginary parts, and we investigated to what extent the ocean effect can explain such a scatter. By performing systematic model calculations we conclude that: (a) the variability due to the ocean effect is substantial, especially at shorter periods, and it is seen for periods up to 40 days or so; (b) the imaginary part of the C -responses is to a larger extent influenced by the oceans; (c) two types of anomalous C -response behaviour associated with the ocean effect can be distinguished. (d) in order to accurately reproduce the ocean effect a lateral resolution of $1^\circ \times 1^\circ$ of the conductance distribution is needed. (e) the ocean effect alone does not explain the whole variability of the observed C -responses.

We also found that part of the variability in the real part of the C -responses is due to the auroral effect. In addition we discovered that the auroral effect in the C -responses reveals strong longitudinal variability, at least in the Northern hemisphere. Europe appears to be the region with smallest degree of distortion compared with North America and northern Asia. We also detected that the imaginary part of the C -responses is practically unaffected by the auroral source, thus confirming the fact that in the considered period range the EM induction from the auroral electrojet is negligible. Assuming independence of the auroral signals on the Earth's conductivity (no EM induction), and longitudinal variability of the auroral effect, we developed a scheme to correct the experimental C -responses for this effect.

With these developments and findings in mind we performed a number of regularized 3-D inversions of our experimental data in order to detect robust features in the recovered 3-D conductivity images. Although differing in details, all our 3-D inversions reveal a substantial level of lateral heterogeneity in the mantle at the depths between 410 and 1600 km. Conductivity values vary laterally by more than one order of magnitude between resistive and conductive regions. The maximum lateral variations of the conductivity have been detected in the layer at depths between 670 and 900 km. By comparing our global 3-D results with the results of independent global and semi-global 3-D conductivity studies, we conclude that 3-D conductivity mantle models produced so far are preliminary as different groups obtain disparate results, thus complicating quantitative comparison with seismic tomography or/and geodynamic models. In spite of this, our 3-D EM study and most other 3-D EM studies reveal at least two robust features: reduced conductivity beneath southern Europe and northern Africa, and enhanced conductivity in north eastern China.

Zusammenfassung

Für das grundsätzliche Verständnis des Erdinneren sind Informationen über dessen physikalische Eigenschaften von grosser Bedeutung. Zur Beschreibung der dreidimensionalen physikalischen Eigenschaften des Erdmantels werden vor allem seismische Methoden angewendet, die jedoch die chemisch-mineralogischen und thermischen Variationen des Mantels nicht ausreichend auflösen können. Eine Kombination von seismischen und elektromagnetischen Methoden ermöglicht jedoch die detaillierte Beschreibung physikalischer und chemischer Eigenschaften von Mineralphasen des Mantels.

Zur Bestimmung der elektrischen Eigenschaften des Mantels wurde in dieser Arbeit ein neuer Ansatz entwickelt, der auf der Analyse von magnetischen Übertragungsfunktionen (*C*-Responsen), die aus den Messungen geomagnetischer Observatorien geschätzt wurden, basiert. Um die "penalty" Funktion (die aus Missfit- und Regulierungs-Funktionen besteht) zu minimieren wurde eine iterative Gradienten-Methode angewendet. Zur Lösung des Vorwärtproblems (der Bestimmung theoretischer *C*-Responsen für ein vorgegebenes Modell der Mantelleitfähigkeit) wurde eine Integralgleichungsmethode verwendet. Die Bestimmung des Missfits-Gradienten wurde mithilfe einer adjungierten Methode optimiert. Um die benötigte Rechenzeit zu verkürzen wurde das Programm in Bezug auf die zu modellierenden Frequenzen parallelisiert und die Berechnung der Green'schen Tensoren vorab durchgeführt. Die Konvergenz und Genauigkeit des Programms wurden an einem numerisch-synthetischen Beispiel und unter Annahme eines dreidimensionalen Leitfähigkeitsmusters im Mantel getestet. Die berechneten synthetische *C*-Responsen wurden anschliessend invertiert und die resultierende Leitfähigkeit mit der ursprünglichen Leitfähigkeitsverteilung verglichen. Dieser Test hat gezeigt, dass der verwendete Algorithmus die Mantelleitfähigkeit mit hoher Genauigkeit aus den *C*-Responsen schätzen kann.

In einem weiteren Schritt wurde dann der Algorithmus verwendet um die Mantelleitfähigkeit im Tiefenbereich zwischen 410 km und 1600 km aus experimentellen *C*-Responsen zu bestimmen. Hierfür mussten letztere optimal geschätzt werden. Dies erfolgte durch eine detaillierte Analyse von Magnetfelddaten von 281 Observatorien der Jahre 1957 bis 2007 (51 Jahre) aus denen *C*-Responsen für 15 Perioden zwischen 2.9 und 104.2 Tagen geschätzt wurden. Spezielles Augenmerk wurde dabei auf eine genaue Bestimmung der Fehler gelegt. Gute Übertragungsfunktionen zeichnen sich durch eine hohe Kohärenz, relativ kleine Fehler und ein glattes Frequenzverhalten aus. *C*-Responsen von 119 Observatorien, gelegen in Dipolbreiten zwischen 11 und 58 Grad Nord oder Süd, erfüllten diese Kriterien.

Diese Übertragungsfunktionen zeigen jedoch eine hohe Variabilität bezüglich ihres Real- und Imaginärteils. Ein relativ hoher Anteil dieser Variabilität wird durch den Einfluss von elektrischen Strömen in den Ozeanen hervorgerufen. Dieser Effekt wurde mithilfe von Modellstudien im Detail untersucht. Es zeigte sich, dass (a) der Einfluss der Ozeane sichtbar ist für Perioden bis zu 40 Tagen; (b) der Imaginärteil stärker beeinflusst ist als der Realteil; (c) die Variabilität jedoch nicht ausschliesslich den Ozeanen zugeschrieben werden kann. Der

Einfluss elektrischer Ströme in der polaren Ionosphäre ist eine zusätzliche Quelle für die Variabilität der *C*-Responsen. Es zeigte sich, dass der Effekt dieser Ströme relativ starke longitudinale Unterschiede aufweist, welche wir vor allem für die Nordhemisphäre beschreiben konnten. Der Einfluss ist in Nordamerika und Asien ausgeprägter als in Europa. Es wurde ein Schema entwickelt, um die durch polare Ströme hervorgerufene Verzerrung der Übertragungsfunktionen abzuschätzen.

Mithilfe all dieser Informationen und dem neu entwickelten analytischen Ansatz einer dreidimensionalen Inversion kann die räumliche Verteilung der elektrischen Leitfähigkeit im Mantelbereich zwischen 410 km und 1600 km Tiefe gut beschrieben werden. Die Robustheit des erhaltenen Leitfähigkeitsmodells wurde durch verschiedene Tests bestätigt. Im Weiteren wurde das erhaltene Leitfähigkeitsmodell mit Resultaten anderer Studien verglichen. Trotz Übereinstimmung in vielen Regionen muss eine genaue Bestimmung der Mantelleitfähigkeit auch weiterhin Gegenstand der Forschung bleiben.

Contents

Abstract	i
Zusammenfassung	iii
1 Introduction	1
1.1 A brief history of early EM induction studies of the Earth	2
1.2 Recent deep electromagnetic studies	3
1.2.1 Response functions used to detect lateral variations of conductivity .	4
1.2.2 Recent regional 1-D studies of the conductivity in the Earth mantle .	6
1.2.3 Semi-global quasi 1-D studies	9
1.2.4 Semi-global and global 3-D EM studies	10
1.2.5 Global multi-dimensional EM studies in time domain	11
1.3 Thesis outline	12
2 Forward modeling	15
2.1 Maxwell's equations	15
2.2 Integral equation approach	16
2.3 Solution of the integral equation	18
2.4 Derivation of explicit forms for Green's tensors for electric current source . .	20
3 Inverse modeling	29
3.1 C-response concept	29
3.2 Inverse problem formulation	33
3.3 Parameterization of the model	34
3.4 Limited-memory quasi-Newton (LMQN) algorithm	35
3.4.1 Line search. The Wolfe conditions	35
3.4.2 Limited-memory BFGS	37
3.5 Adjoint approach for efficient calculation of the misfit gradient	38
3.5.1 Definition of the operators G_{3D}^{ej} and G_{3D}^{eh}	38
3.5.2 Derivatives of the C-responses	39
3.5.3 Gradient of the data misfit	43

3.5.4	Derivation of explicit forms for Green's tensor for a magnetic dipole source	45
3.5.5	Tests of calculation of Green's tensor G_{1D}^{eh}	50
3.5.6	Numerical verification of the adjoint approach	51
3.6	Optimization and numerical verification of the 3-D inverse solution	53
3.6.1	Optimization of the inverse solution	53
3.6.2	Numerical verification	54
4	Estimation of experimental <i>C</i>-responses	57
4.1	Data collection	57
4.2	Determination of <i>C</i> -responses	58
4.2.1	Least squares approach	59
4.2.2	The jackknife method	62
4.2.3	<i>C</i> -responses selection	65
4.3	Ocean effect in <i>C</i> -responses	67
4.3.1	Resolution studies	69
4.3.2	Two types of anomalous behavior due to ocean effect	69
4.3.3	Dependence of the responses on 1-D conductivity structure beneath oceans	72
4.3.4	Correction for the ocean effect	74
4.4	Auroral effect in <i>C</i> -responses	75
4.4.1	Existence of the auroral effect	75
4.4.2	Longitudinal dependence	77
4.4.3	Correction for the auroral effect	79
5	3-D inversion of the experimental responses	85
5.1	Detecting lateral variations in mantle conductivity	85
5.2	Comparison with semi-global 3-D studies	90
5.3	Comparison with global 3-D studies	93
5.4	Comparison with global 3-D seismic studies	96
6	Conclusions and outlook for future studies	99
6.1	Conclusions	99
6.2	Outlook for future studies	102
6.2.1	Extending the data for global 3-D EM inversions	102
6.2.2	Proper account/correction for the auroral effect	103
6.2.3	Further developments of our global 3-D EM inversion solution	103
6.2.4	Implementation of the alternative approach to global 3-D EM inversion	104

A	Mathematical basics	105
A.1	Analytic functions	105
A.2	Properties of C -responses as analytic functions	106
A.3	Spherical harmonics	109
A.3.1	Laplace's equation	109
A.3.2	Associated Legendre functions	109
A.4	Helmholtz representation	110
A.5	Scalar Green's functions	111
A.5.1	Definition and properties	111
A.5.2	Derivation of scalar Green's functions	113
A.5.3	Calculation of admittances	114
A.5.4	Calculation of scalar Green functions	116
B	Representation of EM field in 1-D conductivity model via external coefficients	118
B.1	Representation of \mathbf{B}^e via equivalent sheet current	118
B.2	Final representation of EM fields	120
C	Tests of different inversion settings	122
C.1	Checkerboard test	122
C.2	The results for different lateral resolutions of the inverse domain	123
C.3	The results for different <i>a priori</i> models	125
D	Mineral physics studies	127
E	Experimental responses	132
	Bibliography	196
	Curriculum Vitae	208
	List of Publications	209
	Acknowledgements	211

List of Figures

1.1	Schematic picture of the Earth. After Gubbins (2008)	2
1.2	Electrical conductivity distributions in the Earth from early deep EM studies. After Constable (2007)	3
1.3	Comparison of conductivity profiles from Changchung (CHC) (light green band) in China (Ichiki et al., 2001) with those at Carty Lake (CLC) (blue dotted line), Tucson (TUC) (red broken line) and Honolulu (HON) (green chain line) (Neal et al., 2000). The mantle transition zone is shown by yellow. After Ichiki et al. (2001)	7
1.4	Smoothed image of the integrated conductance, in kiloSiemens, from the surface down to the depth of 770 km in the mantle beneath Europe. After Semenov and Joswiak (2006)	8
1.5	Conductivity models beneath Fürstenfeldbruck (FUR) in Europe, Hermanus (HER) in South Africa, Langzhou (LZH) in China, Alice Springs (ASP) in Australia, Tucson (TUC) in North America, and Honolulu (HON) in North Pacific. For comparison, two other one-dimensional conductivity models (from Olsen (1999) and Kuvshinov and Olsen (2006)) are indicated by colored lines. After Khan et al. (2011)	9
1.6	Comparison of two-jump model beneath the North Pacific obtained by Utada et al. (2003) (black line), by Kuvshinov et al. (2005) (red line) and by Shimizu et al. (2010a) . After Shimizu et al. (2010a)	10
1.7	Two-layer, latitudinally dependent conductivity model of the upper part of the lower mantle and the upper mantle (left and right panels). The model best fitting the 2001 CHAMP data (red lines), the starting model for the CG minimization (blue lines) and the model after the first iteration (dotted line) are compared to the best 1-D conductivity model. After Martinec and Velimsky (2009)	12

3.1	$ Q_n^{(r)} $ for different periods as a function of degree n . Solid lines $ Q_n^{(r)} $ for a typical global 1-D conductivity profile. Dashed lines $ Q_n^{(r)} $ for the same 1-D model overlain by a uniform ocean of 15,000 S. For comparison, the dotted line in the figure shows an upper limit, 1, for $ Q_n^{(r)} $ which corresponds to a perfectly conducting Earth. After Kuvshinov (2008).	30
3.2	Example of C -response estimation at Fürstenfeldbruck (FUR) observatory in southern Germany. Blue circles represent the real part of the C -responses, red circles - the imaginary part.	32
3.3	Sketch of 3-D conductivity model.	34
3.4	Comparison of results calculated in spherical (left-hand plots) and Cartesian (right-hand plots) geometries. Upper plots: real parts of southward component of electric field (V/m). Lower plots: imaginary parts (V/m). Excitation: radial magnetic dipole. See details in the text.	51
3.5	Comparison of results calculated in spherical (left-hand plots) and Cartesian (right-hand plots) geometries. Upper plots: real parts of southward component of electric field (V/m). Lower plots: imaginary parts (V/m). Excitation: southward magnetic dipole. See details in the text.	52
3.6	Comparison of results calculated in spherical (left-hand plots) and Cartesian (right-hand plots) geometries. Upper plots: real parts of southward component of electric field (V/m). Lower plots: imaginary parts (V/m). Excitation: eastward magnetic dipole. See details in the text.	52
3.7	Comparison of data misfit gradients calculated by adjoint method (right-hand plot) and straightforward numerical differentiation (left-hand plot).	53
3.8	Comparison of the data misfit gradients along the profile depicted as a dashed line in right-hand plot of Fig. 3.7.	53
3.9	Normalized misfit with respect to the iterations. Synthetic modeling results.	54
3.10	3-D Model and results of conductivity recovery at initial stage of inversion at (0, 10, 50, 150 and 450 iterations) in logarithmic scale.	55
4.1	Location of 281 observatories, data from which have been retrieved from Edinburgh World Data Center for Geomagnetism.	58
4.2	Time series of hourly mean values X (upper plots), Y (middle plots) and Z (lower plots) components of the magnetic field for Fürstenfeldbruck (FUR) observatory (left-hand plots) in Germany and Hermanus (HER) observatory (right-hand plots) in South Africa.	58
4.3	Time series of hourly mean values of X (upper plots), Y (middle plots) and Z (lower plots) components of the magnetic field for Papete (PPT) observatory (left-hand plots) in Pacific Ocean and Sheshan (SSH) observatory (right-hand plots) in China.	59

4.4	<i>C</i> -responses for Fürstenfeldbruck observatory estimated with the use of eq. (4.3) and eq. (4.13) (for details see the text). Circles signify the results obtained from “single site” estimation (using eq. (4.3)), triangles and crosses denote the results obtained using remote reference technique (see eq. (4.13)) with Kakioka (KAK) and Chambon-la-Forêt (CLF) as respective reference observatories. Blue circles represent the real part of the <i>C</i> -responses, red circles – the imaginary part.	62
4.5	Comparison of least squares and jackknife techniques used to calculate <i>C</i> -responses on the Hermanus observatory (left-hand plot) and the Alice Springs observatory in Australia (right-hand plot). Blue circles represent the real part of the <i>C</i> -responses, red circles - the imaginary part.	63
4.6	Averaged over all periods squared coherencies at 262 preselected observatories. Upper plot shows averaged coherency at a given observatory, where the circles stand for averaged coherencies; the larger the size of the circle the higher the coherency (5 different sizes correspond to the following intervals: 0-0.2; 0.2-0.4; 0.4-0.6; 0.6-0.8, 0.8-1). Lower plot presents the distribution of the averaged coherency with respect to geomagnetic latitude.	64
4.7	Examples of <i>C</i> -responses at equatorial observatories. Left upper plot – at Guam (GUA) observatory in the Pacific Ocean (5°N GM), right upper plot – at Hyderabad (HYD) observatory in India (8°N GM), left lower plot – at Huancayo (HUA) in South America (1°S GM) and right lower plot – at Addis Ababa in Africa (5°N GM). Blue circles represent the real part of the <i>C</i> -responses, red circles – the imaginary part.	65
4.8	Examples of <i>C</i> -responses at high-latitude observatories. Left upper plot – at Sitka observatory in North America (60°N GM), right upper plot – at Yakutsk observatory in Siberia (52°N GM), left lower plot – at Arkhangelsk observatory in north-west of Russia (59°N GM), and right lower plot – at Tromsø observatory in Norway (67°N GM). Blue circles represent the real part of the <i>C</i> -responses, red circles – the imaginary part.	66
4.9	Upper plot shows conductance map using a logarithmic scale and location of the 119 mid-latitude observatories employed here. Lower plots present the variability of the real (left-hand plot) and imaginary (right-hand plot) parts of experimental responses at these observatories.	68
4.10	Ocean effect due to different ocean resolutions in the “1D+ocean” models. Upper plots present the results for $0.3^\circ \times 0.3^\circ$ resolution of the surface conductance, middle plots – the results for $1^\circ \times 1^\circ$ resolution, and lower plots – the results for $3^\circ \times 3^\circ$ resolution. Blue circles (left-hand column) represent the real part of the <i>C</i> -responses, red circles (right-hand column) - the imaginary part.	70

- 4.11 *C*-responses from the Hermanus observatory (left-hand plot) and from Kanoya observatory (right-hand plot) that are predicted in “ocean+1D” model. Blue circles represent the real part of *C*-responses, red circles – the imaginary part. Black circles represent the “global” *C*-responses (see text for explanation). 71
- 4.12 *C*-responses from the Port Stanley (PST) observatory in South America (left-hand plot) and from Faraday Island (AIA) observatory in Antarctic (right-hand plot) which are predicted in “ocean+1D” model. Blue circles represent the real part of *C*-responses, red circles - the imaginary part. Black circles represent the “global” *C* – responses (see text for explanation). 71
- 4.13 Variability of the predicted responses due to the changes in lithosphere resistivity. Upper and lower plots show the variability of the responses when the lithosphere resistivities in the “ocean+1D” model are 300 Ohm-m and 30000 Ohm-m, respectively. Blue circles (left-hand column) represent the real part of the *C*-responses, red circles (right-hand column) - the imaginary part. 72
- 4.14 Dependence of the predicted responses at Hermanus observatory on lithosphere resistivity. Blue circles represent the real part of the *C*-responses, red circles – the imaginary part. Black circles show the responses for 1-D conductivity model, colored circles, triangles and crosses are the responses for the “ocean+1D” model with 300 Ohm-m, 3000 Ohm-m and 30000 Ohm-m lithosphere, respectively. 73
- 4.15 Variability of the predicted responses when the oceanic layer was underlain by 1-D profile recovered by [Khan et al. \(2011\)](#) from the Hermanus observatory data. Blue circles (left-hand plot) represent the real part of the *C*-responses, red circles (right-hand plot) – the imaginary part. 73
- 4.16 Dependence of the predicted responses at Hermanus observatory on 1-D conductivity profile. Blue circles represent the real part of the *C*-responses, red circles - the imaginary part. Black circles show the responses for 1-D conductivity model from [Kuvshinov and Olsen \(2006\)](#), colored circles are the responses for the “ocean+1D” model with 1-D conductivity profile from [Kuvshinov and Olsen \(2006\)](#), and triangles are the responses for the “ocean+1D” model with 1D conductivity profile recovered by [Khan et al. \(2011\)](#) from the Hermanus observatory data. 74
- 4.17 Results of the ocean correction for the Hermanus observatory and Kakioka observatories. Blue circles represent the real part of the *C*-responses, red circles - the imaginary part. Circles with error bars show original experimental responses, triangles depict the responses corrected for the ocean effect. 75
- 4.18 Adopted model of the auroral electrojet current system. This current system is represented by a circular infinitesimally thin line current flowing 23° apart from geomagnetic pole, at an altitude of 100 km. 76

- 4.19 Real (blue) and imaginary (red) parts of the C -responses estimated for all observatories at periods of 3.7 days (upper left-hand plot), 10.5 days (upper right-hand plot), 22.5 days (lower left-hand plot), and 37.4 days (lower right-hand plot). The responses are shown as a function of GM latitude. 77
- 4.20 Experimental responses at two observatories located in geomagnetic latitude band between 40° and 58° . Left-hand plot shows the responses at Brorfelde (BFE; Denmark) observatory, right-hand plot – the responses at Ekaterinburg (SVD; Russia) observatory. Blue circles represent the real part of the C -responses, red circles – the imaginary part. Black circles depict the predicted responses from global 1-D conductivity profile derived by Kuvshinov and Olsen (2006). 78
- 4.21 Z (left-hand plot) and H components (right-hand plot) of the real part of the magnetic fields at the Earth's surface excited by an auroral current. Blue curves depict external field, black and red curves show the results for the models with and without ocean, respectively. The results are for period of 22.5 days. 78
- 4.22 Comparison of the auroral effect in experimental C -responses in different regions. Left-hand plots show the comparison of the responses in Europe and North America, right-hand plots – comparison of the responses in Europe and North Asia. Circles represent the real part of the C -responses, crosses - the imaginary part. Blue, magenta and red colours depict the results for Europe, North Asia and North America, respectively. From the top to the bottom are the responses for periods 3.7 and 10.5 days. 79
- 4.23 Comparison of the auroral effect in experimental C -responses in different regions. Left-hand plots show the comparison of the responses in Europe and North America, right-hand plots – comparison of the responses in Europe and North Asia. Circles represent the real part of the C -responses, crosses - the imaginary part. Blue, magenta and red colours depict the results for Europe, North Asia and North America, respectively. From the top to the bottom are the responses for periods 22.5 and 37.4 days. 80
- 4.24 Intensity of the main magnetic field at Earth's surface in 2010 from IGRF-11 (Finlay et al., 2010). The units are in 10000 nT. 81
- 4.25 The results of fitting of experimental responses, C_s^{exp} , and modelled responses C_s^{mod} for Europe (upper plot), North America (middle plot), and northern Asia (lower plot). Blue color represents the real part of the C -responses, red color – the imaginary part. Circles with error bars show the experimental responses, C_s^{exp} , whereas crosses depict modelled responses, C_s^{mod} . The results are for the period of 10.5 days. 82

4.26	Results of the correction of the European responses for the auroral effect at period 13.5 days (see eq. (4.23). Blue line is the real part of the 1-D C -response, $\Re\{C_{1D}^R(\omega)\}$, at observatory PAG ($\vartheta = 40^\circ N$ GM), red crosses are the real parts of the modeled (see eq. (4.22)) C -responses, $\Re\{C_s^{mod}(\omega)\}$. Black circles are experimental values of the real parts of C -responses, $\Re\{C_s^{exp}(\omega)\}$. Magenta triangles are the real parts of the corrected responses, $\Re\{C_s^{exp,corr}(\omega)\}$.	83
4.27	Results of the auroral correction for the Niemegk (NGK) observatory in Germany. Blue color represent the real part of the C -responses, red color - the imaginary part. Circles with error bars show original experimental responses, triangles – real part of responses corrected for the auroral effect.	83
4.28	Experimental responses at Faraday Island (AIA) observatory. Blue circles represent the real part of the C -responses, red circles – the imaginary part. Black circles are the responses for 1-D profile from Kuvshinov and Olsen (2006).	84
5.1	Side view of the model.	86
5.2	Typical shape of L-curve for our 3-D inversions. Regularization term is from eq. (3.20).	86
5.3	Results of our 3-D inversion. Left-hand column of plots presents the results of inversion of uncorrected responses. Middle column – the results of inversion of the responses corrected for the auroral effect. Right-hand column – the results of inversion of the responses corrected for the auroral and the ocean effects.	87
5.4	Starting misfit (left-hand plot) versus final misfit (right-hand plot).	89
5.5	Misfit evolution during the 3-D inversion.	89
5.6	Left-hand plot presents the locations of geomagnetic observatories and Trans-Pacific telegraph cables. Right-hand plot illustrates the concept of voltage measurement using the cables.	90
5.7	Comparison of our results (left-hand column of plots) with results from Shimizu et al. (2010b) study (two right-hand columns of plots).	91
5.8	Location of observatories used in Utada et al. (2009) study.	92
5.9	Comparison of our results (left column) with results from Utada et al. (2009) study.	92
5.10	Comparison of our results (left-hand plots) with results from Kelbert et al. (2009) study (right-hand plots).	94
5.11	Comparison of our results (left-hand plots) with Tarits and Mandeia (2010) study (right-hand plot).	95

5.12	Comparison of our results (left-hand column of plots) P-wave (middle column of plots) and S-wave (right-hand column of plots) distributions from Becker and Boschi (2002).	97
5.13	Comparison of our results (left-hand column of plots) with the P-wave (middle column of plots) and S-wave (right-hand column of plots) distributions from Della Mora et al. (2011).	98
C.1	Checkerboard test. Left-hand plots are original (“true”) conductivity distributions in five layers. Right-hand plots – results of 3-D inversion. See details in the text.	123
C.2	Unfiltered results for different lateral resolutions of the inverse domain. Left-hand, middle and right-hand plots are the results for grids of lateral resolution $6^\circ \times 6^\circ$, $9^\circ \times 9^\circ$, and $15^\circ \times 15^\circ$, respectively.	124
C.3	Filtered results for different lateral resolutions of the inverse domain. The same legend as in Fig. C.2.	125
C.4	Filtered results for different <i>a priori</i> models. Left-hand plots are the inverse results when the local 1-D profile derived from analysis of Hermanus data was taken as <i>a priori</i> model. Middle plots are the results when global profile from (Kuvshinov and Olsen, 2006) was taken as <i>a priori</i> model. Right-hand plots correspond to the case when inversion was performed without <i>a priori</i> model.	126
D.1	Mineral proportions and phase transition in the Earth’s mantle. Shaded areas indicate the mantle transition zone between 410 and 660 km discontinuities. <i>PX</i> -Pyroxene, <i>OPX</i> - orthopyroxene, <i>CPX</i> - clinopyroxene, <i>GRT</i> - garnet, <i>MJ</i> - majorite garnet, <i>OL</i> - olivine, <i>WD</i> - wadsleyite, <i>RW</i> - ringwoodite, <i>FP</i> - ferropericlase, <i>PV</i> - silicate perovskite, <i>PPV</i> - silicate post-perovskite, <i>Ca – PV</i> Ca-perovskite. After Yoshino (2009).	128
D.2	Laboratory mineral electrical conductivity measurements as a function of inverse temperature (A upper mantle, B transition zone and C upper part of lower mantle) and variations in mineral phase proportions and laboratory-based conductivity profile computed on the basis of a homogeneous adiabatic pyrolite mantle as a function of pressure (depth) and transition zone water content (B and D). The solid and dotted lines in (D) are bulk conductivity and adiabat, respectively. Phases are: Ol (olivine), Opx,(orthopyroxene), Cpx (clinopyroxene), C2/c (highpressure Mgrich Cpx), Gt (garnet), Wads (wadsleyite), Ring (ringwoodite), Aki (akimotoite), Ca-pv (calcium perovskite), Wus (magnesiowustite), Pv (perovskite) and CF (calcium ferrite). After Khan et al. (2011).	131

Chapter 1

Introduction

From seismic studies we know that the Earth has a solid inner core (~ 1221 km from the Earth's center), liquid outer core (~ 1221 - ~ 3481 km), a solid mantle (~ 3481 - ~ 6100 km) and a crust (~ 6100 - ~ 6172 km) (Fig. 1.1). There is great interest in characterizing the three-dimensional (3-D) physical properties of Earth's mantle on a global scale. One technique that has reached a level of maturity is seismic tomography, which recovers the 3-D variations in seismic wave speed in the mantle (e.g. [Becker and Boschi, 2002](#); [Romanowicz, 2003](#), among others). This information is crucial in characterizing the dynamics of the mantle. For example, geodynamic processes such as mantle convection, the fate of subducting slabs and the origin of continents all have signatures in seismic wave speed. Although seismic tomography has proven important as a means of mapping mantle velocity heterogeneities, it suffers from the limited ability to separate effects arising from compositional and thermal variations (see e.g. [Trampert et al., 2004](#); [Khan et al., 2009](#)). In this context global electromagnetic (EM) studies, by recovering the electrical conductivity distribution in the mantle, provide independent and complementary information about the Earth's interior. This is indeed an important issue since conductivity reflects the connectivity of constituents as fluids, partial melt, and volatiles (all of which may have profound effects on rheology and, ultimately, mantle convection and tectonic activity), while seismology ascertains bulk mechanical properties. To separate the effects of composition and temperature, or in illuminating the role of fluids (especially water) in the mantle, both techniques are likely to be important. The latter issue - to what extent the mantle is wet - is very topical because water content in the mantle not only governs physical rock properties but also transport properties such as viscosity, thermal and not least electrical conductivity (e.g. [Karato, 1990, 2006](#)). But it is still not clear how the water enhances the electrical conductivity of the mantle minerals. Laboratory results at mantle conditions have so far proved controversial, with the two main groups (Yoshino, Katsura & coworkers, and Karato, Dai & coworkers) reaching different conclusions, as regards the effect of water on the conductivity of upper mantle and transition zone (TZ; depths between 410 and 670 km) minerals. Since the minerals in the transition zone (i.e. wadsleyite and ringwoodite) are known to have high H_2O solubility ([Inoue et al., 1995](#)) the actual water content is a key parameter to understand their

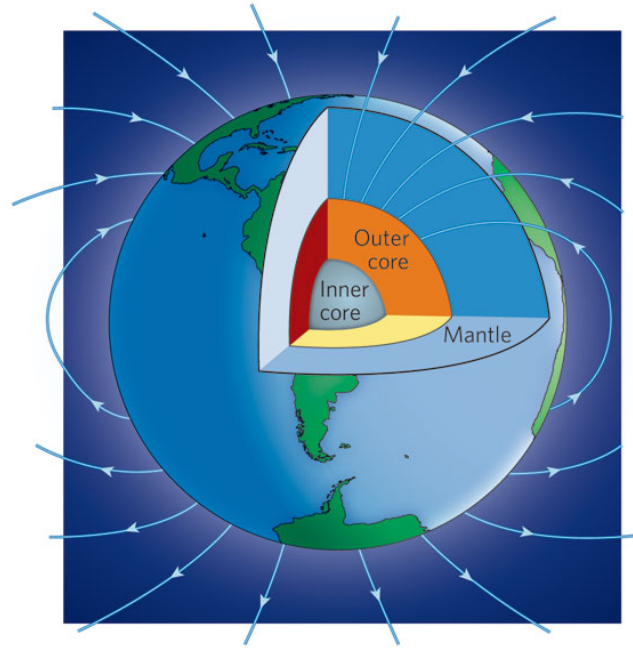


Figure 1.1: Schematic picture of the Earth. After Gubbins (2008).

physical properties. An overview of laboratory studies on electrical conductivity is presented in Appendix D.

1.1 A brief history of early EM induction studies of the Earth

The history of terrestrial EM induction studies is connected to the development of the fundamental physics of electromagnetic energy, closely following Oersted's 1820 observation that an electric current deflected a magnet (Dibner, 1962) and Ampere's quantification of this phenomena in 1826 (Ampere, 1826). Ampere also found out that a current in a wire exerted a magnetic force, and that two such wires therefore interact magnetically. In 1831 Faraday observed that moving a magnet through a coil produces an electric current (Faraday, 1839). In 1832 he predicted that salt water moving through a magnetic field should also produce an electric field, an effect that was observed much later in 1918.

The first observations that associated induction effects with geomagnetic storms were seen in telegraph cables. The storm of 1838 produced a noticeable effect on Norwegian telegraph cables (Constable, 2007), and Barlow (1849) reports spontaneous currents in telegraph lines in England, while Clement (1860) observed that the aurora of 29 August 1859 disrupted the telegraphic connection. The mathematical developments of the subject started in 1839, when Gauss published a method describing Earth's magnetic field by a spherical harmonic expansion, which allows the separation of "internal" and "external" magnetic sources. Later Maxwell (1865) introduced Maxwell's equations to describe the world of electromagnetism. In 1865 the Greenwich Observatory started to observe Earth's potentials on 15 km ground

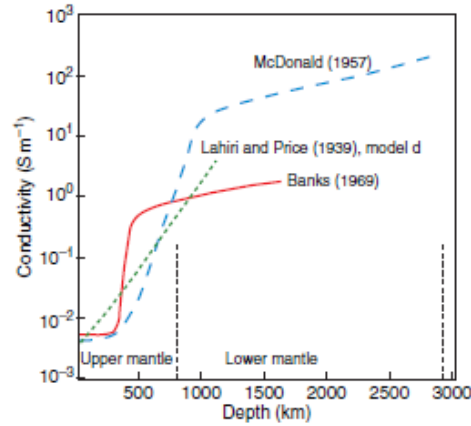


Figure 1.2: Electrical conductivity distributions in the Earth from early deep EM studies. After Constable (2007).

lines. In the beginning of the XXth century the relationship between Earth's currents and magnetic activity was already well known.

The possibility of obtaining knowledge about Earth's electrical conductivity distribution from observations of Earth's magnetic field, was first considered by Schuster (1889). He separated daily magnetic variations observed on a number of observatories into parts of external and internal origin, and then applied the theory of electromagnetic induction in a uniform sphere (Lamb, 1883) to show that the internal part could be connected to electric currents induced in the Earth by the external part. Chapman (1919) inferred that the Earth's interior must be more conductive than the crustal rocks, and modeled the magnetic field of the model sphere having a conductive core surrounded by a nonconducting shell of about 250 km thickness. Chapman and Whitehead (1922) found, however, that a highly conducting ocean has a significant effect on the internal field, and thus introduced some uncertainty in previous estimates of core conductivity. Lahiri and Price (1939) made further investigations of terrestrial conductivity; they modeled the internal and external parts of the magnetic field using a radially-symmetric conductivity profile down to 1000 km. Banks (1969) proposed that the P_1^0 spherical harmonic adequately describes the variation of the magnetic field over the surface of the Earth in the period range between 2 days and 2 months and modeled the conductivity profile down to 2000 km. In order to get an estimate of the electrical conductivity of the lowermost mantle, McDonald (1957) modeled the outward propagation of an inferred geomagnetic secular variation signal originating in the core. Fig. 1.2, taken from Constable (2007), summarizes one-dimensional (1-D) conductivity distributions from these early studies.

1.2 Recent deep electromagnetic studies

Since the presented work aims to detect lateral variations in mantle conductivity in this chapter we review results that are relevant to this topic (Kuvshinov, 2011).

In most deep EM studies, time series of hourly mean values of three geomagnetic field components measured on a global net of geomagnetic observatories have been used to probe electrical conductivity structure of the mantle. The data are Fourier transformed, and then analyzed and interpreted in the frequency domain. The source, caused by modulation of ring electric current in the magnetosphere, is most frequently used for deep EM induction studies. This source generates irregular geomagnetic variations (*Dst* variations) in the period range between a few days and a few months; namely the results based on the analysis of these variations will be discussed in the manuscript. The geometry of this source is dominated by a P_1^0 spherical harmonic function in the geomagnetic coordinate system.

By analyzing the *Dst* variations one relies on the solution of Maxwell's equations in the frequency domain

$$\nabla \times \mathbf{H}(\mathbf{r}, \omega) = \sigma(\mathbf{r})\mathbf{E}(\mathbf{r}, \omega) + \mathbf{j}^{ext}(\mathbf{r}, \omega), \quad (1.1a)$$

$$\nabla \times \mathbf{E}(\mathbf{r}, \omega) = i\omega\mathbf{B}(\mathbf{r}, \omega). \quad (1.1b)$$

Here $\mathbf{E}(\mathbf{r}, \omega)$ and $\mathbf{B}(\mathbf{r}, \omega)$ are frequency-dependent complex-valued electric and magnetic fields, respectively, $\mathbf{H}(\mathbf{r}, \omega) = \mathbf{B}(\mathbf{r}, \omega)/\mu(\mathbf{r})$ is the magnetic field intensity, $\mathbf{j}^{ext}(\mathbf{r}, \omega)$ is the extraneous source current, $\sigma(\mathbf{r})$ is the conductivity distribution in the Earth, \mathbf{r} is the position vector, the time factor is $e^{-i\omega t}$, $\omega = \frac{2\pi}{T}$, where T is period and $i = \sqrt{-1}$. $\mu(\mathbf{r})$ is the magnetic permeability which is assumed to be equal everywhere to the permeability of free space $\mu_0 = 4\pi \cdot 10^{-7} \frac{N}{A^2}$.

1.2.1 Response functions used to detect lateral variations of conductivity

Responses of GDS method

If the source magnetic potential (see Section 3.1 for details) is described by a single spherical harmonic function, $S_1^0 \equiv P_1^0 = \cos \vartheta$, and if the Earth is assumed to be regionally 1-D, the *C*-response can be introduced at a given site (Banks, 1969) as

$$C(\mathbf{r}, \omega) = -\frac{a \tan \vartheta}{2} \frac{B_r(\mathbf{r}, \omega)}{B_\vartheta(\mathbf{r}, \omega)}, \quad (1.2)$$

where ϑ is the geomagnetic colatitude. The complex-valued *C*-response has physical dimension of length and for 1-D conductivity models its real part provides an estimation of the depth to which EM field penetrates (Weidelt, 1972). Other important properties of *C*-responses are discussed in Appendix A.2. This technique of estimating *C*-responses will be referred to below as the geomagnetic depth sounding (GDS) method. There is a common consensus that the GDS method works fairly well in the period range between a few days and a few months (cf. Banks, 1969; Roberts, 1984; Schultz and Larsen, 1987; Fujii and Schultz, 2002, among others), thus allowing for the recovery of electrical conductivities in the depth range from 400 km down to 1600 km. More details about the GDS method are provided in Chapter 3.

Responses of HSG method

For the case where the source is described by more than one spherical harmonic, the horizontal spatial gradient (HSG) method is applied (Schmucker, 1970; Olsen, 1998, among others) to determine C -responses. Using this method the C -response is calculated as

$$C(\mathbf{r}, \omega) = -\frac{B_r(\mathbf{r}, \omega)}{\nabla_{\perp} \cdot \mathbf{B}_{\tau}(\mathbf{r}, \omega)}, \quad (1.3)$$

where $\nabla_{\perp} \cdot \mathbf{B}_{\tau}(\mathbf{r}, \omega)$ is the angular part of the divergence of the horizontal magnetic field component. In reality, one does not directly measure spatial derivatives of the field. The common practice while applying the HSG method is to interpolate the field using low-order polynomials or spherical harmonics and then analytically estimate the derivatives. Since the global net of geomagnetic observatories is strongly irregular such an approach to approximating $\nabla_{\perp} \cdot \mathbf{B}_{\tau}(\mathbf{r}, \omega)$ works reasonably well only for Europe where the spatial coverage of observatories is rather dense and uniform.

Responses of HSG+GDS method

The GDS and HSG methods are inherently limited in that they have only been developed to deal with 1-D conductivity models of the Earth. Schmucker (2003) presented a new approach to remove the one-dimensionality constraint. He introduced a new relation, which locally connects the radial magnetic component with the angular part of the divergence of the normal horizontal component and the normal horizontal components themselves

$$B_r(\mathbf{r}, \omega) \approx -C(\mathbf{r}, \omega) \nabla_{\perp} \cdot \mathbf{B}_{\tau}(\mathbf{r}, \omega) + z_H(\mathbf{r}, \omega) B_{\theta}(\mathbf{r}, \omega) - z_D(\mathbf{r}, \omega) B_{\varphi}(\mathbf{r}, \omega). \quad (1.4)$$

The normal fields in our context are the fields which are induced in a 1-D conducting Earth. It is seen from eq. (1.4) that in order to estimate response functions C , z_H and z_D , source fields of sufficient spatial and temporal variability are required to guarantee robust determination of these responses. This means, that this method can't be used for periods larger than a few days, since the single term, P_1^0 , is dominating the spatial source structure at these periods.

Long-period magnetotelluric (MT) responses

If, along with magnetic field measurements, the horizontal component of the electric field is measured, conventional MT responses can be estimated using

$$E_{\theta} = Z_{\theta\theta} B_{\theta} + Z_{\theta\varphi} B_{\varphi}, \quad (1.5a)$$

$$E_{\varphi} = Z_{\varphi\theta} B_{\theta} + Z_{\varphi\varphi} B_{\varphi}. \quad (1.5b)$$

The use of the MT method allows one to estimate responses at periods shorter than a few days, which provides the information about the conductivity structure for depths shallower than 400 km. Moreover, the MT method works in areas where GDS method fails. For example, it works near the geomagnetic equator, where the radial component of the magnetic field B_r is close to zero, thus preventing the use of the GDS method. At high latitudes the MT method is also preferable, since in this region GDS responses suffer from strong contamination by non- P_1^0 sources. However, since the strength of electric field signals drops significantly as the period increases combined with long-term drift of the electrodes that are used to measure the electric field, it is rather difficult to obtain good quality MT responses at very long periods; a period of 10 days is the longest period at which reliable MT responses have been obtained so far (Utada et al., 2003; Shimizu et al., 2010a).

1.2.2 Recent regional 1-D studies of the conductivity in the Earth mantle

During the last decade a number of studies have estimated mantle 1-D conductivity profiles in different regions of the world using the magnetic field variations in the Dst period range.

Olsen (1998) using data from 24 European observatories, obtained European averaged C -responses in the period range between 3 hours and one month, using the HSG method. The author also observed lateral variations in the real part of the C -responses, which he principally attributed to the effect from ionospheric current system at high latitudes. In Olsen (1999) the same methodology was employed to obtain averaged C -responses for periods between 1 month and 1 year. In both studies special effort was given to obtaining unbiased C -response estimates.

Neal et al. (2000) analyzed long-period MT and GDS responses from diverse tectonic regions in North America and the Pacific Ocean. They obtained 1-D conductivity profiles beneath Carty Lake (CLC) in the Canadian Shield, Tucson (TUC) in the southwest United States, Honolulu (HON) and Midway (MID) in the north central Pacific. The authors found significant lateral variations in conductivity associated with the various tectonic settings. In particular, the upper mantle beneath Carty Lake appeared to be approximately an order of magnitude more resistive than the upper mantle beneath Tucson and nearly 1.5 orders of magnitude more resistive than Honolulu and Midway Island. The authors suggested that the observed conductivity variations may be interpreted as lateral variations in temperature, partial melt and/or dissolved hydrogen in olivine.

Ichiki et al. (2001) obtained a 1-D conductivity model of the upper mantle including TZ beneath the Pacific back-arc of North East China. The conductivity distributions were investigated through long-period MT and GDS experiments. The electric field data were acquired using land telephone lines to obtain long-period MT responses at three different (but close) locations. GDS responses were obtained using Changchun (CHN) geomagnetic observatory data. Authors compared their profiles with those at CLC, TUC and HON. The most distinct

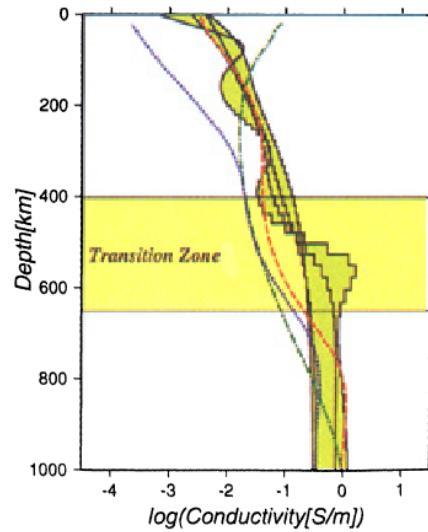


Figure 1.3: Comparison of conductivity profiles from Changchung (CHC) (light green band) in China (Ichiki et al., 2001) with those at Carty Lake (CLC) (blue dotted line), Tucson (TUC) (red broken line) and Honolulu (HON) (green chain line) (Neal et al., 2000). The mantle transition zone is shown by yellow. After Ichiki et al. (2001).

difference revealed in their study was that the TZ beneath North East China is significantly more conductive than the others by about one order of magnitude. This led the authors to suggest that the high conductivity is most probably related to the presence of water in the stagnant slab. For depths shallower than 400 km, their conductivity profile has a slope and conductivity values similar to TUC, which is also more conductive than observed elsewhere. Ichiki et al. (2001) noted that this common feature is probably typical for the continental upper mantle beneath the region of active tectonics as also pointed out by Neal et al. (2000). The results of their study and comparison with the results of Neal et al. (2000) are presented in Fig. 1.3.

Tarits et al. (2004) presented the results of long-period MT sounding in the French Alps from which a vertical electrical conductivity profile between 200 and 1000 km was obtained. The authors speculated that for depths between 200 and 400 km their model favors a wet mantle. The authors noted that the data do not require the conductivity to change throughout the TZ; conductivity in the TZ is at least an order of magnitude smaller compared with the conductivity reported by Ichiki et al. (2001) suggesting that a small amount of water has been transported into the TZ by the subduction in the Mediterranean.

Semenov and Joswiak (2006) compiled the response functions for 35 European observatories in the period range between 6 h and 11 years using various data sets including data by Roberts (1984), Schultz and Larsen (1987) and Olsen (1998). The combined responses have been inverted individually and the resulting 1-D profiles have been merged to obtain a mantle conductance image down to a depth of ~ 770 km (see Fig. 1.4). The authors noticed that their conductance image can be correlated with major European tectonic units like the Baltic Shield

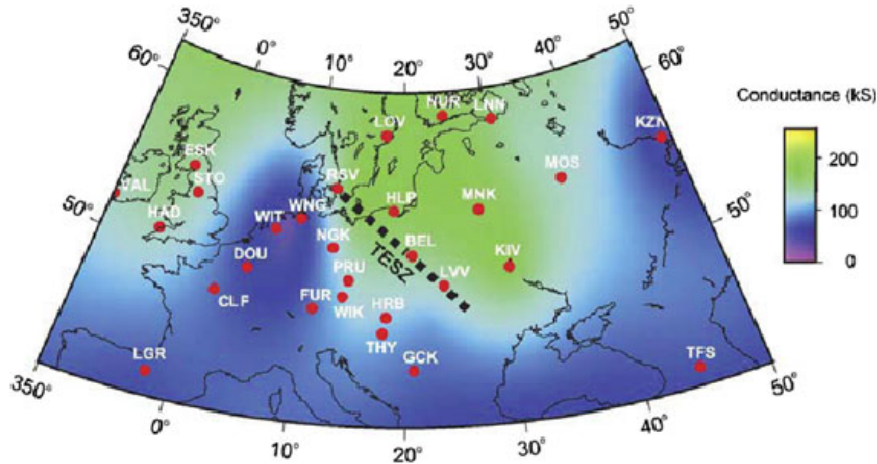


Figure 1.4: Smoothed image of the integrated conductance, in kiloSiemens, from the surface down to the depth of 770 km in the mantle beneath Europe. After [Semenov and Joswiak \(2006\)](#).

and the Trans-European Suture zone.

[Khan et al. \(2011\)](#) investigated the electrical conductivity structure of the mantle at six different locations around the globe that cover different geological settings. The selected observatories were: Fürstenfeldbruck (FUR), Europe; Hermanus (HER), South Africa; Langzhou (LZH), China; Alice Springs (ASP), Australia; Tucson (TUC), North America; and Honolulu (HON), North Pacific. They inverted the response functions beneath each observatory for a local 1-D conductivity profile using a probabilistic approach (e.g. [Mosegaard, 1998](#)) already successfully implemented in an earlier study ([Khan et al., 2006](#)). Resolution is limited to 500-1200 km depth. The authors found large variations in conductivity throughout the depth range studied. Mean conductivity varies between 0.1 and 0.4 S/m at 600 km depth, with a marked increase in conductivity (1.3-2.0 S/m) occurring at 800 km depth for all stations except HER (0.5 S/m). Conductivity at 900 km depth increases further to 1.4-2.4 S/m with HER, HON and ASP being most conductive. This trend persists to a depth of 1200 km. A comparison with conductivity profiles constructed from the most recent laboratory mineral conductivity measurements and models of Earth's mantle composition and thermal state revealed that significant variations in mantle composition and temperature are at the origin of the observed heterogeneous mantle conductivity structure. The authors remarked that due to the somewhat large error bounds on sampled conductivity profiles and the reduced sensitivity of their responses in the upper mantle and TZ, constraints on TZ water content are not conclusive. The conductivity profiles beneath each of the stations are shown in Fig. 1.5.

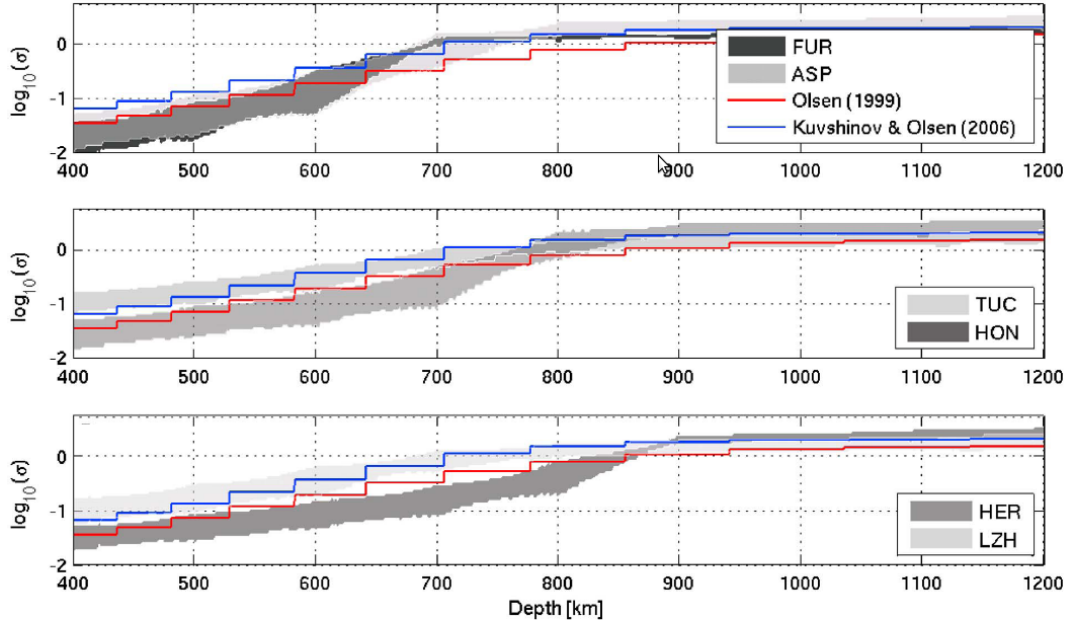


Figure 1.5: Conductivity models beneath Fürstenfeldbruck (FUR) in Europe, Hermanus (HER) in South Africa, Langzhou (LZH) in China, Alice Springs (ASP) in Australia, Tucson (TUC) in North America, and Honolulu (HON) in North Pacific. For comparison, two other one-dimensional conductivity models (from Olsen (1999) and Kuvshinov and Olsen (2006)) are indicated by colored lines. After Khan et al. (2011).

1.2.3 Semi-global quasi 1-D studies

In all studies discussed in the previous section (except for the study of Khan et al. (2011)), various 1-D interpretation schemes were used to obtain local/regional profiles. The study of Utada et al. (2003) commenced quasi 1-D studies (continued by Kuvshinov et al. (2005) and Shimizu et al. (2010a)), which aimed at obtaining semi-global 1-D mantle electric conductivity structure beneath the North Pacific using 3-D modeling of the ocean effect. It is well recognized that the ocean has a large influence on the coastal responses (cf. Kuvshinov et al., 1999, 2002b). In particular, Kuvshinov et al. (2002b) demonstrated that a nonuniform ocean is a major contributor to the anomalous behavior of the C -responses at coastal observatories up to periods of 20 days. The authors also showed that the effects arising from the oceans may be corrected using predictions in the conductivity Earth's models with and without oceans (we will discuss their correction scheme later, in Chapter 4). Utada et al. (2003) suggested an iterative correction based on a similar procedure, and showed that with a few iterations good agreement between observed and predicted responses can be achieved. Utada et al. (2003) (and later Kuvshinov et al. (2005) and Shimizu et al. (2010a)) used this technique to obtain reference 1-D structures beneath the North Pacific. Further discussion in this section is based on the most recent results of Shimizu et al. (2010a). They used the experimental responses in the period range from 1.7 to 113 days to construct the reference 1-D model. The authors examined three different models of conductivity variation with depth: (1) a model with no

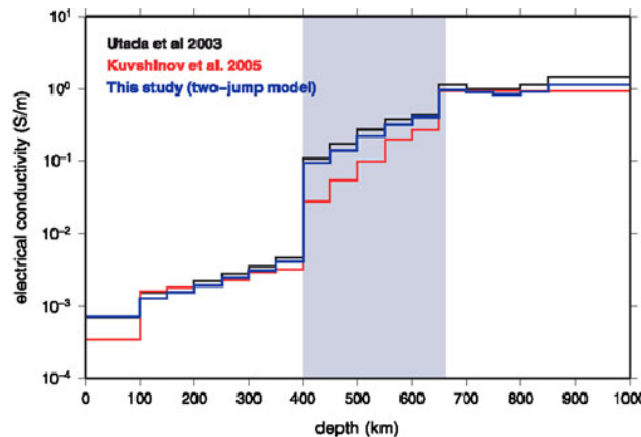


Figure 1.6: Comparison of two-jump model beneath the North Pacific obtained by Utada et al. (2003) (black line), by Kuvshinov et al. (2005) (red line) and by Shimizu et al. (2010a). After Shimizu et al. (2010a).

discontinuities; (2) a model with two jumps at 400 and 650 km depths; and (3) a model with three jumps at 400, 500 and 650 km depths. Fig. 1.6 compares their “two-jump” model with the two-jump models by Utada et al. (2003) and Kuvshinov et al. (2005). The authors concluded that the conductivity of the two-jump model in the TZ is higher than the experimentally determined conductivity of dry wadsleyite and ringwoodite. If the difference is entirely due to the effect of water in the TZ, then the conductivity is consistent with water contents around 0.5 wt %. However, if an additional discontinuity of electrical conductivity is allowed at the 500 km depth, the obtained conductivity for the upper 100 km of the TZ is lower, and can be explained by a lower water content of 0.1 wt % in wadsleyite.

1.2.4 Semi-global and global 3-D EM studies

The first attempt to invert global induction data in a 3-D frame was performed by Schultz and Pritchard (1999). Their study was based on inversion of the augmented Schultz and Larsen (1987) set of C -responses. Their approximate forward modeling approach used for this inversion was accurate only for small perturbations about a reference 1-D model, and it was found that no model satisfying this limitation could fit the European subset of observatories. Later on, two rigorous frequency-domain 3-D global EM inverse solutions to deal with ground-based data have been developed at the Earthquake Research Institute (Tokyo University, Japan) and Oregon State University (Corvallis, USA).

Koyama (2001) pioneered the development and application of a rigorous 3-D inversion scheme to interpret ground-based C -responses on a (semi) global scale. His inversion exploits a quasi-Newton optimization method whereas the forward solver is based on a modern version of the volume integral equation (IE) approach (cf. Singer, 1995; Pankratov et al., 1995; Kuvshinov, 2008). In subsequent studies (Fukao et al., 2004; Koyama et al., 2006; Utada et al.,

2009; Shimizu et al., 2010b) his 3-D inverse solution was used to interpret long-period EM data, mostly in the north Pacific region (termed semi-global studies). In all these investigations voltage data from trans-Pacific submarine cables and magnetic field data from circum-Pacific geomagnetic observatories were analyzed. The exception is the study of Utada et al. (2009) where data from Europe were analyzed.

Kelbert et al. (2008) developed a 3-D EM inversion scheme for the whole globe. Their scheme is based on a non-linear conjugate gradient method. To calculate responses and misfit gradients they generalized and extended an existing staggered-grid finite difference solver by Uyeshima and Schultz (2000). Using spherical harmonics in each inhomogeneous layer to parameterize the model space, they inverted a suite of synthetic data sets generated using checkerboard models to test the inversion and to study vertical and horizontal resolution of currently available data sets. The inversion was regularized by minimizing deviations from the reference model, with a norm that penalized higher degree and order terms and jumps between layers. Kelbert et al. (2008) concluded that responses in the period range 5–107 days resolve large scale (300–500 km vertically, and thousands of km horizontally) heterogeneities in mantle electrical conductivity reliably in the depth range 670–1600 km. They also demonstrated that by extending induction responses to 0.2–5 days (assuming a dipole source), upper-mantle structure could be resolved. However, the authors notice that interpreting data at these shorter periods is a challenging task due to much more complex source structure. Kelbert et al. (2009) used the developed scheme to obtain the first global 3-D mantle conductivity model. We will discuss their 3-D global results and the semi-global results in Chapter 5 where these will be compared to our results.

1.2.5 Global multi-dimensional EM studies in time domain

So far we discussed the frequency-domain results only. However, in recent years much attention has been paid to implementation of time-domain approach to global induction studies using mostly satellite data (Velimsky et al., 2006; Velimsky, 2010). In particular, Martinec and Velimsky (2009) interpreted satellite data in the frame of 2-D conductivity models where conductivity varies with latitude and radius. The authors developed an adjoint approach (analogous to that used in frequency domain studies) allowing for calculation of the gradient of their misfit with respect to model parameters for the price of only one additional (backward in time) forward calculation irrespective of the number of conductivity parameters. Using this approach they applied conjugate gradient methods to infer the 2-D conductivity structures of the Earth from one year (2001) of CHAMP data. They showed that a one-year time series is capable of resolving 2-D structures in the upper mantle and the upper part of the lower mantle down to ~ 1500 km depth. The results of their 2-D inversion are summarized in Fig. 1.7. From these results Martinec and Velimsky (2009) concluded that the mantle conductivity variations in the latitudinal direction reach about 20 % of the mean value in upper mantle and about 4 %

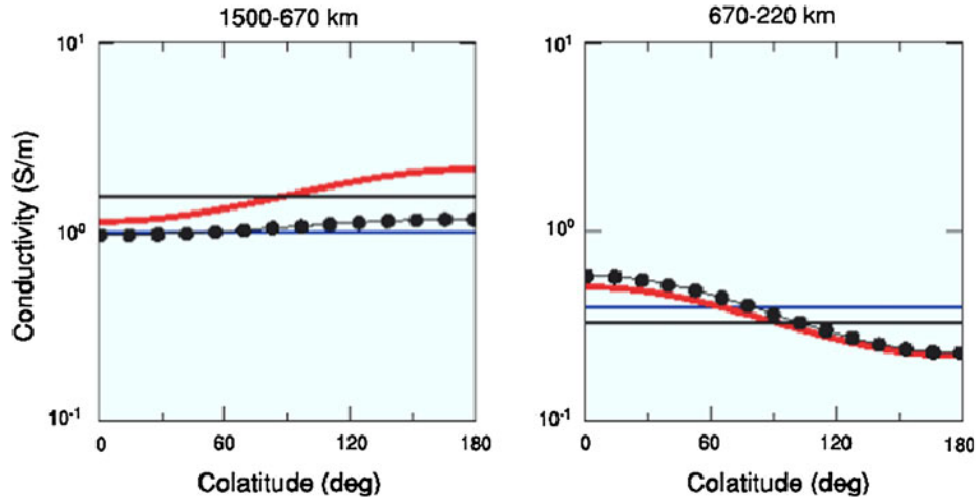


Figure 1.7: Two-layer, latitudinally dependent conductivity model of the upper part of the lower mantle and the upper mantle (left and right panels). The model best fitting the 2001 CHAMP data (red lines), the starting model for the CG minimization (blue lines) and the model after the first iteration (dotted line) are compared to the best 1-D conductivity model. After [Martinec and Velimsky \(2009\)](#).

in the upper part of the lower mantle. Later on Jakub Velimsky has developed a time-domain approach which deals with a 3-D inversion of time series of internal coefficients (cf. Chapter 3 of [Kuvshinov et al., 2010](#)). This 3-D time-domain inverse solution has been successfully verified on a number of realistic models but as far as we know no attempt has been made so far to apply this method to experimental data.

The first attempt to apply time-domain approach to real data in order to recover 3-D mantle conductivity has been performed recently by [Tarits and Manda \(2010\)](#). They developed a 3-D EM time-domain technique to invert time series of the magnetic field observed on a global net of observatories. We will also discuss their results in Chapter 5 where we compare them with our results.

The final remark of this section is that important information about conductivity of the minerals under mantle conditions (high pressures and high temperatures) comes from mineral physics laboratory studies. The results of these studies are summarized in Appendix D.

1.3 Thesis outline

The objectives of this work are three-fold: a) to develop a novel and efficient global 3-D EM inverse solution to recover (3-D) electrical conductivity distribution in the mantle. The solution is based on analysis of the experimental C -responses from the global net of geomagnetic observatories; b) to obtain a new set of reliable C -responses which cover the broadest possible period range from the largest possible number of observatories; c) to invert these new

C-responses in order to image the 3-D mantle conductivity distribution in the depth range between 400 and 1600 km.

The structure of the manuscript is as follows. Chapter 2 discusses the essentials of an integral equation solution which is used as a forward problem engine to calculate the responses and data misfit gradients during 3-D inversion. Chapter 3 presents our 3-D inverse solution. It exploits an iterative gradient-type technique – limited-memory quasi-Newton method – for minimizing the penalty function consisting of data misfit and regularization terms. An adjoint approach is implemented to compute misfit gradients efficiently. Further improvements in computational load come from the parallelizing the scheme with respect to frequencies, and from setting the most time-consuming part of the forward calculations – calculation of Green’s tensors – apart from the inversion loop. Convergence, performance, and accuracy of our 3-D inverse solution are demonstrated with a synthetic numerical example. Chapter 2 mostly follows the papers of Kuvshinov et al. (2002b) and Kuvshinov (2008). Chapter 3 closely follows the papers by Pankratov and Kuvshinov (2010) and Kuvshinov and Semenov (2011). Chapter 4 describes estimation and analysis of new set of *C*-responses. To estimate the responses we collected very long time series (up to 51 years; 1957-2007) of hourly means of three components of the geomagnetic field from 281 observatories. Special attention was given to data processing in order to obtain unbiased, smoothed *C*-responses with realistic estimates of experimental errors. After careful inspection of the obtained responses we left for further analysis the responses from 119 mid-latitude observatories in period range between 2.9 to 104.2 days. In the Chapter 4 we also investigate in what extent ocean and auroral effects can explain huge variability of the observed responses, and develop schemes to correct the observed responses for these two effects. Chapter 5 outlines the results of our 3-D inversion of the experimental responses. We investigate the robustness of the recovered 3-D mantle conductivity images, and compared our results with the results of independent global and semi-global 3-D EM studies, as well as with the results of seismic tomography. Chapter 6 presents conclusions and an outlook for future studies as seen by author. Chapters 4-5 closely follow the paper by Semenov and Kuvshinov (2011).

The thesis also includes 5 Appendices complementing the main text. In particular lengthy Appendix E presents experimental responses, their uncertainties and squared coherencies for all 119 observatories in the form of plots and Tables. In addition, this appendix shows time series of hourly mean values of three components of the magnetic field for the relevant time interval.

Chapter 2

Forward modeling

2.1 Maxwell's equations

Time dependent electric and magnetic fields obey Maxwell's equations

$$\nabla \times \mathbf{H}(\mathbf{r}, t) = \mathbf{J}(\mathbf{r}, t), \quad (2.1a)$$

$$\nabla \times \mathbf{E}(\mathbf{r}, t) = -\frac{\partial \mathbf{B}(\mathbf{r}, t)}{\partial t}, \quad (2.1b)$$

where $\mathbf{r} = (r, \vartheta, \varphi)$ is the position vector, ϑ , φ and r are colatitude, longitude and radial distance from the Earth's center, respectively, \mathbf{J} is the current density (A/m^2), \mathbf{E} is the electric field (V/m), \mathbf{B} is the magnetic flux density or induction (T), \mathbf{H} is the magnetic field intensity (A/m). We neglect displacement currents, as they are not significant at the frequencies and conductivities relevant to our long-period studies. Note also that \mathbf{B} is a solenoidal field

$$\nabla \cdot \mathbf{B}(\mathbf{r}) = 0. \quad (2.2)$$

\mathbf{B} and \mathbf{H} are related by the magnetic permeability μ

$$\mathbf{B}(\mathbf{r}, t) = \mu(\mathbf{r})\mathbf{H}(\mathbf{r}, t). \quad (2.3)$$

It is common to assume the magnetic permeability $\mu(\mathbf{r})$ to be constant and equal to the magnetic permeability of free space μ_0 . \mathbf{J} and \mathbf{E} are connected by

$$\mathbf{J}(\mathbf{r}, t) = \sigma(\mathbf{r})\mathbf{E}(\mathbf{r}, t) + \mathbf{j}^{ext}(\mathbf{r}, t), \quad (2.4)$$

where σ is the electrical conductivity, \mathbf{j}^{ext} is the impressed current density.

If we consider sinusoidally varying fields of angular frequency $\omega = \frac{2\pi}{T}$, where T is a

period, we can write

$$\mathbf{E}(t) = \hat{\mathbf{E}}e^{-i\omega t}, \quad \mathbf{j}^{ext}(t) = \hat{\mathbf{j}}^{ext}e^{-i\omega t}, \quad \mathbf{H}(t) = \hat{\mathbf{H}}e^{-i\omega t} \quad \longrightarrow \quad \frac{\partial \mathbf{H}}{\partial t} = -i\omega \mathbf{H}. \quad (2.5)$$

Substituting eqs (2.5) into eqs (2.1) we obtain Maxwell's equations in frequency domain

$$\nabla \times \hat{\mathbf{H}}(\mathbf{r}, \omega) = \sigma(\mathbf{r})\hat{\mathbf{E}}(\mathbf{r}, \omega) + \hat{\mathbf{j}}^{ext}(\mathbf{r}, \omega), \quad (2.6a)$$

$$\nabla \times \hat{\mathbf{E}}(\mathbf{r}, \omega) = i\omega\mu_0\hat{\mathbf{H}}(\mathbf{r}, \omega). \quad (2.6b)$$

Further we will work only with frequency dependent EM field, therefore we denote frequency dependent fields $\hat{\mathbf{E}}$, $\hat{\mathbf{H}}$ and $\hat{\mathbf{j}}^{ext}$ as \mathbf{E} , \mathbf{H} and \mathbf{j}^{ext} , and finally write

$$\nabla \times \mathbf{H}(\mathbf{r}) = \sigma(\mathbf{r})\mathbf{E}(\mathbf{r}) + \mathbf{j}^{ext}(\mathbf{r}), \quad (2.7a)$$

$$\nabla \times \mathbf{E}(\mathbf{r}) = i\omega\mu_0\mathbf{H}(\mathbf{r}). \quad (2.7b)$$

2.2 Integral equation approach

We solve eqs (2.7) using the integral equation (IE) approach which is based on a contraction operator (Singer, 1995; Pankratov et al., 1995, among others). We consider 3-D Earth's conductivity model, which consist of a number of inhomogeneous layers, embedded in 1-D background section of conductivity $\sigma_b(r)$.

We start with introducing "reference" radially symmetric (1-D) model of conductivity $\sigma_0(r)$. The reference magnetic and electric fields, \mathbf{H}^0 and \mathbf{E}^0 , in this model obey Maxwell's equations

$$\nabla \times \mathbf{H}^0(\mathbf{r}) = \sigma_0(r)\mathbf{E}^0(\mathbf{r}) + \mathbf{j}^{ext}(\mathbf{r}), \quad (2.8a)$$

$$\nabla \times \mathbf{E}^0(\mathbf{r}) = i\omega\mu_0\mathbf{H}^0(\mathbf{r}). \quad (2.8b)$$

If we can construct and calculate fundamental solutions (tensor Green's functions) of eqs (2.8), G_{1D}^{ej} and G_{1D}^{hj} , then \mathbf{H}^0 and \mathbf{E}^0 can be determined via convolution integrals

$$\mathbf{H}^0(\mathbf{r}) = \int_{V^{ext}} G_{1D}^{hj}(\mathbf{r}, \mathbf{r}') \mathbf{j}^{ext}(\mathbf{r}') dv'. \quad (2.9)$$

$$\mathbf{E}^0(\mathbf{r}) = \int_{V^{ext}} G_{1D}^{ej}(\mathbf{r}, \mathbf{r}') \mathbf{j}^{ext}(\mathbf{r}') dv', \quad (2.10)$$

Here $\mathbf{r} \in \mathbb{R}^3$, $\mathbf{r}' \in V^{ext}$, V^{ext} is the volume occupied by \mathbf{j}^{ext} , $dv' = r'^2 \sin \vartheta' d\vartheta' d\varphi' dr'$. Note that in all quantities discussed (except conductivities) the dependence on ω is implied but omitted for the simplicity of presentation. The subscript "1D" means that Green's functions depend

not only on \mathbf{r} , \mathbf{r}' and ω but also depend on 1-D conductivity distribution $\sigma_0(r)$. A formalism how the entries of such kind of tensors can be derived and calculated will be presented further in this chapter (Section 2.4).

Introducing further "scattered" fields, $\mathbf{E}^s = \mathbf{E} - \mathbf{E}^0$ and $\mathbf{H}^s = \mathbf{H} - \mathbf{H}^0$ and subtracting eqs (2.8) from eqs (2.7), Maxwell's equations for scattered fields can be written in the form

$$\nabla \times \mathbf{H}^s(\mathbf{r}) = \sigma_0(r)\mathbf{E}^s(\mathbf{r}) + \mathbf{j}^q(\mathbf{r}), \quad (2.11a)$$

$$\nabla \times \mathbf{E}^s(\mathbf{r}) = i\omega\mu_0\mathbf{H}^s(\mathbf{r}), \quad (2.11b)$$

where

$$\mathbf{j}^q(\mathbf{r}) = [\sigma(\mathbf{r}) - \sigma_0(r)]\mathbf{E}^s(\mathbf{r}) + \mathbf{j}^s(\mathbf{r}), \quad (2.12)$$

and

$$\mathbf{j}^s(\mathbf{r}) = [\sigma(\mathbf{r}) - \sigma_0(r)]\mathbf{E}^0(\mathbf{r}). \quad (2.13)$$

Comparing eqs (2.8) and eqs (2.11) one can deduce that the scattered magnetic and electric fields, in analogy with eqs (2.10) and (2.9) can be written as

$$\mathbf{H}^s(\mathbf{r}) = \int_{V^{mod}} G_{1D}^{hj}(\mathbf{r}, \mathbf{r}') \mathbf{j}^q(\mathbf{r}') dv', \quad (2.14)$$

$$\mathbf{E}^s(\mathbf{r}) = \int_{V^{mod}} G_{1D}^{ej}(\mathbf{r}, \mathbf{r}') \mathbf{j}^q(\mathbf{r}') dv', \quad (2.15)$$

where $\mathbf{r} \in \mathbb{R}^3$, $\mathbf{r}' \in V^{mod}$, and V^{mod} is a region where $\sigma(\mathbf{r}) - \sigma_0(r)$ differs from 0. If we restrict ourselves to $\mathbf{r} \in V^{mod}$ we obtain from eq. (2.15) conventional scattering equation with respect to unknown scattered field \mathbf{E}^s

$$\mathbf{E}^s(\mathbf{r}) - \int_{V^{mod}} G_{1D}^{ej}(\mathbf{r}, \mathbf{r}') [\sigma(\mathbf{r}') - \sigma_0(r')] \mathbf{E}^s(\mathbf{r}') dv' = \mathbf{E}_f(\mathbf{r}), \quad (2.16)$$

where free term $\mathbf{E}_f(\mathbf{r})$ has a form

$$\mathbf{E}_f(\mathbf{r}) = \int_{V^{mod}} G_{1D}^{ej}(\mathbf{r}, \mathbf{r}') \mathbf{j}^s(\mathbf{r}') dv'. \quad (2.17)$$

2.3 Solution of the integral equation

The formal solution of eq. (2.16) can be written as an infinite Neumann series, starting from \mathbf{E}_f as zero-th order approximation to \mathbf{E}^s

$$\begin{aligned} \mathbf{E}^s(\mathbf{r}) = & \mathbf{E}_f(\mathbf{r}) + \int_{V^{mod}} G_{1D}^{ej}(\mathbf{r}, \mathbf{r}') [\sigma(\mathbf{r}') - \sigma_0(r')] \mathbf{E}_f(\mathbf{r}') dv' + \\ & + \int_{V^{mod}} G_{1D}^{ej}(\mathbf{r}, \mathbf{r}') [\sigma(\mathbf{r}') - \sigma_0(r')] \left\{ \int_{V^{mod}} G_{1D}^{ej}(\mathbf{r}', \mathbf{r}'') [\sigma(\mathbf{r}'') - \sigma_0(r'')] \mathbf{E}_f(\mathbf{r}'') dv'' \right\} dv' + \dots \end{aligned} \quad (2.18)$$

It is known, however, that series (2.18) does not necessarily converge, especially when models with strong scatterers are considered. The remedy is to modify eq. (2.16) to integral equation with contraction operator (cf. Pankratov et al., 1995)

$$\chi(\mathbf{r}) - \int_{V^{mod}} K(\mathbf{r}, \mathbf{r}') R(\mathbf{r}') \chi(\mathbf{r}') dv' = \chi_0(\mathbf{r}), \quad (2.19)$$

where

$$R(\mathbf{r}') = \frac{\sigma(\mathbf{r}') - \sigma_0(r')}{\sigma(\mathbf{r}') + \sigma_0(r')}, \quad (2.20a)$$

$$K(\mathbf{r}, \mathbf{r}') = \delta(\mathbf{r} - \mathbf{r}') I + 2 \sqrt{\sigma_0(r)} G_{1D}^{ej}(\mathbf{r}, \mathbf{r}') \sqrt{\sigma_0(r')}, \quad (2.20b)$$

$$\chi_0(\mathbf{r}) = \int_{V^{mod}} K(\mathbf{r}, \mathbf{r}') \frac{\sqrt{\sigma_0(r')}}{\sigma(\mathbf{r}') + \sigma_0(r')} \mathbf{j}^s(\mathbf{r}') dv', \quad (2.20c)$$

$$\chi(\mathbf{r}') = \frac{1}{2 \sqrt{\sigma_0(r')}} \{ [\sigma(\mathbf{r}') + \sigma_0(r')] \mathbf{E}^s(\mathbf{r}') + \mathbf{j}^s(\mathbf{r}') \}. \quad (2.20d)$$

Here $\delta(\mathbf{r} - \mathbf{r}')$ is Dirac's delta function, I is the identity matrix. Note that in order to derive eq. (2.19) we add term $(\sigma - \sigma_0)\mathbf{E}^0/2\sigma_0$ to both sides of eq. (2.16) and change variables in the way defined by eq. (2.20d). The specific form of equation (2.19) is motivated by the energy inequality for the scattered EM field, which expresses a fundamental physical fact that the energy flow of the scattered field outside the domain with inhomogeneities is always non-negative (cf. Singer, 1995; Pankratov et al., 1995, 1997). In an operator form, eq. (2.19) can be written as

$$A\chi = \chi_0, \quad (2.21)$$

where $A = I - KR$. Equation (2.19) possesses a contracting integral kernel (Pankratov et al., 1995), where

$$\left\| \int_{V^{mod}} K(\mathbf{r}, \mathbf{r}') R(\mathbf{r}') \chi(\mathbf{r}') dv' \right\| < \|\chi\|, \quad \forall \chi, \quad (2.22)$$

for any choice of “reference” conductivity profile $\sigma_0(r)$. Here $\|\chi\| = \sqrt{\int_{V^{mod}} |\chi(\mathbf{r})|^2 dV}$. Property (2.22) allows one to find the solution of eq. (2.19) by simple iteration

$$\chi^{(n+1)}(\mathbf{r}) = \chi_0(\mathbf{r}) + \int_{V^{mod}} K(\mathbf{r}, \mathbf{r}') R(\mathbf{r}') \chi^{(n)}(\mathbf{r}') dV', \quad (2.23)$$

for $n = 1, 2, \dots$, with any initial guess $\chi^{(1)}(\mathbf{r})$. Moreover, this iteration procedure, when using $\chi_0(\mathbf{r})$ as an initial guess, produces convergent Neumann series (NS) for eq. (2.19)

$$\begin{aligned} \chi(\mathbf{r}) = & \chi_0(\mathbf{r}) + \int_{V^{mod}} K(\mathbf{r}, \mathbf{r}') R(\mathbf{r}') \chi_0(\mathbf{r}') dV' + \\ & + \int_{V^{mod}} K(\mathbf{r}, \mathbf{r}') R(\mathbf{r}') \left\{ \int_{V^{mod}} K(\mathbf{r}', \mathbf{r}'') R(\mathbf{r}'') \chi_0(\mathbf{r}'') dV'' \right\} dV' + \dots \end{aligned} \quad (2.24)$$

It was shown by [Singer \(1995\)](#) that in case of quasi-static field and isotropic media the fastest convergence is achieved if the reference medium is chosen in an “optimal” way, namely: outside the depths occupied by inhomogeneities, it coincides with the conductivity of the background section, $\sigma_b(r)$, but at depths with laterally inhomogeneous distribution of conductivity it has form

$$\sigma_0(r) = \sqrt{\min_{\vartheta, \varphi} \sigma(r, \vartheta, \varphi) \max_{\vartheta, \varphi} \sigma(r, \vartheta, \varphi)}. \quad (2.25)$$

For this specific choice of reference medium, the number, N , of simple iterations (or NS terms) is proportional to \sqrt{C} , where C is maximum lateral contrast of conductivity in the model

$$C = \max_r \frac{\max_{\vartheta, \varphi} \sigma(r, \vartheta, \varphi)}{\min_{\vartheta, \varphi} \sigma(r, \vartheta, \varphi)}. \quad (2.26)$$

By replacing simple iteration with conjugate gradient (cf. [Greenbaum, 1997](#)) iteration, significant convergence acceleration has been reported by [Avdeev et al. \(2002\)](#) and [Kuvshinov et al. \(2005\)](#). It can be explained by the following fact. It is well known that for well-conditioned systems conjugate gradient (CG) iteration are far more efficient than simple iteration (cf. [Greenbaum, 1997](#)). It can be shown (cf. [Avdeev et al., 2000](#)), that for an optimal reference medium, a condition number, $k(A) = \|A\| \cdot \|A^{-1}\|$, can be estimated as

$$k(A) \simeq \sqrt{C}. \quad (2.27)$$

From this estimate it follows that even for the media with extremely large lateral contrasts of conductivity (say, on land-ocean contacts), the operator A of eq. (2.21) still appears to be well conditioned, with $k(A) \sim 100$.

At this stage it is important to remark that eqs (2.10) and (2.9) are valid for any distribution

of the impressed current, \mathbf{j}^{ext} , of any location. However, since in this work we deal with the responses generated by the external currents that are usually considered in the form of spherical harmonic expansion (SHE) of the equivalent sheet currents, general expressions for \mathbf{H}^0 and \mathbf{E}^0 in eqs (2.10) and (2.9) are also transformed to SHE which will be explained in Appendix B.

A 3-D IE forward modeling solution which provides magnetic field prediction at $\mathbf{r}_a \in Sites$ (location of observatories) can be represented as a sequence of the following steps.

1. $G_{1D}^{ej}(\mathbf{r}, \mathbf{r}')$ and consequently $K(\mathbf{r}, \mathbf{r}')$ are calculated for $\mathbf{r}' \in V^{mod}$ and $\mathbf{r} \in V^{mod}$
2. $G_{1D}^{hj}(\mathbf{r}_a, \mathbf{r}')$ is calculated for $\mathbf{r}' \in V^{mod}$ and $\mathbf{r}_a \in Sites$
3. $\mathbf{E}^0(\mathbf{r})$, $\mathbf{r} \in V^{mod}$ is calculated using eqs (B.14)-(B.15)
4. $\mathbf{j}^s(\mathbf{r}) = (\sigma(\mathbf{r}) - \sigma_0(r))\mathbf{E}^0(\mathbf{r})$, $\mathbf{r} \in V^{mod}$ is calculated
5. $\chi_0(\mathbf{r})$ is calculated on $\mathbf{r} \in V^{mod}$ with K obtained at step 1
6. The scattering equation (2.19) is solved on V^{mod} using CG method
7. $\mathbf{E}^s(\mathbf{r})$, $\mathbf{r} \in V^{mod}$ is calculated using eq. (2.20d) with \mathbf{j}^s obtained at step 4
8. $\mathbf{j}^q(\mathbf{r})$, $\mathbf{r} \in V^{mod}$ is calculated using eq. (2.12) with \mathbf{j}^s obtained at step 4
9. $\mathbf{H}^s(\mathbf{r}_a)$, $\mathbf{r}_a \in Sites$ is calculated using eq. (2.14) with G_{1D}^{hj} obtained at step 2
10. $\mathbf{H}^0(\mathbf{r}_a)$, $\mathbf{r}_a \in Sites$ is calculated using eqs (B.16)-(B.17)
11. $\mathbf{H}(\mathbf{r}_a)$, $\mathbf{r}_a \in Sites$ is calculated as a sum of \mathbf{H}^s and \mathbf{H}^0 obtained at steps 9 and 10

Henceforce, this scheme will be referred as the “IE-C” solution. One can see that the key point in constructing the forward problem solution is the derivation of tensor Green’s functions G_{1D}^{ej} and G_{1D}^{hj} .

2.4 Derivation of explicit forms for Green’s tensors for electric current source

In this section we derive the explicit forms of 3×3 tensor “current-to-electric” and “current-to-magnetic” Green’s functions for a case of the Earth’s model with radially-symmetric distribution of the electrical conductivity $\sigma_0(r)$. These tensor functions allow for calculating magnetic and electric fields that obey Maxwell’s equations

$$\nabla \times \mathbf{H}(\mathbf{r}) = \sigma_0(r)\mathbf{E}(\mathbf{r}) + \mathbf{j}(\mathbf{r}), \quad (2.28a)$$

$$\nabla \times \mathbf{E}(\mathbf{r}) = i\omega\mu_0\mathbf{H}(\mathbf{r}), \quad (2.28b)$$

in the following integral form

$$\mathbf{E}(r, \vartheta, \varphi) = \int_V G_{1D}^{ej}(r, r', \vartheta, \vartheta', \varphi - \varphi') \mathbf{j}(r', \vartheta', \varphi') dv', \quad (2.29)$$

$$\mathbf{H}(r, \vartheta, \varphi) = \int_V G_{1D}^{hj}(r, r', \vartheta, \vartheta', \varphi - \varphi') \mathbf{j}(r', \vartheta', \varphi') dv'. \quad (2.30)$$

Here V is a 3-D volume occupied by a current \mathbf{j} , and

$$G_{1D}^{ej(hj)} = \mathbf{e}_\vartheta g_{\vartheta\vartheta'}^{ej(hj)} \mathbf{e}_{\vartheta'} + \mathbf{e}_\vartheta g_{\vartheta\varphi'}^{ej(hj)} \mathbf{e}_{\varphi'} + \dots + \mathbf{e}_r g_{rr'}^{ej(hj)} \mathbf{e}_{r'}, \quad (2.31)$$

where $\mathbf{e}_r, \mathbf{e}_\vartheta, \mathbf{e}_\varphi$ and $\mathbf{e}_{r'}, \mathbf{e}_{\vartheta'}, \mathbf{e}_{\varphi'}$ are the unit vectors of spherical coordinate system at points $\mathbf{r} = (r, \vartheta, \varphi)$ and $\mathbf{r}' = (r', \vartheta', \varphi')$, respectively.

First, we consider vector spherical functions, which are determined via scalar spherical functions $S_m^n(\vartheta, \varphi)$ as (cf. [Morse and Feshbach, 1953](#))

$$\mathbf{S}_{nm}^r(\vartheta, \varphi) = S_m^n(\vartheta, \varphi) \mathbf{e}_r, \quad (2.32a)$$

$$\mathbf{S}_{nm}^t(\vartheta, \varphi) = \frac{1}{\sqrt{n(n+1)}} \mathbf{e}_r \times \nabla_\perp S_m^n(\vartheta, \varphi), \quad (2.32b)$$

$$\mathbf{S}_{nm}^p(\vartheta, \varphi) = \frac{1}{\sqrt{n(n+1)}} \nabla_\perp S_m^n(\vartheta, \varphi), \quad (2.32c)$$

where ∇_\perp is the angular part of operator $\nabla = \mathbf{e}_r \frac{\partial}{\partial r} + \frac{1}{r} \nabla_\perp$, \mathbf{e}_r is the outward unit vector. The coefficient $\frac{1}{\sqrt{n(n+1)}}$ is introduced to provide that \mathbf{S}_{nm}^t and \mathbf{S}_{nm}^p have the same norm as \mathbf{S}_{nm}^r . Following Helmholtz representation discussed in Appendix A.4, the tangential and radial components of the electric field \mathbf{E} and current \mathbf{j} can be decomposed as follows

$$\mathbf{E}_\tau(r, \vartheta, \varphi) = \frac{1}{r} \sum_{n,m} \left\{ \varepsilon_{nm}^t(r) \mathbf{S}_{nm}^t(\vartheta, \varphi) + \varepsilon_{nm}^p(r) \mathbf{S}_{nm}^p(\vartheta, \varphi) \right\}, \quad (2.33a)$$

$$E_r(r, \vartheta, \varphi) \mathbf{e}_r = \frac{1}{r} \sum_{n,m} \varepsilon_{nm}^r(r) \mathbf{S}_{nm}^r, \quad (2.33b)$$

$$\mathbf{j}_\tau(r, \vartheta, \varphi) = \frac{1}{r} \sum_{n,m} \left\{ j_{nm}^t(r) \mathbf{S}_{nm}^t(\vartheta, \varphi) + j_{nm}^p(r) \mathbf{S}_{nm}^p(\vartheta, \varphi) \right\}, \quad (2.33c)$$

$$j_r(r, \vartheta, \varphi) \mathbf{e}_r = \frac{1}{r} \sum_{n,m} j_{nm}^r(r) \mathbf{S}_{nm}^r. \quad (2.33d)$$

Hereinafter $\sum_{n,m}$ denotes summation $\sum_{n=1}^{\infty} \sum_{m=-n}^n$. Note that for radial parts of electric field and current the terms for $n = 0$ are equal to zero, as will be clear later. For magnetic field we have similar decomposition but we write tangential part of the field in slightly different way leaving

the same (as for electric field and impressed current) decomposition of the radial part

$$\mathbf{e}_r \times \mathbf{H}_r(r, \vartheta, \varphi) = \frac{1}{r} \sum_{n,m} \left\{ h_{nm}^t(r) \mathbf{S}_{nm}^t(\vartheta, \varphi) + h_{nm}^p(r) \mathbf{S}_{nm}^p(\vartheta, \varphi) \right\}, \quad (2.34a)$$

$$H_r(r, \vartheta, \varphi) \mathbf{e}_r = \frac{1}{r} \sum_{n,m} h_{nm}^r(r) \mathbf{S}_{nm}^r(\vartheta, \varphi). \quad (2.34b)$$

Substituting eqs (2.33a)-(2.34b) into eqs (2.28) and gathering terms involving functions \mathbf{S}_{nm}^t and \mathbf{S}_{nm}^p , we get the system of equations

$$\begin{cases} \partial_r \varepsilon_{nm}^t &= -i\omega\mu_0 h_{nm}^t, \\ \partial_r h_{nm}^t &= \frac{\kappa}{i\omega\mu_0} \varepsilon_{nm}^t + j_{nm}^t, \end{cases} \quad (2.35)$$

to determine coefficients ε_{nm}^t and h_{nm}^t , and the system

$$\begin{cases} \partial_r \varepsilon_{nm}^p &= \frac{\kappa}{\sigma_0} h_{nm}^p - \frac{\sqrt{n(n+1)}}{r\sigma_0} j_{nm}^r, \\ \partial_r h_{nm}^p &= \sigma_0 \varepsilon_{nm}^p + j_{nm}^p, \end{cases} \quad (2.36)$$

to determine coefficients ε_{nm}^p and h_{nm}^p . Here $\kappa = \frac{n(n+1)}{r^2} - i\omega\mu_0\sigma_0$. For determination of the coefficients ε_{nm}^r and h_{nm}^r we, in its turn, get the following equations

$$\sigma_0 \varepsilon_{nm}^r = \frac{\sqrt{n(n+1)}}{r} h_{nm}^p - j_{nm}^r, \quad (2.37)$$

$$i\omega\mu_0 h_{nm}^r = -\frac{\sqrt{n(n+1)}}{r} \varepsilon_{nm}^t. \quad (2.38)$$

From eqs (2.36) and (2.37) it follows that for radial parts of electric field and current the terms for $n = 0$ are equal to zero. Systems of equations (2.35) and (2.36) can be written in the following generic form

$$\begin{cases} \partial_r \varepsilon(r) = p(r)h(r) + f_h(r), \\ \partial_r h(r) = q\varepsilon(r) + f_\varepsilon(r), \end{cases} \quad (2.39)$$

where

$$\begin{aligned} \varepsilon(r) &= \varepsilon_{nm}^t, & h(r) &= h_{nm}^t, \\ p(r) &= -i\omega\mu_0, & q(r) &= -\frac{\kappa}{i\omega\mu_0}, \\ f_\varepsilon(r) &= j_{nm}^t, & f_h(r) &= 0, \end{aligned} \quad (2.40)$$

for system (2.35) and

$$\begin{aligned}\varepsilon(r) &= \varepsilon_{nm}^p, & h(r) &= h_{nm}^p, \\ p(r) &= \frac{\kappa}{\sigma_0}, & q(r) &= \sigma_0, \\ f_\varepsilon(r) &= j_{nm}^p, & f_h(r) &= -\frac{\sqrt{n(n+1)}}{r\sigma_0} j_{nm}^r,\end{aligned}\tag{2.41}$$

for system (2.36). System (2.39) can be reduced to the second order ordinary differential equation

$$\partial_r \left(\frac{1}{p(r)} \partial_r \varepsilon(r) \right) - q(r) \varepsilon(r) = f(r),\tag{2.42}$$

where

$$f(r) = f_\varepsilon(r) + \partial_r \left(\frac{f_h(r)}{p(r)} \right).\tag{2.43}$$

The solution of eq. (2.42) can be written as

$$\varepsilon(r) = \int_0^\infty G(n, r, r') f(r') dr',\tag{2.44}$$

where $G(n, r, r')$ is (scalar) Green's function of eq. (2.42). The explicit forms of $G(n, r, r')$ are presented in Appendix A.5.2. We impose boundary conditions on the solution of (2.42) in the form $\varepsilon(r) \rightarrow 0$, when $r \rightarrow 0$ and $r \rightarrow \infty$.

Substituting eq. (2.43) into eq. (2.44) and integrating by parts, we have

$$\varepsilon(r) = \int_0^\infty G(n, r, r') f_\varepsilon(r') dr' - \int_0^\infty \beta(n, r, r') G(n, r, r') f_h(r') dr',\tag{2.45}$$

where we define β as

$$\beta(n, r, r') = \frac{\partial_r G(n, r, r')}{p(r') G(n, r, r')}.\tag{2.46}$$

Then, substituting eq. (2.45) into the first equation of the system (2.39), we obtain in a similar way

$$\begin{aligned}h(r) &= \int \alpha(n, r, r') G(n, r, r') f_\varepsilon(r') dr' - \\ &\quad - \int \alpha(n, r, r') \beta(n, r, r') G(n, r, r') f_h(r') dr',\end{aligned}\tag{2.47}$$

where we denote

$$\alpha(n, r, r') = \beta(n, r', r).\tag{2.48}$$

An explicit formula for $\alpha(n, r, r')$ is presented in eq. (2.52). Let us show how we derive eq. (2.47)

$$\begin{aligned}
h(r) &= \frac{1}{p(r)}(\partial_r \varepsilon(r) - f_h(r)) = \\
&= \frac{\partial_r}{p(r)} \int G f_\varepsilon(r') dr' - \frac{\partial_r}{p(r)} \int \frac{\partial_{r'} G}{p(r')} f_h(r') dr' - \frac{1}{p(r)} f_h(r) \stackrel{(2.50)}{=} \\
&\stackrel{(2.50)}{=} \int \frac{\partial_r G}{p(r)} f_\varepsilon(r') dr' - \frac{1}{p(r)} \int \frac{\partial_r G}{p(r') G} \frac{\partial_{r'} G}{G} G f_h(r') dr' - \\
&- \frac{1}{p(r)} \int \partial_r \left(\frac{\partial_{r'} G}{p(r') G} \right) G f_h(r') dr' - \frac{1}{p(r)} f_h(r) \stackrel{(2.51)}{=} \\
&\stackrel{(2.51)}{=} \int \alpha G f_\varepsilon(r') dr' - \int \alpha \beta G f_h(r') dr' + \\
&+ \frac{1}{p(r)} \int \frac{\delta(r-r')}{G} G f_h(r') dr' - \frac{1}{p(r)} f_h(r) = \\
&= \int \alpha G f_\varepsilon(r') dr' - \int \alpha \beta G f_h(r') dr'.
\end{aligned} \tag{2.49}$$

Here $G \equiv G(n, r, r')$, $\alpha \equiv \alpha(n, r, r')$, $\beta \equiv \beta(n, r, r')$. While deriving eq. (2.49) we also used

$$\partial_r \left(\frac{\partial_{r'} G}{p(r') G} \right) = \frac{\partial_r}{p(r')} \left(\frac{\partial_{r'} G}{G} \right) = \frac{\partial_r \partial_{r'} G}{p(r') G} - \frac{\partial_r G \partial_{r'} G}{p(r') G^2}, \tag{2.50}$$

and

$$\partial_r \left(\frac{\partial_{r'} G(n, r, r')}{p(r') G(n, r, r')} \right) = \partial_r \beta(n, r, r') \stackrel{(2.55)}{=} - \frac{\delta(r-r')}{G(n, r, r')}. \tag{2.51}$$

Four equations in the following frame explain how we obtain the derivatives of the spectral functions

Derivatives of the spectral functions

$$\alpha(n, r, r') = \beta(n, r', r) = \begin{cases} -Y^u(n, r), & r > r' \\ Y^l(n, r), & r < r' \end{cases} \tag{2.52}$$

(see Appendix A.5). Therefore

$$\partial_{r'} \alpha(n, r, r') = (-Y^u(n, r') - Y^l(n, r')) \delta(r - r'), \tag{2.53}$$

because $\partial_{r'} \theta(r' - r) = \delta(r' - r)$, where θ is a Heaviside step function and δ is a Dirac's delta function. This leads to

$$\partial_{r'} \alpha(n, r, r') = \frac{\delta(r - r')}{G(n, r', r')} = - \frac{\delta(r' - r)}{G(n, r', r')}, \tag{2.54}$$

and

$$\partial_r \beta(n, r, r') = \partial_r \alpha(n, r', r) = - \frac{\delta(r - r')}{G(n, r, r')}. \tag{2.55}$$

Substituting further eqs (2.40) and (2.41) into eqs (2.45) and (2.47) we express coefficients

$\varepsilon_{nm}^t, \varepsilon_{nm}^p, h_{nm}^t$ and h_{nm}^p via coefficients q_{nm}^t, q_{nm}^p and q_{nm}^r

$$\varepsilon_{nm}^t(r) = \int_0^\infty G^t(n, r, r') j_{nm}^t(r') dr', \quad (2.56)$$

$$\begin{aligned} \varepsilon_{nm}^p(r) = & \int_0^\infty G^p(n, r, r') j_{nm}^p(r') dr' + \\ & + \int_0^\infty \frac{\sqrt{n(n+1)}}{r' \sigma_0(r')} \beta^p(n, r, r') G^p(n, r, r') j_{nm}^r(r') dr', \end{aligned} \quad (2.57)$$

$$h_{nm}^t(r) = \int_0^\infty \alpha^t(n, r, r') G^t(n, r, r') j_{nm}^t(r') dr', \quad (2.58)$$

$$\begin{aligned} h_{nm}^p(r) = & \int_0^\infty \alpha^p(n, r, r') G^p(n, r, r') j_{nm}^p(r') dr' + \\ & + \int_0^\infty \frac{\sqrt{n(n+1)}}{r' \sigma_0(r')} \alpha^p(n, r, r') \beta^p(n, r, r') G^p(n, r, r') j_{nm}^r(r') dr'. \end{aligned} \quad (2.59)$$

Then, using decompositions (2.33c) and (2.33d), the coefficients $j_{nm}^t(r')$, $j_{nm}^p(r')$ and $j_{nm}^r(r')$ are written as

$$j_{nm}^t(r') = \frac{r'}{\|S_n^m\|^2 \sqrt{n(n+1)}} \int_\Omega \nabla'_\perp \cdot (\mathbf{e}_r \times \mathbf{j}_\tau) \widetilde{S_n^m} d\Omega', \quad (2.60)$$

$$j_{nm}^p(r') = -\frac{r'}{\|S_n^m\|^2 \sqrt{n(n+1)}} \int_\Omega (\nabla'_\perp \cdot \mathbf{j}_\tau) \widetilde{S_n^m} d\Omega', \quad (2.61)$$

$$j_{nm}^r(r') = \frac{r'}{\|S_n^m\|^2} \int_\Omega j_r \widetilde{S_n^m} d\Omega'. \quad (2.62)$$

Here Ω' is complete solid angle, $d\Omega' = \sin \vartheta' d\vartheta' d\varphi'$, $\widetilde{S_n^m}$ stands for complex conjugation of $S_n^m = S_n^m(\vartheta', \varphi')$, $\|S_n^m\|^2$ is a squared norm of S_n^m . While deriving eqs. (2.60) and (2.61) we used that

$$\nabla_\perp \cdot (\mathbf{e}_r \times \nabla_\perp) = 0, \quad (2.63)$$

$$\Delta_\perp S_n^m = -n(n+1) S_n^m. \quad (2.64)$$

Here operators $\nabla_\perp \cdot$ and Δ_\perp stand for angular parts of the divergence and the Laplacian, respectively. More explicitly, the action of these operators on any entry functions $\mathbf{a}_\tau = a_\vartheta \mathbf{e}_\vartheta + a_\varphi \mathbf{e}_\varphi$ and u is defined as

$$\nabla_\perp \cdot \mathbf{a}_\tau = \frac{1}{\sin \vartheta} \frac{\partial(a_\vartheta \sin \vartheta)}{\partial \vartheta} + \frac{1}{\sin \vartheta} \frac{\partial a_\varphi}{\partial \varphi}, \quad (2.65)$$

$$\Delta_{\perp} u = \nabla_{\perp} \cdot (\nabla_{\perp} u) = \frac{1}{\sin \vartheta} \frac{\partial}{\partial \vartheta} (\sin \vartheta \frac{\partial u}{\partial \vartheta}) + \frac{1}{\sin^2 \vartheta} \frac{\partial^2 u}{\partial \varphi^2}. \quad (2.66)$$

Substituting eqs (2.60)-(2.62) into eqs (2.56)-(2.57) and further eqs (2.56)-(2.57) into eq. (2.33a) we obtain for the horizontal part of the electric field, after rearranging the operations of integration and summation

$$\begin{aligned} \mathbf{E}_{\tau}(r, \vartheta, \varphi) &= \int_{\Omega} \int_0^{\infty} (\mathbf{e}_r \times \nabla_{\perp}) \{ [\mathbf{e}_{r'} \times \nabla'_{\perp}] \mathcal{P}[\frac{r'}{r} \frac{G'(n, r, r')}{n(n+1)}] \} \cdot \mathbf{j}_{\tau}(r', \vartheta', \varphi') \} dr' d\Omega' + \\ &+ \int_{\Omega} \int_0^{\infty} \nabla_{\perp} \{ [\nabla'_{\perp} \mathcal{P}[\frac{r'}{r} \frac{G^p(n, r, r')}{n(n+1)}] \} \cdot \mathbf{j}_{\tau}(r', \vartheta', \varphi') \} dr' d\Omega' - \\ &- \int_{\Omega} \int_0^{\infty} \nabla_{\perp} \{ \mathcal{P}[\frac{\beta^p(n, r, r') G^p(n, r, r')}{r \sigma_0(r')}] j_r(r', \vartheta', \varphi') \} dr' d\Omega'. \end{aligned} \quad (2.67)$$

Here “.” stands for the scalar product of two vectors, and $\mathcal{P}[f]$ denotes the summation of series

$$\mathcal{P}[f(n, r, r')] = \sum_{n=1}^{\infty} \frac{2n+1}{4\pi} f(n, r, r') P_n(\cos \gamma), \quad (2.68)$$

where P_n are the Legendre polynomials, and $\cos \gamma$ is determined by

$$\cos \gamma = \cos \vartheta \cos \vartheta' + \sin \vartheta \sin \vartheta' \cos(\varphi - \varphi'). \quad (2.69)$$

Note that while deriving eq. (2.67) we used the theorem of summation for spherical functions (Jackson, 1975)

$$\sum_{n,m} \frac{S_n^m(\vartheta, \varphi) \widetilde{S_n^m}(\vartheta', \varphi')}{\|S_n^m\|^2} = \sum_{n=1}^{\infty} \frac{2n+1}{4\pi} P_n(\cos \gamma), \quad (2.70)$$

and the following equalities

$$\int_{\Omega} Q \nabla'_{\perp} \cdot \mathbf{P} d\Omega' = - \int_{\Omega} \mathbf{P} \nabla_{\perp} Q d\Omega', \quad (2.71)$$

$$\mathbf{a}(\mathbf{b} \times \mathbf{c}) = -(\mathbf{b} \times \mathbf{a})\mathbf{c}, \quad (2.72)$$

that are valid for any scalar function Q and any vector functions \mathbf{P} , \mathbf{a} , \mathbf{b} and \mathbf{c} . In a similar way we obtain the expressions for the radial component of the electric field

$$\begin{aligned} E_r(r, \vartheta, \varphi) &= -\frac{1}{\sigma_0(r)} j_r(r', \vartheta', \varphi') - \\ &- \int_{\Omega} \int_0^{\infty} [\Delta'_{\perp} \mathcal{P}[\frac{\alpha^p(n, r, r') \beta^p(n, r, r') G^p(n, r, r')}{r^2 \sigma_0(r) \sigma_0(r')}] j_r(r', \vartheta', \varphi') dr' d\Omega' + \\ &+ \int_{\Omega} \int_0^{\infty} [\nabla'_{\perp} \mathcal{P}[\frac{r'}{r^2} \alpha^p(n, r, r') G^p(n, r, r')]] \cdot \mathbf{j}_{\tau}(r', \vartheta', \varphi') dr' d\Omega', \end{aligned} \quad (2.73)$$

and for the horizontal and radial components of the magnetic field

$$\begin{aligned}
 \mathbf{H}_\tau(r, \vartheta, \varphi) = & \int_{\Omega} \int_0^{\infty} \nabla_{\perp} \{ [(\mathbf{e}_{r'} \times \nabla'_{\perp}) \mathcal{P}[\frac{r'}{r} \frac{\alpha^t(n, r, r') G^t(n, r, r')}{n(n+1)}]] \cdot \mathbf{j}_{\tau}(r', \vartheta', \varphi') \} dr' d\Omega' - \\
 & - \int_{\Omega} \int_0^{\infty} (\mathbf{e}_r \times \nabla_{\perp}) \{ [\nabla'_{\perp} \mathcal{P}[\frac{r'}{r} \frac{\alpha^p(n, r, r') G^p(n, r, r')}{n(n+1)}]] \cdot \mathbf{j}_{\tau}(r', \vartheta', \varphi') \} dr' d\Omega' - \\
 & - \int_{\Omega} \int_0^{\infty} (\mathbf{e}_r \times \nabla_{\perp}) \{ \mathcal{P}[\frac{\alpha^p(n, r, r') \beta^p(n, r, r') G^p(n, r, r')}{r \sigma_0(r')}] j_r(r', \vartheta', \varphi') \} dr' d\Omega',
 \end{aligned} \tag{2.74}$$

$$H_r(r, \vartheta, \varphi) = - \int_{\Omega} \int_0^{\infty} [(\mathbf{e}_{r'} \times \nabla'_{\perp}) \mathcal{P}[\frac{r'}{r^2} \frac{G^p(n, r, r')}{i\omega\mu_0}]] \cdot \mathbf{j}_{\tau}(r', \vartheta', \varphi') dr' d\Omega'. \tag{2.75}$$

Now from eqs (2.67) and (2.73) we write the expressions for elements $g_{\vartheta\vartheta}^{ej}$, $g_{\vartheta\varphi'}^{ej}$, ..., $g_{rr'}^{ej}$ of eq. (2.31)

$$g_{\vartheta\vartheta}^{ej} = \frac{1}{\sin \vartheta} \frac{1}{\sin \vartheta'} \partial_{\varphi} \partial_{\varphi'} \mathcal{P}[\frac{1}{r'r} \frac{G^t}{n(n+1)}] + \partial_{\vartheta} \partial_{\vartheta'} \mathcal{P}[\frac{1}{r'r} \frac{G^p}{n(n+1)}], \tag{2.76a}$$

$$g_{\vartheta\varphi'}^{ej} = -\frac{1}{\sin \vartheta} \partial_{\varphi} \partial_{\vartheta'} \mathcal{P}[\frac{1}{r'r} \frac{G^t}{n(n+1)}] + \frac{1}{\sin \vartheta'} \partial_{\vartheta} \partial_{\varphi'} \mathcal{P}[\frac{1}{r'r} \frac{G^p}{n(n+1)}], \tag{2.76b}$$

$$g_{\vartheta r'}^{ej} = -\partial_{\vartheta} \mathcal{P}[\frac{1}{r'^2 r} \frac{\beta^p G^p}{\sigma_0(r')}], \tag{2.76c}$$

$$g_{\varphi\vartheta'}^{ej} = -\frac{1}{\sin \vartheta'} \partial_{\vartheta} \partial_{\varphi'} \mathcal{P}[\frac{1}{r'r} \frac{G^t}{n(n+1)}] + \frac{1}{\sin \vartheta} \partial_{\varphi} \partial_{\vartheta'} \mathcal{P}[\frac{1}{r'r} \frac{G^p}{n(n+1)}], \tag{2.76d}$$

$$g_{\varphi\varphi'}^{ej} = \partial_{\vartheta} \partial_{\vartheta'} \mathcal{P}[\frac{1}{r'r} \frac{G^t}{n(n+1)}] + \frac{1}{\sin \vartheta} \frac{1}{\sin \vartheta'} \partial_{\varphi} \partial_{\varphi'} \mathcal{P}[\frac{1}{r'r} \frac{G^p}{n(n+1)}], \tag{2.76e}$$

$$g_{\varphi r'}^{ej} = -\frac{1}{\sin \vartheta} \partial_{\varphi} \mathcal{P}[\frac{1}{r'^2 r} \frac{\beta^p G^p}{\sigma_0(r')}], \tag{2.76f}$$

$$g_{r\vartheta'}^{ej} = \partial_{\vartheta'} \mathcal{P}[\frac{1}{r' r^2} \frac{\alpha^p G^p}{\sigma_0(r)}], \tag{2.76g}$$

$$g_{r\varphi'}^{ej} = \frac{1}{\sin \vartheta'} \partial_{\varphi'} \mathcal{P}[\frac{1}{r' r^2} \frac{\alpha^p G^p}{\sigma_0(r)}], \tag{2.76h}$$

$$g_{rr'}^{ej} = -\frac{\delta(r-r')\delta(\vartheta-\vartheta')\delta(\varphi-\varphi')}{r'^2 \sin \vartheta' \sigma_0(r)} + \mathcal{P}[\frac{1}{r'^2 r^2} \frac{n(n+1)\alpha^p \beta^p G^p}{\sigma_0(r)\sigma_0(r')}]. \tag{2.76i}$$

In a similar way from eqs (2.74) and (2.75) we write the expressions for elements $g_{\vartheta\vartheta}^{hj}$, $g_{\vartheta\varphi'}^{hj}$, ..., $g_{rr'}^{hj}$ of eq. (2.31)

$$g_{\vartheta\vartheta'}^{hj} = -\frac{1}{\sin\vartheta'}\partial_{\vartheta}\partial_{\varphi'}\mathcal{P}\left[\frac{1}{r'r}n(n+1)\frac{\alpha^t G^t}{n(n+1)}\right] + \frac{1}{\sin\vartheta}\partial_{\varphi}\partial_{\vartheta'}\mathcal{P}\left[\frac{1}{r'r}n(n+1)\frac{\alpha^p G^p}{n(n+1)}\right], \quad (2.77a)$$

$$g_{\vartheta\varphi'}^{hj} = \partial_{\vartheta}\partial_{\vartheta'}\mathcal{P}\left[\frac{1}{r'r}n(n+1)\frac{\alpha^t G^t}{n(n+1)}\right] + \frac{1}{\sin\vartheta}\frac{1}{\sin\vartheta'}\partial_{\varphi}\partial_{\varphi'}\mathcal{P}\left[\frac{1}{r'r}n(n+1)\frac{\alpha^p G^p}{n(n+1)}\right], \quad (2.77b)$$

$$g_{\vartheta r'}^{hj} = \frac{1}{\sin\vartheta}\partial_{\varphi}\mathcal{P}\left[\frac{1}{r'^2 r}\frac{\alpha^p \beta^p G^p}{\sigma_0(r')}\right], \quad (2.77c)$$

$$g_{\varphi\vartheta'}^{hj} = -\frac{1}{\sin\vartheta}\frac{1}{\sin\vartheta'}\partial_{\varphi}\partial_{\varphi'}\mathcal{P}\left[\frac{1}{r'r}n(n+1)\frac{\alpha^t G^t}{n(n+1)}\right] - \partial_{\vartheta}\partial_{\vartheta'}\mathcal{P}\left[\frac{1}{r'r}n(n+1)\frac{\alpha^p G^p}{n(n+1)}\right], \quad (2.77d)$$

$$g_{\varphi\varphi'}^{hj} = \frac{1}{\sin\vartheta}\partial_{\varphi}\partial_{\vartheta'}\mathcal{P}\left[\frac{1}{r'r}n(n+1)\frac{\alpha^t G^t}{n(n+1)}\right] - \frac{1}{\sin\vartheta'}\partial_{\vartheta}\partial_{\varphi'}\mathcal{P}\left[\frac{1}{r'r}n(n+1)\frac{\alpha^p G^p}{n(n+1)}\right], \quad (2.77e)$$

$$g_{\varphi r'}^{hj} = -\partial_{\vartheta}\mathcal{P}\left[\frac{1}{r'^2 r}\frac{\alpha^p \beta^p G^p}{\sigma_0(r')}\right], \quad (2.77f)$$

$$g_{r\vartheta'}^{hj} = \frac{1}{\sin\vartheta'}\partial_{\varphi'}\mathcal{P}\left[\frac{1}{r'r^2}\frac{G^t}{i\omega\mu_0}\right], \quad (2.77g)$$

$$g_{r\varphi'}^{hj} = -\partial_{\vartheta'}\mathcal{P}\left[\frac{1}{r'r^2}\frac{G^t}{i\omega\mu_0}\right], \quad (2.77h)$$

$$g_{rr'}^{hj} = 0. \quad (2.77i)$$

Chapter 3

Inverse modeling

3.1 C-response concept

Above the conducting Earth ($r > a$, $a = 6371.2$ km is the mean Earth's radius) and beneath the external (magnetospheric and ionospheric) sources, the magnetic field in a frequency domain, $\mathbf{B}(\mathbf{r}, \omega) = \mu_0 \mathbf{H}(\mathbf{r}, \omega) = -\nabla V(\mathbf{r}, \omega)$, can be derived from a scalar magnetic potential, V , which is represented by a spherical harmonic expansion

$$V(r, \vartheta, \varphi, \omega) = a \sum_{n=1}^{\infty} \sum_{m=-n}^n \left[\varepsilon_n^m(\omega) \left(\frac{r}{a}\right)^n + i_n^m(\omega) \left(\frac{a}{r}\right)^{n+1} \right] P_n^m(\cos \vartheta) e^{im\varphi}, \quad (3.1)$$

where ε_n^m and i_n^m are the complex-valued expansion coefficients of the external (inducing) and internal (induced) parts of the potential. Further we will again use $\sum_{n,m}$ to designate $\sum_{n=1}^{\infty} \sum_{m=-n}^n$.

Components of the magnetic field following from eq. (3.1) can be written as

$$B_r(r, \vartheta, \varphi, \omega) = - \sum_{n,m} \left[n \varepsilon_n^m(\omega) \left(\frac{r}{a}\right)^{n-1} - (n+1) i_n^m(\omega) \left(\frac{a}{r}\right)^{n+2} \right] P_n^m(\cos \vartheta) e^{im\varphi}, \quad (3.2a)$$

$$B_{\vartheta}(r, \vartheta, \varphi, \omega) = - \sum_{n,m} \left[\varepsilon_n^m(\omega) \left(\frac{r}{a}\right)^{n-1} + i_n^m(\omega) \left(\frac{a}{r}\right)^{n+2} \right] \frac{dP_n^m(\cos \vartheta)}{d\vartheta} e^{im\varphi}, \quad (3.2b)$$

$$B_{\varphi}(r, \vartheta, \varphi, \omega) = - \sum_{n,m} \left[\varepsilon_n^m(\omega) \left(\frac{r}{a}\right)^{n-1} + i_n^m(\omega) \left(\frac{a}{r}\right)^{n+2} \right] \frac{im}{\sin \vartheta} P_n^m(\cos \vartheta) e^{im\varphi}. \quad (3.2c)$$

From eqs (3.2) one can see, in particular, that the radial component is to a greater extent than the horizontal components influenced by induction. For the horizontal components the degree of this influence is governed by the complex Q -response, which is the ratio of the internal to the external coefficients for a specific degree, order and frequency. In the case of only radially dependent (1-D) conductivity distribution, each external coefficient induces only one internal coefficient (of the same degree n and order m), and their ratio is independent of m

$$Q_n(\omega) = \frac{i_n^m(\omega)}{\varepsilon_n^m(\omega)}, \quad (3.3)$$

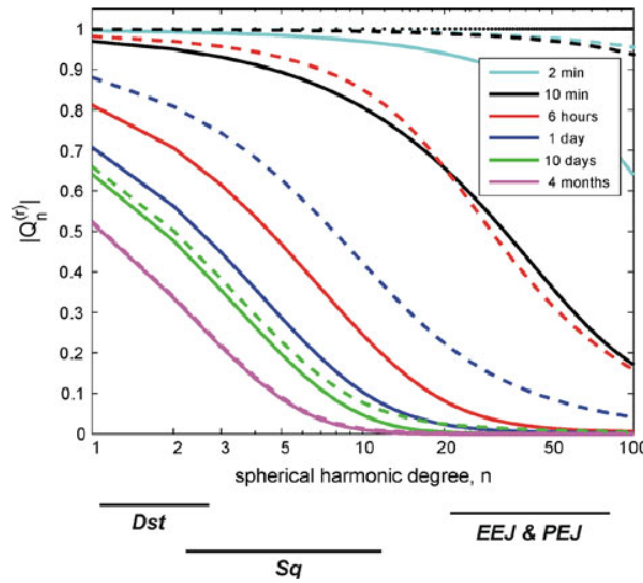


Figure 3.1: $|Q_n^{(r)}|$ for different periods as a function of degree n . Solid lines $|Q_n^{(r)}|$ for a typical global 1-D conductivity profile. Dashed lines $|Q_n^{(r)}|$ for the same 1-D model overlain by a uniform ocean of 15,000 S. For comparison, the dotted line in the figure shows an upper limit, 1, for $|Q_n^{(r)}|$ which corresponds to a perfectly conducting Earth. After Kuvshinov (2008).

and can be calculated using appropriate recurrence formulas (see Appendix B.2, eqs A.71 and (B.27)). For the radial component, the degree of the influence is governed by the quantity

$$Q_n^{(r)}(\omega) = \frac{n+1}{n} Q_n(\omega). \quad (3.4)$$

This means that the relative amount of induction in the radial part is $\frac{n+1}{n}$ times larger than for the horizontal components (Kuvshinov, 2008). In addition, due to subtraction in eq. (3.2a) the ratio of induced signal to total (inducing+induced) signal is larger in the radial component. Figure 3.1 presents $|Q_n^{(r)}|$ for a range of periods as a function of harmonic of degree n for two global 1-D conductivity profiles (with and without ocean of uniform conductance). Solid black lines below the plot show the range of degree n for the different sources. For comparison, the dotted line in the plot shows an upper limit of 1, for $|Q_n^{(r)}|$, which corresponds to a perfectly conducting Earth. In this case, induction cancels the radial component at the surface of the Earth and more or less doubles the horizontal component. For all n , we observe that the longer the period the smaller $|Q_n^{(r)}|$. In addition, $|Q_n^{(r)}|$ also decreases with increasing of n . For example, at a period of 24 h $|Q_n^{(r)}|$ drops from 0.56 for $n = 2$ (degree of fundamental spherical harmonic of Sq at this period) down to less than 0.03 for $n = 20$, when inland (without ocean) 1-D profile is considered. The latter result is very important since it means that one cannot expect an induction signal from the polar electrojet (requiring $n \geq 20$) at periods longer than a few days. Contamination of deep EM results by the polar electrojet will be discussed in Chapter 4.

The C -response concept was introduced by [Schmucker \(1970\)](#). For a radially symmetric conductivity distribution in the Earth it is connected to the Q -response by means of

$$C_n(\omega) = \frac{a}{n+1} \frac{1 - \frac{n+1}{n} Q_n(\omega)}{1 + Q_n(\omega)} = \frac{a}{n+1} \frac{z_n^m(\omega)}{v_n^m(\omega)}, \quad (3.5)$$

([Schmucker, 1970, 1987](#); [Olsen, 1998](#)), where $z_n^m = n\varepsilon_n^m - (n+1)i_n^m$ and $v_n^m = \varepsilon_n^m + i_n^m$. We can rewrite eq. (3.2) for a specific site on the surface with coordinates ($r = a, \vartheta, \varphi$) as

$$B_r(a, \vartheta, \varphi, \omega) = - \sum_{n,m} z_n^m(\omega) P_n^m(\cos \vartheta) e^{im\varphi}, \quad (3.6a)$$

$$B_\vartheta(a, \vartheta, \varphi, \omega) = - \sum_{n,m} v_n^m(\omega) \frac{dP_n^m(\cos \vartheta)}{d\vartheta} e^{im\varphi}, \quad (3.6b)$$

$$B_\varphi(a, \vartheta, \varphi, \omega) = - \sum_{n,m} v_n^m(\omega) \frac{im}{\sin \vartheta} P_n^m(\cos \vartheta) e^{im\varphi}. \quad (3.6c)$$

Inserting eq. (3.5) into eq. (3.6a) we can write

$$B_r(a, \vartheta, \varphi, \omega) = - \frac{1}{a} \sum_{n,m} C_n(\omega) n(n+1) v_n^m(\omega) P_n^m(\cos \vartheta) e^{im\varphi}. \quad (3.7)$$

This equation has been derived with the assumption of a 1-D conductivity distribution, it has a general validity, provided that the scale length of lateral conductivity anomalies beneath the site is large compared with $|C_n|$.

C_n depends only weakly on the source field geometry (cf. [Olsen, 1998](#)), i.e. on the degree n of the spherical harmonic, and is therefore, to a first approximation, equal to the asymptotic value $C = C_0$ (C_0 is the zero wave-number flat-earth response, which differs from C_1 insignificantly). This yields

$$B_r = -C \frac{1}{a} \sum_{n,m} n(n+1) v_n^m(\omega) P_n^m(\cos \vartheta) e^{im\varphi}. \quad (3.8)$$

Further we can write

$$\frac{1}{a} \sum_{n,m} n(n+1) v_n^m(\omega) P_n^m(\cos \vartheta) e^{im\varphi} = \frac{1}{\sin \vartheta} \left[\frac{\partial(\sin \vartheta B_\vartheta)}{\partial \vartheta} + \frac{\partial B_\varphi}{\partial \varphi} \right] = \nabla_\perp \cdot \mathbf{B}_\tau, \quad (3.9)$$

and therefore

$$B_r(a, \vartheta, \varphi, \omega) = -C \nabla_\perp \cdot \mathbf{B}_\tau(a, \vartheta, \varphi, \omega). \quad (3.10)$$

Let us assume that the source field potential is proportional to $P_1^0 = \cos \vartheta$ (here ϑ is the geomagnetic colatitude). This gives

$$V(a, \vartheta, \varphi, \omega) = a v_1^0(\omega) \cos \vartheta, \quad (3.11)$$

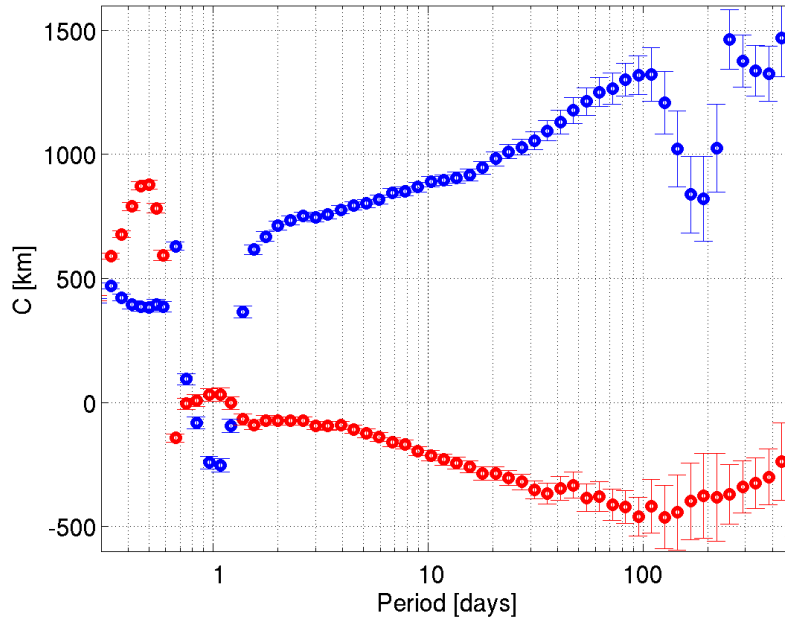


Figure 3.2: Example of C -response estimation at Fürstenfeldbruck (FUR) observatory in southern Germany. Blue circles represent the real part of the C -responses, red circles - the imaginary part.

and

$$B_r(a, \vartheta, \varphi, \omega) = -z_1^0(\omega) \cos \vartheta, \quad (3.12a)$$

$$B_\vartheta(a, \vartheta, \varphi, \omega) = v_1^0(\omega) \sin \vartheta, \quad (3.12b)$$

$$B_\varphi(a, \vartheta, \varphi, \omega) = 0. \quad (3.12c)$$

From eqs (3.10) and (3.12) one can write

$$B_r = -\frac{z_1^0(\omega) \cos \vartheta}{v_1^0(\omega) \sin \vartheta} B_\vartheta = -C(\omega) \frac{2}{a} \tan \vartheta B_\vartheta, \quad (3.13)$$

and then the C -response is written as

$$C(\omega) = -\frac{a \tan \vartheta}{2} \frac{B_r}{B_\vartheta} = -\frac{a \tan \vartheta}{2} \frac{H_r}{H_\vartheta}. \quad (3.14)$$

Figure 3.2 shows an example of experimental C -response at the observatory Fürstenfeldbruck in southern Germany. In Chapter 4 we discuss in detail the estimation of C -responses from experimental data.

Weidelt (1972) derived several key properties of C -responses. We present them in Appendix A.2. In this section we summarize the three most important properties.

1. The C -response does not depend on the amplitude of the external source.
2. The real part of C -response reflects the mean depth of EM field penetration into the

Earth.

3. In case of a 1-D Earth the real part of C -response increases monotonically to z_m , the depth to a perfect conductor, which in the case of the Earth is the depth to the core-mantle boundary. In Fig. 3.2 one can see the violation of this property at periods smaller than 1.5 days, which is explained by completely different spatial structure of the source (Sq current system) at these periods. At periods larger than 110 days this property also violates, hinting at either non- P_1^0 source structure and/or contamination by the sources originated in the core.

3.2 Inverse problem formulation

We formulate the inverse problem of conductivity recovery as an optimization problem such that

$$\phi(\mathbf{m}, \lambda) \underbrace{\rightarrow}_{\mathbf{m}} \min, \quad (3.15)$$

with the penalty function

$$\phi(\mathbf{m}, \lambda) = \phi_d(\mathbf{m}) + \lambda \phi_s(\mathbf{m}), \quad (3.16)$$

where λ and $\phi_s(\mathbf{m})$ are a regularization parameter and a regularization term, respectively, $\phi_d(\mathbf{m})$ is the data misfit

$$\phi_d(\mathbf{m}) = \sum_{\omega \in Freqs} \sum_{\mathbf{r}_a \in Sites} \left| \frac{C^{mod}(\mathbf{r}_a, \omega, \mathbf{m}) - C^{exp}(\mathbf{r}_a, \omega)}{\delta C^{exp}(\mathbf{r}_a, \omega)} \right|^2. \quad (3.17)$$

Here $C^{mod}(\mathbf{r}_a, \omega, \mathbf{m})$ and $C^{exp}(\mathbf{r}_a, \omega)$ are the (complex-valued) predicted and observed C -responses at observation site \mathbf{r}_a and at frequency ω , and $\delta C^{exp}(\mathbf{r}_a, \omega)$ is the uncertainties of the observed responses. "Sites" define the locations of the geomagnetic observatories

$$Sites := \{(r = a, \vartheta_i, \varphi_i), i = 1, 2, \dots, N_{sites}\}, \quad (3.18)$$

where ϑ_i and φ_i are respectively colatitude and longitude of the observation site. "Freqs" define the frequencies under consideration

$$Freqs := \{\omega_k, k = 1, 2, \dots, N_{freq}\}. \quad (3.19)$$

Vector \mathbf{m} represents the model parameters that describe the 3-D conductivity distribution in the model. Parameterization of the model is explained in Section 3.3.

We work with a regularization term of the form

$$\phi_s(\mathbf{m}) = \{W\mathbf{m}\}^T \{W\mathbf{m}\}, \quad (3.20)$$

where the superscript T means transpose and W presents a regularization matrix which –

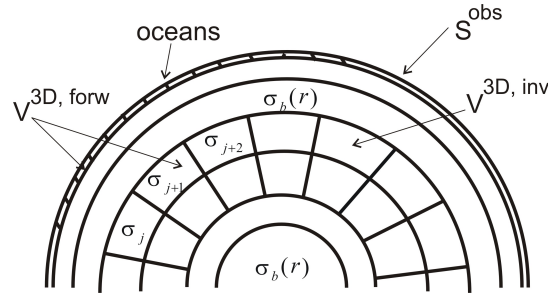


Figure 3.3: Sketch of 3-D conductivity model.

together with the regularization parameter λ – controls the model smoothness. As a smoothing matrix the finite difference approximation to the gradient operator is used.

3.3 Parameterization of the model

Let V^{inv} be the inversion problem domain where we seek a 3-D conductivity distribution. Also let V^{mod} be the forward problem domain where we solve eqs (2.7). We assume that V^{inv} is confined to N_r^{inv} laterally nonuniform spherical layers embedded into the Earth's model, which consists of a surface shell of known laterally varying conductance, $S(\vartheta, \varphi)$, and background 1-D section of known conductivity $\sigma_b(r)$ (see the sketch of the 3-D model in Fig. 3.3). For our problem statement it is important to include the surface shell (which approximates nonuniform distribution of the conducting oceans and resistive continents) into V^{mod} , since this shell greatly affects the responses at coastal observatories (Kuvshinov et al., 2002a). Thus V^{mod} consists of V^{inv} and the thin surface layer. V^{mod} is discretized by $N^{mod} = N_r^{mod} \times N_{\vartheta}^{mod} \times N_{\varphi}^{mod}$ volume cells, $V_j (j = 1, 2, \dots, N^{mod})$, with the edges of the cells stretching along r , ϑ and φ . Here $N_r^{mod} = N_r^{inv} + 1$.

The model parameterization \mathbf{m} is defined as follows. Let V^{inv} be subdivided onto $N^{inv} = N_r^{inv} \times N_{\tau}^{inv}$ volume cells, $V_m (m = 1, 2, \dots, N^{inv})$. We assume that the conductivity is constant within V_m .

$$\sigma(\mathbf{r}) = \sigma_m, \quad \mathbf{r} \in V_m. \quad (3.21)$$

Then the vector

$$\mathbf{m} = (\ln(\sigma_1), \ln(\sigma_2), \dots, \ln(\sigma_{N^{inv}}))^T \quad (3.22)$$

defines the set of model parameters. The choice of $\ln(\sigma)$ instead σ as unknowns guarantees the positiveness of the conductivities during the inversion and provides a better scaling of the problem. We also notice that the sizes of the cells along r and ϑ can be variable.

Note that V_m might coincide with V_j within V^{inv} , or might be some combinations of V_j . In the present version of the inverse solution only one type of combination of V_j (to comprise V_m) is allowed, namely simultaneous merging in both lateral directions of L^2 cells V_j within each of N_r^{inv} inhomogeneous layers. Thus, for this merging scheme $N_{\tau}^{inv} = \frac{N_{\vartheta}^{mod}}{L} \times \frac{N_{\varphi}^{mod}}{L}$.

3.4 Limited-memory quasi-Newton (LMQN) algorithm

To minimize $\phi(\mathbf{m}, \lambda)$ we apply the quasi-Newton (QN) method. This method is based on the update formula

$$\mathbf{m}_{k+1} = \mathbf{m}_k + \alpha_k \mathbf{p}_k, \quad (3.23)$$

where \mathbf{p}_k is determined as

$$\mathbf{p}_k = -B_k^{-1} \nabla \phi_k. \quad (3.24)$$

Here k is the iteration number, $\nabla \phi_k = (\frac{\partial \phi_k}{\partial m_1}, \frac{\partial \phi_k}{\partial m_2}, \dots, \frac{\partial \phi_k}{\partial m_{N^{inv}}})^T$ is the gradient vector with respect to the current model parameters \mathbf{m}_k , α_k is the step length and B_k^{-1} is an approximation of the inverse Hessian matrix.

This updating procedure requires three basic operations:

1. Update of $\nabla \phi_k$;
2. Update of B_k^{-1} using, for example, Broyden-Fletcher-Goldfarb-Shanno (BFGS) formula;
3. Inexact line search to find appropriate α_k .

Since the inverse Hessian approximation is generally dense, the cost of storing and manipulating it is computationally high when the number, N^{inv} , of variables is large. Indeed we need $O([N^{inv}]^2)$ bytes and operations to respectively store B_k^{-1} and calculate $B_k^{-1} \nabla \phi_k$ at each iteration. To circumvent this problem, a limited-memory variant of QN was introduced which works with a modified version of B_k^{-1} and requires manipulations with m vector pairs $\{\mathbf{m}_i - \mathbf{m}_{i-1}, \nabla \phi_i - \nabla \phi_{i-1}\}$. In this case we need $O(mN^{inv})$ bytes and operations to store B_k^{-1} and calculate $B_k^{-1} \nabla \phi_k$ in each iteration (see Section 3.4.2 for details).

Note that the efficiency (rate of convergence to the solution) of the inversion strongly depends on the accuracy of the line search scheme. We used a scheme, following the reasonings presented in Nocedal and Wright (2006).

3.4.1 Line search. The Wolfe conditions

Computing the step length α_k is a tradeoff. It is desirable to obtain a substantial reduction of the functional, but at the same time not spending too much time finding α_k . The ideal choice would be the global minimizer of the univariate function $f(\alpha)$ defined by

$$f(\alpha) = \phi(\mathbf{m}_k + \alpha \mathbf{p}_k), \quad \alpha > 0, \quad (3.25)$$

but in general it is too expensive to identify this value. To find even a local minimizer of f generally requires too many evaluations of the objective function ϕ and $\nabla \phi$. More practical strategies perform an inexact line search to identify a step length that achieves adequate reductions of ϕ at minimal cost.

A popular inexact line search stipulates that α_k should, first of all, give sufficient decrease in the objective function ϕ , as measured by the inequality:

$$\phi(\mathbf{m}_k + \alpha \mathbf{p}_k) \leq \phi(\mathbf{m}_k) + c_1 \alpha \nabla \phi_k^T \mathbf{p}_k, \quad (3.26)$$

for some constant $c_1 \in (0, 1)$. Usually the value for c_1 is very small, for example, $c_1 = 10^{-4}$. Simply to say, the reduction in ϕ should be proportional to both the step length α_k and the directional derivative $\nabla \phi_k^T \mathbf{p}_k$. Often inequality (3.26) is called *Armijo condition*.

The sufficient decrease condition is not enough to ensure the reasonable decrease in ϕ . To rule out unacceptably short steps, a second requirement, called a curvature condition, is introduced. It requires α_k to satisfy

$$\nabla \phi(\mathbf{m}_k + \alpha_k \mathbf{p}_k)^T \mathbf{p}_k \geq c_2 \nabla \phi_k^T \mathbf{p}_k, \quad (3.27)$$

for some constant $c_2 \in (c_1, 1)$, where c_1 is the constant from eq. (3.26). The left-hand side of eq. (3.27) is simply the derivative $f'(\alpha_k)$, so the curvature condition ensures that the slope of f at α_k is greater than c_2 times the initial slope $f'(0)$.

On the other hand, if $f'(\alpha_k)$ is only slightly negative or even positive, that means that we cannot expect much more decrease in ϕ in this direction, so it makes sense to terminate the line search. Typical values of c_2 are 0.9.

The sufficient decrease and curvature conditions together are known as *Wolfe conditions*

$$\phi(\mathbf{m}_k + \alpha \mathbf{p}_k) \leq \phi(\mathbf{m}_k) + c_1 \alpha \nabla \phi_k^T \mathbf{p}_k, \quad (3.28a)$$

$$\nabla \phi(\mathbf{m}_k + \alpha_k \mathbf{p}_k)^T \mathbf{p}_k \geq c_2 \nabla \phi_k^T \mathbf{p}_k, \quad (3.28b)$$

with $0 < c_1 < c_2 < 1$.

The *strong Wolfe conditions* require α_k to satisfy

$$\phi(\mathbf{m}_k + \alpha \mathbf{p}_k) \leq \phi(\mathbf{m}_k) + c_1 \alpha \nabla \phi_k^T \mathbf{p}_k, \quad (3.29a)$$

$$|\nabla \phi(\mathbf{m}_k + \alpha_k \mathbf{p}_k)^T \mathbf{p}_k| \geq c_2 |\nabla \phi_k^T \mathbf{p}_k|, \quad (3.29b)$$

with $0 < c_1 < c_2 < 1$. The only difference with the Wolfe conditions is that $f'(\alpha_k)$ is no longer allowed to be positive. Hence, the points that are far from stationary points of f are excluded. The proof of existence of the step lengths satisfying the Wolfe conditions (3.28) and the strong Wolfe conditions (3.29) can be found in Nocedal and Wright (2006).

3.4.2 Limited-memory BFGS

The most popular quasi-Newton algorithm is the BFGS method, named for its discoverers Broyden, Fletcher, Goldfarb and Shanno. The details of this algorithm are presented in Nocedal and Wright (2006). Each step of the BFGS method has the form

$$\mathbf{m}_{k+1} = \mathbf{m}_k - \alpha_k H_k \nabla \phi_k, \quad (3.30)$$

where the update formula for the $H_k = B_k^{-1}$, approximation of the inverse Hessian matrix, at each iteration is given by

$$H_{k+1} = (I - \rho_k \mathbf{s}_k \mathbf{y}_k^T) H_k (I - \rho_k \mathbf{s}_k \mathbf{y}_k^T) + \rho_k \mathbf{s}_k \mathbf{s}_k^T, \quad (3.31)$$

where

$$\mathbf{s}_k = \mathbf{m}_{k+1} - \mathbf{m}_k = \alpha_k \mathbf{p}_k, \quad (3.32a)$$

$$\mathbf{y}_k = \nabla \phi_{k+1} - \nabla \phi_k, \quad (3.32b)$$

and

$$\rho_k = \frac{1}{\mathbf{y}_k^T \mathbf{s}_k}. \quad (3.33)$$

Unfortunately there is no formula for H_0 that works well in all cases. Some specific information is usually used. Otherwise, one can simply set it to be identity matrix, or a multiple of the identity matrix, where the multiple is chosen to reflect the scaling of the variables.

It is reasonable to ask whether the updating formula (3.31) can produce unsatisfactory results in certain cases. This question was studied analytically and experimentally (Nocedal and Wright, 2006), and these studies show that the BFGS formula has very effective self-correcting property. If the matrix H_k incorrectly estimates the curvature in the objective function, and this bad estimate slows down the convergence, the Hessian approximation will tend to correct itself within a few steps.

Let us now discuss the limited-memory version of BFGS method (L-BFGS). Since the inverse Hessian approximation H_k is generally dense, the cost of storing and manipulating it is high when the number of variables is large. To overcome this problem, one can store a modified version of H_k implicitly, by storing a certain number (say, m) of the vector pairs $\{\mathbf{s}_i, \mathbf{y}_i\}$. The product $H_k \nabla \phi_k$ can be obtained by performing a sequence of inner products and vector summations involving $\nabla \phi_k$ and the pairs $\{\mathbf{s}_i, \mathbf{y}_i\}$. After the new iterate is computed, the oldest vector pair in the set is replaced by $\{\mathbf{s}_k, \mathbf{y}_k\}$. Practical experience has shown that modest values of number of pairs ($3 \leq m \leq 20$) often produce satisfactory results.

Let us describe the updating process in more detail. At iteration k , the current iterate is \mathbf{m}_k and the set of vector pairs $\mathbf{s}_i, \mathbf{y}_i$, for $i = k - m, \dots, k - 1$. We first choose some initial Hessian approximation H_k^0 (in contrast to standard BFGS iteration, this initial approximation

is allowed to vary from iteration to iteration) and find by repeated application of the formula (3.31), that the L-BFGS approximation satisfies the following formula:

$$\begin{aligned}
 H_k = & (V_{k-1}^T \cdots V_{k-m}^T) H_k^0 (V_{k-m} \cdots V_{k-1}) + \\
 & + \rho_{k-m} (V_{k-1}^T \cdots V_{k-m+1}^T) \mathbf{s}_{k-m} \mathbf{s}_{k-m}^T (V_{k-m+1} \cdots V_{k-1}) + \\
 & + \rho_{k-m+1} (V_{k-1}^T \cdots V_{k-m+2}^T) \mathbf{s}_{k-m+1} \mathbf{s}_{k-m+1}^T (V_{k-m+2} \cdots V_{k-1}) + \cdots + \\
 & + \rho_{k-1} \mathbf{s}_{k-1} \mathbf{s}_{k-1}^T.
 \end{aligned} \tag{3.34}$$

It is effective in practice to set $H_k^0 = \gamma_k I$, where

$$\gamma_k = \frac{\mathbf{s}_{k-1}^T \mathbf{y}_{k-1}}{\mathbf{y}_{k-1}^T \mathbf{y}_{k-1}} \tag{3.35}$$

is the scaling factor that attempts to estimate the size of the true Hessian matrix along the most recent search direction. This choice helps to ensure that the search direction \mathbf{p}_k is well scaled, and as a result the step length $\alpha_k = 1$ is accepted in most iterations.

3.5 Adjoint approach for efficient calculation of the misfit gradient

In the method discussed above one has to calculate the gradient of the penalty function $\nabla \phi = \nabla \phi_d + \lambda \nabla \phi_s$. As for regularization term introduced by eq. (3.20), an evaluation of $\nabla \phi_s$ leads immediately to

$$\nabla \phi_s = 2W^T W \mathbf{m}. \tag{3.36}$$

For the computation of $\nabla \phi_d$ we adopt the adjoint approach (cf. Dorn et al., 1999; Newman and Alumbaugh, 2000; Rodi and Mackie, 2000; Kelbert et al., 2008; Avdeev and Avdeeva, 2009, among others), which allows for calculating the gradient with only a few forward calculations. Pankratov and Kuvshinov (2010) presented a general formalism for the efficient calculation of the derivatives of EM frequency-domain responses and the derivatives of the misfit with respect to variations of 3-D isotropic/anisotropic conductivity. Using this formalism one can readily obtain appropriate formulae for the specific sounding methods. Below we overview this approach to the calculation of the gradient of our misfit function.

3.5.1 Definition of the operators G_{3D}^{ej} and G_{3D}^{eh}

Let us again consider Maxwell's equations

$$\nabla \times \mathbf{H} = \sigma \mathbf{E} + \mathbf{j}^{ext}, \tag{3.37a}$$

$$\nabla \times \mathbf{E} = i\omega \mu_0 \mathbf{H}, \tag{3.37b}$$

and define the operator G_{3D}^{ej} as

$$\mathbf{E} = G_{3D}^{ej}(\mathbf{j}^{ext}) \Leftrightarrow \begin{cases} \nabla \times \mathbf{H} = \sigma \mathbf{E} + \mathbf{j}^{ext}, \\ \nabla \times \mathbf{E} = i\omega\mu_0 \mathbf{H}, \\ \mathbf{E}, \mathbf{H} \rightarrow 0 \text{ as } \mathbf{r} \rightarrow \infty, \end{cases} \quad (3.38)$$

where

$$\mathbf{j}^{ext} = \mathbf{j}^{ext}(r, \vartheta, \varphi, \omega), \quad (3.39)$$

is the given impressed current, and $\sigma \equiv \sigma(r, \vartheta, \varphi)$ is the given three-dimensional (3-D) conductivity distribution in the Earth's model. The operator $G_{3D}^{ej}(\cdot)$ acts on the input distribution of electric current \mathbf{j}^{ext} and yields the electric field due to this current.

Further we define the operator G_{3D}^{eh}

$$\mathbf{E} = G_{3D}^{eh}(\mathbf{h}^{ext}) \Leftrightarrow \begin{cases} \nabla \times \mathbf{H} = \sigma \mathbf{E}, \\ \nabla \times \mathbf{E} = i\omega\mu_0 \mathbf{H} + \mathbf{h}^{ext}, \\ \mathbf{E}, \mathbf{H} \rightarrow 0 \text{ as } \mathbf{r} \rightarrow \infty, \end{cases} \quad (3.40)$$

which calculates the electric field $G_{3D}^{eh}(\mathbf{h}^{ext})$ provided that the input \mathbf{h}^{ext} has the spatial distribution

$$\mathbf{h}^{ext} = \mathbf{h}^{ext}(r, \vartheta, \varphi, \omega), \quad (3.41)$$

of the imposed magnetic dipoles. G_{3D}^{ej} and G_{3D}^{eh} are linked through

$$G_{3D}^{eh}(\mathbf{h}^{ext}) = G_{3D}^{ej}\left(\nabla \times \left(\frac{\mathbf{h}^{ext}}{i\omega\mu_0}\right)\right). \quad (3.42)$$

3.5.2 Derivatives of the C-responses

Since it is most natural to relate the 3-D conductivity distribution to the geographic coordinate system, all (forward and inverse) calculations are performed in geographic coordinates. Bearing this in mind H_ϑ in eq. (3.14) can be rewritten as

$$H_\vartheta(\mathbf{r}_a, \omega) = \cos \alpha(\mathbf{r}_a) H_\vartheta^g(\mathbf{r}_a, \omega) - \sin \alpha(\mathbf{r}_a) H_\varphi^g(\mathbf{r}_a, \omega), \quad (3.43)$$

where H_ϑ^g and H_φ^g are the components directed toward geographic south and east, respectively, and $\alpha(\mathbf{r}_a)$ is the angle between directions to geographic and geomagnetic north at observation site \mathbf{r}_a . Then the C-responses can be written as

$$C_a(\omega) = \left(K \frac{H_r}{\cos \alpha H_\vartheta^g - \sin \alpha H_\varphi^g} \right) \Big|_{\mathbf{r}=\mathbf{r}_a}, \quad (3.44)$$

where $K = \frac{a}{2} \tan \vartheta$. By denoting

$$U = \cos \alpha H_{\theta}^g - \sin \alpha H_{\varphi}^g, \quad (3.45)$$

we have

$$C_a(\omega) = \left(K \frac{H_r}{U} \right) \Big|_{\mathbf{r}=\mathbf{r}_a}. \quad (3.46)$$

Thus we can write

$$dC_a = \left(K \left(\frac{\partial C}{\partial U} dU + \frac{\partial C}{\partial H_r} dH_r \right) \right) \Big|_{\mathbf{r}=\mathbf{r}_a} = \left(K \left(-\frac{H_r}{U^2} dU + \frac{1}{U} dH_r \right) \right) \Big|_{\mathbf{r}=\mathbf{r}_a}. \quad (3.47)$$

Let us consider the calculation of $\frac{1}{U} dH_r$:

$$\begin{aligned} \left(\frac{1}{U} dH_r \right) \Big|_{\mathbf{r}=\mathbf{r}_a} &= \left(\frac{1}{U} d \left[\frac{\nabla \times \mathbf{E}}{i\omega\mu_0} \right]_r \right) \Big|_{\mathbf{r}=\mathbf{r}_a} = \left(\frac{1}{i\omega\mu_0} \frac{1}{U} [\nabla \times d\mathbf{E}]_r \right) \Big|_{\mathbf{r}=\mathbf{r}_a} = \\ &= \left(\frac{1}{i\omega\mu_0} \frac{1}{U} [\nabla \times (G_{3D}^{ej} (G_{3D}^{ej} (\mathbf{j}^{ext}) d\sigma))]_r \right) \Big|_{\mathbf{r}=\mathbf{r}_a} = \\ &= \left\langle \frac{1}{i\omega\mu_0} \frac{1}{U} \mathbf{e}_r \delta_a, \nabla \times (G_{3D}^{ej} (G_{3D}^{ej} (\mathbf{j}^{ext}) d\sigma)) \right\rangle, \end{aligned} \quad (3.48)$$

where $\delta_a = \delta(\mathbf{r} - \mathbf{r}_a)$ is Dirac's delta function, $[\mathbf{v}]_r$ denotes the r -component of a vector \mathbf{v} , and pair in angle brackets $\langle \cdot, \cdot \rangle$ denotes complex bilinear pairing

$$\langle \mathbf{a}, \mathbf{b} \rangle = \int_{R^3} (a_r(\mathbf{r})b_r(\mathbf{r}) + a_{\theta}(\mathbf{r})b_{\theta}(\mathbf{r}) + a_{\varphi}(\mathbf{r})b_{\varphi}(\mathbf{r}))r^2 \sin \vartheta d\vartheta d\varphi. \quad (3.49)$$

Note that in eq. (3.48) we used the following expression for differential of electric field with respect to variation of conductivity σ

$$d\mathbf{E} = G_{3D}^{ej} (G_{3D}^{ej} (\mathbf{j}^{ext}) d\sigma). \quad (3.50)$$

Let us show how we derive this equation. We consider Maxwell's equations for $\sigma + \Delta\sigma$ and denote their solutions as $\mathbf{H} + \Delta\mathbf{H}$ and $\mathbf{E} + \Delta\mathbf{E}$

$$\nabla \times (\mathbf{H} + \Delta\mathbf{H}) = (\sigma + \Delta\sigma)(\mathbf{E} + \Delta\mathbf{E}) + \mathbf{j}^{ext}, \quad (3.51a)$$

$$\nabla \times (\mathbf{E} + \Delta\mathbf{E}) = i\omega\mu_0(\mathbf{H} + \Delta\mathbf{H}). \quad (3.51b)$$

By subtracting eq. (3.37) from eq. (3.51) we obtain

$$\nabla \times \Delta\mathbf{H} = (\sigma + \Delta\sigma)\Delta\mathbf{E} + \Delta\sigma\mathbf{E}, \quad (3.52a)$$

$$\nabla \times \Delta\mathbf{E} = i\omega\mu_0\Delta\mathbf{H}. \quad (3.52b)$$

But we notice, from eq. (3.38), that

$$\Delta\sigma\mathbf{E} = G_{3D}^{ej}(\mathbf{j}^{ext})\Delta\sigma. \quad (3.53)$$

By tending $\Delta\sigma$ to zero we arrive at the following equation

$$\nabla \times d\mathbf{H} = \sigma d\mathbf{E} + G_{3D}^{ej}(\mathbf{j}^{ext})d\sigma, \quad (3.54a)$$

$$\nabla \times d\mathbf{E} = i\omega\mu_0 d\mathbf{H}. \quad (3.54b)$$

By comparing eq. (3.54) with eq. (3.38) we obtain the desired eq. (3.50). Let us continue with eq. (3.48). Since the $\nabla \times$ is a self-adjoint operator, i.e.

$$\langle \nabla \times \mathbf{a}, \mathbf{b} \rangle = \langle \mathbf{a}, \nabla \times \mathbf{b} \rangle, \quad (3.55)$$

for any fields \mathbf{a} and \mathbf{b} , we obtain

$$\left(\frac{1}{U} dH_r \right) \Big|_a = \left\langle \nabla \times \left(\frac{1}{i\omega\mu_0} \frac{1}{U} \mathbf{e}_r \delta_a \right), G_{3D}^{ej}(G_{3D}^{ej}(\mathbf{j}^{ext})d\sigma) \right\rangle. \quad (3.56)$$

Now we will show that G_{3D}^{ej} is also self-adjoint operator

$$\langle G_{3D}^{ej}(\mathbf{a}), \mathbf{b} \rangle = \langle \mathbf{a}, G_{3D}^{ej}(\mathbf{b}) \rangle. \quad (3.57)$$

First let us obtain, from Maxwell's equations (3.37), the equation for electric field. By substituting the second equation of (3.37) into the first equation we have

$$\nabla \times \left(\frac{\nabla \times \mathbf{E}}{i\omega\mu_0} \right) - \sigma\mathbf{E} = \mathbf{j}^{ext}. \quad (3.58)$$

Let $\mathbf{A} = G_{3D}^{ej}(\mathbf{a})$ and $\mathbf{B} = G_{3D}^{ej}(\mathbf{b})$, i.e.

$$\nabla \times \left(\frac{\nabla \times \mathbf{A}}{i\omega\mu_0} \right) - \sigma\mathbf{A} = \mathbf{a}, \quad (3.59)$$

and

$$\nabla \times \left(\frac{\nabla \times \mathbf{B}}{i\omega\mu_0} \right) - \sigma\mathbf{B} = \mathbf{b}. \quad (3.60)$$

Using the reciprocity of $\nabla \times$ operator we obtain the following sequence of equalities

$$\begin{aligned}\langle G_{3D}^{ej}(\mathbf{a}), \mathbf{b} \rangle &= \langle \mathbf{A}, \nabla \times \left(\frac{\nabla \times \mathbf{B}}{i\omega\mu_0} \right) - \sigma \mathbf{B} \rangle = \langle \mathbf{A}, \nabla \times \left(\frac{\nabla \times \mathbf{B}}{i\omega\mu_0} \right) \rangle - \\ &\langle \mathbf{A}, \sigma \mathbf{B} \rangle = \langle \nabla \times \mathbf{A}, \frac{\nabla \times \mathbf{B}}{i\omega\mu_0} \rangle - \langle \sigma \mathbf{A}, \mathbf{B} \rangle = \langle \nabla \times \left(\frac{\nabla \times \mathbf{B}}{i\omega\mu_0} \right), \mathbf{B} \rangle - \\ &\langle \sigma \mathbf{A}, \mathbf{B} \rangle = \langle \nabla \times \left(\frac{\nabla \times \mathbf{A}}{i\omega\mu_0} \right) - \sigma \mathbf{A}, \mathbf{B} \rangle = \langle \mathbf{a}, G_{3D}^{ej}(\mathbf{b}) \rangle,\end{aligned}\quad (3.61)$$

which proves eq. (3.57). Using eq. (3.57) we obtain

$$\left(\frac{1}{U} dH_r \right) \Big|_{\mathbf{r}=\mathbf{r}_a} = \left\langle G_{3D}^{ej} \left(\nabla \times \left(\frac{1}{i\omega\mu_0} \frac{1}{U} \mathbf{e}_r \delta_a \right) \right), G_{3D}^{ej}(\mathbf{j}^{ext}) d\sigma \right\rangle. \quad (3.62)$$

Further using the link between G_{3D}^{ej} and G_{3D}^{eh} , described by eq. (3.42) we arrive to the final expression for $\left(\frac{1}{U} dH_r \right) \Big|_{\mathbf{r}=\mathbf{r}_a}$

$$\left(\frac{1}{U} dH_r \right) \Big|_{\mathbf{r}=\mathbf{r}_a} = \left\langle G_{3D}^{eh} \left(\frac{1}{U} \mathbf{e}_r \delta_a \right), G_{3D}^{ej}(\mathbf{j}^{ext}) d\sigma \right\rangle. \quad (3.63)$$

In a similar way as in eqs (3.47-3.63) we calculate the first term in right-hand side of eq. (3.47)

$$\begin{aligned}\left(\frac{1}{U^2} dU \right) \Big|_{\mathbf{r}=\mathbf{r}_a} &= \left(\frac{1}{U^2} d(\cos \alpha H_\vartheta^g - \sin \alpha H_\varphi^g) \right) \Big|_{\mathbf{r}=\mathbf{r}_a} = \left(\frac{1}{U^2} d(\cos \alpha H_\vartheta^g - \sin \alpha H_\varphi^g) \right) \Big|_{\mathbf{r}=\mathbf{r}_a} = \\ &= \left(\left[\frac{1}{U^2} d(\cos \alpha H_\vartheta^g) \right] - \left[\frac{1}{U^2} d(\sin \alpha H_\varphi^g) \right] \right) \Big|_{\mathbf{r}=\mathbf{r}_a} = \\ &= \left(\frac{\cos \alpha}{i\omega\mu_0 U^2} [\nabla \times d\mathbf{E}]_\vartheta - \frac{\sin \alpha}{i\omega\mu_0 U^2} [\nabla \times d\mathbf{E}]_\varphi \right) \Big|_{\mathbf{r}=\mathbf{r}_a} = \\ &= \left\langle \frac{1}{i\omega\mu_0} \frac{\cos \alpha}{U^2} \mathbf{e}_\vartheta \delta_a, \nabla \times (G_{3D}^{ej} (G_{3D}^{ej}(\mathbf{j}^{ext}) d\sigma)) \right\rangle - \\ &\quad - \left\langle \frac{1}{i\omega\mu_0} \frac{\sin \alpha}{U^2} \mathbf{e}_\varphi \delta_a, \nabla \times (G_{3D}^{ej} (G_{3D}^{ej}(\mathbf{j}^{ext}) d\sigma)) \right\rangle = \\ &= \left\langle G_{3D}^{eh} \left(\frac{1}{U^2} (\cos \alpha \mathbf{e}_\vartheta - \sin \alpha \mathbf{e}_\varphi) \delta_a \right), G_{3D}^{ej}(\mathbf{j}^{ext}) d\sigma \right\rangle.\end{aligned}\quad (3.64)$$

Here $[\mathbf{v}]_\vartheta$ and $[\mathbf{v}]_\varphi$ denote the ϑ - and the φ - components of a vector \mathbf{v} respectively. Substituting eqs (3.63)-(3.64) into eq. (3.47) we obtain the desired differential, dC_a , with respect to variation of σ

$$dC_a = \left\langle G_{3D}^{eh} \left(\left(-\frac{KH_r}{U^2} (\cos \alpha \mathbf{e}_\vartheta - \sin \alpha \mathbf{e}_\varphi) + \frac{K}{U} \mathbf{e}_r \right) \delta_a \right), G_{3D}^{ej}(\mathbf{j}^{ext}) d\sigma \right\rangle. \quad (3.65)$$

3.5.3 Gradient of the data misfit

The differential of the misfit function defined by eq. (3.17) with respect to variation of σ can be written in the form

$$\begin{aligned} d\phi_d &= d \sum_{\omega \in Freqs} \sum_{\mathbf{r}_a \in Sites} \left| \frac{C^{mod}(\mathbf{r}_a, \omega, \mathbf{m}) - C^{exp}(\mathbf{r}_a, \omega)}{\delta C^{exp}(\mathbf{r}_a, \omega)} \right|^2 = \\ &= 2 \Re \left\{ \sum_{\omega \in Freqs} \sum_{\mathbf{r}_a \in Sites} \frac{(C^{mod}(\mathbf{r}_a, \omega, \mathbf{m}) - C^{exp}(\mathbf{r}_a, \omega))^*}{(\delta C^{exp}(\mathbf{r}_a, \omega))^2} dC_a \right\}, \end{aligned} \quad (3.66)$$

where \Re stands for the real part of the expression in brackets and the sign “*” stands for complex conjugation. Deriving eq. (3.66) we used the equality

$$d|B|^2 = d(BB^*) = B^*dB + BdB^* = B^*dB + (B^*dB)^* = 2\Re(B^*dB), \quad (3.67)$$

which is true for any complex-valued variable B . Substituting eq. (3.65) into the eq. (3.66) we obtain

$$d\phi_d = 2 \Re \left\{ \sum_{\omega \in Freqs} \langle G_{3D}^{eh}(\mathbf{h}^{ext}), G_{3D}^{ej}(\mathbf{j}^{ext}) d\sigma \rangle \right\}, \quad (3.68)$$

where adjoint, “magnetic”, source is given by

$$\mathbf{h}(\mathbf{r}) = \sum_{\mathbf{r}_a \in Sites} \mathbf{M}(\mathbf{r}_a) \delta(\mathbf{r} - \mathbf{r}_a), \quad (3.69)$$

with

$$\mathbf{M}(\mathbf{r}) = K \frac{[C^{mod}(\mathbf{r}, \mathbf{m}) - C^{exp}(\mathbf{r})]^*}{[\delta C^{exp}(\mathbf{r})]^2} \left\{ \frac{1}{U(\mathbf{r})} \mathbf{e}_r - \frac{H_r(\mathbf{r})}{U^2(\mathbf{r})} [\cos \alpha(\mathbf{r}) \mathbf{e}_\theta - \sin \alpha(\mathbf{r}) \mathbf{e}_\phi] \right\}. \quad (3.70)$$

Thus the adjoint source is an array of magnetic dipoles located at observation sites, with the magnitudes determined via the residuals of the responses. Taking in mind our model parametrization we obtain the expressions for the partial derivatives $\frac{\partial \phi_d}{\partial m_l}$ in the form

$$\frac{\partial \phi_d}{\partial \sigma_l} = \frac{\partial \phi_d}{\partial \ln \sigma_l} \frac{\partial \ln \sigma_l}{\partial \sigma_l} \longrightarrow \frac{\partial \phi_d}{\partial m_l} = \frac{\partial \phi_d}{\partial \ln \sigma_l} = \sigma_l \frac{\partial \phi_d}{\partial \sigma_l}, \quad (3.71)$$

where

$$\frac{\partial \phi_d}{\partial \sigma_l} = 2 \Re \left\{ \sum_{\omega \in Freqs} \left(\int_{V_l} G_{3D}^{eh}(\mathbf{h}^{ext}) \cdot G_{3D}^{ej}(\mathbf{j}^{ext}) dv \right) \right\}. \quad (3.72)$$

Summing up, the individual entries of $\nabla \phi_d$ can be calculated as

$$\frac{\partial \phi_d}{\partial m_l} = \frac{1}{\sigma_l} \Re \left\{ \sum_{\omega \in Freqs} \int_{V_l} (E_r(\mathbf{r}') E_r^a(\mathbf{r}') + E_\theta(\mathbf{r}') E_\theta^a(\mathbf{r}') + E_\phi(\mathbf{r}') E_\phi^a(\mathbf{r}')) dv' \right\}, \quad (3.73)$$

where $V_l \in V^{inv}$, $l = 1, 2, \dots, N^{inv}$, \mathbf{E} is the "electric" solution of system of eqs (2.7) and \mathbf{E}^a is the electric solution of the following Maxwell's equations

$$\begin{aligned}\nabla \times \mathbf{H}^a(\mathbf{r}) &= \sigma(\mathbf{r})\mathbf{E}^a(\mathbf{r}), \\ \nabla \times \mathbf{E}^a(\mathbf{r}) &= i\omega\mu_0\mathbf{H}^a(\mathbf{r}) + \mathbf{h}(\mathbf{r}),\end{aligned}\tag{3.74}$$

where adjoint, "magnetic", source is determined as in eq. (3.69) (note again that all the fields and currents under discussion depend on frequency ω). These equations demonstrate the essence of the adjoint approach: in order to calculate the gradient of the misfit one needs to perform only one (per frequency) additional forward modeling with the excitation provided by the adjoint source. This forward modeling differs from that described in Chapter 2 in the following point: now we have to consider Maxwell's equations for the reference fields with the magnetic source

$$\begin{aligned}\nabla \times \mathbf{H}^{0,a}(\mathbf{r}) &= \sigma_0(r)\mathbf{E}^{0,a}(\mathbf{r}), \\ \nabla \times \mathbf{E}^{0,a}(\mathbf{r}) &= i\omega\mu_0\mathbf{H}^{0,a}(\mathbf{r}) + \mathbf{h}(\mathbf{r}).\end{aligned}\tag{3.75}$$

Then, if we are able to construct and calculate "magnetic-to-electric" fundamental solution (tensor Green's function) of eqs (3.75), G_{1D}^{eh} , then $\mathbf{E}^{0,a}$ can be represented via the following convolution integral

$$\mathbf{E}^{0,a}(\mathbf{r}) = \int_{V^{ext}} G_{1D}^{eh}(\mathbf{r}, \mathbf{r}') \mathbf{h}^{ext}(\mathbf{r}') dV'. \tag{3.76}$$

Substituting eq. (3.69) into eq. (3.76) we obtain for $\mathbf{E}^{0,a}$

$$\mathbf{E}^{0,a}(\mathbf{r}) = \sum_{\mathbf{r}_a \in Sites} G_{1D}^{eh}(\mathbf{r}, \mathbf{r}_a) \mathbf{M}(\mathbf{r}_a). \tag{3.77}$$

With $\mathbf{E}^{0,a}(\mathbf{r})$ at hand we can proceed exactly in the same way as we did in Chapter 2. A 3-D IE forward modeling solution which provides the misfit gradient can be summarized with the following steps

1. $G_{1D}^{ej}(\mathbf{r}, \mathbf{r}')$ and consequently $K(\mathbf{r}, \mathbf{r}')$ (2.20b) are calculated for $\mathbf{r}' \in V^{mod}$ and $\mathbf{r} \in V^{mod}$
2. $G_{1D}^{eh}(\mathbf{r}, \mathbf{r}_a)$ is calculated for $\mathbf{r}_a \in Sites$ and $\mathbf{r} \in V^{mod}$
3. $\mathbf{E}^{0,a}(\mathbf{r})$, $\mathbf{r} \in V^{mod}$ is calculated using eq. (3.77) with G_{1D}^{eh} obtained at step 2
4. $\mathbf{j}^{s,a}(\mathbf{r})$, $\mathbf{r} \in V^{mod}$ is calculated using eq. (2.13) and $\mathbf{E}^{0,a}$ obtained at step 3
5. $\chi_{0,a}(\mathbf{r})$, $\mathbf{r} \in V^{mod}$ is calculated using eq. (2.20c) with K obtained at step 1
6. The scattering equation (2.19) is solved on V^{mod} using CG method
7. $\mathbf{E}^{s,a}(\mathbf{r})$, $\mathbf{r} \in V^{mod}$ is calculated using eq. (2.20d) and $\mathbf{j}^{s,a}$ obtained at step 4
8. $\mathbf{E}^a(\mathbf{r})$, $\mathbf{r} \in V^{mod}$ is calculated as a sum of $\mathbf{E}^{s,a}$ and $\mathbf{E}^{0,a}$ obtained at steps 3 and 7
9. $\mathbf{E}(\mathbf{r})$ is calculated from IE-C solution (see Chapter 2)

10. Misfit gradient is calculated using eq. (3.73) with \mathbf{E}^a and \mathbf{E} obtained at steps 8 and 9

Henceforce, this scheme will be referred as the "IE-G" solution. In Chapter 2.4 we presented the derivation of G_{1D}^{ej} and G_{1D}^{hj} . In the next section we will present the derivation of G_{1D}^{eh} and

$$G_{1D}^{hh}.$$

3.5.4 Derivation of explicit forms for Green's tensor for a magnetic dipole source

In this section we derive the explicit forms of 3×3 tensor "magnetic-to-electric", G_{1D}^{eh} , and "magnetic-to-magnetic", G_{1D}^{hh} , Green's functions. These tensor functions allow for calculating magnetic and electric fields that obey Maxwell's equations

$$\nabla \times \mathbf{H}(\mathbf{r}) = \sigma_0(r)\mathbf{E}(\mathbf{r}), \quad (3.78a)$$

$$\nabla \times \mathbf{E}(\mathbf{r}) = i\omega\mu_0\mathbf{H}(\mathbf{r}) + \mathbf{h}(\mathbf{r}), \quad (3.78b)$$

If we can construct and calculate fundamental solutions (tensor Green's functions) of eqs (2.8), G_{1D}^{ej} and G_{1D}^{hj} , then \mathbf{H} and \mathbf{E} can be calculated via convolution integrals

$$\mathbf{E}(\mathbf{r}) = \int_{V^{ext}} G_{1D}^{eh}(\mathbf{r}, \mathbf{r}') \mathbf{h}(\mathbf{r}') dv', \quad (3.79)$$

$$\mathbf{H}(\mathbf{r}) = \int_{V^{ext}} G_{1D}^{hh}(\mathbf{r}, \mathbf{r}') \mathbf{h}(\mathbf{r}') dv'. \quad (3.80)$$

Here

$$G_{1D}^{eh(hh)} = \mathbf{e}_\vartheta g_{\vartheta\vartheta'}^{eh(hh)} \mathbf{e}_{\vartheta'} + \mathbf{e}_\vartheta g_{\vartheta\varphi'}^{eh(hh)} \mathbf{e}_{\varphi'} + \dots + \mathbf{e}_r g_{rr'}^{eh(hh)} \mathbf{e}_{r'}. \quad (3.81)$$

We then decompose the electric $\mathbf{E}(\mathbf{r})$ and magnetic $\mathbf{H}(\mathbf{r})$ fields via spherical functions defined by eqs (2.32) in the same way as we did in Chapter 2

$$\mathbf{E}_\tau(r, \vartheta, \varphi) = \frac{1}{r} \sum_{n,m} \left\{ \varepsilon_{nm}^t(r) \mathbf{S}_{nm}^t(\vartheta, \varphi) + \varepsilon_{nm}^p(r) \mathbf{S}_{nm}^p(\vartheta, \varphi) \right\}, \quad (3.82a)$$

$$E_r(r, \vartheta, \varphi) \mathbf{e}_r = \frac{1}{r} \sum_{n,m} \varepsilon_{nm}^r(r) \mathbf{S}_{nm}^r, \quad (3.82b)$$

and

$$\mathbf{e}_r \times \mathbf{H}_\tau(r, \vartheta, \varphi) = \frac{1}{r} \sum_{n,m} \left\{ h_{nm}^t(r) \mathbf{S}_{nm}^t(\vartheta, \varphi) + h_{nm}^p(r) \mathbf{S}_{nm}^p(\vartheta, \varphi) \right\}, \quad (3.83a)$$

$$H_r(r, \vartheta, \varphi) \mathbf{e}_r = \frac{1}{r} \sum_{n,m} h_{nm}^r(r) \mathbf{S}_{nm}^r(\vartheta, \varphi). \quad (3.83b)$$

Similarly to magnetic field we decompose the magnetic source as

$$\mathbf{e}_r \times \mathbf{h}_\tau^{ext}(r, \vartheta, \varphi) = \frac{1}{r} \sum_{n,m} \left\{ q_{nm}^t(r) \mathbf{S}_{nm}^t(\vartheta, \varphi) + q_{nm}^p(r) \mathbf{S}_{nm}^p(\vartheta, \varphi) \right\}, \quad (3.84)$$

$$h_r^{ext}(r, \vartheta, \varphi) \mathbf{e}_r = \frac{1}{r} \sum_{n=0}^{\infty} \sum_{m=-n}^n q_{nm}^r(r) \mathbf{S}_{nm}^r(\vartheta, \varphi). \quad (3.85)$$

We can rewrite eq. (3.83a) and eq. (3.84) as

$$\mathbf{H}_\tau(r, \vartheta, \varphi) = \frac{1}{r} \sum_{n,m} \{-h_{nm}^p(r) \mathbf{S}_{nm}^t(\vartheta, \varphi) + h_{nm}^t(r) \mathbf{S}_{nm}^p(\vartheta, \varphi)\}, \quad (3.86)$$

$$\mathbf{h}_\tau^{ext}(r, \vartheta, \varphi) = \frac{1}{r} \sum_{n,m} \{-q_{nm}^p(r) \mathbf{S}_{nm}^t(\vartheta, \varphi) + q_{nm}^t(r) \mathbf{S}_{nm}^p(\vartheta, \varphi)\}. \quad (3.87)$$

Substituting eqs (3.82)-(3.85) into Maxwell's equations (3.78) and gathering terms involving functions \mathbf{S}_{nm}^t and \mathbf{S}_{nm}^p , we obtain the systems of equations

$$\begin{cases} \partial_r \varepsilon_{nm}^t &= -i\omega\mu_0 h_{nm}^t - q_{nm}^t, \\ \partial_r h_{nm}^t &= \varepsilon_{nm}^t \left(\sigma_0 - \frac{n(n+1)}{r^2 i\omega\mu_0} \right) - \frac{\sqrt{n(n+1)}}{r i\omega\mu_0} q_{nm}^r, \end{cases} \quad (3.88)$$

$$\begin{cases} \partial_r \varepsilon_{nm}^p &= h_{nm}^p \left(\frac{n(n+1)}{r^2 \sigma_0} - i\omega\mu_0 \right) - q_{nm}^p, \\ \partial_r h_{nm}^p &= \sigma_0 \varepsilon_{nm}^p, \end{cases} \quad (3.89)$$

$$\begin{cases} \sigma_0 \varepsilon_{nm}^r &= \frac{h_{nm}^p \sqrt{n(n+1)}}{r}, \\ i\omega\mu_0 h_{nm}^r &= -\frac{\varepsilon_{nm}^t \sqrt{n(n+1)}}{r} - q_{nm}^r, \end{cases} \quad (3.90)$$

where $\varepsilon_{nm}^{r(t,p)} = \varepsilon_{nm}^{r(t,p)}(r)$, $h_{nm}^{r(t,p)} = h_{nm}^{r(t,p)}(r)$, $q_{nm}^{r(t,p)} = q_{nm}^{r(t,p)}(r)$ and $\sigma_0 = \sigma_0(r)$. One can see that from eq. (3.88) it follows that $q_{00}^r(r) = 0$ and further from eq. (3.90) – that $\varepsilon_{00}^r(r) = 0$ and $h_{00}^r(r) = 0$. This means that the $n = 0$ terms are equal to zero in eqs (3.82b), (3.83b) and (3.85).

Systems of eqs (3.88) and (3.89) can be rewritten in a same generic form as in eq. (2.39)

$$\begin{cases} \partial_r \varepsilon(r) &= p(r)h(r) + f_h(r), \\ \partial_r h(r) &= q\varepsilon(r) + f_\varepsilon(r), \end{cases} \quad (3.91)$$

where

$$\begin{aligned} \varepsilon(r) &= \varepsilon_{nm}^t, & h(r) &= h_{nm}^t, \\ p(r) &= -i\omega\mu_0, & q(r) &= \sigma_0 - \frac{n(n+1)}{r^2 i\omega\mu_0}, \\ f_h(r) &= -q_{nm}^t, & f_\varepsilon(r) &= -\frac{\sqrt{n(n+1)}}{r i\omega\mu_0} q_{nm}^r, \end{aligned} \quad (3.92)$$

for system (3.88) and

$$\begin{aligned} \varepsilon(r) &= \varepsilon_{nm}^p, & h(r) &= h_{nm}^p, \\ p(r) &= \frac{n(n+1)}{r^2 \sigma_0} - i\omega\mu_0, & q(r) &= \sigma_0, \\ f_h(r) &= -q_{nm}^p, & f_\varepsilon(r) &= 0, \end{aligned} \quad (3.93)$$

for system of eqs (3.89). In a similar way like in eqs (2.42)-(2.49) we write expressions

$$\varepsilon(r) = \int_0^\infty G(r, r') f_\varepsilon(r') dr' - \int_0^\infty \beta G(r, r') f_h(r') dr', \quad (3.94)$$

and

$$h(r) = \int \alpha G f_\varepsilon(r') dr' - \int \alpha \beta G f_h(r') dr', \quad (3.95)$$

where $\beta(n, r, r') = \frac{\partial_r G(r, r')}{p(r') G(r, r')}$ and $\alpha(n, r, r') = \beta(n, r', r)$.

Substituting further eq. (3.92) and eq. (3.93) into eq. (3.94) and eq. (3.95) we express coefficients $\varepsilon_{nm}^t, \varepsilon_{nm}^p, h_{nm}^t, h_{nm}^p$ via coefficients $q_{nm}^t, q_{nm}^p, q_{nm}^r$

$$\varepsilon_{nm}^t(r) = - \int_0^\infty G^t \frac{\sqrt{n(n+1)}}{r' i \omega \mu_0} q_{nm}^r(r') dr' + \int_0^\infty \beta^t G^t q_{nm}^t(r') dr', \quad (3.96)$$

$$\varepsilon_{nm}^p(r) = \int_0^\infty \beta^p G^p q_{nm}^p(r') dr', \quad (3.97)$$

$$h_{nm}^t(r) = - \int_0^\infty \alpha^t G^t \frac{\sqrt{n(n+1)}}{r' i \omega \mu_0} q_{nm}^r(r') dr' + \int_0^\infty \alpha^t \beta^t G^t q_{nm}^t(r') dr', \quad (3.98)$$

$$h_{nm}^p(r) = \int_0^\infty \alpha^p \beta^p G^p q_{nm}^p(r') dr', \quad (3.99)$$

where $G^{t(p)} \equiv G^{t(p)}(n, r, r')$, $\alpha^{t(p)} \equiv \alpha^{t(p)}(n, r, r')$ and $\beta^{t(p)} \equiv \beta^{t(p)}(n, r, r')$. Then, using decompositions (3.84)-(3.85), the coefficients $q_{nm}^t(r')$, $q_{nm}^p(r')$ and $q_{nm}^r(r')$ are written as

$$\begin{aligned} q_{nm}^t(r') &= \frac{r'}{\|S_n^m\|^2 \sqrt{n(n+1)}} \int_\Omega \nabla'_\perp \cdot (\mathbf{e}_{r'} \times \mathbf{e}_{r'} \times \mathbf{h}_\tau) \widetilde{S}_n^m d\Omega' = \\ &= - \frac{r'}{\|S_n^m\|^2 \sqrt{n(n+1)}} \int_\Omega \nabla'_\perp \cdot \mathbf{h}_\tau \widetilde{S}_n^m d\Omega', \end{aligned} \quad (3.100)$$

$$\begin{aligned} q_{nm}^p(r') &= - \frac{r'}{\|S_n^m\|^2 \sqrt{n(n+1)}} \int_\Omega \nabla'_\perp \cdot (\mathbf{e}_{r'} \times \mathbf{h}_\tau) \widetilde{S}_n^m d\Omega' = \\ &= \frac{r'}{\|S_n^m\|^2 \sqrt{n(n+1)}} \int_\Omega (\mathbf{e}_{r'} \times \nabla'_\perp) \cdot \mathbf{h}_\tau \widetilde{S}_n^m d\Omega', \end{aligned} \quad (3.101)$$

$$q_{nm}^r(r') = \frac{r'}{\|S_n^m\|^2} \int_\Omega h_r \widetilde{S}_n^m d\Omega'. \quad (3.102)$$

While deriving eq. (3.100) and eq. (3.101) we used eqs (2.63)-(2.66). Substituting eqs (3.100)-(3.102) into eqs (3.96)-(3.99) and further eqs (3.96)-(3.99) into eqs (3.82) after some algebra we obtain

$$\begin{aligned} \mathbf{E}_\tau(r, \vartheta, \varphi) &= \frac{1}{r} \sum_{n,m} (\varepsilon_{nm}^t(r) \mathbf{S}_{nm}^t(\vartheta, \varphi) + \varepsilon_{nm}^p(r) \mathbf{S}_{nm}^p(\vartheta, \varphi)) = \\ &= \frac{1}{r} \sum_{n,m} \left\{ \left[\int_0^\infty G^t \frac{\beta^t}{\sqrt{n(n+1)}} q_{nm}^t(r') dr' - \int_0^\infty G^t \frac{\sqrt{n(n+1)}}{r' i \omega \mu_0} q_{nm}^r(r') dr' \right] \mathbf{S}_{nm}^t(\vartheta, \varphi) + \right. \\ &\quad \left. + \int_0^\infty \beta^p G^p q_{nm}^p(r') dr' \mathbf{S}_{nm}^p(\vartheta, \varphi) \right\}, \end{aligned} \quad (3.103)$$

$$\begin{aligned} E_r(r, \vartheta, \varphi) &= \frac{1}{r} \sum_{n,m} \varepsilon_{nm}^r(r) S_n^m(\vartheta, \varphi) = \frac{1}{r} \sum_{n,m} \frac{h_{nm}^p \sqrt{n(n+1)}}{\sigma_0 r} S_n^m(\vartheta, \varphi) = \\ &= \frac{1}{r} \sum_{n,m} \frac{\sqrt{n(n+1)}}{\sigma_0 r} \int_0^\infty \alpha^p \beta^p G^p q_{nm}^p(r') dr' S_n^m(\vartheta, \varphi). \end{aligned} \quad (3.104)$$

Then substituting eqs (3.100)-(3.102) into eqs (3.103)-(3.104) we obtain for the electric field, after rearranging the operations of integration and summation

$$E_r(r, \vartheta, \varphi) = \int_\Omega \int_0^\infty \left\{ (\mathbf{e}_{r'} \times \nabla'_\perp) P \left[\frac{\alpha^p \beta^p G^p r'}{\sigma_0 r^2} \right] \right\} \cdot \mathbf{h}_\tau dr' d\Omega', \quad (3.105)$$

$$\begin{aligned} \mathbf{E}_\tau(r, \vartheta, \varphi) &= \int_\Omega \int_0^\infty (\mathbf{e}_r \times \nabla'_\perp) \left\{ \nabla'_\perp P \left[\frac{r' \beta^t G^t}{r n(n+1)} \right] \cdot \mathbf{h}_\tau \right\} dr' d\Omega' - \\ &- \int_\Omega \int_0^\infty (\mathbf{e}_r \times \nabla'_\perp) \left\{ P \left[\frac{G^t}{r i \omega \mu_0} \right] h_r \right\} dr' d\Omega' - \\ &- \int_\Omega \int_0^\infty \nabla'_\perp \left\{ [(\mathbf{e}_{r'} \times \nabla'_\perp) P \left[\frac{r' \beta^p G^p}{r n(n+1)} \right]] \cdot \mathbf{h}_\tau \right\} dr' d\Omega', \end{aligned} \quad (3.106)$$

where $P[f]$ denotes the summation of series (see eq. (2.68)). In a similar way we obtain the expressions for the magnetic fields components

$$\begin{aligned} \mathbf{H}_\tau(r, \vartheta, \varphi) &= \frac{1}{r} \sum_{n,m} (-h_{nm}^p(r) \mathbf{S}_{nm}^t(\vartheta, \varphi) + h_{nm}^t(r) \mathbf{S}_{nm}^p(\vartheta, \varphi)) = \\ &= \frac{1}{r} \sum_{n,m} \left\{ - \int_0^\infty \alpha^p \beta^p G^p q_{nm}^p(r') dr' \mathbf{S}_{nm}^t(\vartheta, \varphi) - \right. \\ &\quad \left. - \left(\int_0^\infty \frac{\alpha^t G^t \sqrt{n(n+1)}}{r' i \omega \mu_0} q_{nm}^r(r') dr' - \int_0^\infty \alpha^t \beta^t G^t q_{nm}^t(r') dr' \right) \mathbf{S}_{nm}^p(\vartheta, \varphi) \right\}, \end{aligned} \quad (3.107)$$

and

$$\begin{aligned} H_r(r, \vartheta, \varphi) &= \frac{1}{r} \sum_{n,m} h_{nm}^r(r) S_n^m(\vartheta, \varphi) = \\ &= \frac{1}{r} \sum_{n,m} \left[-\frac{q_{nm}^r(r)}{i\omega\mu_0} - \frac{\varepsilon_{nm}^t(r) \sqrt{n(n+1)}}{i\omega\mu_0 r} \right] S_n^m(\vartheta, \varphi). \end{aligned} \quad (3.108)$$

Finally, substituting eqs (3.100)-(3.102) into eqs (3.107)-(3.108) after similar rearranging of the operations we obtain the expressions for magnetic field in the following form

$$\begin{aligned} \mathbf{H}_\tau(r, \vartheta, \varphi) &= \int_{\Omega} \int_0^\infty (\mathbf{e}_r \times \nabla_\perp) \{ (\mathbf{e}_{r'} \times \nabla'_\perp) P \left[\frac{r' \alpha^p \beta^p G^p}{rn(n+1)} \right] \cdot \mathbf{h}_\tau \} dr' d\Omega' - \\ &- \int_{\Omega} \int_0^\infty \nabla_\perp \{ P \left[\frac{\alpha^t G^t}{ri\omega\mu_0} \right] h_r \} dr' d\Omega' - \int_{\Omega} \int_0^\infty \nabla_\perp \{ \left[\nabla'_\perp P \left[\frac{r' \alpha^t \beta^t G^t}{rn(n+1)} \right] \right] \cdot \mathbf{h}_\tau \} dr' d\Omega', \end{aligned} \quad (3.109)$$

$$\begin{aligned} H_r(r, \vartheta, \varphi) &= -\frac{1}{i\omega\mu_0} h_r - \int_{\Omega} \int_0^\infty \nabla'_\perp P \left[\frac{r' \beta^t G^t}{r^2 i\omega\mu_0} \right] \cdot \mathbf{h}_\tau d\Omega' dr' - \\ &- \int_{\Omega} \int_0^\infty P \left[\frac{G^t n(n+1)}{\omega^2 \mu_0 r^2} \right] h_r d\Omega' dr'. \end{aligned} \quad (3.110)$$

Now from eqs (3.106)-(3.105) we write the expressions for elements $g_{\vartheta\vartheta'}^{eh}, g_{\vartheta\varphi'}^{eh}, \dots$

$$g_{\vartheta\vartheta'}^{eh} = -\frac{1}{\sin \vartheta} \partial_\varphi \partial_{\vartheta'} P \left[\frac{\beta^t G^t}{rr'n(n+1)} \right] + \frac{1}{\sin \vartheta'} \partial_\vartheta \partial_{\varphi'} P \left[\frac{\beta^p G^p}{rr'n(n+1)} \right], \quad (3.111a)$$

$$g_{\vartheta\varphi'}^{eh} = -\frac{1}{\sin \vartheta} \frac{1}{\sin \vartheta'} \partial_\varphi \partial_{\varphi'} P \left[\frac{\beta^t G^t}{rr'n(n+1)} \right] - \partial_\vartheta \partial_{\vartheta'} P \left[\frac{\beta^p G^p}{rr'n(n+1)} \right], \quad (3.111b)$$

$$g_{\vartheta r'}^{eh} = \frac{1}{\sin \vartheta} \partial_\varphi P \left[\frac{G^t}{r'^2 ri\omega\mu_0} \right], \quad (3.111c)$$

$$g_{\varphi\vartheta'}^{eh} = \partial_\vartheta \partial_{\vartheta'} P \left[\frac{\beta^t G^t}{rr'n(n+1)} \right] + \frac{1}{\sin \vartheta} \frac{1}{\sin \vartheta'} \partial_\varphi \partial_{\varphi'} P \left[\frac{\beta^p G^p}{rr'n(n+1)} \right], \quad (3.111d)$$

$$g_{\varphi\varphi'}^{eh} = \frac{1}{\sin \vartheta'} \partial_\vartheta \partial_{\varphi'} P \left[\frac{\beta^t G^t}{rr'n(n+1)} \right] - \frac{1}{\sin \vartheta} \partial_\varphi \partial_{\vartheta'} P \left[\frac{\beta^p G^p}{rr'n(n+1)} \right], \quad (3.111e)$$

$$g_{\varphi r'}^{eh} = -\partial_\vartheta P \left[\frac{G^t}{r'^2 ri\omega\mu_0} \right], \quad (3.111f)$$

$$g_{r\vartheta'}^{eh} = \frac{1}{\sin \vartheta'} \partial_{\varphi'} P \left[\frac{\alpha^p \beta^p G^p}{r^2 r' \sigma_0} \right], \quad (3.111g)$$

$$g_{r\varphi'}^{eh} = -\partial_{\vartheta'} P \left[\frac{\alpha^p \beta^p G^p}{r^2 r' \sigma_0} \right], \quad (3.111h)$$

$$g_{rr'}^{eh} = 0. \quad (3.111i)$$

Lastly from eqs (3.109) - (3.110) we obtain the expressions for elements $g_{\vartheta\vartheta'}^{hh}, g_{\vartheta\varphi'}^{hh}, \dots$

$$g_{\vartheta\vartheta'}^{hh} = \frac{1}{\sin \vartheta} \frac{1}{\sin \vartheta'} \partial_\varphi \partial_{\varphi'} P \left[\frac{\alpha^p \beta^p G^p}{rr'n(n+1)} \right] - \partial_\vartheta \partial_{\vartheta'} P \left[\frac{\alpha^t \beta^t G^t}{rr'n(n+1)} \right], \quad (3.112a)$$

$$g_{\vartheta\varphi'}^{hh} = -\frac{1}{\sin \vartheta} \partial_\varphi \partial_{\vartheta'} P \left[\frac{\alpha^p \beta^p G^p}{rr'n(n+1)} \right] - \frac{1}{\sin \vartheta'} \partial_\vartheta \partial_{\varphi'} P \left[\frac{\alpha^t \beta^t G^t}{rr'n(n+1)} \right], \quad (3.112b)$$

$$g_{\vartheta r'}^{hh} = -\partial_\vartheta P \left[\frac{\alpha^t G^t}{rr'^2 i \omega \mu_0} \right], \quad (3.112c)$$

$$g_{\varphi\vartheta'}^{hh} = -\frac{1}{\sin \vartheta'} \partial_\vartheta \partial_{\varphi'} P \left[\frac{\alpha^p \beta^p G^p}{rr'n(n+1)} \right] + \frac{1}{\sin \vartheta} \partial_\varphi \partial_{\vartheta'} P \left[\frac{\alpha^t \beta^t G^t}{rr'n(n+1)} \right], \quad (3.112d)$$

$$g_{\varphi\varphi'}^{hh} = \partial_\vartheta \partial_{\vartheta'} P \left[\frac{\alpha^p \beta^p G^p}{rr'n(n+1)} \right] - \frac{1}{\sin \vartheta} \frac{1}{\sin \vartheta'} \partial_\varphi \partial_{\varphi'} P \left[\frac{\alpha^t \beta^t G^t}{rr'n(n+1)} \right], \quad (3.112e)$$

$$g_{\varphi r'}^{hh} = -\frac{1}{\sin \vartheta} \partial_\varphi P \left[\frac{\alpha^t G^t}{rr'^2 i \omega \mu_0} \right], \quad (3.112f)$$

$$g_{r\vartheta'}^{hh} = -\partial_{\vartheta'} P \left[\frac{\beta^t G^t}{r^2 r' i \omega \mu_0} \right], \quad (3.112g)$$

$$g_{r\varphi'}^{hh} = \frac{1}{\sin \vartheta'} \partial_{\varphi'} P \left[\frac{\beta^t G^t}{r^2 r' i \omega \mu_0} \right], \quad (3.112h)$$

$$g_{rr'}^{hh} = -\frac{\delta(r-r')\delta(\vartheta-\vartheta')\delta(\varphi-\varphi')}{i\omega\mu_0 r'^2 \sin \vartheta} - P \left[\frac{G^t n(n+1)}{\omega\mu_0 r^2 r'^2} \right]. \quad (3.112i)$$

Note that for the misfit gradient calculations we need only Green's tensor G_{1D}^{eh} . The expressions for the elements of this tensor are presented for the first time, and therefore have to be tested. Final remark of this section is that the expressions for the elements of G_{1D}^{hh} are presented for completeness of the exposition.

3.5.5 Tests of calculation of Green's tensor G_{1D}^{eh}

For testing the calculation of elements of the Green's tensor G_{1D}^{eh} we consider a radially symmetric Earth model consisting of a 400 km thick upper layer of 0.004 S/m, a 100 km thick transition layer of 0.04 S/m, and an inner uniform sphere of 2 S/m. The left-hand plots of Fig. 3.4 present real (upper) and imaginary (lower) parts of southward component of the electric field at depth of 450 km, induced by radial magnetic dipole. The period of excitation is 1 day. The dipole is located at the equator on the surface of the Earth. For comparison, right-hand plots present the same component of electric field calculated by the IE Cartesian code of Avdeev et al. (2002). Note that we don't plot the eastward component since it has similar geometry (but rotated anticlockwise 90°) and similar amplitudes. Figs. 3.5 and 3.6 show in a similar manner the electric fields induced by southward and eastward directed magnetic dipoles. It is seen that the results for spherical and Cartesian cases as a whole agree very well, but some disagreement exists, most probably due to the different coordinate systems used.

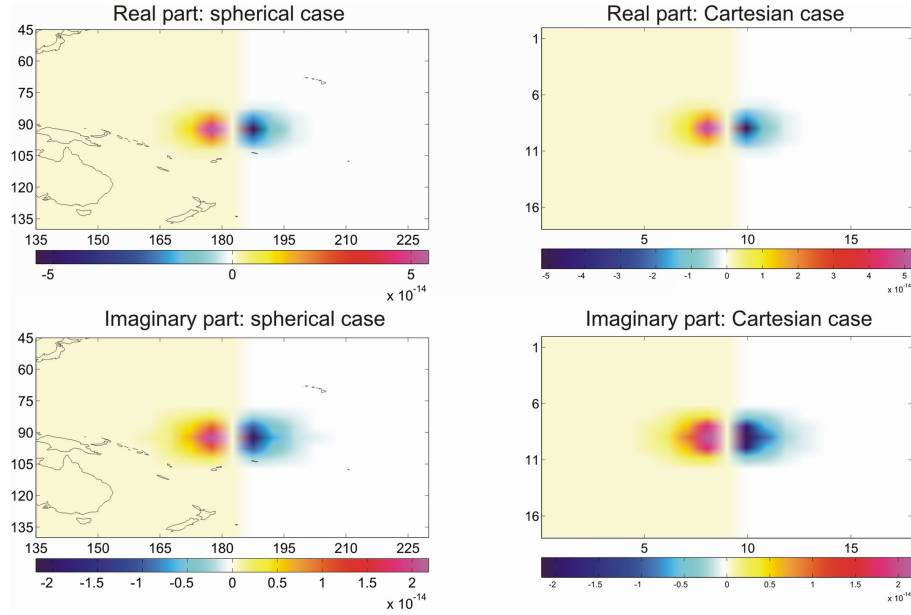


Figure 3.4: Comparison of results calculated in spherical (left-hand plots) and Cartesian (right-hand plots) geometries. Upper plots: real parts of southward component of electric field (V/m). Lower plots: imaginary parts (V/m). Excitation: radial magnetic dipole. See details in the text.

3.5.6 Numerical verification of the adjoint approach

To verify calculation of the misfit gradient using the adjoint approach we consider a 3-D model which consists of a deep-seated nonuniform layer located between 500 and 600 km depth. The conductivity distribution in the layer (in logarithmic scale) is shown in the upper left-hand plot of Fig. 3.10. The anomaly has a conductivity of 1 S/m, whereas the surrounding area has a conductivity of 0.04 S/m. Above the nonuniform layer (from top to the bottom) sits a resistive 100 km lithosphere of conductivity 0.00001 S/m, and a 400 km upper mantle of conductivity 0.01 S/m. Below the nonuniform layer the conductivity is fixed to be 2 S/m. The model is excited by a source which is described by the first zonal harmonic. The layer is discretized in 72×36 cells of horizontal size $5^\circ \times 5^\circ$ and radial size of 100 km. We calculate C -responses on the surface of the Earth on a mesh of $5^\circ \times 5^\circ$ at 25 periods from 3.9 to 109,6 days, with a geometric step of 1.14. The gradient is calculated for model vector \mathbf{m} with $\sigma_i = 0.04$ S/m for all i ($i = 1, 2, \dots, N^{inv}$). The right-hand plot of Fig. 3.7 presents (in the form of global maps) the data misfit gradient calculated by the adjoint approach. The left-hand plot shows the data misfit gradient calculated by numerical differentiation

$$\frac{\partial \phi_d}{\partial m_i} \approx \frac{\phi_d(m_i + \delta m_i) - \phi_d(m_i)}{\delta m_i}, \quad i = 1, 2, \dots, N^{inv}. \quad (3.113)$$

Note that in our calculations we take $\frac{\delta m_i}{m_i} = 0.01$ for all i . It is seen from the Fig. 3.7 that the gradients calculated by the adjoint scheme and by numerical differentiation agree remarkably well. Fig. 3.8 supports this conclusion in a more quantitative way. It presents the results

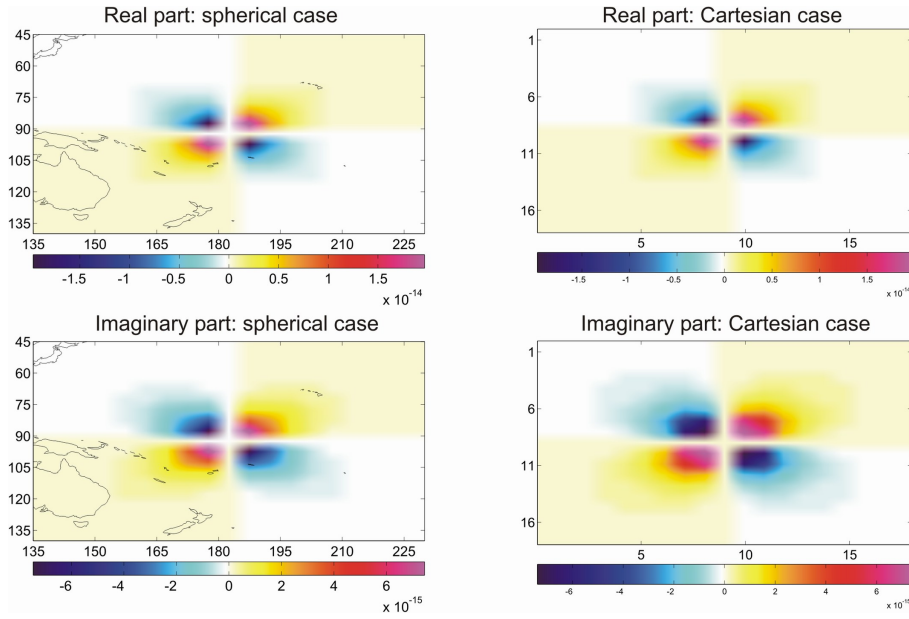


Figure 3.5: Comparison of results calculated in spherical (left-hand plots) and Cartesian (right-hand plots) geometries. Upper plots: real parts of southward component of electric field (V/m). Lower plots: imaginary parts (V/m). Excitation: southward magnetic dipole. See details in the text.

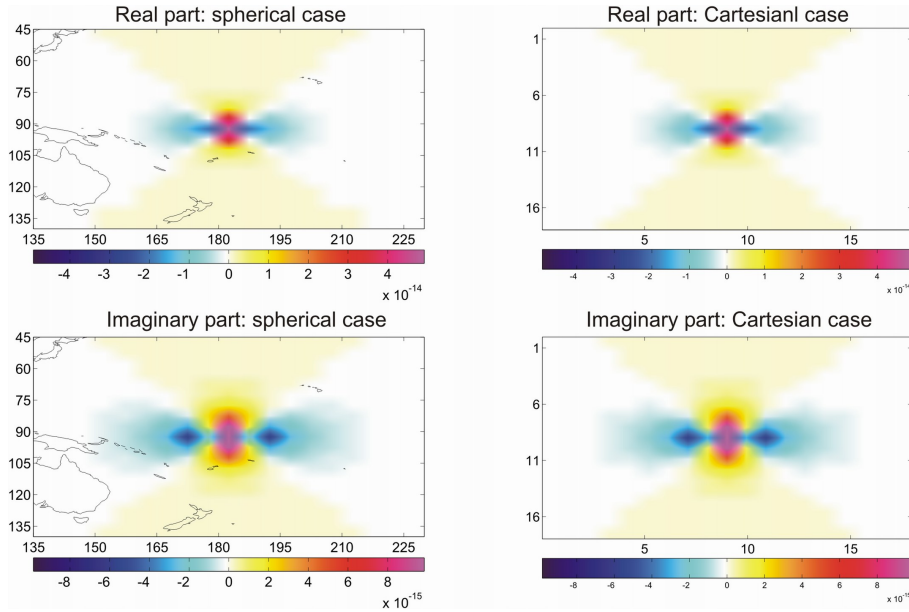


Figure 3.6: Comparison of results calculated in spherical (left-hand plots) and Cartesian (right-hand plots) geometries. Upper plots: real parts of southward component of electric field (V/m). Lower plots: imaginary parts (V/m). Excitation: eastward magnetic dipole. See details in the text.

of comparison along the profile that is depicted by a dashed line in right-hand plot of Fig. 3.7. Again, one can see almost perfect agreement between two approaches for calculating data misfit gradients. But numerical differentiation required $N^{inv} + 1 = 72 \times 36 + 1$ forward modelings (per frequency) whereas the adjoint procedure required only 2 forward modelings

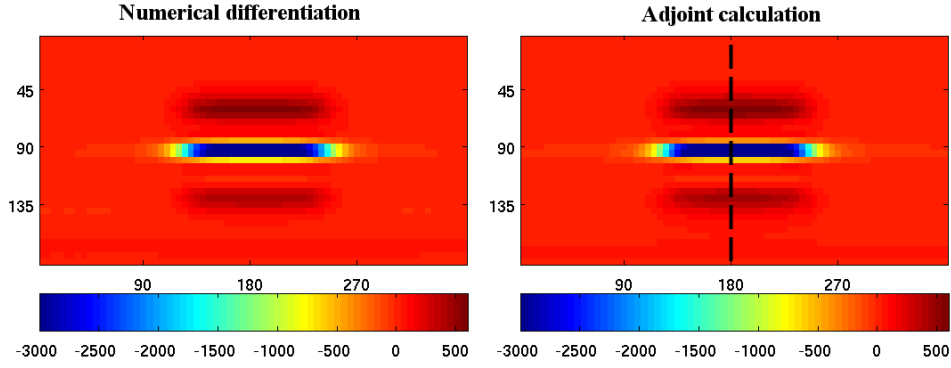


Figure 3.7: Comparison of data misfit gradients calculated by adjoint method (right-hand plot) and straightforward numerical differentiation (left-hand plot).

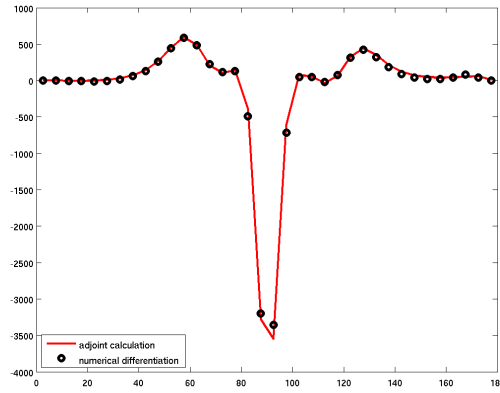


Figure 3.8: Comparison of the data misfit gradients along the profile depicted as a dashed line in right-hand plot of Fig. 3.7.

per frequency.

3.6 Optimization and numerical verification of the 3-D inverse solution

3.6.1 Optimization of the inverse solution

Massive 3-D forward calculations of the responses (cf. IE-C scheme of Section 2.3) and misfit gradients (cf. IE-G scheme of Section 3.5.3) during the 3-D inversion dictate that these calculations have to be performed as fast as possible. Since our forward numerical schemes are based on IE formulation we can take advantage of the IE approach and perform the most time-consuming part of the forward calculations – calculation of the Green’s tensors, G_{1D}^{ej} (G_{1D}^{ej} is the same in IE-C and IE-G schemes), G_{1D}^{hj} (needed in IE-C scheme) and G_{1D}^{eh} (needed in IE-G scheme) only once, prior to the inversion loop. The reason for this is that Green’s

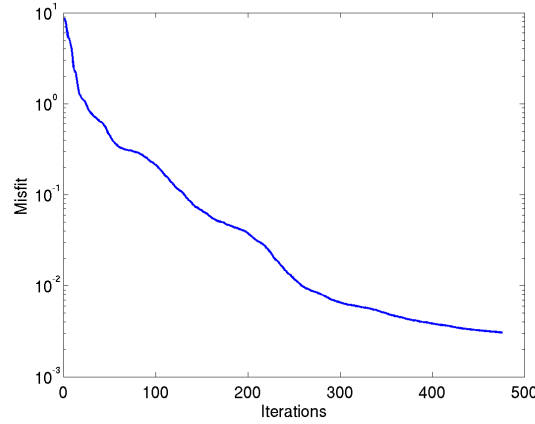


Figure 3.9: Normalized misfit with respect to the iterations. Synthetic modeling results.

tensors do not depend on the 3-D conductivity distribution in the model but only on a 1-D reference conductivity distribution, which remains the same during 3-D inversion. In order to illustrate the gain in efficiency by using this separation scheme we provide below the CPU times (on a single processor of the ETH cluster Brutus) for major (in a sense of time consumption) components of IE forward solution at a specific frequency for a 3-D conductivity model discretized by $N_r \times N_\theta \times N_\varphi = 6 \times 36 \times 72 = 15552$ cells.

- Calculation of $G_{1D}^{ej}(\mathbf{r}, \mathbf{r}')$ for $\mathbf{r}, \mathbf{r}' \in V_{mod}$ takes 270 sec
- Numerical solution of scattering equation takes 30 sec
- Calculation of $G_{1D}^{hj}(\mathbf{r}_a, \mathbf{r}')$ for $\mathbf{r}_a \in Sites$ and $\mathbf{r}' \in V_{mod}$ takes 50 sec
- Calculation of $G_{1D}^{eh}(\mathbf{r}, \mathbf{r}_a)$ for $\mathbf{r} \in V_{mod}$ and $\mathbf{r}_a \in Sites$ takes 50 sec

These estimates show that separating the calculation of Green's tensors gives more than one order of magnitude acceleration (in this particular case $370/30=12.3$ times acceleration) of the forward calculations during inversion.

Another substantial saving of the computational load comes from parallelization of the IE solution. Since forward calculations are independent with respect to frequency we perform the modelings at N_{freq} frequencies in parallel on N_{freq} processors. This results in an additional $N_{freq} \times$ acceleration of the forward/inversion solutions.

3.6.2 Numerical verification

To test our inverse scheme we considered the same data, model and excitation as in Section 3.5.6. Our aim is to recover from the input data the conductivity distribution within the deep-seated inhomogeneous layer. The vector of parameters to be determined, \mathbf{m} , is the vector of

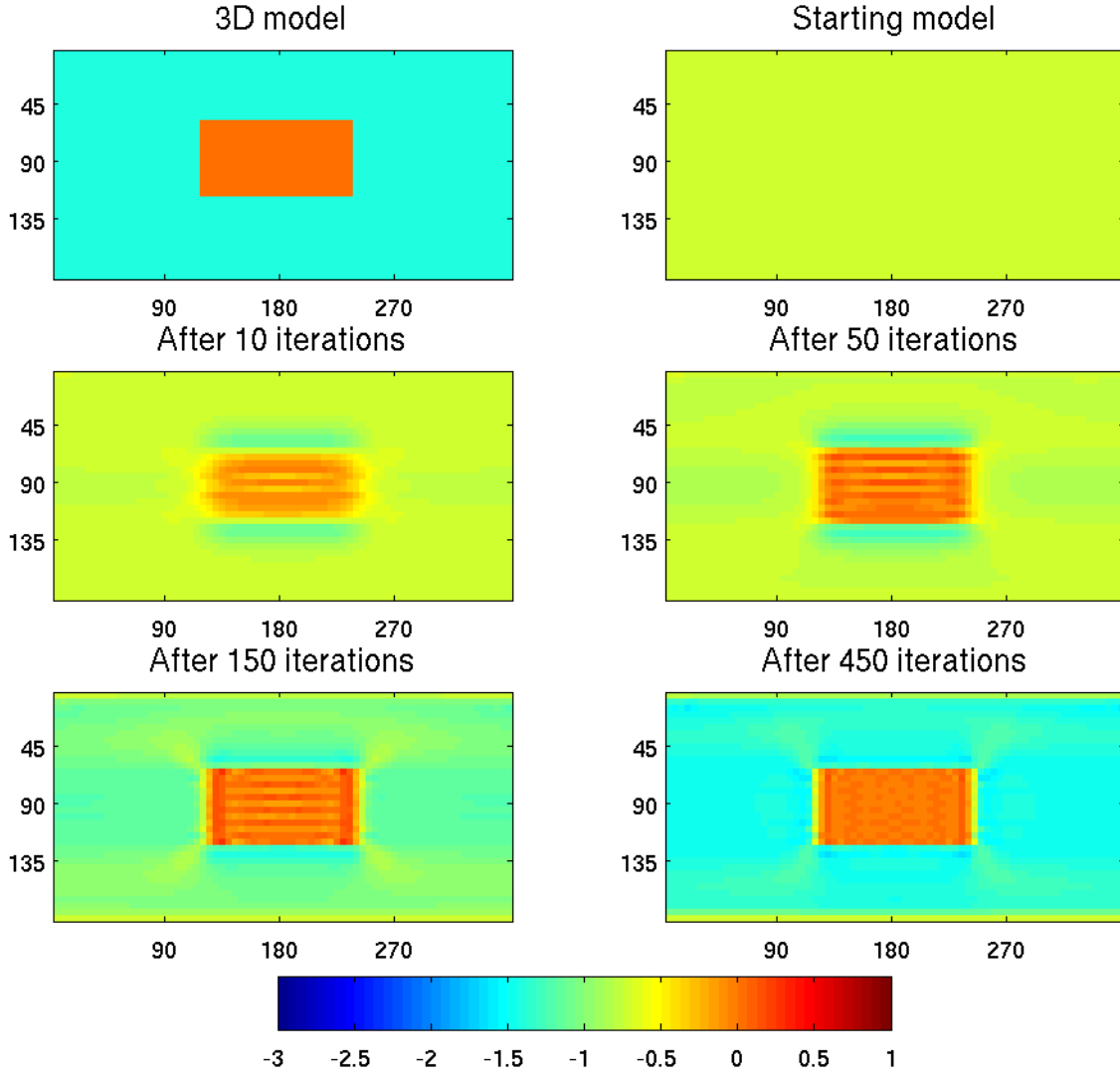


Figure 3.10: 3-D Model and results of conductivity recovery at initial stage of inversion at (0, 10, 50, 150 and 450 iterations) in logarithmic scale.

logarithms of unknown electrical conductivities in $N^{inv} = 72 \times 36$ cells (of 100 km thickness) comprising the inhomogeneous layer. For this test we assume known: a) the background 1-D conductivity; b) the geometry of the source; and c) the location (depth and thickness) of the deep-seated inhomogeneous layer. No noise is added to the data, and no regularization is applied. Thus, this test is considered as a proof of concept, i.e. we verify whether our implementation of the LMQN method along with the adjoint approach, and an optimization of the inverse solution discussed in Section 3.6 works correctly. We start the inversion using a homogeneous layer of conductivity 0.2 S/m which is far away from both the conductivity of anomaly (1 S/m) and background conductivity (0.04 S/m).

Figs. 3.9 and 3.10 summarize the results of our 3-D inversion test. Fig 3.9 presents the misfit with respect to the number of iterations. It is seen that within 150 iteration the

normalized misfit drops from 10.058 to 0.067, and after 450 to 0.003.

The upper left-hand plot of Fig. 3.10 shows the “true” (which has to be recovered) conductivity distribution in the layer, while other plots show the evolution of conductivity recovery with respect to the number of iterations in the inversion. It is seen that after 50 iterations the deep-seated anomaly is recovered fairly well, after which a further 400 iterations are necessary to recover properly the background conductivity. The final image (lower right-hand plot) almost perfectly agrees with the true conductivity.

Chapter 4

Estimation of experimental *C*-responses

4.1 Data collection

We assembled very long time series (up to 51 years; 1957-2007) of hourly mean values of three components of the geomagnetic field from 281 geomagnetic observatories, including polar and equatorial observatories. These data were retrieved from Edinburgh World Data Center for Geomagnetism (<http://www.wdc.bgs.ac.uk>). The spatial distribution of observatories is shown in Fig. 4.1.

We first visually inspected all the data and found that very few observatories (mostly in Europe and Japan) provide continuous time series of good quality (without baseline jumps and gaps) for the whole 51 year interval. As an example Fig. 4.2 shows time series of the geomagnetic field components for two of the best (with respect to data quality) geomagnetic observatories – Hermanus (HER) in South Africa and Fürstentfeldbruck (FUR) in Germany. Data found to have gaps and/or involve baseline jumps were excluded. No attempt has been made to edit the data. This decision is motivated by the intention to avoid any uncertainties associated with the necessarily subjective editing schemes. Our hope was that using very long time series the above simple criteria would provide enough data for further analysis. Fig. 4.3 demonstrates the data of “moderate” quality from Chinese observatory, Sheshan (SSH), and from Papete (PPT) observatory in Pacific Ocean. In spite of clear baseline jumps and lengthy gaps in the data time intervals of considerable duration showing continuous observations without jumps and outliers are nonetheless extant. Note that usable data from many observatories exist only for periods as little as few months down to a few days (e.g. EIC, Easter Island in Pacific Ocean), preventing their use. After initial processing step data from 262 observatories remained. Based on the results of time series analysis to be discussed below we further decreased more than twice this subset of observatories.

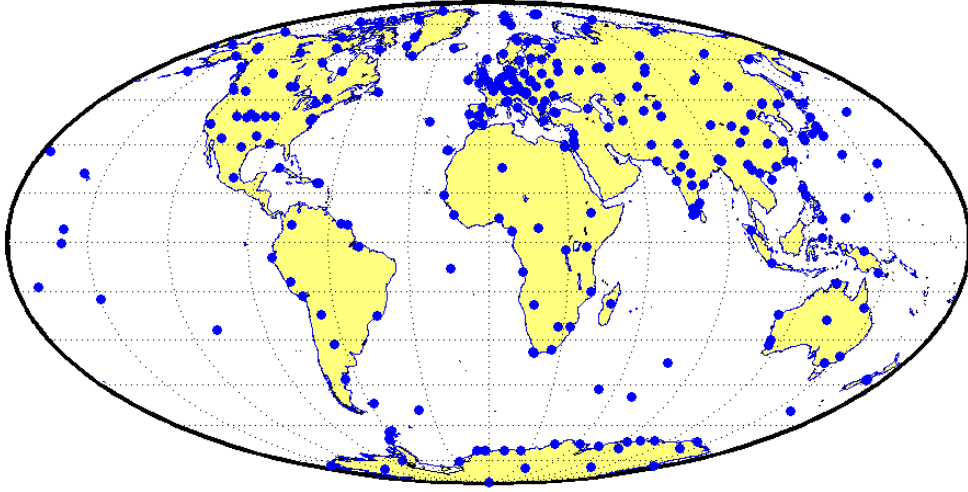


Figure 4.1: Location of 281 observatories, data from which have been retrieved from Edinburgh World Data Center for Geomagnetism.

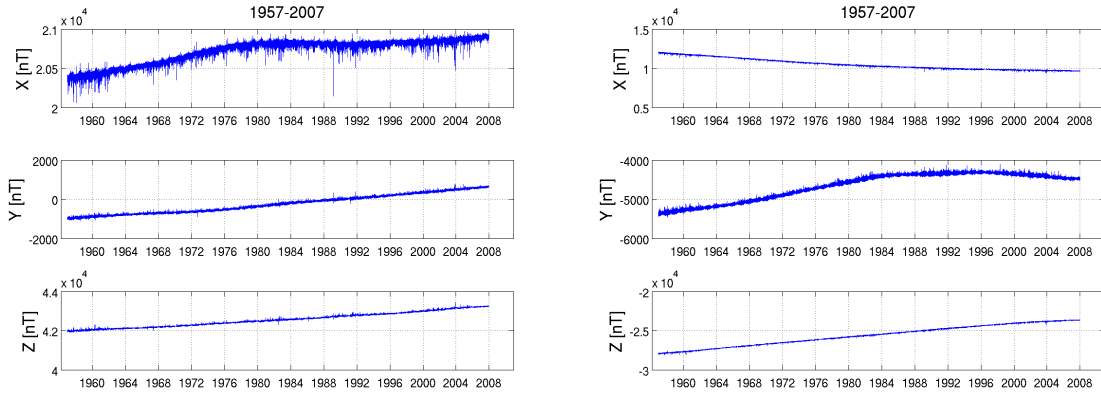


Figure 4.2: Time series of hourly mean values X (upper plots), Y (middle plots) and Z (lower plots) components of the magnetic field for Fürstenfeldbruck (FUR) observatory (left-hand plots) in Germany and Hermanus (HER) observatory (right-hand plots) in South Africa.

4.2 Determination of C -responses

In this section we discuss details of time series analysis to estimate C -responses, which we write here in the following form

$$C(\mathbf{r}_a, \omega) = -\frac{a \tan \vartheta}{2} \frac{Z(\mathbf{r}_a, \omega)}{H(\mathbf{r}_a, \omega)}, \quad (4.1)$$

where we denote $Z \equiv -B_r$ and $H \equiv -B_\theta$.

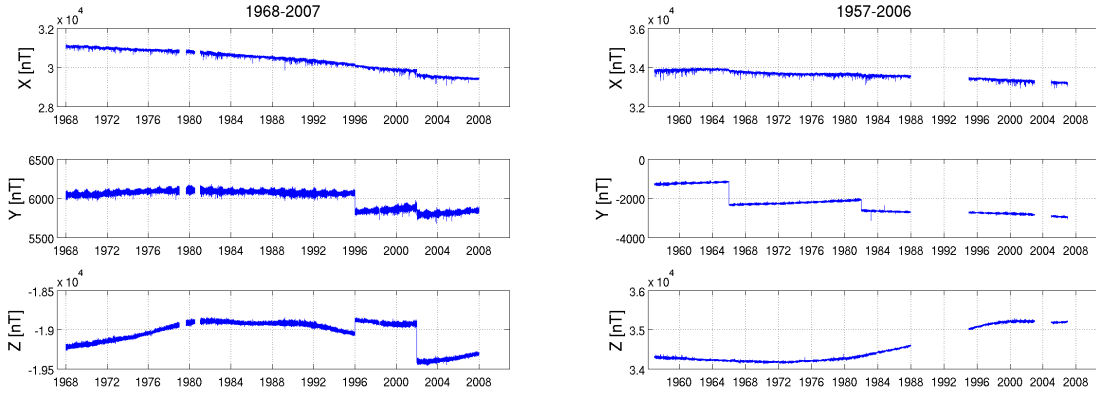


Figure 4.3: Time series of hourly mean values of X (upper plots), Y (middle plots) and Z (lower plots) components of the magnetic field for Papete (PPT) observatory (left-hand plots) in Pacific Ocean and Sheshan (SSH) observatory (right-hand plots) in China.

4.2.1 Least squares approach

The procedure presented below describes how we estimated C -responses.

1. Secular variation is removed from the original time series. For each component the secular variation is treated by means of cubic B-splines (cf. De Boor, 1978; Eilers and Marx, 1996; Dierckx, 1993, among others) with a knot separation of 2 years.

2. The resulting time series of the horizontal component are transformed by a rotation from geographic to geomagnetic (dipolar) coordinate system. Location of the geomagnetic pole has been obtained from three dipole components of the IGRF 1985 model. The secular motion of the pole is not relevant because this rate is much slower than the period range of interest.

3. Segments of Z and H time series of length KT_j (hereinafter referred to as realizations) are taken for estimating time harmonics of Z and H at various periods T_j , $j = 1, \dots, N_T$, with N_T being the number of considered periods and K being a constant. The responses were estimated at 15 periods between 2.9 and 104.2 days, evenly spaced on a logarithmic scale. There is a consensus that the GDS method works well in this period range (cf. Banks, 1969; Roberts, 1984; Schultz and Larsen, 1987; Fujii and Schultz, 2002, among others). We varied K between 3 and 10 and finally choose $K = 7$, considering this value as a good compromise between resolution and accuracy of the response estimates. In order to increase the number of realizations, successive realizations overlap 50% with preceding ones. If a given realization contains gaps in either component (Z or H), we exclude it from further analysis. To reduce sidelobes a Kaiser window (Kuo and Kaiser, 1966) is applied to each realization. This window is an approximation to the prolate-spheroidal window, for which the ratio of the main lobe energy to the side lobe energy is maximized.

4. For each realization and for each period T_j , we calculate a frequency dependent \hat{Z}_l and \hat{H}_l using the Fourier transform

$$\hat{Z}_l(\omega_j) = \int_{t_l}^{t_l+KT_j} Z(t)e^{-i\omega_j t} dt, \quad \hat{H}_l(\omega_j) = \int_{t_l}^{t_l+KT_j} H(t)e^{-i\omega_j t} dt, \quad (4.2)$$

where $l = 1, \dots, L$, L is the number of realizations, and t_l is the first time instant of the realization. Hereinafter we will use the symbols Z and H for frequency dependent fields in place of \hat{Z} and \hat{H} .

5. Least squares C -responses are then estimated as

$$C = -\frac{a \tan \vartheta}{2} \frac{\langle ZWH^* \rangle}{\langle HWH^* \rangle}, \quad (4.3)$$

where H^* is the complex conjugate of H , and $\langle \dots \rangle$ denotes summation over the L realizations

$$\langle AWH^* \rangle = \sum_{l=1}^L A_l W_l H_l^*, \quad (4.4)$$

where A is either Z or H . Non-Gaussian noise is handled with an iterative robust (Huber) weight W which reduces the effect of outliers (Huber, 1981). The corresponding errors are calculated as follows (Schmucker, 1999)

$$\delta C(\omega) = |C| \sqrt{\frac{1 - coh^2}{coh^2} \left(\frac{1}{\beta}\right)^{\frac{1}{L-1}}}, \quad (4.5)$$

where $1 - \beta$ is the confidence level, i.e. probability that the absolute value $|C|$ lies within error limits $|C| \pm \delta C$. In our calculations the confidence level is chosen to be 0.9. Squared coherence coh^2 is calculated as

$$coh^2 = \frac{|\langle ZWH^* \rangle|^2}{\langle ZWZ^* \rangle \langle HWH^* \rangle}. \quad (4.6)$$

In Section 4.2.3 the squared coherence will be used as the quality indicator, which allows for detecting sites with large noise-to-signal ratio. Let us provide the reasonings for this decision. Following Olsen (1998) we denote true signals of magnetospheric origin (for each realization l) as $Z_{0,l}$ and $H_{0,l}$, and noise parts in Z_l and H_l as δZ_l and δH_l

$$\begin{aligned} Z_l &= Z_{0,l} + \delta Z_l, \\ H_l &= H_{0,l} + \delta H_l, \end{aligned} \quad (4.7)$$

Eq. (4.1) should then be written as

$$C = -\frac{a \tan \vartheta}{2} \frac{Z_{0,l} + \delta Z_l}{H_{0,l} + \delta H_l}, \quad (4.8)$$

where $Z_{0,l}$ and $H_{0,l}$ are assumed to be exactly correlated

$$-\frac{a \tan \vartheta}{2} Z_{0,l} = E(C) H_{0,l}. \quad (4.9)$$

Here $E(C)$ denotes expected value for C . Let us further assume that

$$\langle \delta H W \delta Z^* \rangle = \langle \delta Z W Z_0^* \rangle = \langle \delta H W H_0^* \rangle = \langle \delta Z W H_0^* \rangle = \langle \delta H W Z_0^* \rangle = 0. \quad (4.10)$$

Then the eq. (4.6) can be rewritten as

$$\begin{aligned} coh^2 &= \frac{|\langle Z W H^* \rangle|^2}{\langle Z W Z^* \rangle \langle H W H^* \rangle} = \frac{\langle Z W H^* \rangle \langle H W Z^* \rangle}{\langle Z W Z^* \rangle \langle H W H^* \rangle} = \\ &= \frac{\langle Z_0 W H_0^* \rangle}{\langle Z_0 W Z_0^* \rangle + \langle \delta Z W \delta Z^* \rangle} \frac{\langle H_0 W Z_0^* \rangle}{\langle H_0 W H_0^* \rangle + \langle \delta H W \delta H^* \rangle} = \\ &= \frac{\langle Z_0 W H_0^* \rangle}{\langle Z_0 W Z_0^* \rangle} \frac{1}{(1 + \frac{\langle \delta Z W \delta Z^* \rangle}{\langle Z_0 W Z_0^* \rangle})} \frac{\langle H_0 W Z_0^* \rangle}{\langle H_0 W H_0^* \rangle} \frac{1}{(1 + \frac{\langle \delta H W \delta H^* \rangle}{\langle H_0 W H_0^* \rangle})} = \\ &= \frac{1}{(1 + \frac{\langle \delta Z W \delta Z^* \rangle}{\langle Z_0 W Z_0^* \rangle})(1 + \frac{\langle \delta H W \delta H^* \rangle}{\langle H_0 W H_0^* \rangle})}, \end{aligned} \quad (4.11)$$

where we have made use of the equality

$$\frac{\langle Z_0 W H_0^* \rangle}{\langle Z_0 W Z_0^* \rangle} = \frac{\langle Z_0 W Z_0^* \rangle}{\langle H_0 W Z_0^* \rangle}, \quad (4.12)$$

which arises from the exact correlation of Z_0 and H_0 (see eq. (4.9)). It is seen from eq. (4.11), that low squared coherence means high relative errors in Z or/and in H . These errors are possible due to a combination of the following cases: 1) instrumental or/and environmental noise; 2) smallness of the true signal; 3) violation of the assumption about P_1^0 structure of the true signal. With regard to the use of eq. (4.3) for estimating C -responses, the question of a possible downward bias of the responses arises (Olsen, 1998). In order to address this issue, we calculate responses using the remote reference technique (Gamble et al., 1979) which allows for a reduction of downward bias of the C -response estimates (should this bias exist). Using this technique the responses are computed as follows

$$C = -\frac{a \tan \vartheta}{2} \frac{\langle Z W H_{ref}^* \rangle}{\langle H W H_{ref}^* \rangle}, \quad (4.13)$$

where H_{ref} are realizations at the reference observatory, which is sufficiently far away so that the noise sources in H and H_{ref} are independent. Applying this technique we found that estimates calculated with the use of eqs (4.3) and (4.13) are very similar for all observatories over the period range of interest. We paired the observatories with different remote reference observatories, but noticed only a negligible difference between the different estimates so com-

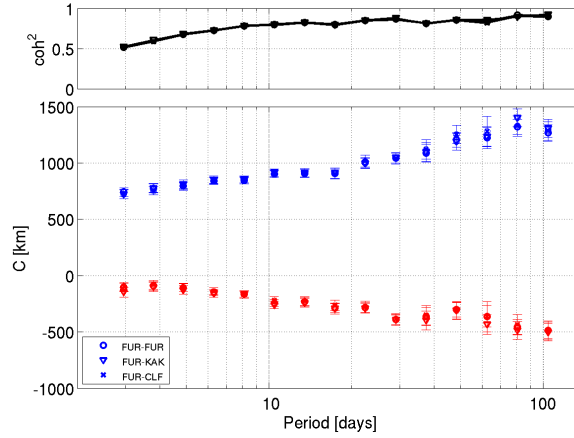


Figure 4.4: C -responses for Fürstfeldbruck observatory estimated with the use of eq. (4.3) and eq. (4.13) (for details see the text). Circles signify the results obtained from “single site” estimation (using eq. (4.3)), triangles and crosses denote the results obtained using remote reference technique (see eq. (4.13)) with Kakioka (KAK) and Chambon-la-Forêt (CLF) as respective reference observatories. Blue circles represent the real part of the C -responses, red circles – the imaginary part.

puted. This is illustrated in Fig. 4.4, which shows the results of C -response estimates for FUR estimated with the use of eqs (4.3) and (4.13). Circles depict the results obtained from “single site” estimation (i.e. using eq. (4.3)), triangles and crosses denote the results obtained using the remote reference technique (see eq. (4.13)), employing Kakioka (KAK) observatory in Japan and Chambon-la-Forêt (CLF) in France as remote reference observatories. The responses are seen to be very close over the whole period range, which means that the use of eq. (4.3) for obtaining unbiased estimates of C -responses seems adequate.

4.2.2 The jackknife method

We also applied an alternative (jackknife) method (cf. [Chave and Thomson, 1989](#)) to estimate C -responses and their uncertainties. The advantage of the jackknife method over the least squares approach discussed above is two-fold. First, jackknife estimates of the responses tend to be bias-free (see [Efron, 1982](#)). Second, the jackknife method does not require assumptions about the statistical distribution of experimental errors and, thus, gives a more realistic estimate of the response uncertainties. The method works as follows. Let’s designate

$$\langle AWH^* \rangle_i = \sum_{j=1}^{i-1} A_j W_j H_j^* + \sum_{j=i+1}^L A_j W_j H_j^*, \quad (4.14)$$

and

$$\hat{C}_i = \frac{\langle ZWH^* \rangle_i}{\langle HWH^* \rangle_i}. \quad (4.15)$$

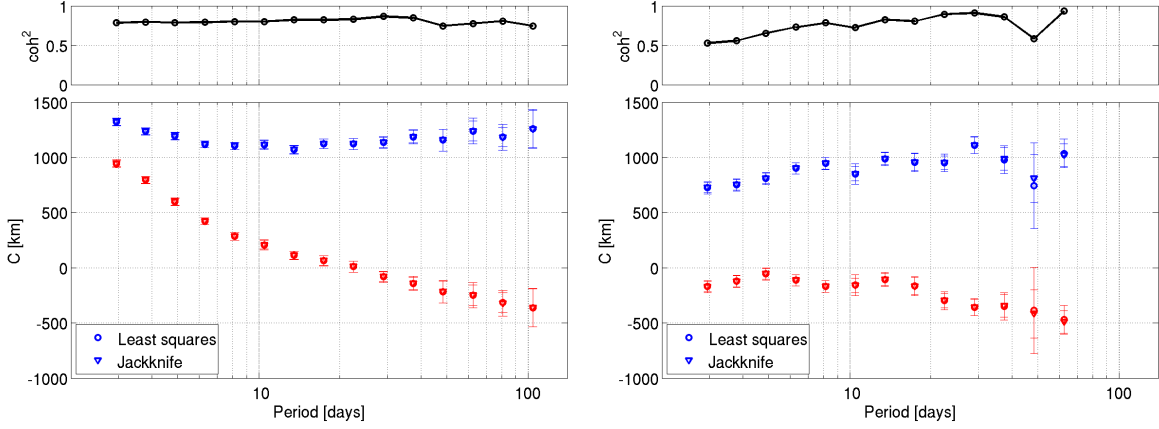


Figure 4.5: Comparison of least squares and jackknife techniques used to calculate C -responses on the Hermanus observatory (left-hand plot) and the Alice Springs observatory in Australia (right-hand plot). Blue circles represent the real part of the C -responses, red circles - the imaginary part.

Then the jackknife estimate of the response, \tilde{C} , is determined as

$$\tilde{C} = L\hat{C} - \frac{(L-1)}{L} \sum_{i=0}^N \hat{C}_i, \quad (4.16)$$

where \hat{C} is calculated as in eq. (4.3) from all available (L) realizations. The jackknife estimate of the variance is written as

$$\tilde{s}^2 = \frac{L-1}{L} \sum_{i=1}^L \left| \hat{C}_i - \frac{1}{L} \sum_{j=1}^L \hat{C}_j \right|^2. \quad (4.17)$$

Under very general conditions, it can be shown (cf. [Chave and Thomson, 1989](#)) that $\frac{\tilde{C}-C}{\tilde{s}}$ is asymptotically normally distributed, allowing the exact value of C with probability $1-\gamma$ to be placed between

$$\tilde{C} - t_\nu(1 - \frac{\gamma}{2})\tilde{s} \leq C \leq \tilde{C} + t_\nu(1 - \frac{\gamma}{2})\tilde{s}, \quad (4.18)$$

where $t_\nu(1 - \frac{\gamma}{2})$ is a value from Student's distribution with ν degrees of freedom. In our calculations we took $\gamma = 0.1$. Thus, within the jackknife approach we can estimate uncertainty, dC , as

$$dC = t_\nu(1 - \frac{\gamma}{2})\tilde{s}. \quad (4.19)$$

Fig. 4.5 presents comparison of estimates of C -responses and their uncertainties obtained by the least squares and the jackknife methods. The results are presented for the observatory Alice Springs (ASP) in Australia and the observatory Hermanus. It is seen from the figure that the two methods give comparable estimates, both of responses and uncertainties. These model studies demonstrate that we are rather safe by using either least squares or jackknife

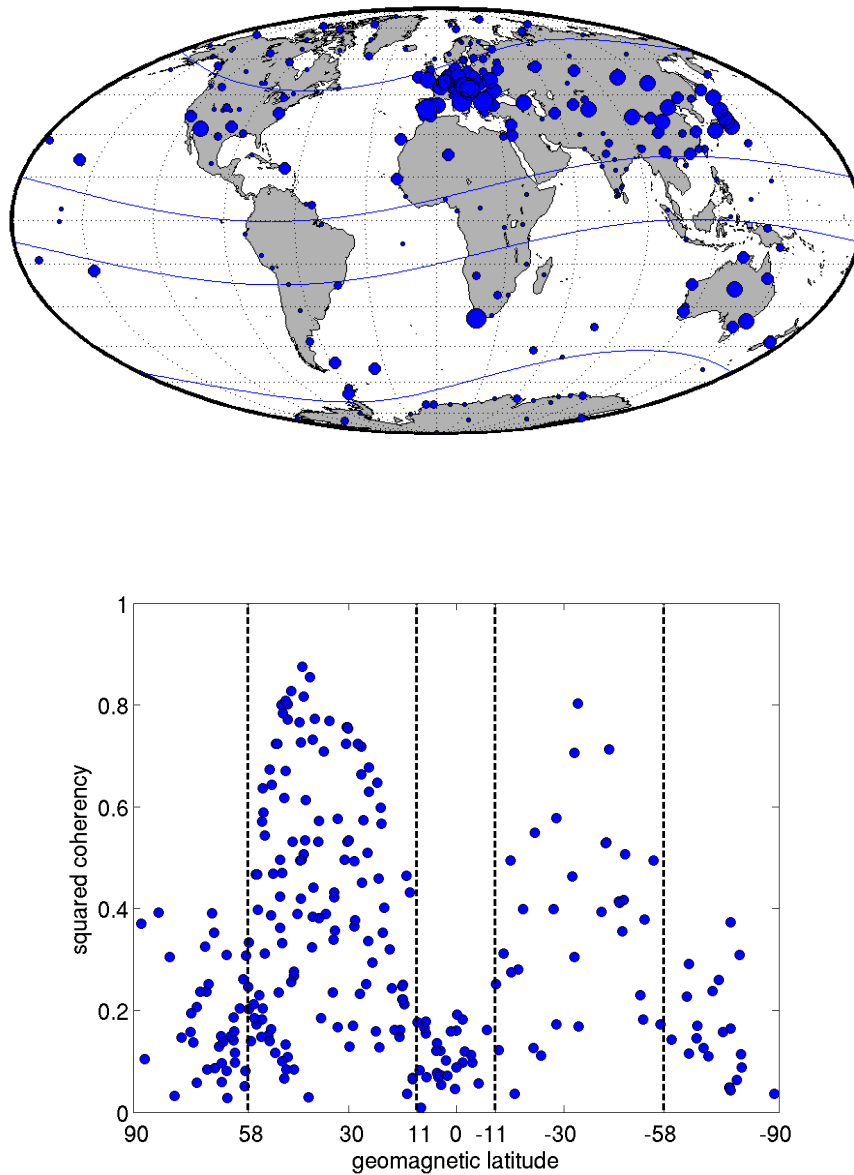


Figure 4.6: Averaged over all periods squared coherencies at 262 preselected observatories. Upper plot shows averaged coherency at a given observatory, where the circles stand for averaged coherencies; the larger the size of the circle the higher the coherency (5 different sizes correspond to the following intervals: 0-0.2; 0.2-0.4; 0.4-0.6; 0.6-0.8, 0.8-1). Lower plot presents the distribution of the averaged coherency with respect to geomagnetic latitude.

methods, however we prepared the final set of C -responses and their uncertainties with the use of the jackknife scheme.

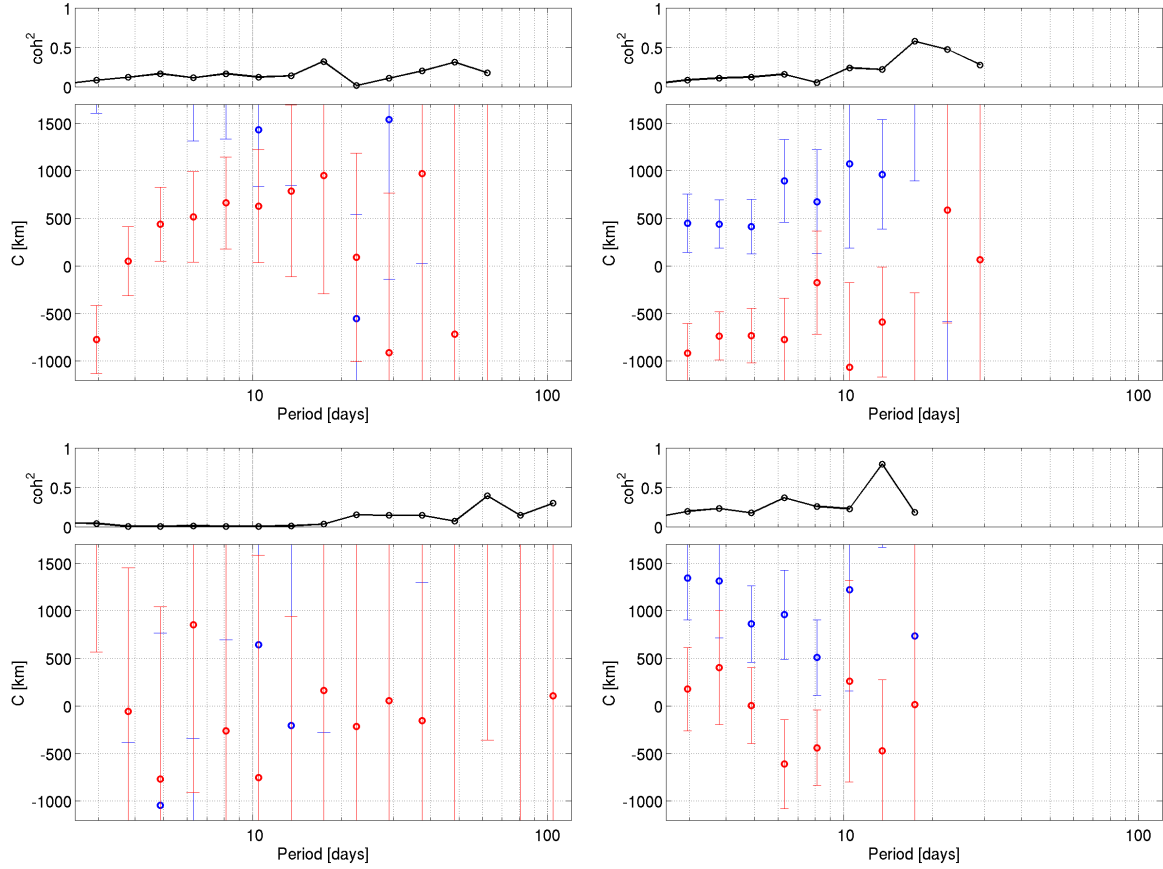


Figure 4.7: Examples of C -responses at equatorial observatories. Left upper plot – at Guam (GUA) observatory in the Pacific Ocean (5°N GM), right upper plot – at Hyderabad (HYD) observatory in India (8°N GM), left lower plot – at Huancayo (HUA) in South America (1°S GM) and right lower plot – at Addis Ababa in Africa (5°N GM). Blue circles represent the real part of the C -responses, red circles – the imaginary part.

4.2.3 C -responses selection

As previously mentioned the (squared) coherency can serve as a proxy either for estimating the quality of the responses at a given observatory. Fig. 4.6 quantitatively summarizes information in a form of coherencies at 262 observatories. The upper plot in Fig. 4.6 presents this information in a form of global map where the circles of different sizes stand for the averaged (over all (15) periods) coherencies at a given observatory. The lower plot shows the same averaged coherencies versus geomagnetic latitude. It is clearly seen from the figure that the coherence dramatically drops at geomagnetic latitudes higher than 58° and below 11° (these latitudes are depicted in the plots by solid (upper plot) and dotted (lower plot) lines).

The decrease in coherency is particularly prominent in the vicinity of the geomagnetic equator, which is likely due to the assumed geometry of the magnetospheric source. For this source (described by the first zonal harmonic, $P_1^0 = \cos \vartheta$, in geomagnetic coordinates) the vertical component, Z , near the geomagnetic equator tends to 0, thus enlarging the noise-to-

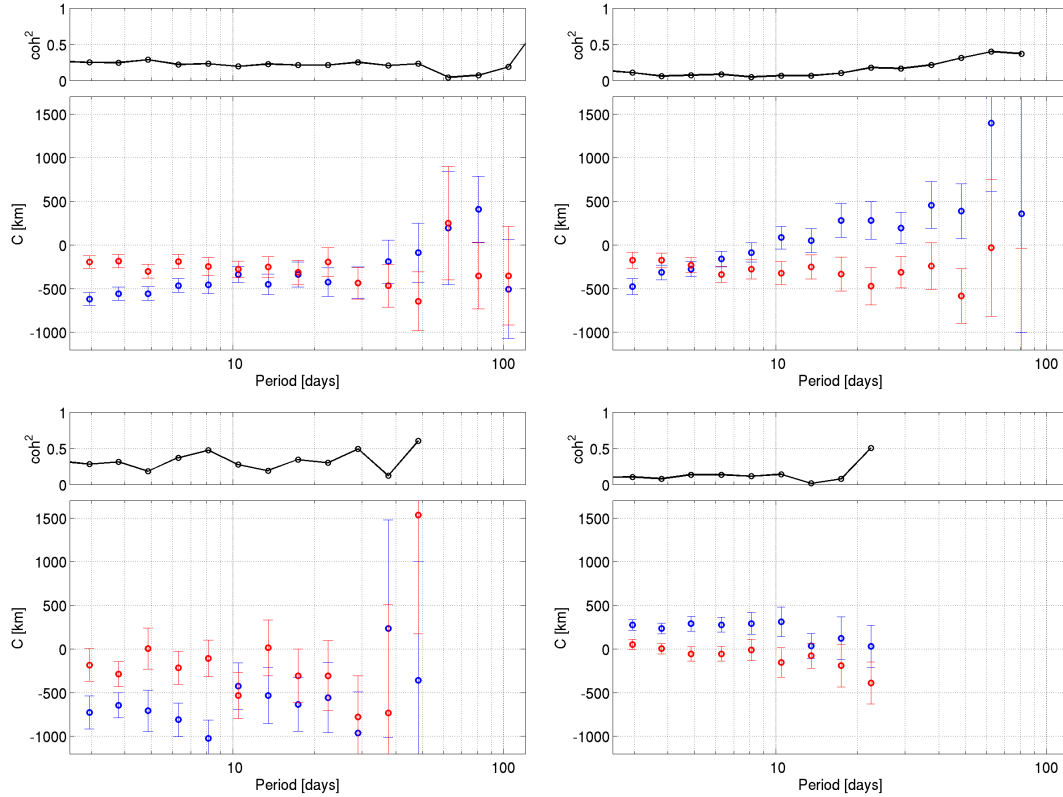


Figure 4.8: Examples of C -responses at high-latitude observatories. Left upper plot – at Sitka observatory in North America (60°N GM), right upper plot – at Yakutsk observatory in Siberia (52°N GM), left lower plot – at Arkhangelsk observatory in north-west of Russia (59°N GM), and right lower plot – at Tromso observatory in Norway (67°N GM). Blue circles represent the real part of the C -responses, red circles – the imaginary part.

signal ratio, as a consequence of which coherency diminishes (see eq. (4.11)). As a result the GDS method fail in this region as is illustrated in Fig. 4.7, showing C -responses, uncertainties and coherencies for four equatorial observatories – Guam (GUA; geomagnetic (GM) latitude, $\vartheta = 5^\circ\text{N}$; North Pacific), Hyderabad (HYD; $\vartheta = 8^\circ\text{N}$; India), Addis-Ababa (AAE; $\vartheta = 5^\circ\text{N}$; Africa), and Huancayo (HUA; $\vartheta = 1^\circ\text{S}$; South America). Indeed, along with the low squared coherency, C -responses are seen to be very scattered and have large uncertainties.

Coherency at high-latitude observatories is also very low, which is explained by the fact that in this region the main source of the magnetic field variations is the ionospheric polar electrojet. This source has spatial structure that is very different from the here assumed P_1^0 structure of our magnetospheric source, which thus prevents us from implementing of the GDS method at high latitudes. Fig. 4.8 shows the results for high-latitude observatories – Sitka (SIT; $\vartheta = 60^\circ\text{N}$; Alaska), Yakutsk (YAK; $\vartheta = 52^\circ\text{N}$; Russia), Arkhangelsk (ARK; $\vartheta = 59^\circ\text{N}$; Russia), Tromso (TRO; $\vartheta = 67^\circ\text{N}$; Norway) and supports this inference. Here the responses have unphysical values (for example, at SIT, YAK and ARK observatories real parts of C -responses are negative for most of the periods) and the coherency between Z and

H signals is very low.

Applying these additional constraints C -responses from 119 mid-latitude observatories remained for further analysis. Fig. 4.9 shows the location of the selected observatories and the surface conductance map, which describes the nonuniform distribution of the conductive oceans and resistive continents. Table 1 in Appendix E summarizes station details such as their acronyms, names, locations (both in geographic and geomagnetic coordinates) and time interval used for estimating C -responses. Appendix E also presents experimental responses, uncertainties and squared coherencies for all 119 observatories. In addition, Appendix E presents time series of hourly mean values of the three components of the magnetic field for the time interval that was used to estimate the C -responses. Note that for many observatories Appendix E also presents the experimental responses corrected for the auroral effect (to be discussed later in this chapter).

In Fig. 4.9 we are also showing the variability of the selected C -responses of both real and imaginary parts. Black circles in these plots show the responses which have been calculated from the global 1-D conductivity profile, derived from 5 years of satellite (CHAMP, Orsted, and SAC-C) magnetic data by Kuvshinov and Olsen (2006).

4.3 Ocean effect in C -responses

There is a common understanding that two 3-D induction effects prevail in the responses: those caused by the distribution of land and sea, and those due to the heterogeneous mantle. Kuvshinov et al. (2002b) demonstrated that up to periods of 20 days a nonuniform ocean is a major contributor to the anomalous behavior of the C -responses at coastal observatories. This was concluded by comparing predicted (in the model with nonuniform oceans) and observed responses at five coastal geomagnetic observatories: Apia (South Pacific), Hermanus (South Africa), Kakioka, Kanoya, and Simosato (all in Japan). The authors also concluded that in order to achieve good agreement between predictions and observations one needs: (a) good lateral resolution of the conductance distribution (grid with a lateral resolution of $2^\circ \times 2^\circ$ or denser); and (b) highly resistive lithosphere. Kuvshinov et al. (2002b) also showed that the effects arising from the oceans may be corrected for by multiplying the observed response, C^{exp} , by the ratio of the synthetic response of a radially symmetric conductive Earth (without oceans), C^{1D} , with the response of the same radially symmetric conductive Earth overlain by an inhomogeneous shell (shell approximates the nonuniform oceans), $C^{1D+shell}$,

$$C^{exp,corr}(\omega) = C^{exp}(\omega) \times \frac{C^{1D}(\omega)}{C^{1D+shell}(\omega)}. \quad (4.20)$$

In this section we analyze the ocean effect in the responses from all 119 observatories that we selected for further analysis. The goal is to understand to what extent the variability of our collection of the experimental responses (see Fig. 4.9) can be understood by the ocean

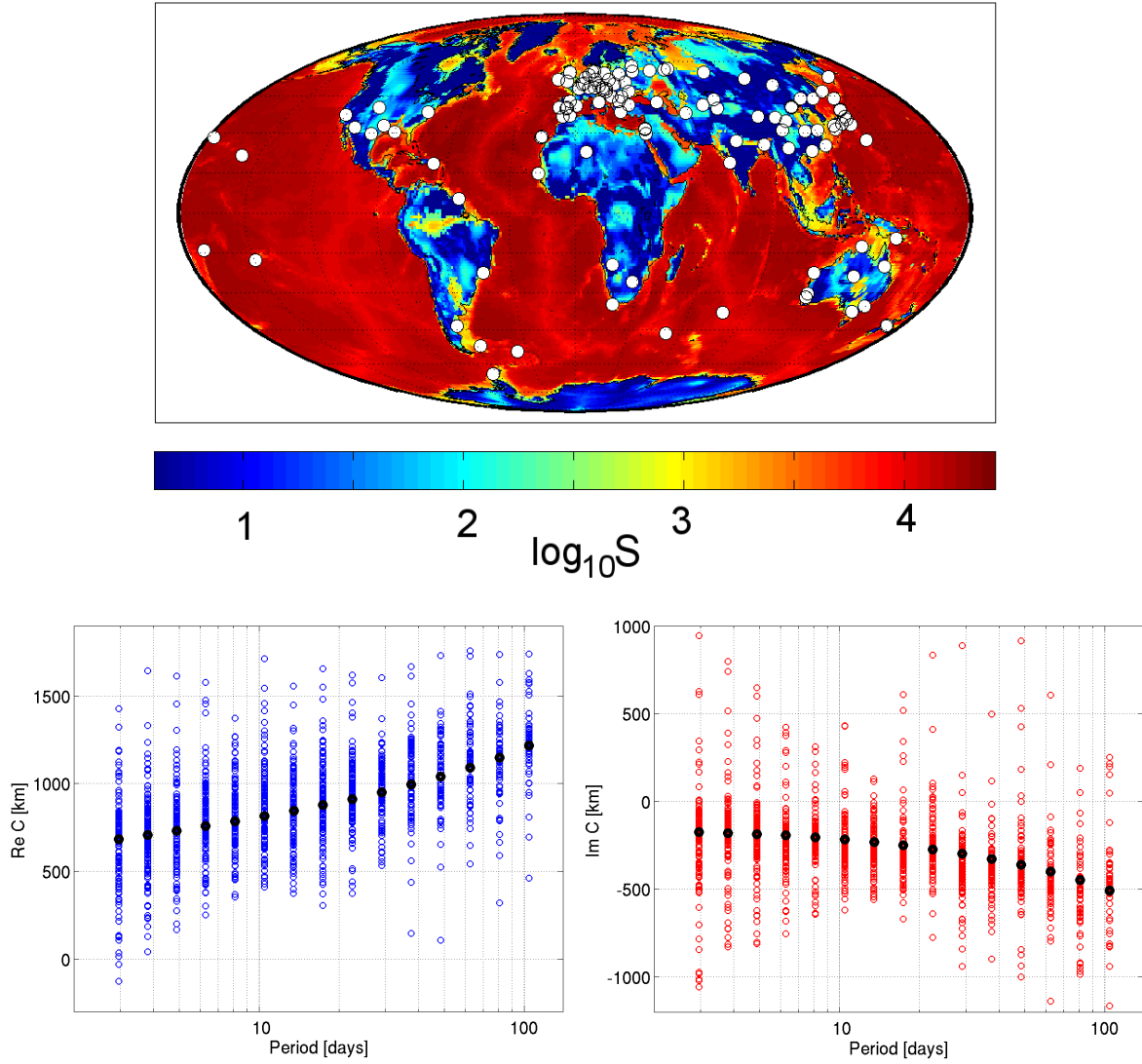


Figure 4.9: Upper plot shows conductance map using a logarithmic scale and location of the 119 mid-latitude observatories employed here. Lower plots present the variability of the real (left-hand plot) and imaginary (right-hand plot) parts of experimental responses at these observatories.

effect. We would also like to know how the ocean effect shows up in the responses in different regions of the world.

The 3-D (“ocean+1D”) model, which is used to predict the ocean effect, consists of a thin spherical layer of laterally varying surface conductance $S(\vartheta, \varphi)$ (see conductance distribution in Fig. 4.9) and a radially symmetric conductivity $\sigma(r)$ underneath. The shell conductance $S(\vartheta, \varphi)$ is obtained by considering contributions from both sea water and from sediments. The conductance of sea water is taken from [Manoj et al. \(2006\)](#), which accounts for ocean bathymetry (taken from the global $5' \times 5'$ NOAA ETOPO map of bathymetry/topography), ocean salinity, temperature and pressure (taken from the World Ocean Atlas 2001). Conductance of the sediments (in continental as well as oceanic regions) is based on the global

sediment thicknesses given by the $1^\circ \times 1^\circ$ map of Laske and Masters (1997) and calculated by a heuristic procedure similar to that described by Everett et al. (2003). The underlying radially symmetric (1-D) conductivity model, $\sigma(r)$, includes a 100 km resistive lithosphere of 3000 Ohm-m and a layered model underneath derived by Kuvshinov and Olsen (2006).

4.3.1 Resolution studies

We first investigate what lateral resolution of the model is needed to adequately represent the ocean effect. We calculated the responses for the selected 119 observatories in an “ocean+1D” model using the three conductance maps of resolution $3^\circ \times 3^\circ$, $1^\circ \times 1^\circ$, and $0.3^\circ \times 0.3^\circ$. Fig. 4.10 shows the variability of the responses for the three resolutions adopted. It is seen that, proper resolution of the conductance map is essential to accurately describe the ocean effect. A lateral resolution of $3^\circ \times 3^\circ$ is, likely, not detailed enough to fully account for the effect. Visual comparison of the results for the $1^\circ \times 1^\circ$ and the $0.3^\circ \times 0.3^\circ$ resolutions indicates that the $1^\circ \times 1^\circ$ grid is able to adequately model the ocean effect. We also observe that the variability due to the ocean effect is substantial, especially at shorter periods, and that it can be traced to periods of 40 days. Variability of the imaginary part is, on average, 1.5 times larger than the variability seen in the real part. Maximum predicted variability at shortest period are 1050 km and 1500 km in real and imaginary parts, respectively. At a period of 40 days this variability drops to 100 km and 300 km, respectively, although in the imaginary part still exceeds the uncertainties of the responses. It is remarkable that the shape of the variability of the imaginary part of the predicted responses to a period of 20 days is in good agreement with the variability of the imaginary part of the experimental responses (cf. right-hand lower plot of Fig. 4.9). The agreement in the real part is worse (cf. left-hand lower plot of Fig. 4.9), where variability of the experimental responses is more or less constant throughout the whole period range and reaches 1600 km which is substantially larger than maximum variability of the predicted responses.

4.3.2 Two types of anomalous behavior due to ocean effect

We discovered that two types of anomalous C -response behavior can be seen due to the ocean effect. The first type is characterized by a substantial increase in both real and imaginary parts of the responses towards shorter periods. Moreover at shorter periods the imaginary part at many coastal observatories becomes positive. Such a behavior is not compatible with any 1-D conductivity structure, the responses of which always show up with a negative imaginary part (we adopted $e^{i\omega t}$ time dependence convention to present the results; note that in Chapters 2 and 3 we work with $e^{-i\omega t}$), and a monotonically descending real part with decreasing period. Three end-member observatories, showing maximum ocean effect of this type, are KOU (Kourou, French Guiana), VSS (Vassouras, Brasil), and HER (Hermanus, South Africa). This is exemplified in Fig. 4.11, which shows the predicted anomalous behavior for Hermanus observatory.

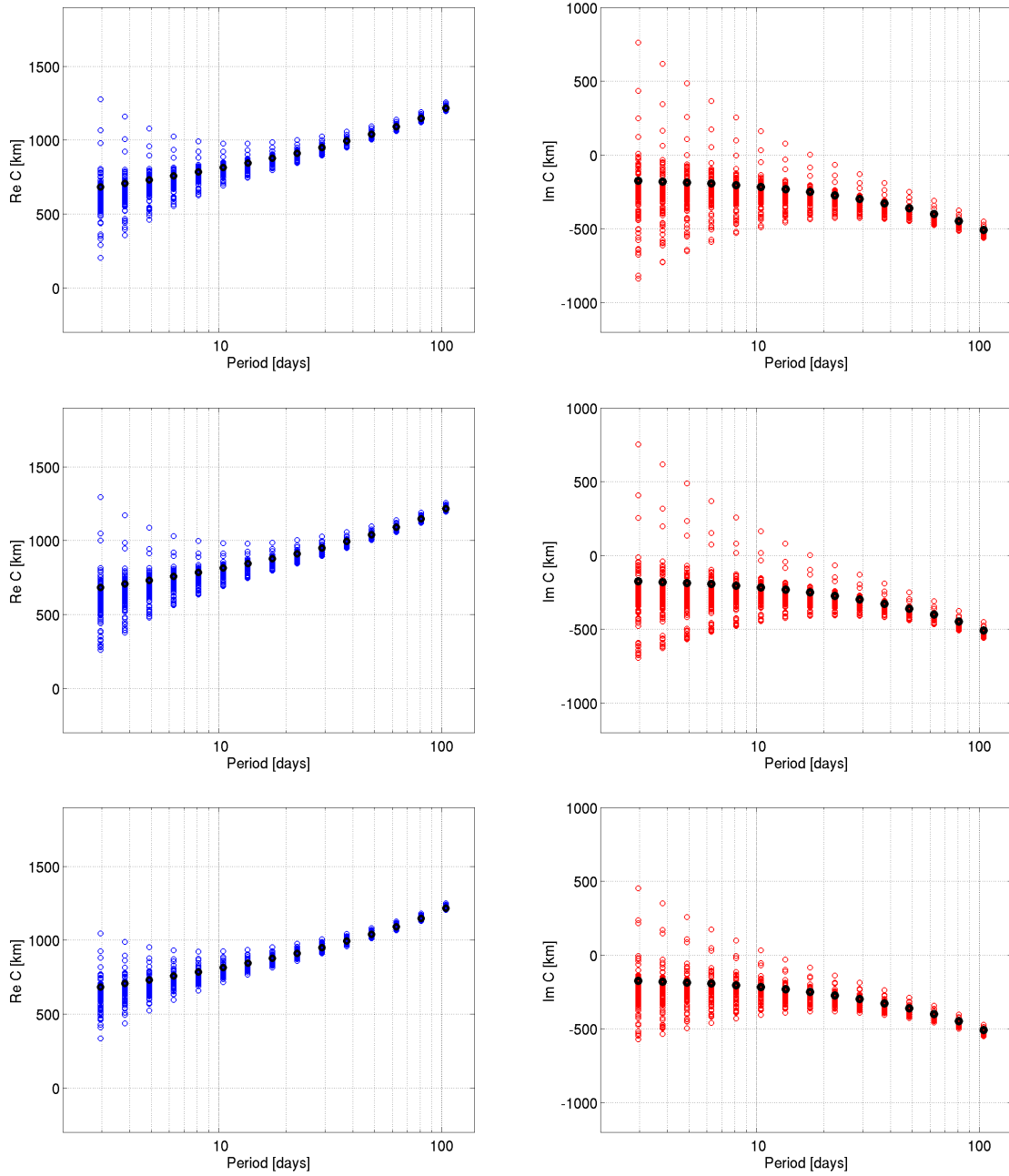


Figure 4.10: Ocean effect due to different ocean resolutions in the “1D+ocean” models. Upper plots present the results for $0.3^\circ \times 0.3^\circ$ resolution of the surface conductance, middle plots – the results for $1^\circ \times 1^\circ$ resolution, and lower plots – the results for $3^\circ \times 3^\circ$ resolution. Blue circles (left-hand column) represent the real part of the C -responses, red circles (right-hand column) - the imaginary part.

For comparison, the global responses discussed above are shown by black circles.

The second type of anomalous behavior is characterized by an excessive (compared to 1-D case) decrease in both real and imaginary parts of the responses for decreasing period. Three observatories that show the maximum ocean effect of this type are the Japanese observatories HTY (Hatizyo), KNY (Kanoya) and SSO (Simosato). Fig. 4.11 shows the anomalous

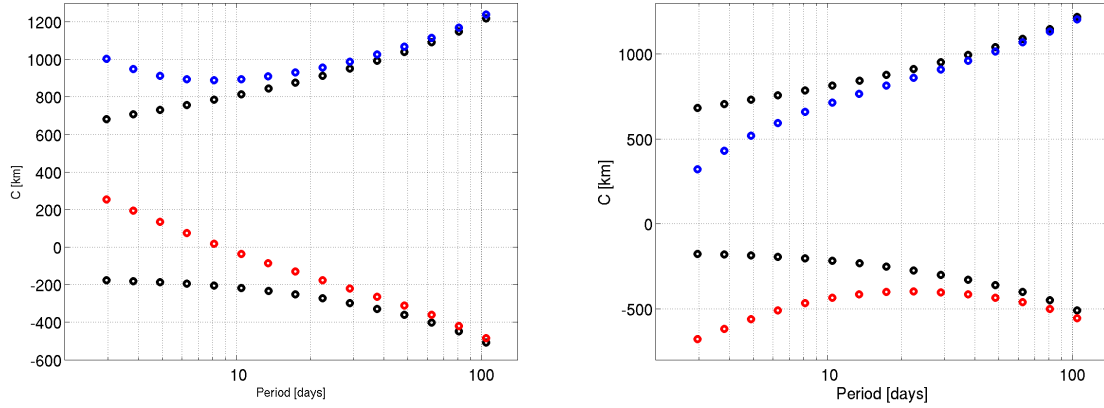


Figure 4.11: C -responses from the Hermanus observatory (left-hand plot) and from Kanoya observatory (right-hand plot) that are predicted in “ocean+1D” model. Blue circles represent the real part of C -responses, red circles – the imaginary part. Black circles represent the “global” C -responses (see text for explanation).

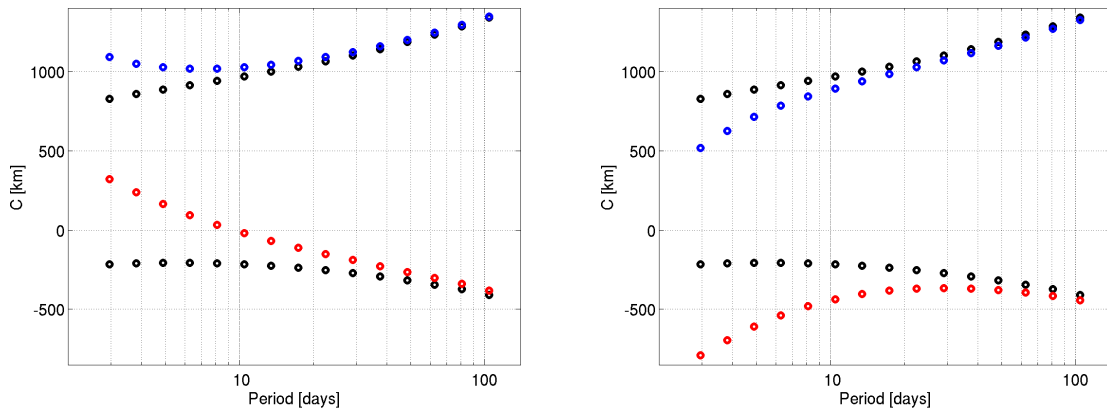


Figure 4.12: C -responses from the Port Stanley (PST) observatory in South America (left-hand plot) and from Faraday Island (AIA) observatory in Antarctica (right-hand plot) which are predicted in “ocean+1D” model. Blue circles represent the real part of C -responses, red circles - the imaginary part. Black circles represent the “global” C – responses (see text for explanation).

behavior of the second type of ocean effect for Kanoya (KNY) observatory in Japan. It is interesting that in some regions the relatively closely located observatories demonstrate the anomalous behavior of different type of ocean effect. Fig. 4.12 illustrates this fact by showing the predicted responses at observatories Port Stanley (PST; South Atlantic) and Faraday island (AIA; Antarctica). The reason for this different behavior in this particular region is that the observatories are situated at opposite sides of a strong electric currents that flow between South America and Antarctica.

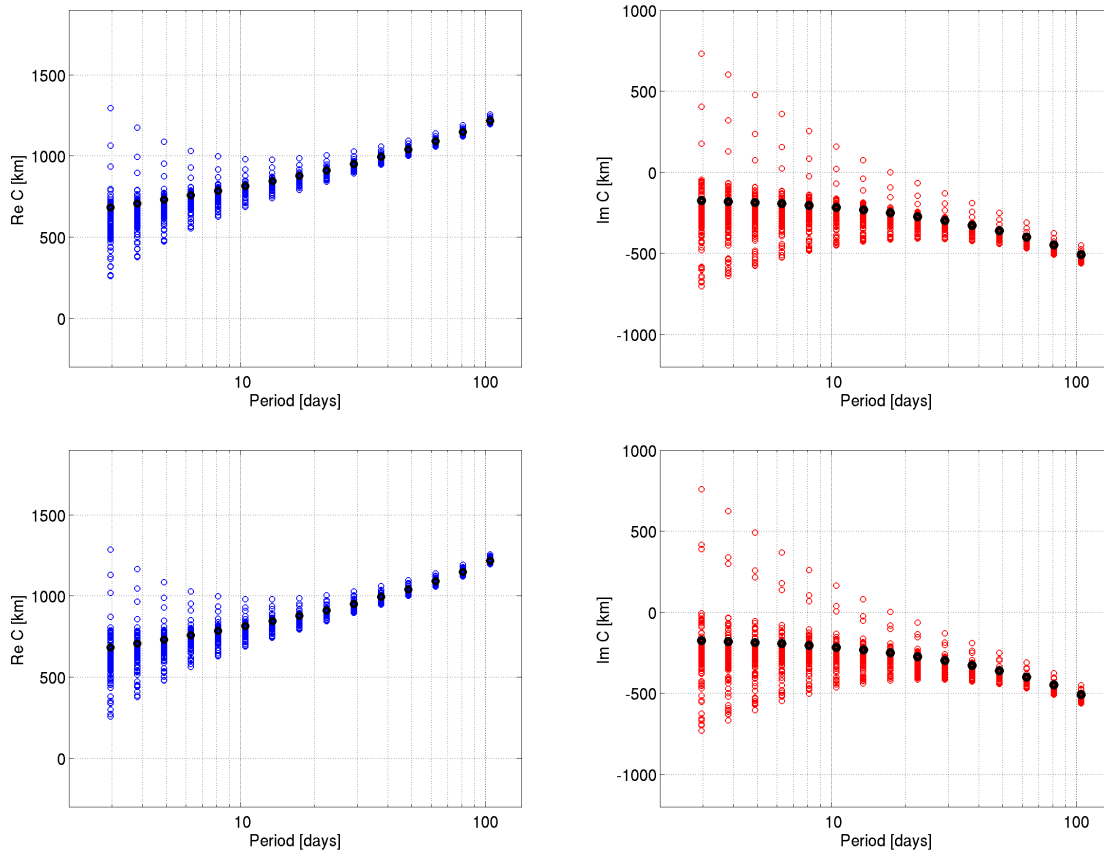


Figure 4.13: Variability of the predicted responses due to the changes in lithosphere resistivity. Upper and lower plots show the variability of the responses when the lithosphere resistivities in the “ocean+1D” model are 300 Ohm-m and 30000 Ohm-m, respectively. Blue circles (left-hand column) represent the real part of the C -responses, red circles (right-hand column) - the imaginary part.

4.3.3 Dependence of the responses on 1-D conductivity structure beneath oceans

We also studied to what extent the variability of the responses depends on the resistivity of the lithosphere. Fig. 4.13 shows the variability calculated in the models (with lateral resolution $1^\circ \times 1^\circ$) in which lithospheric resistivities were chosen to be 300 Ohm-m (upper plot) and 30000 Ohm-m (lower plot), while below this the model was fixed to 1-D obtained by Kuvshinov and Olsen (2006). From this figure and the corresponding (middle) plot in Fig. 4.10, it is seen that the overall variability, both in real and imaginary parts, only slightly depends on the resistivity of the lithosphere. However, for coastal observatories, like Hermanus, the dependence is rather pronounced, as is seen in Fig. 4.14, which shows the responses calculated in the “ocean+1D” model for the three values of lithospheric resistivity.

Finally, we investigated how the results change if we vary the underlying 1-D section. For this purpose we take as global 1-D section the local conductivity model derived by Khan et al.

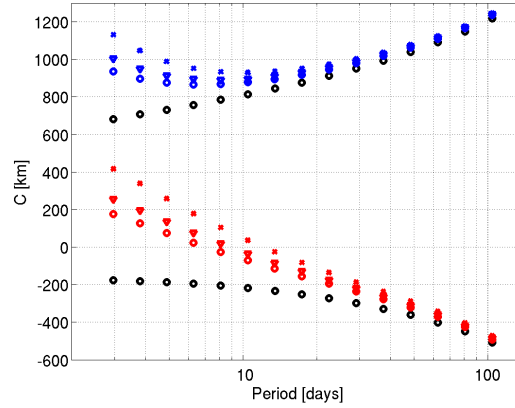


Figure 4.14: Dependence of the predicted responses at Hermanus observatory on lithosphere resistivity. Blue circles represent the real part of the C -responses, red circles – the imaginary part. Black circles show the responses for 1-D conductivity model, colored circles, triangles and crosses are the responses for the “ocean+1D” model with 300 Ohm-m, 3000 Ohm-m and 30000 Ohm-m lithosphere, respectively.

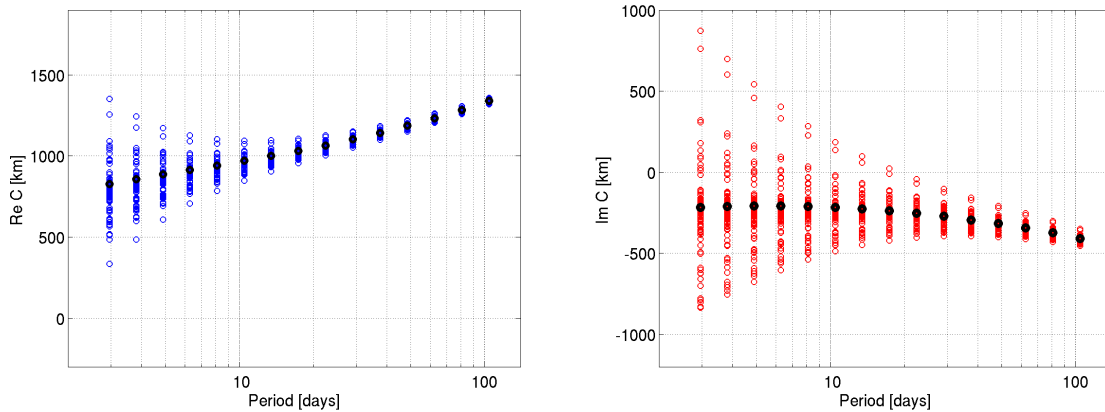


Figure 4.15: Variability of the predicted responses when the oceanic layer was underlain by 1-D profile recovered by Khan et al. (2011) from the Hermanus observatory data. Blue circles (left-hand plot) represent the real part of the C -responses, red circles (right-hand plot) – the imaginary part.

(2011) from the analysis of the responses estimated at Hermanus observatory. Note that Khan et al. (2011) achieved excellent agreement between very anomalous observed and predicted (in the model with oceans) responses at this observatory (see their Figure 4) by applying iteratively the correction scheme described by eq. (4.20). Fig. 4.15 shows the variability of the predicted responses when the oceanic layer was underlain by the 1-D profile recovered from the Hermanus data. It is seen that the variability in the real part remains the same, but that the variability in the imaginary part is visibly enhanced. As for the case when we varied lithospheric resistivity, the responses for coastal observatories vary substantially if we change the underlying 1-D section. Fig. 4.16 illustrates this for the responses at Hermanus

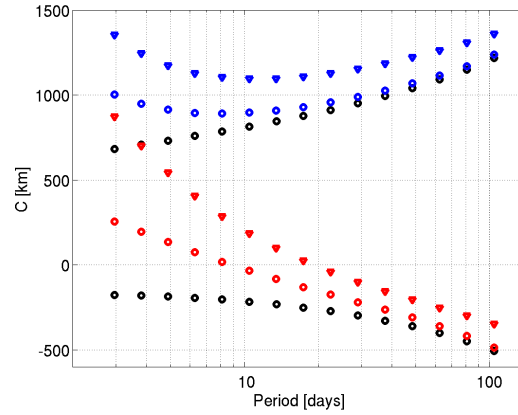


Figure 4.16: Dependence of the predicted responses at Hermanus observatory on 1-D conductivity profile. Blue circles represent the real part of the C -responses, red circles - the imaginary part. Black circles show the responses for 1-D conductivity model from Kuvshinov and Olsen (2006), colored circles are the responses for the “ocean+1D” model with 1-D conductivity profile from Kuvshinov and Olsen (2006), and triangles are the responses for the “ocean+1D” model with 1D conductivity profile recovered by Khan et al. (2011) from the Hermanus observatory data.

observatory.

4.3.4 Correction for the ocean effect

The model studies in this section demonstrate that we must account for the ocean effect as accurately as possible in order not to interpret this effect as arising from deeper structures. The best strategy to account for the distortions associated with a nonuniform distribution of the oceans and continents would be to include an oceanic layer of known conductance (with a lateral resolution of $1^\circ \times 1^\circ$) in the 3-D conductivity model, the deeper part of which we aim to image when inverting the data. However, only a coarser grid with a lateral resolution of $3^\circ \times 3^\circ$ is presently computationally feasible when performing our global 3-D inversion. (Note that in our present version of the inverse solution all nonuniform layers have the same lateral resolution.)

Alternatively, observed responses can be corrected for the ocean effect using eq. (4.20) where the predicted results in the model with oceans are calculated on a $1^\circ \times 1^\circ$ grid. This correction was employed by Kelbert et al. (2009) to isolate the influence of the oceans during their global 3-D inversion. However, our modeling studies have shown that the amount of correction (at least at very coastal observatories) depends strongly on the 1-D profile used during forward modelings. In order to apply corrections as consistently as possible we consider a more sophisticated correction scheme, which is described below.

We took the 1-D regional conductivity profiles recovered by Khan et al. (2011) for the six observatories distributed across the globe (Europe (FUR), South Africa (HER), China (LZH),

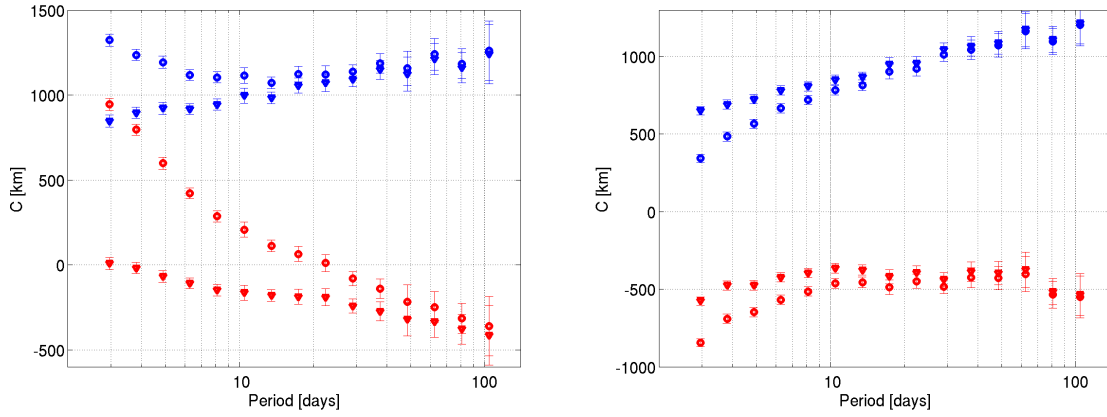


Figure 4.17: Results of the ocean correction for the Hermanus observatory and Kakioka observatories. Blue circles represent the real part of the C -responses, red circles - the imaginary part. Circles with error bars show original experimental responses, triangles depict the responses corrected for the ocean effect.

Australia (ASP), North America (TUC) and North Pacific (HON)). The localities are representative of a number of different tectonic settings, covering regions of continental extension (TUC), ocean (HON), relatively young continents (FUR and HER) and the stable archaean Australian craton (ASP). Next we subdivided the selected (119) observatories into six clusters depending on distance to these six (reference) observatories. Finally, for each cluster of observatories we corrected the responses using eq. (4.20) but exploiting as a 1-D model the regional 1-D profile for the corresponding reference observatory. Fig. 4.17 illustrates the result exemplified with observatories Hermanus and Kakioka.

4.4 Auroral effect in C -responses

4.4.1 Existence of the auroral effect

Another source of the variability of the experimental responses comes from auroral currents (polar electrojet) flowing in the ionosphere at an altitude of 110 km. This current system can to a first approximation be represented by a circular infinitesimally thin line current flowing 23° apart from the geomagnetic pole (see Fig. 4.18). Fujii and Schultz (2002) demonstrated that the influence of this current system (auroral effect) is seen in the responses down to geomagnetic latitudes of 40° . In this section we investigate in detail the morphology of the auroral effect and propose a scheme to correct the experimental responses for this effect.

To start with, Fig. 4.19 presents the experimental responses at periods of 3.7, 10.5, 22.5, and 37.4 days from all observatories as a function of GM latitude. Two features in the response behavior are clearly visible.

First, the behavior of the responses both in real and imaginary parts show abrupt changes

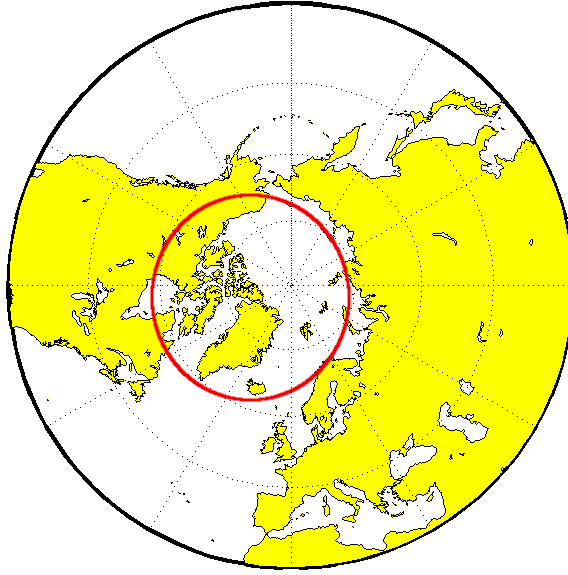


Figure 4.18: Adopted model of the auroral electrojet current system. This current system is represented by a circular infinitesimally thin line current flowing 23° apart from geomagnetic pole, at an altitude of 100 km.

around 58° latitude. Note that in Section 4.2.3 we – based on the analysis of the squared coherency (cf. Fig. 4.6) – provided the reasons why we exclude the responses from the observatories higher than 58° latitude from the final data set. In this section we present the responses from those observatories just to demonstrate again that these data cannot be used for the interpretation.

Second, one can see that in the latitudinal band between 40° and 58° the real part of the responses clearly decays towards higher latitudes. Note that this behavior of the real part is observed for all considered periods. In contrast, the imaginary part of the responses does not reveal a dependency on geomagnetic latitude in this band. Below we argue that this can be explained by the fact that there is no induction effect from the auroral current system in the considered period range.

Fig. 4.20 shows a typical manifestation of the auroral effect in the responses at observatories located in the discussed latitudinal range, for example, the experimental responses at observatory Brorfelde (BFE; Denmark; $\vartheta = 55^\circ N$ GM), and at observatory Ekaterinburg (SVD; Russia; $\vartheta = 49^\circ N$ GM). For comparison black circles depict the predicted responses from the global 1-D conductivity profile derived by [Kuvshinov and Olsen \(2006\)](#). The auroral effect is seen as a strong decrease of the real part of the responses towards shorter periods. We also notice that the imaginary part of the responses is not influenced by the auroral electrojet as there is no induction occurring from this source. Moreover, the squared coherency for these observatories is substantially smaller than those obtained at lower latitude observatories (cf. Fig. 4.4).

To confirm this conclusion quantitatively we calculated magnetic fields at the Earth's sur-

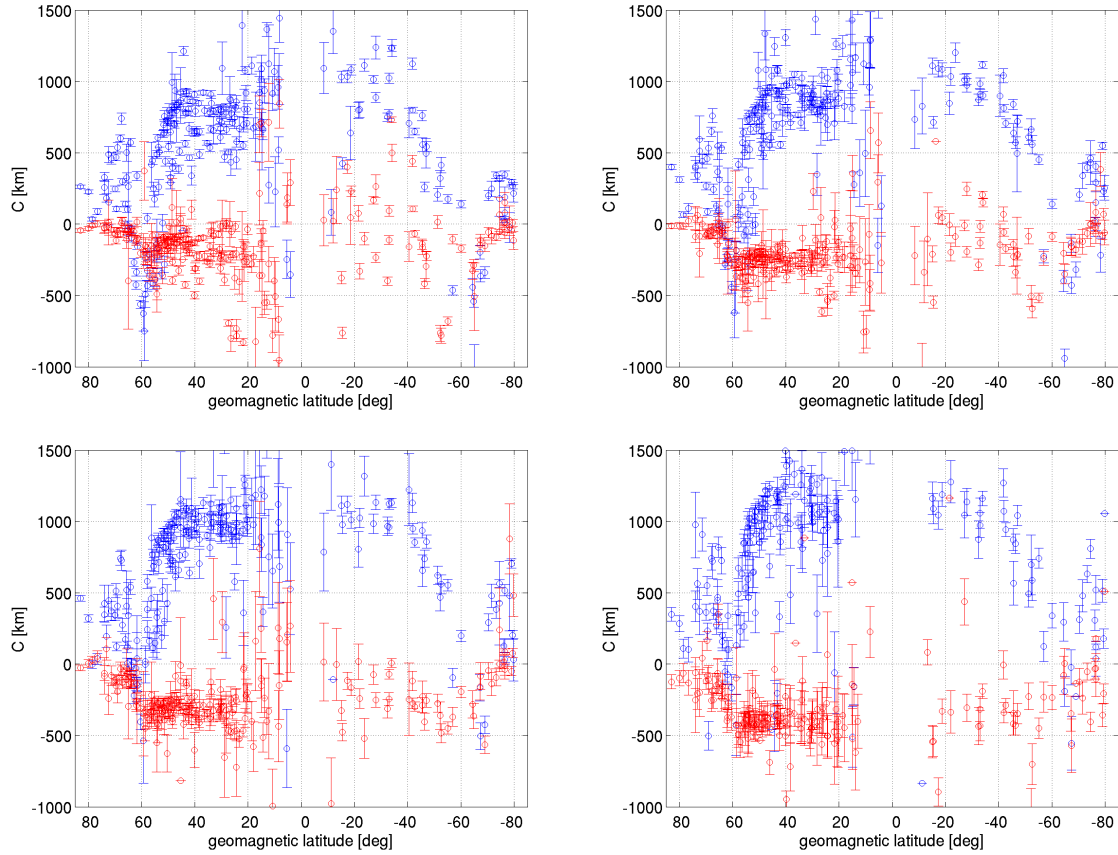


Figure 4.19: Real (blue) and imaginary (red) parts of the C -responses estimated for all observatories at periods of 3.7 days (upper left-hand plot), 10.5 days (upper right-hand plot), 22.5 days (lower left-hand plot), and 37.4 days (lower right-hand plot). The responses are shown as a function of GM latitude.

face induced by the auroral current which has the geometry shown in Fig. 4.18. Fig. 4.21 presents the results for the Z and H components for a period of 22.5 days along the profile $\varphi = 30^\circ$ (in geomagnetic coordinates). Blue curves represent the external field, black and red curves show the results for the models with and without an ocean, respectively. One observes that the conducting Earth (either with or without an ocean) only negligibly affects the external field (see a discussion in Section 3.1), which also supports the fact that the induction effect from the auroral source at the considered periods is negligible.

4.4.2 Longitudinal dependence

Having found that the influence of the auroral current system can be traced in C -responses down to geomagnetic latitude of 40° *globally*, we next discovered that the auroral effect in the responses reveals a strong longitudinal variability, at least in the Northern hemisphere. Figs 4.22 and 4.23 display responses at four periods as a function of geomagnetic latitude for three regions: Europe, North America and North Asia. It is clearly seen that for all periods the decay

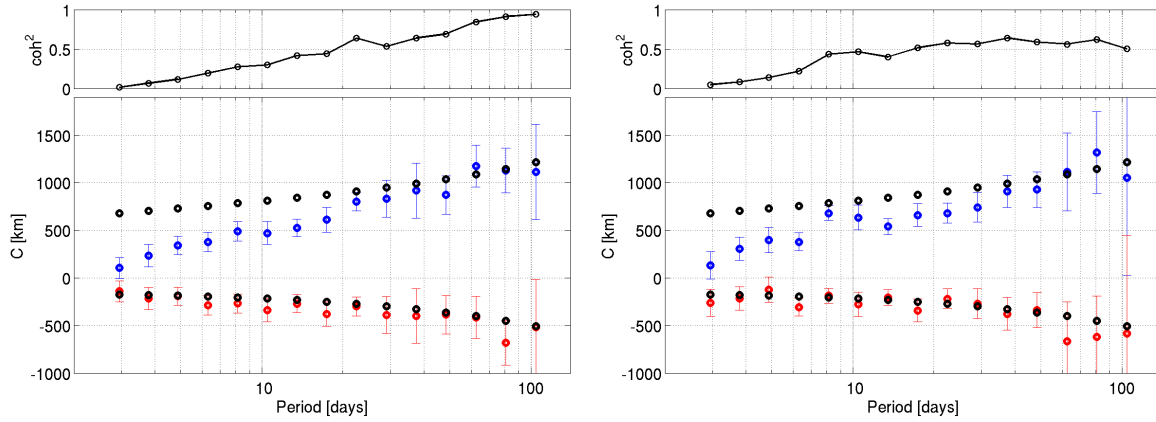


Figure 4.20: Experimental responses at two observatories located in geomagnetic latitude band between 40° and 58° . Left-hand plot shows the responses at Brorfelde (BFE; Denmark) observatory, right-hand plot – the responses at Ekaterinburg (SVD; Russia) observatory. Blue circles represent the real part of the C -responses, red circles – the imaginary part. Black circles depict the predicted responses from global 1-D conductivity profile derived by Kuvshinov and Olsen (2006).

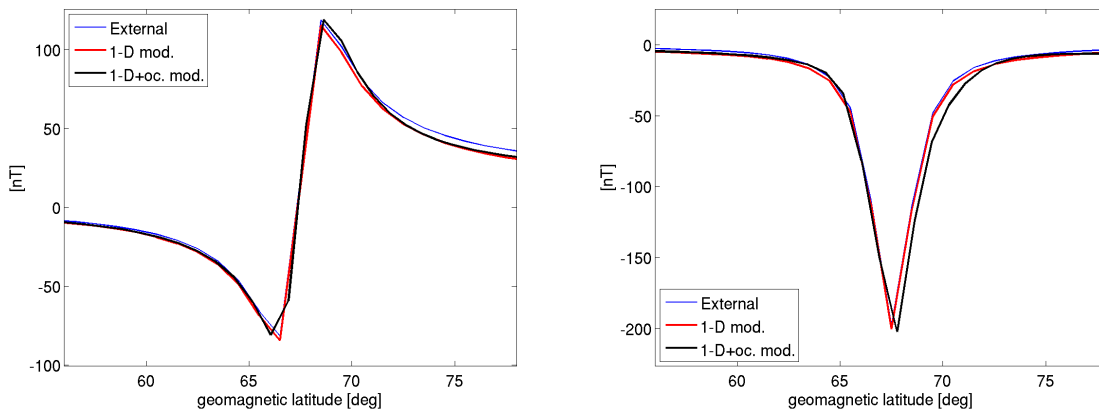


Figure 4.21: Z (left-hand plot) and H components (right-hand plot) of the real part of the magnetic fields at the Earth's surface excited by an auroral current. Blue curves depict external field, black and red curves show the results for the models with and without ocean, respectively. The results are for period of 22.5 days.

pattern of the real part of the responses towards geomagnetic pole varies with region. Europe appears to be the region with the smallest level of distortion. (Note again, that the imaginary parts are almost unaffected by the auroral source in the latitudinal band between 40° and 58°). This strong longitudinal variability of the responses is observed (not shown) for all periods. This suggests that the auroral electrojet has longitudinal variations either in strength or/and in spatial distribution. We have no conclusive explanation so far for what physical process is behind such variability of the auroral source. One can speculate (personal communication, C. Finlay; 2010) that the longitudinal variability of the auroral source can be governed by spatial

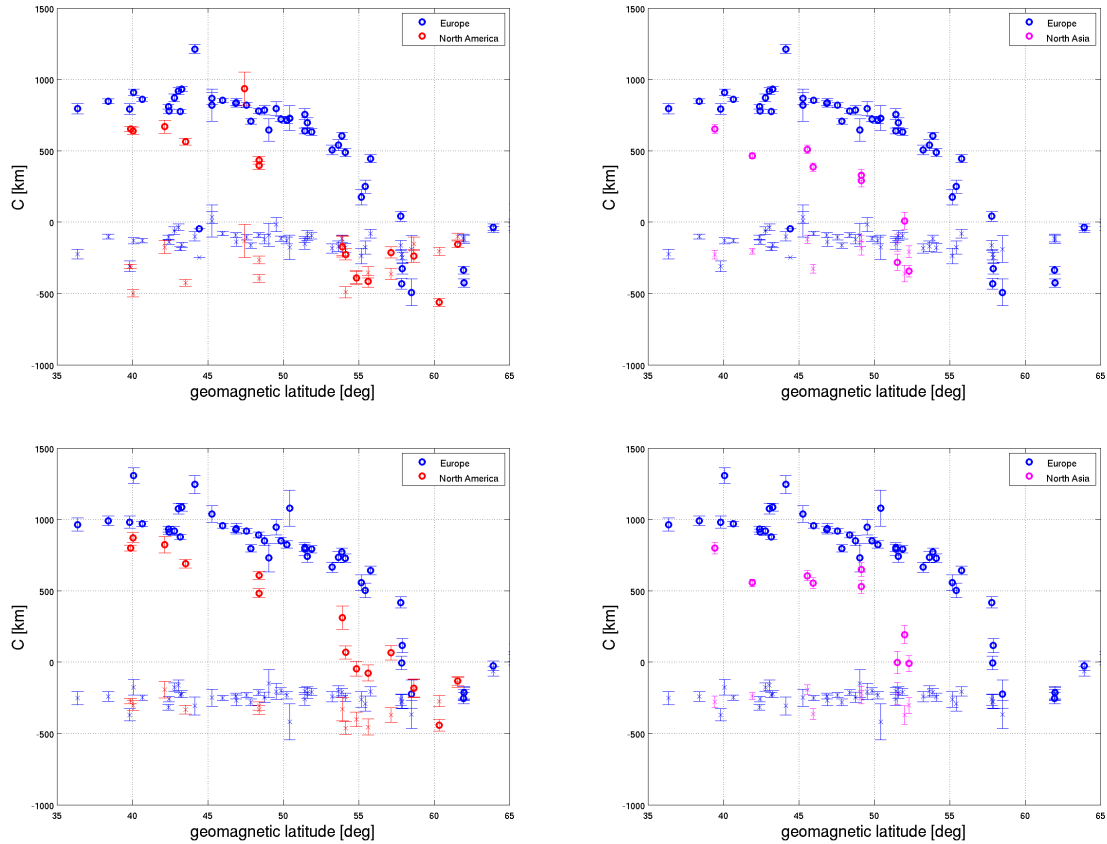


Figure 4.22: Comparison of the auroral effect in experimental C -responses in different regions. Left-hand plots show the comparison of the responses in Europe and North America, right-hand plots – comparison of the responses in Europe and North Asia. Circles represent the real part of the C -responses, crosses - the imaginary part. Blue, magenta and red colours depict the results for Europe, North Asia and North America, respectively. From the top to the bottom are the responses for periods 3.7 and 10.5 days.

inhomogeneity of the main field intensity which strongly deviates from dipolar structure in auroral regions and has pronounced patches exactly over North America and North Asia (see Fig. 4.24). Upward continuation of this map to 110 km, the altitude of the current, reveals the same high latitude flux concentrations will still be evident. The enhanced field strength in these regions could perhaps help to explain this asymmetry in auroral ionospheric currents.

4.4.3 Correction for the auroral effect

Given that the auroral signals appear independent of Earth's conductivity, in addition to the longitudinal variability of the auroral effect, we have developed a scheme to correct the responses from observatories located between 40° and 58° latitude for this effect. We consider as before the model of the auroral current described in the beginning of Section 4.4. The correction scheme works as follows.

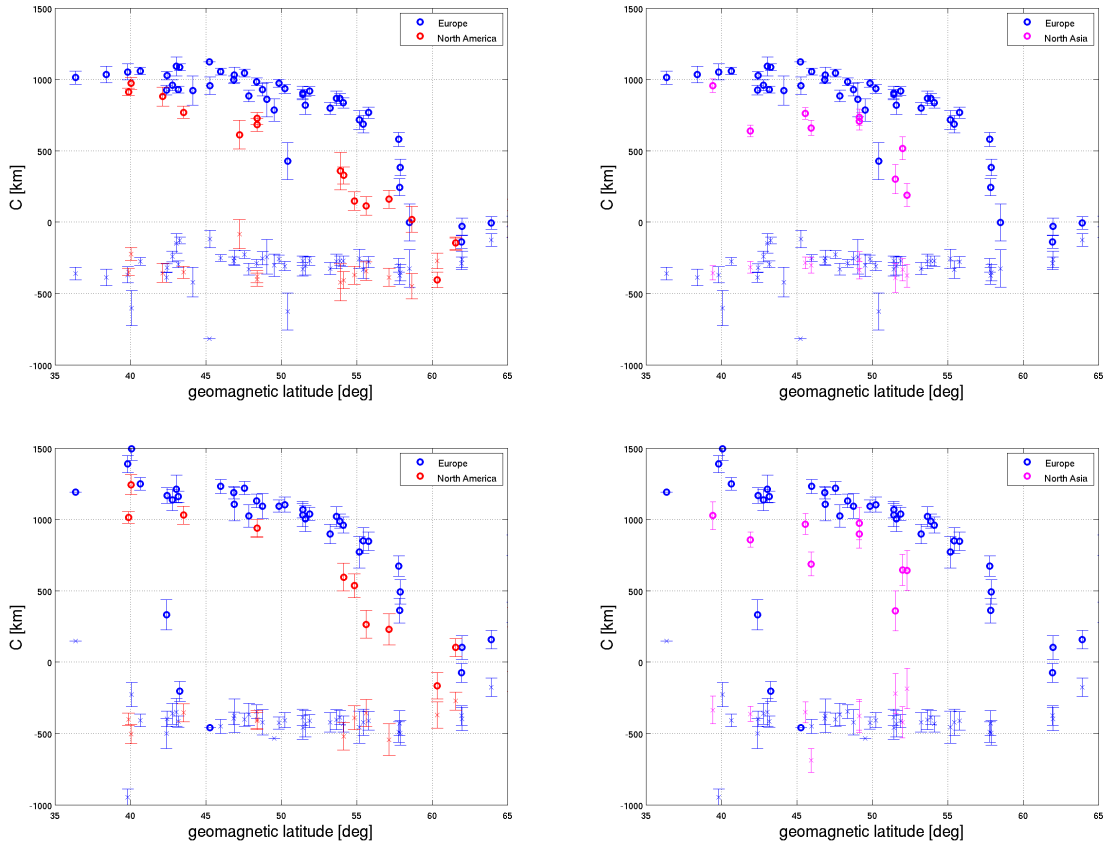


Figure 4.23: Comparison of the auroral effect in experimental C -responses in different regions. Left-hand plots show the comparison of the responses in Europe and North America, right-hand plots – comparison of the responses in Europe and North Asia. Circles represent the real part of the C -responses, crosses - the imaginary part. Blue, magenta and red colours depict the results for Europe, North Asia and North America, respectively. From the top to the bottom are the responses for periods 22.5 and 37.4 days.

1. Magnetic fields from the auroral current source, $Z_s^{aur}(\omega)$ and $H_s^{aur}(\omega)$, are calculated at the location of all considered observatories, with s denoting the specific observatory. During these calculations the choice of the conductivity model of the Earth is not relevant, since it does not influence the results as discussed above (cf. Fig. 4.21).

2. Magnetic fields from a magnetospheric ring current source, $Z_s^R(\omega)$ and $H_s^R(\omega)$, are calculated for each of three regions, R . These regions are Europe (with geographic longitude from 330° to 45°), northern Asia (with geographic longitude from 45° to 180°), and North America (with geographic longitude from 180° to 330°). For these regions we used three different 1-D conductivity profiles derived by inversion of C -responses from the observatories of these regions, for which data are assumed not to be influenced by the auroral effect. For North America, Europe and northern Asia these observatories were Tucson (TUC; $\vartheta = 40^\circ N$ GM), Panagyurishte (PAG; $\vartheta = 40^\circ N$ GM) and Manzhouli (MZL; $\vartheta = 39^\circ N$ GM), respectively.

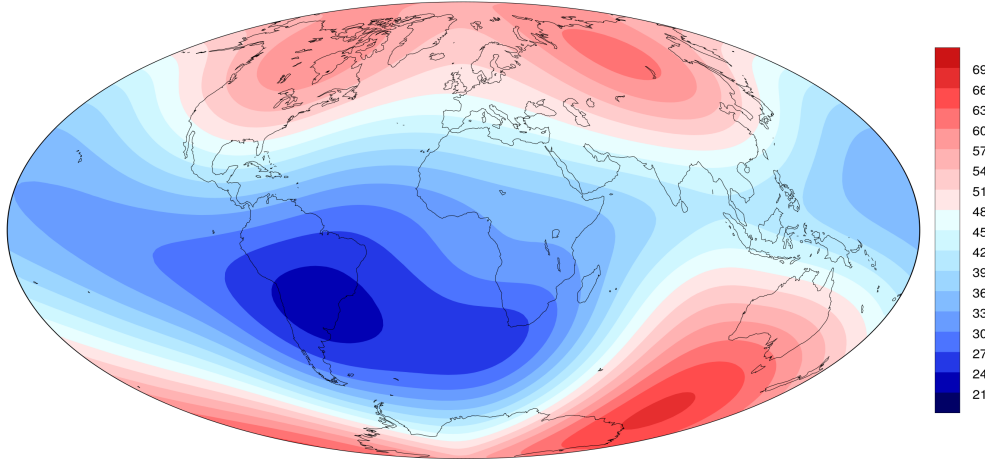


Figure 4.24: Intensity of the main magnetic field at Earth's surface in 2010 from IGRF-11 (Finlay et al., 2010). The units are in 10000 nT.

3. We introduce complex-valued coefficients, $k_R(\omega)$, which we assume are specific for each region, R , and frequency, ω , and estimate the size of the auroral effect in this region by minimizing (with respect to k_R) the following functional

$$\sum_{s \in R} \left| \frac{C_s^{mod}(\omega) - C_s^{exp}(\omega)}{\delta C_s^{exp}(\omega)} \right|^2 \xrightarrow{k_R(\omega)} \min, \quad (4.21)$$

where

$$C_s^{mod}(\omega) = -\frac{a \tan \vartheta_s}{2} \frac{Z_s^R(\omega) + k_R(\omega) Z_s^{aur}(\omega)}{H_s^R(\omega) + k_R(\omega) H_s^{aur}(\omega)}. \quad (4.22)$$

Fig. 4.25 demonstrates the results of fitting experimental responses using eq. (4.22) at period of 10.5 days in Europe, North America, and North Asia, respectively. Circles with error bars show the experimental responses, C_s^{exp} , whereas crosses depict modelled responses, C_s^{mod} . It is remarkable that coefficients, $k_R(\omega)$, indeed vary from region to region, showing, as expected, the smallest magnitude in Europe. For the particular period the coefficients are $k = -0.8 - 0.1i$, $k = -2.3 + 1.1i$ and $k = -1.5 + 0.4i$ for Europe, North America and northern Asia, respectively.

4. Finally, we correct the real parts of the experimental responses, for each region R and frequency ω as

$$\Re\{C_s^{exp,corr}(\omega)\} = \Re\{C_s^{exp}(\omega)\} + \Re\{C_{1D}^R(\omega)\} - \Re\{C_s^{mod}(\omega)\}. \quad (4.23)$$

Fig. 4.26 illustrates the application of this scheme for European observatories. Fig. 4.27 illustrates the results of the correction on the observatory Niemegk (NGK; $\vartheta = 51^\circ N$ GM; Germany). One can see that the correction made the responses more compatible with the responses at lower latitude (cf. Fig. 4.4).

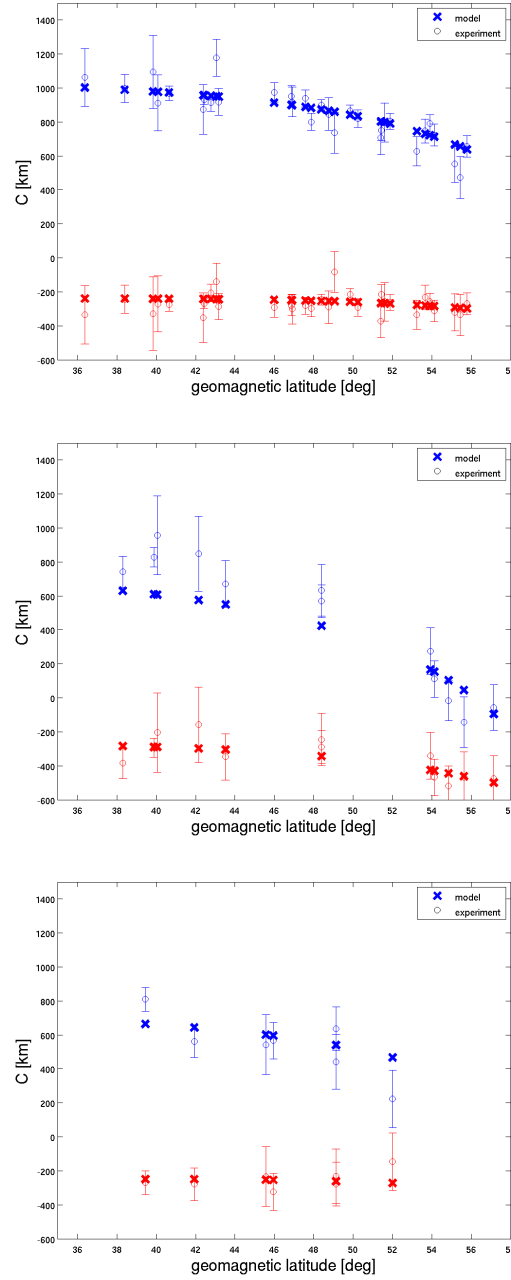


Figure 4.25: The results of fitting of experimental responses, C_s^{exp} , and modelled responses C_s^{mod} for Europe (upper plot), North America (middle plot), and northern Asia (lower plot). Blue color represents the real part of the C -responses, red color – the imaginary part. Circles with error bars show the experimental responses, C_s^{exp} , whereas crosses depict modelled responses, C_s^{mod} . The results are for the period of 10.5 days.

Note that we applied this scheme only for the observatories located in the Northern hemisphere. In the Southern hemisphere no definitive conclusion could be made about the longitudinal variability of the auroral effect due to the lack of observatories in this region. Moreover, the responses from the very few Southern hemisphere observatories located between 40° and 58° latitudes are also influenced by the ocean effect (fortunately, this is not the case for most

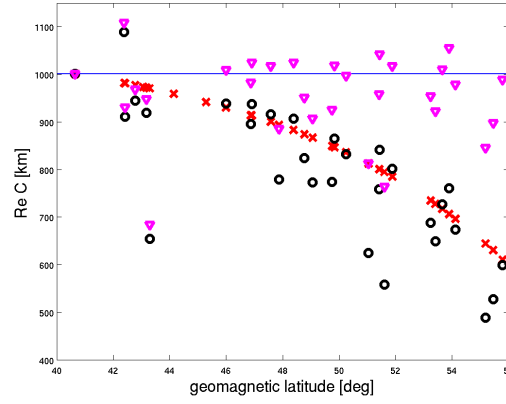


Figure 4.26: Results of the correction of the European responses for the auroral effect at period 13.5 days (see eq. (4.23)). Blue line is the real part of the 1-D C -response, $\Re\{C_{1D}^R(\omega)\}$, at observatory PAG ($\vartheta = 40^\circ N$ GM), red crosses are the real parts of the modeled (see eq. (4.22)) C -responses, $\Re\{C_s^{mod}(\omega)\}$. Black circles are experimental values of the real parts of C -responses, $\Re\{C_s^{exp}(\omega)\}$. Magenta triangles are the real parts of the corrected responses, $\Re\{C_s^{exp,corr}(\omega)\}$.

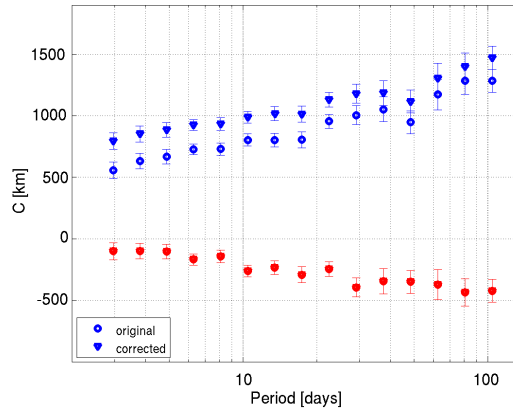


Figure 4.27: Results of the auroral correction for the Niemegk (NGK) observatory in Germany. Blue color represent the real part of the C -responses, red color - the imaginary part. Circles with error bars show original experimental responses, triangles – real part of responses corrected for the auroral effect.

of the observatories in this latitude band in Northern hemisphere), complicating the analysis. The latter fact is illustrated in Fig. 4.28, which demonstrates experimental responses at Faraday Island (AIA; $\vartheta = -55^\circ S$ GM; Antarctic) observatory. Here, a very strong decay in the real part of the responses at shorter periods is most probably due to cumulative effect of both – auroral electrojet and ocean. Note that here the imaginary part is also affected, because of the ocean effect.

A final remark of this section concerns the question of whether we have to use the responses from the observatories located in latitude band between 40° and 58° at all? We be-

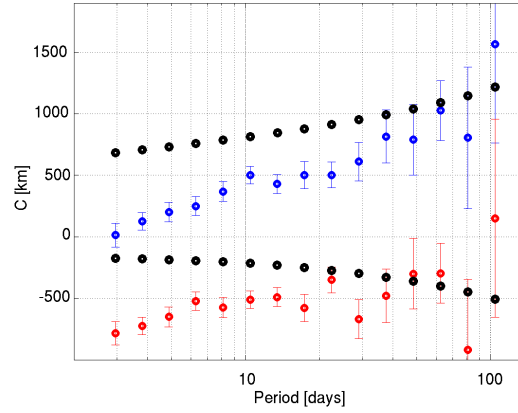


Figure 4.28: Experimental responses at Faraday Island (AIA) observatory. Blue circles represent the real part of the C -responses, red circles – the imaginary part. Black circles are the responses for 1-D profile from Kuvshinov and Olsen (2006).

lieve that answer on this question should be “yes” for three reasons. First, our correction scheme makes the real parts of the responses more consistent with the responses at lower latitudes. Second, the imaginary parts of the responses are not distorted by the auroral effect. By excluding these data from analysis we diminish by as much as a half the amount of usable observatories, since 58 of our 119 observatories from our preselected set are located in this latitude band.

Chapter 5

3-D inversion of the experimental responses

5.1 Detecting lateral variations in mantle conductivity

For the 3-D inversion of our data set it was assumed that lateral heterogeneities are present in the depth range 410 – 1600 km. We parameterized the 3-D conductivity distribution at these depths by 5 spherical inhomogeneous layers of 110, 150, 230, 300 and 400 km thickness. The thicknesses of the two upper layers were chosen in accordance with seismic studies which show compositional changes at depths 410, 520 and 670 km. The thicknesses of three lower layers coincide with those used by Kelbert et al. (2009) to simplify the comparison with their results which will be discussed later in this chapter. Note that we did not attempt to recover 3-D variations at depths shallower than 410 km and deeper than 1600 km, assuming that our responses in the considered period range between 2.9 and 104.2 days have limited sensitivity to conductivity variations at these depths (see also the results of Kelbert et al. (2008) which support this reasoning). The layers were embedded into an *a priori* 1-D section obtained by Kuvshinov and Olsen (2006). Introducing *a priori* means that we will consider as a vector of our model parameters

$$\mathbf{m} = \left(\ln\left(\frac{\sigma_1}{\sigma_1^0}\right), \frac{\sigma_2}{\sigma_2^0} \right) \cdots, \ln\left(\frac{\sigma_{N^{inv}}}{\sigma_{N^{inv}}^0}\right), \quad (5.1)$$

where σ_i^0 , $i = 1, 2, \dots, N^{inv}$ are the conductivities of the *a priori* section. This 1-D section remains unchanged during 3-D inversion. The sketch of the model is shown in Fig. 5.1. The model is excited by a source which is described by the first zonal harmonic in a geomagnetic coordinate frame. All forward problem calculations were performed on a $3^\circ \times 3^\circ$ grid. The lateral resolution of the inverse domain was chosen to be $9^\circ \times 9^\circ$. We also tried resolutions $6^\circ \times 6^\circ$ and $15^\circ \times 15^\circ$ for the inverse domain but observed only minor changes in the recovered images (see these model studies in Appendix C). The details of our 3-D inverse solution are presented in Chapter 3. For each inversion run the regularization parameter was determined

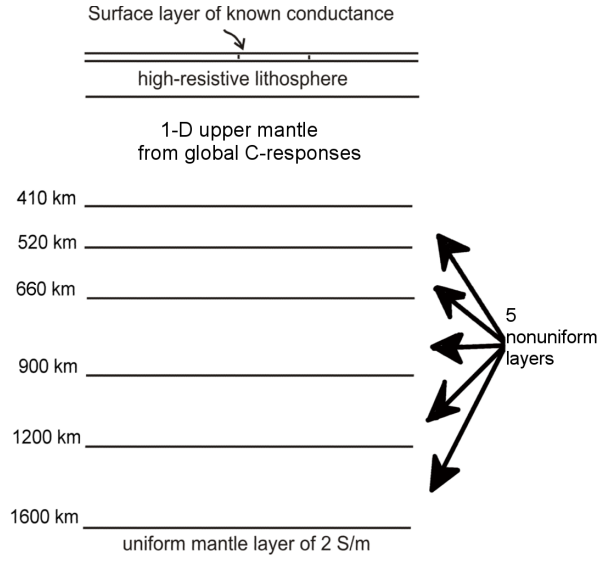


Figure 5.1: Side view of the model.

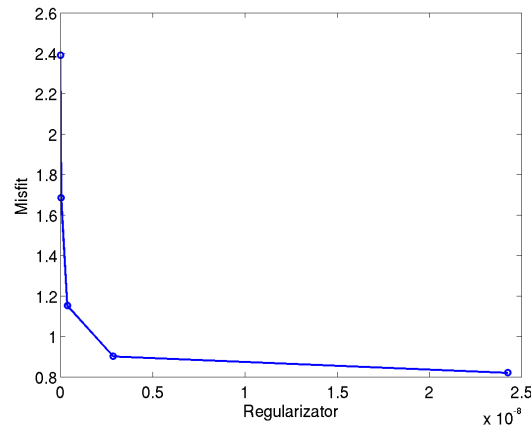


Figure 5.2: Typical shape of L-curve for our 3-D inversions. Regularization term is from eq. (3.20).

using the L-curve criterion (cf. [Zhdanov, 2002](#)). Fig. 5.2 presents a typical L-curve for one of our 3-D inversions; for all runs the regularization parameter was taken to be in the vicinity of the knee of the L-curve. Note that hereinafter the misfit stands for the normalized misfit defined as

$$\phi_d^N = \frac{1}{N_{data}} \sum_{i=1}^{N_{obs}} \sum_{j=1}^{N_T(i)} \left| \frac{C_{ij}^{pred} - C_{ij}^{exp}}{\delta C_{ij}} \right|^2. \quad (5.2)$$

Here $N_{data} = \sum_{i=1}^{N_{obs}} N_T(i)$, and C_{ij}^{exp} , C_{ij}^{pred} and δC_{ij} are experimental responses, predicted responses, and uncertainties of experimental responses, respectively, of the i -th observatory and at the j -th period. The expression for N_{data} means that for some observatories a number of

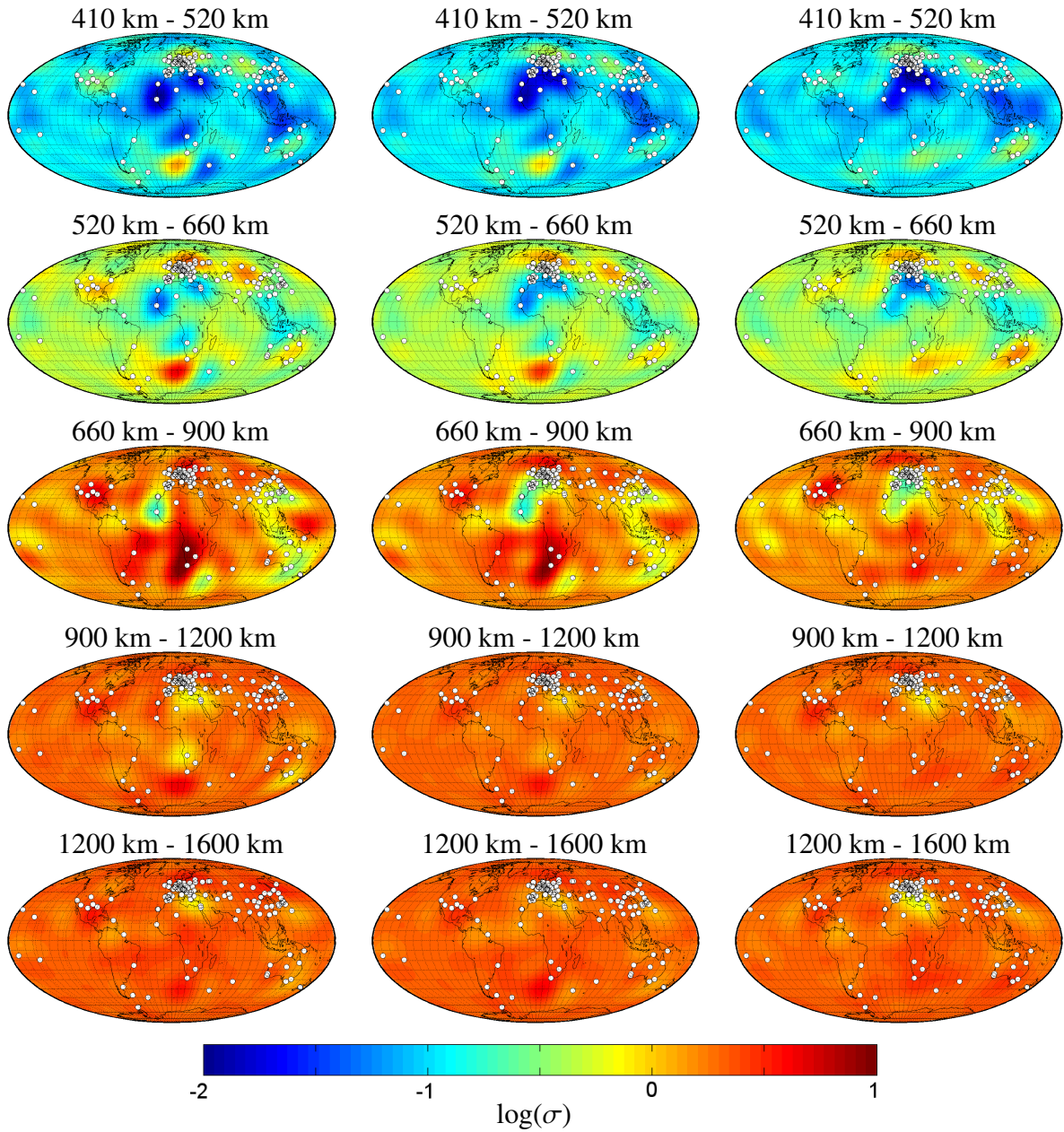


Figure 5.3: Results of our 3-D inversion. Left-hand column of plots presents the results of inversion of uncorrected responses. Middle column – the results of inversion of the responses corrected for the auroral effect. Right-hand column – the results of inversion of the responses corrected for the auroral and the ocean effects.

analyzed periods are less than 15.

To detect robust features in the conductivity images we performed three 3-D inversion runs which differ by an amount of the corrections applied to the data. In the first run data were not corrected neither for ocean nor for auroral effects. The ocean was included in the model as an additional thin (surface) inhomogeneous layer with a prescribed and fixed (during the inversion) conductance with a lateral resolution of $3^\circ \times 3^\circ$. Results from this 3-D inversion (global conductivity distributions in five inhomogeneous layers) are presented in the left-hand column of Fig. 5.3. Note that we present in this Figure not the raw results – which are piece-wise

constant conductivity distributions – but their smoothed version. The smoothing procedure is based on a spherical harmonic filtering of the raw results up to spherical harmonics of degree 9. We present the filtered results only when we discuss the global images. This is motivated by the fact that we aim to compare these images with the global results of Kelbert et al. (2009), who used a spherical harmonic parameterization (up to degree 9) of their inverse domain, as well as with the global filtered results of Tarits and Mandeia (2010). Note also that here our results are shown as decimal logarithms of conductivities. To be able to compare the results at different depths the same scale is employed for all five layers. A scale range between -2 and 1 corresponds to a range in conductivity between 0.01 S/m and 10 S/m. It is also important to emphasize at this stage that one must interpret the results of inversion in many regions (for example, in equatorial and oceanic regions) with extreme care – lack of observation precludes any conclusive inferences about conductivity distributions in these regions. For example, the decrease in conductivity beneath Indonesia in first three layers is not supported by data.

In the second run we also included the oceanic layer in the model but corrected the data for the auroral effect (see Section 4.4 for details of the correction scheme). The recovered conductivities are shown in the middle column of Fig. 5.3. Unfortunately our sophisticated scheme of data correction for the auroral effect only partly improves the results of the inversion (normalized misfit appeared to be slightly less). We nonetheless observe enhanced conductivity in our images in Northern Europe (at least in the first three layers) which is – we believe – an artefact dictated to a large extent by an inappropriate correction for the auroral effect. Discernible differences are seen only beneath North America (in the two first layers) where an implementation of the correction led to a less pronounced conductivity anomaly.

Finally, in the third run we inverted data corrected both for ocean and auroral effects. Our correction scheme for the ocean effect is outlined in Section 4.3. We exclude the surface layer from the model, assuming that our correction scheme suppresses the effect of the ocean in the responses. The results of this inversion run are shown in the right-hand column of Fig. 5.3. Here we observe substantial changes in the conductivity distribution in the three first layers beneath two regions: South Africa and Australia. The spurious anomaly to the south of the African continent, which was seen in the results of the two first runs is much decreased in amplitude. We think that this last (third) run produces the most plausible images which will be compared with results from other semi-global and global 3-D studies.

A closer look at the results presented in Fig. 5.3 reveal the following common features: (1) at depths between 410 and 900 km lateral variations in conductivity are rather prominent reaching 1.5 order of magnitude and below 900 km the conductivity variations diminish with depth; (2) all inversions show a decrease in conductivity beneath southern Europe and northern Africa at all considered depths, this feature will be discussed later in this section; (3) an increase of conductivity is discernable beneath China at depths between 520 and 900 km. This is in agreement with the results of Ichiki et al. (2001). We also see a prominent anomaly beneath the northern Europe but we attribute this feature to an artefact associated with an

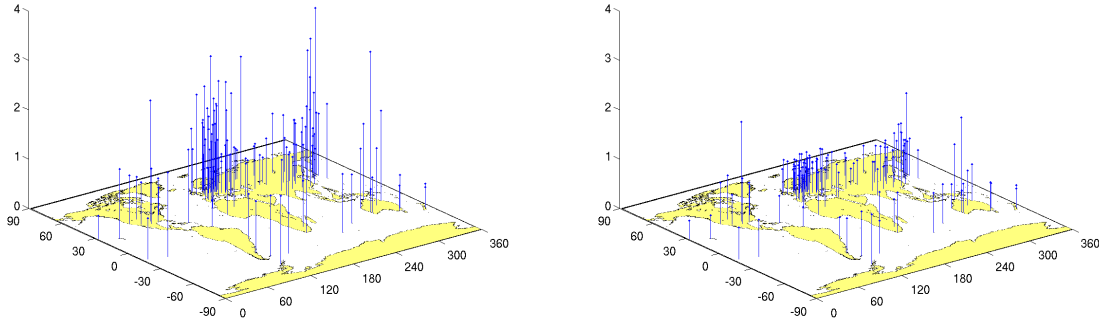


Figure 5.4: Starting misfit (left-hand plot) versus final misfit (right-hand plot).

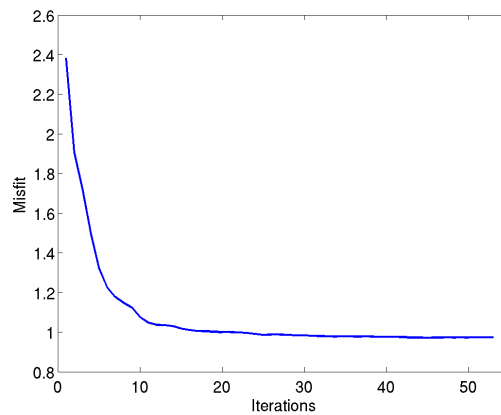


Figure 5.5: Misfit evolution during the 3-D inversion.

underestimation of the auroral effect in the corrected responses. Alternatively, one could also speculate about the presence of an enhanced conductivity beneath Australia and South Africa. However, prior to scrutinizing the conductivity maps it is also important to emphasize that results for equatorial and oceanic regions have to be interpreted with extreme care given lack of observatory data from these regions, and since the amount and the shape of this anomalous behavior strongly varies with inversion settings.

Fig. 5.4 shows how well the results of the 3-D inversion (third run) fit the data. The figure presents the misfits at each observatory for a starting 1-D conductivity model (left-hand plot) and for the recovered 3-D model (right-hand plot). It is seen that for most of the observatories the 3-D inversion substantially decreases the misfit. This is especially true for European and Japanese observatories.

Fig. 5.5 shows the evolution of the overall misfit with respect to number of iterations performed. During inversion the misfit drops from 2.4 to 0.98, and after 20 iterations the solution has converged with almost no improvement of misfit. For comparison, the two first inversion runs achieved misfits of 1.7 and 1.6, respectively.

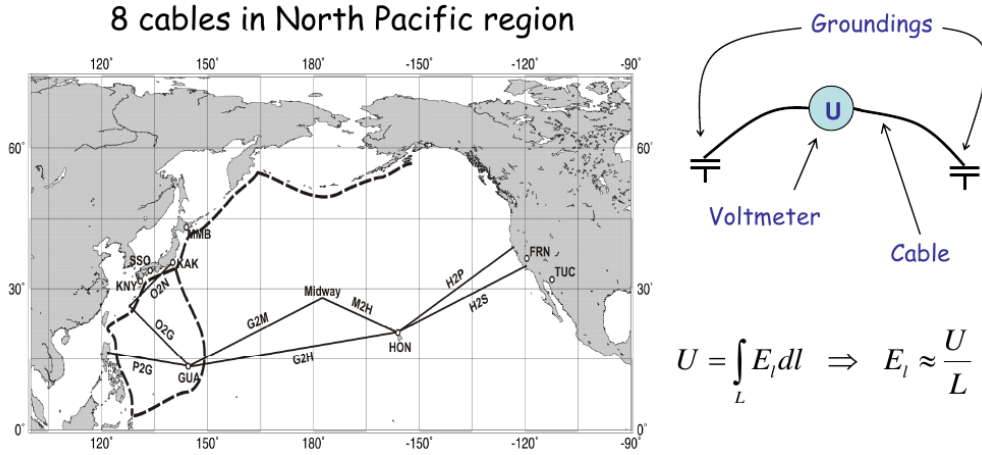


Figure 5.6: Left-hand plot presents the locations of geomagnetic observatories and Trans-Pacific telegraph cables. Right-hand plot illustrates the concept of voltage measurement using the cables.

5.2 Comparison with semi-global 3-D studies

Koyama (2001) was the first to develop and apply a rigorous 3-D inversion scheme to interpret ground-based C -responses on a semi-global scale. In later studies (Fukao et al., 2004; Koyama et al., 2006; Utada et al., 2009; Shimizu et al., 2010b) his inverse solution was exploited to analyze EM data, mostly beneath the northern Pacific region. The authors investigated voltage data from trans-Pacific submarine cables and magnetic field data from circum-Pacific geomagnetic observatories (see location of observatories and cables in Fig. 5.6). We note that Utada et al. (2009) also analyzed data from Europe (to be discussed later in this section). In the above studies lateral heterogeneity was assumed to exist between 350 and 850 km depth, thus aiming to resolve the electrical conductivity structures in and around the TZ.

We compare our results with the most recent results obtained by Shimizu et al. (2010b). Shimizu et al. (2010b) inverted GDS responses at 9 periods between 5 and 35 days from 13 observatories, and MT responses at 9 periods between 1.7 to 10.5 from 8 trans-Pacific cables. The 1-D conductivity model beneath the North Pacific obtained by Shimizu et al. (2010a) was employed as an *a priori* model in this inversion. The grid spacing for the forward problem was $2^\circ \times 2^\circ$ laterally and 50 km radially. The size of each block in the final inversion domain was $10^\circ \times 10^\circ$ laterally and 100 km radially, comprising a total of $N = 19 \times 9 \times 5$ unknowns. Absolute values of the Laplacian of $\mathbf{m} - \mathbf{m}_0$ represented the regularization term in horizontal directions. No regularization of the model parameters in the vertical direction was applied. The right-hand plots of Figure 5.7 show the resulting 3-D conductivity model. The authors detected three features in the TZ: (a) a high conductivity anomaly beneath the Philippine Sea; (b) a high conductivity anomaly beneath the Hawaiian Islands, and (c) a low conductivity anomaly beneath and in the vicinity of northern Japan.

Left-hand plots in the same Figure show our results for the same region and for similar

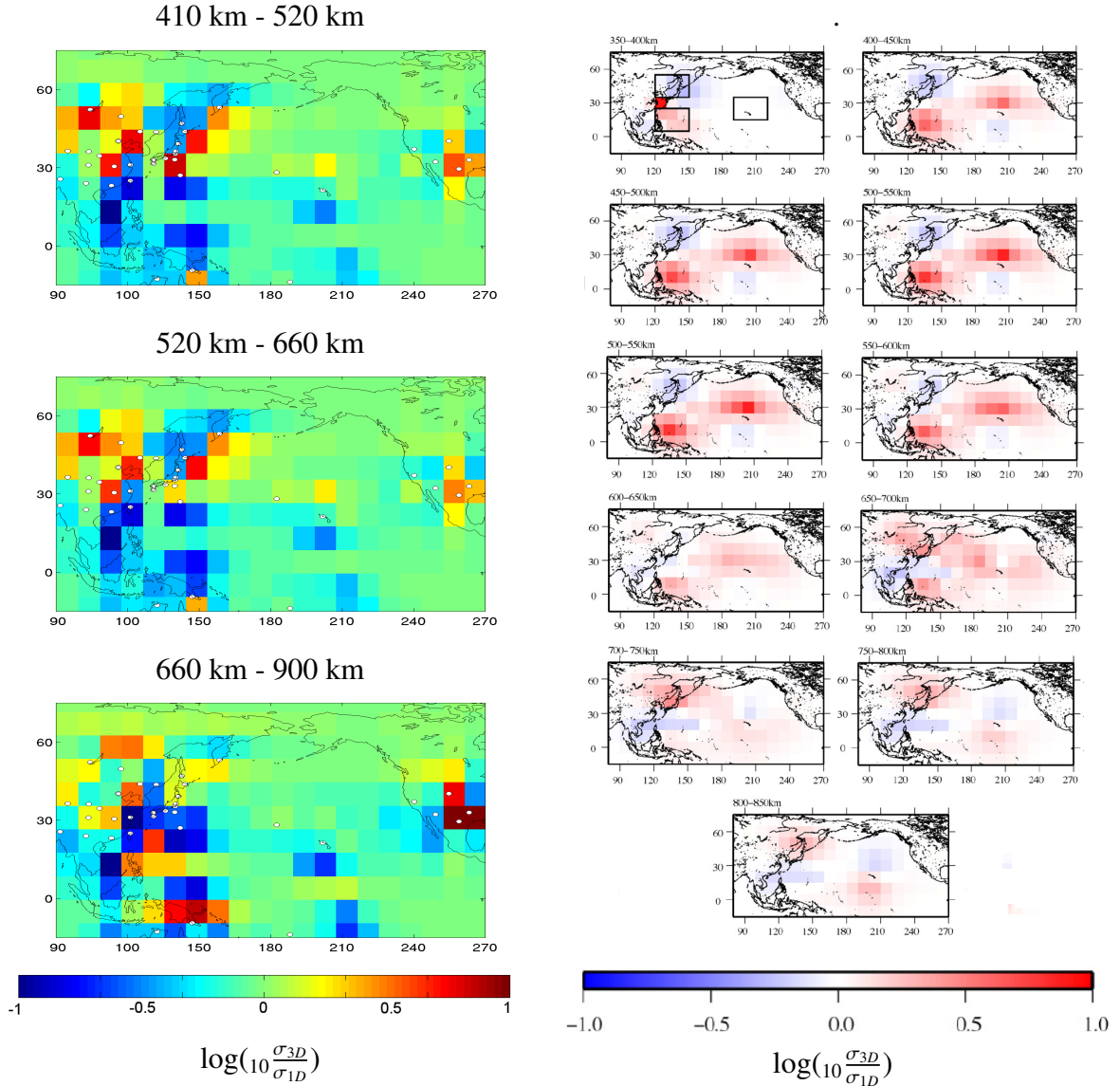


Figure 5.7: Comparison of our results (left-hand column of plots) with results from Shimizu et al. (2010b) study (two right-hand columns of plots).

depths. We plot $\log_{10}(\frac{\sigma_{3D}}{\sigma_{1D}})$, where σ_{3D} is our resulting conductivity and σ_{1D} is the 1-D *a priori* conductivity profile of Kuvshinov and Olsen (2006). Note that since the authors of these semi-global studies presented the piece-wise constant conductivity distributions we apply the same strategy showing in this section the raw (blocky) 3-D results. Surprisingly, our results mostly anti-correlate with the results of Shimizu et al. (2010b). It should be noted that their results beneath Philippine Sea and Hawaiian Islands are probably more conclusive than ours due to the fact that they used additional (“cable”) data in these regions. As for regions beneath Japan and China our results seem to be closer to the results of the global 3-D model by Kelbert et al. (2009), which we will discuss in the next section.

Utada et al. (2009) constructed a 3-D conductivity model beneath Europe in depth range between 400 and 800 km. They inverted *C*-responses obtained in the period range between 5

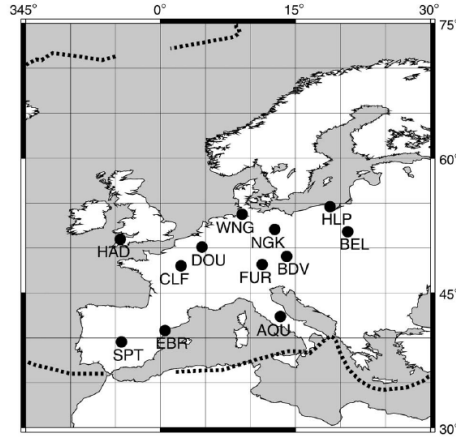


Figure 5.8: Location of observatories used in Utada et al. (2009) study.

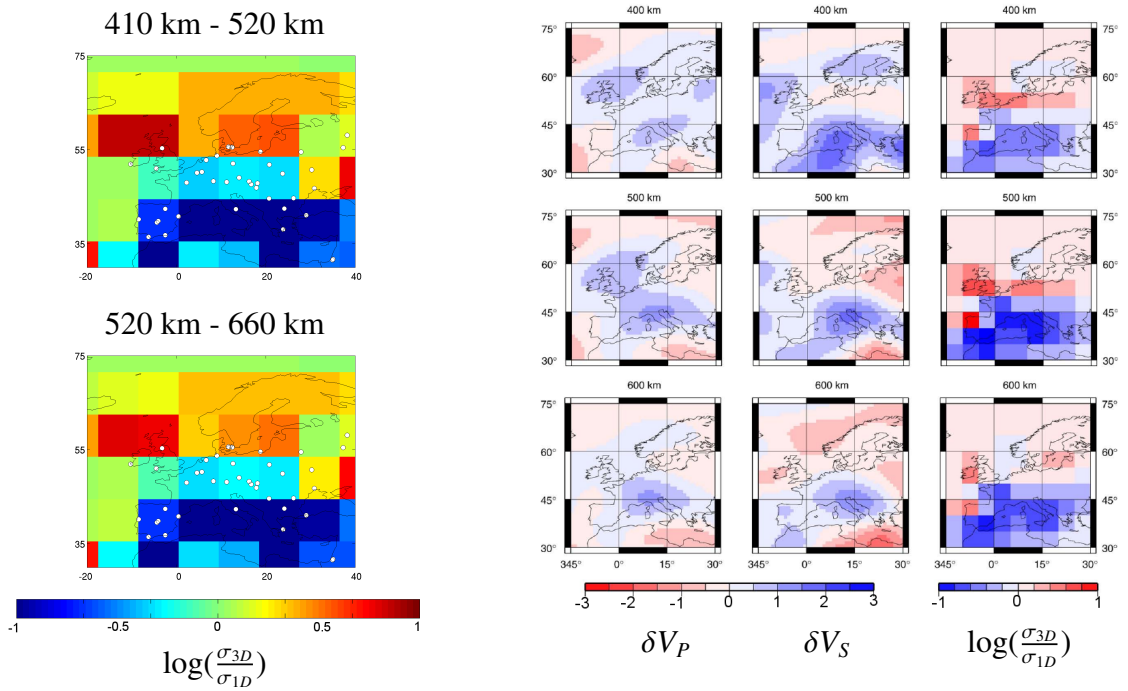


Figure 5.9: Comparison of our results (left column) with results from Utada et al. (2009) study.

and 50 days from 12 European observatories (see location of the observatories in Fig. 5.8). As an *a priori* model they used the 1-D model for the northern Pacific region (Utada et al., 2003). The grid spacing for the forward problem calculations was $1^\circ \times 1^\circ$ laterally and 50 km radially. The size of each block in the inversion domain was $5^\circ \times 5^\circ$ laterally and 100 km radially, resulting in a total of $N = 9 \times 9 \times 5$ unknowns. No regularization was applied during inversion. The authors were interested in the conductivity distribution in the TZ, at depths between 400 and 700 km. The right-hand side of Fig. 5.9 shows their conductivity anomaly maps as well as the results of global P- and S-wave tomography studies (Megnin and

Romanowicz, 2000; Obayashi et al., 2006), with $\delta V_{P(S)}$ defined as

$$\delta V_{P(S)} = \frac{V_{P(S)}^{mod} - V_{P(S)}^{PREM}}{V_{P(S)}^{PREM}} \cdot 100\%, \quad (5.3)$$

where $V_{P(S)}^{mod}$ are the P(S)-wave velocities from the 3-D study, and $V_{P(S)}^{PREM}$ are the P(S)-wave velocities from preliminary reference Earth model (PREM; Dziewonski and Anderson, 1981).

The authors found that the most notable feature in their results is the correlation between the low-conductivity and high-velocity anomalies beneath the central and southern parts of Europe, where slab material subducted from the Tyrrhenian trench stagnates in the transition zone (Faccena et al., 2003). They claim that such a correlation implies that the low-conductivity and high-velocity characteristics of the stagnant slab (Fukao et al., 2001) have a common origin, most likely temperature, and thus that there is no need to assume an additional conduction mechanism (e.g., hydrogen conduction) to explain a particular conductivity anomaly. These results led the authors to the inference that the TZ beneath Europe is relatively dry. Our results (left-hand plots) – using a different data set and different modeling technique – confirm this conclusion, with low conductivity regions beneath the central and southern parts of Europe. In the images from both studies we see enhancement of conductivity in the northern and north-western parts of Europe, but we believe that this may be an artefact related to the auroral effect, which is still present in the corrected experimental data.

5.3 Comparison with global 3-D studies

Kelbert et al. (2009) obtained the first global 3-D model of mantle electrical conductivity. They parameterized the 3-D conductivity distribution at depths between the surface and 1600 km by 8 spherical inhomogeneous layers of 100, 150, 160, 110, 150, 230, 300 and 400 km thickness, in each of which lateral conductivity variations around the 1-D reference model of Kuvshinov and Olsen (2006) are parameterized by spherical harmonics up to degree and order 9. Conductivity jumps at 410, 520 and 670 km were allowed to mimic major mineral phase transitions in mantle. Below 1600 km the layers were assumed to be homogeneous with a fixed conductivity value. They used a compilation of the *C*-responses at 59 observatories from the studies of Fujii and Schultz (2002) (responses from 53 observatories) and Schultz and Larsen (1987) (responses from 6 observatories). The responses were estimated at 28 periods from 5 to 106.7 days. The lateral grid for forward problem calculations was chosen as $10^\circ \times 10^\circ$. To account for the ocean effect the eq. (4.20) was applied, where the predicted responses were calculated with the use of integral equation (IE) solver of Kuvshinov (2008) (the IE solution is summarized in Chapter 2) using a much denser grid ($1^\circ \times 1^\circ$) to represent nonuniform oceans. The right-hand plots in Fig. 5.10 show the results of Kelbert et al. (2009). The authors note that in regions with poor data coverage, including most of Africa, South America,

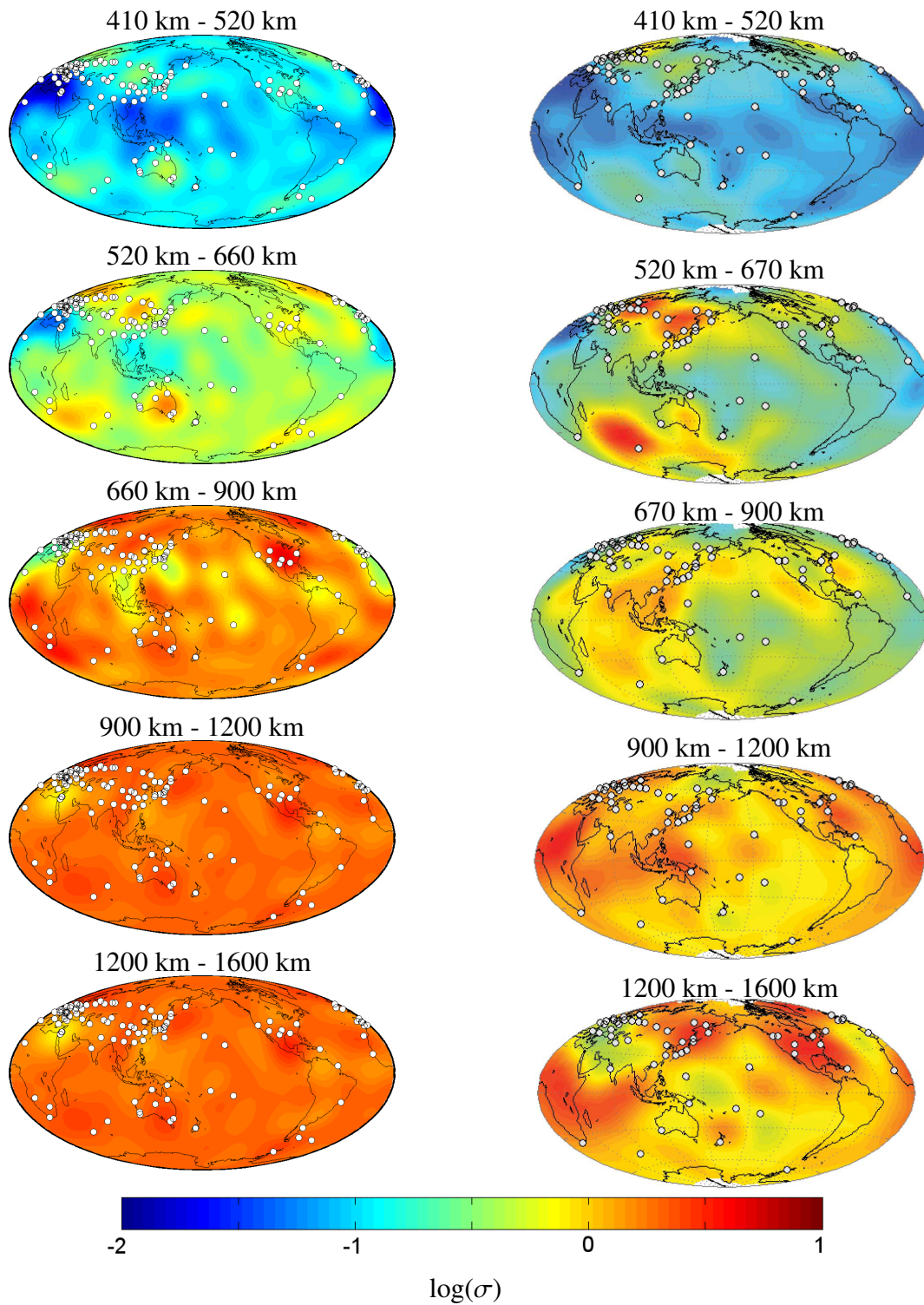


Figure 5.10: Comparison of our results (left-hand plots) with results from Kelbert et al. (2009) study (right-hand plots).

and the Indian and South Pacific Oceans, conductivity is poorly constrained at all depths. Their inversion suggests enhanced conductivity at TZ depths along the circum-Pacific margin extending from western North America, through the Aleutian arc and East Asia, and into the Indian Ocean and Australia. Most notably, higher conductivities are found beneath Japan,

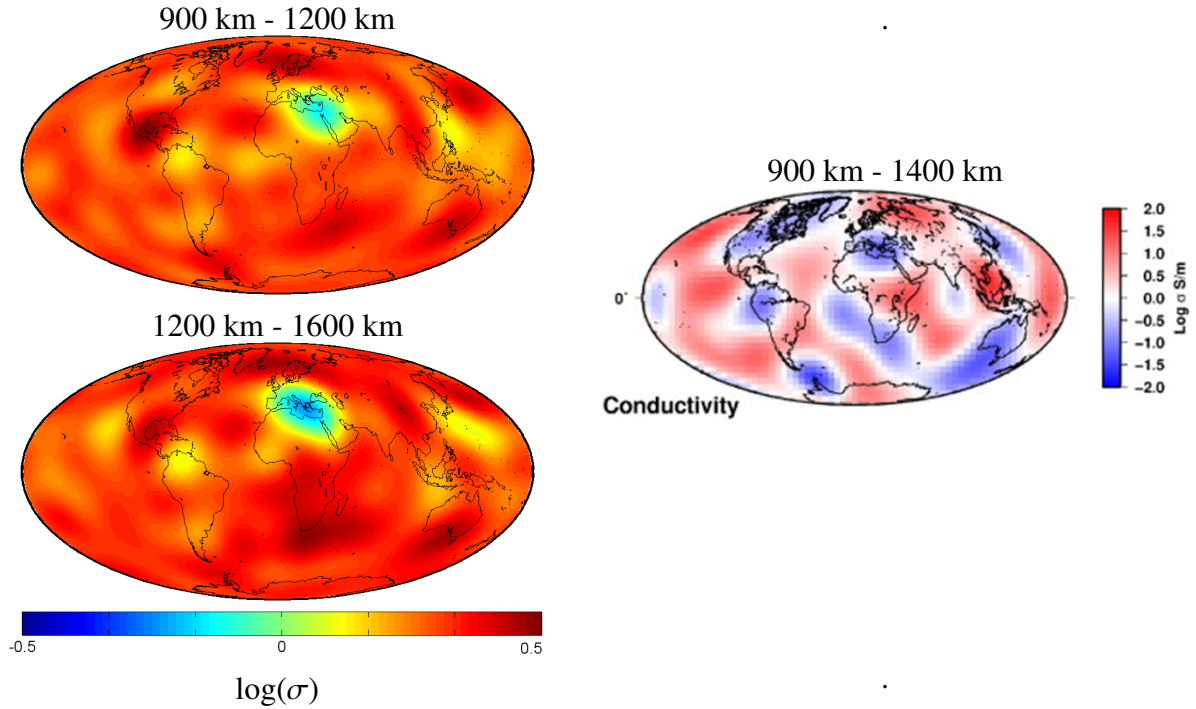


Figure 5.11: Comparison of our results (left-hand plots) with Tarits and Manda (2010) study (right-hand plot).

eastern China, and in the areas of the Izu-Bonin and Tonga slabs. The central Pacific basin is seen to be more than an order of magnitude more resistive than the surrounding conductive regions. The left-hand plots in Fig. 5.10 show our results for comparison. The images differ in detail (for example, they differ beneath North America), but nonetheless reveal two common features: (1) reduced conductivity beneath southern Europe and northern Africa; (2) enhanced conductivity beneath Japan and eastern China. The former is in agreement with the results of the semi-global study of Utada et al. (2009), while the latter, an enhanced conductivity beneath eastern China is in accord with the results of Ichiki et al. (2001). However, high conductivities beneath Japan and low conductivities beneath Hawaii contrast with the results of Shimizu et al. (2010b). In addition, both inversions show enhanced conductivities in polar regions. This is, as already remarked, likely an artefact due to inappropriate accounting/correction for the auroral source effect. Visible differences are also present in lower layers, where our results are more conductive and show less lateral variability.

Recently Tarits and Manda (2010) developed a 3-D EM time-domain technique to invert 32 years (1958-1990) of magnetic monthly mean values from 120 geomagnetic observatories to image the conductivity in the middle mantle. Their interpretation scheme includes two steps. As a first step a source field model and an initial 1-D conductivity profile are determined. To find a source they used a potential representation of the magnetic field. The authors obtained time series of external and internal coefficients up to degree $n = 3$ using a regularized least squares method. A 1-D conductivity profile was then obtained by performing a

regularized inversion of global C -responses. C -responses were estimated using time series of external and internal coefficients from dominant term ($n = 1, m = 0$) of spherical harmonic expansion, using eq. (3.1).

3-D inversion was initiated with a 1-D conductivity model obtained in an initial step. The parameters for the inversion are the conductivity in the cells of the inversion grid. Only the layer between 900 km and 1400 km was assumed to be heterogeneous. Other layers were fixed to be homogeneous with conductivities fixed to their initial 1-D model. Tarits and Mandeia (2010) used a grid with lateral resolution of $15^\circ \times 15^\circ$ (in both forward and inverse domains), thus estimating conductivity in $12 \times 24 = 288$ cells. The right-hand plots in Fig. 5.11 present their results filtered up to spherical harmonic degree 7. Our results for overlapping depth ranges are shown in the left-hand plots. The results of Tarits and Mandeia (2010) reveal low conductivities beneath the Australian region, Western Africa, near Japan, North and Central America, and high conductivities in Eastern Africa, South-East Asia and Eurasia. When compared with our results significant discrepancies can be observed. The most striking feature of the model by Tarits and Mandeia (2010) is that it shows much stronger conductivity contrasts (up to 3 decimal logarithmic units) than our model (less than 1 log unit). It is interesting however that the reduced conductivity anomaly beneath southern Europe and northern Africa is recovered in both studies.

5.4 Comparison with global 3-D seismic studies

Lateral variation of electrical conductivity and seismic velocity are caused by compositional and temperature changes in the mantle in relation with global geodynamics. Good (anti)correlation is expected when temperature variations are the leading process in a dry mantle (e.g. Shankland et al., 1993; Verhoeven et al., 2008; Utada et al., 2009): in regions with increasing temperature, the velocity decreases while the conductivity increases. This means that high conductivity corresponds to low velocity or vice versa.

There are several tomography models of the mid-mantle available (e.g. Becker and Boschi, 2002; Romanowicz, 2003). Becker and Boschi (2002) synthesized the common large scale features, which are observed in P-wave and S-wave models, and created mean models, shown in two right-hand columns of plots in Fig. 5.12. In the middle column the resulting P-wave distributions of the P-mean model of Becker and Boschi (2002) in 5 layers are presented. The results are for depths between: 399 and 498 km, 498 and 598 km, 678 and 797 km, 997 and 1096 km, 1395 and 1495 km. The depths of these layers were chosen to correspond to the depths of our 5 inhomogeneous layers. In the right-hand column of Fig. 5.12 the S-wave distributions in the S-mean model of Becker and Boschi (2002) are shown for the same layers. $\delta V_{P(S)}$ is defined as in eq. (5.3). The left-hand column in Fig. 5.12 shows our 3-D results. Fig. 5.13 in a similar manner shows the comparison of our global 3-D EM results with the most recent global 3-D seismic results of Della Mora et al. (2011). It is remarkable how well the

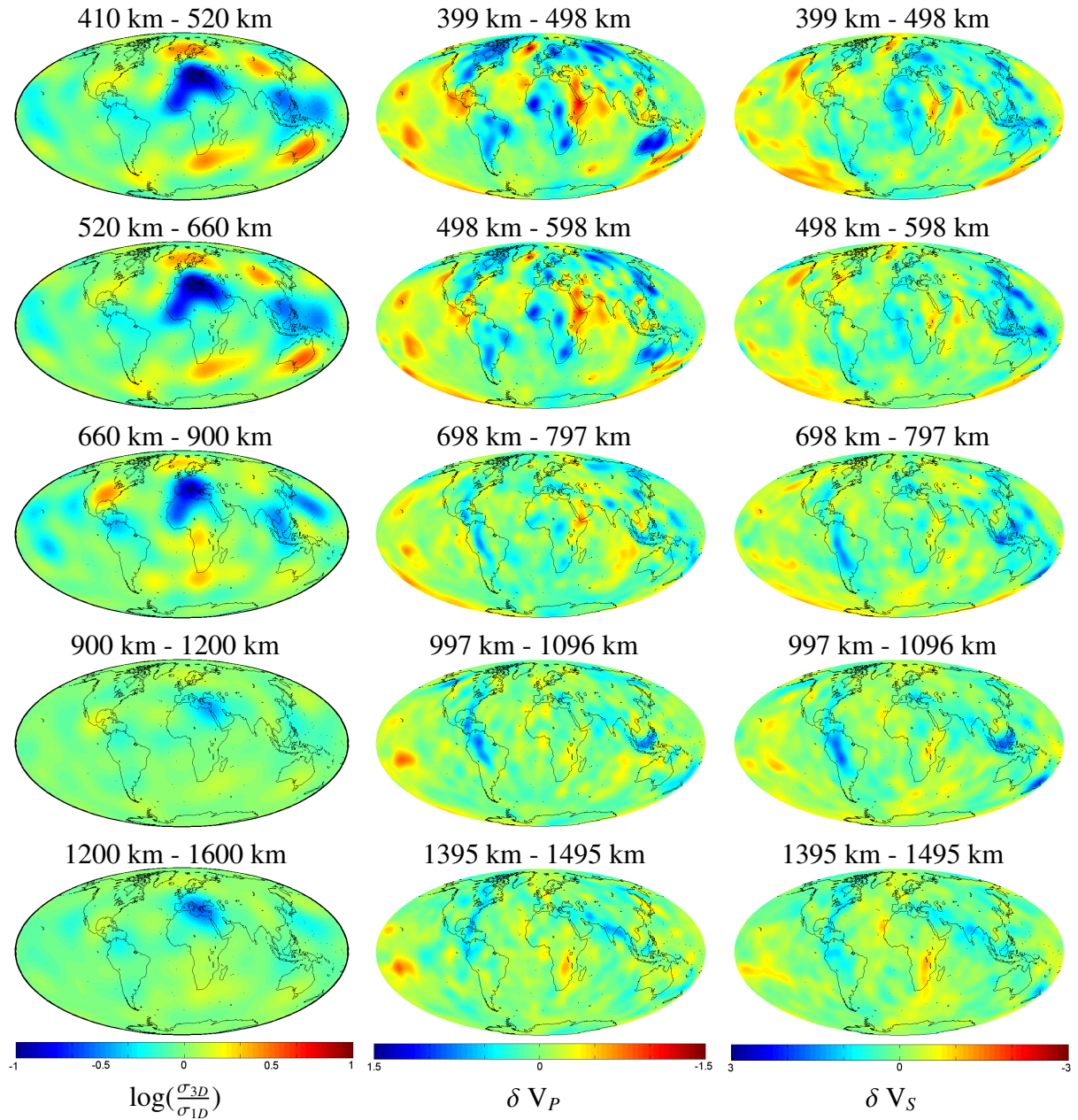


Figure 5.12: Comparison of our results (left-hand column of plots) P-wave (middle column of plots) and S-wave (right-hand column of plots) distributions from Becker and Boschi (2002).

models by Becker and Boschi (2002) and Della Mora et al. (2011) agree with each other, at least visually.

A very tentative comparison of our EM results with those from seismic studies, shows that different trends are observed (at least in two shallower layers). In northern Africa, for example, low conductivity corresponds to high velocity. But in Australia we see opposite trend: EM inversion reveals high conductivity anomaly, whereas seismic tomography suggests high velocity structure. This could be an indication of the processes that act differently on conductivity and seismic velocities. A weak correlation between high (low) conductivities and low (high) velocities may be attributed for example to the water effect (Koyama et al.,

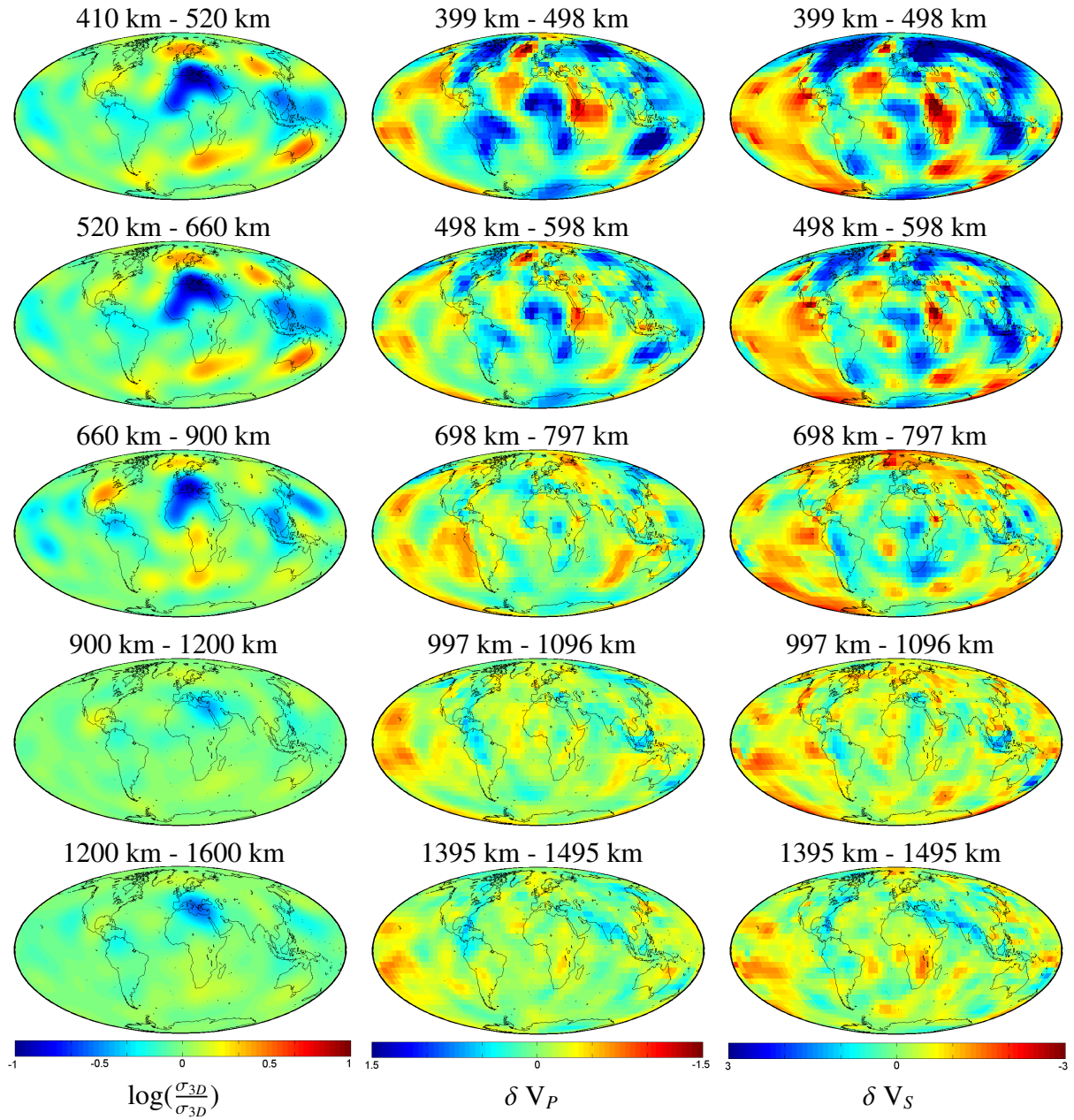


Figure 5.13: Comparison of our results (left-hand column of plots) with the P-wave (middle column of plots) and S-wave (right-hand column of plots) distributions from Della Mora et al. (2011).

2006). But we have to state that more work is still needed to ascertain the full robustness of the features observed in our 3-D EM images.

Chapter 6

Conclusions and outlook for future studies

6.1 Conclusions

A novel 3-D inversion tool for global electromagnetic studies in the frequency domain has been developed and verified with synthetic data. The technique is based on the analysis of local C -responses and exploits a limited-memory quasi-Newton optimization method. As with most other types of optimization methods, this method requires multiple calculations of the gradient of the data misfit with respect to model parameters. We implemented the adjoint method to allow efficient calculation of the gradient. In support of the gradient calculation the formulas for “magnetic-to-electric” Green’s tensor (fundamental solution of Maxwell’s equation in the Earth’s models with radially symmetric conductivity distribution, excited by arbitrarily oriented magnetic dipoles) have been derived and tested.

It is known that the efficiency of 3-D inversions depends critically on the ability to execute the forward problem promptly. Since our forward solver is based on an integral equation formulation, we take the advantage of this approach and conduct the most time-consuming part of the simulations – calculation of the tensor Green’s functions – only once, prior to the inversion. Model experiments demonstrated that separating the calculation of Green’s tensors accelerates the inverse problem solution by more than one order of magnitude.

Further improvement in computational time stems from the parallelization of the forward solver. Since forward calculations are independent with respect to frequencies, they are performed at different frequencies in parallel on N_f processors, where N_f is the number of analyzed periods.

The developed 3-D inverse solution has been applied to real ground-based geomagnetic data. The goal was to obtain three-dimensional images of the electrical conductivity distribution in the mantle at depths between 400 and 1600 km. As a first step we collected and analyzed very long time series (up to 51 years; 1957-2007) of hourly means of three com-

ponents of the geomagnetic field from 281 geomagnetic observatories. Special attention was given to data processing in order to obtain unbiased C -responses with trustworthy estimates of experimental errors in the period range from 2.9 to 104.2 days.

After careful inspection of the obtained C -responses we chose the data from 119 observatories for the further analysis. Squared coherency was used as a main quality indicator to detect (and then to exclude from consideration) observatories with large noise-to-signal ratio. During this analysis we found that – along with the C -responses from high-latitude observatories (geomagnetic latitudes higher than 58°) – the C -responses from all low-latitude observatories (geomagnetic latitudes below 11°) also have very low squared coherencies, and thus cannot be used for global induction studies.

We found that the C -responses from the selected 119 mid-latitude observatories show a huge variability both in real and imaginary parts, and we investigated to what extent the ocean effect can explain such a scatter. By performing the systematic model calculations we conclude that: (a) the variability due to the ocean effect is substantial, especially at shorter periods, and it is seen for periods up to 40 days or so; (b) the imaginary part of the C -responses is to a larger extent (compared with the real part) influenced by the oceans; (c) two types of anomalous C -response behaviour associated with the ocean effect can be distinguished. The first type is characterized by substantial increase in both real and imaginary parts towards shorter periods. In addition, at small periods (of our period range) the imaginary part becomes positive. Such behavior of the C -responses is not compatible with any 1-D conductivity structure, which always have a negative imaginary part (for adopted $e^{i\omega t}$ time dependence convention), and a descending real part with decreasing period. Three end-member observatories, showing maximum ocean effect of this type, are KOU (Kourou, French Guiana), VSS (Vassouras, Brasil), and HER (Hermanus, South Africa). The second type of anomalous behaviour is apparent as an excessive (compared with a 1-D case) decrease in both real and imaginary parts of the C -responses with decreasing period. Three observatories, showing maximum ocean effect of this type, are the Japanese observatories SSO (Simosato), HTY (Hatizyo), and KNY (Kanoya); (d) in order to accurately reproduce the ocean effect a lateral resolution of $1^\circ \times 1^\circ$ of the conductance distribution is needed. Note that from the point of view of practicality such a resolution in the case of 3-D inversion still requires prohibitively high computational loads, and the applied correction scheme to account for the ocean effect is only approximate; (e) the ocean effect alone does not explain the whole variability of the observed C -responses in particular the variability observed in the real part.

We also found that part of the variability in the real part of the C -responses is due to the auroral effect, which manifests itself as an excessive decrease of the real part at shorter periods. In addition to the observation of [Fujii and Schultz \(2002\)](#) that the influence of the auroral current system can be traced in C -responses to a geomagnetic latitude of 40° *globally*, we also found that the auroral effect in the C -responses reveals strong longitudinal variability, at least in the Northern hemisphere. Moreover, as the auroral effect is seen as the decay of the real

part of the C -responses towards higher latitudes, we clearly showed that the latitudinal pattern of the decay varies with the region and that this pattern persists in the whole period range. Europe appears to be the region with smallest degree of distortion compared with North America and northern Asia. It is interesting that the imaginary part of the C -responses is practically unaffected by the auroral source, thus confirming the fact that in the considered period range the EM induction from the auroral electrojet is negligible (due to the small scale spatial pattern of this source). Assuming the independence of the auroral signals on the Earth's conductivity (no EM induction), and longitudinal variability of the auroral effect, we developed an approximate scheme to correct the experimental C -responses for this effect.

With these developments and findings in mind we performed a number of regularized 3-D inversions of our experimental data in order to detect robust features in the recovered 3-D conductivity images. The proper choice of the regularization parameter (for each inversion run) was based on the standard L-curve formalism.

Although differing in details, all our 3-D inversions reveal a substantial level of lateral heterogeneity in the mantle at the depths between 410 and 1600 km. Conductivity values vary laterally by more than one order of magnitude between resistive and conductive regions. The maximum lateral variations of the conductivity have been detected in the layer at depths between 670 and 900 km. In the layers below (between 900 and 1600 km) the overall tendency is that lateral conductivity variations diminish in magnitude with depth. As expected, polar, equatorial and oceanic regions, where we lack data, are poorly resolved. It is believed that the forthcoming *Swarm* geomagnetic satellite mission will improve the situation providing a much better spatial data coverage.

By comparing our global 3-D results with the results of independent global and semi-global 3-D conductivity studies, we conclude that 3-D conductivity mantle models produced so far are preliminary as different groups obtain disparate results, thus complicating quantitative comparison with seismic tomography or/and geodynamic models. The present discrepancy is most probably due to: (a) strong non-uniqueness of the inverse problem arising from spatial sparsity and irregularity of data distribution, variable data quality and limited period range; (b) different data sets; (c) different inversion settings, including forward problem gridding, model parameterization, form of regularization term employed, and choice of regularisation parameter; (d) inconsistency of external field models, for example improper account/correction for the auroral effect and/or ignoring asymmetric part of the ring current; (e) possible inaccuracy in forward and inverse solutions.

In spite of this, our 3-D study and most other 3-D studies reveal at least two robust features: a) reduced conductivity beneath southern Europe and northern Africa and b) enhanced conductivity in north eastern China.

6.2 Outlook for future studies

6.2.1 Extending the data for global 3-D EM inversions

While the data from geomagnetic satellite missions are believed to be very important, we think that the major input for 3-D conductivity studies will still come from ground-based data. There are still large gaps in the ground-based network, especially in oceanic areas and in the Southern hemisphere. In the last decade a number of geomagnetic observatory projects have been initiated to improve the coverage by long-term measurements in those regions. From 2007 GFZ (Helmholtz-Zentrum Potsdam) operates an observatory in the South Atlantic Ocean on St. Helena Island (Korte et al., 2009). In 2008, a new observatory on Easter Island (South Pacific Ocean) was installed by Institut de Physique du Globe de Paris (France) and Direccion Meteorologica de Chile (Chulliat et al., 2009). Since 2009 the National Space Institute at the Technical University of Denmark runs an observatory on Tristan da Cunha Island also located in the South Atlantic Ocean (Matzka et al., 2009). The Institute of Geophysics, ETH Zurich (Switzerland) is on the way to install and run two geomagnetic observatories in the Indian Ocean – on Gan island, Maldives (in cooperation with Maldives Meteorological Service and National Geophysical Research Institute, Hyderabad, India), and on Cocos Island (in cooperation with Geoscience Australia and the Ionospheric Prediction Service).

A few long-term geomagnetic stations have been installed by Ocean Hemisphere Research Center (OHRC) of ERI (Shimizu and Utada, 1999) in the Pacific Ocean. Five stations at Majuro (Marshall Islands), Pohnpei (Micronesia), Muntinlupa (Philippines), Atele (Tonga), Marcus Island (Japan) are running and OHRC plans to continue observations at these sites.

The irregular distribution of the land/island geomagnetic observatories is improved by extending the geomagnetic observatories to the seafloor. Toh et al. (2004, 2006, 2010) reported running of two long-term seafloor stations. One station operates in the North West Pacific since 2001 and another – operates in the West Philippine Basin since 2006. Their seafloor data consist of the geomagnetic vector and scalar field measurements along with attitude measurements for both orientation and tilt. In addition, horizontal components of the electric field are measured, thus allowing for long period MT sounding.

Note that long period electric field measurements more often complement magnetic field observations. During 2001-2003 MT data have been collected at positions of 11 geomagnetic observatories situated within a few 100 km along the South West margin of the East European Craton (Semenov et al., 2008). Long period MT measurements have been conducted at 7 backbone MT stations across North America in the frame of Earthscope project (Schultz, 2010). These data are very relevant for global induction studies since the use of electric fields allows us to obtain *C*-responses at periods shorter than a few days and thus to provide information on conductivities at depths shallower than 400 km. Another merit of the MT technique is that it works in regions where the GDS method fails. For example, MT measurements might

be helpful in the vicinity of the geomagnetic equator where B_r of magnetospheric origin is close to zero thus preventing the use of the GDS method. High latitudes are also favorable for MT experiments since in these regions the GDS method also fails to work due to the fact that here the source structure is completely different from the P_1^0 structure (that is assumed by default in the GDS method). Finally, use of the electric field allows us to probe relatively resistive structures in the mantle that is not readily possible using magnetic observations only.

In addition to local MT observations, variations of the voltage differences measured with the use of the retired transoceanic submarine cables provide unique information in oceanic regions (Lizarralde et al., 1995; Utada et al., 2003, among others). Note that there exist already first successful examples of 3-D semi-global joint analysis of the data from geomagnetic observatories and trans-Pacific cables (Koyama et al., 2006; Shimizu et al., 2010b). In summary, we believe that complementing the existing data with the above-mentioned data should improve the reliability and resolution of the global 3-D images of mantle electrical conductivity.

Lastly, the analysis of forthcoming satellite data from *Swarm* or joint analysis of satellite and ground-based data should enhance the capability to detect lateral conductivity variations, especially in the vast oceanic regions where the ground-based data are still rare. But the 3-D EM inversion of satellite data is a challenging problem since satellite data analysis is more difficult compared to observatory data, because satellites move typically with a speed of 7-8 km/s and thus measure a mixture of temporal and spatial changes of the magnetic field. A review of the approaches for induction studies from space is given by Kuvshinov (2011).

6.2.2 Proper account/correction for the auroral effect

Our attempt to correct for the auroral effect in 3-D inversion of ground-based C-responses cannot be said to be fully successful. Artefacts are still present in global 3-D conductivity images at polar latitudes. A future goal, albeit challenging, would be to understand the physical processes occurring in the auroral regions in order to obtain quantitative models of the polar electrojets and incorporate these into global 3-D EM inversion schemes.

6.2.3 Further developments of our global 3-D EM inversion solution

Our experience with the development of global 3-D EM inversion and its implementation to real data allows us to formulate some possible directions for how this can be improved and extended. These directions are as follows.

1. The forward problem gridding of $3^\circ \times 3^\circ$ used during 3-D inversion is most probably not enough to account accurately for the ocean effect. Our attempt to run inversion on a dense grid of $1^\circ \times 1^\circ$ were computationally prohibitive. We also tried to correct the data for the ocean effect using dense gridding, but found that such correction only slightly influenced the results. Modification of the forward modeling scheme to allow for different lateral gridding in surface (denser grid) and deeper (coarser grid) layers could resolve this problem.

2. In existing inversion solution the volume cells, where the conductivities are searched for, are assumed to cover uniformly (in lateral directions) the inverse volume. More flexible options of the inverse volume parameterization seems to be more appropriate for ground-based data. For example discretization of the inverse volume can be made denser beneath the regions with better data coverage and sparser in the regions with no data. However, this will require development of numerical algorithm(s) to perform it in the most consistent way. Such flexibility in the model parameterization will also require elaboration of new regularization schemes which will account for this spatially nonuniform parameterization.

3. If long period MT responses and the voltage difference will be included in the interpretation one has to derive the formulas for the adjoint sources, which are needed to calculate efficiently data misfit gradient. This can be done by applying a general formalism developed by Pankratov and Kuvshinov (2010).

4. In all existing 3-D EM solutions that are based on a deterministic approaches, the resolution estimates are generally deficient. Part of the problem is the inherently non-linear relation between the Earth's conductivity structure and the responses that leads to misfit functionals with multiple local minima. In the vicinity of the global minimum the Hessian matrix (matrix of second derivatives of the misfit functional with respect to Earth model parameters) can be used to infer the resolution of and the trade-offs between model parameters. Recently, Fichtner and Trampert (2011) presented an extension of the adjoint method that allows them to compute the second derivatives of seismic data functionals with respect to Earth model parameters. Perhaps this approach can be adopted for EM studies, and thus can serve as a prelude to the development of quantitative resolution analyses.

6.2.4 Implementation of the alternative approach to global 3-D EM inversion

Alternatively a probabilistic approach, which uses a stochastic-based sampling algorithm (Mosegaard, 1998) can be applied to invert our data set in a 3-D frame. The advantage of this approach lies in its inherent ability to fully incorporate nonlinearities into the final solution, obviating any form of linearization of the original problem that is typical of deterministic approaches. This means that probabilistic approaches are capable of finding the global minimum, and allows us to obtain reliable resolution estimates. The main disadvantage of the method are huge computational resources required, since it involves thousands (at least) calls of the forward problem. To date this approach has been applied only for 1-D (or quasi 1-D) interpretation of global induction data (Khan et al., 2006, 2011). Keeping in mind our developments in solving the forward problem (separating calculations of Green's tensors, parallelization of the solution with respect to the frequencies) – along with the progress in computer hardware – we believe that implementation of a probabilistic approach for 3-D inversion of the data as implemented here will become feasible in the near future.

Appendix A

Mathematical basics

A.1 Analytic functions

The material presented below will be used in Appendix A.2. A function $f(x)$ is complex analytic on an open set $A \subset \mathbb{C}$, complex plane, if for any $x_0 \in A$ one can write

$$f(x) = \sum_{n=0}^{\infty} a_n (x - x_0)^n. \quad (\text{A.1})$$

An analytic function is an infinitely differentiable function such that the Taylor series at any point $x_0 \in A$

$$T(x) = \sum_{n=0}^{\infty} \frac{f^{(n)}(x_0)}{n!} (x - x_0)^n, \quad (\text{A.2})$$

converges to $f(x)$ in a neighborhood of x_0 .

Properties of analytic functions are as follows

- If $f(z)$ and $g(z)$ are analytic on $G \subset \mathbb{C}$ then $f(z) \pm g(z)$, $f(z) \cdot g(z)$ and $f(g(z))$ are analytic in G . If $g(z)$ is also not equal to 0 on G , then $\frac{f(z)}{g(z)}$ is analytic;
- If $f(z)$ is analytic on $G \subset \mathbb{C}$, then $f(z)$ is infinitely differentiable. The converse is not true.

There are four kinds of singularity for analytic functions

- Isolated singularities. This kind of singularity appear when function $f(x)$ is not defined at some point $a \in G$, but defined everywhere else on $G \setminus \{a\}$
 - If there exists such an analytic function $g(x)$ defined on G , that $f(x) = g(x)$ for all $x \in G \setminus \{a\}$, the point a is called a *removable singularity*;
 - If there exists such an analytic function $g(x)$, that $f(x) = \frac{g(x)}{(x-a)^n}$ for all $x \in G \setminus \{a\}$, the point a is called a *pole of order n* ;

- If the isolated singularity is neither removable, nor a pole, it is called an *essential point*;
- *Branch points* appear as a result of multi-valued functions, like \sqrt{x} or $\log(x)$, defined in a certain domain in such a way, that function can be made single-valued for this domain.

A.2 Properties of C -responses as analytic functions

Weidelt (1972) discussed in detail properties of the response function, as an analytic function. Here we sum up the most important and descriptive of them. For simplicity, only a flat Earth and uniform inducing magnetic field are considered here. Conductivity is assumed to vary with depth only.

Neglecting the displacement current and assuming free space magnetic permeability, considering the time factor to be $e^{i\omega t}$, horizontal magnetic and electric field (in x and y directions respectively) are interconnected by

$$\frac{\partial H_x(z, \omega)}{\partial z} = \sigma(z)E_y(z, \omega), \quad (\text{A.3a})$$

$$\frac{\partial E_y(z, \omega)}{\partial z} = i\omega\mu_0 H_x(z, \omega), \quad (\text{A.3b})$$

which leads to

$$\frac{\partial^2 E_y(z, \omega)}{\partial z^2} = i\omega\mu_0\sigma(z)E_y(z, \omega). \quad (\text{A.4})$$

In this case the response function $C(\omega)$ is defined as

$$C(\omega) = -\frac{E_y(0, \omega)}{E'_y(0, \omega)} = -\frac{E_y(0, \omega)}{i\omega\mu_0 H_x(0, \omega)}, \quad (\text{A.5})$$

where $E'_y(0, \omega) = \left. \frac{\partial E_y(z, \omega)}{\partial z} \right|_{z=0}$.

Let z_m be the maximum depth to which the electromagnetic field can penetrate,

$$z_m = \begin{cases} \infty, & \text{if there is no perfect conductor} \\ \text{the depth of the perfect conductor} & \end{cases} \quad (\text{A.6})$$

a) Analytic properties in the complex frequency plane

The response function $C(\omega)$ is zero-free and analytic in the whole ω -plane except on the positive imaginary axis, where it has either infinite series of interlacing simple poles and zeros, or a finite number of poles and zeros and two branch points (one at $\omega = +i\infty$), according whether integral

$$\lim_{z \rightarrow z_m} \int_0^z \sqrt{\sigma(r)} dr, \quad (\text{A.7})$$

converges or not. A possible perfect conductor at $z = z_m$ is not to be included in eq. (A.7).

The proof follows from general theorems on second order differential equations (Titchmarsh, 1962; Weidelt, 1972).

Let $w_1(z, \omega)$ and $w_2(z, \omega)$ be two solutions of eq. (A.4) with the initial conditions

$$w_1(0, \omega) = 1, \quad w_1'(0, \omega) = 0, \quad w_2(0, \omega) = 0, \quad w_2'(0, \omega) = 1. \quad (\text{A.8})$$

Their Wronskian

$$w_1(z)w_2'(z) - w_2(z)w_1'(z) = 1, \quad (\text{A.9})$$

is not zero everywhere, those solutions are linearly independent for all z , and the solution for electric field E_y from eq. (A.4) is a linear combination of them. From eqs (A.3) and (A.8) we can withdraw

$$\begin{aligned} E_y(z, \omega) &= E_y(0, \omega)w_1(z, \omega) + i\omega\mu_0 H_x(0, \omega)w_2(z, \omega), \\ &\Updownarrow \\ \frac{E_y(z, \omega)}{E_y(0, \omega)} &= w_1(z, \omega) - \frac{1}{C(\omega)}w_2(z, \omega). \end{aligned} \quad (\text{A.10})$$

Thus for any conductivity profile

$$C(\omega) = \lim_{z \rightarrow z_m} \frac{w_2(z, \omega)}{w_1(z, \omega)}. \quad (\text{A.11})$$

All singularities of $C(\omega)$ are either poles or zeroes (zeroes of w_1 and w_2 respectively), and lie on the positive imaginary ω -axis (Weidelt, 1972).

b) *Symmetry relation for $C(\omega)$*

$$C(-\omega^*) = C^*(\omega). \quad (\text{A.12})$$

It follows from eq. (A.11) and the fact, that $w_{1(2)}^*(z, \omega)$ and $w_{1(2)}(z, -\omega^*)$ satisfy the same differential equations and initial conditions.

c) *Limiting values for large and small frequencies*

For large frequencies we have

$$C(\omega) = k^{-1} - \frac{1}{4} \frac{\sigma'(0)}{\sigma(0)} k^{-2} + \mathcal{O}(k^{-3}), \quad \omega \rightarrow \infty, \quad k^2 = i\omega\mu_0\sigma(0), \quad (\text{A.13})$$

(Kamke, 1959; Siebert, 1964), and for small frequencies

$$\lim_{\omega \rightarrow 0} C(\omega) = z_m, \quad (\text{A.14})$$

which follows from eq. (A.11).

d) *Dispersion relations*

Let us for real frequencies define

$$C(\omega) = g(\omega) - ih(\omega). \quad (\text{A.15})$$

Then for real part $g(\omega)$ and imaginary part $h(\omega)$ we can write

$$g(\omega) = \frac{1}{\pi} \oint_{-\infty}^{+\infty} \frac{h(x)dx}{x - \omega} = \frac{2}{\pi} \int_0^{+\infty} \frac{xh(x)dx}{x^2 - \omega^2}, \quad (\text{A.16a})$$

$$h(\omega) = -\frac{1}{\pi} \oint_{-\infty}^{+\infty} \frac{g(x)dx}{x - \omega} = -\frac{2}{\pi} \int_0^{+\infty} \frac{\omega g(x)dx}{x^2 - \omega^2}, \quad (\text{A.16b})$$

where \oint denotes the Cauchy principal value $\oint = \lim_{\varepsilon \rightarrow 0} \left(\int_{-\infty}^{\omega - \varepsilon} + \int_{\omega + \varepsilon}^{+\infty} \right)$. For details we again refer to (Weidelt, 1972).

e) Inequalities

Let $\omega > 0$ and define an operator D by

$$Df = \omega \frac{df}{d\omega} = \frac{df}{d \ln \omega} = -\frac{df}{d \ln T}, \quad (\text{A.17})$$

where $T = \frac{2\pi}{\omega}$ is a period. Recalling the definition (A.15) following inequalities apply

$$g \geq 0, \quad h \geq 0, \quad (\text{A.18a})$$

$$Dg \leq 0, \quad (\text{A.18b})$$

$$0 \leq -D|C| \leq |C|, \quad (\text{A.18c})$$

$$|DC| \leq h, \quad |C + DC| \leq g, \quad (\text{A.18d})$$

$$|D^2C| \leq h, \quad |C + 2DC + D^2C| \leq g. \quad (\text{A.18e})$$

f) Physical meaning of the real part of $C(\omega)$

Let $j(z, \omega) = \sigma(z)E_y(z, \omega)$ be the density of the induced currents. Then from eq. (A.3), integrating by parts we can write

$$\int_0^{z_m} j(z, \omega) dz = H_x(0, \omega), \quad \int_0^{z_m} z j(z, \omega) dz = -\frac{1}{\omega \mu_0} E_y(0, \omega). \quad (\text{A.19})$$

Hence applying eq. (A.5) we get

$$g(\omega) = \frac{\int_0^{z_m} z \operatorname{Re}\{j(z, \omega)\} dz}{\int_0^{z_m} \operatorname{Re}\{j(z, \omega)\} dz}. \quad (\text{A.20})$$

Thus, $g(\omega)$ can be interpreted as the mean depth of induced current propagation for a certain frequency. Recalling eq. (A.18b), $g'(\omega) \leq 0$ shows that the mean depth of induced current system increases if the frequency is diminished, and limiting values are $g(\infty) = 0$ and $g(0) = z_m$.

A.3 Spherical harmonics

A.3.1 Laplace's equation

Spherical harmonics come from solution of Laplace's equation $\nabla^2 V = 0$ in spherical polar coordinates. In this coordinate system Laplace's equation has a form

$$\frac{1}{r} \frac{\partial^2(rV)}{\partial r^2} + \frac{1}{r^2} \frac{1}{\sin \vartheta} \frac{\partial}{\partial \vartheta} \left(\sin \vartheta \frac{\partial V}{\partial \vartheta} \right) + \frac{1}{r^2} \frac{1}{\sin^2 \vartheta} \frac{\partial^2 V}{\partial \varphi^2} = 0. \quad (\text{A.21})$$

If we separate the solution $V(r, \vartheta, \varphi) = R(r)\Theta(\vartheta)\Phi(\varphi)$, we can find that

$$R(r) = r^n \quad \text{or} \quad r^{-(n+1)}, \quad (\text{A.22a})$$

$$\Theta(\vartheta) = P_n^m(\cos \vartheta), \quad (\text{A.22b})$$

$$\Phi(\varphi) = \sin(m\varphi) \quad \text{or} \quad \cos(m\varphi), \quad (\text{A.22c})$$

where n and m are integers with $m \leq n$. $P_n^m(x)$ is an associated Legendre function, being a solution of

$$(1-x^2) \frac{d^2 P_n^m}{dx^2} - 2x \frac{dP_n^m}{dx} + \left\{ n(n+1) - \frac{m^2}{1-x^2} \right\} P_n^m = 0, \quad (\text{A.23})$$

where $x = \cos \vartheta$, n is called the degree and m – the order.

A.3.2 Associated Legendre functions

The Legendre polynomials satisfy eq. (A.23) with $m = 0$. They can be written as (e.g. Abramowitz and Stegun, 1984)

$$P_n(x) = \frac{1}{2^n n!} \frac{d^n (x^2 - 1)^n}{dx^n}. \quad (\text{A.24})$$

The associated Legendre functions are related by

$$P_n^m(x) = (1-x^2)^{\frac{m}{2}} \frac{d^m P_n(x)}{dx^m}, \quad (\text{A.25})$$

and are orthogonal to each other:

$$\int_0^\pi P_n^m(\cos \vartheta) P_k^m(\cos \vartheta) \sin \vartheta d\vartheta = \begin{cases} \frac{2}{2n+1} \frac{(n+m)!}{(n-m)!} & n = k \\ 0 & n \neq k. \end{cases} \quad (\text{A.26})$$

One can rewrite eq. (A.25) as

$$P_n^m(\cos \vartheta) = \sin^m \vartheta \frac{d^m P_n(\cos \vartheta)}{d(\cos \vartheta)^m}. \quad (\text{A.27})$$

From eq. (A.23) one can see, that $P_n(-x) = (-1)^n P_n(x)$.

A.4 Helmholtz representation

In this Appendix we introduce Helmholtz representation (on a sphere) of a general vector field; this representation is used in Chapters 2-3. Consider vector field \mathbf{F} . Then the equation

$$\mathbf{F} = U\mathbf{e}_r + \nabla_\perp V + \mathbf{e}_r \times \nabla_\perp W, \quad (\text{A.28})$$

defines the Helmholtz representation of \mathbf{F} in terms of a radial vector field $U\mathbf{e}_r$ and horizontal vector field $\nabla_\perp V + \mathbf{e}_r \times \nabla_\perp W$. This representation can be shown to be unique (cf. Backus et al., 1996) if for any value r within a shell, the average values of V and W over the sphere of radius r (denoted as $\langle \rangle_{S(r)}$) is such that

$$\langle V \rangle_{S(r)} = \langle W \rangle_{S(r)} = 0. \quad (\text{A.29})$$

Each of scalar function U , V , W can be expanded in terms of spherical harmonics in the form

$$U(r, \theta, \varphi) = \sum_{n=0}^{\infty} \sum_{m=-n}^n U_{mn}(r) S_n^m(\theta, \varphi), \quad (\text{A.30})$$

where $S_n^m(\vartheta, \varphi) = P_n^m(\cos \vartheta) e^{im\varphi}$, P_n^m are the associated Legendre polynomials of degree n ($n = 0, 1, \dots$) and of order m ($m = 0, \pm 1, \pm 2, \dots, \pm n$). Note that for V and W the $n = 0$ term is zero because of eq. (A.29). Substituting eq. (A.30) and similar expansions for V and W into eq. (A.28) we obtain

$$\begin{aligned} \mathbf{F}(r, \theta, \varphi) = & \sum_{n=0}^{\infty} \sum_{m=-n}^n U_{mn}(r) S_n^m(\theta, \varphi) \mathbf{e}_r + \\ & + \sum_{n=1}^{\infty} \sum_{m=-n}^n V_{mn}(r) \nabla_\perp S_n^m(\theta, \varphi) + \\ & + \sum_{n=1}^{\infty} \sum_{m=-n}^n W_{mn}(r) \mathbf{e}_r \times \nabla_\perp S_n^m(\theta, \varphi). \end{aligned} \quad (\text{A.31})$$

Note that if \mathbf{F} stands for the magnetic field or electric current then the terms for $n = 0$, in corresponding radial components, are also zero, since the magnetic field and electric current are solenoidal vector fields (cf. Backus et al., 1996).

A.5 Scalar Green's functions

A.5.1 Definition and properties

Definition. A Green's function, $G(r, r')$, of a linear differential operator $L = L(r)$ acting on distribution over a subset of the Euclidean space \mathbb{R}^n , at points r' , is any solution of

$$LG(r, r') = \delta(r - r'), \quad (\text{A.32})$$

where δ is the Dirac's delta function. If the kernel of L is nontrivial, then the Green's function is not unique (Eyges, 1972). However, in practice, some combination of symmetry, boundary conditions and/or other externally imposed criteria will give a unique Green's function.

This property of a Green's function can be exploited to solve differential equations of the form

$$Lu(r) = f(r). \quad (\text{A.33})$$

So, if such a function G can be found for the operator L , then if we multiply the eq. (A.32) by $f(r')$, and then integrate in the r' variable, we obtain

$$\int LG(r, r')f(r')dr' = \int \delta(r - r')f(r')dr' = f(r) = Lu(r). \quad (\text{A.34})$$

Because the operator $L = L(r)$ is linear and acts only on the variable r

$$Lu(r) = L\left(\int G(r, r')f(r')dr'\right) \Leftrightarrow u(r) = \int G(r, r')f(r')dr'. \quad (\text{A.35})$$

In our case we determine Green's function, $G(r, r') \equiv G(n, r, r')$, as a continuous (with respect to r) solution of the following equation

$$\partial_r\left(\frac{1}{p(r)}\partial_r G(n, r, r')\right) - q(r)G(n, r, r') = \delta(r - r'), \quad (\text{A.36})$$

where $p(r)$ and $q(r)$ (assumed to be continuous) are defined in Section 2.4. We also require that

$$G(n, r, r') \rightarrow 0 \begin{cases} r \rightarrow \infty \\ r \rightarrow 0 \end{cases} \quad (\text{A.37})$$

The two properties arise from our definition of the Green's function.

1. The first one is

$$\left[\frac{1}{p(r)} \partial_r G(n, r, r') \right]_{r=r'-0}^{r=r'+0} = 1. \quad (\text{A.38})$$

This property comes from continuity of the Green's function. Indeed, integrating eq. (A.36) from $r' - \Delta$ to $r' + \Delta$

$$\int_{r'-\Delta}^{r'+\Delta} \partial_r \left(\frac{1}{p(r)} \partial_r G(n, r, r') \right) dr = \int_{r'-\Delta}^{r'+\Delta} q(r) G(n, r, r') dr + \int_{r'-\Delta}^{r'+\Delta} \delta(r - r') dr, \quad (\text{A.39})$$

and tending Δ to zero we obtain the desired property. Here we used that $q(r)G(n, r, r')$ is continuous with respect to r .

2. The second property reads

$$G(n, r, r') = G(n, r', r). \quad (\text{A.40})$$

Indeed, let us write

$$\partial_r \left(\frac{1}{p(r)} \partial_r G(n, r, r') \right) = q(r) G(n, r, r') + \delta(r - r') \quad (\text{A.41})$$

and

$$\partial_r \left(\frac{1}{p(r)} \partial_r G(n, r, r'') \right) = q(r) G(n, r, r'') + \delta(r - r''). \quad (\text{A.42})$$

Multiplying the first one by $G(n, r, r'')$ and the second one by $G(n, r, r')$, subtracting then one from another, and integrating over r we have

$$\begin{aligned} \int_0^\infty \partial_r \left(\frac{1}{p(r)} \partial_r G(n, r, r') \right) G(n, r, r'') dr - \int_0^\infty \partial_r \left(\frac{1}{p(r)} \partial_r G(n, r, r'') \right) G(n, r, r') dr = \\ = \int_0^\infty G(n, r, r'') \delta(r - r') dr - \int_0^\infty G(n, r, r') \delta(r - r'') dr = \\ = G(n, r', r'') - G(n, r'', r') \end{aligned} \quad (\text{A.43})$$

The left-hand part after integrating by parts leads to

$$\frac{1}{p(r)} G(n, r, r'') \partial_r G(n, r, r') \Big|_0^\infty - \frac{1}{p(r)} G(n, r, r') \partial_r G(n, r, r'') \Big|_0^\infty = 0, \quad (\text{A.44})$$

because of the boundary conditions (A.37). Thus we obtain the symmetry of Green's function

$$G(n, r', r'') = G(n, r'', r'). \quad (\text{A.45})$$

A.5.2 Derivation of scalar Green's functions

As was stated in previous section the scalar Green's functions $G^{(p)}(n, r, r')$ are solutions of the equation

$$\partial_r \left[\frac{1}{p^{(p)}(r)} \partial_r G^{(p)}(n, r, r') \right] = q^{(p)}(r) G^{(p)}(n, r, r') + \delta(r - r'), \quad (\text{A.46})$$

with the imposed boundary conditions: $G^{(p)}(n, r, r') \rightarrow 0$ when $r \rightarrow 0$ and $r \rightarrow \infty$. The coefficients for the two modes ("t" and "p") are defined in eq. (2.40) and eq. (2.41), respectively. From eq. (A.38) we obtain the following matching condition

$$\frac{1}{p(r' + 0)} \partial_r G(n, r' + 0, r') = \frac{1}{p(r' - 0)} \partial_r G(n, r' - 0, r') + 1. \quad (\text{A.47})$$

Here and later in this section we will omit superscripts "t" and "p" for the simplicity of presentation. By fixing r' we write

$$G(n, r, r') = \begin{cases} v^u(n, r), & r > r' \\ v^l(n, r), & r < r' \end{cases}, \quad (\text{A.48})$$

where functions $v^u(n, r)$ and $v^l(n, r)$ satisfy the equation

$$\partial_r \left[\frac{1}{p(r)} \partial_r v^{(u)}(n, r) \right] = q(r) v^{(u)}(n, r), \quad (\text{A.49})$$

and where $v^u(n, r) \rightarrow 0$, when $r \rightarrow \infty$, and $v^l(n, r) \rightarrow 0$, when $r \rightarrow 0$. We introduce further "lower", Y^l , and "upper", Y^u , admittances as follows

$$Y^l(n, r) = \frac{1}{p(r)} \frac{\partial_r v^l(n, r)}{v^l(n, r)}, \quad Y^u(n, r) = -\frac{1}{p(r)} \frac{\partial_r v^u(n, r)}{v^u(n, r)}. \quad (\text{A.50})$$

Using eq. (A.50) we write

$$v^l(n, r) = v^l(n, r') \exp \left[\int_{r'}^r p(\xi) Y^l(n, \xi) d\xi \right], \quad v^u(n, r) = v^u(n, r') \exp \left[- \int_{r'}^r p(\xi) Y^u(n, \xi) d\xi \right]. \quad (\text{A.51})$$

Then substituting eq. (A.51) into eq. (A.48) and using eq. (A.47) we obtain

$$\frac{1}{p(r' + 0)} \partial_r v^u(n, r' + 0) = \frac{1}{p(r' - 0)} \partial_r v^l(n, r' - 0) + 1. \quad (\text{A.52})$$

Noting the continuity of $G(n, r, r')$ with respect to r we use that

$$v^u(n, r' + 0) = v^u(n, r') = v^l(n, r') = v^l(n, r' - 0). \quad (\text{A.53})$$

Then using eq. (A.50) we represent $v^u(n, r)$ and $v^l(n, r)$ as

$$v^u(n, r') = v^l(n, r') = -\frac{1}{Y^l(n, r') + Y^u(n, r')}. \quad (\text{A.54})$$

And finally from eqs (A.48), (A.51) - (A.54) we write the explicit form of scalar Green's function as

$$G(n, r, r') = -\frac{1}{Y^l(n, r') + Y^u(n, r')} \cdot \exp \left[\int_{r'}^r p(n, \xi) \alpha(n, \xi, r') d\xi \right], \quad (\text{A.55})$$

where the spectral function α is defined as

$$\alpha(n, r, r') = \begin{cases} -Y^u(n, r), & r > r' \\ Y^l(n, r), & r < r' \end{cases}. \quad (\text{A.56})$$

A.5.3 Calculation of admittances

In order to calculate the admittances $Y^{l,t(p)}(n, r)$ and $Y^{u,t(p)}(n, r)$ we assume that the radially symmetric reference section consists of N layers $\{r_{k+1} < r \leq r_k\}_{k=1,2,\dots,N}$. We construct the set $\{r_k\}_{k=1,2,\dots,N}$ in such a way that it includes all levels r_j , where we will calculate the admittances and the Green's scalar functions. We assume that within each layer the conductivity varies as

$$\sigma_o(r) = \sigma_k \left(\frac{r_k}{r} \right)^2, \quad r_{k+1} < r \leq r_k, \quad (\text{A.57})$$

where $r_1 = a$, $r_{N+1} = 0$, σ_k is an appropriate constant. Distribution (A.57) (cf. [Rokityansky \(1982\)](#); [Fainberg et al. \(1990\)](#)) is chosen to make recurrent calculations of $Y^{l,t(p)}(n, r)$ and $Y^{u,t(p)}(n, r)$ for any n as accurate and stable as possible. Since N can be taken as large as necessary, the distribution (A.57) allows for the approximation of any radially symmetric conductivity distribution. Let us show, with an example of $Y^{l,p}(n, r)$, how these recurrences are derived.

According to eq. (2.41) and using eq. (A.57), eq. (A.49) for $v^{l,p}$ within k -th layer is written as

$$\frac{\partial^2}{\partial r^2} v^{l,p}(n, r) - \frac{n(n+1) - i\omega\mu_0\sigma_k r_k^2}{r^2} v^{l,p}(n, r) = 0. \quad (\text{A.58})$$

The solution of equation

$$\frac{\partial^2}{\partial r^2} v(r) = \frac{C}{r^2} v(r), \quad (\text{A.59})$$

where C is constant can generally be written in form

$$Ar^{x_1} + Br^{x_2}, \quad (\text{A.60})$$

where A and B are constants and x_1 and x_2 are the roots of quadratic equation

$$x(x-1) = C \quad \leftrightarrow \quad x^2 - x - C = 0, \quad (\text{A.61})$$

and therefore

$$v(r) = Ar^{\frac{1}{2}+} \sqrt{\frac{1}{4}+C} + Br^{\frac{1}{2}-} \sqrt{\frac{1}{4}+C}. \quad (\text{A.62})$$

The solution of eq. (A.58) has the form

$$v^{l,p}(n, r) = A_k^{l,p} \left(\frac{r_{k+1}}{r} \right)^{b_k^-} + B_k^{l,p} \left(\frac{r}{r_{k+1}} \right)^{b_k^+}, \quad (\text{A.63})$$

where

$$b_k^- = b_k - \frac{1}{2}, \quad b_k^+ = b_k + \frac{1}{2}, \quad b_k = \left\{ \left(n + \frac{1}{2} \right)^2 - i\omega\mu_0\sigma_k r_k^2 \right\}^{\frac{1}{2}}. \quad (\text{A.64})$$

From eq. (A.63) we get

$$\partial_r v^{l,p}(n, r) = \frac{-b_k^- A_k^{l,p}}{r_{k+1}} \left(\frac{r_{k+1}}{r} \right)^{b_k^-+1} + \frac{b_k^+ B_k^{l,p}}{r_{k+1}} \left(\frac{r}{r_{k+1}} \right)^{b_k^+-1}. \quad (\text{A.65})$$

Substituting eq. (A.63) and eq. (A.65) into eq. (A.50), taking into account eq. (2.41), we obtain

$$Y^{l,p}(n, \omega, r) = \frac{\sigma_k r_k^2 - \frac{b_k^- C_k^{l,p}}{r_{k+1}} \left(\frac{r_{k+1}}{r} \right)^{b_k^-+1} + \frac{b_k^+}{r_{k+1}} \left(\frac{r}{r_{k+1}} \right)^{b_k^+-1}}{\frac{b_k^+ b_k^-}{C_k^{l,p} \left(\frac{r_{k+1}}{r} \right)^{b_k^-} + \left(\frac{r}{r_{k+1}} \right)^{b_k^+}}}, \quad (\text{A.66})$$

where $C_k^{l,p} = \frac{A_k^{l,p}}{B_k^{l,p}}$. By setting $r = r_{k+1}$ in eq. (A.66) we obtain for $C_k^{l,p}$

$$C_k^{l,p} = \frac{\frac{\sigma_k r_k^2}{b_k^- r_{k+1}} - Y_{k+1}^{l,p}}{\frac{\sigma_k r_k^2}{b_k^+ r_{k+1}} + Y_{k+1}^{l,p}}, \quad (\text{A.67})$$

where $Y_{k+1}^{l,p} \equiv Y^{l,p}(n, \omega, r_{k+1})$. Substituting eq. (A.67) into eq. (A.66) we finally have the recurrence

$$Y_k^{l,p} \equiv Y^{l,p}(n, \omega, r_k) = g_k \frac{Y_{k+1}^{l,p} (b_k - 0.5\tau_k) - g_l \eta_k \tau_k}{g_k \eta_k (b_k + 0.5\tau_k) - b_k^+ b_k^- \tau_k Y_{k+1}^{p,l}}, \quad k = N-1, N-2, \dots, 1, \quad (\text{A.68})$$

where

$$\eta_k = \frac{r_k}{r_{k+1}}, \quad \tau_k = \frac{1 - \zeta_k}{1 + \zeta_k}, \quad \zeta_k = \eta_k^{2b_k}, \quad g_k = \sigma_k r_k, \quad (\text{A.69})$$

and

$$Y_N^{l,p} = \frac{\sigma_N r_N}{b_N^-}. \quad (\text{A.70})$$

Deriving eq. (A.68) we used continuity of admittance at the boundaries of the spherical layers. In addition, while deriving eq. (A.70) we used the fact that $A_N^{p,l} = 0$, what follows from

boundary condition $v^{l,p} \rightarrow 0$, when $r \rightarrow 0$. In a similar way we derive the recurrences for $Y^{u,p}$, $Y^{l,t}$, $Y^{u,t}$

$$Y_k^{l,t} = \frac{1}{q_k} \frac{q_{k+1} Y_{k+1}^{l,t} (b_k - 0.5\tau_k) + b_k^+ b_k^- \tau_k}{(b_k + 0.5\tau_k) + q_{k+1} \tau_k Y_{k+1}^{l,t}}, \quad k = N-1, N-2, \dots, 1, \quad Y_N^{l,t} = -\frac{b_N^+}{q_N}, \quad (\text{A.71})$$

$$Y_{k+1}^{u,t} = \frac{1}{q_{k+1}} \frac{q_k Y_k^{u,t} (b_k + 0.5\tau_k) + b_k^+ b_k^- \tau_k}{(b_k - 0.5\tau_k) + q_k \tau_k Y_k^{u,t}}, \quad k = 1, 2, \dots, N-1, \quad Y_1^{u,t} = -\frac{b_1^-}{q_1}, \quad (\text{A.72})$$

$$Y_{k+1}^{u,p} = g_k \eta_k \frac{Y_k^{u,p} (b_k + 0.5\tau_k) - g_k \tau_k}{g_k (b_k - 0.5\tau_k) - b_k^+ b_k^- \tau_k Y_k^{u,p}}, \quad k = 1, 2, \dots, N-1, \quad Y_1^{u,p} = \frac{\sigma_1 r_1}{b_1^+}, \quad (\text{A.73})$$

where

$$q_k = i\omega\mu_0 r_k. \quad (\text{A.74})$$

A.5.4 Calculation of scalar Green functions

Finally we show how to calculate $G^{(p)}(n, r, r')$ when $r \neq r'$. Let us consider the calculation of $G^t(n, r_i, r_j)$ when $r_i \leq r_j$. From eqs (A.55) and (A.56) it follows that $G^t(n, r_i, r_j)$ can be written as

$$G^t(n, r_i, r_j) = -\frac{1}{Y_j^{t,l} + Y_j^{t,u}} \prod_{k=j}^i F_k^t, \quad r_i \leq r_j, \quad (\text{A.75})$$

where F_k^t is defined as

$$F_k^t = \exp\left(\int_{r_{k+1}}^{r_k} i\omega\mu_0 Y^{t,l}(n, r) dr\right), \quad (\text{A.76})$$

and $Y^{t,l}$ (in analogy with $Y^{p,l}$) has the form

$$Y^{t,l}(n, r) = -\frac{1}{i\omega\mu_0} \frac{-\frac{b_k^- C_k^{t,l}}{r_{k+1}} \left(\frac{r_{k+1}}{r}\right)^{b_k^-+1} + \frac{b_k^+}{r_{k+1}} \left(\frac{r}{r_{k+1}}\right)^{b_k^+-1}}{C_k^{t,l} \left(\frac{r_{k+1}}{r}\right)^{b_k^-} + \left(\frac{r}{r_{k+1}}\right)^{b_k^+}}. \quad (\text{A.77})$$

Substituting eq. (A.77) into eq. (A.76) we derive

$$\begin{aligned} \int_{r_{k+1}}^{r_k} i\omega\mu_0 Y^{t,l}(n, r) dr &= \frac{1}{r_{k+1}} \int_{r_{k+1}}^{r_k} \frac{b_k^- C_k^{t,l} - b_k^+ \left(\frac{r}{r_{k+1}}\right)^{2b_k}}{\left(\frac{r}{r_{k+1}}\right) \left(C_k^{t,l} + \left(\frac{r}{r_{k+1}}\right)^{2b_k}\right)} dr = \\ &= \frac{1}{b_k} \int_1^{\zeta_k} \frac{C_k^{t,l} b_k^- - b_k^+ \gamma_k}{\gamma_k (C_k^{t,l} + \gamma_k)} d\gamma_k = \ln \left(\frac{C_k^{t,l} + 1}{C_k^{t,l} + \gamma_k} \eta_k^{b_k^-} \right). \end{aligned} \quad (\text{A.78})$$

While integrating we used the change of variables, $\gamma_k = \eta^{2b_k}$, where $\eta = \frac{r}{r_{k+1}}$, and tabular integrals $\int \frac{dx}{a+bx} = \frac{1}{b} \ln(a+bx)$, $\int \frac{dx}{x(a+bx)} = -\frac{1}{a} \ln\left(\frac{a+bx}{x}\right)$. Setting further in eq. (A.77) $r = r_{k+1}$ we obtain for $C_k^{t,l}$

$$C_k^{t,l} = \frac{b_k^+ + i\omega\mu_0 Y_{k+1}^{t,l}}{b_k^- - i\omega\mu_0 Y_{k+1}^{t,l}}. \quad (\text{A.79})$$

Substituting eq. (A.79) into eq. (A.78) and then eq. (A.78) into eq. (A.76) we obtain for F_k^t

$$F_k^t = \frac{1}{1 + \zeta_k} \frac{2b_k \eta_k^{b_k^-}}{(b_k + 0.5\tau_k) + q_k \tau_k Y_{k+1}^{t,l}}. \quad (\text{A.80})$$

In a similar way we obtain the expressions for another mode

$$G^p(n, r_i, r_j) = -\frac{1}{Y_j^{p,l} + Y_j^{p,u}} \prod_{k=j}^i F_k^p, \quad r_i \leq r_j, \quad (\text{A.81})$$

where

$$F_k^p = \frac{1}{1 + \zeta_k} \frac{2g_k b_k \eta_k^{b_k^-}}{g_k \eta_k (b_k + 0.5\tau_k) - b_k^+ b_k^- \tau_k Y_{k+1}^{l,p}}. \quad (\text{A.82})$$

Due to symmetry of scalar Green's functions, $G^{(p)}(n, r, r') = G^{(p)}(n, r', r)$ (see eq. (A.40)), one derives the results for $r_i > r_j$.

Appendix B

Representation of EM field in 1-D conductivity model via external coefficients

B.1 Representation of \mathbf{B}^e via equivalent sheet current

The results presented below will be used in Appendix B.2. It is known that in the source-free (and insulating) region, the magnetic field \mathbf{B} can be represented via the scalar magnetic potential V

$$\mathbf{B} = \mu_0 \mathbf{H} = -\nabla V. \quad (\text{B.1})$$

Since magnetic field is solenoidal

$$\nabla \cdot \mathbf{B} = 0, \quad (\text{B.2})$$

potential V satisfies Laplace's equation

$$\Delta V = 0. \quad (\text{B.3})$$

The general solution of Laplace's equation in spherical coordinates in this region is given by

$$V = a \sum_{n,m} \left[\epsilon_n^m \left(\frac{r}{a} \right)^n + \iota_n^m \left(\frac{a}{r} \right)^{n+1} \right] S_n^m(\vartheta, \varphi), \quad (\text{B.4})$$

where $\epsilon_n^m \equiv \epsilon_n^m(\omega)$ and $\iota_n^m \equiv \iota_n^m(\omega)$ are the complex-valued expansion coefficients of inducing (external) and induced (internal) parts of the potential. Using eqs (B.1) and (B.4) one can write magnetic field, \mathbf{B} , in the form

$$\mathbf{B} = \mathbf{B}^e + \mathbf{B}^i, \quad (\text{B.5})$$

where

$$\mathbf{B}^e = -\nabla \left\{ a \sum_{n,m} \epsilon_n^m \left(\frac{r}{a} \right)^n S_n^m(\vartheta, \varphi) \right\}, \quad (\text{B.6})$$

$$\mathbf{B}^i = -\nabla \left\{ a \sum_{n,m} \iota_n^m \left(\frac{a}{r} \right)^{n+1} S_n^m(\vartheta, \varphi) \right\}. \quad (\text{B.7})$$

Let us introduce a spherical, infinitely thin shell of radius b and assume that the shell is surrounded by the insulator. We also assume that the current system flows in the shell, and therefore is described by the sheet current density, \mathbf{J}_τ^{ext} . In the region above the shell $r > b$ the source is seen as internal, producing a magnetic field of the form of eq. (B.7). Below the shell $r < b$ the source is seen as external, producing a field with a magnetic potential of the form of eq. (B.6). However, because \mathbf{B} is solenoidal, one can obtain (using Gauss theorem) that the radial component, B_r , is continuous across the shell, and thus

$$B_r^i|_{r=b} = B_r^e|_{r=b}. \quad (\text{B.8})$$

Substituting expressions for B_r^e and B_r^i from eqs (B.6) and (B.7) into eq. (B.8) we find that coefficients ϵ_n^m and ι_n^m are connected via relation

$$\iota_n^m = -\frac{n}{n+1} \left(\frac{b}{a} \right)^{2n+1} \epsilon_n^m. \quad (\text{B.9})$$

In contrast to the radial component of magnetic field which is continuous across the shell, horizontal components have a jump across the shell

$$\mathbf{J}_\tau^{ext} = \frac{\delta(r-b)}{\mu_0} \mathbf{e}_r \times (\mathbf{B}_\tau^+ - \mathbf{B}_\tau^-), \quad (\text{B.10})$$

which follows from Ampere's law. Here

$$\mathbf{B}_\tau^+ = \mathbf{B}_\tau|_{r \rightarrow b+0} = \mathbf{B}_\tau^i|_{r=b}, \quad (\text{B.11})$$

$$\mathbf{B}_\tau^- = \mathbf{B}_\tau|_{r \rightarrow b-0} = \mathbf{B}_\tau^e|_{r=b}. \quad (\text{B.12})$$

Substituting expressions for \mathbf{B}_τ^e and \mathbf{B}_τ^i from eqs (B.11) and (B.12) into eq. (B.10), and using eqs (B.6)-(B.7) and relation (B.9) we express \mathbf{J}_τ^{ext} via the external coefficients ϵ_n^m as

$$\mathbf{J}_\tau^{ext} = \frac{\delta(r-b)}{\mu_0} \sum_{n,m} \frac{2n+1}{n+1} \epsilon_n^m \left(\frac{b}{a} \right)^{n-1} \mathbf{e}_r \times \nabla_\perp S_n^m(\vartheta, \varphi). \quad (\text{B.13})$$

Thus, the currents in the form of eq. (B.13) flowing in a shell $r = b \geq a$ (embedded in an insulator) produce exactly the external magnetic field \mathbf{B}^e below the shell in the region $a \leq r < b$.

B.2 Final representation of EM fields

In Appendix B.1 we discussed a representation of our impressed (magnetospheric) source in the form of a SHE of an equivalent sheet current, \mathbf{J}_τ^{ext} . Now we obtain the representation for \mathbf{E}^0 and \mathbf{H}^0 (cf. eqs (2.10)-(2.9)) via \mathbf{J}_τ^{ext} (and thus via inducing coefficients ϵ_n^m). Substituting eq. (B.13) into eq. (2.60), then the resulting expression into eq. (2.56), by accounting eqs (2.32b) and (2.33a), and rearranging operations of integration and summation, we write the SHE for the horizontal electric field, \mathbf{E}_τ^0 , in the following form

$$\mathbf{E}_\tau^0(r, \vartheta, \varphi) = \frac{1}{\mu_0} \frac{b}{r} \sum_{n,m} \frac{2n+1}{n+1} \epsilon_n^m \left(\frac{b}{a}\right)^{n-1} G^t(n, r, b) \mathbf{e}_r \times \nabla_\perp S_n^m(\vartheta, \varphi). \quad (\text{B.14})$$

Since the sheet current is horizontal and, moreover, contains only one (“ t ”) mode, then

$$E_r^0(r, \vartheta, \varphi) = 0. \quad (\text{B.15})$$

In a similar way, using eqs (2.32a), (2.32b), (2.34a), (2.34b), (2.38), and (2.58) we write SHE for the magnetic field, \mathbf{H}^0 , as

$$H_r^0(r, \vartheta, \varphi) = -\frac{1}{i\omega\mu_0} \frac{b}{\mu_0 r^2} \sum_{n,m} (2n+1)n\epsilon_n^m \left(\frac{b}{a}\right)^{n-1} G^t(n, r, b) S_n^m(\vartheta, \varphi), \quad (\text{B.16})$$

$$\mathbf{H}_\tau^0(r, \vartheta, \varphi) = \frac{1}{\mu_0} \frac{b}{r} \sum_{n,m} \frac{2n+1}{n+1} \epsilon_n^m \left(\frac{b}{a}\right)^{n-1} \alpha^t(n, r, b) G^t(n, r, b) \nabla_\perp S_n^m(\vartheta, \varphi). \quad (\text{B.17})$$

Let us obtain expressions for electric and magnetic field at the surface of the Earth. Assume that \mathbf{J}_τ^{ext} flows just above the Earth’s surface, i.e. at $b = a+$. From eqs (A.55), (A.64), (A.71), (A.72) and (A.74) we then have

$$G^t(n, a, a+) = -\frac{i\omega\mu_0 a}{i\omega\mu_0 a Y_1^{l,t} - n}, \quad (\text{B.18})$$

and from eq. (A.56)

$$\alpha^t(n, a, a+) = Y_1^{l,t}. \quad (\text{B.19})$$

Using eqs (B.18) and (B.19) we finally derive expressions for the electric and magnetic fields on the surface of the Earth

$$\mathbf{E}_\tau^0(a, \vartheta, \varphi) = -\frac{1}{\mu_0} \sum_{n,m} \frac{2n+1}{n+1} \epsilon_n^m \frac{i\omega\mu_0 a}{i\omega\mu_0 a Y_1^{l,t} - n} \mathbf{e}_r \times \nabla_\perp S_n^m(\vartheta, \varphi), \quad (\text{B.20})$$

$$H_r^0(a, \vartheta, \varphi) = \frac{1}{\mu_0} \sum_{n,m} (2n+1)n\epsilon_n^m \frac{1}{i\omega\mu_0 a Y_1^{l,t} - n} S_n^m(\vartheta, \varphi), \quad (\text{B.21})$$

$$\mathbf{H}_\tau^0(a, \vartheta, \varphi) = -\frac{1}{\mu_0} \sum_{n,m} \frac{2n+1}{n+1} \epsilon_n^m \frac{i\omega\mu_0 a Y_1^{l,t}}{i\omega\mu_0 a Y_1^{l,t} - n} \nabla_\perp S_n^m(\vartheta, \varphi). \quad (\text{B.22})$$

Note that the C -responses at the Earth's surface, $C_n(\omega, a)$, are connected to $Y_1^{l,t}(n, \omega) \equiv Y^{l,t}(n, \omega, a)$ as

$$C_n(\omega, a) = -\frac{1}{i\omega\mu_0 Y_1^{l,t}(n, \omega)}. \quad (\text{B.23})$$

If we assume that ϑ and φ correspond to geomagnetic coordinate system then C_1 gives the response discussed in Section 3.1.

A final remark concerns the connection between $Y_1^{l,t}(n, \omega)$ and $Q_n(\omega)$ which is defined as

$$Q_n(\omega) = \frac{\epsilon_n^m(\omega)}{\iota_n^m(\omega)}. \quad (\text{B.24})$$

Note, that in the case of a 1-D conductivity distribution this ratio is independent of m . With the use of eq. (B.24) and eqs (B.5)-(B.7) the magnetic field at the surface of the Earth can be written in an alternative manner as

$$H_r^0(a, \vartheta, \varphi) = -\frac{1}{\mu_0} \sum_{n,m} \epsilon_n^m (n - (n+1)Q_n) S_n^m(\vartheta, \varphi), \quad (\text{B.25})$$

$$\mathbf{H}_\tau^0(a, \vartheta, \varphi) = -\frac{1}{\mu_0} \sum_{n,m} \epsilon_n^m (1 + Q_n) \nabla_\perp S_n^m(\vartheta, \varphi). \quad (\text{B.26})$$

Equating eq. (B.25) with eq. (B.21) (or eq. (B.26) with eq. (B.22)) one can deduce that

$$Q_n(\omega) = \frac{n}{n+1} \frac{i\omega\mu_0 a Y_1^{l,t}(n, \omega) + n+1}{i\omega\mu_0 a Y_1^{l,t}(n, \omega) - n}. \quad (\text{B.27})$$

Appendix C

Tests of different inversion settings

In this appendix we present the results of checkerboard test (Section C.1) and the results of the inversions in which we varied the resolution of the inverse domain (Section C.2) and an *a priori* model (Section C.3). The inverse problem settings, such as discretization of the forward problem and inverse problem domains, the geometry of the source, conductivity distribution in the background 1-D section, are explained in the beginning of Chapter 5.

C.1 Checkerboard test

The discussed period range of our study is 2.9 – 104.2 days, and in this period range the real part of experimental *C*-responses shows on average the values between ~ 600 and ~ 1000 km. Since the real part gives an estimate of the depth where EM field penetrates, we assume that our third inhomogeneous layer located at depths between 660 km and 900 km should be best resolved. To understand, how well we can resolve the conductivity in this layer with our spatial distribution of the data, we perform the following “checkerboard” test. We prepared a set of synthetic responses in the considered period range and at location of our 119 observatories. The responses were calculated in a 3-D model which included surface oceanic layer of fixed conductance, and checkerboard structure in the third layer with the lowest conductivity values equal to the 1-D conductivity value divided by $\sqrt{10}$ and the highest value equal to that of 1-D conductivity times $\sqrt{10}$. The size of single anomaly of checkerboard structure is $60^\circ \times 60^\circ$. During 3-D inversion we recover conductivity distributions in all 5 layers. The resolution of the inverse domain was taken as $30^\circ \times 30^\circ$. Fig. C.1 shows the results of inversion. As expected the conductivities is better resolved in the regions with good data coverage. The worst resolution is obviously detected in the polar and oceanic regions where there is no data present.

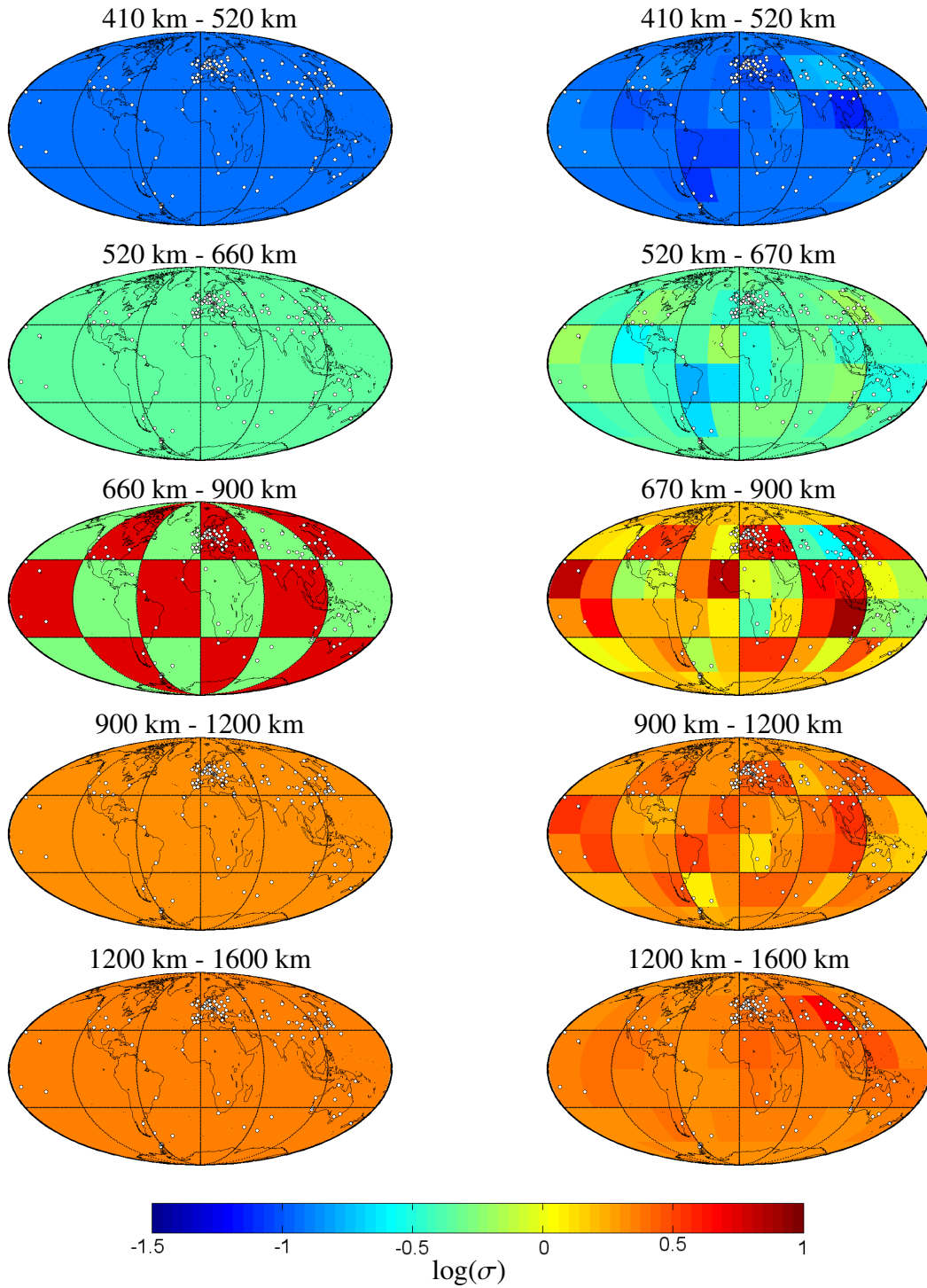


Figure C.1: Checkerboard test. Left-hand plots are original ("true") conductivity distributions in five layers. Right-hand plots – results of 3-D inversion. See details in the text.

C.2 The results for different lateral resolutions of the inverse domain

The aim of this model study is to understand how robust are the results of our inversion with respect to different lateral resolutions in the inversion domain. We run our 3-D inversion for

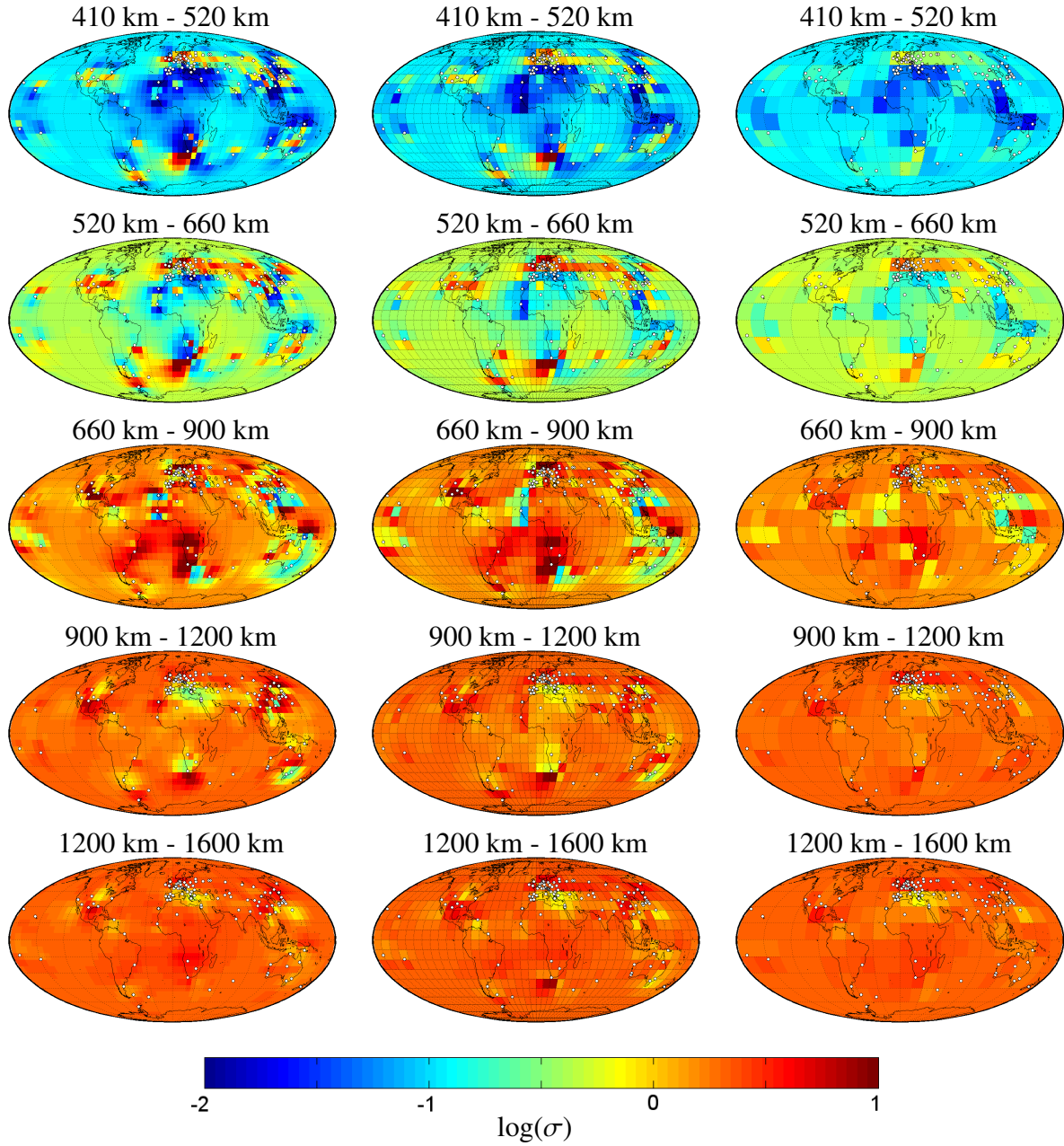


Figure C.2: Unfiltered results for different lateral resolutions of the inverse domain. Left-hand, middle and right-hand plots are the results for grids of lateral resolution $6^\circ \times 6^\circ$, $9^\circ \times 9^\circ$, and $15^\circ \times 15^\circ$, respectively.

the data set, which is not corrected for the ocean and auroral effects. This, in particular, means that the surface (oceanic) layer of known conductance was included in the model. Figs C.2 and C.3 present the unfiltered and filtered results, respectively, for three different lateral resolutions of the inverse domain. From these figures it is seen that irrespectively of the resolution we recover similar structures in all layers. Note that in Chapter 5, where we discussed our inverse results, the lateral resolution of the inverse domain was adopted as $9^\circ \times 9^\circ$.

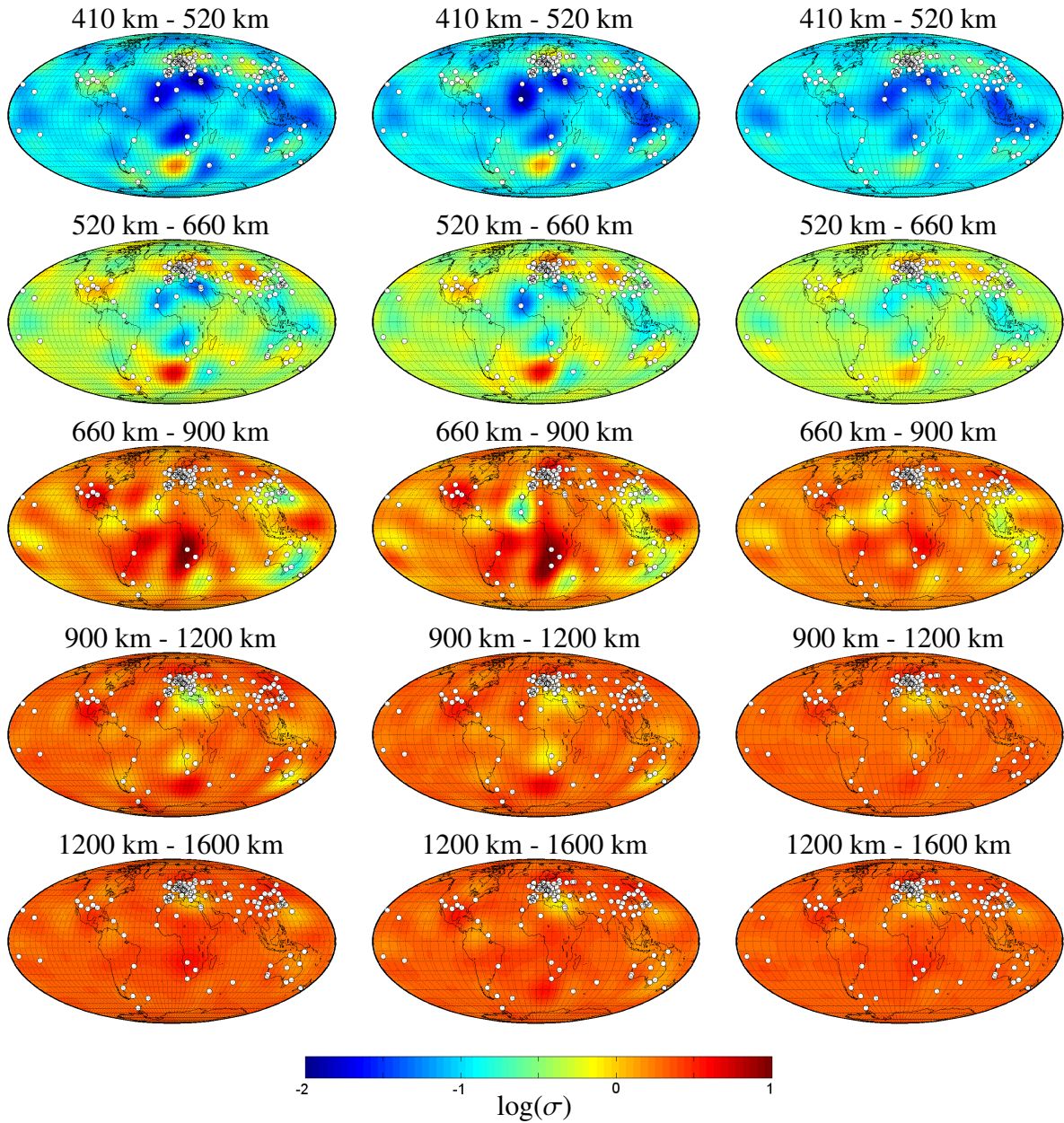


Figure C.3: Filtered results for different lateral resolutions of the inverse domain. The same legend as in Fig. C.2.

C.3 The results for different *a priori* models

The goal of the last model study is to understand how robust are the results of our inversion with respect to different *a priori* models. We run our 3-D inversion for the same data set (not corrected for the ocean and auroral effects). Fig. C.4 shows the filtered results for three different *a priori* models. From this figure one can see that, again, irrespectively of an *a priori* model we are able, more or less, to detect common anomalous features in all layers. We notice that in regions that are far away from observatories, the conductivity tends to be close to the predefined *a priori* value.

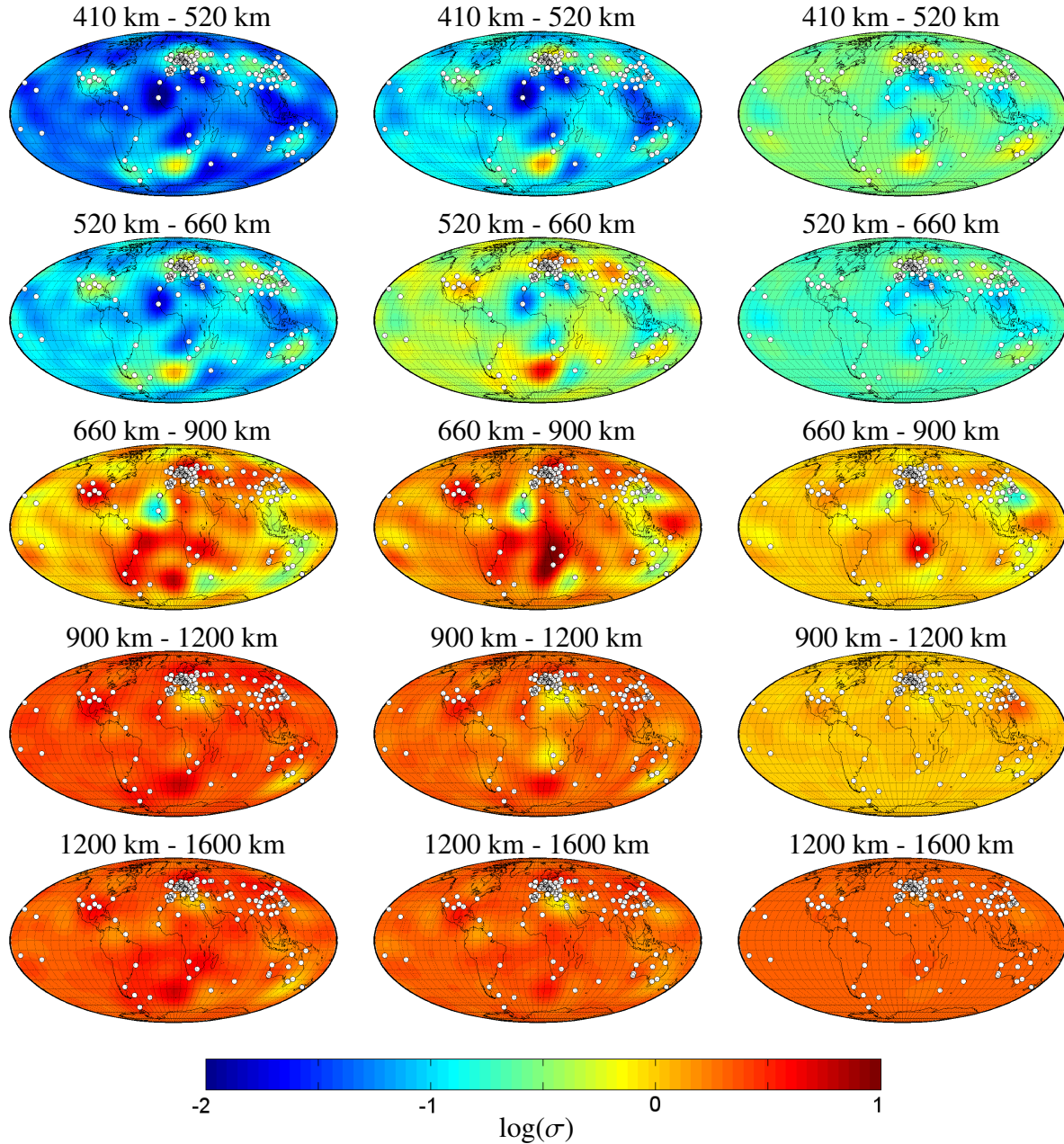


Figure C.4: Filtered results for different *a priori* models. Left-hand plots are the inverse results when the local 1-D profile derived from analysis of Hermanus data was taken as *a priori* model. Middle plots are the results when global profile from (Kuvshinov and Olsen, 2006) was taken as *a priori* model. Right-hand plots correspond to the case when inversion was performed without *a priori* model.

Appendix D

Mineral physics studies

It was shown during seismological studies that the Earth's interior has conditions of pressure up to 360 GPa and temperatures up to thousands of degrees Kelvin (K). To estimate conductivity of the minerals under such circumstances high-pressure and high-temperature experiments on hypothetical Earth's forming materials have been carried out, to find out what structures and properties they have under such extreme conditions (Yoshino, 2009). In the following frame we describe the chemical composition of the major mineral in the mantle.

Mineral composition

Pyroxene – mineral with the formula $XY(\text{Si},\text{Al})_2\text{O}_6$. X represents Ca, Na or Fe^{2+} and rarely Zn, Mg and Li. Y represents ions of smaller size - Cr, Al, Fe^{3+} , Mg, Sc, Ti, V or even Fe^{2+} .

Garnet – nesosilicate having the general formula $X_3Y_2(\text{Si},\text{O}_4)_3$. X is usually occupied by divalent cations (Ca^{2+} , Mg^{2+} , Fe^{2+}) and Y by trivalent cations (Al^{3+} , Fe^{3+} , Cr^{3+}).

Majorite garnet – garnet with composition $\text{Mg}_3Y_2(\text{Si},\text{O}_4)_3$, where Y is Fe, Al or Si.

Olivine – magnesium iron silicate with the formula $X_2\text{SiO}_4$, where X is Mg or Fe.

Wadsleyite and *Ringwoodite* – high-pressure transformations from olivine with different structure of Mg or Fe elements.

Ferro-periclase or *Magnesiowüstite* – a magnesium/iron oxide XO, where X is Mg or Fe.

Silicate perovskite – mineral with formula $X\text{SiO}_3$, where X is Mg or Fe.

Silicate post-perovskite – a high pressure phase of perovskite MgSiO_3 .

Although many different pressure devices have been designed, usually the solid pressure media is exploited to generate high pressures corresponding to the mantle conditions. Three types of devices are widely used in the scientific community: piston-cylinder appara-

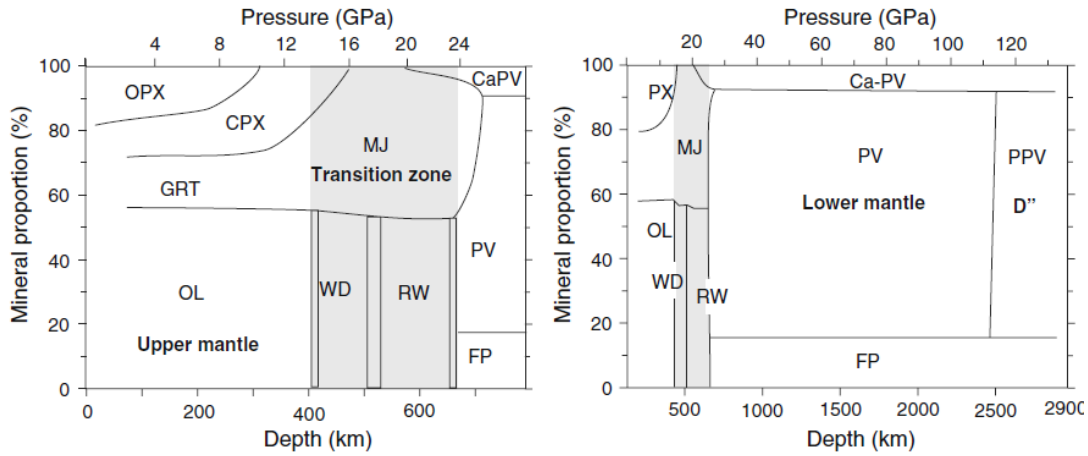


Figure D.1: Mineral proportions and phase transition in the Earth's mantle. Shaded areas indicate the mantle transition zone between 410 and 660 km discontinuities. *PX*-Pyroxene, *OPX* - ortopyroxene, *CPX* - clinopyroxene, *GRT* - garnet, *MJ* - majorite garnet, *OL* - olivine, *WD* - wadsleyite, *RW* - ringwoodite, *FP* - ferro-periclase, *PV* - silicate perovskite, *PPV* - silicate post-perovskite, *Ca - PV* Ca-perovskite. After Yoshino (2009).

tus, Kawai-type multi-anvil press, and diamond anvil cell (DAC). Each of them has different pressure and temperature generating possibilities. The advantage of piston-cylinder apparatus is characterized by relatively large sample space ($< 500 \text{ mm}^3$) and small thermal gradient. But pressure generation is limited only up to 4 GPa. The Kawai-type multi-anvil press has some remarkable advantages: accurate temperature control, large sample volume. Disadvantage of this press is also a limit of pressure generation. Recently an accessible pressure range for electrical conductivity measurement in such devices has been extended to 35 GPa by adopting sintered diamond (SD) anvils (Katsura et al., 2007). The DAC is one of the simplest high-pressure apparatus composed of the opposed anvils of single crystal diamond with flat faces at the top. It can covers the mantle pressure conditions up to the core mantle boundary (above 135 GPa). In addition with laser-heating system it can realize extremely high temperature conditions ($< 4000 \text{ K}$). The problem of the DAC is that the sample size is very limited. To generate pressure above 100 GPa, the sample size should be less than $50 \mu\text{m}$, but the smaller size of the sample would lead to the larger error of the calculated conductivity.

In the Earth's mantle some seismic velocity discontinuities have been globally observed, and are thought to be caused by the phase transformations of mantle minerals (see Fig. D.1). We shortly review the electrical conductivities of the major mantle constituents minerals. Olivine is the most abundant mineral in the upper mantle and transforms to wadsleyite and ringwoodite in the mantle transition zone at 410 and 520 km seismic discontinuities, respectively.

Pyroxene is another important constituent mineral in the mantle. In the depth range from 300 to 500 km, pyroxenes progressively dissolve into garnet with increasing pressure (Takahashi and Ito, 1987; Irifune and Ringwood, 1993). With increasing pressure majorite garnet gradually dissolves into silicate perovskite. Near the core-mantle boundary perovskite trans-

forms into post-perovskite (Murakami et al., 2004). Although most mantle minerals are silicates, non-silicate oxide ferro-periclase appears as a second abundant mineral in the lower mantle (Ito and Takahashi, 1989).

The electrical conductivity of olivine increases with increasing oxygen fugacity (Wanamaker and Duba, 1993; Hirsch and Shankland, 1993; Du Frane et al., 2005) and total iron content (Hirsch et al., 1993). It has been modeled as a function of temperature and oxygen fugacity (Shankland and Duba, 1990; Constable et al., 1992; Constable, 2006). Different conduction mechanisms were studied and the resulting conductivities strongly depend on them. But in general the results for conductivity on a certain pressure (3 GPa) and water content with the same conducting mechanism vary from 1.45 S/m for lower temperatures (723-973 K) to 9.23 S/m for higher ones (973-1473 K) (Yoshino et al., 2006). For higher pressures (10 GPa) it can go up to 113.2 S/m (Yoshino et al., 2009).

Wadsleyite and Ringwoodite are the main constituent minerals in the mantle transition zone (410-660 km depth), and are able to store rather large amount of water in their crystal structure. Xu et al. (1998b) reported that electrical conductivities of wadsleyite and ringwoodite are similar and two orders of magnitude higher than that of olivine, but these values are too high to explain the conductivity depth profiles obtained by electromagnetic induction studies (Neal et al., 2000; Tarits et al., 2004; Kuvshinov et al., 2005). However Yoshino et al. (2008a) in their studies argued, that electrical conductivity of ringwoodite is around one magnitude higher than that of wadsleyite and for mantle temperature condition the dominant conduction mechanism is the same as for olivine.

Garnet is stable on a wide range of pressure conditions from the Earth's crust down to the lower mantle. Xu and Shankland (1999) firstly measured electrical conductivity of garnet under pressure of 21 GPa at temperatures 1473-1773 K and received 28.5 S/m for the conductivity. However their recovered sample was a mixture of ilmenite and garnet. Romano et al. (2006) reported the electrical conductivity of garnet as a function of iron content ($\text{Fe}_3\text{Al}_2\text{Si}_3\text{O}_{12} \rightarrow \text{Mg}_3\text{Al}_2\text{Si}_3\text{O}_{12}$) at pressures from 10 to 19 GPa. His results for conductivity vary from 1.5 S/m for high pressures (19 GPa) and high temperatures (1173-1923 K) to 80.6 at lower pressures (10 GPa) and lower temperatures (573-873 K). Yoshino et al. (2008b) measured electrical conductivities of majorite garnet with compositions of pyrolite minus olivine (pyrolite majorite) at 18 and 23 GPa and temperatures up to 2000 K. According to their results pyrolite majorite has only slightly higher and lower conductivity than dry wadsleyite and ringwoodite, respectively, and will not largely change the conductivity depth profile predicted from the electrical conductivities of wadsleyite and ringwoodite.

The major phase in the Earth's lower mantle is thought to be silicate perovskite. It can store much of aluminium and iron (Ito and Takahashi, 1989; Wood and Rubie, 1996). Electrical conductivity of silicate perovskite was firstly measured in DAC (Peyronneau and Poirer, 1989; Li and Jeanloz, 1990; Shankland et al., 1993). Shankland et al. (1993) estimated the maximum conductivity value of 3-10 S/m at the base of the lower mantle using the extrapolation of low

temperature data on the mantle condition. On the other hand Li and Jeanloz (1990) reported extremely lower conductivity values (10^{-4} S/m) at temperature above 2000 K compared with geophysical observations (Egbert et al., 1992). Two groups (Katsura et al., 1998; Xu et al., 1998a) in the end of 1990s measured the conductivity of the silicate perovskite in an Kawai-type multi-anvil press under physical conditions of the uppermost lower mantle. These studies show, that perovskite has slightly higher conductivity than ringwoodite with the same Mg#. A presence of impurities in perovskite significantly affects the electrical conductivity of silicate perovskite (Yoshino, 2009). Xu et al. (1998a) reported a significant effect of aluminium on the conductivity of perovskite.

Lower mantle pressures increase from 23 GPa at the 660 km seismic discontinuity up to 136 GPa at the core-mantle boundary, and above 30 GPa, the conductivity measurements were conducted in a DAC, using laser heating system. Ohta et al. (2008) reported that electrical conductivity of perovskite with composition ($\text{Mg}_{0.9}\text{Fe}_{0.1}\text{SiO}_3$) decreases with pressure.

Ferro-periclase is the second abundant mineral in the lower mantle. The conductivity measurements of ferropericlase have been performed separately at high (> 1300 K) and low (< 1000 K) temperatures. Wood and Nell (1991) showed that the conductivity of ferropericlase at atmospheric pressure is largely higher than that of co-existing silicate perovskite. Same results are reported by Katsura and Ito (1996), who linked the higher conductivity of ferropericlase to higher iron content. Lin et al. (2007) measured electrical conductivity of the ferropericlase ($\text{Mg}_{0.75}\text{Fe}_{0.25}\text{O}$) using DAC at pressures over 100 GPa. The electrical conductivity gradually increases by an order of magnitude up to 50 GPa but decreases by a factor of approximately 3 between 50 and 70 GPa. Although the absolute conductivity values are largely different from each other due to usage of samples with different iron content, a trend showing a gradual decrease of electrical conductivity between 50 and 80 GPa is quite consistent.

Large seismic anomalies have been observed at the bottom of lower mantle with a thickness of several kilometers (D'' layer) (Lay et al., 1998). Those anomalies are difficult to explain with known physical properties of MgSiO_3 perovskite - the main constituent of the lower mantle. A first report on electrical conductivity of silicate post-perovskite with a composition ($\text{Mg}_{0.89}\text{Fe}_{0.11}\text{SiO}_3$) at 129 and 143 GPa using laser heating DAC showed extremely high conductivity ($> 10^2$ S/m) in comparison with that of silicate perovskite and little temperature dependence at the conditions of D'' layer (Ohta et al., 2008). If the electrical conductivity of the post-perovskite has positive pressure dependence, temperature may have a small negative effect. But further studies including the effect of Al and Fe contents on the electrical conductivity of the post-perovskite phase are needed to characterize the conductivity structure near the core-mantle boundary.

There is still some results inconsistency among laboratories, but nevertheless, the comprehensive collection of high-pressure conductivity data for mantle minerals yields some important features. Electrical conductivity of the main mantle constituents increases in order of olivine, wadsleyite, ringwoodite, perovskite and post-perovskite. At least three conductivity

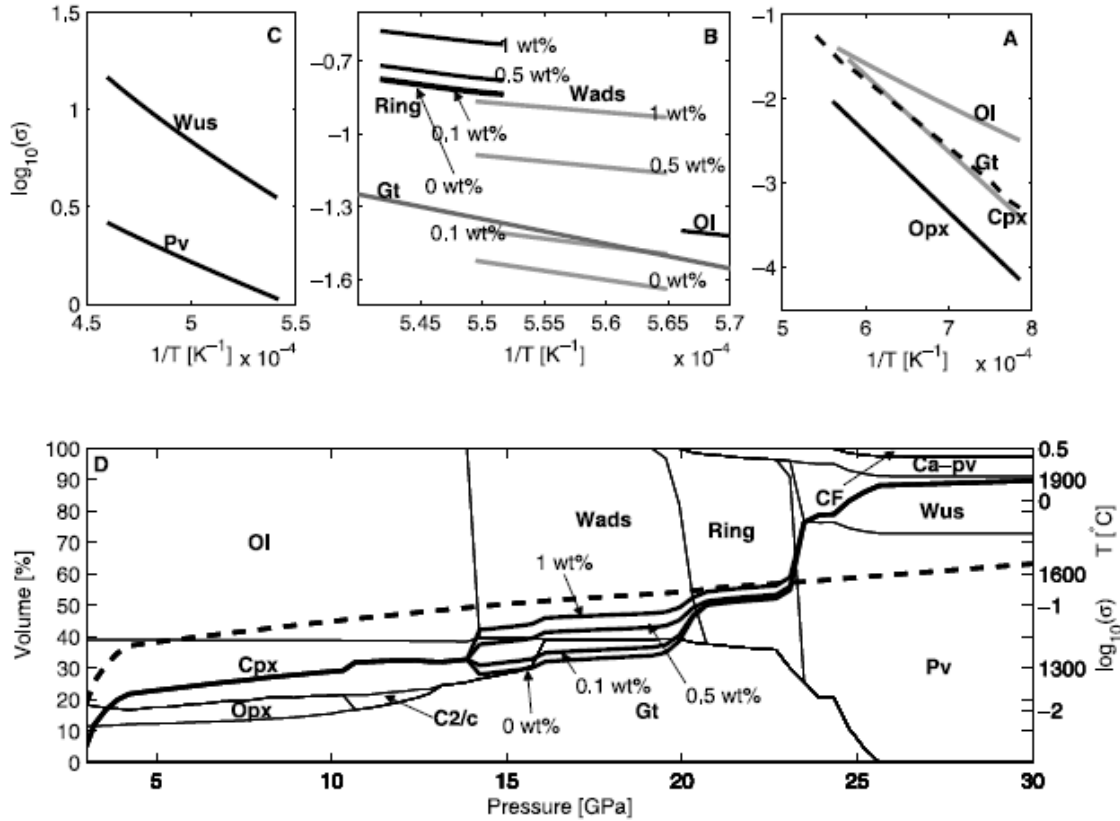


Figure D.2: Laboratory mineral electrical conductivity measurements as a function of inverse temperature (A upper mantle, B transition zone and C upper part of lower mantle) and variations in mineral phase proportions and laboratory-based conductivity profile computed on the basis of a homogeneous adiabatic pyrolite mantle as a function of pressure (depth) and transition zone water content (B and D). The solid and dotted lines in (D) are bulk conductivity and adiabat, respectively. Phases are: Ol (olivine), Opx, (orthopyroxene), Cpx (clinopyroxene), C2/c (high-pressure Mg-rich Cpx), Gt (garnet), Wads (wadsleyite), Ring (ringwoodite), Aki (akimotoite), Ca-pv (calcium perovskite), Wus (magnesiowüstite), Pv (perovskite) and CF (calcium ferrite). After Khan et al. (2011).

jumps would be present at 410, 520 and 660 km discontinuities due to phase transformation. Electrical conductivity increases with increasing water and iron content. Small difference of iron content may produce the large difference of conductivity (Yoshino, 2009).

Combining laboratory measurements and numerical modeling results it should be possible to infer mantle water content and other physical properties of the mantle (Khan et al., 2011). The comparison hinges on the construction of a reliable laboratory-based conductivity profile using a technique where laboratory data are combined with a self-consistently computed mineralogical model of the Earth's mantle from a specific composition and geotherm using Gibbs free energy minimization (Connolly, 2005). Fig. D.2 represents the resulting distribution of the minerals in the mantle.

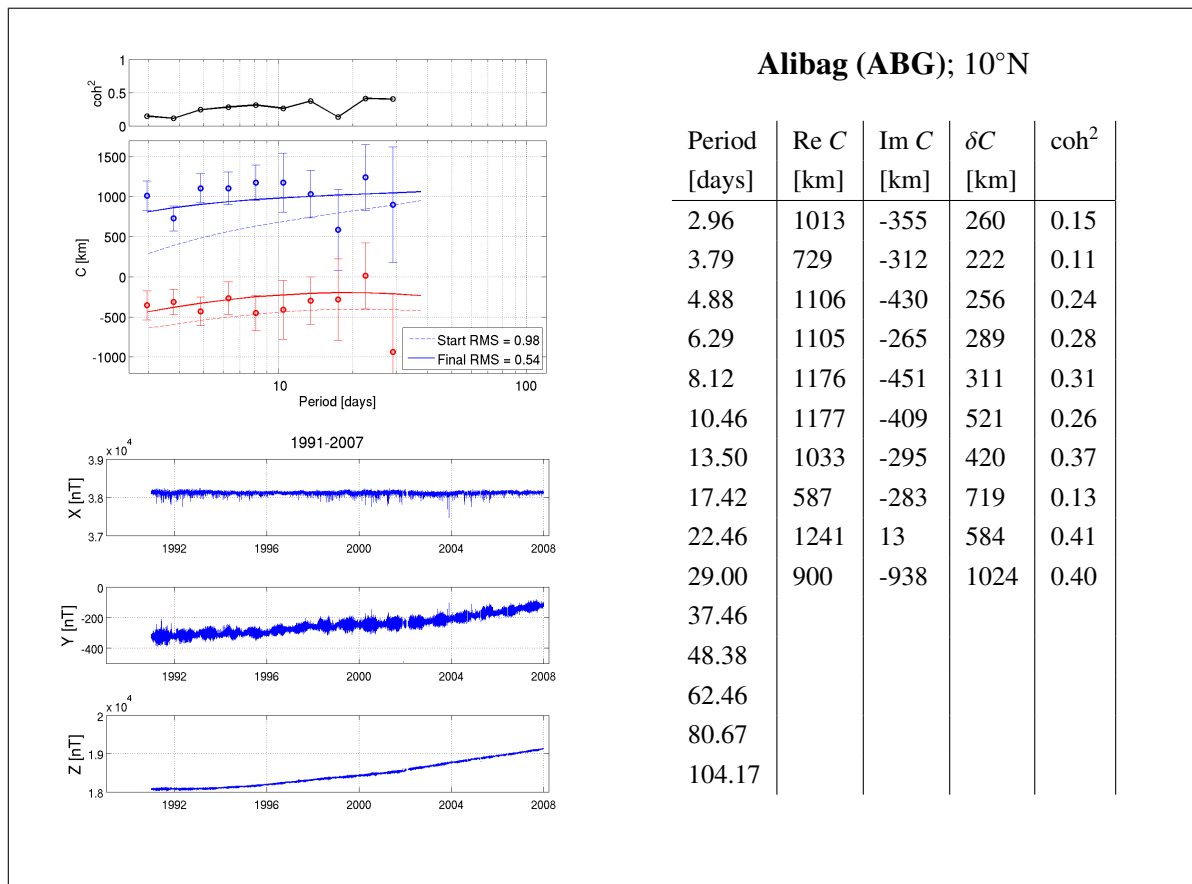
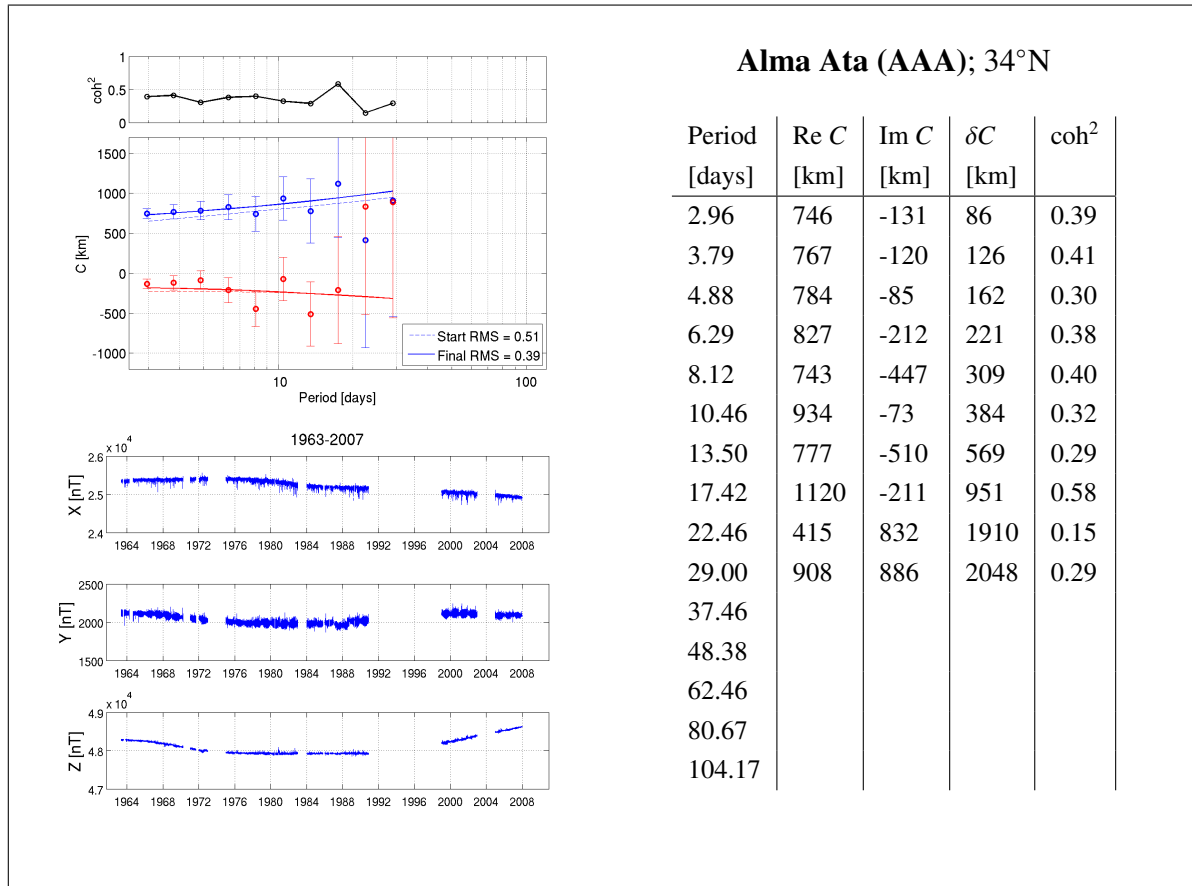
Appendix E

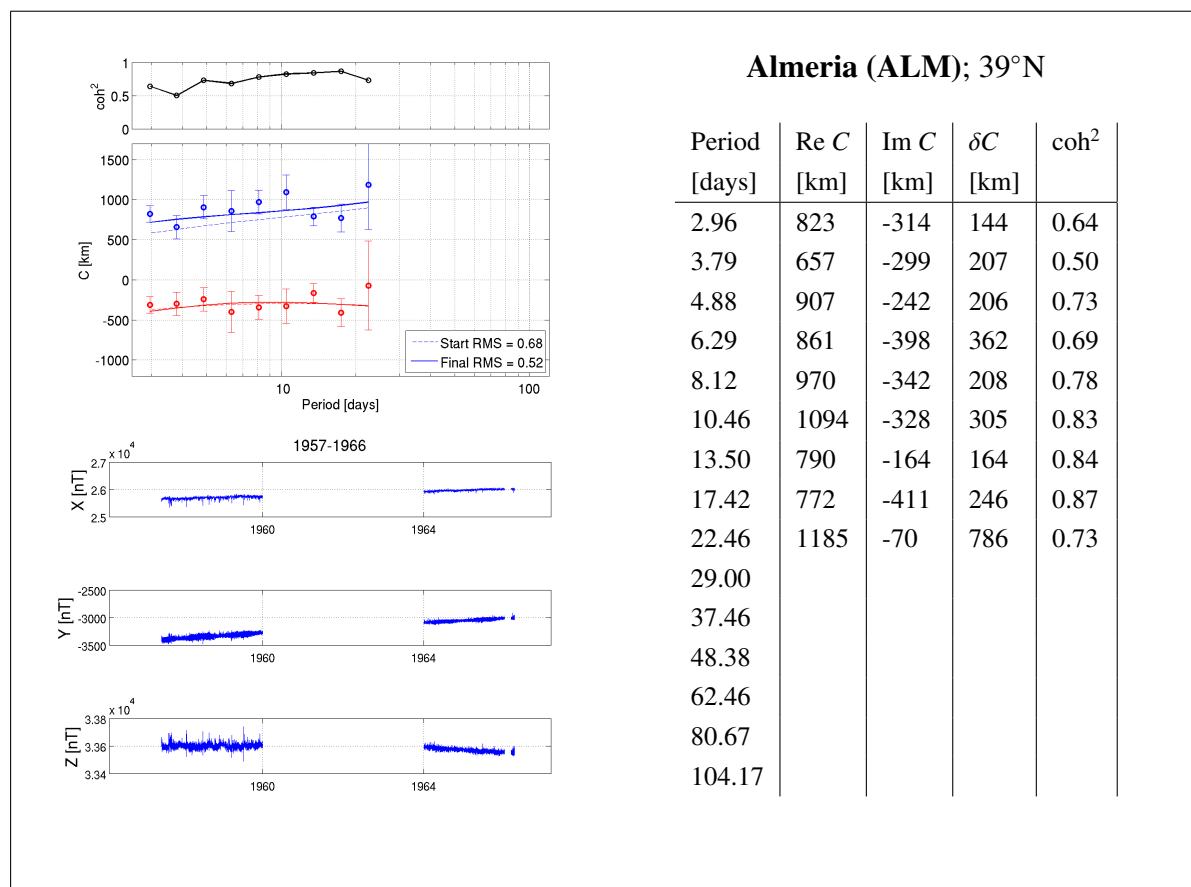
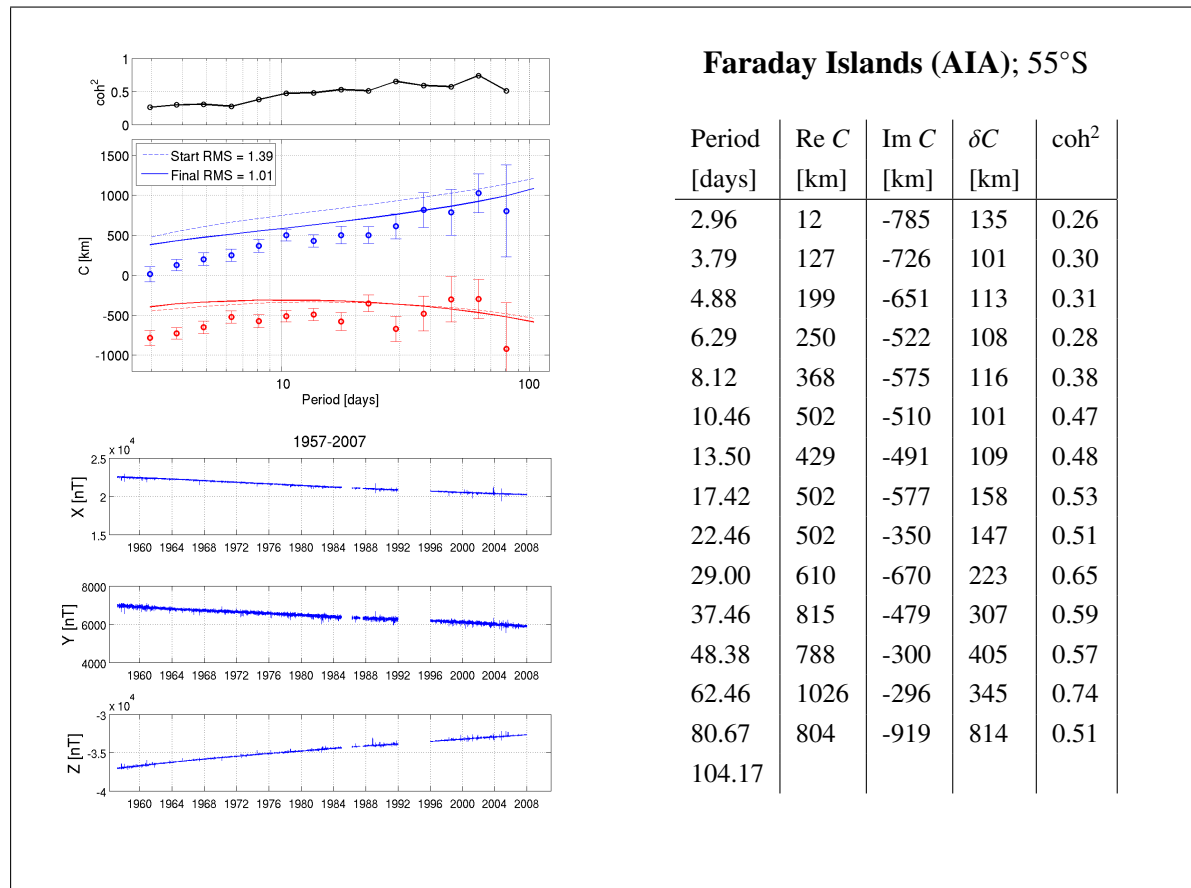
Experimental responses

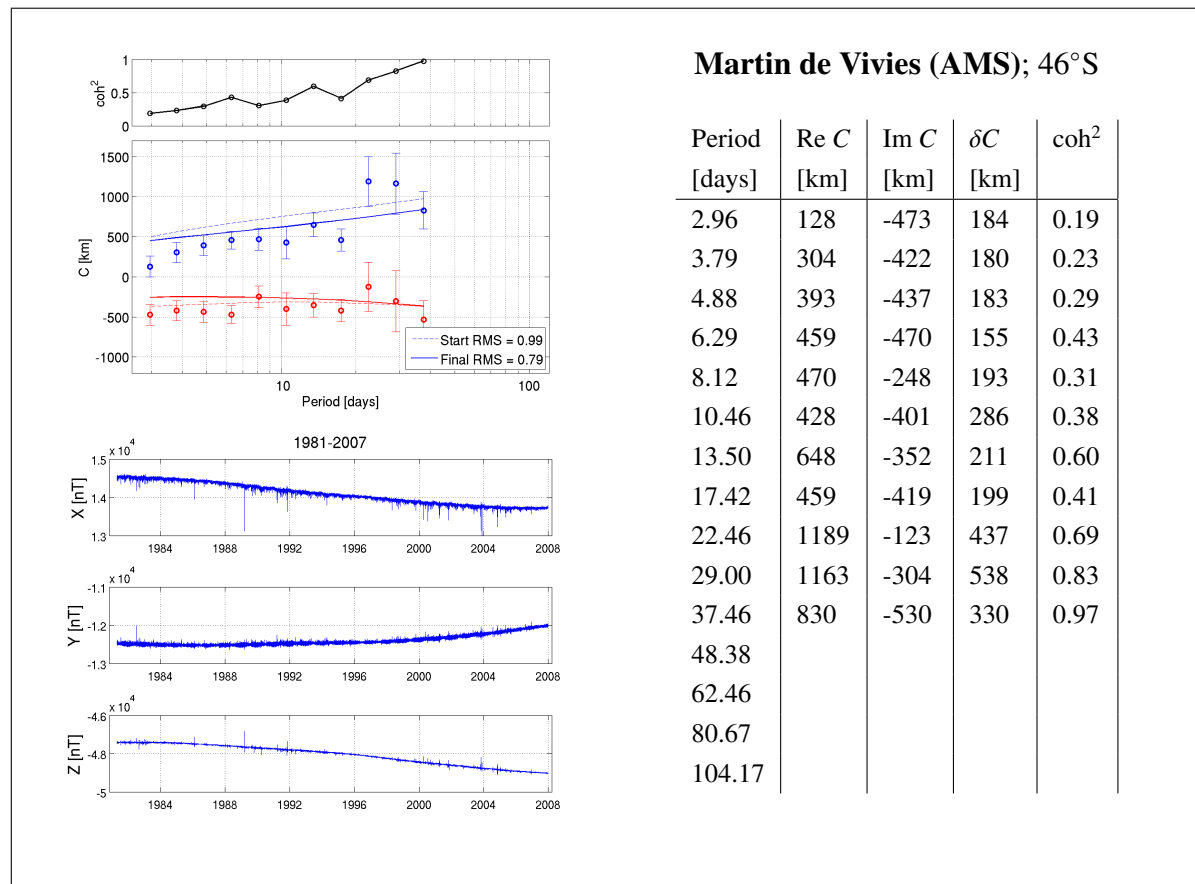
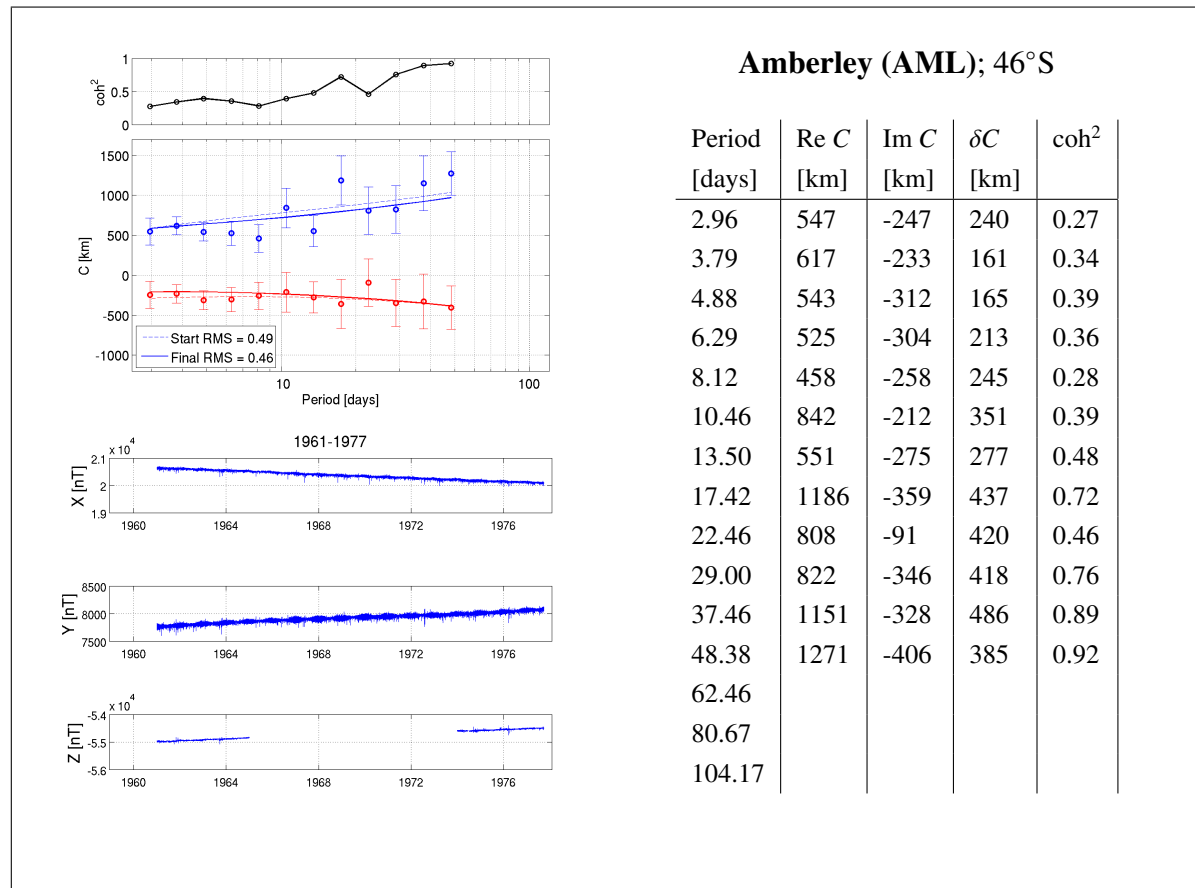
This Appendix presents collection of experimental responses from 119 observatories which we used in our 3-D inversions. Each page summarizes the results for two observatories. Tables on the right consist of 6 columns for 55 observatories above 40° geomagnetic latitude in the Northern hemisphere, and 5 columns for all other observatories. For the latter observatories Tables present period (in days), real (Re C) and imaginary (Im C) parts of experimental responses (in km), uncertainty of the responses (δC ; in km) and squared coherency (coh^2). For 55 observatories above 40° geomagnetic latitude the extra column includes real part of the experimental responses corrected for the auroral effect (Re C^* ; in km). Title of the Tables contains the name of observatory, its acronym and geomagnetic latitude of the observatory. Left-hand lower plots of each semi-page shows three components (X, Y and Z (from the top to the bottom); in geographic coordinate system; in nT) of time-varying magnetic field for the years, the data from which are used to estimate the C -responses. Upper left plots present the experimental responses (circle with error bars). The real and imaginary parts are depicted by blue and red colors, respectively. Also shown are the predicted responses for starting model (dashed lines), and predicted responses, which correspond to the recovered 3-D conductivity model (solid lines). The latter responses are obtained as follows. First, the 3-D inversion was performed using the data set corrected for the ocean and the auroral effects (thus ignoring the ocean layer during inversion). Second, the recovered 3-D model was complemented by the oceanic layer, and the resulting responses were calculated in the “extended” 3-D model with the lateral resolution of $1^\circ \times 1^\circ$. In addition in these plots we also present the RMS which are calculated as follows

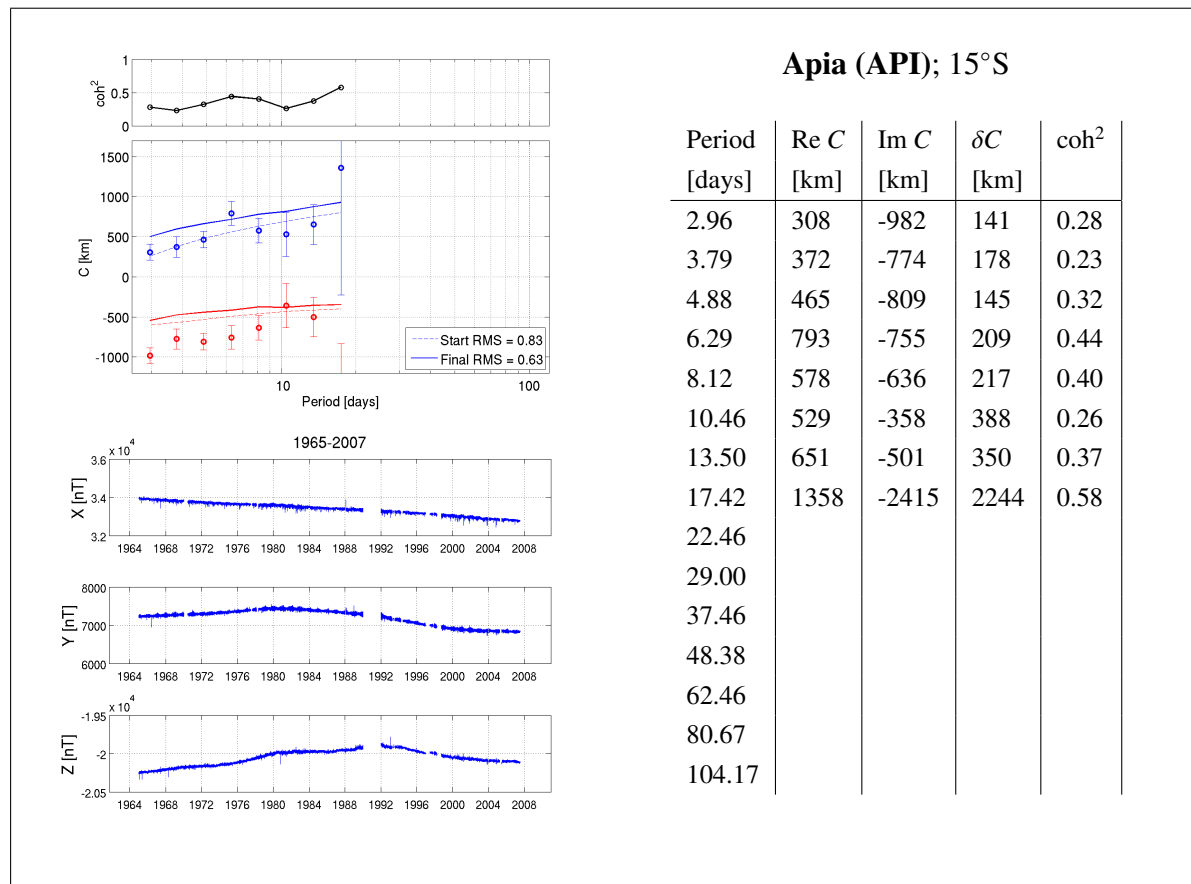
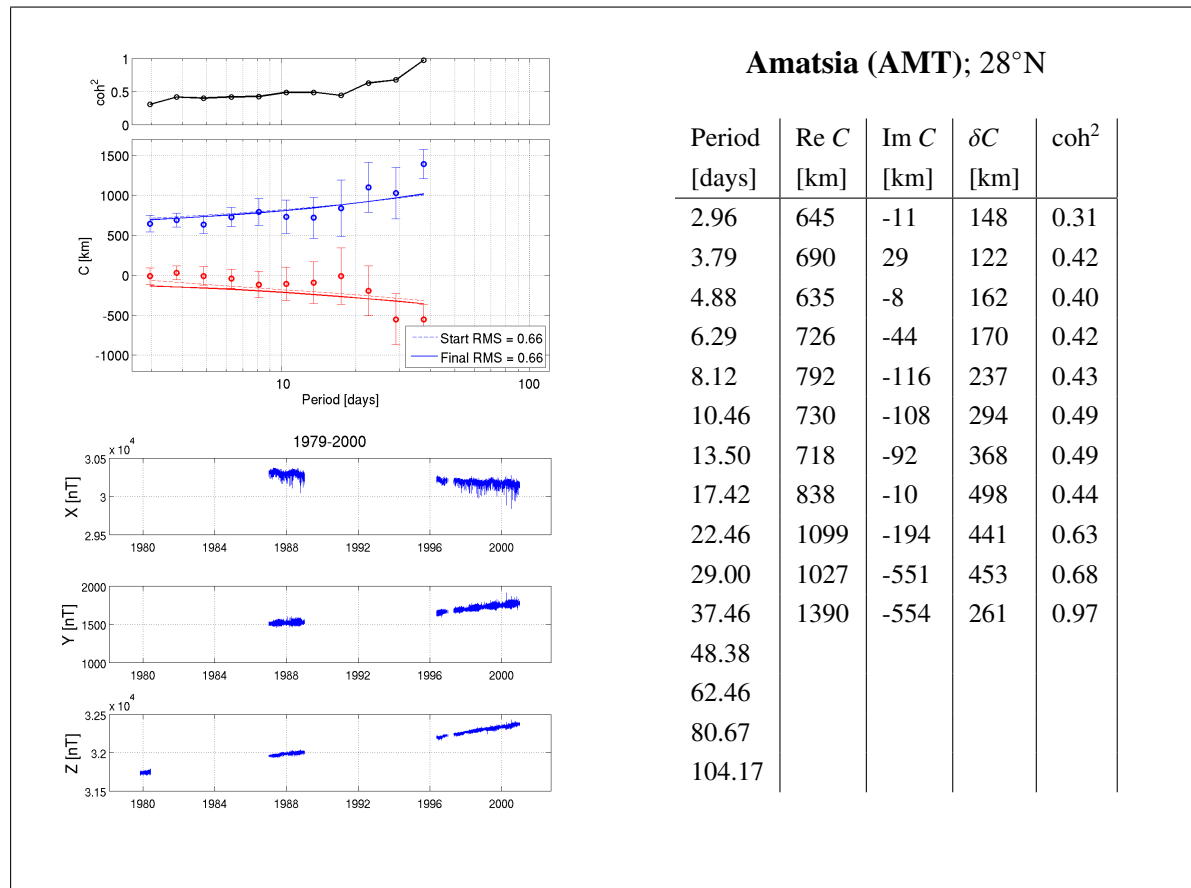
$$RMS = \sqrt{\frac{1}{N_T(i)} \sum_{j=1}^{N_T(i)} \left| \frac{C_{ij}^{pred} - C_{ij}^{exp}}{\delta C_{ij}} \right|^2}, \quad (E.1)$$

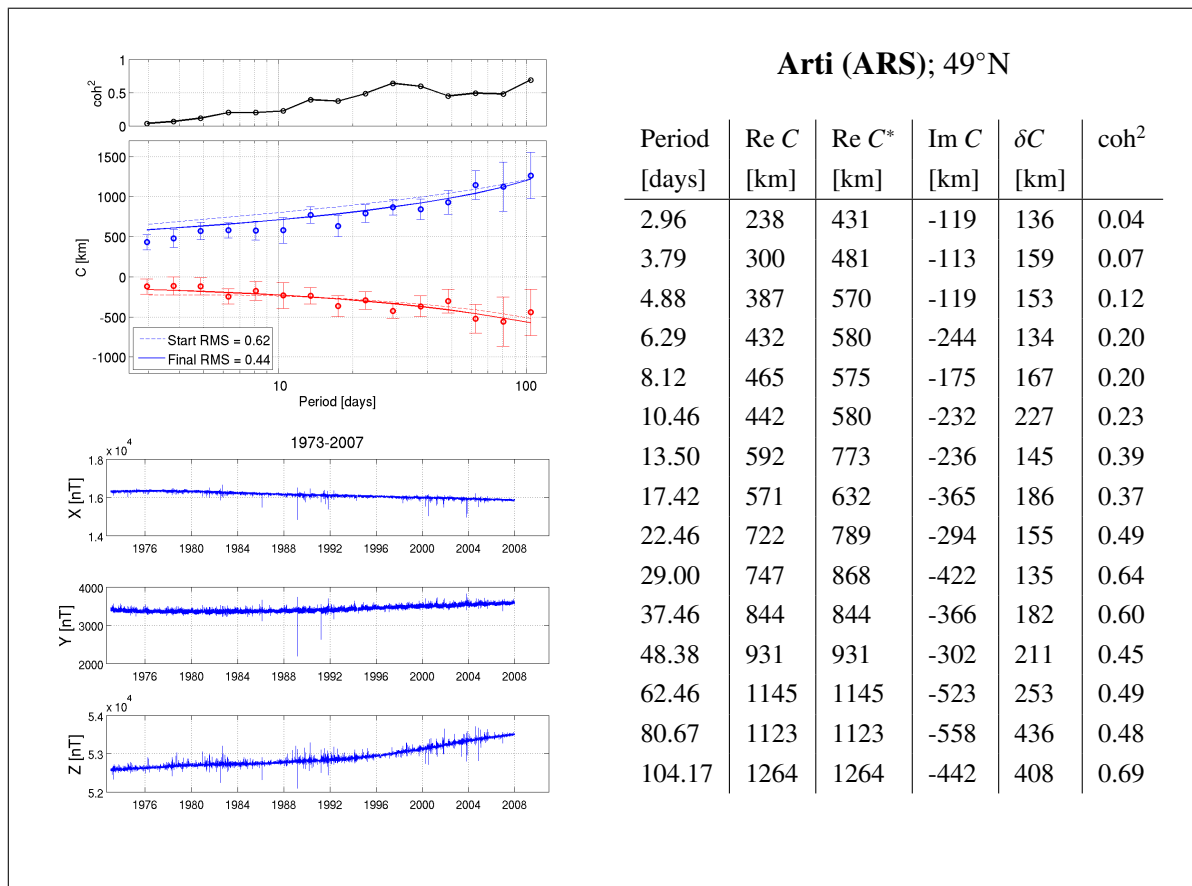
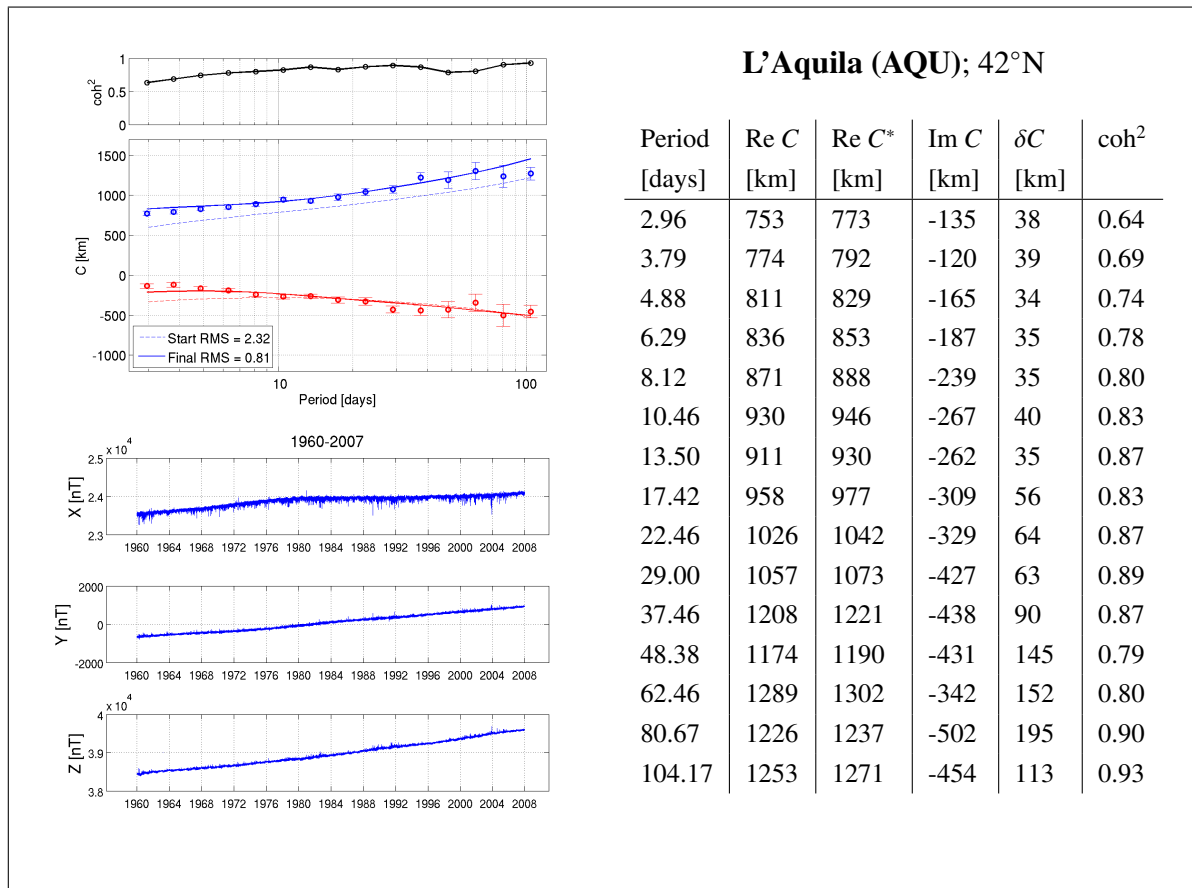
where $N_T(i)$ is the number of periods used for a certain observatory, and subscript “ ij ” stands for the results for i -th observatory and for j -th period, respectively.

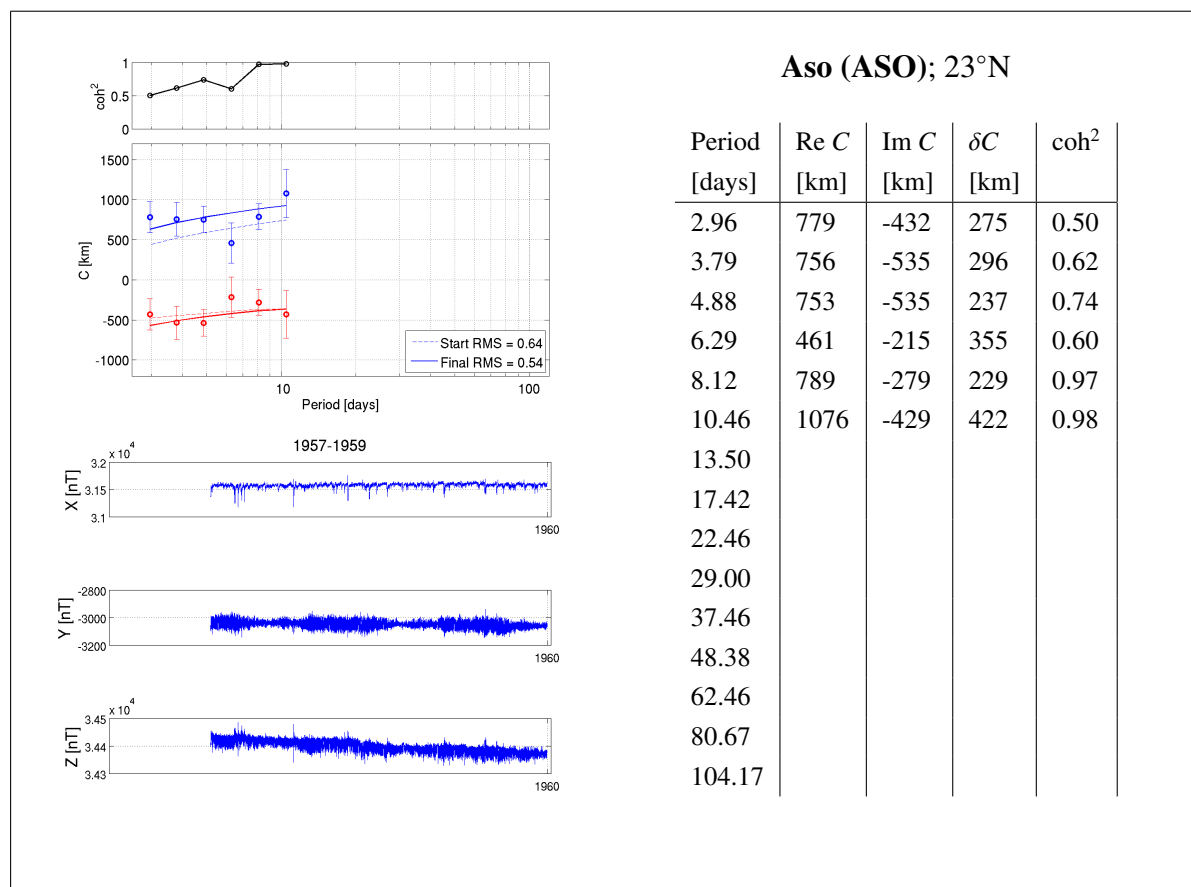
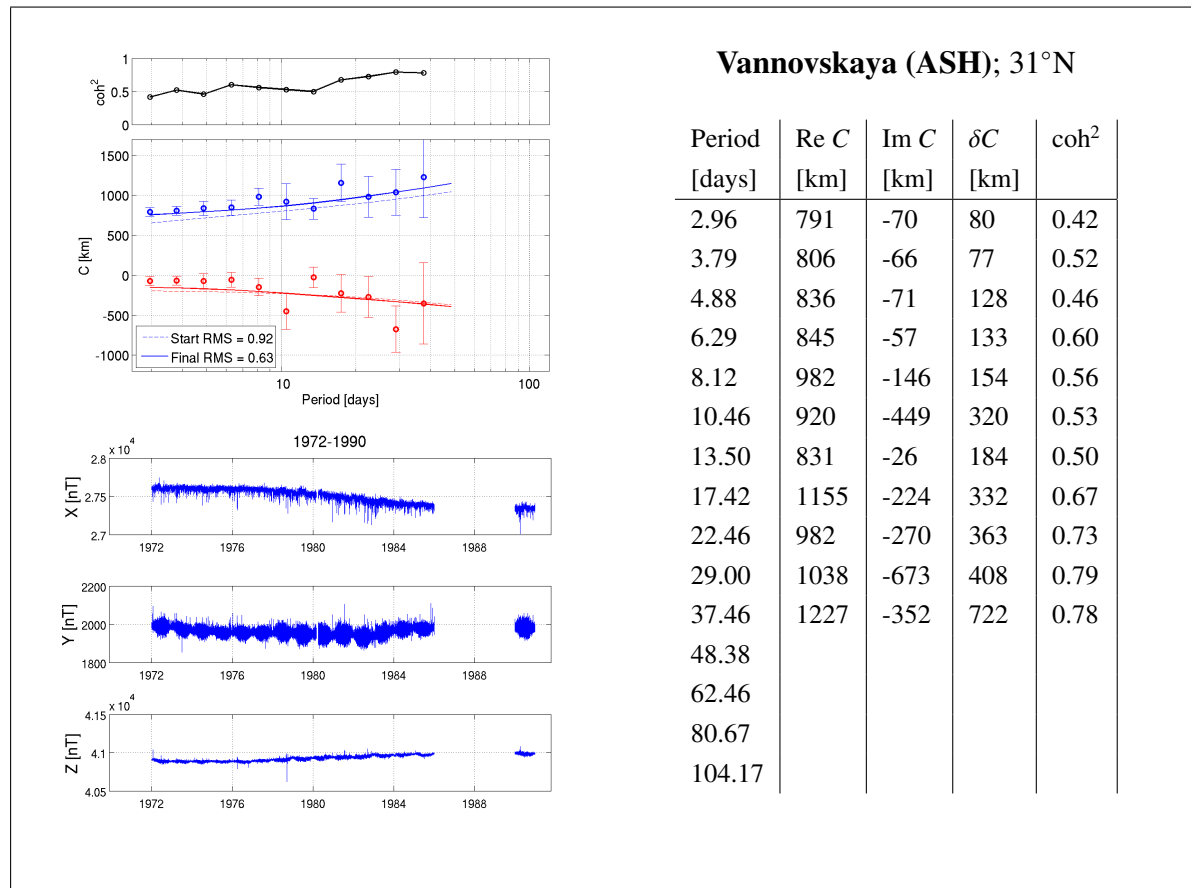


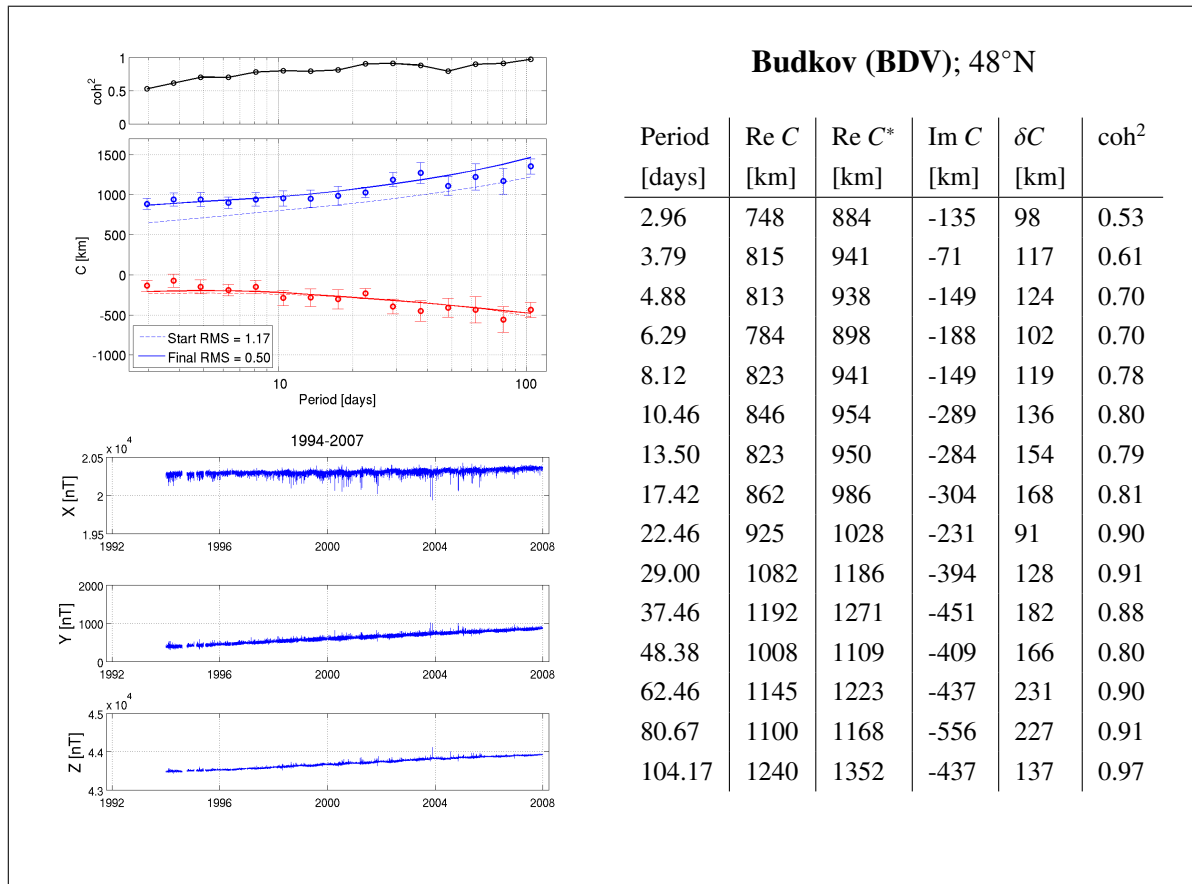
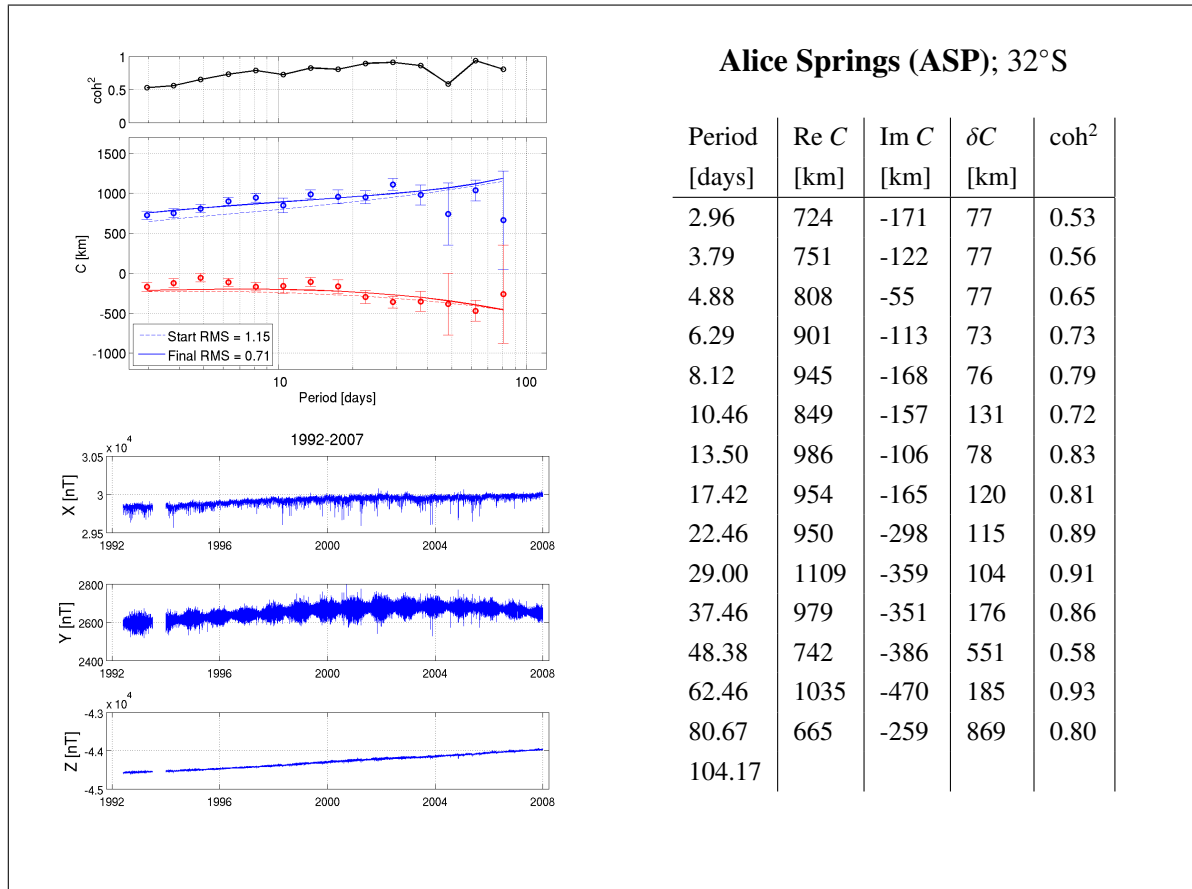


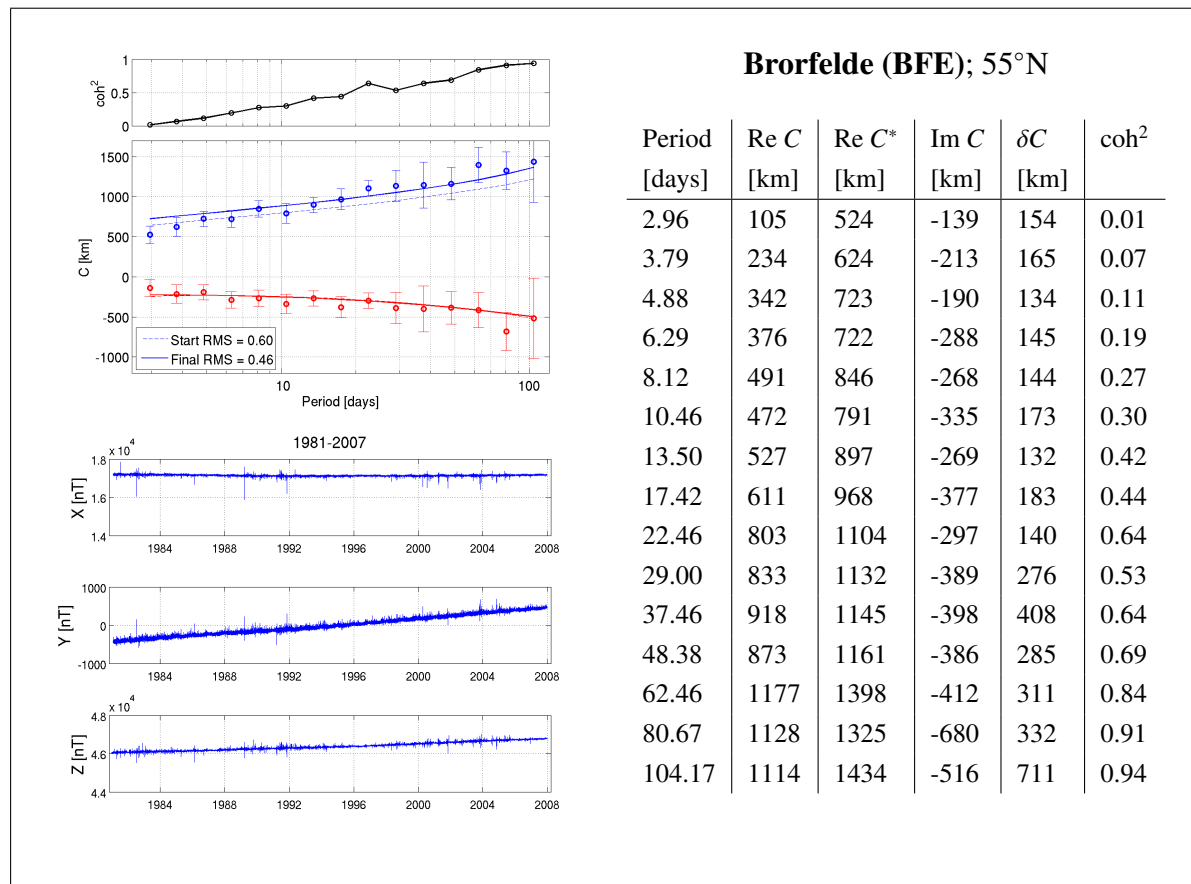
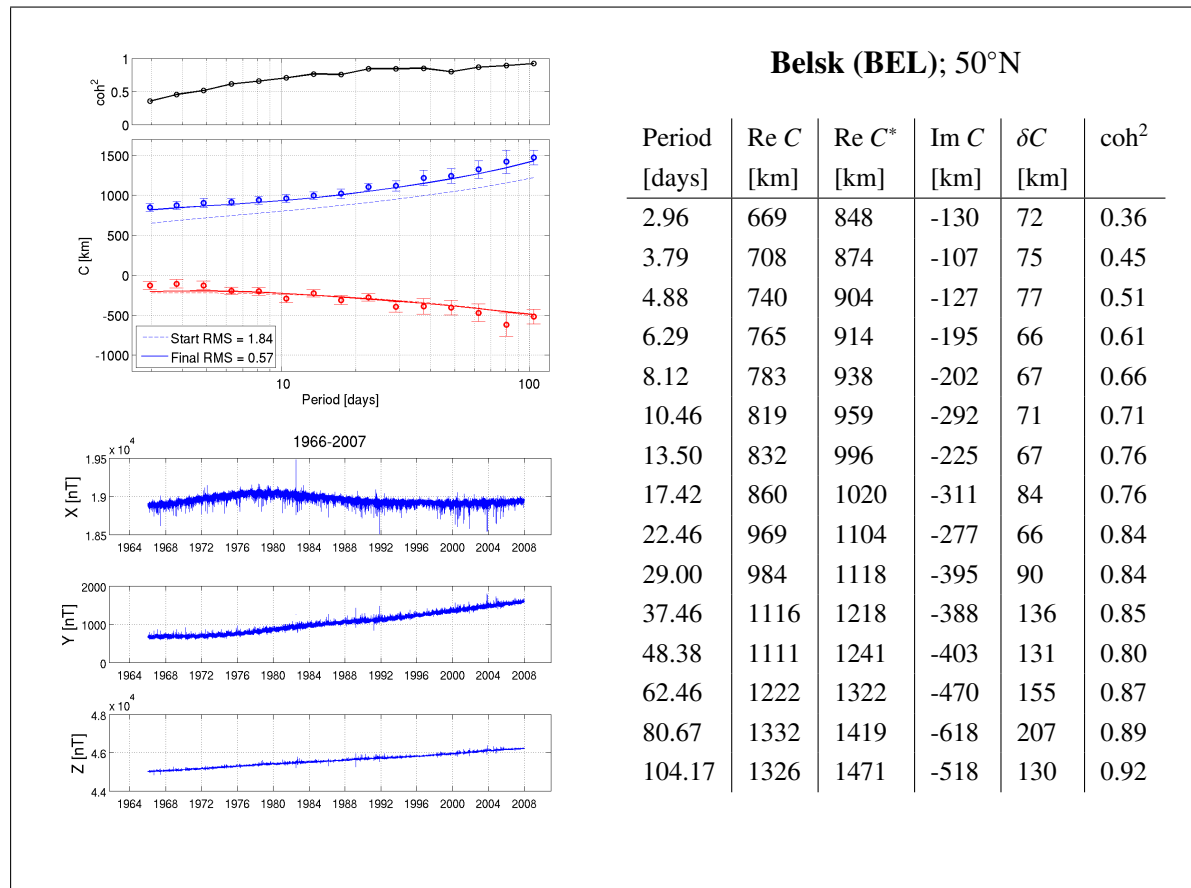


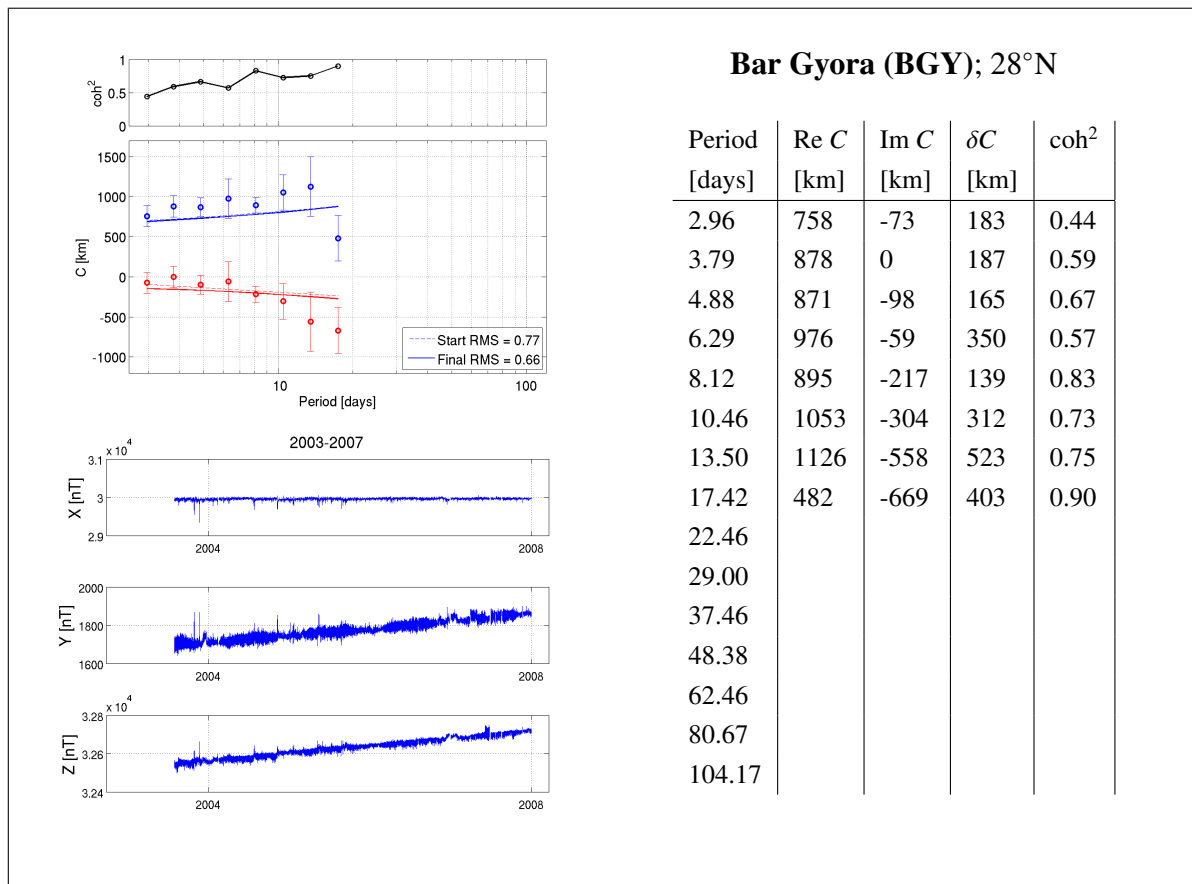
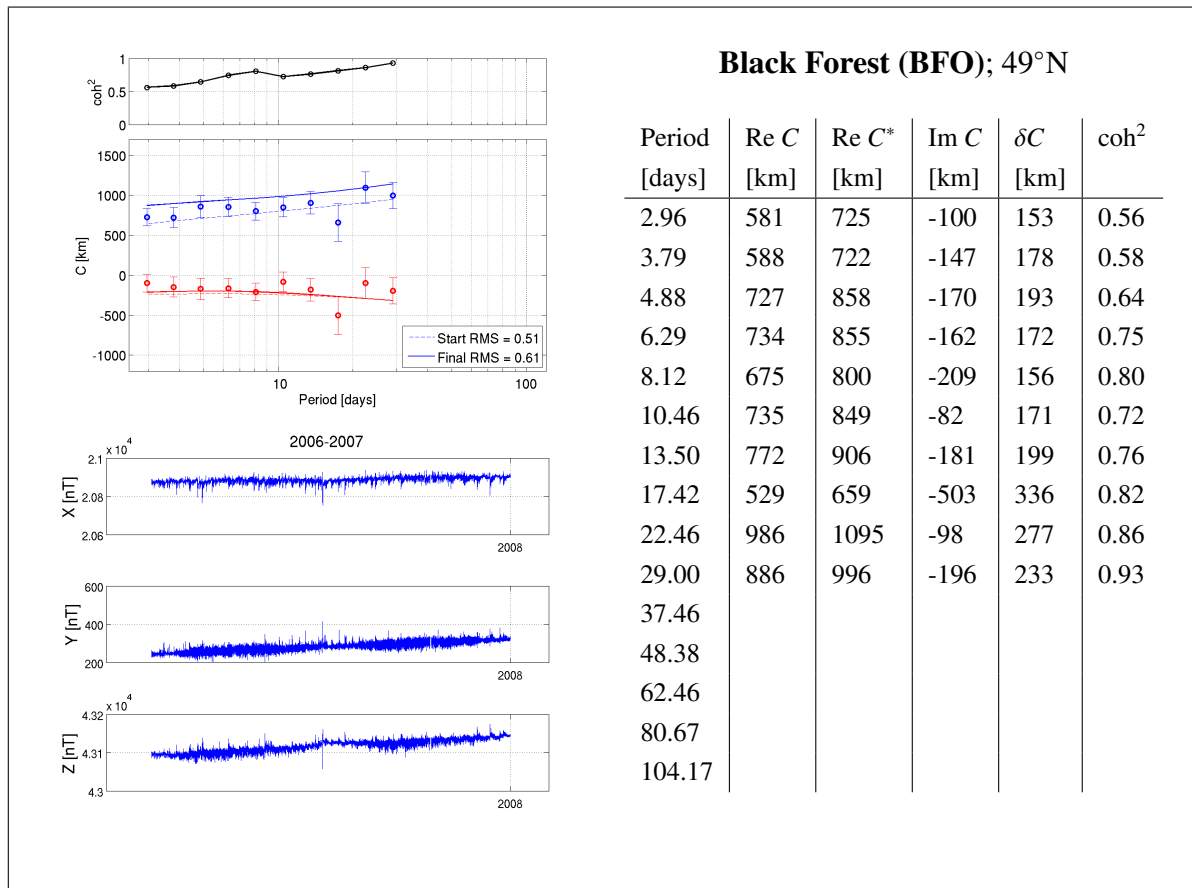


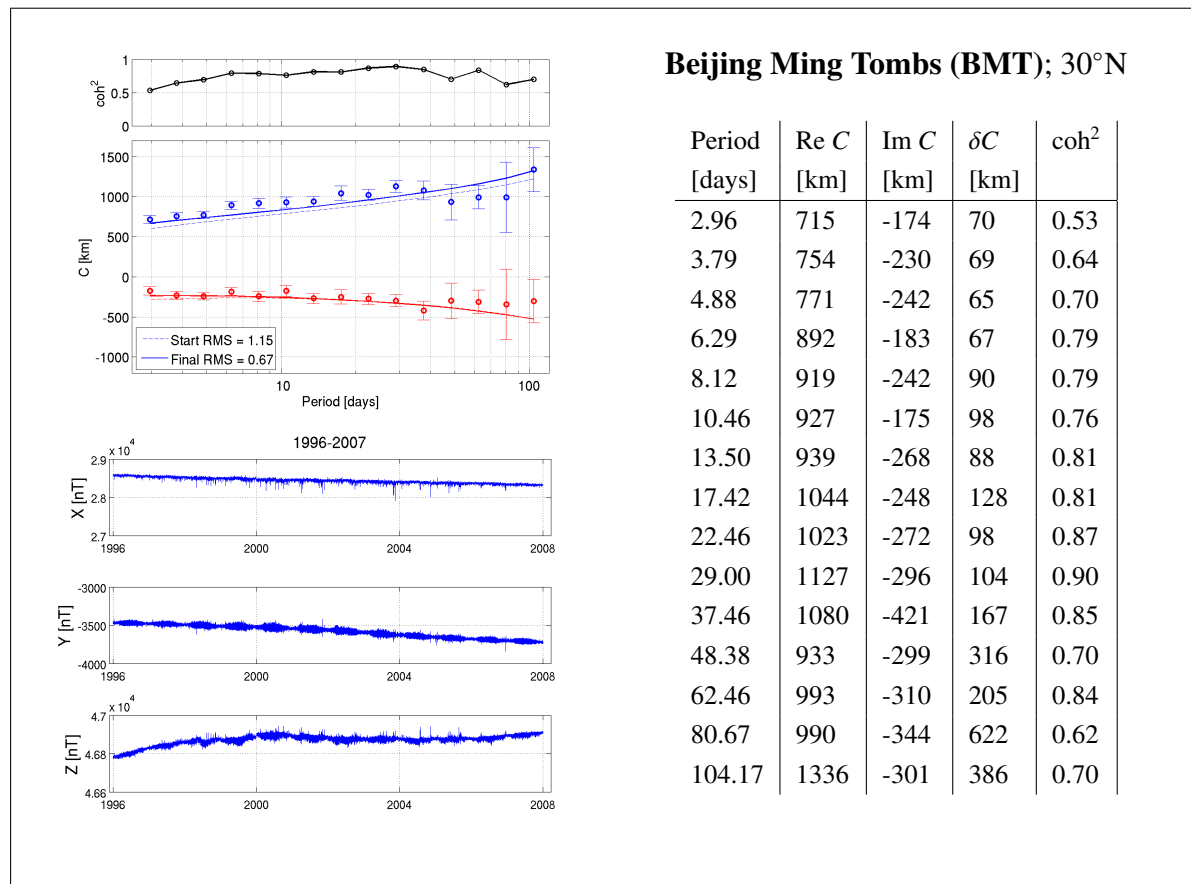
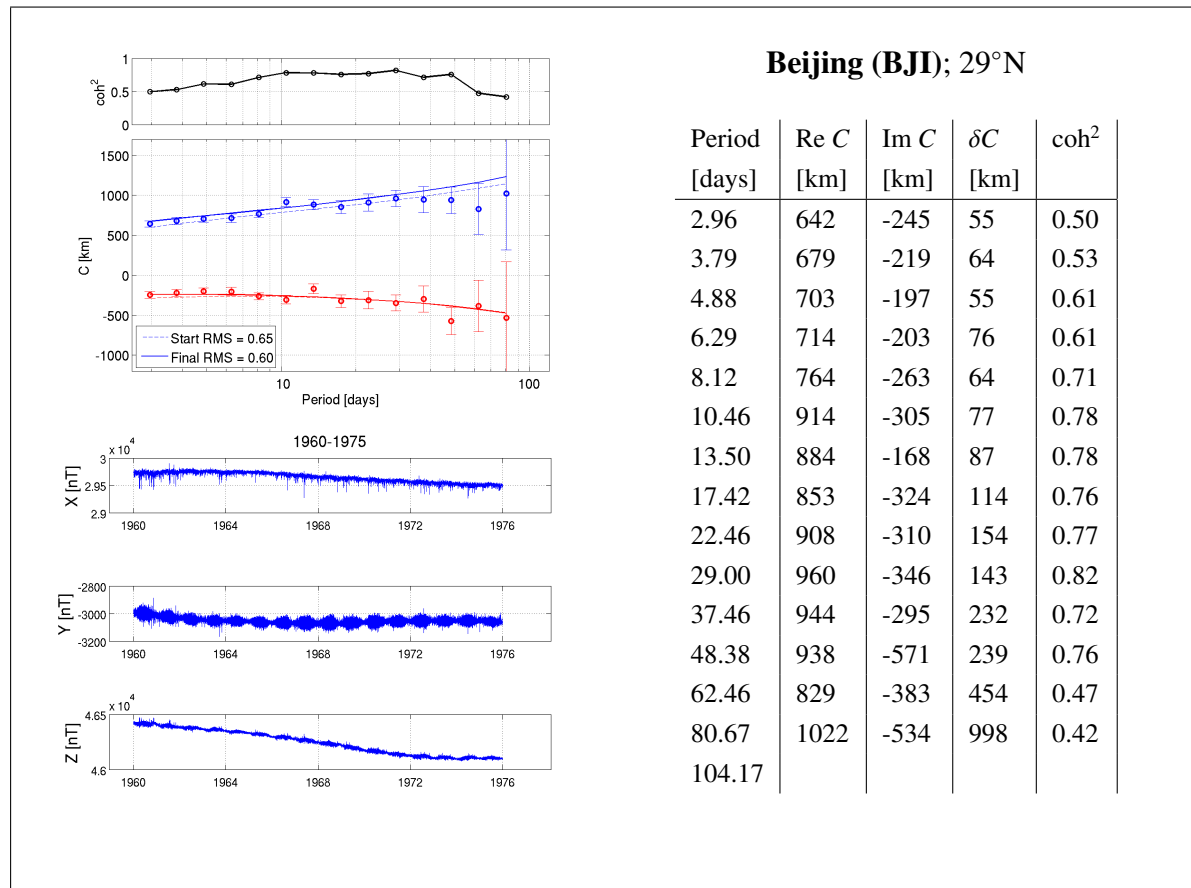


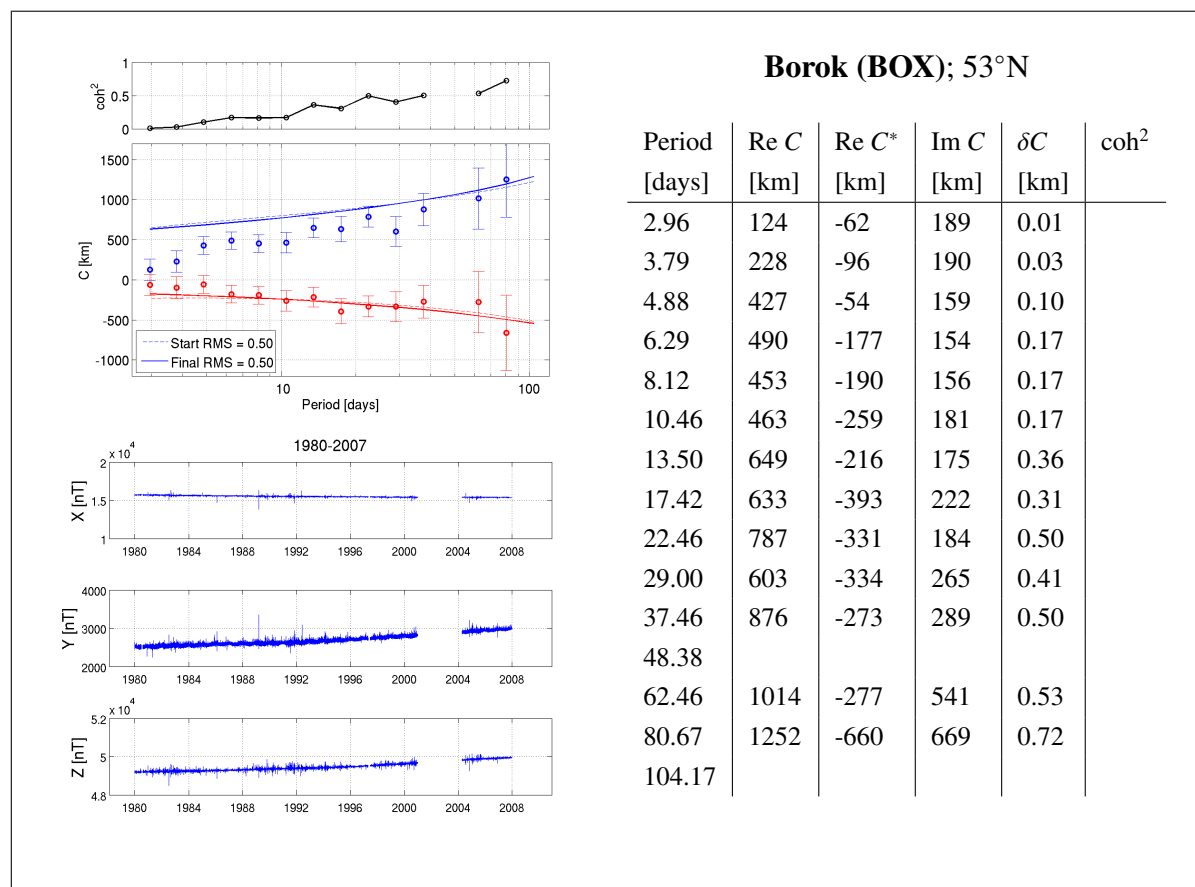
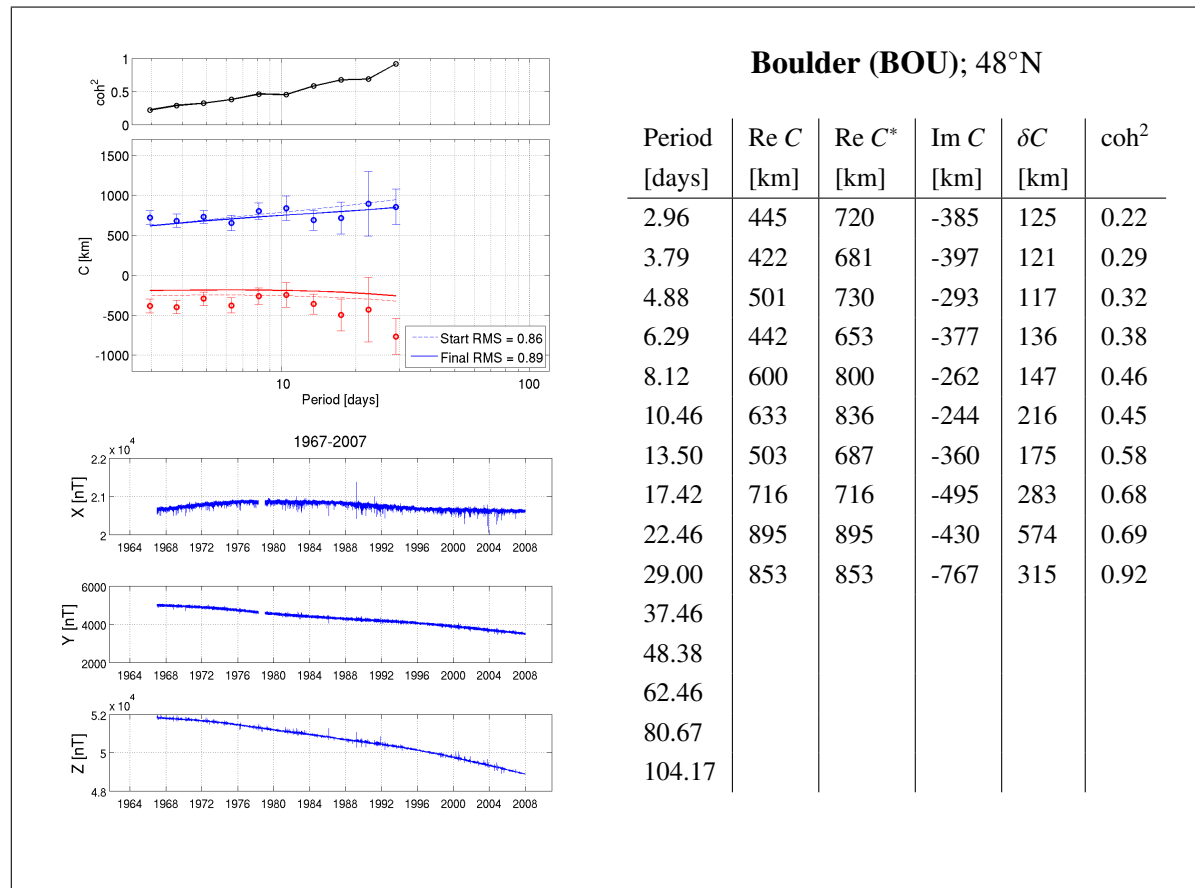


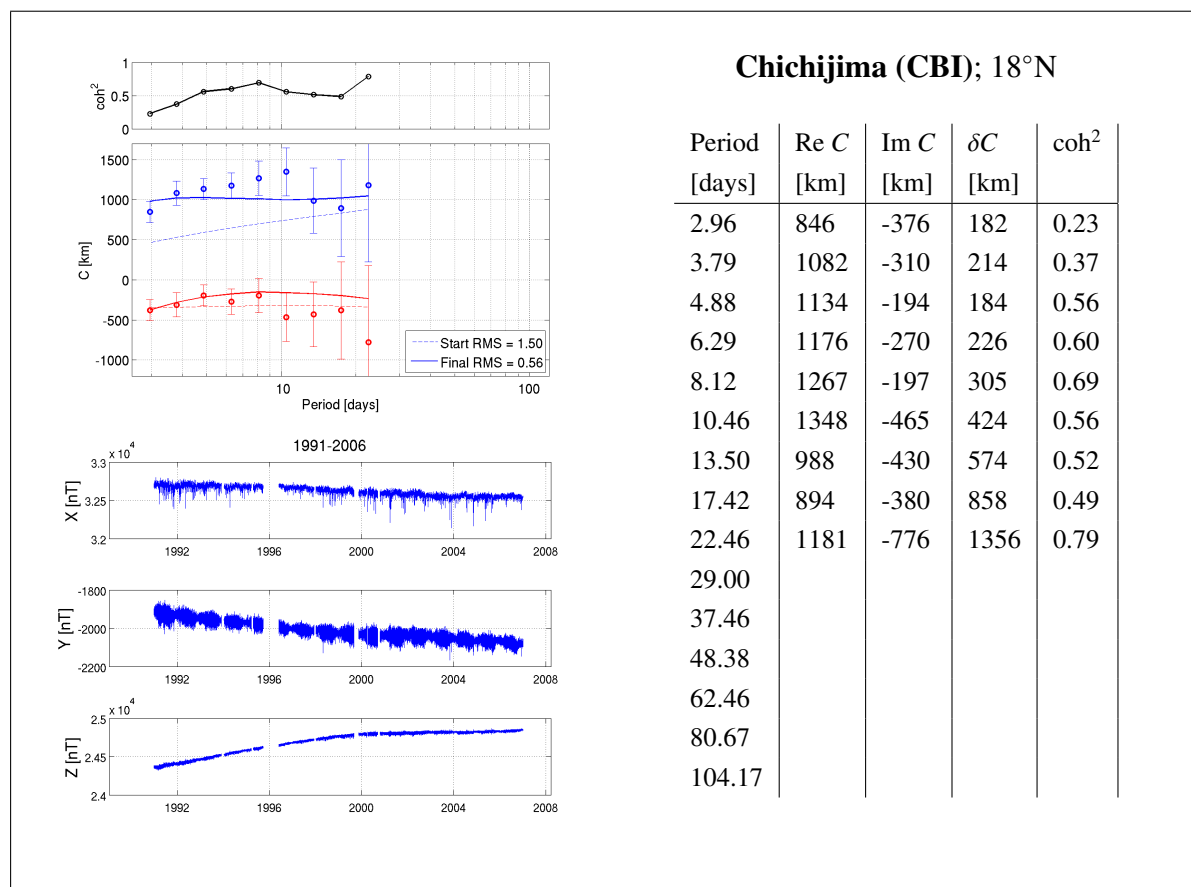
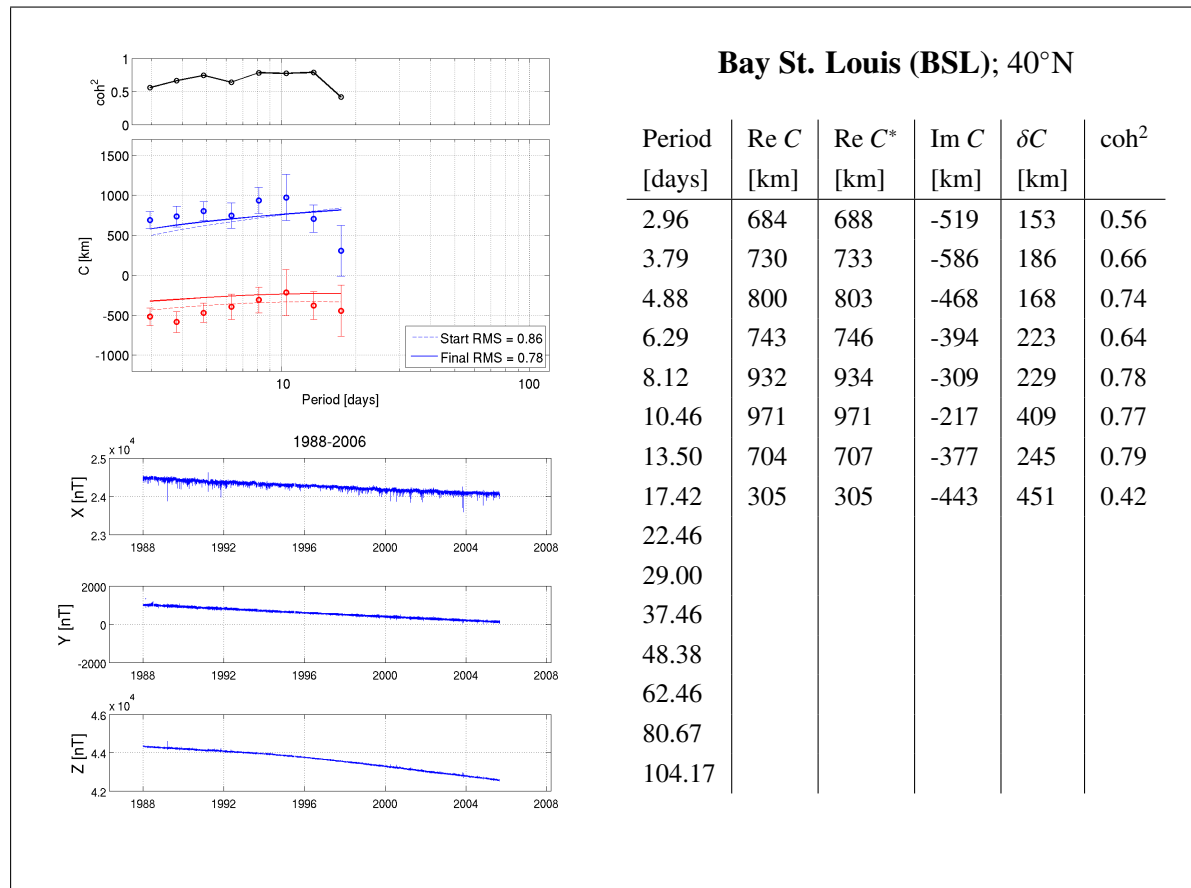


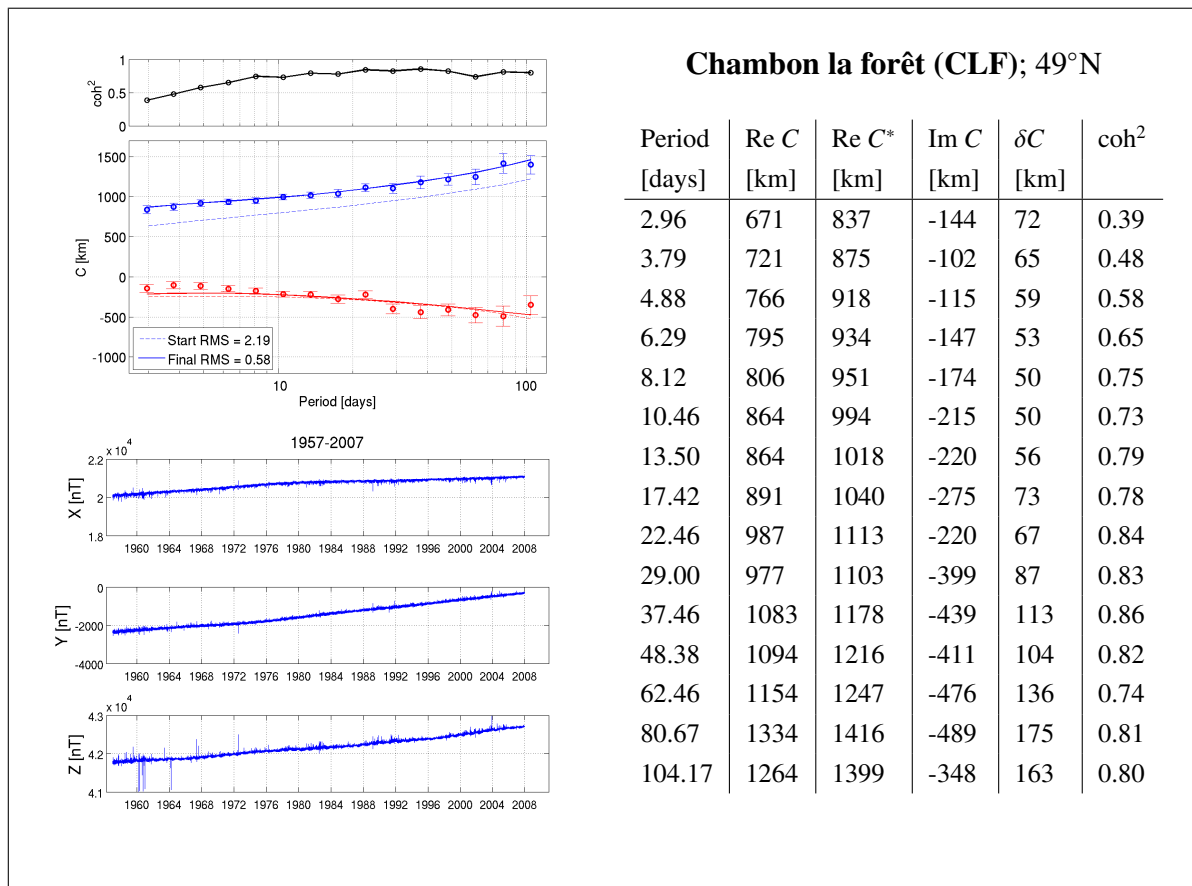
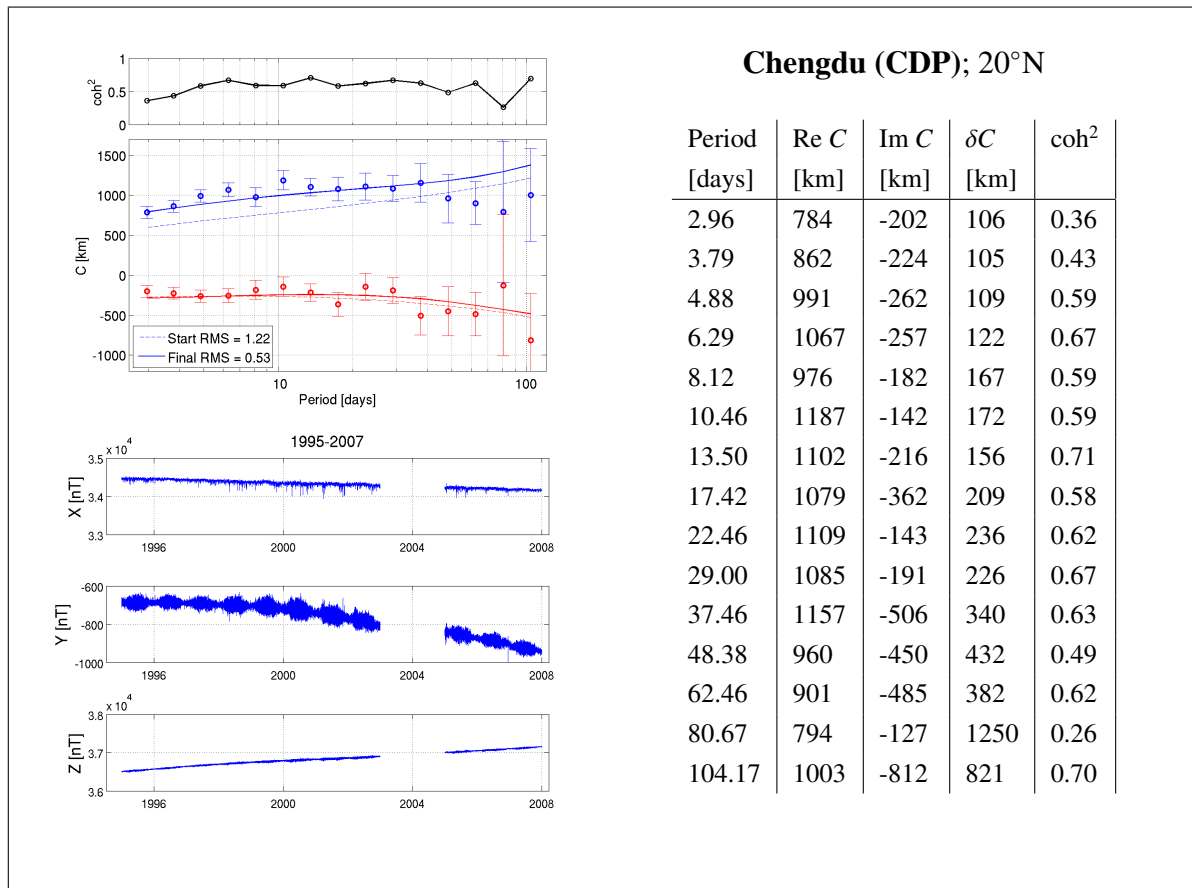


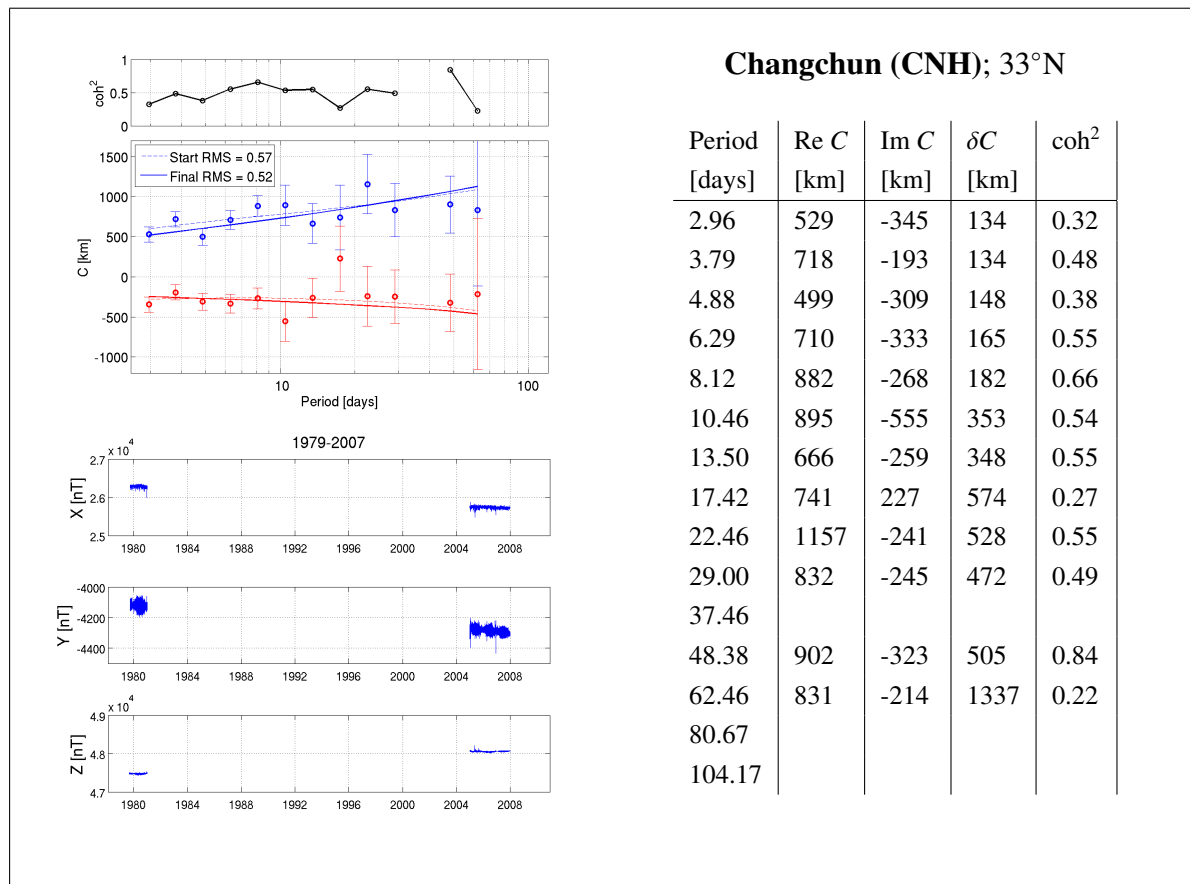
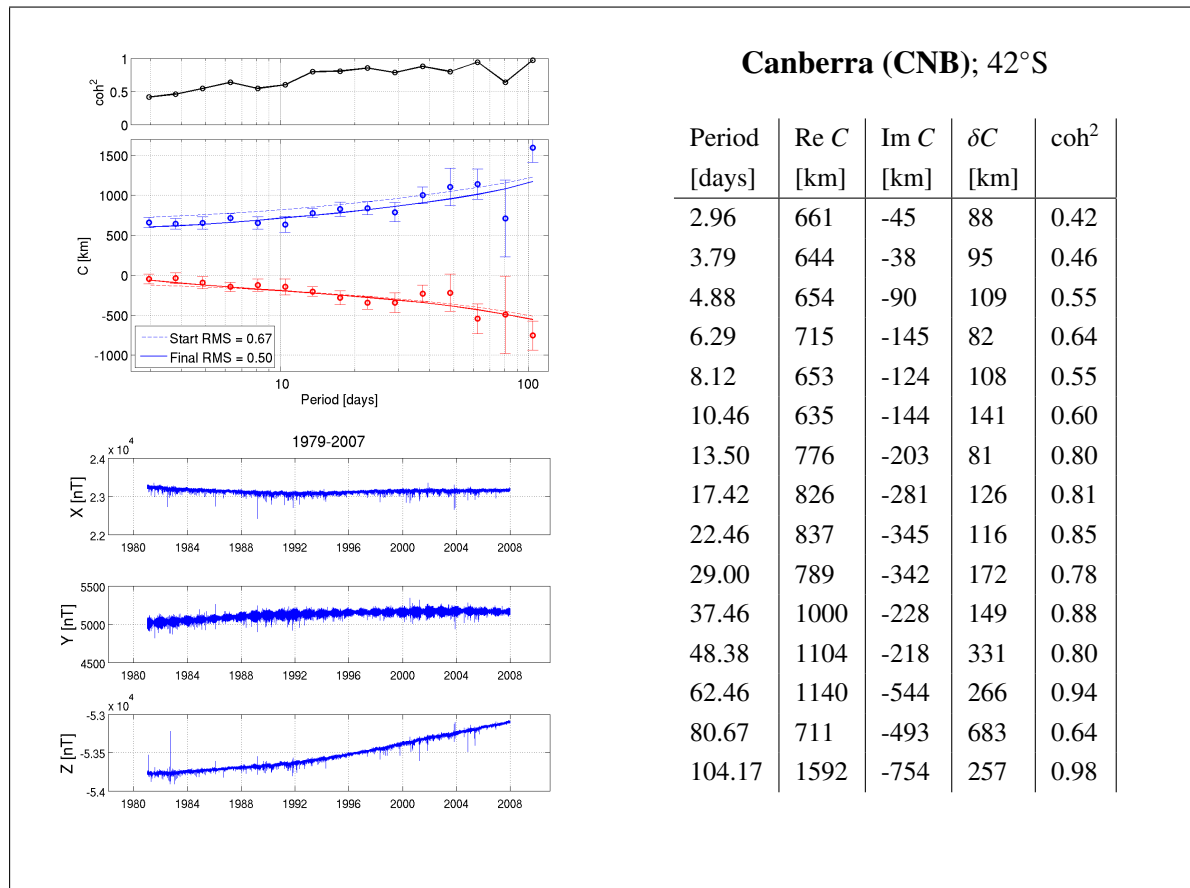


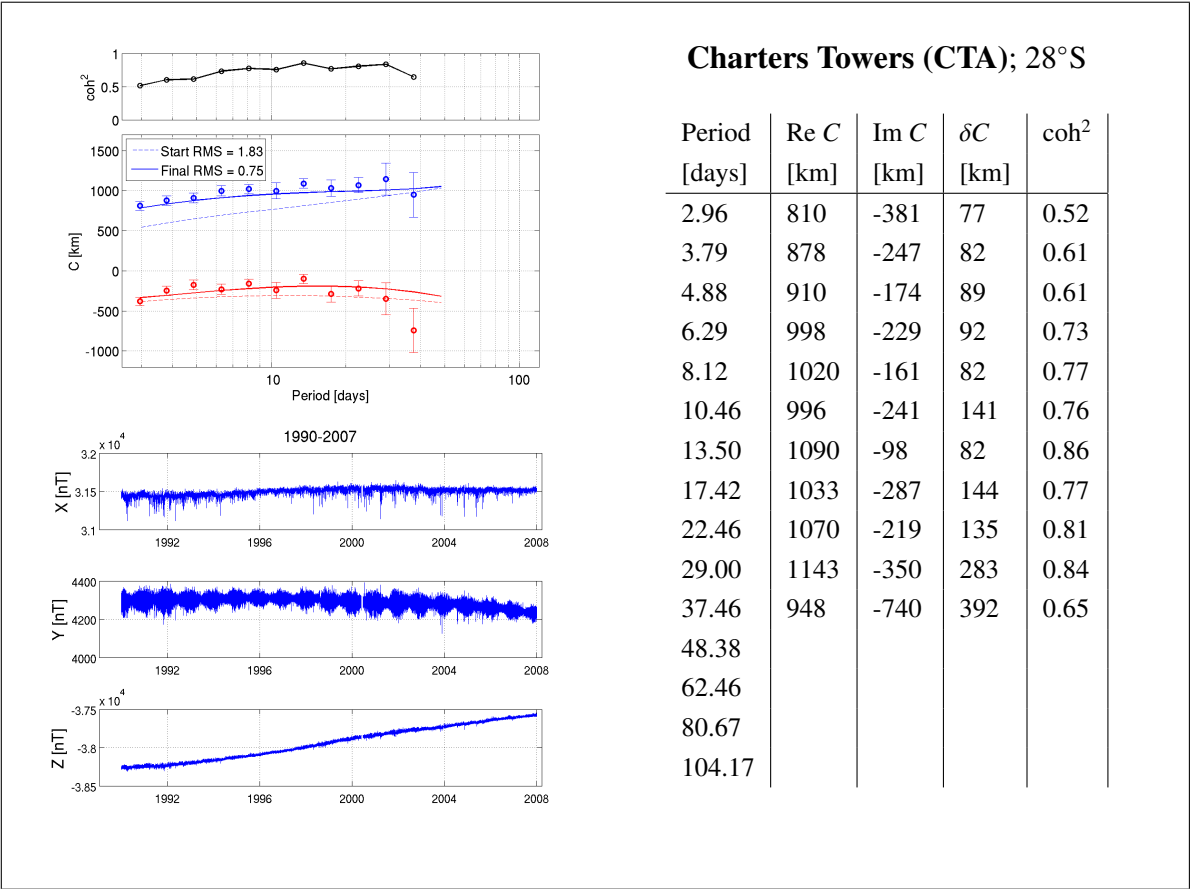
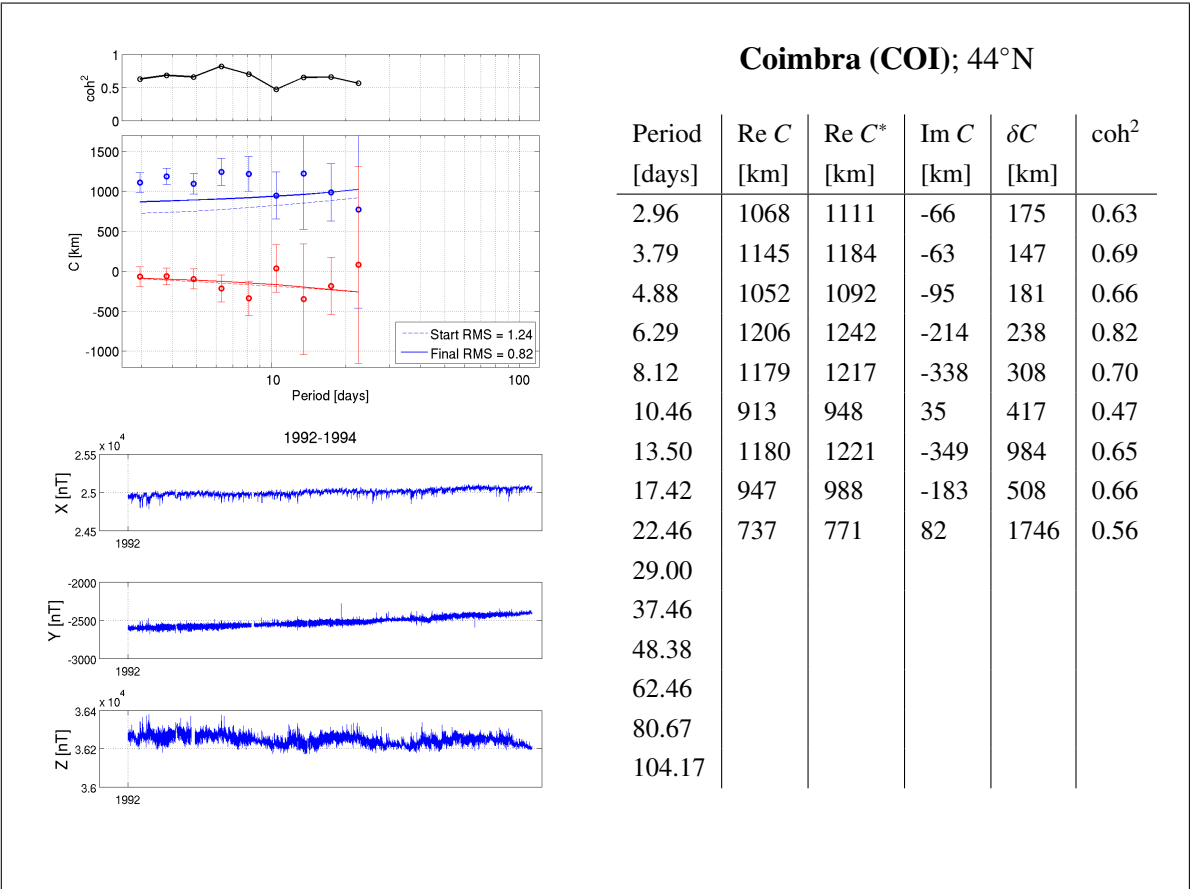


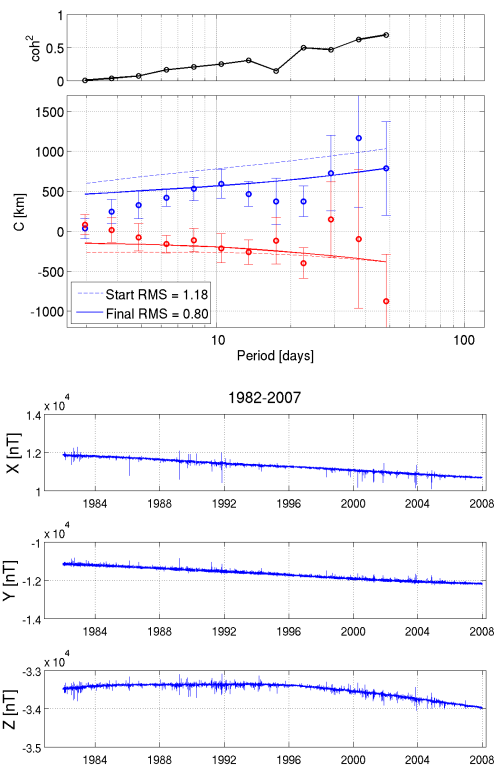




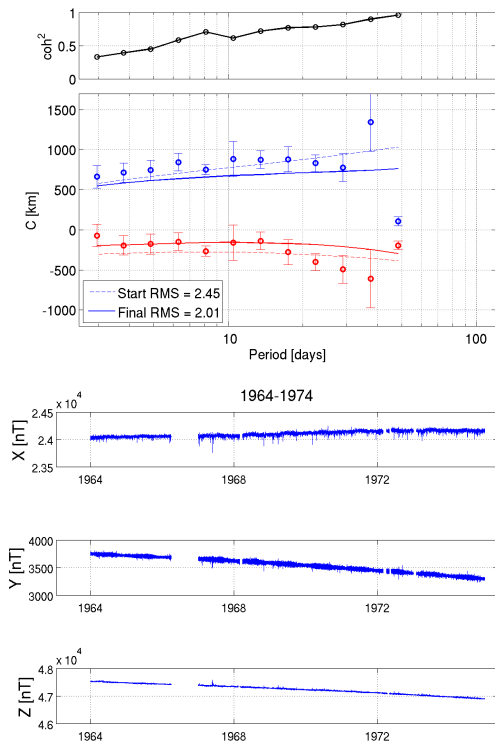




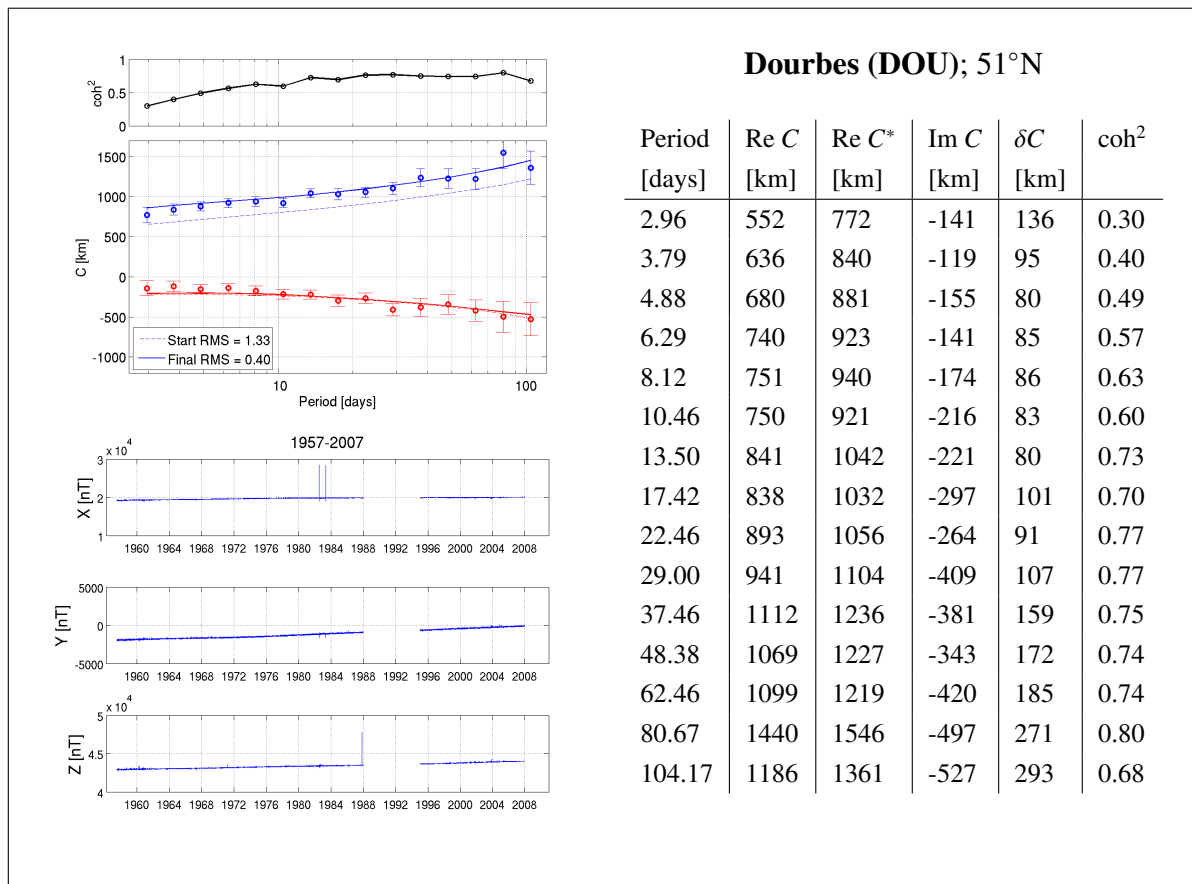
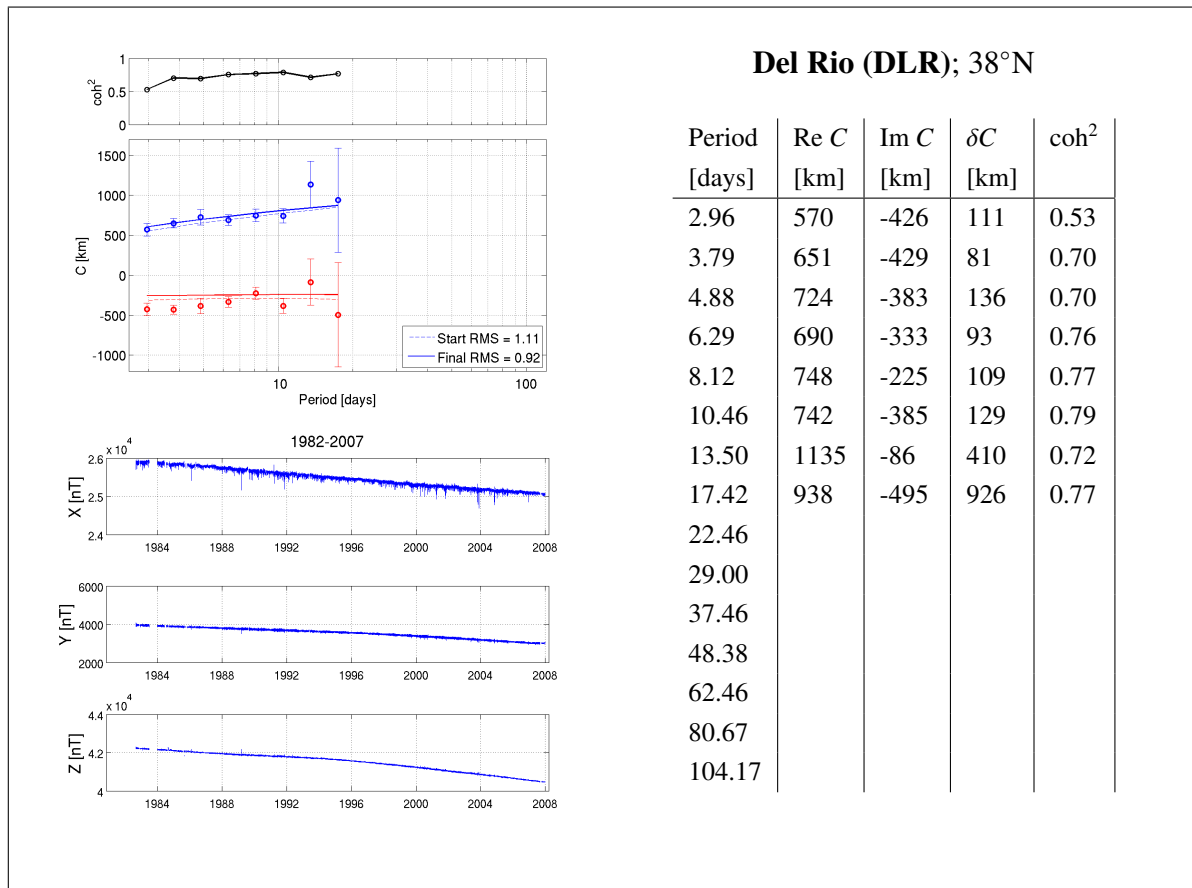


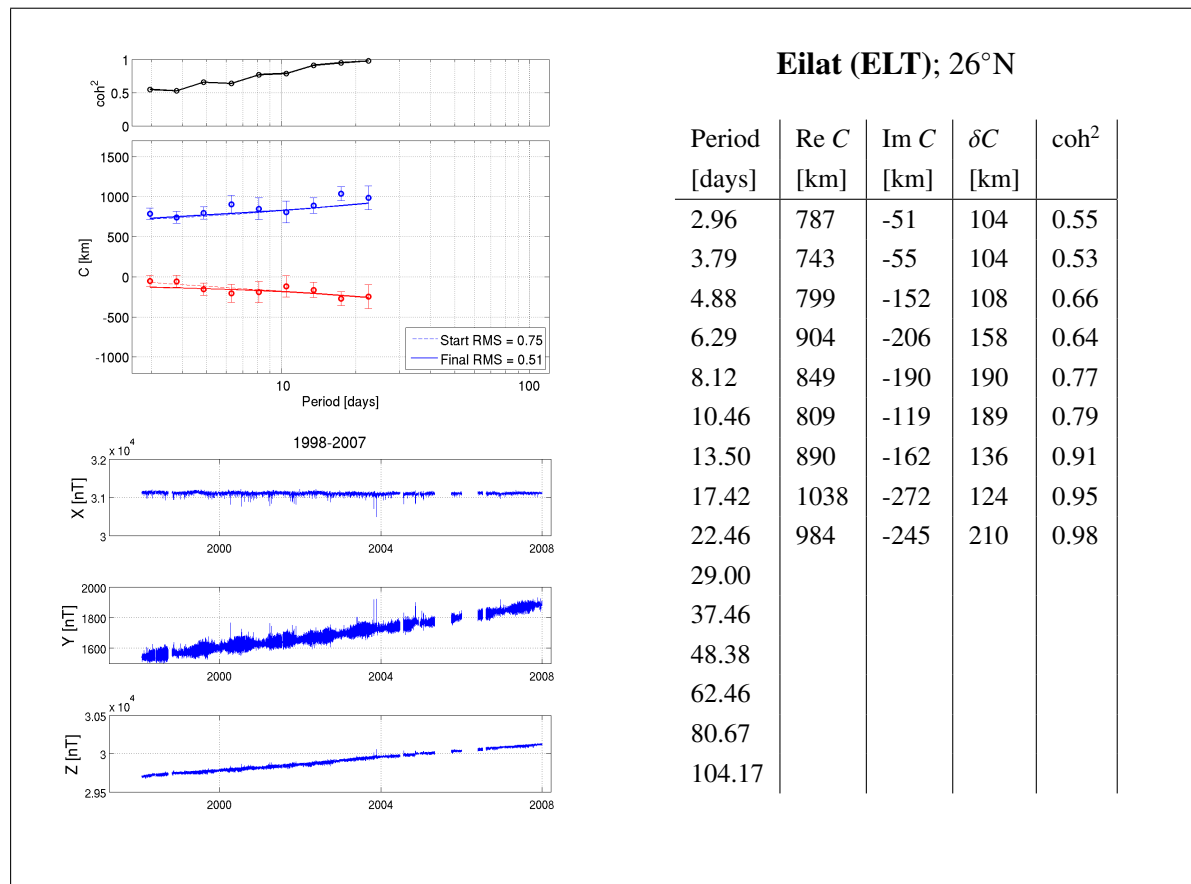
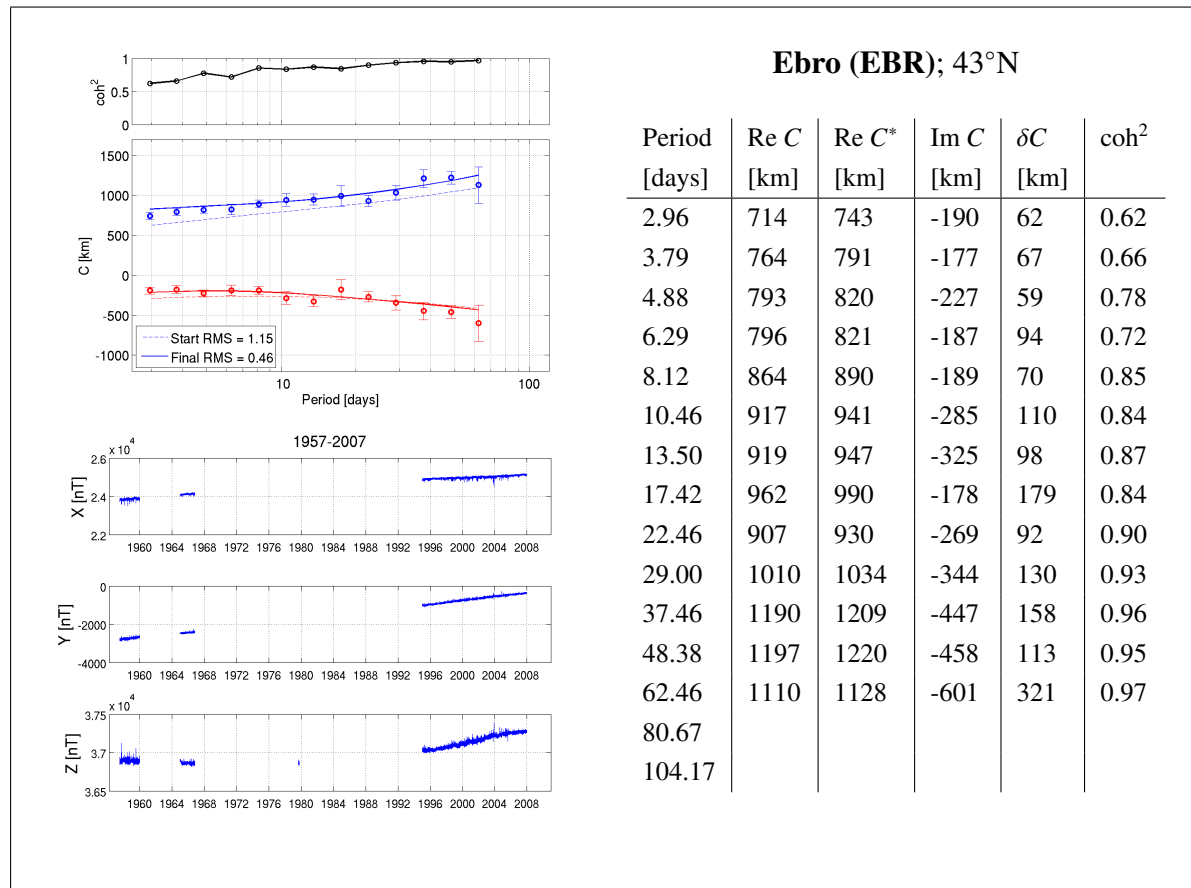
**Port Alfred (CZT); 51°S**

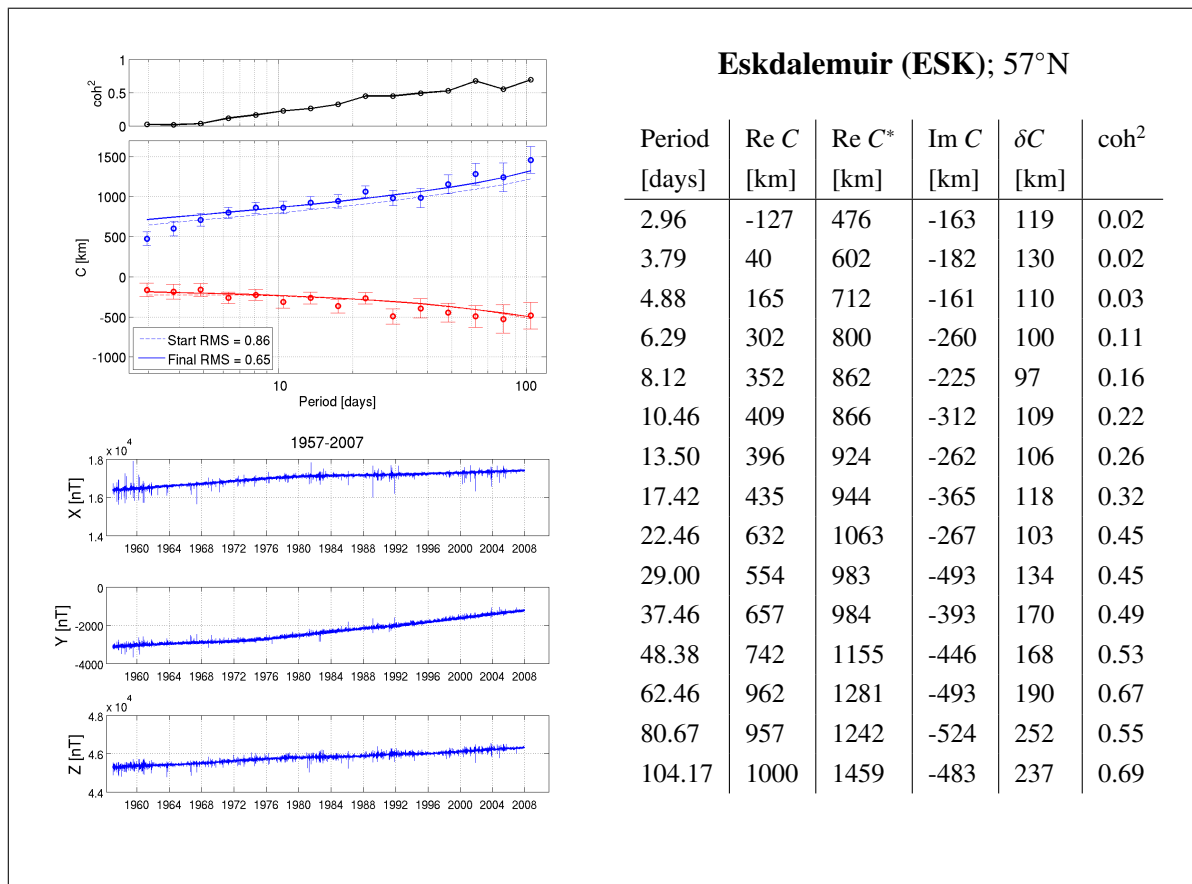
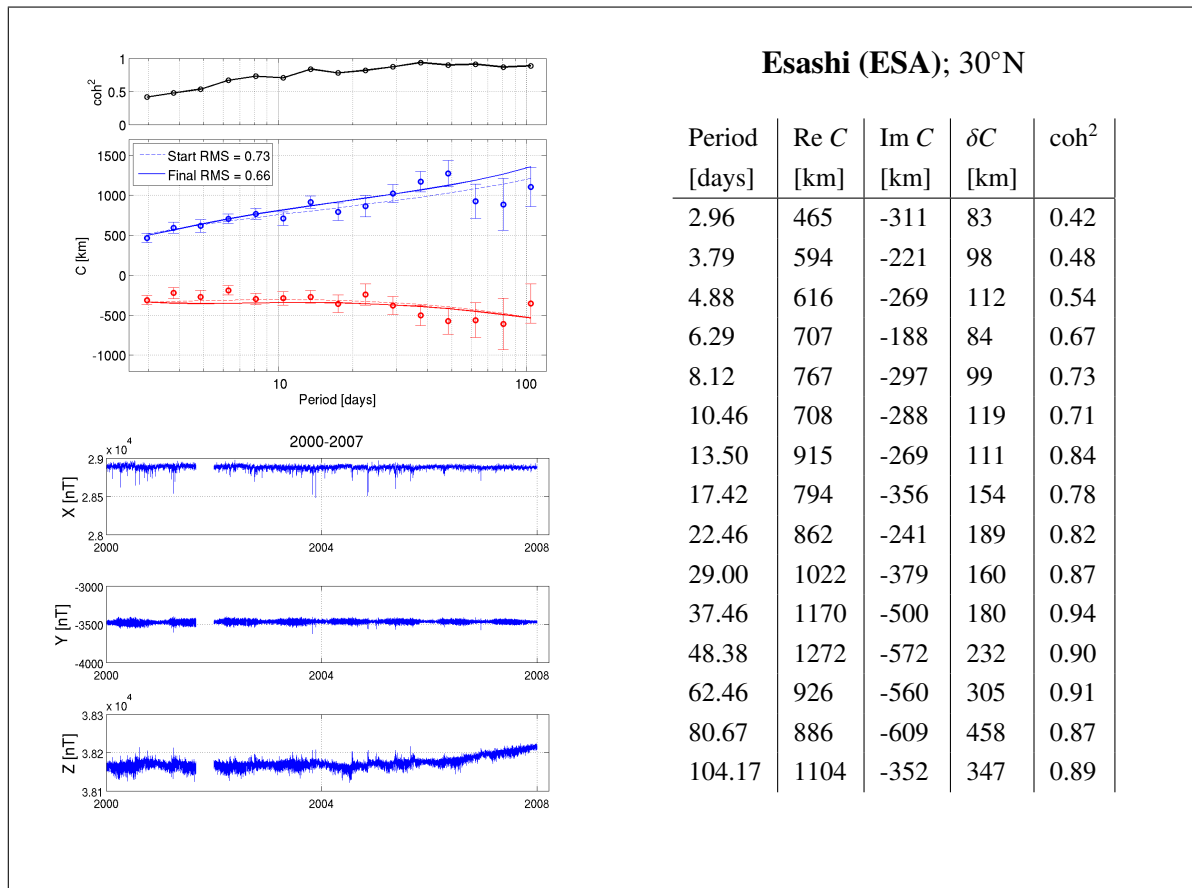
Period [days]	Re C [km]	Im C [km]	δC [km]	coh^2
2.96	33	83	179	0.00
3.79	247	14	215	0.04
4.88	328	-75	241	0.07
6.29	420	-161	157	0.16
8.12	530	-111	207	0.20
10.46	593	-214	256	0.25
13.50	466	-261	220	0.30
17.42	372	-118	416	0.15
22.46	373	-397	272	0.49
29.00	728	149	667	0.47
37.46	1167	-95	1227	0.62
48.38	785	-873	829	0.69
62.46				
80.67				
104.17				

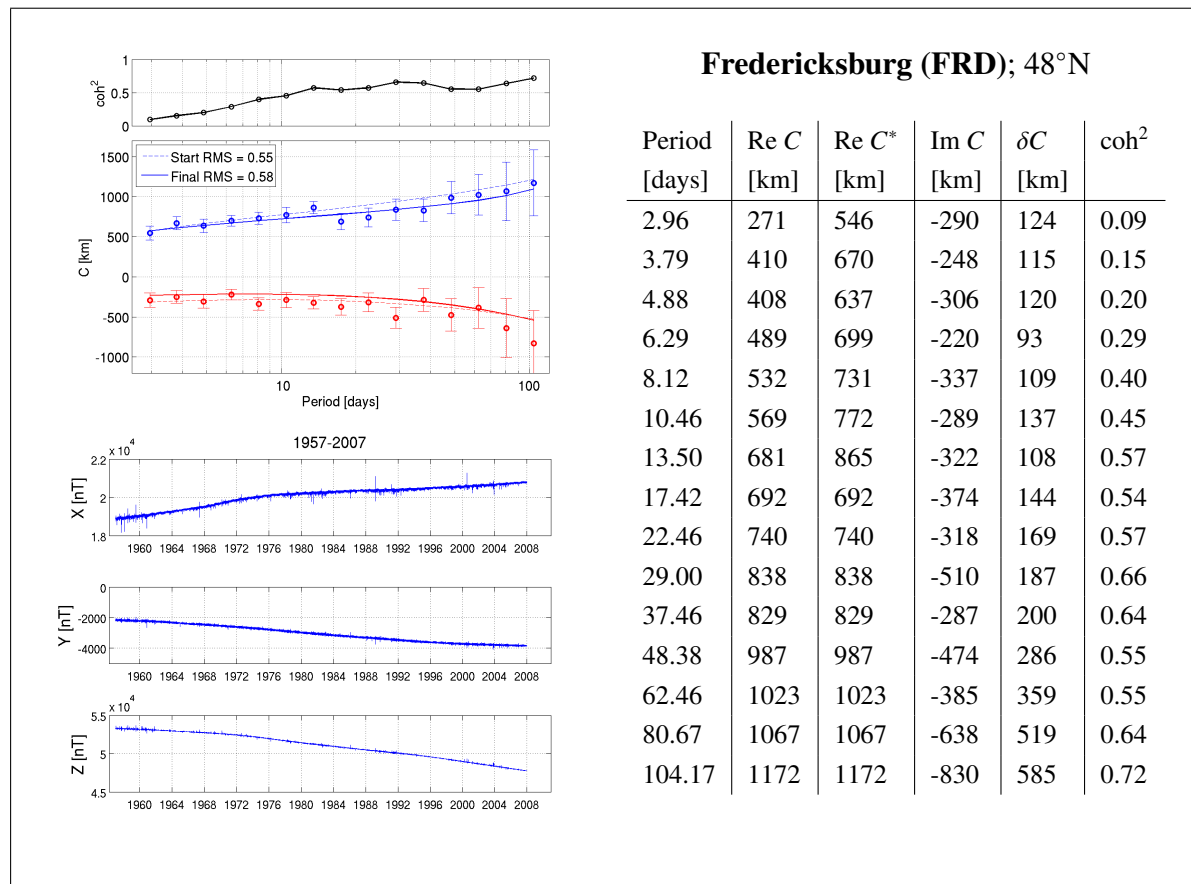
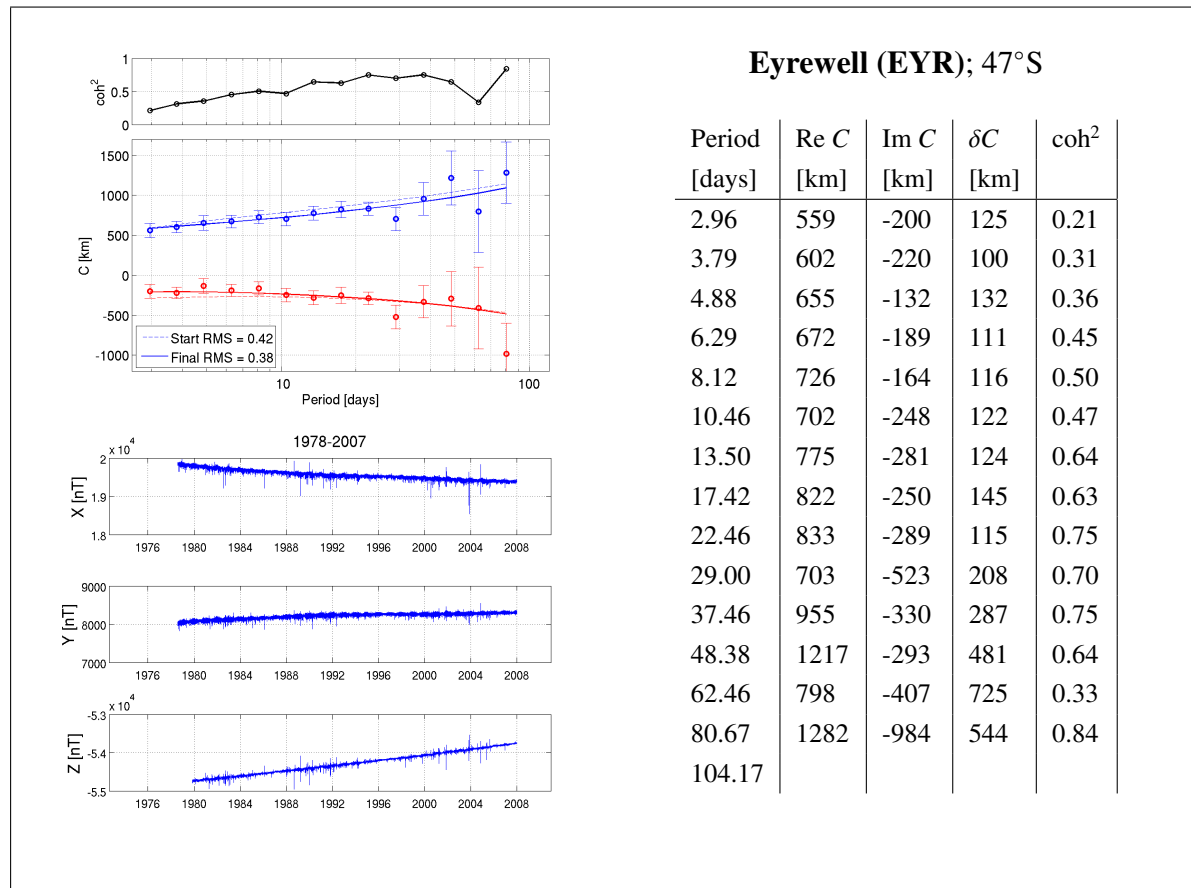
**Dallas (DAL); 42°N**

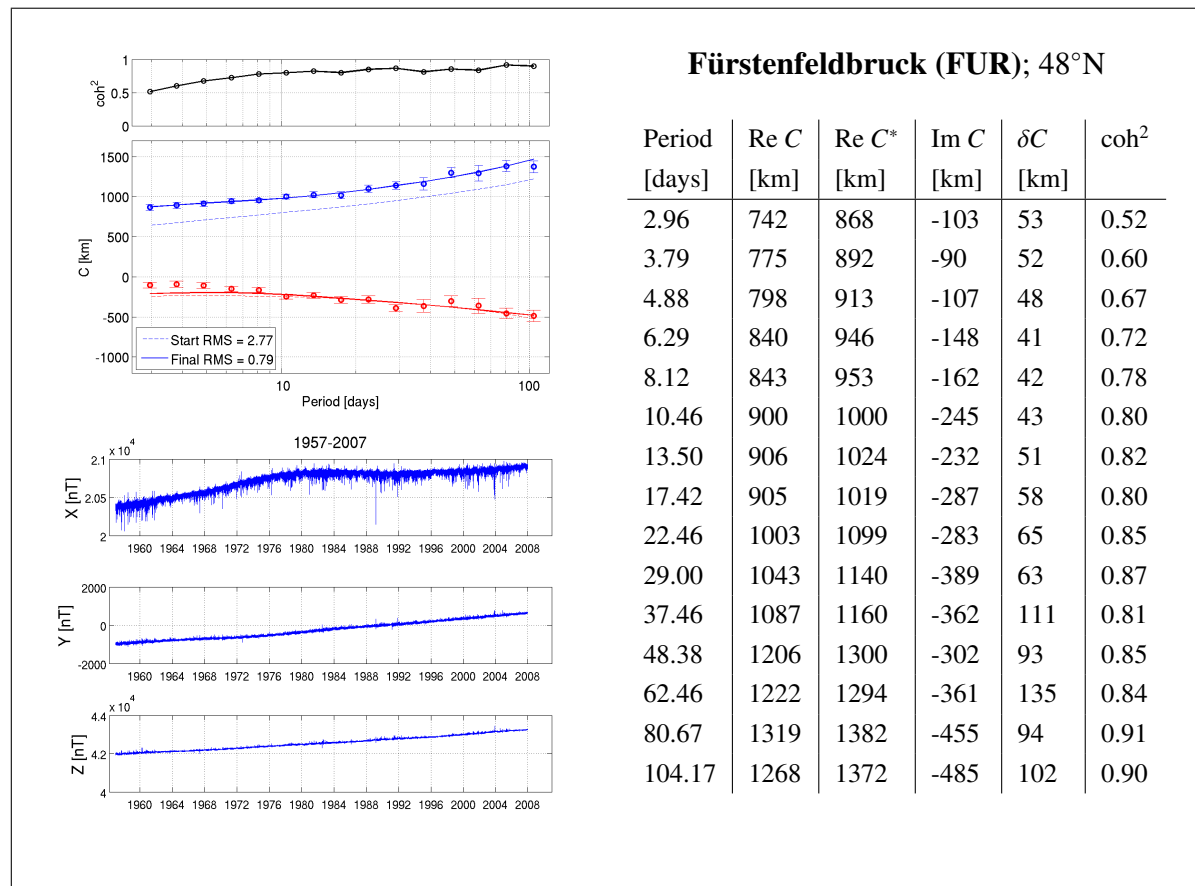
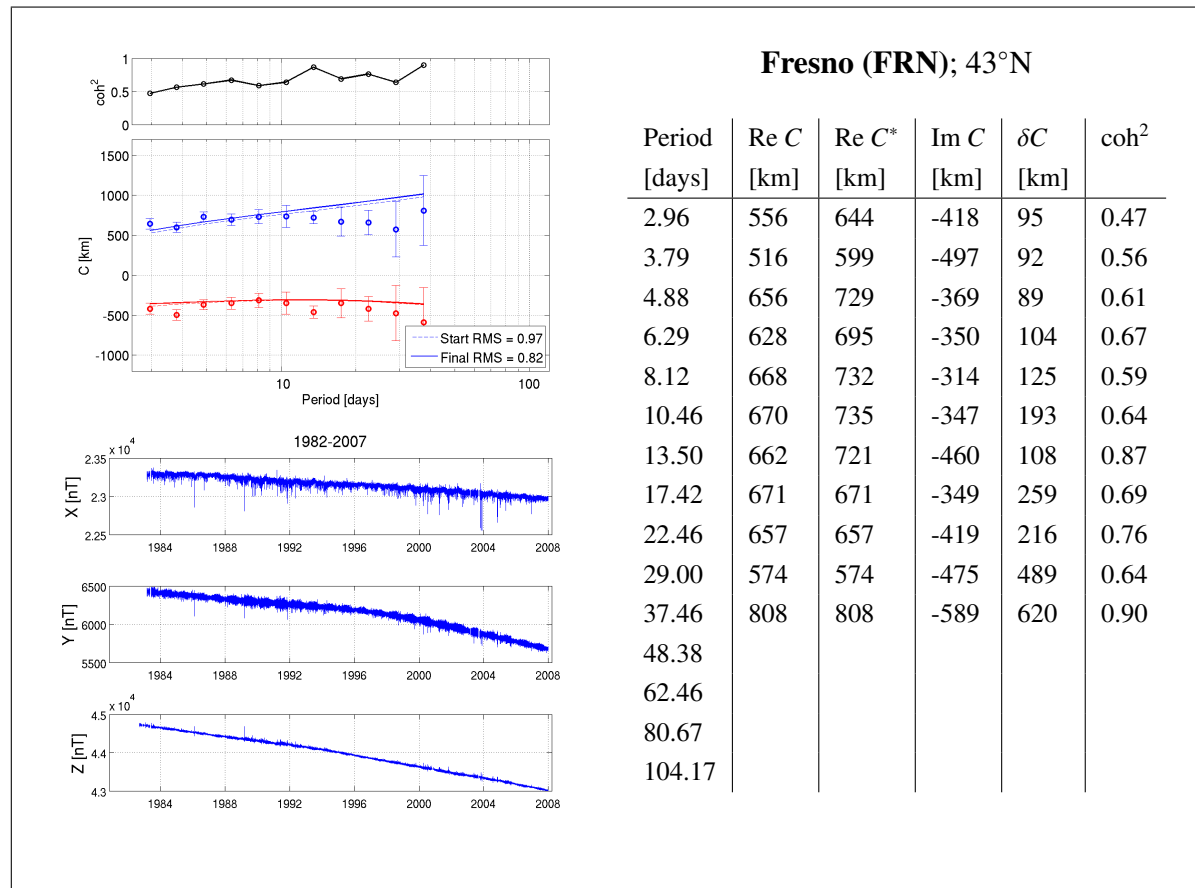
Period [days]	Re C [km]	Re C* [km]	Im C [km]	δC [km]	coh^2
2.96	612	663	-71	200	0.33
3.79	666	714	-193	170	0.39
4.88	701	744	-177	177	0.45
6.29	806	845	-146	153	0.58
8.12	712	749	-264	88	0.71
10.46	847	885	-158	313	0.61
13.50	841	875	-136	153	0.72
17.42	881	881	-278	220	0.77
22.46	832	832	-400	148	0.78
29.00	776	776	-492	247	0.82
37.46	1344	1344	-610	514	0.90
48.38	106	106	-192	76	0.96
62.46					
80.67					
104.17					

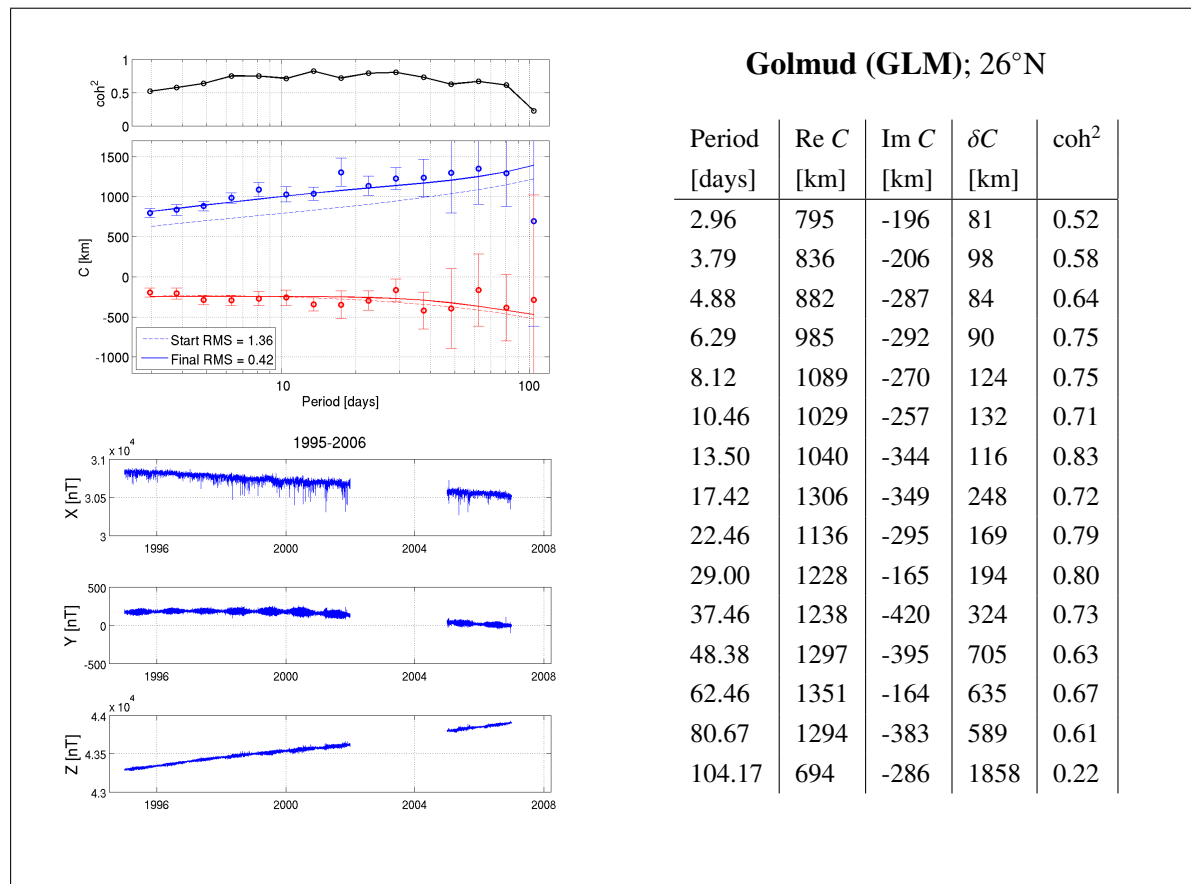
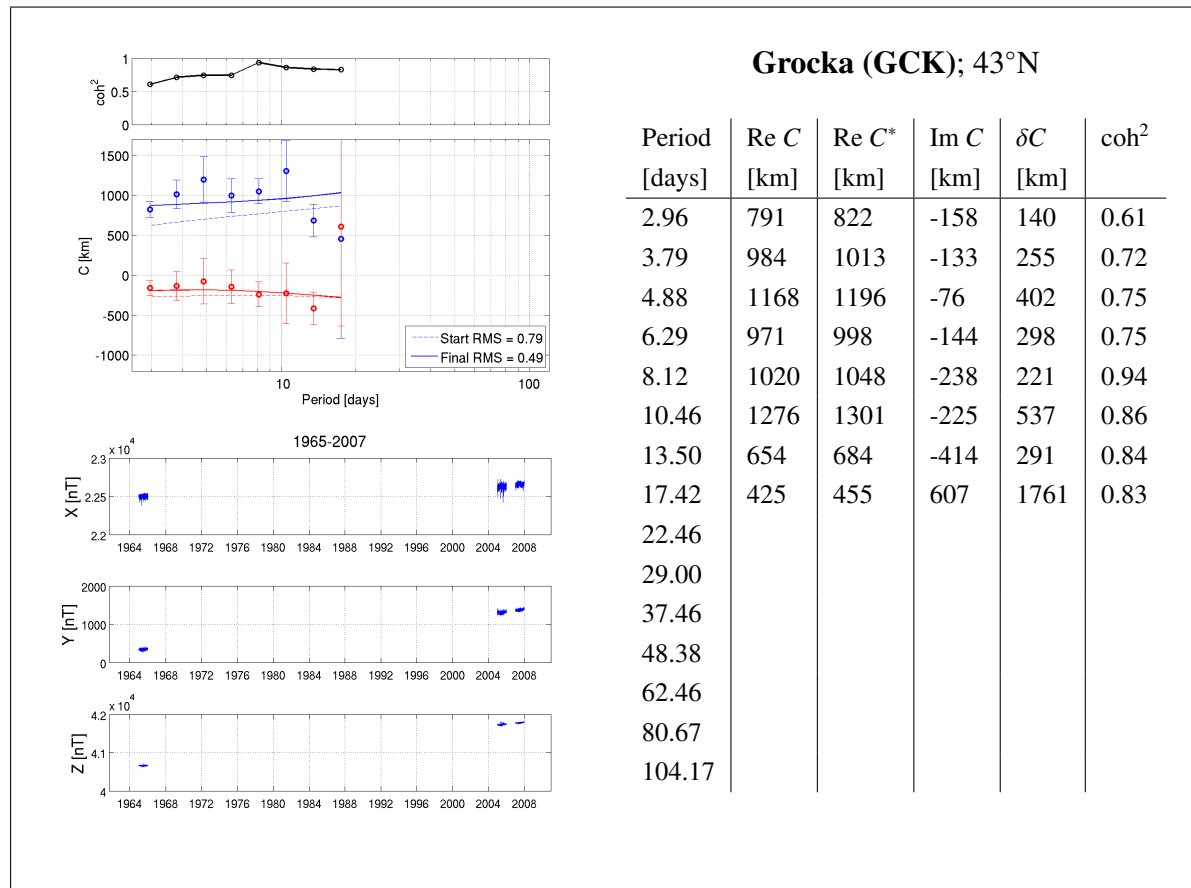


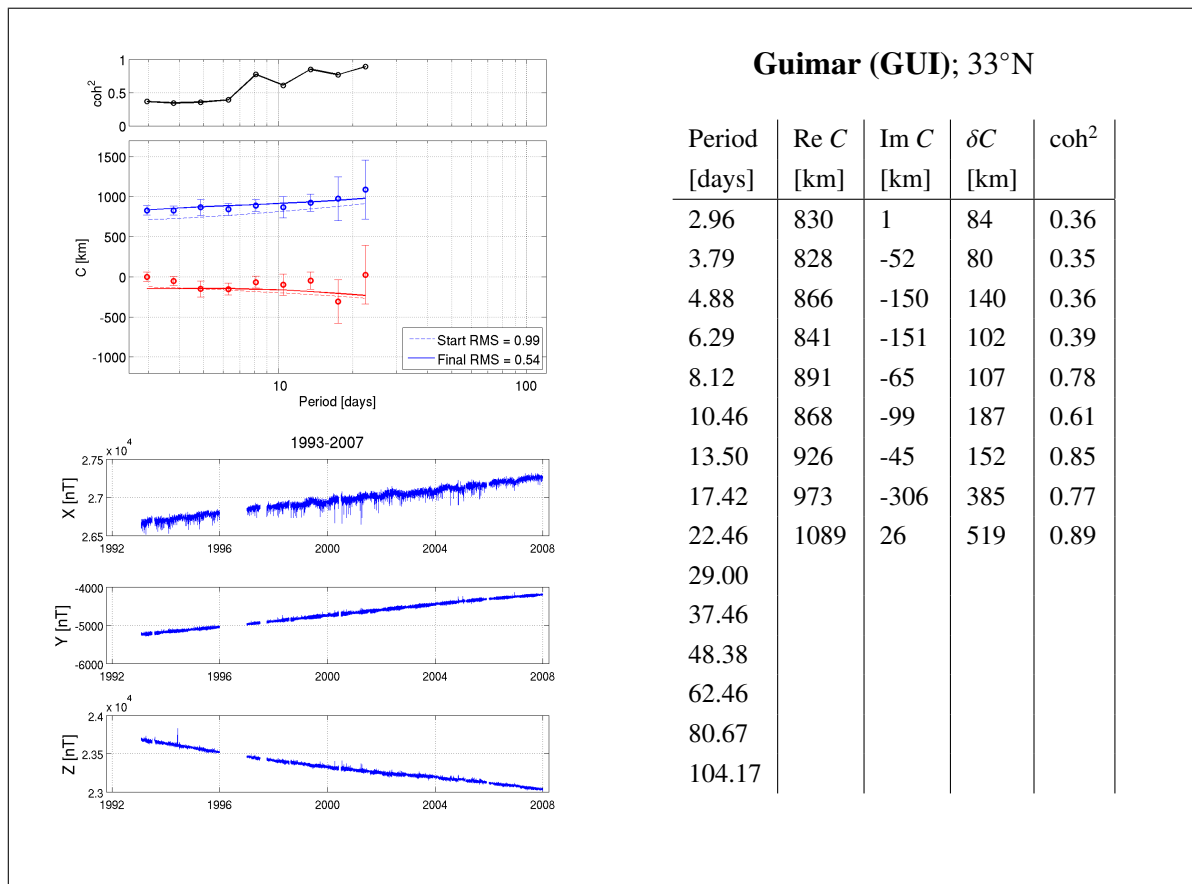
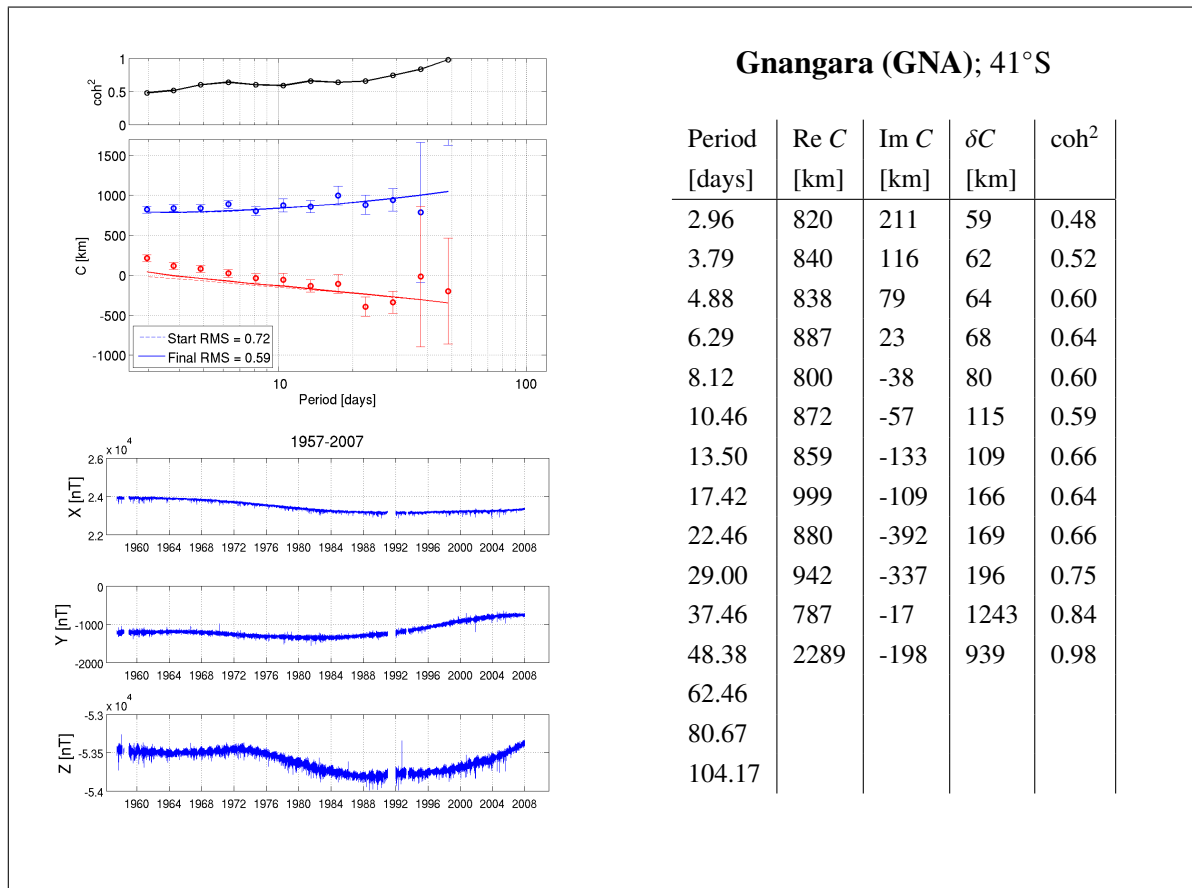


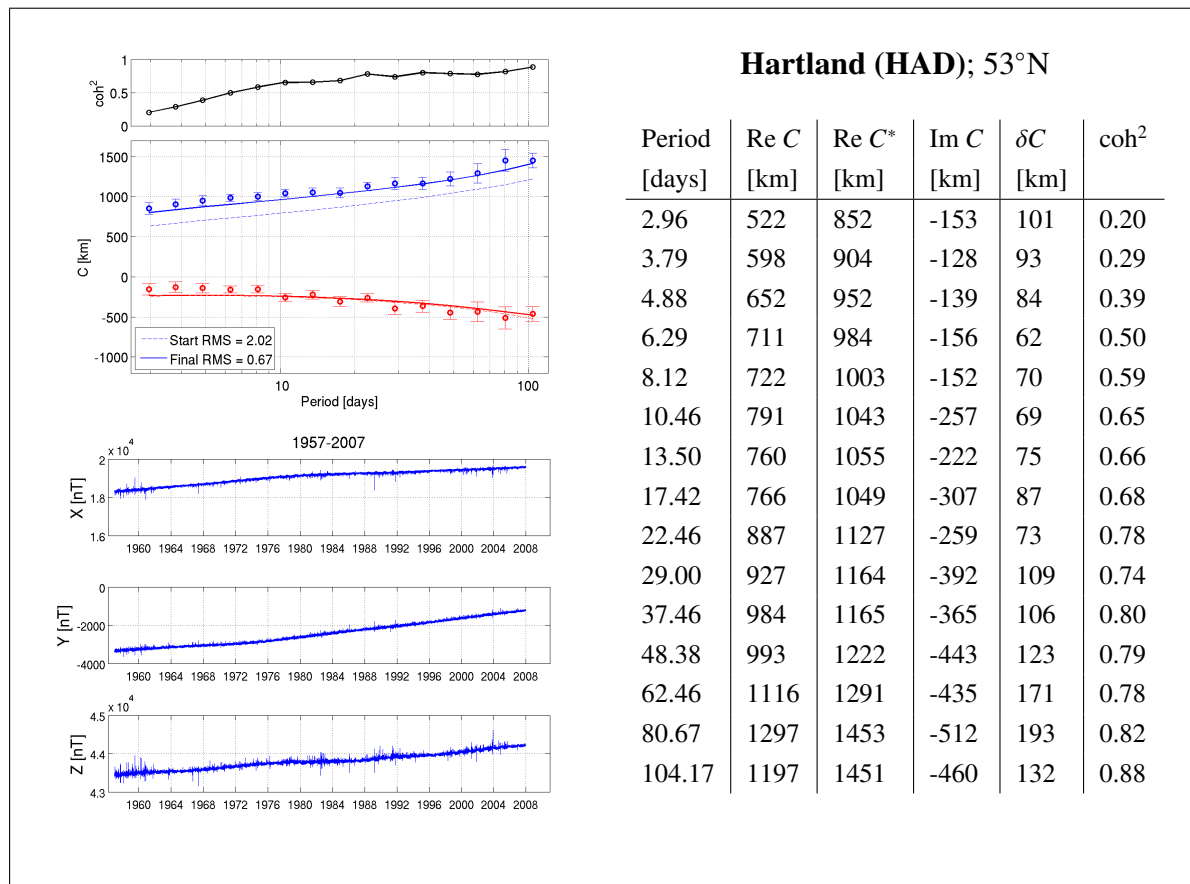
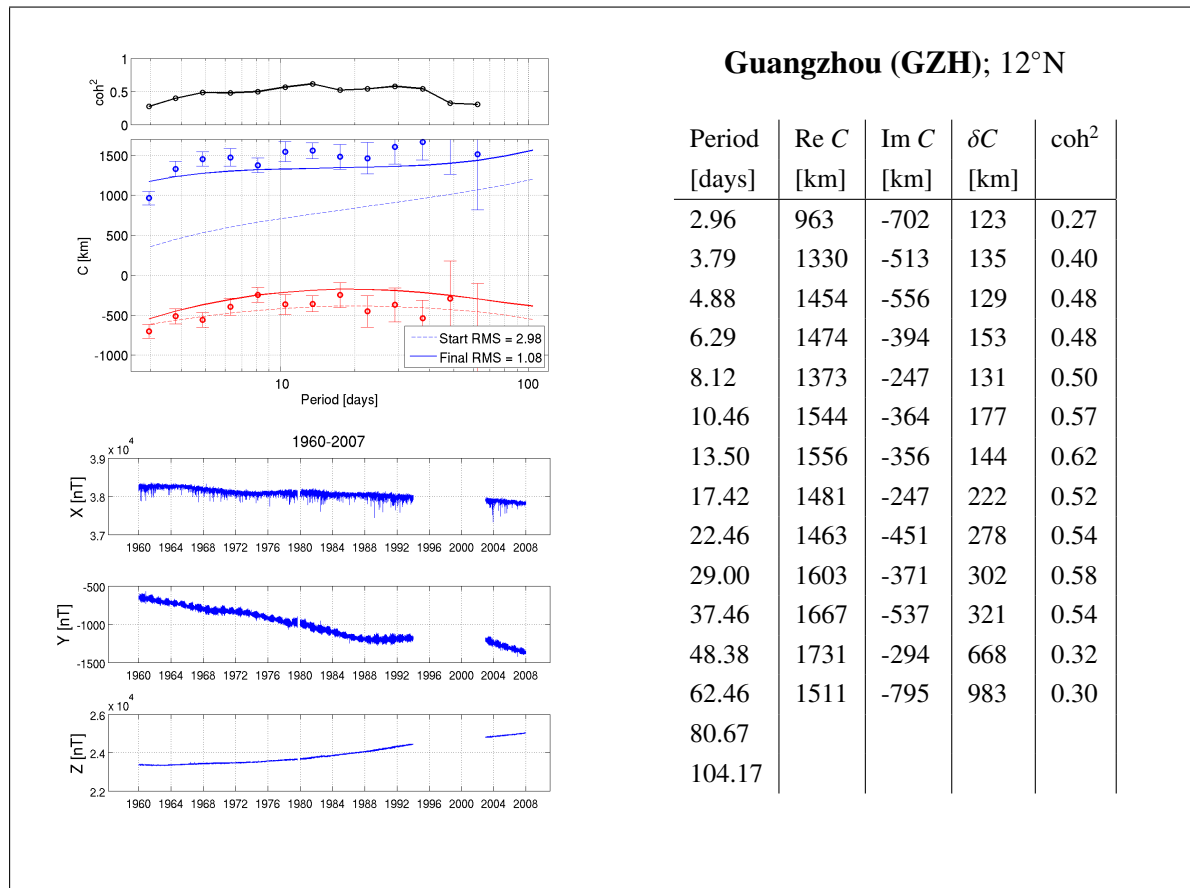


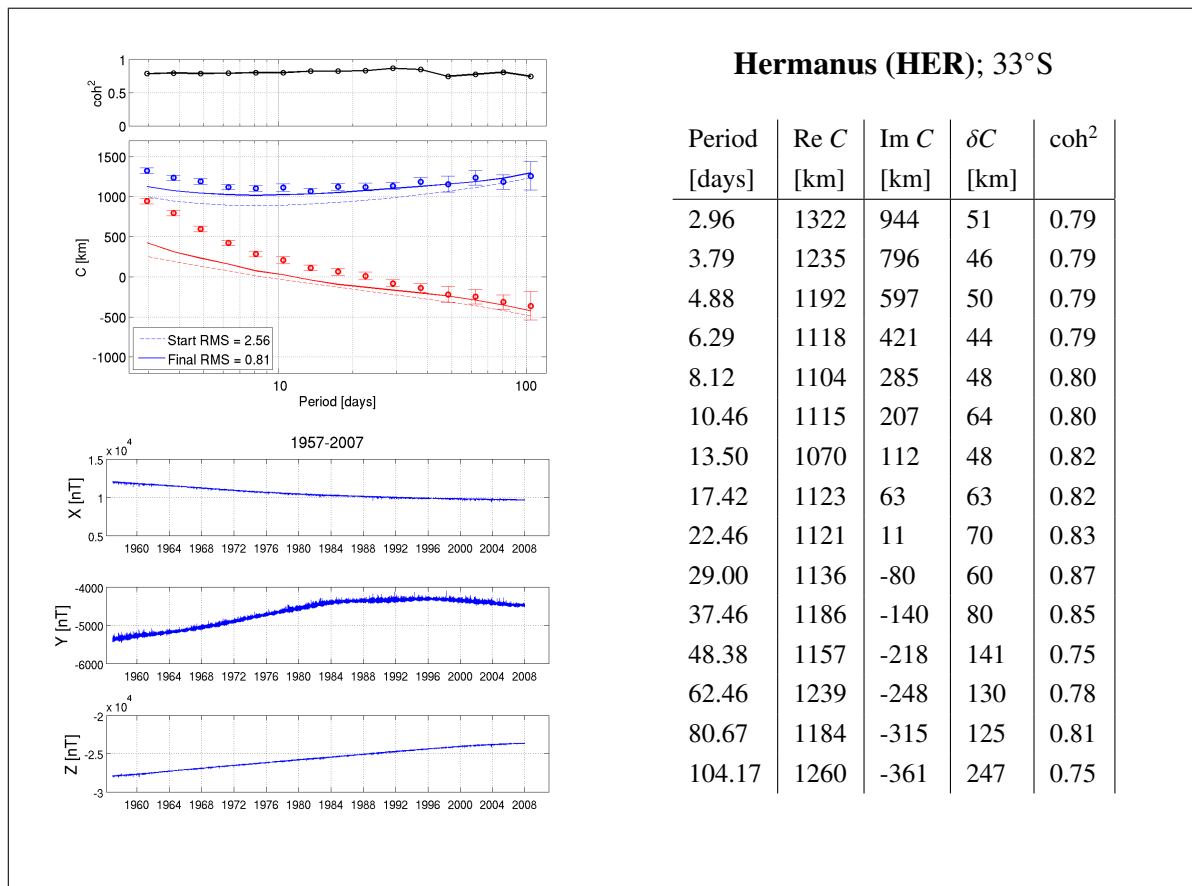
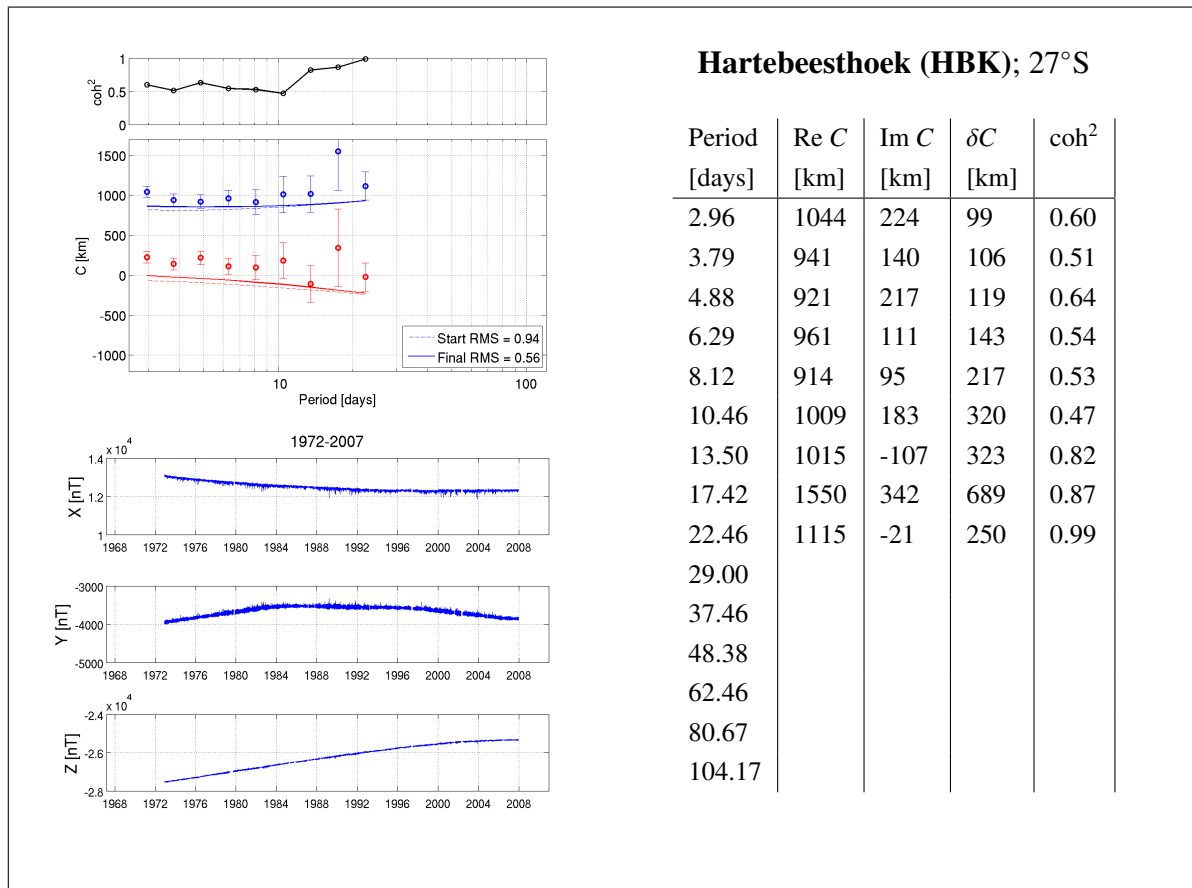


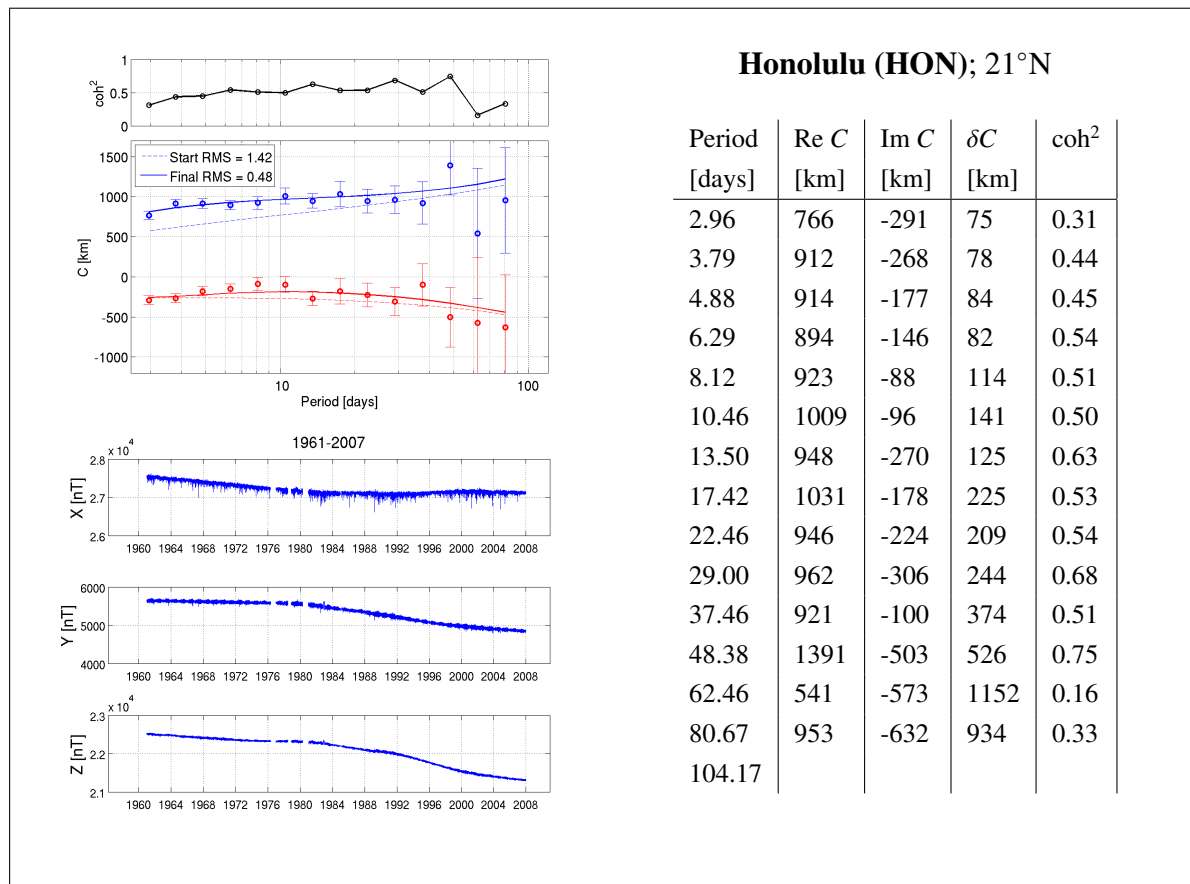
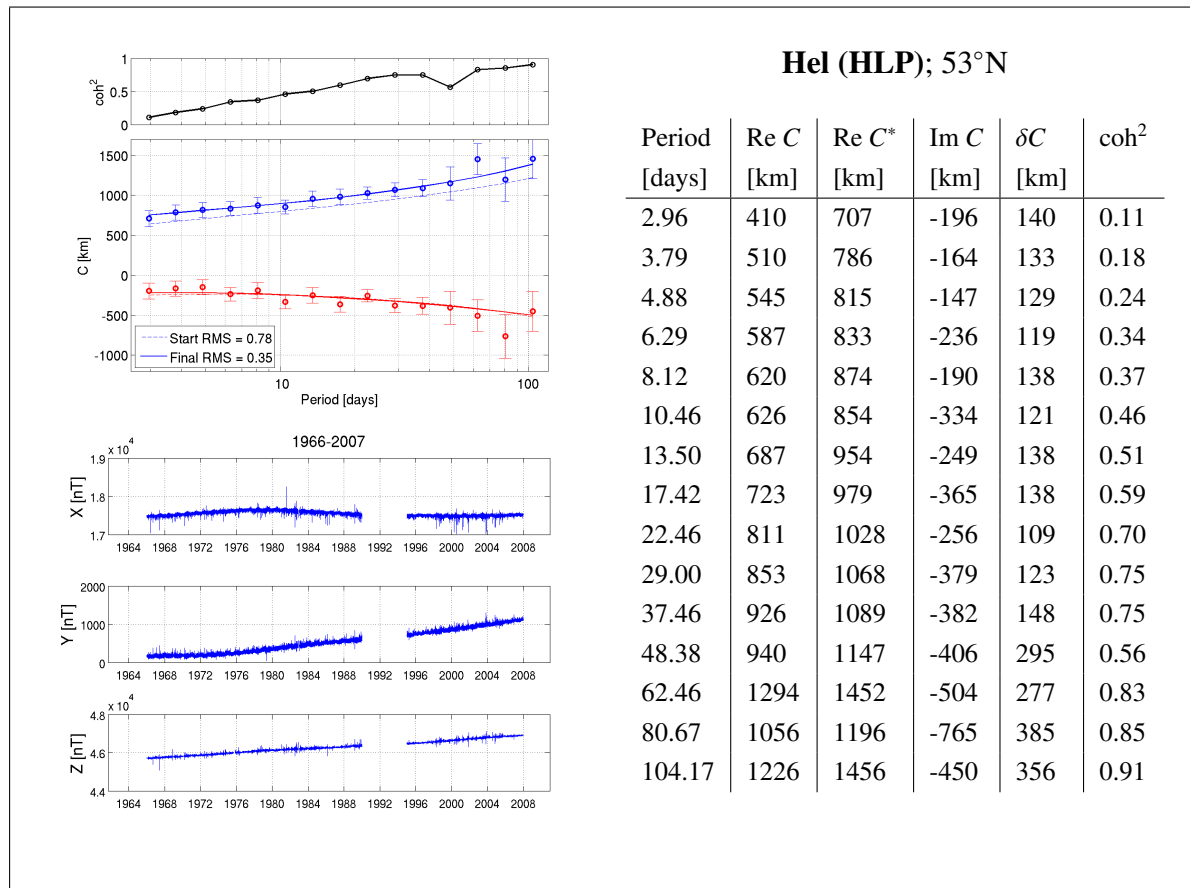


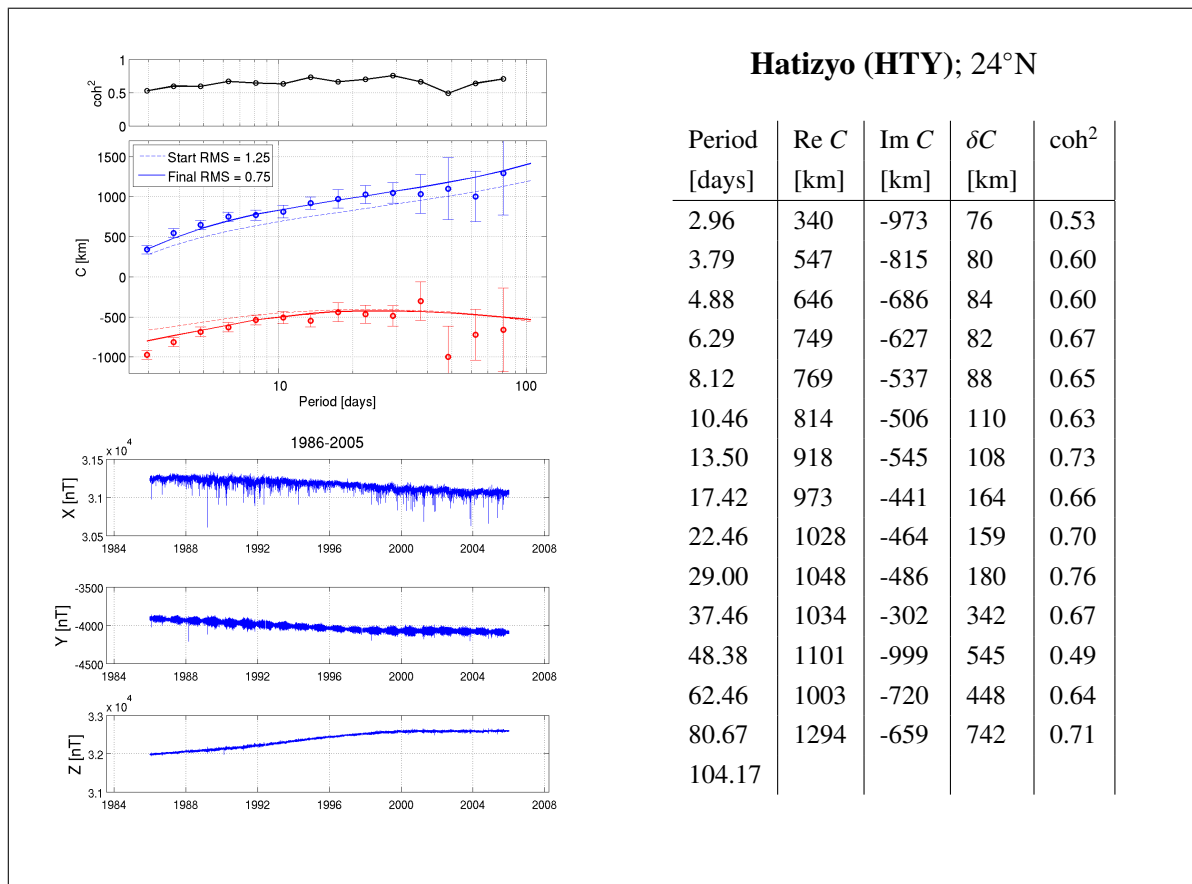
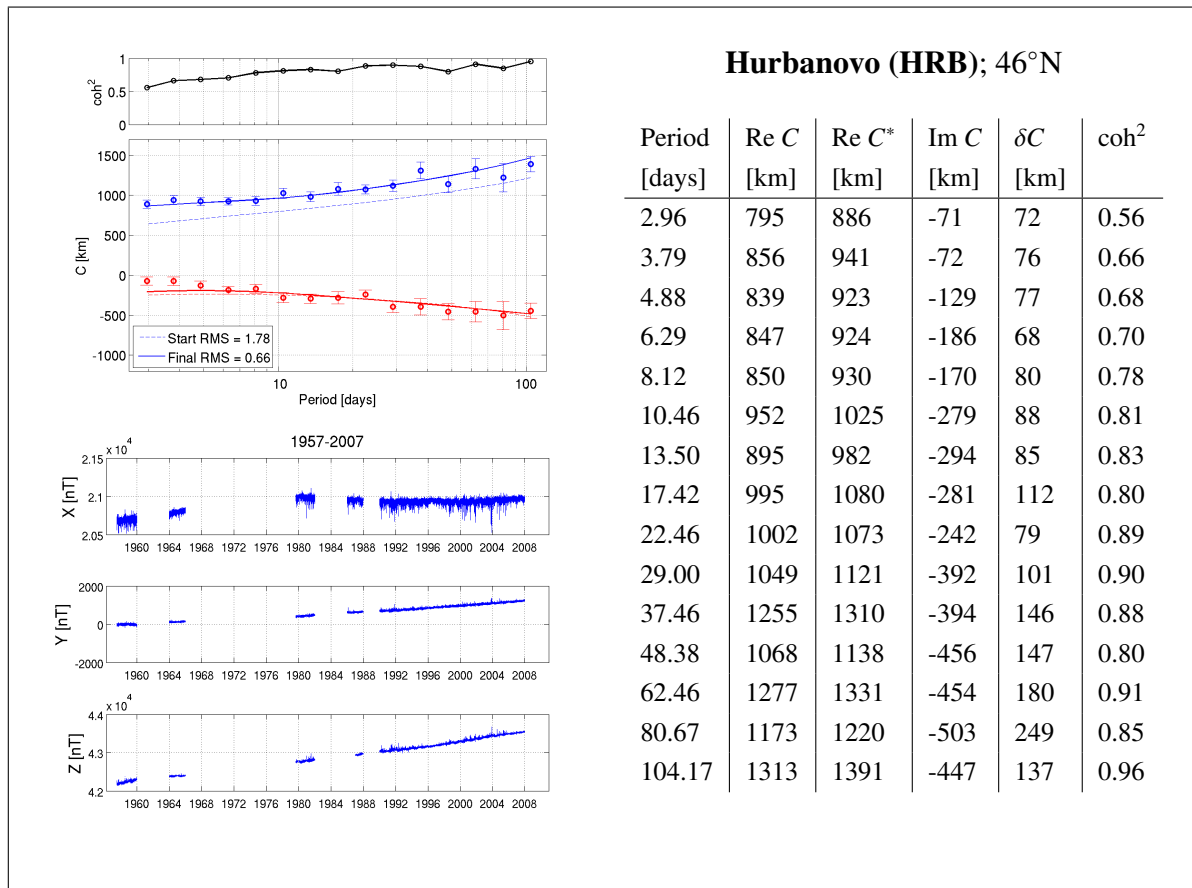


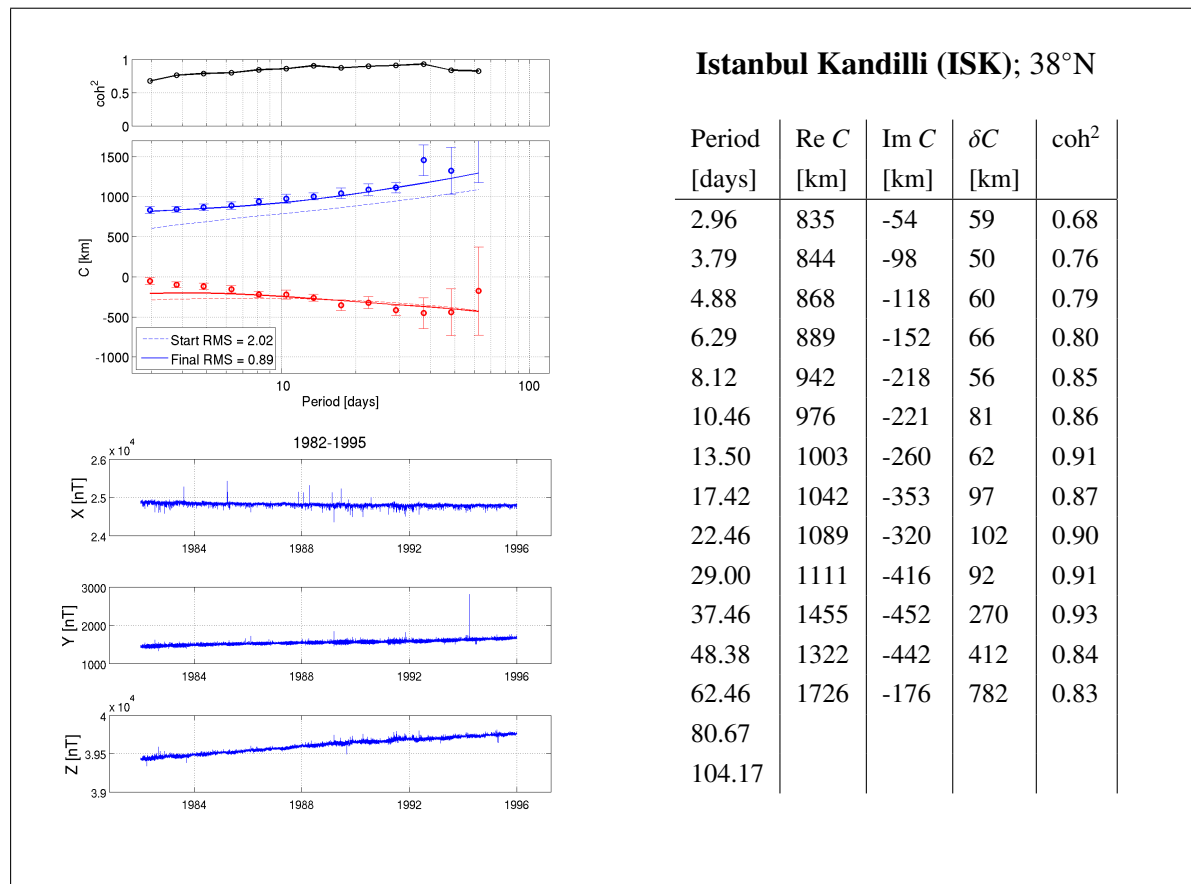
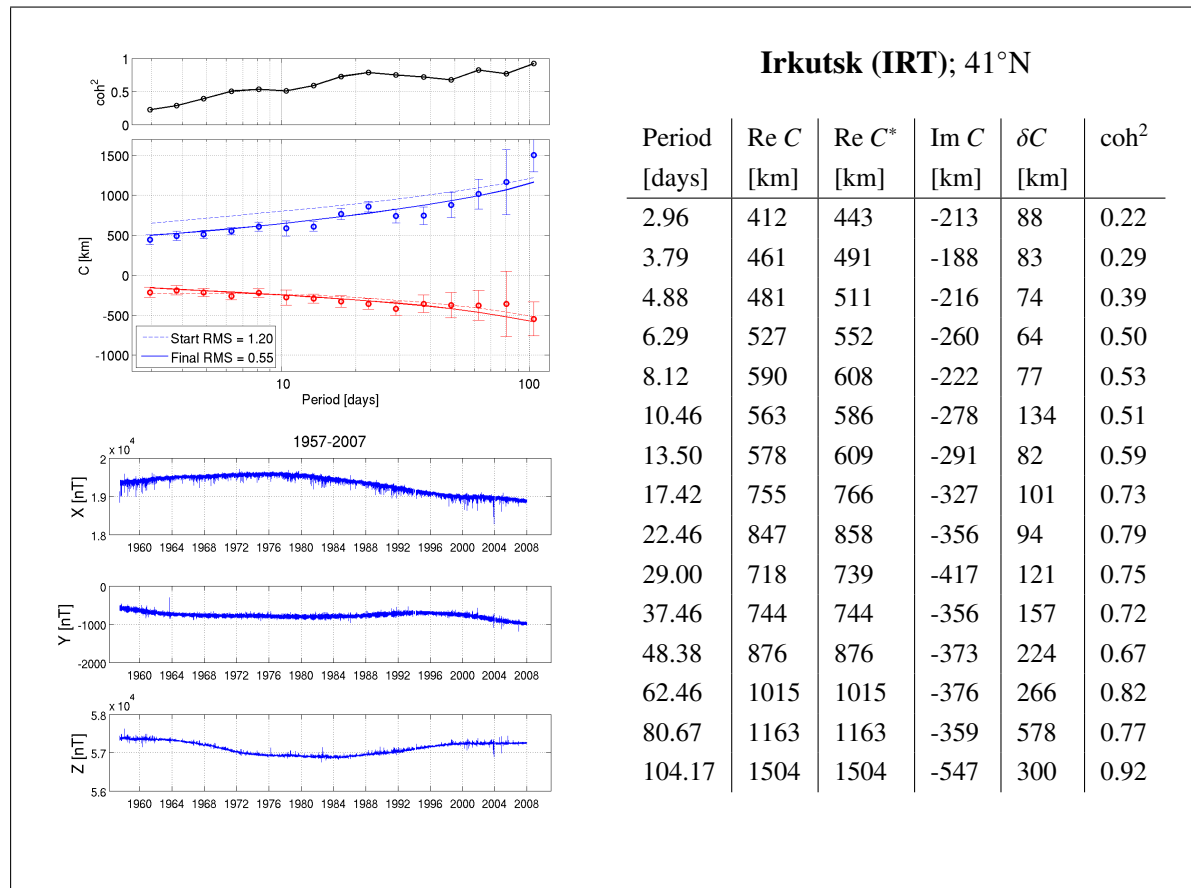


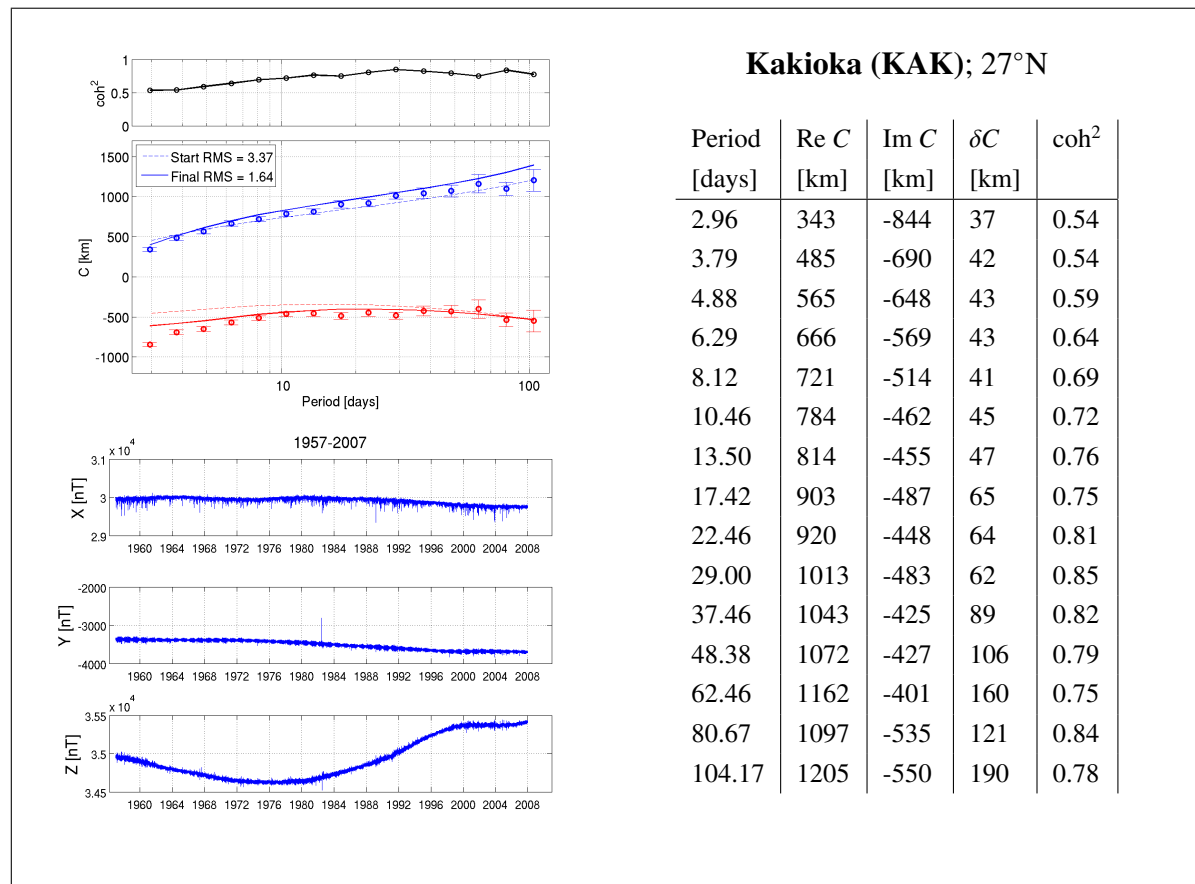
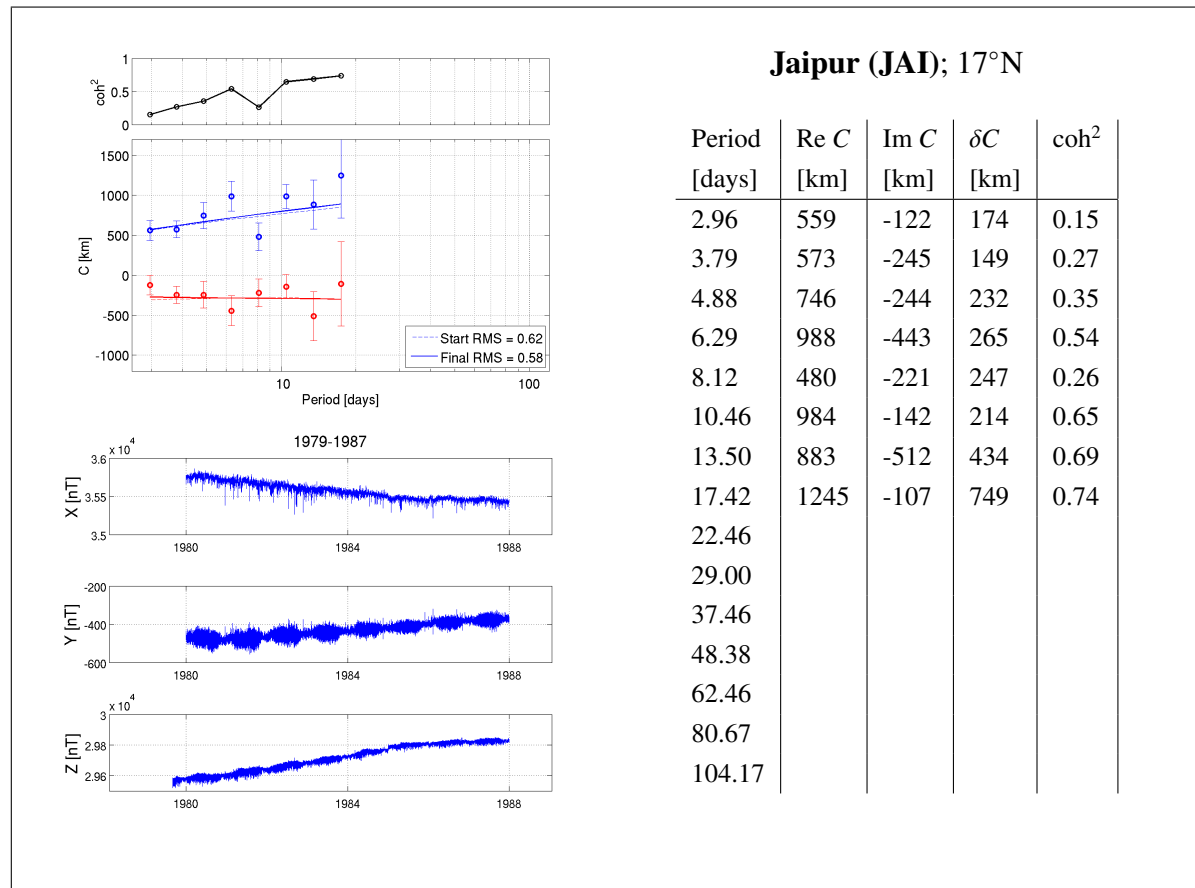


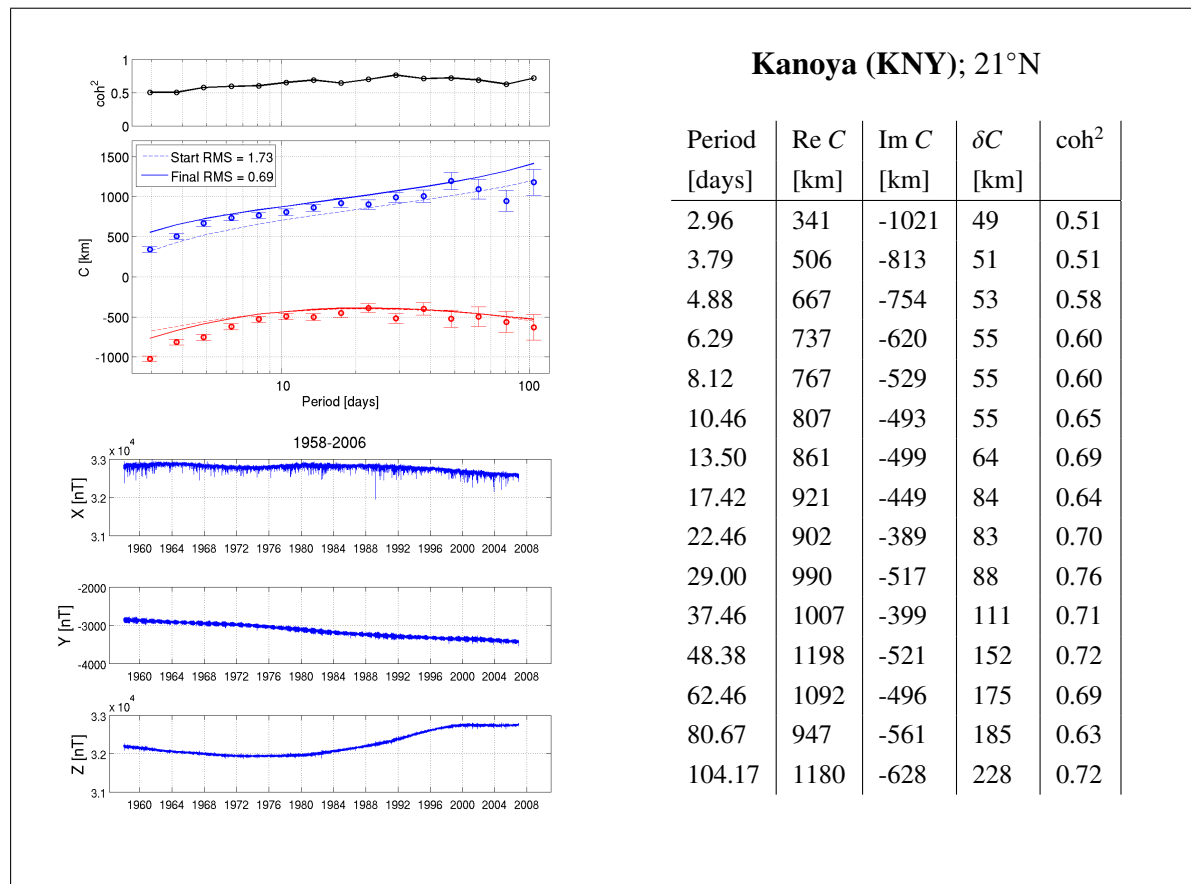
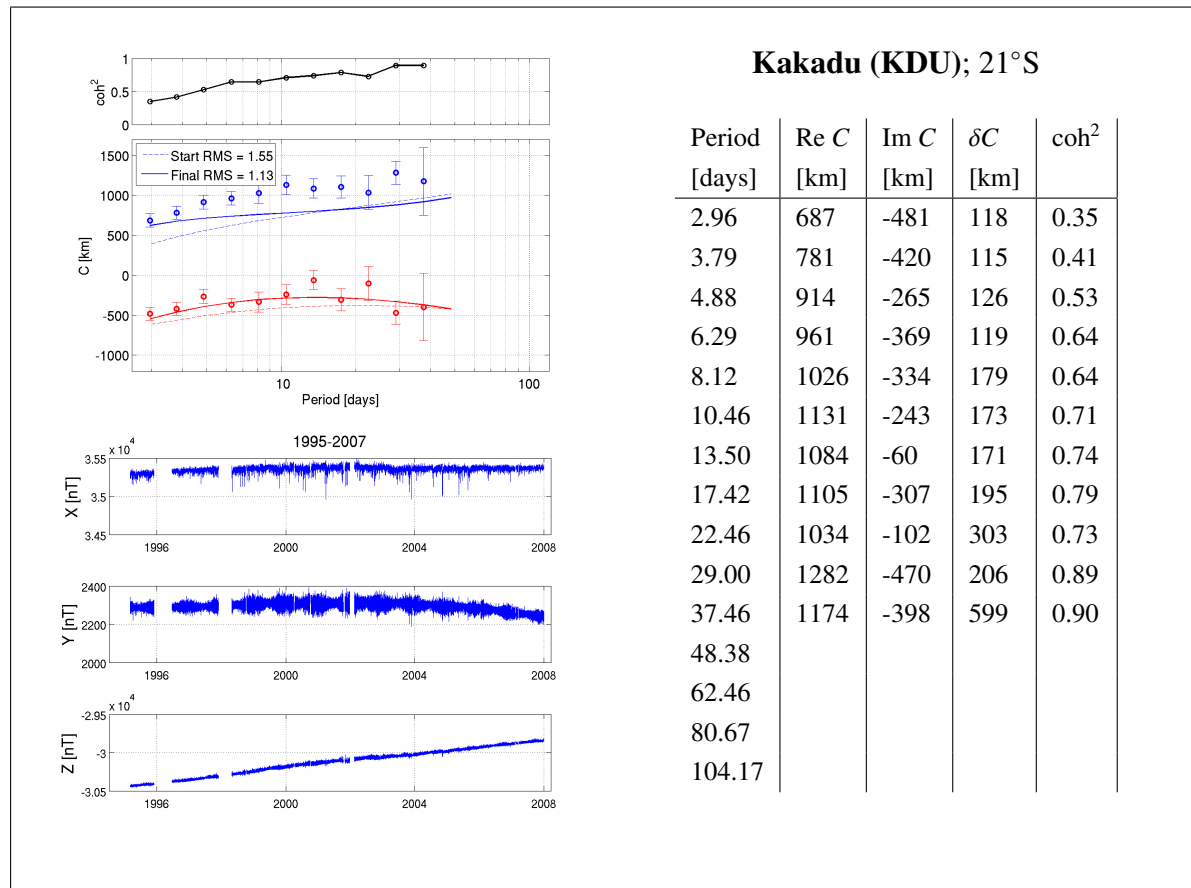


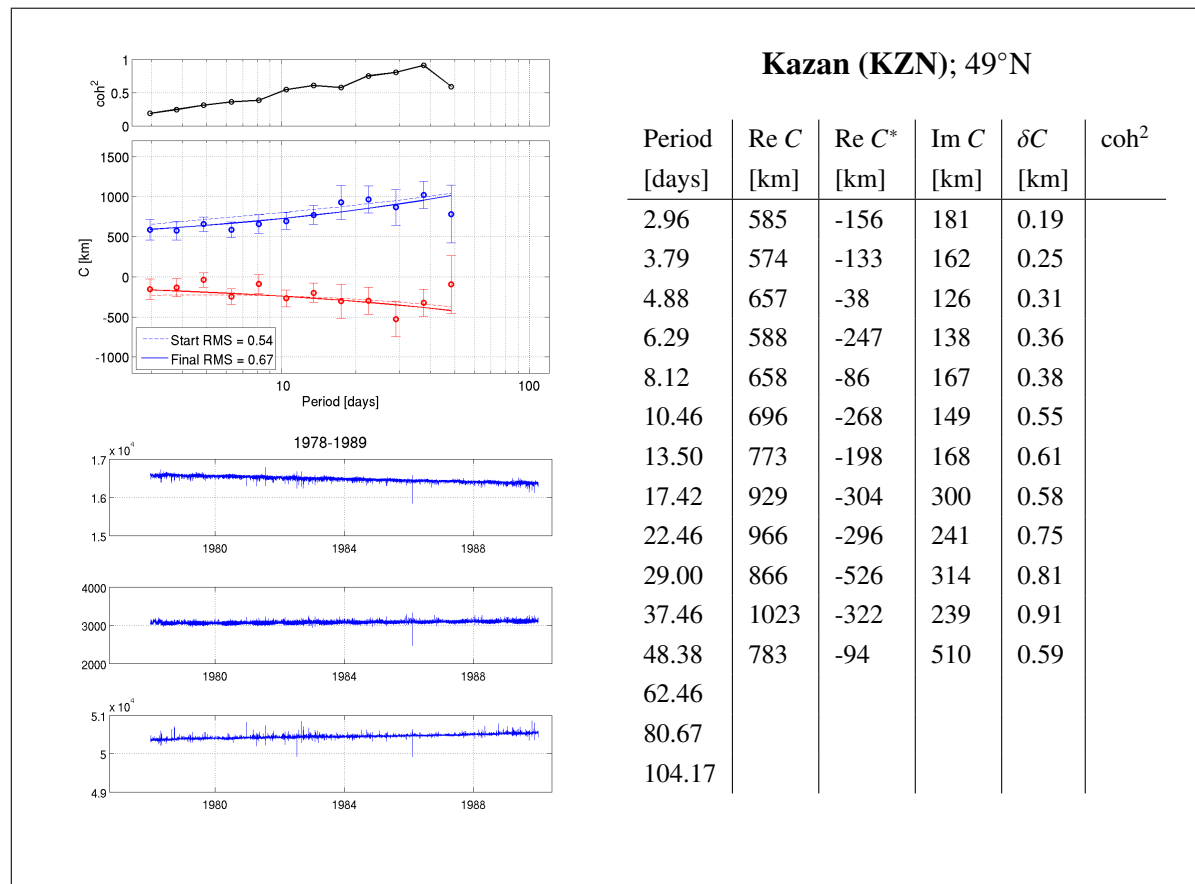
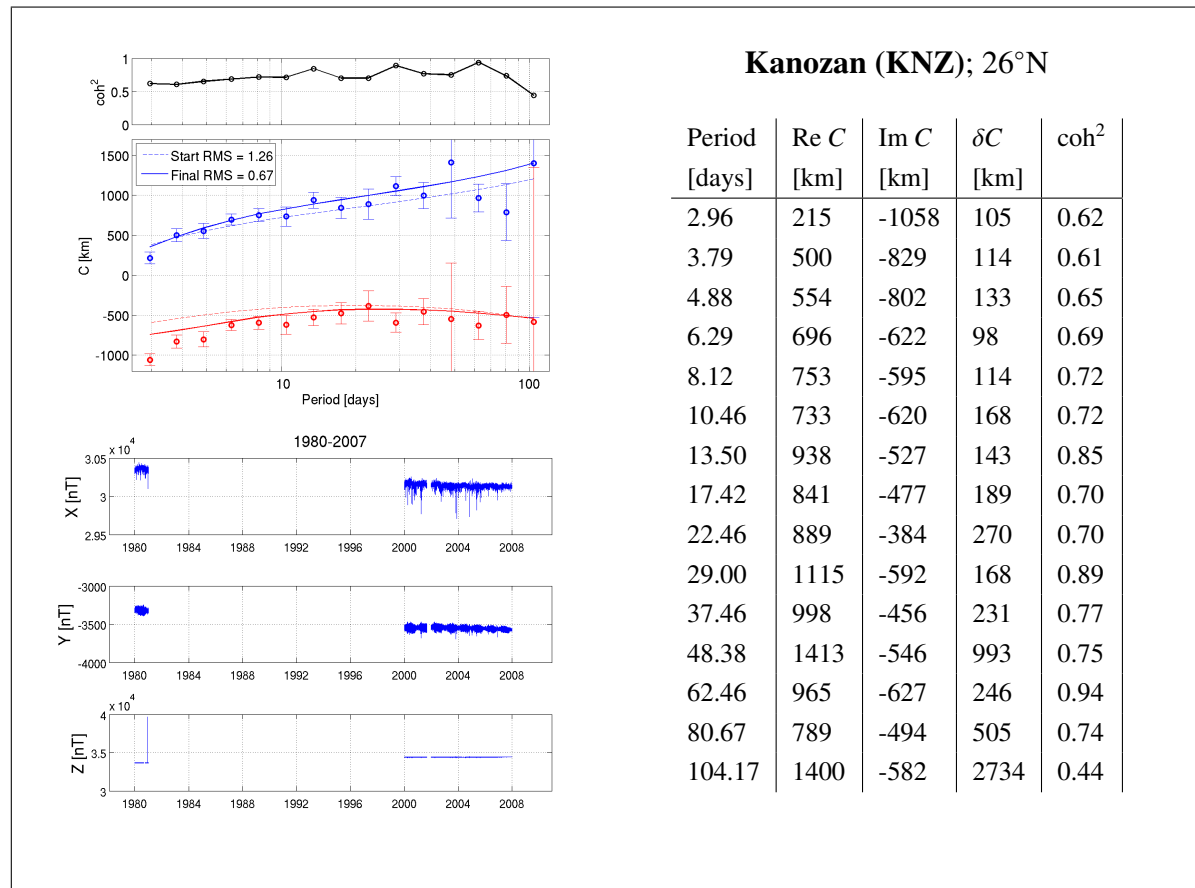


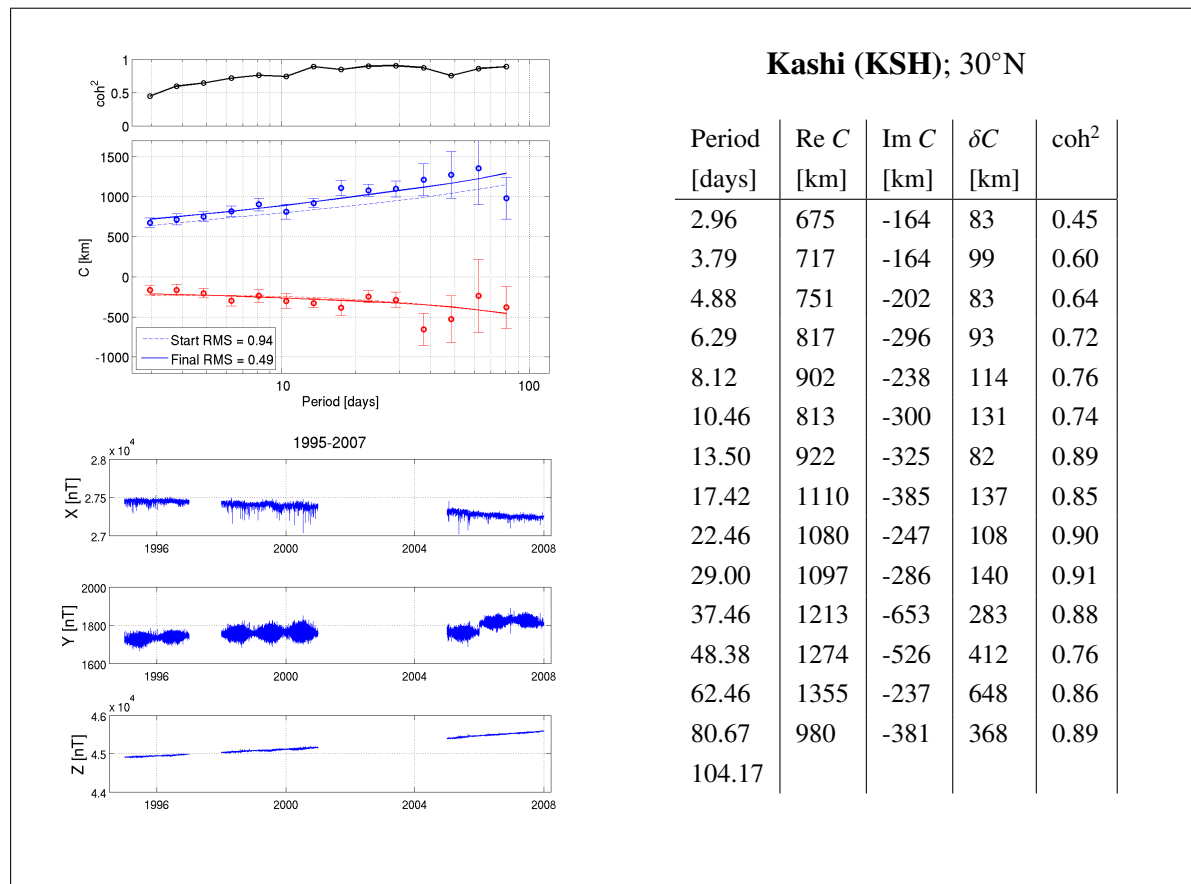
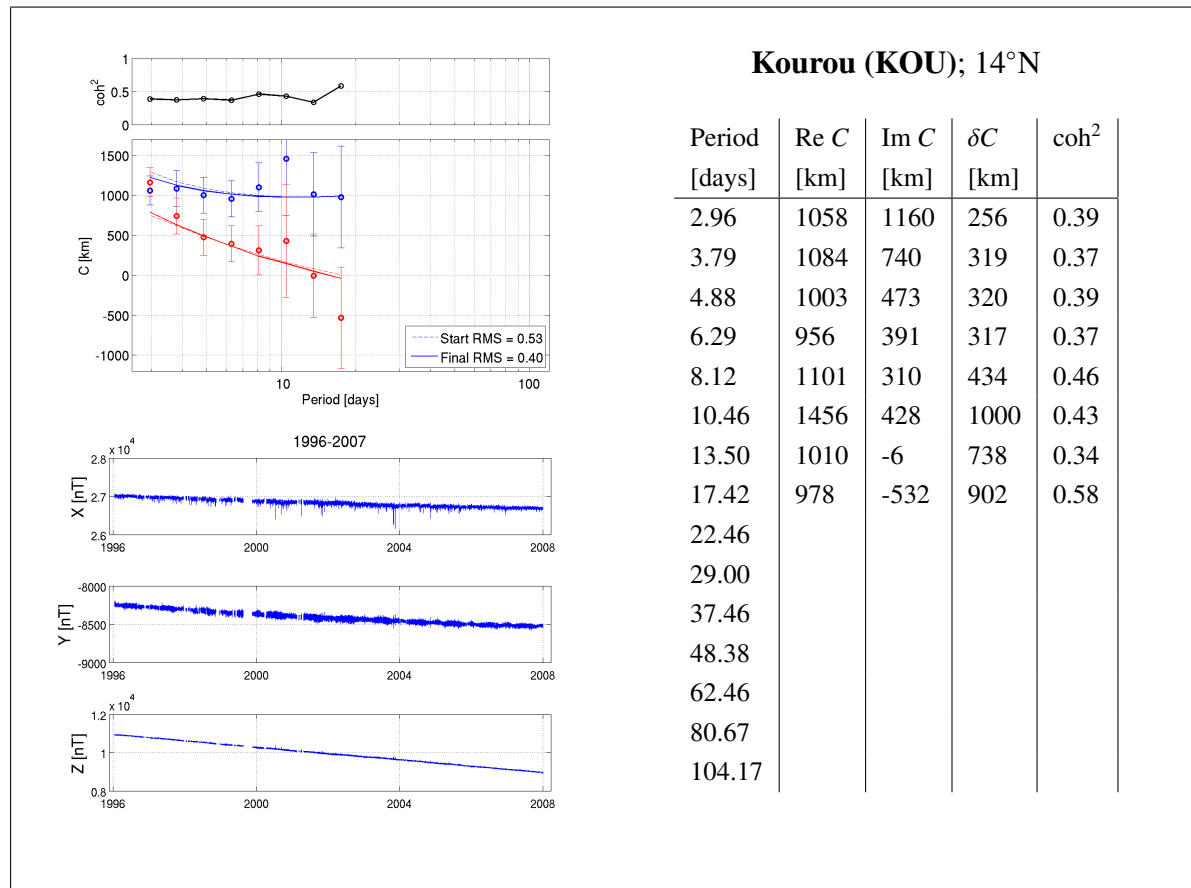


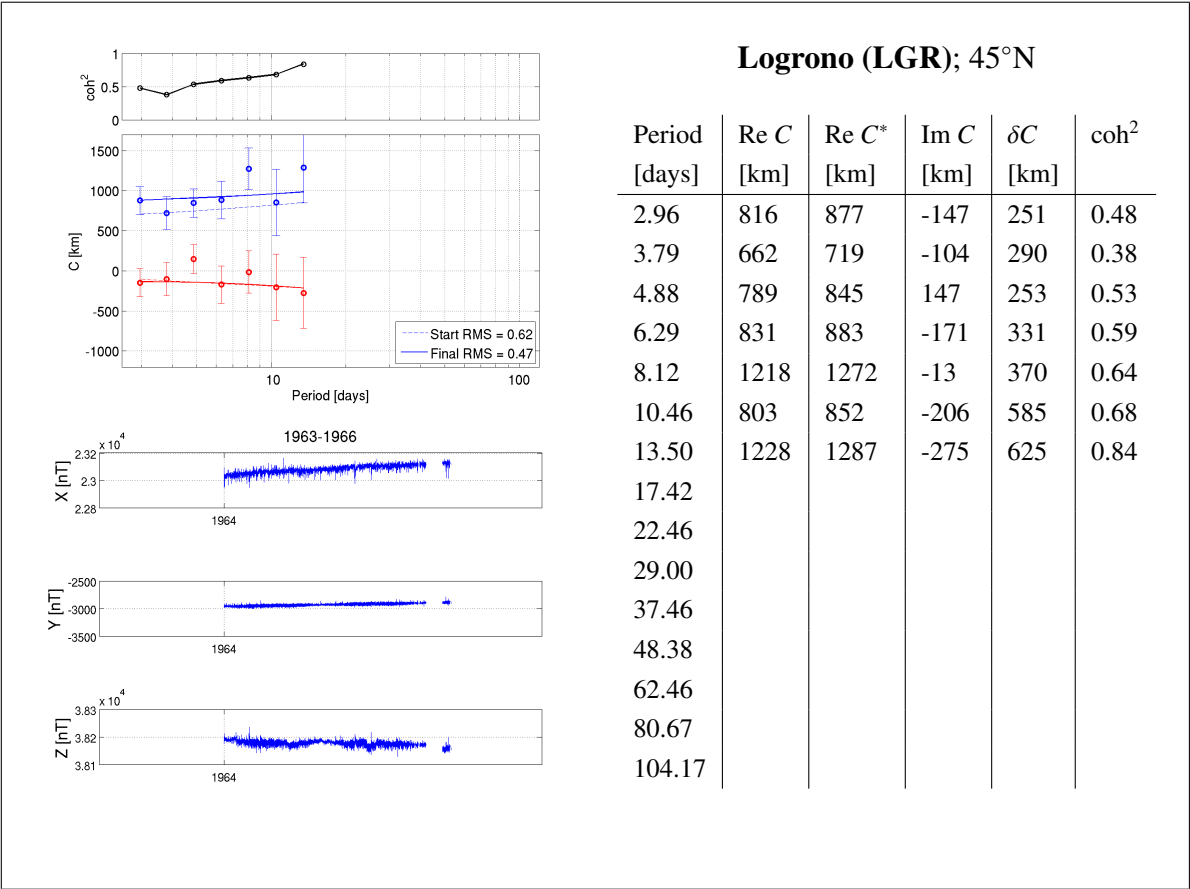
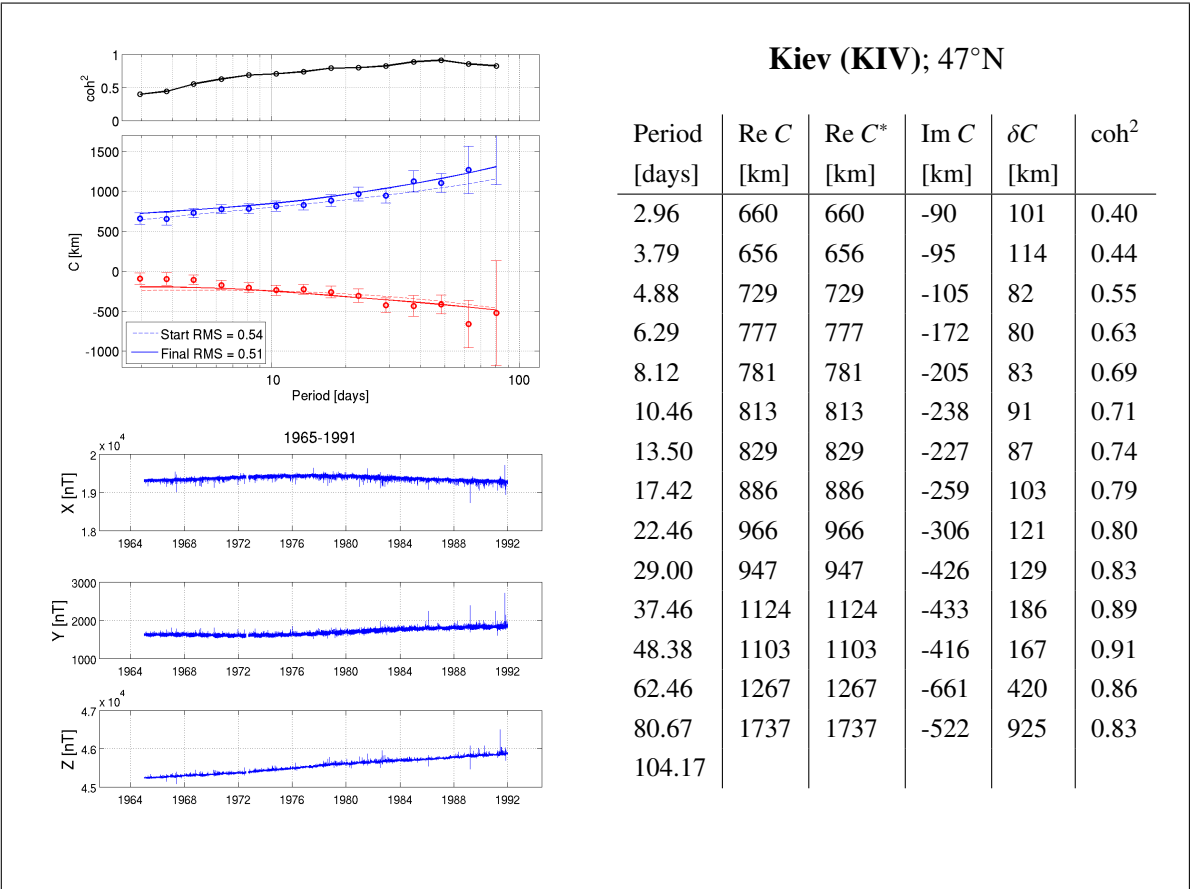


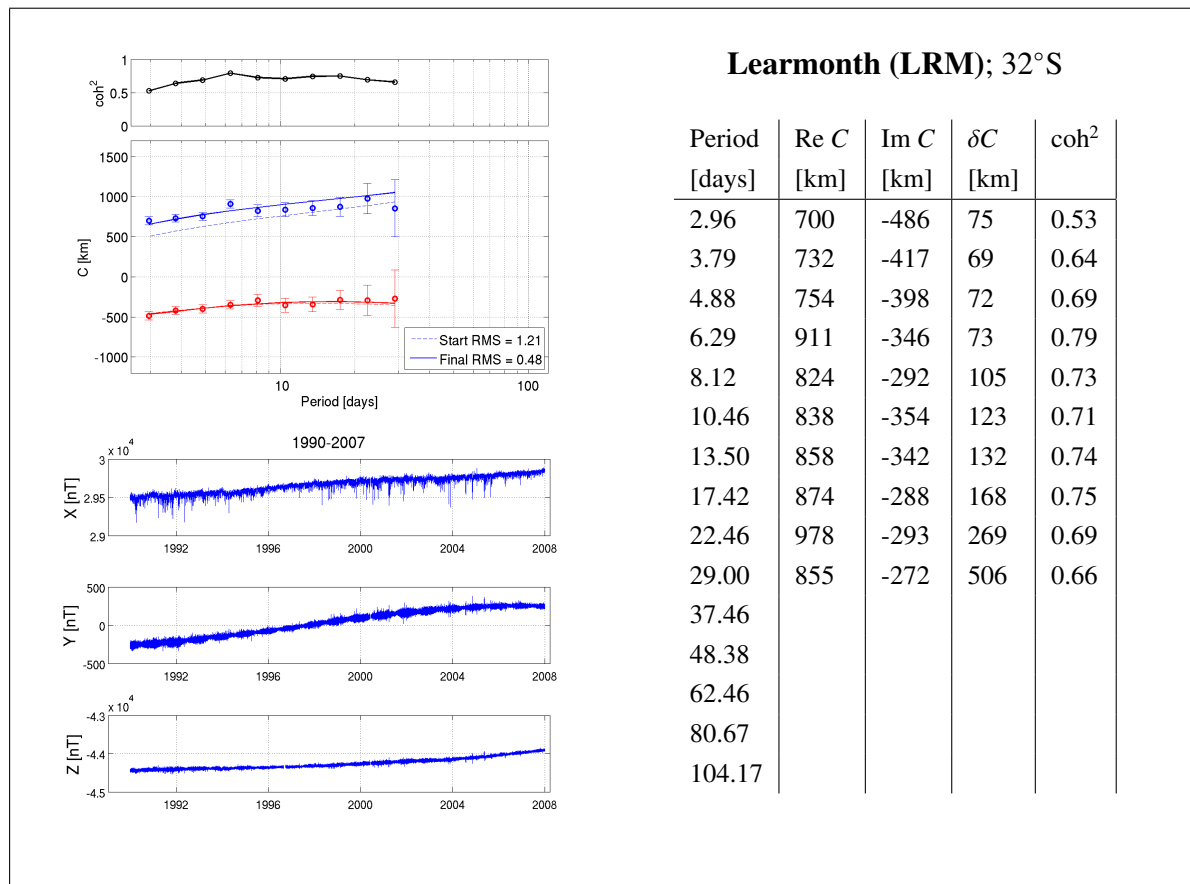
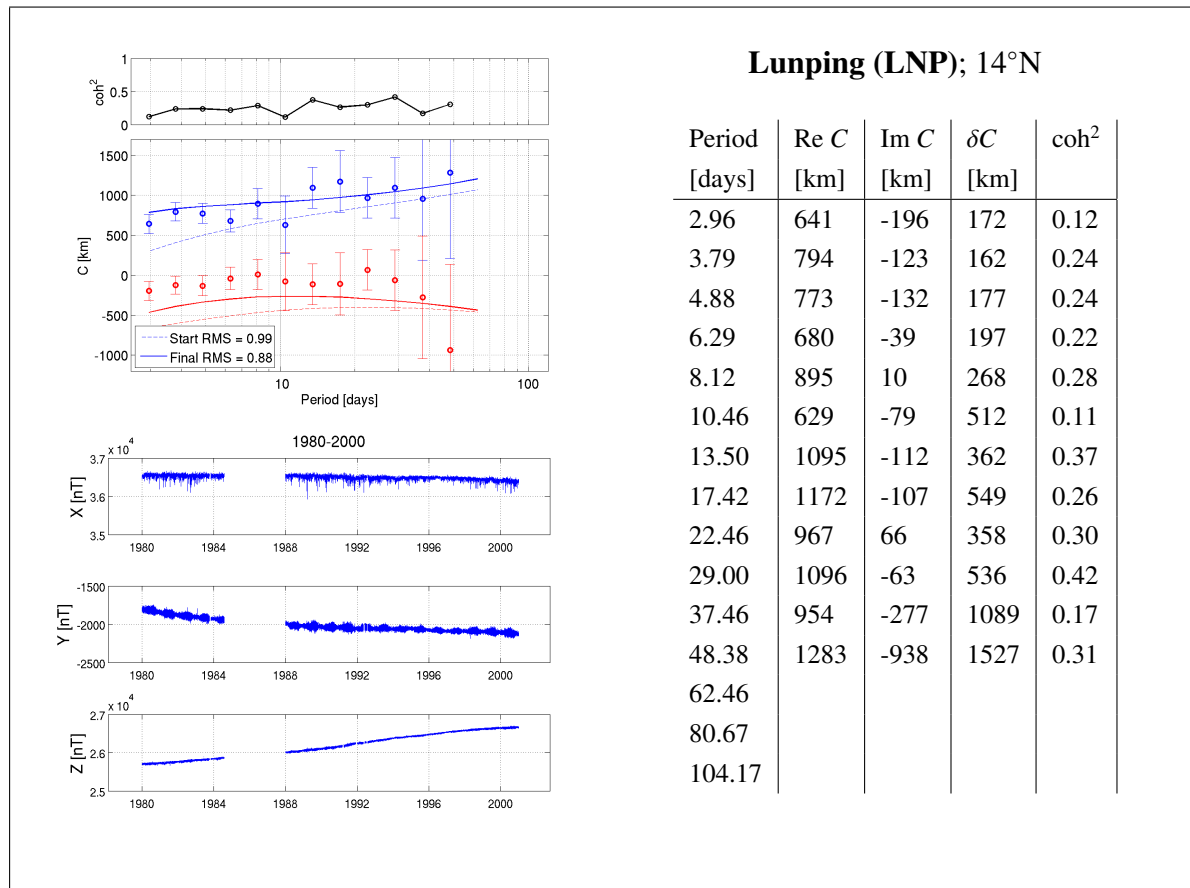


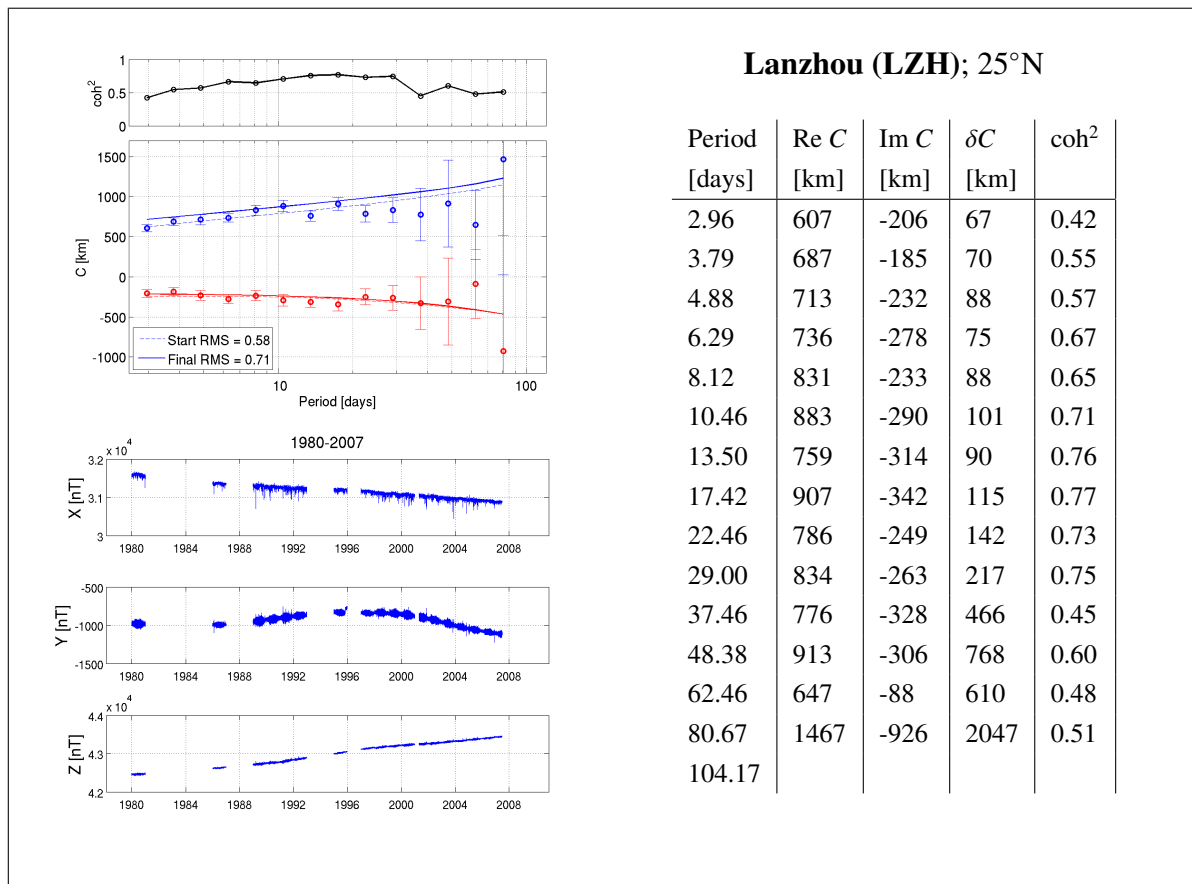
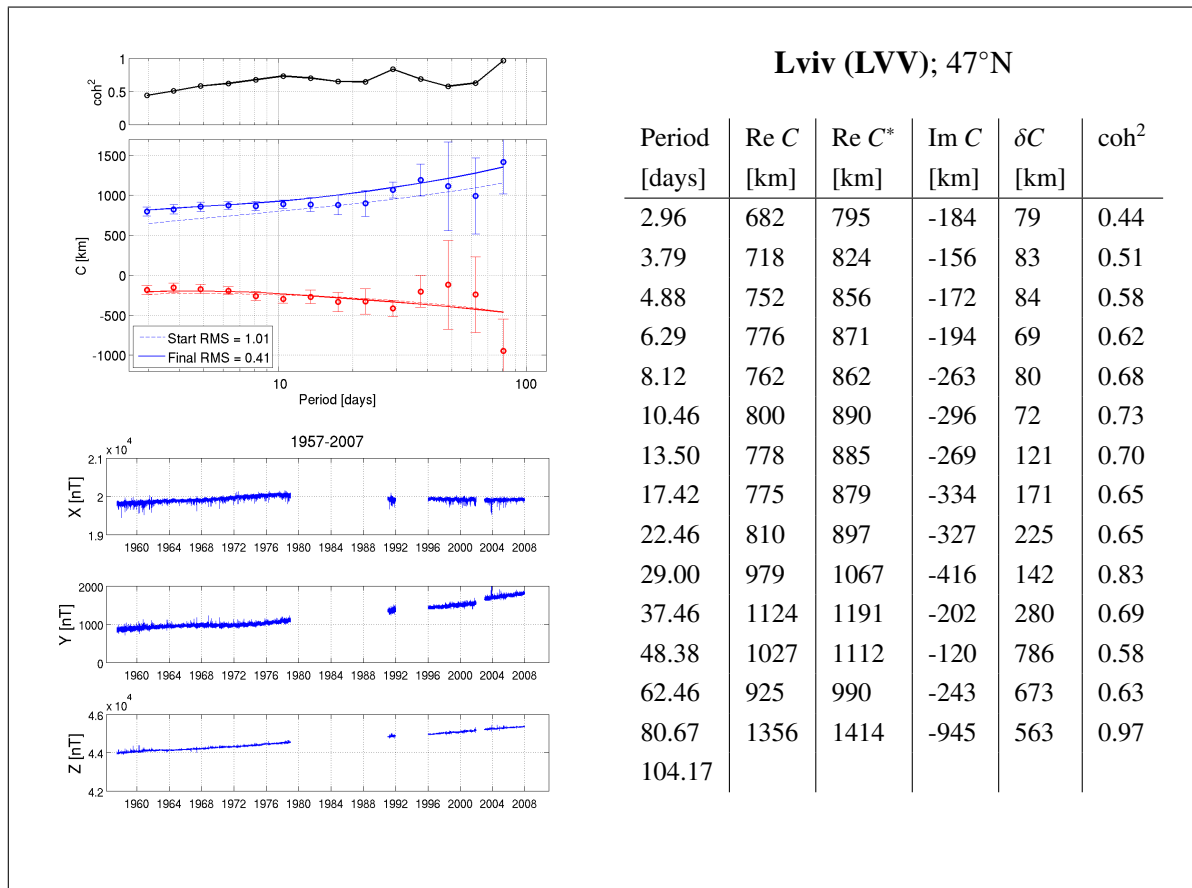


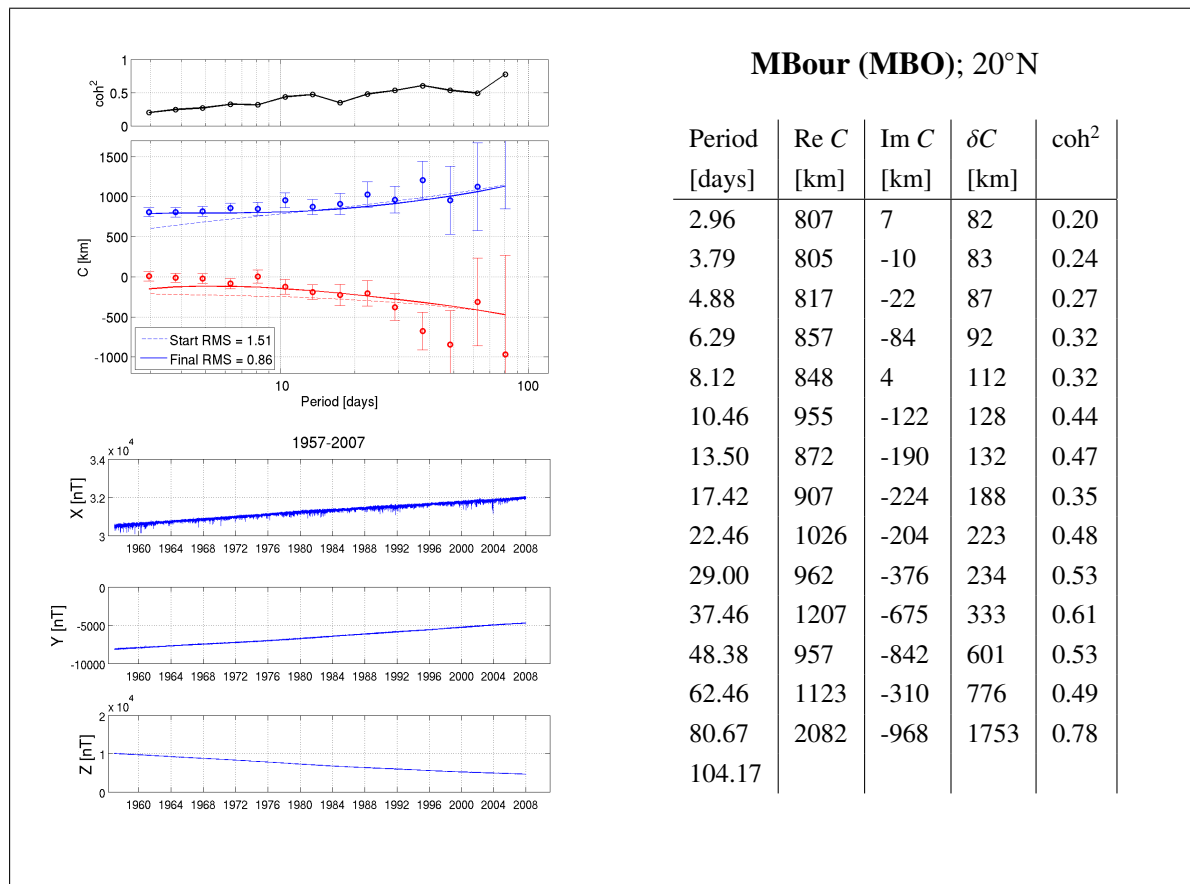
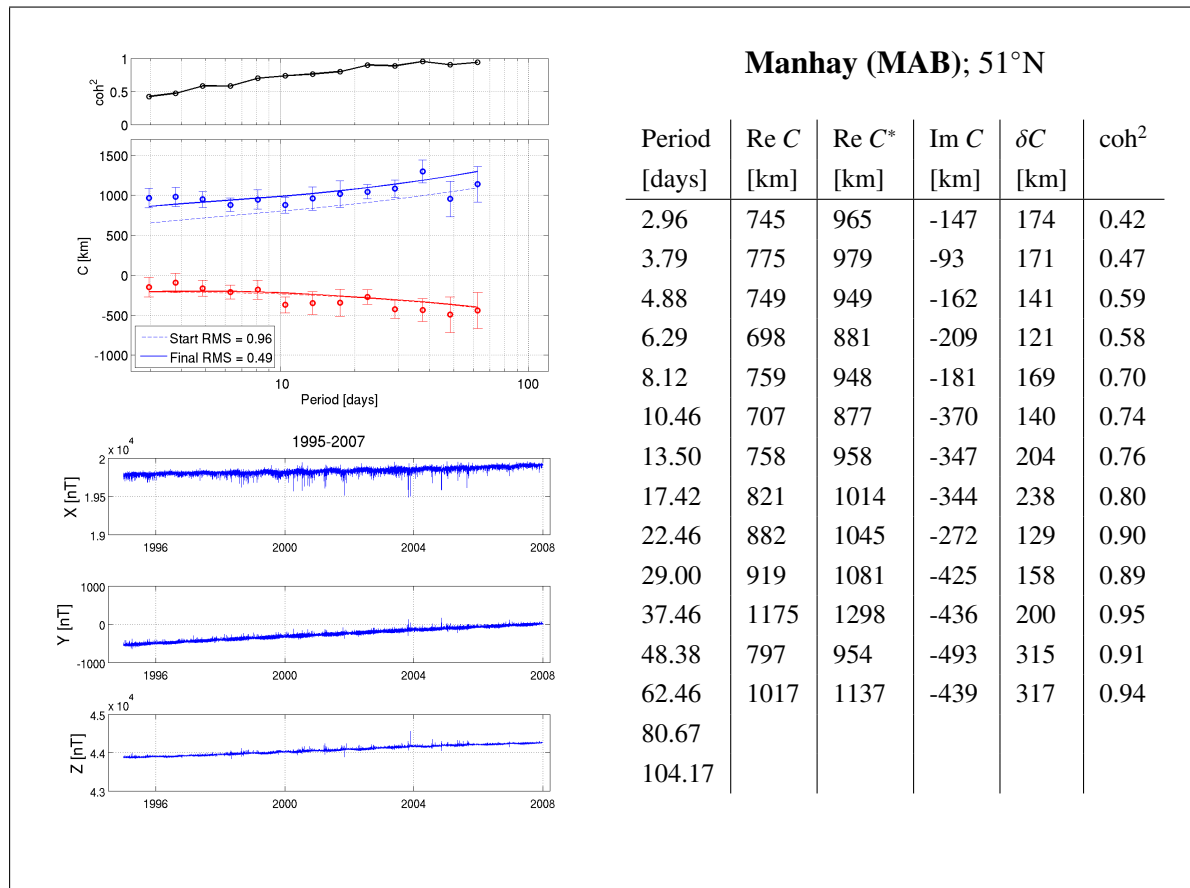


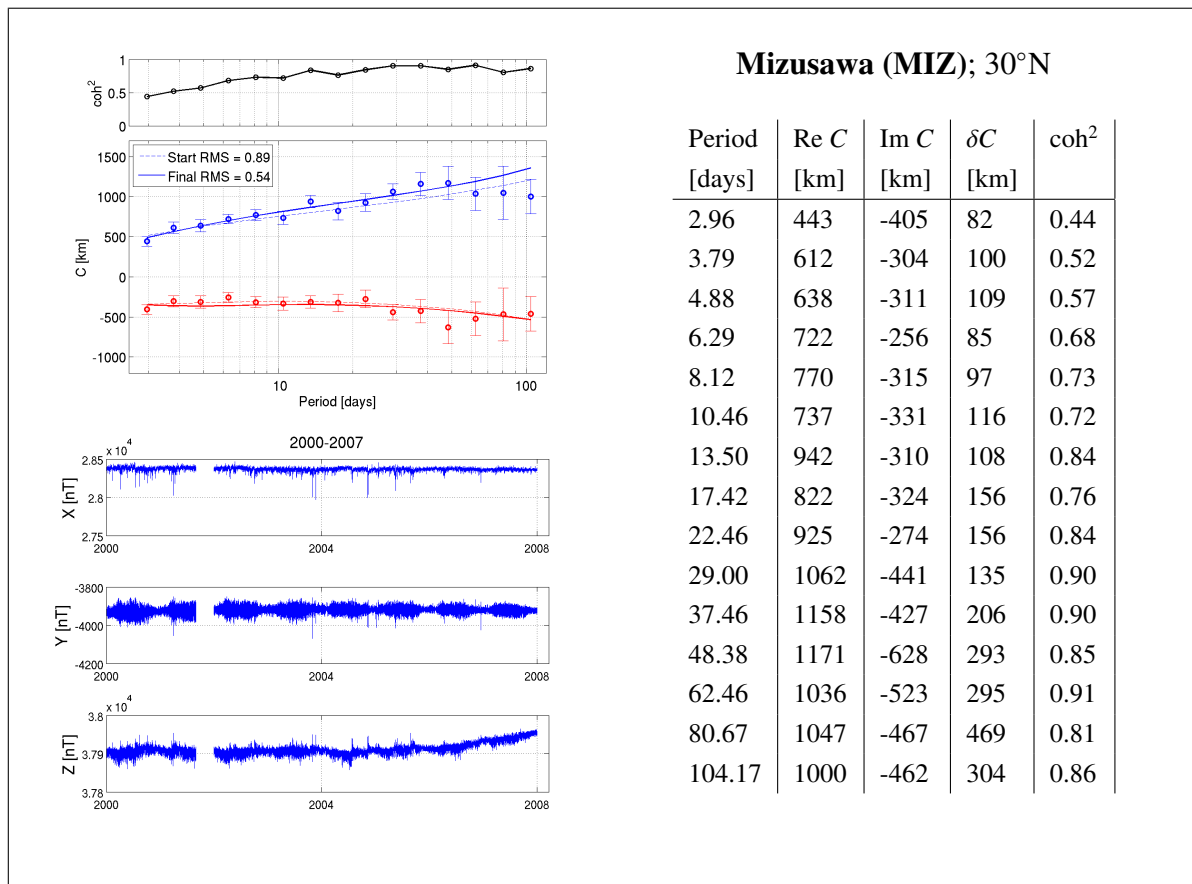
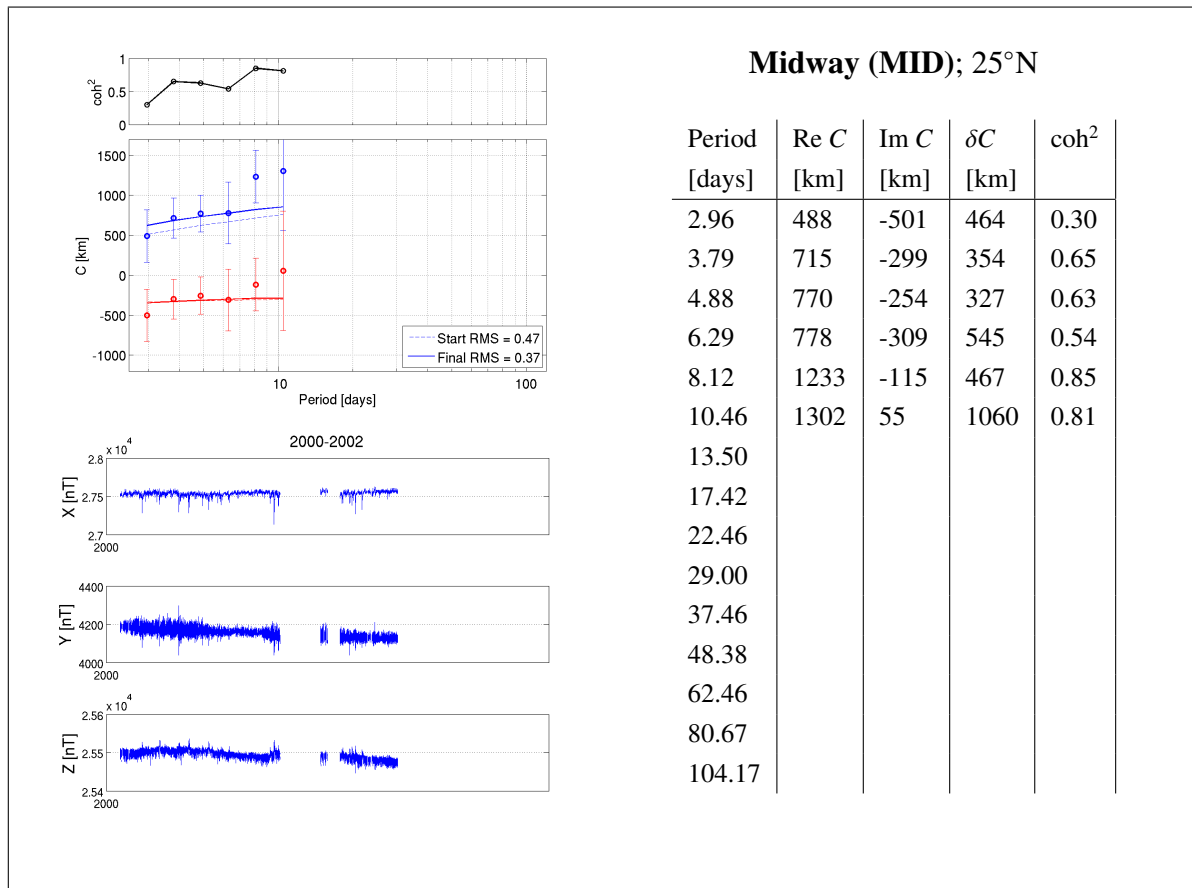


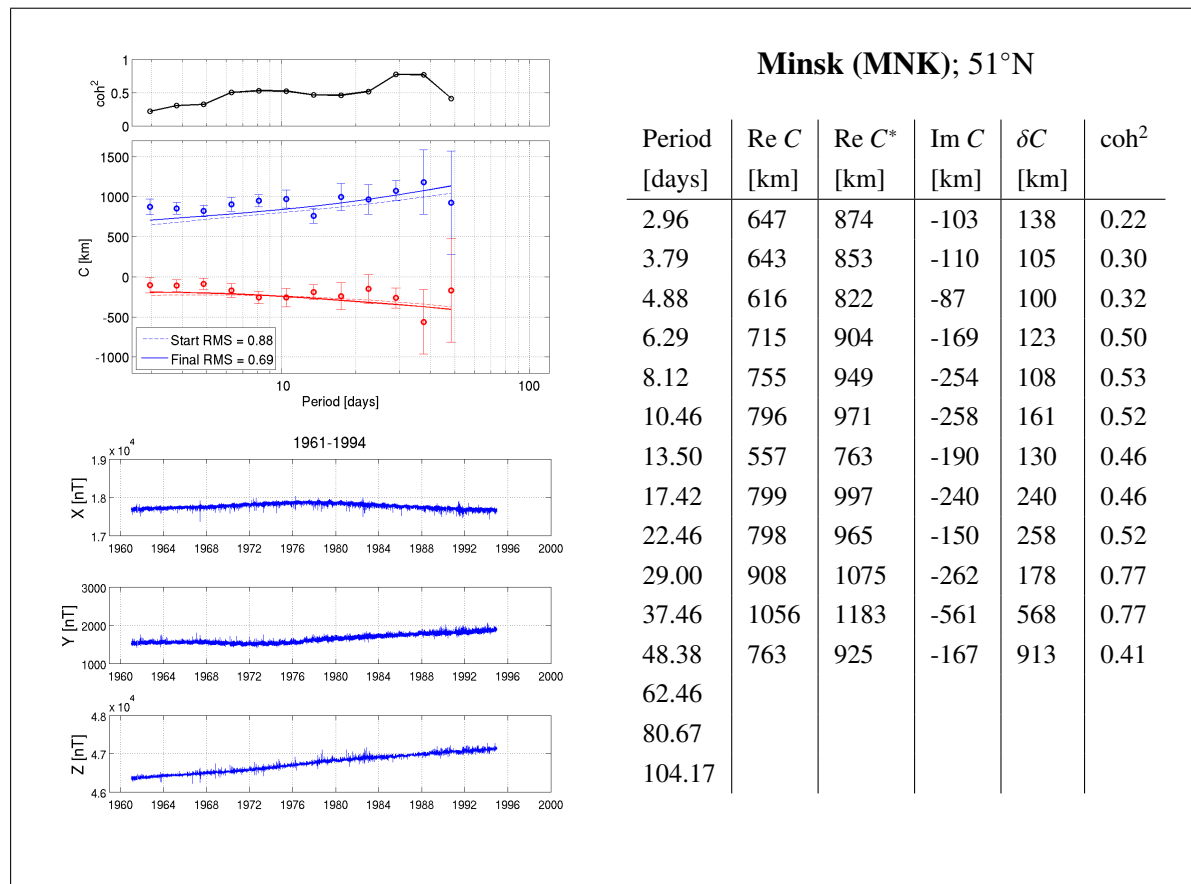
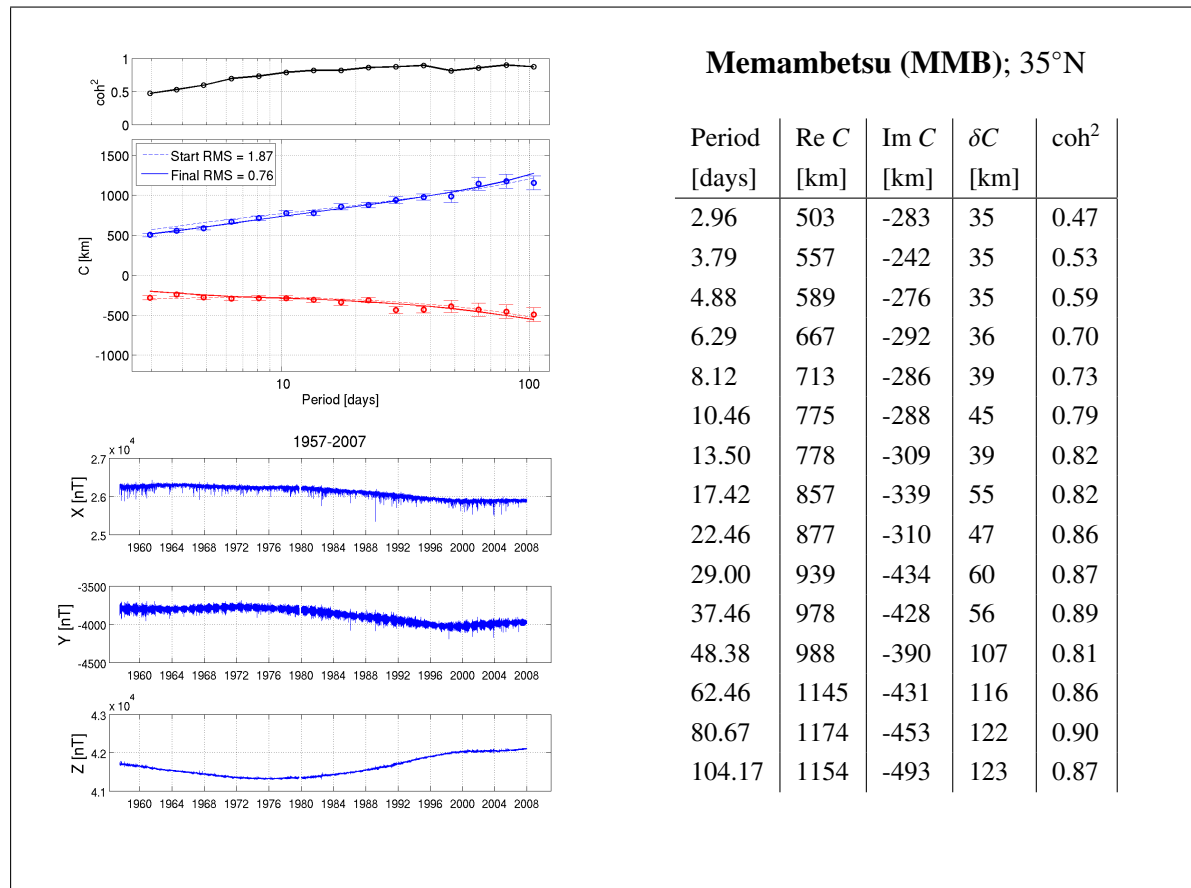


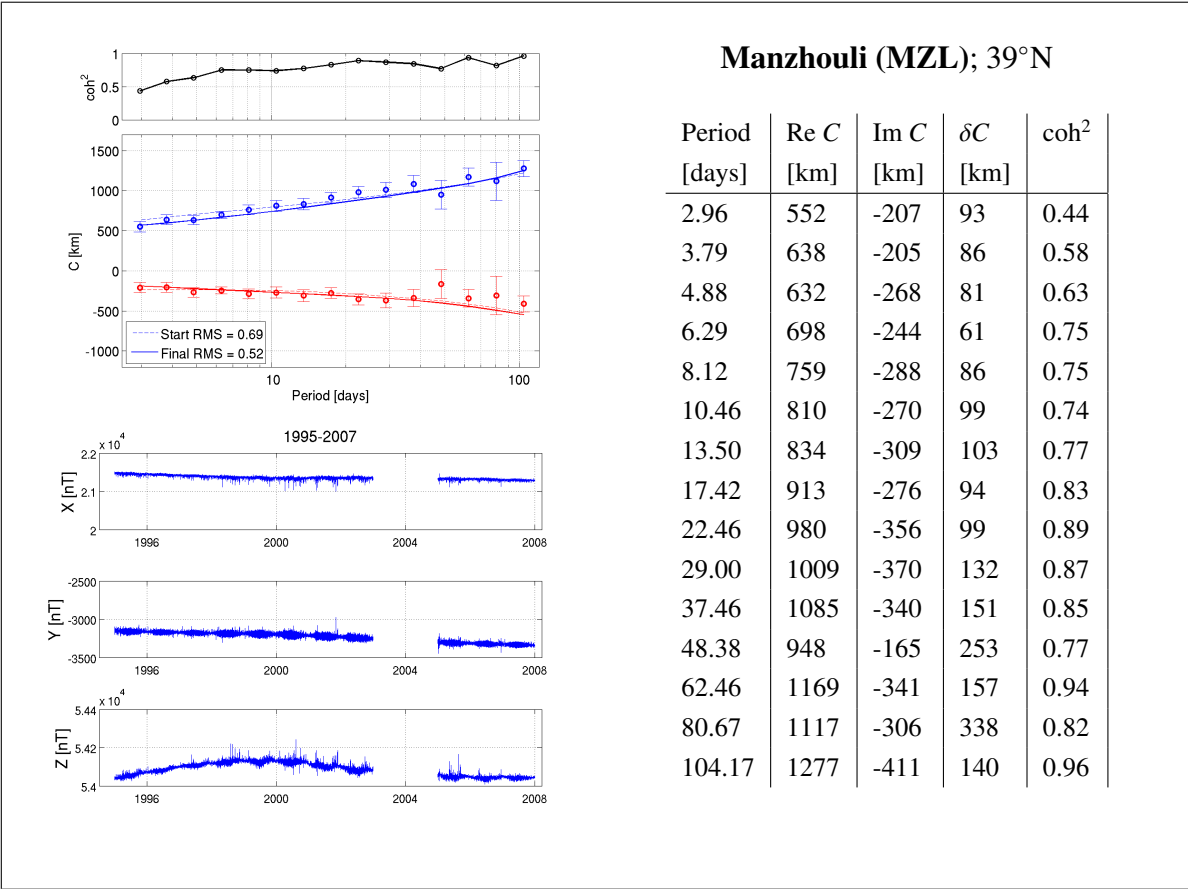
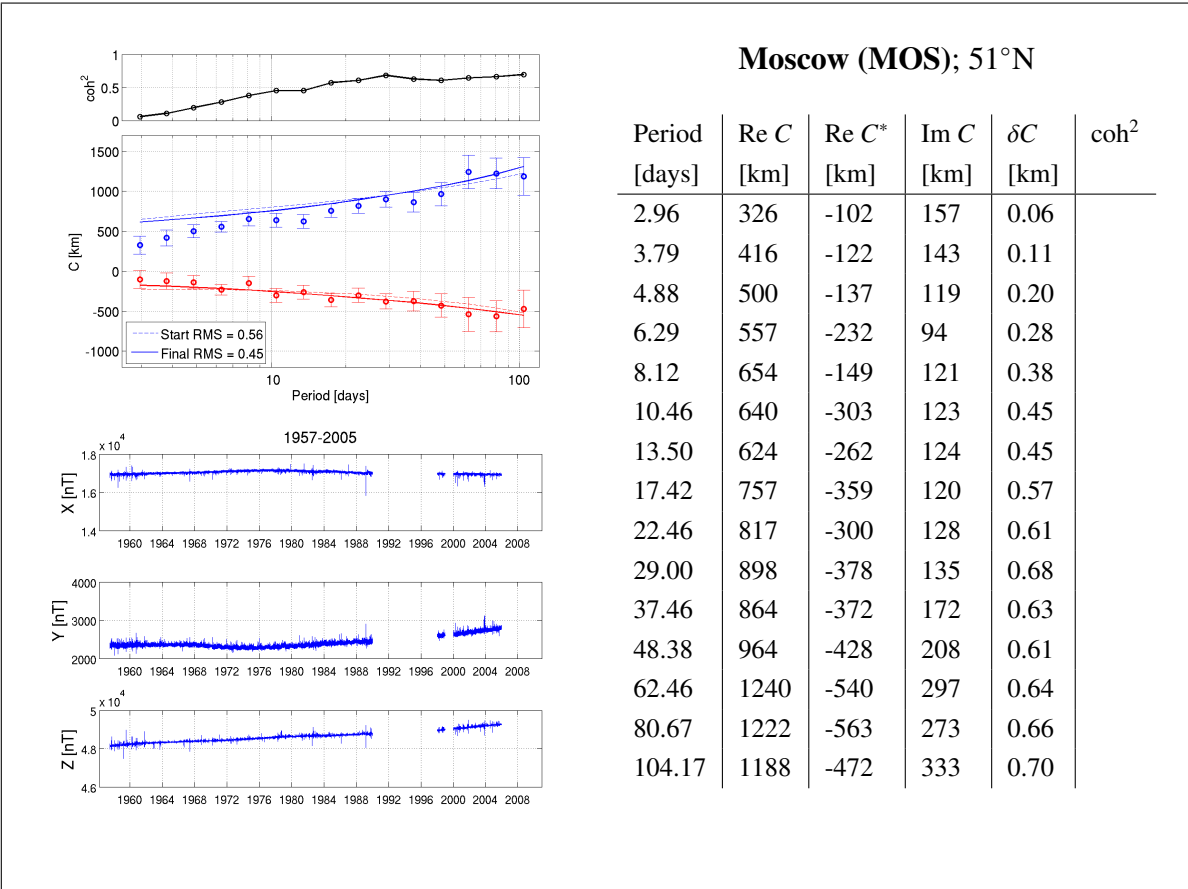


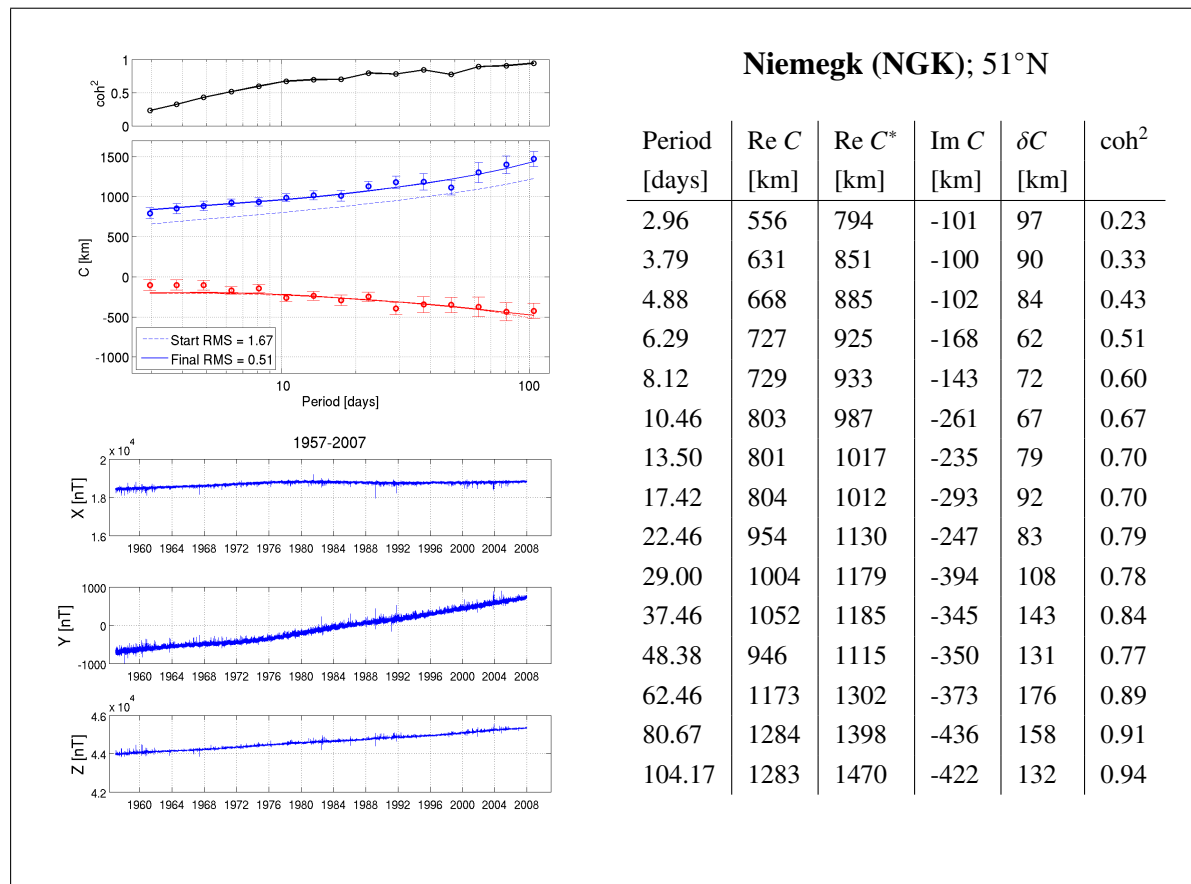
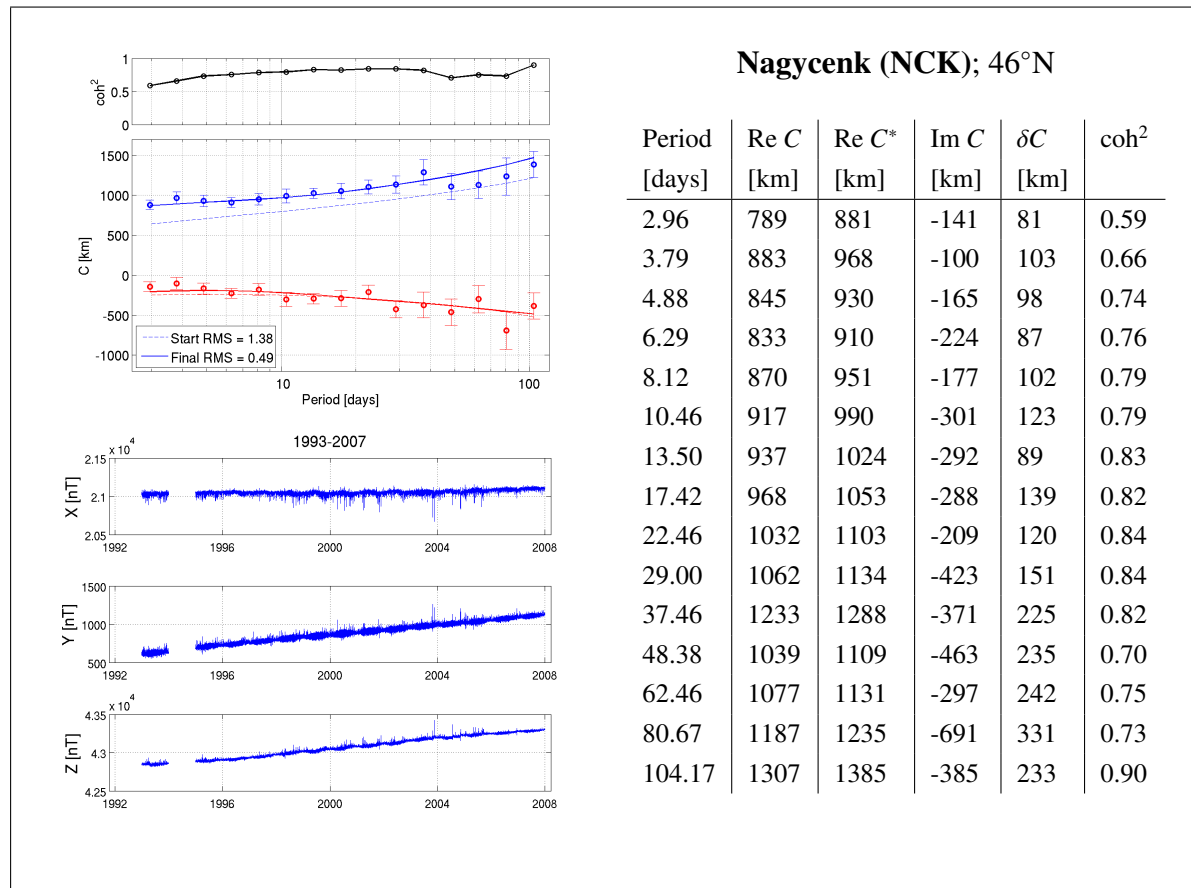


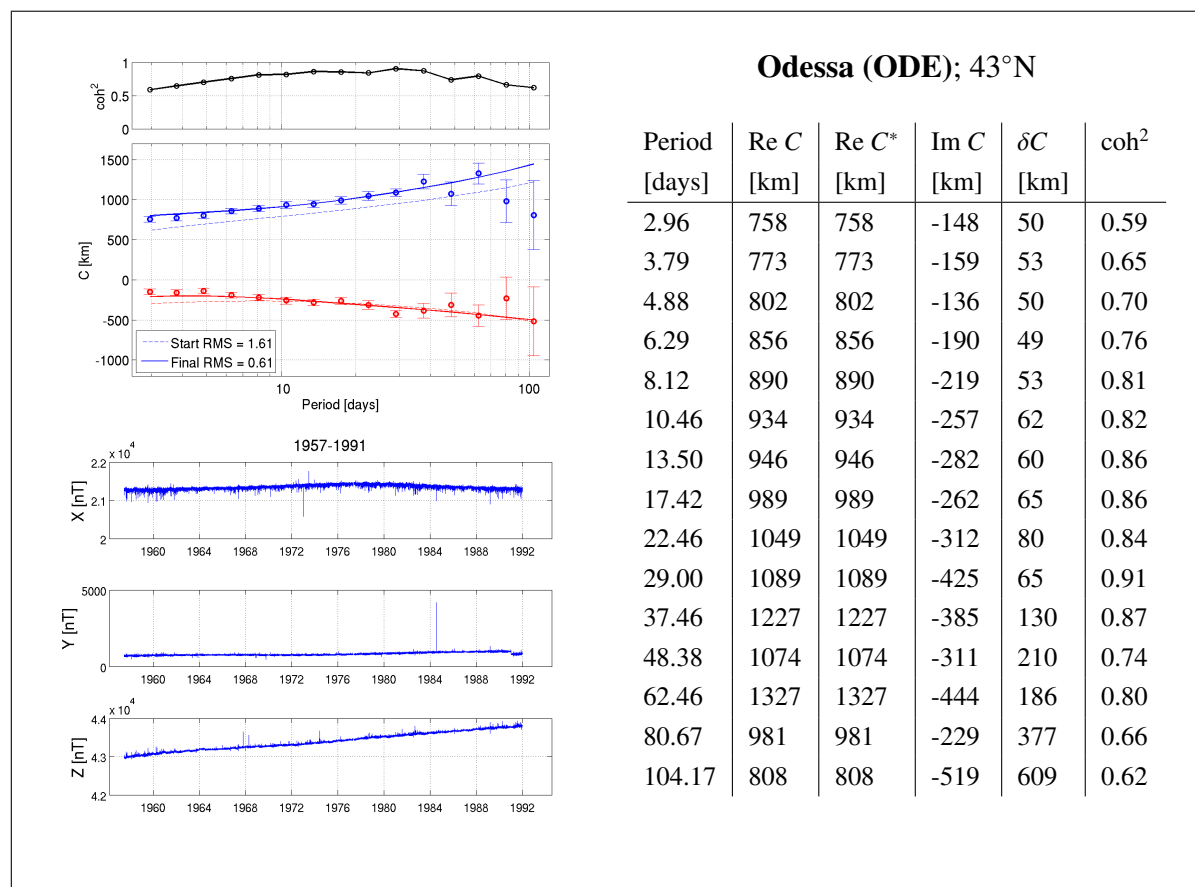
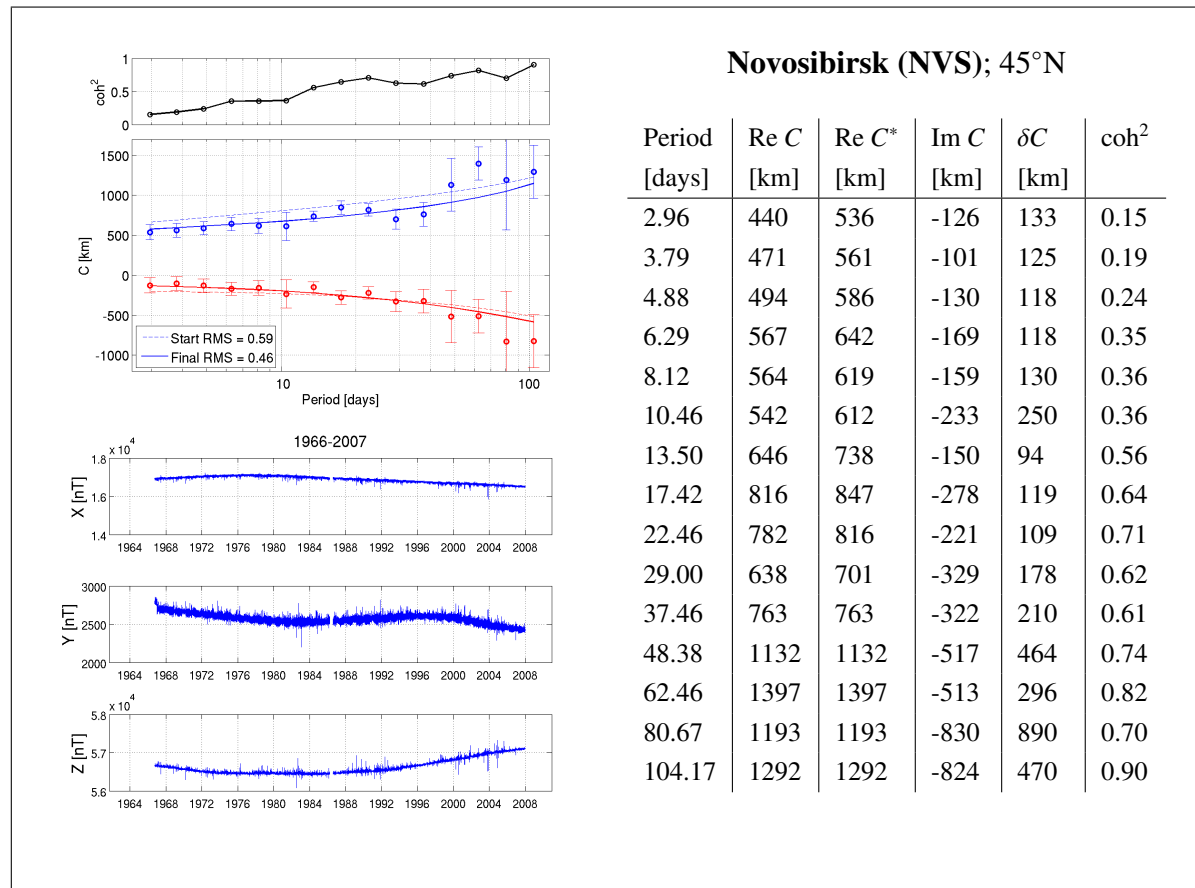


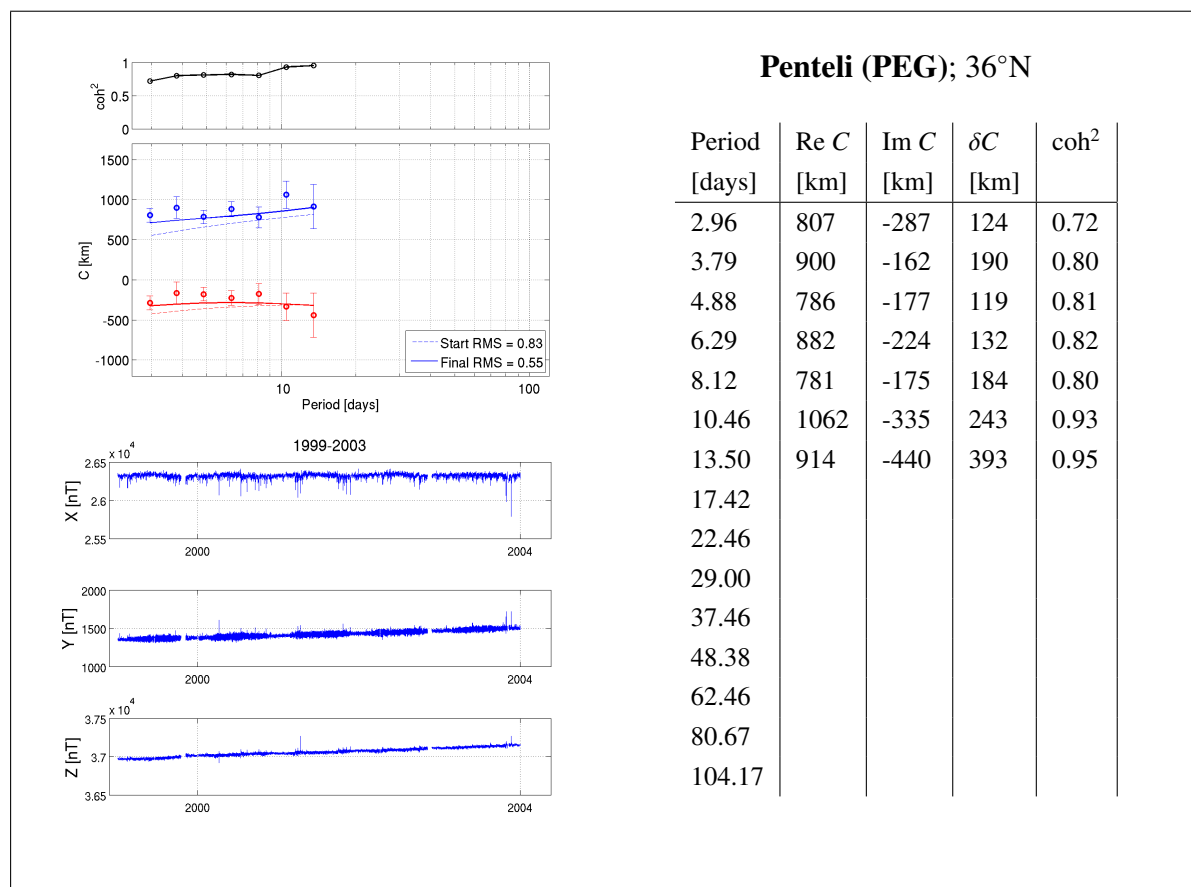
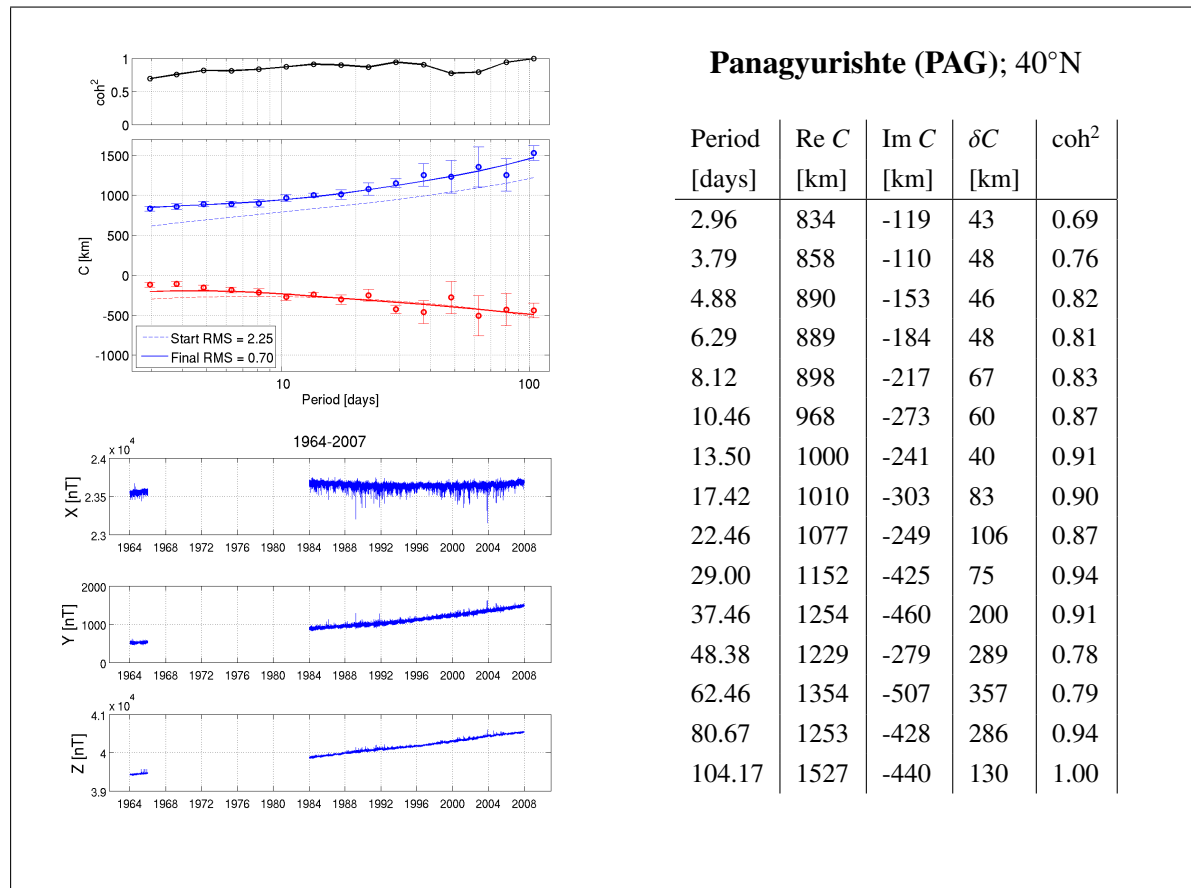


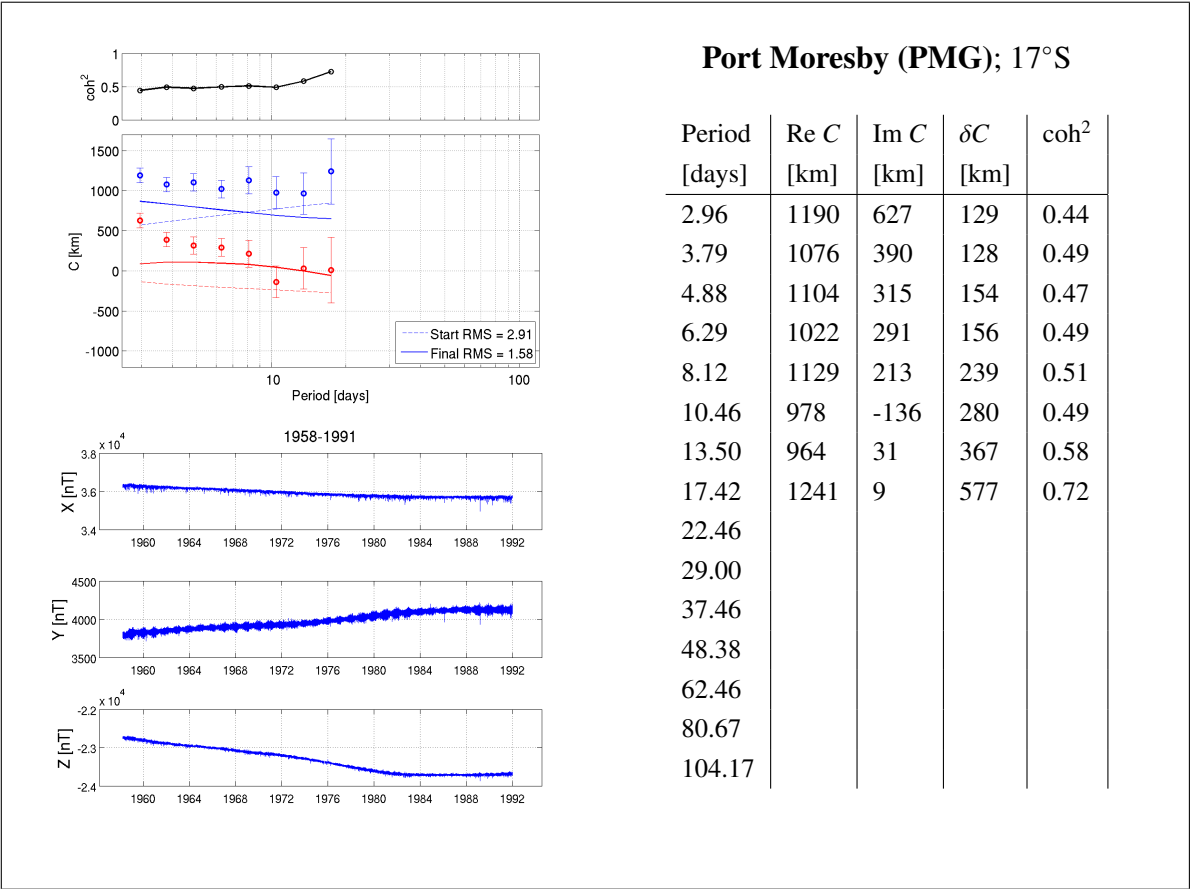
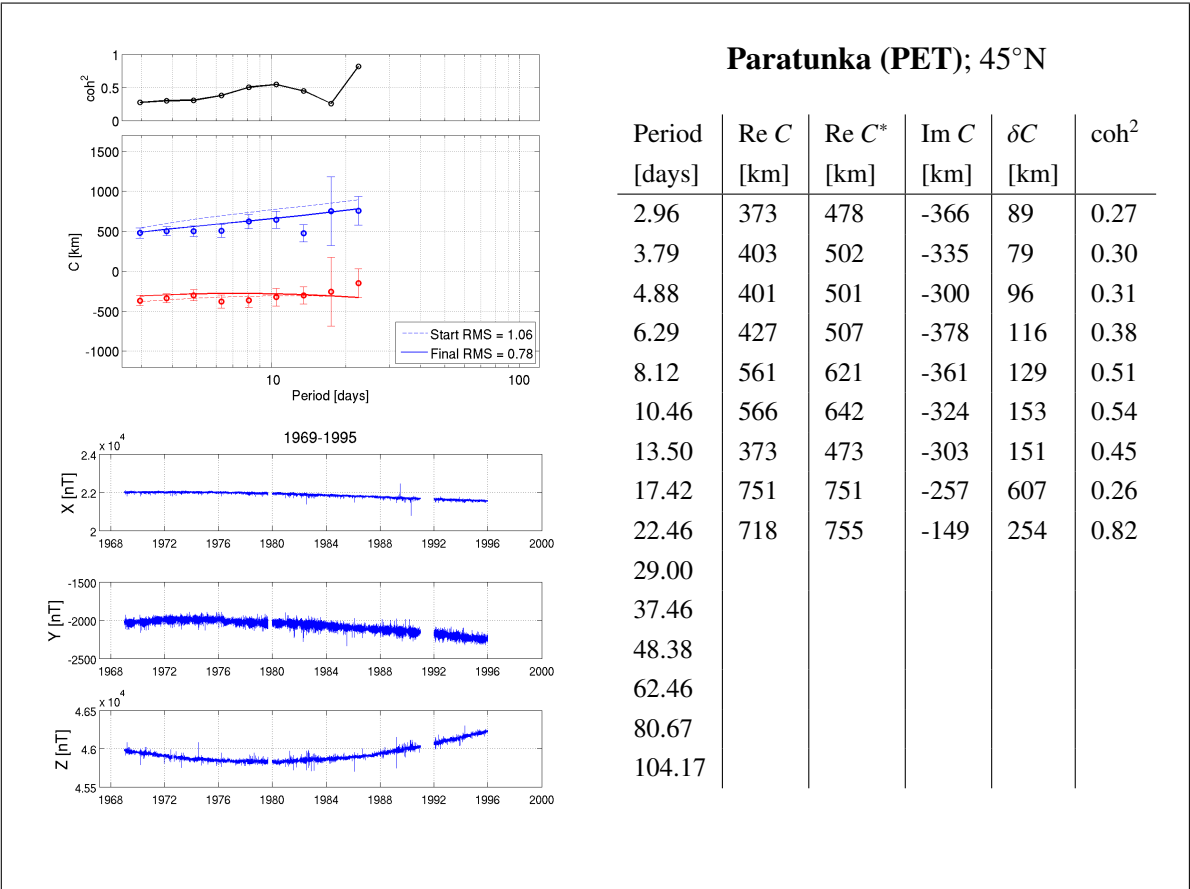


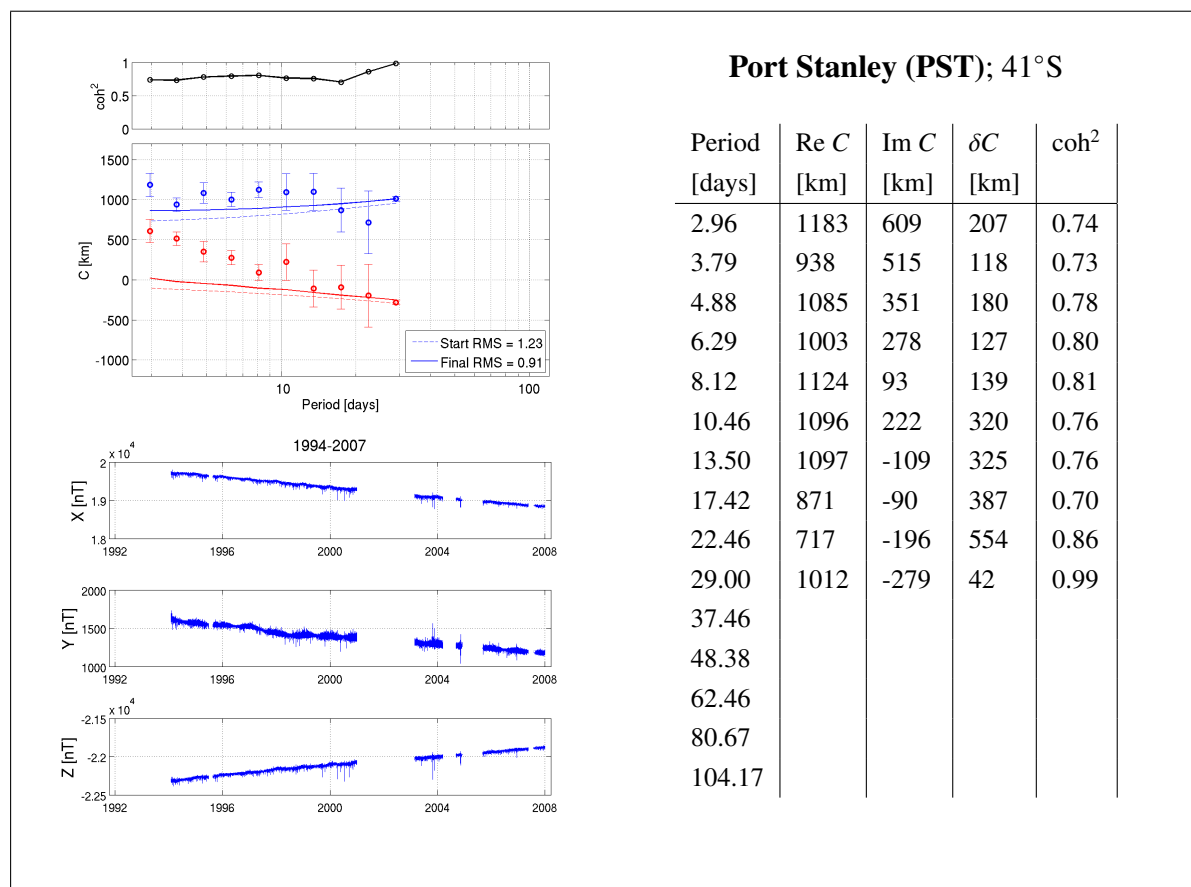
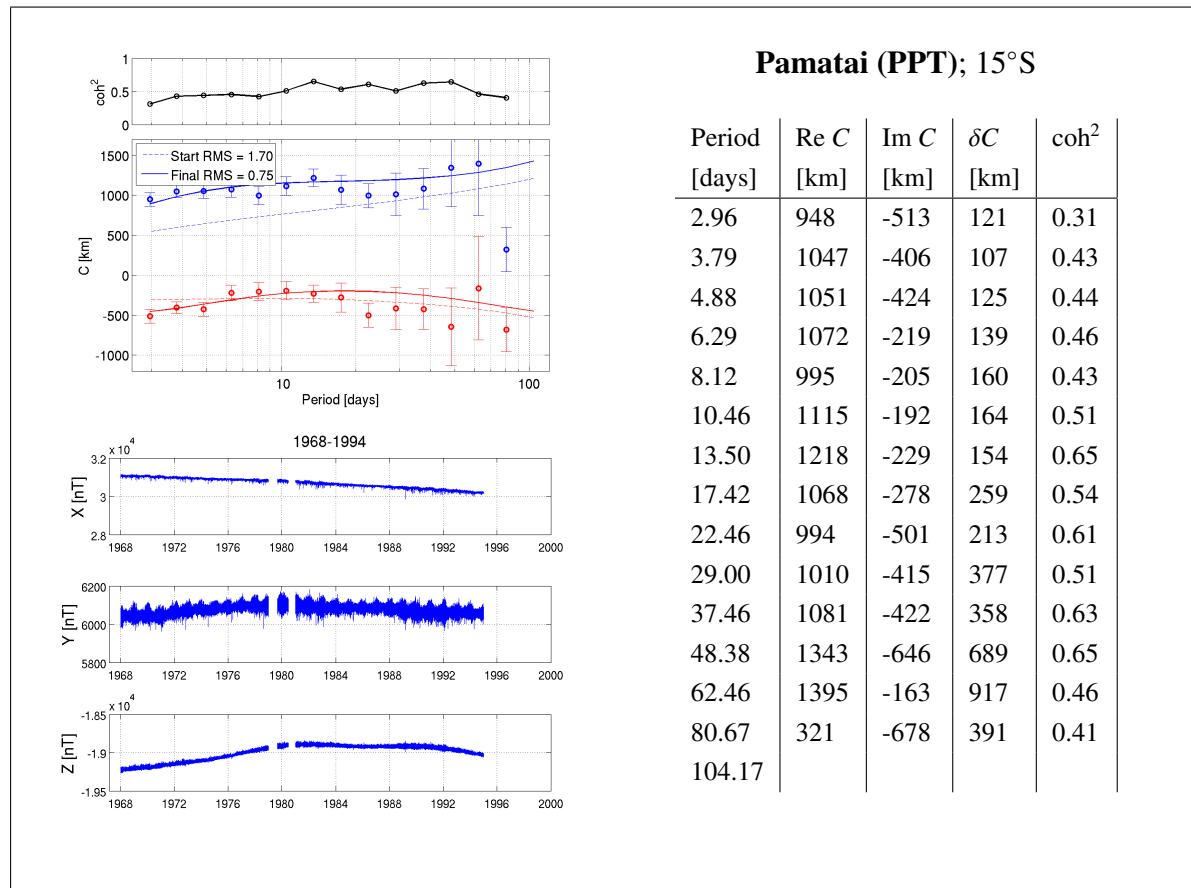


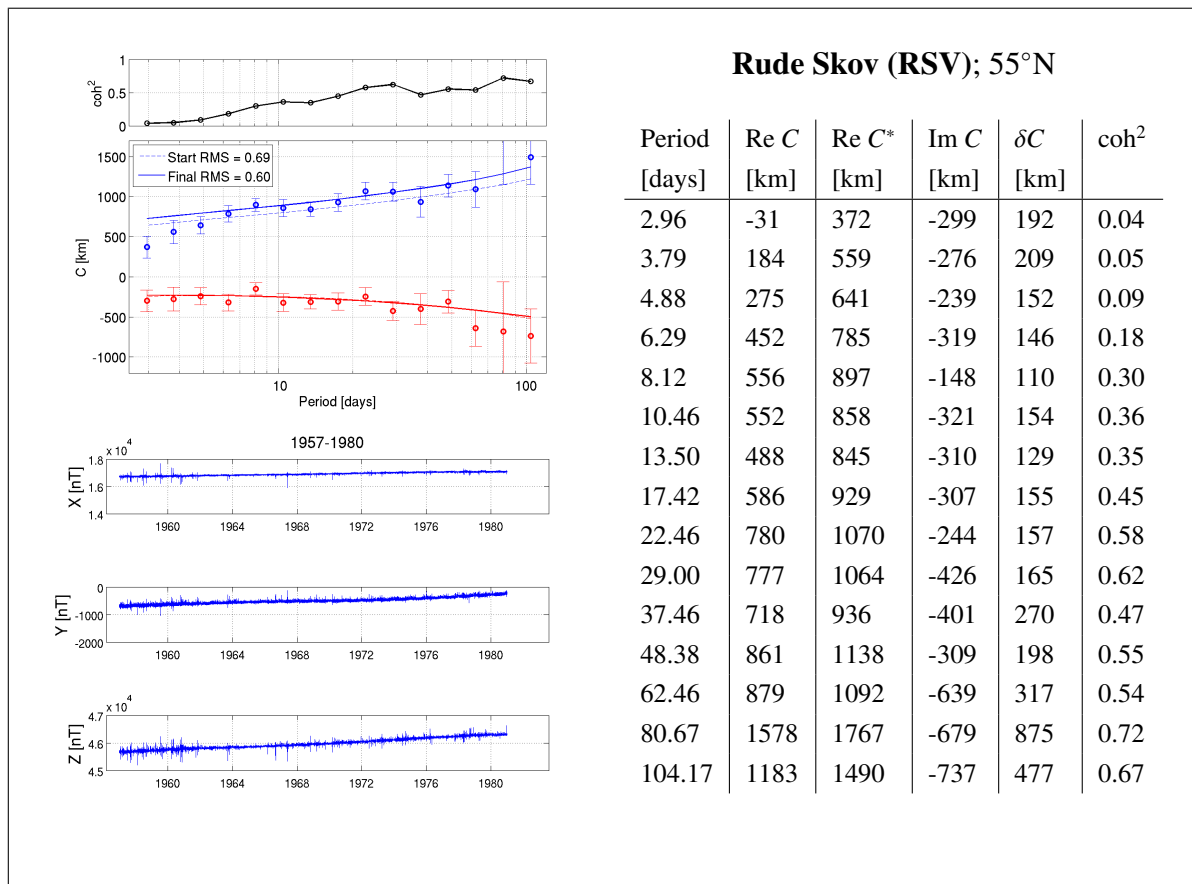
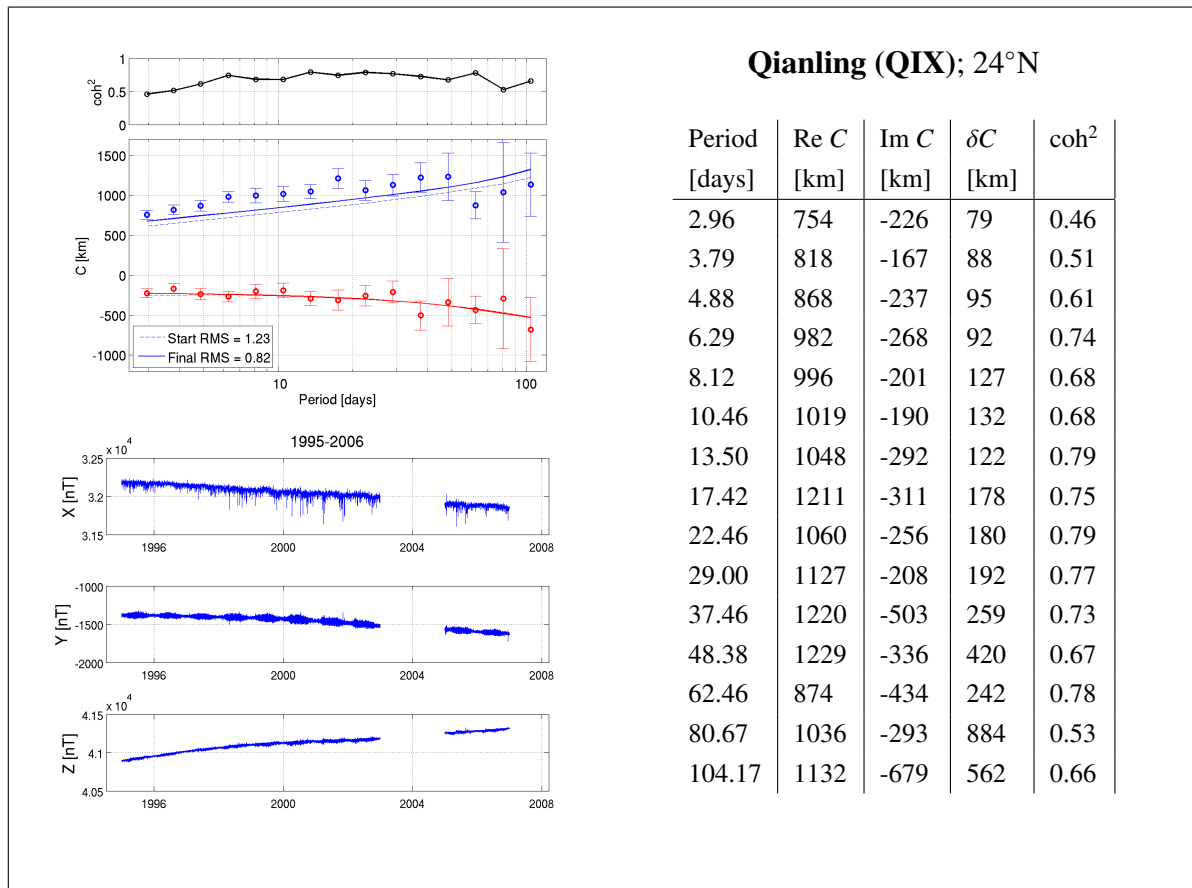


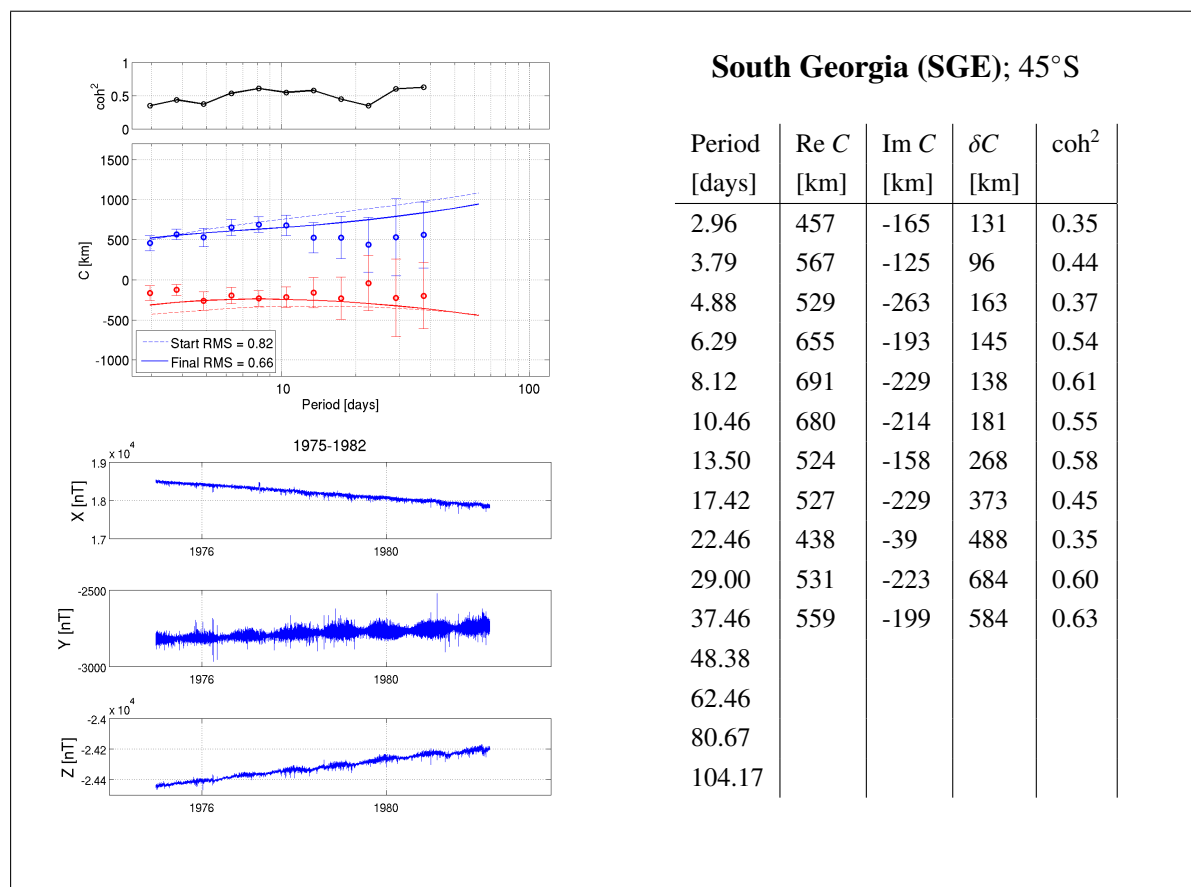
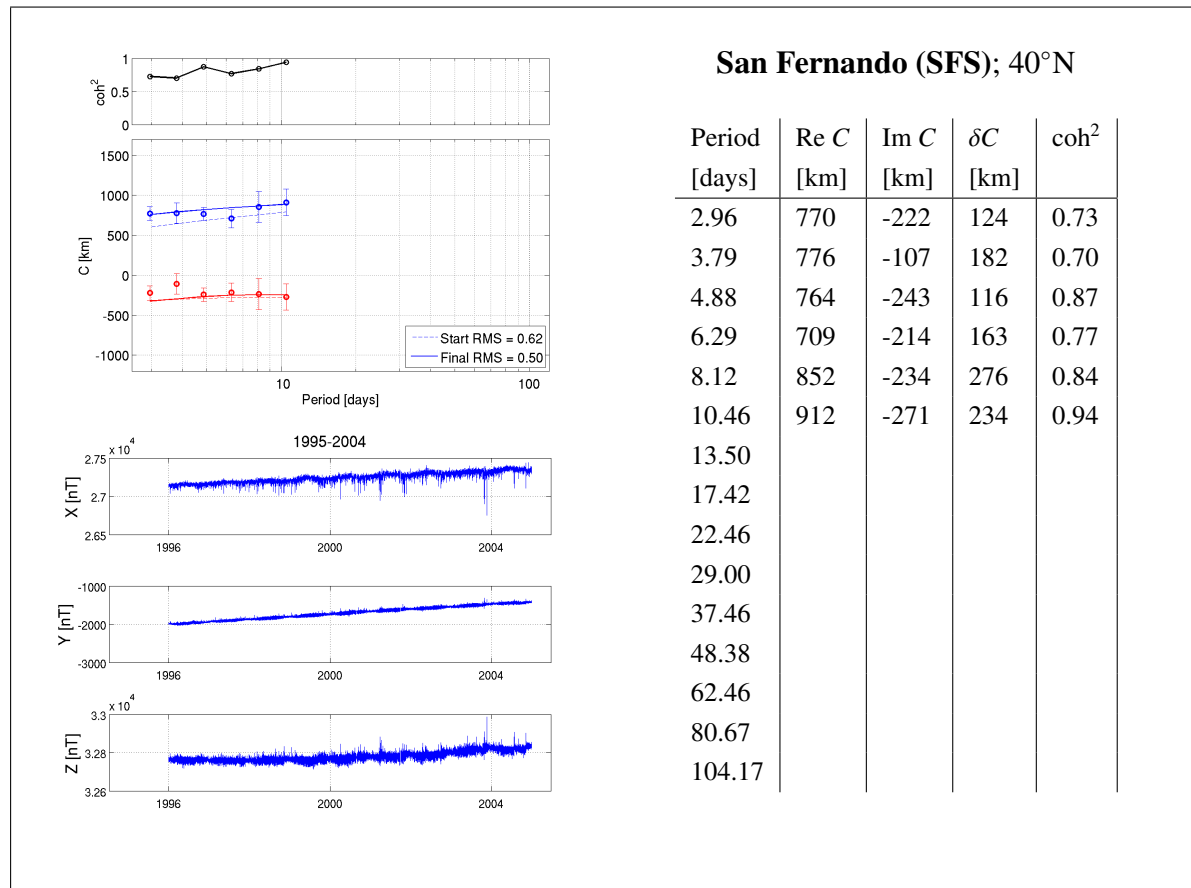


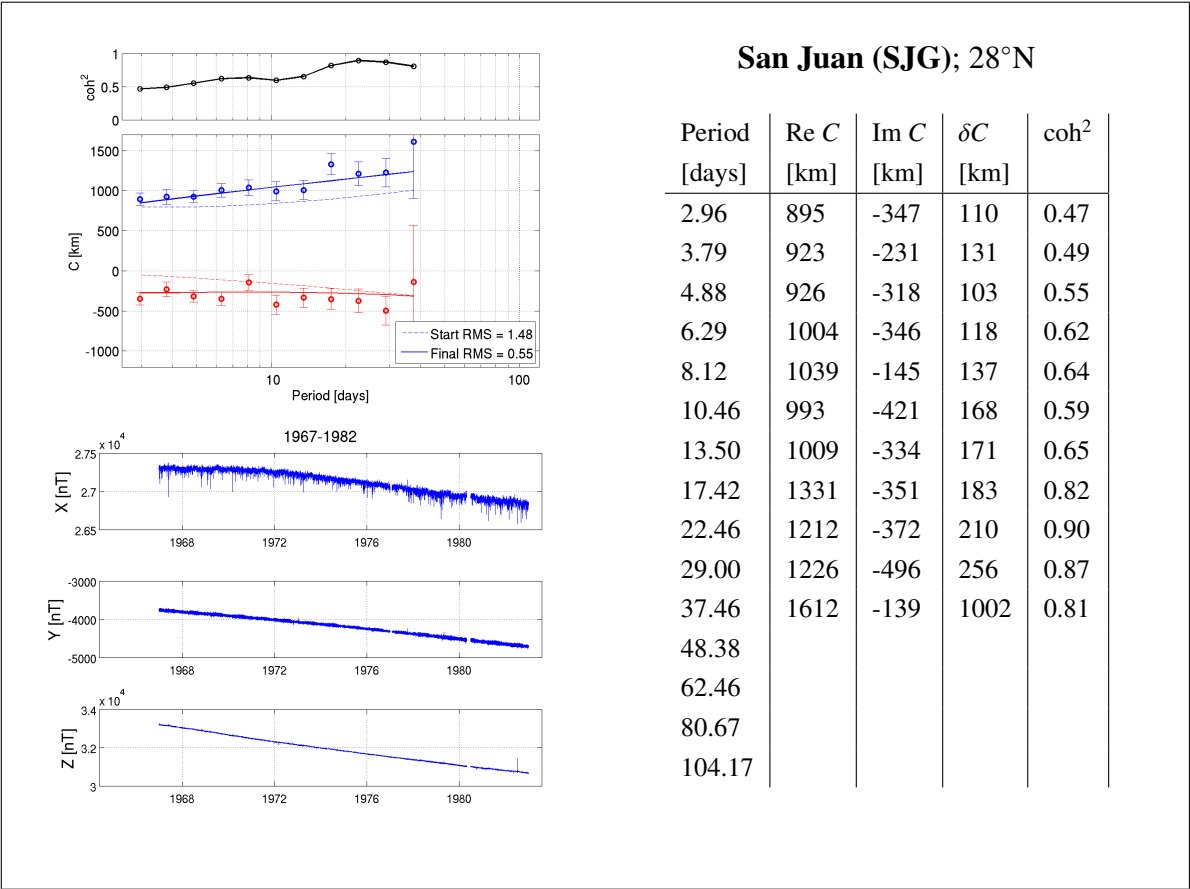
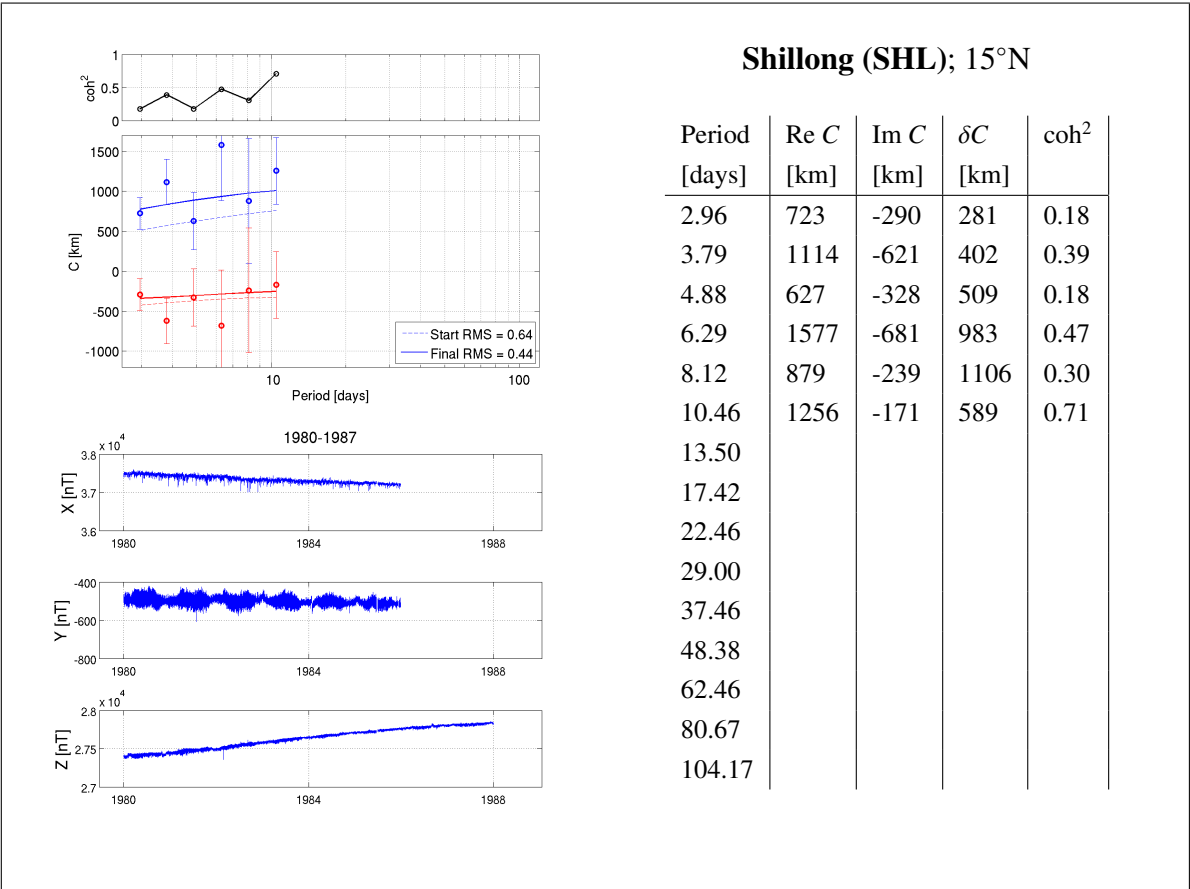


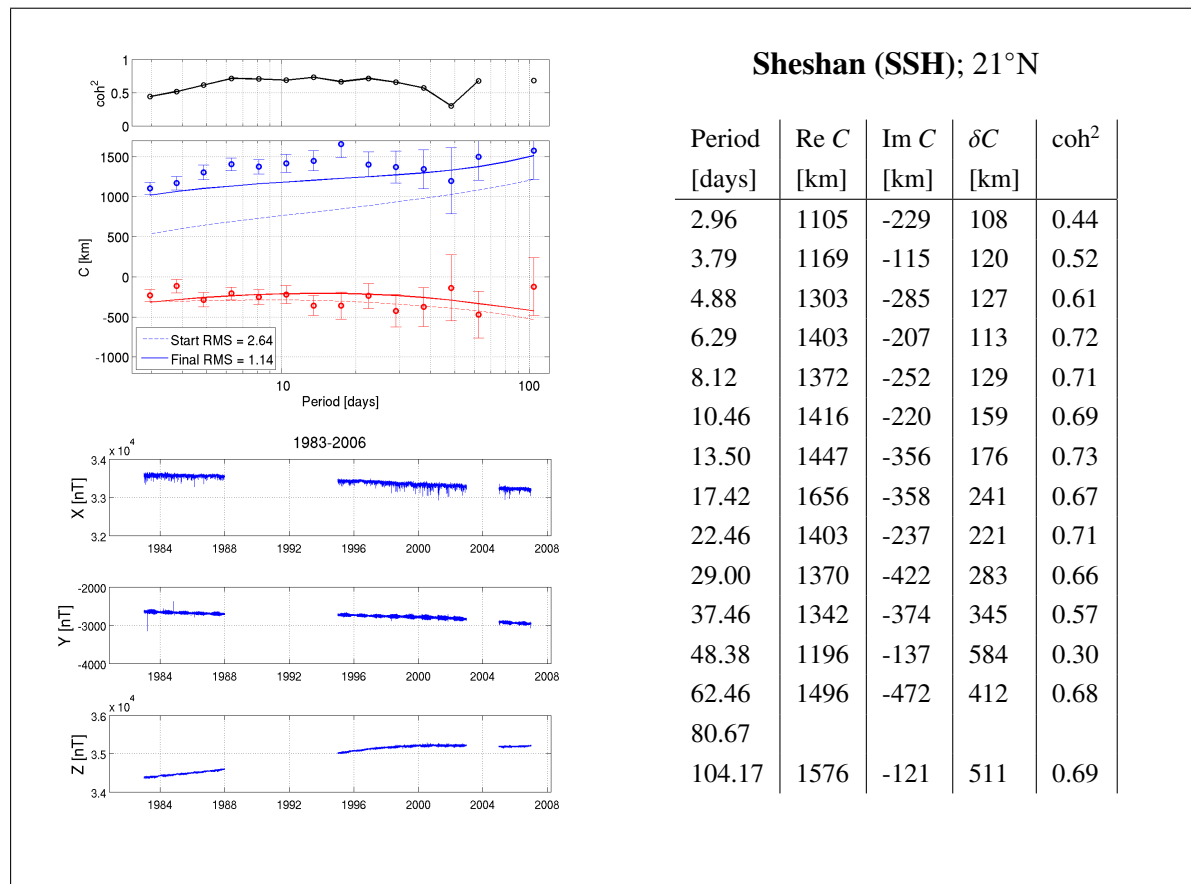
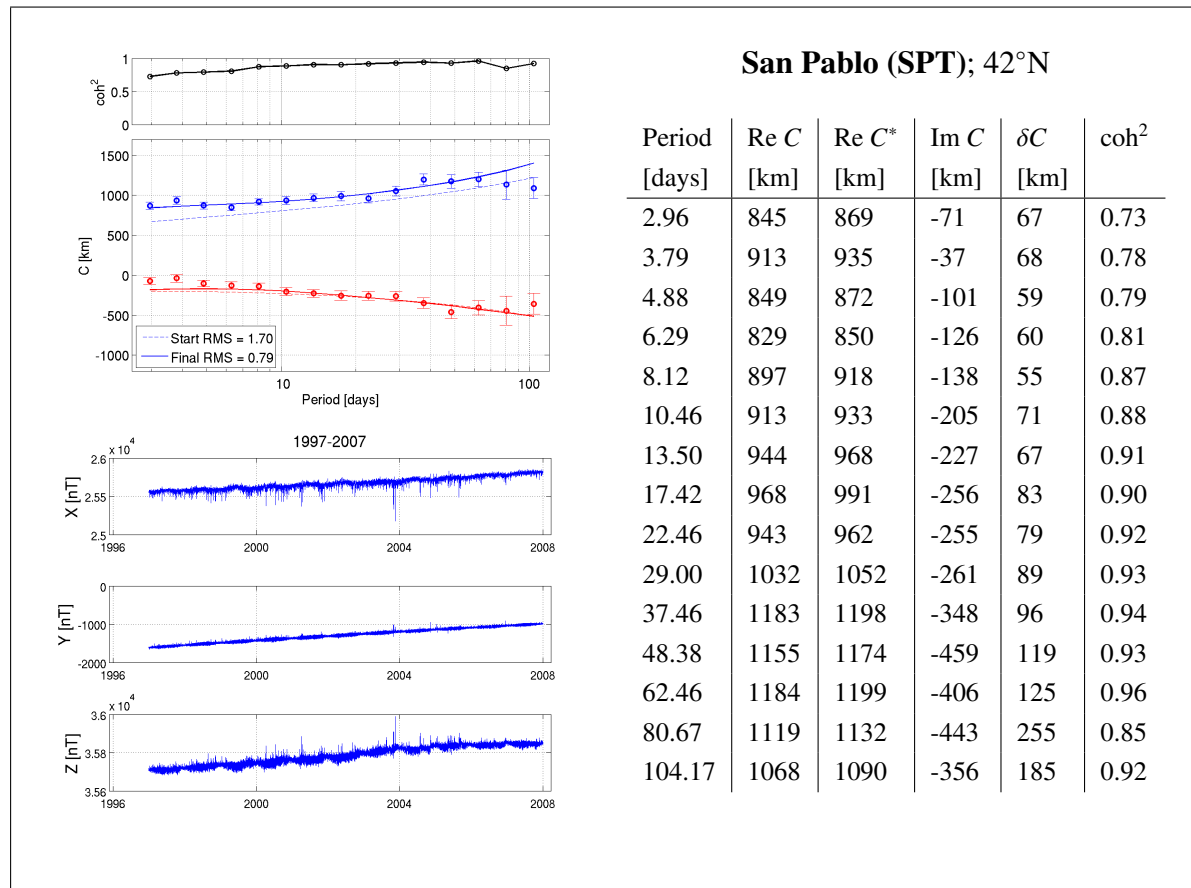


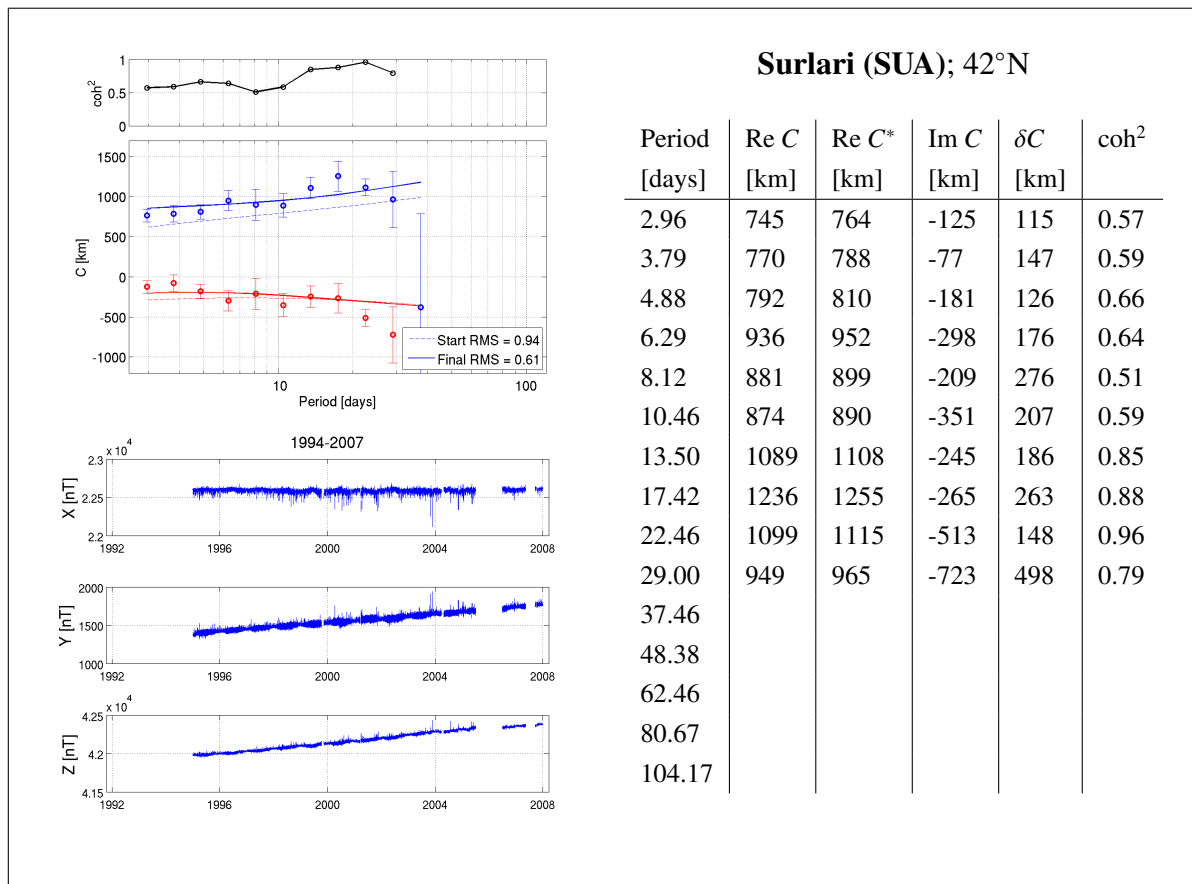
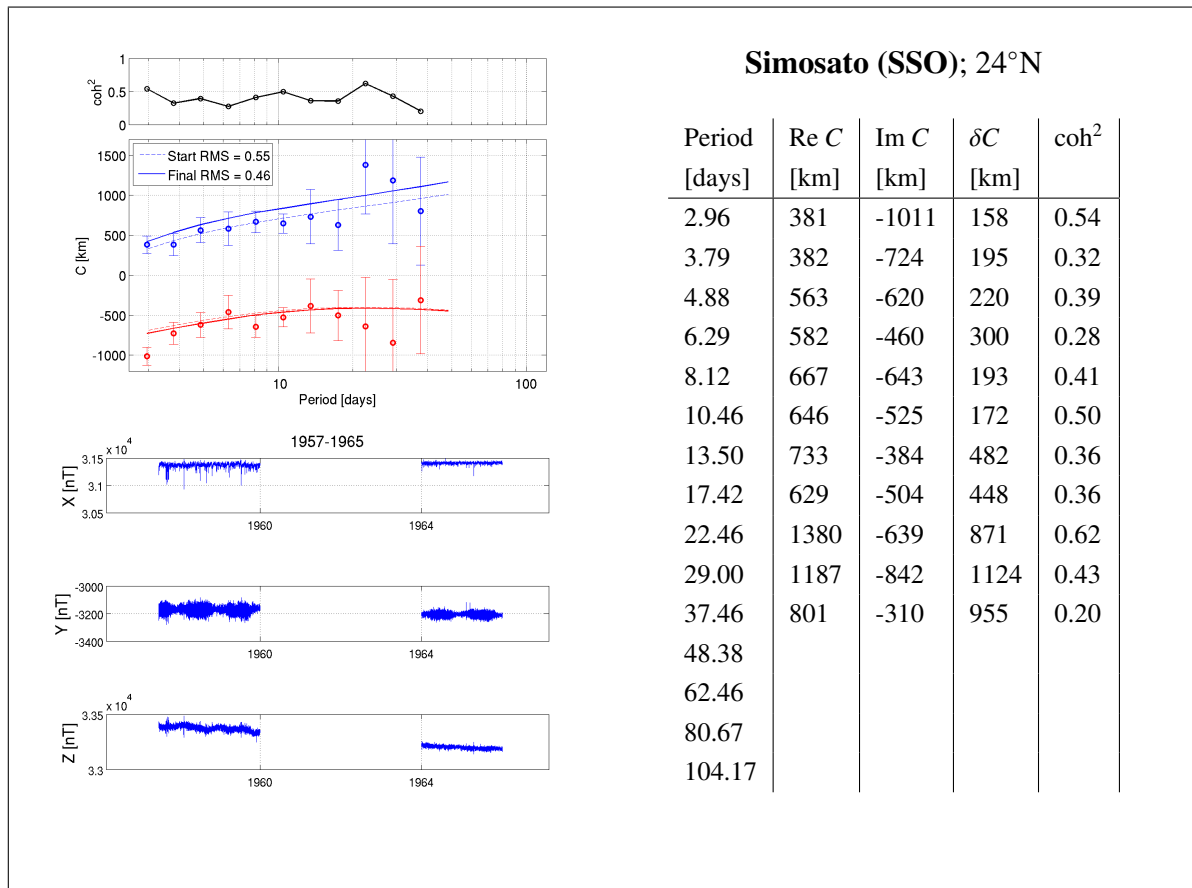


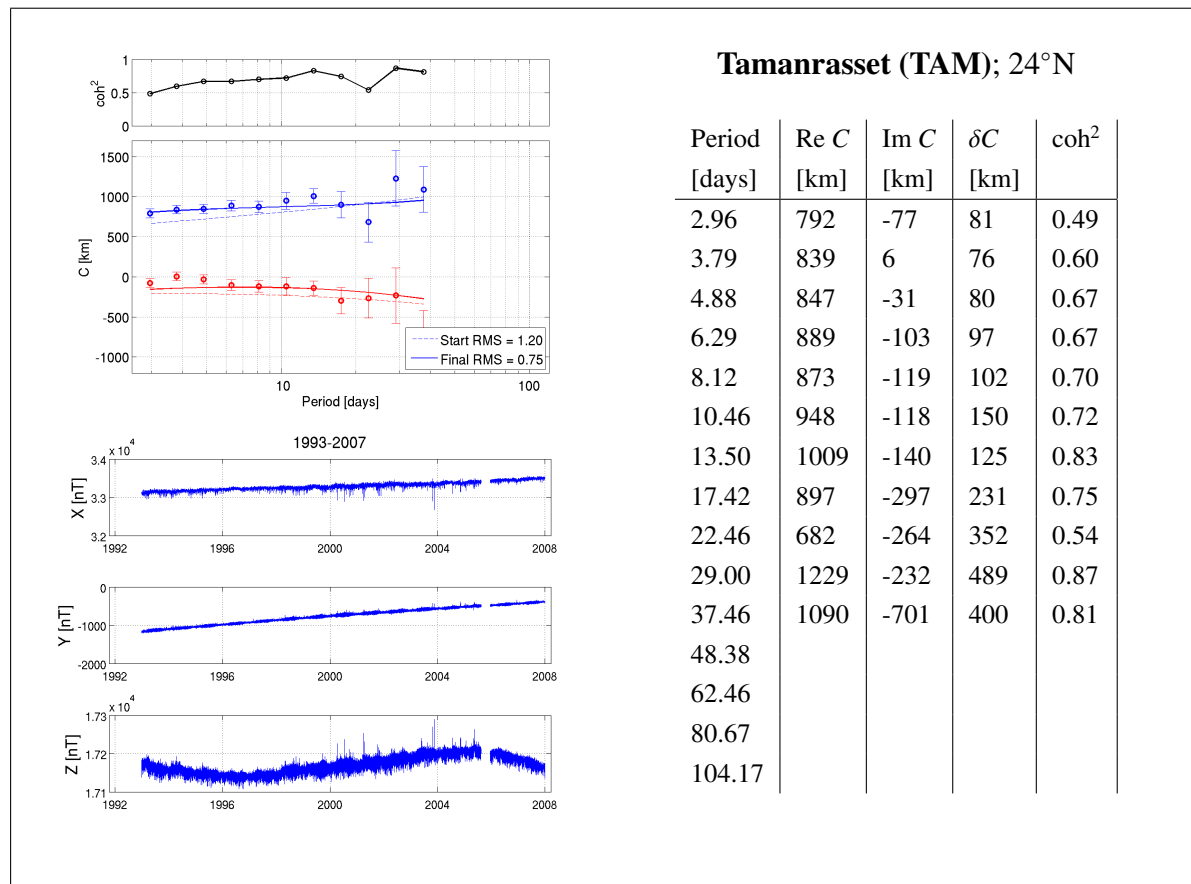
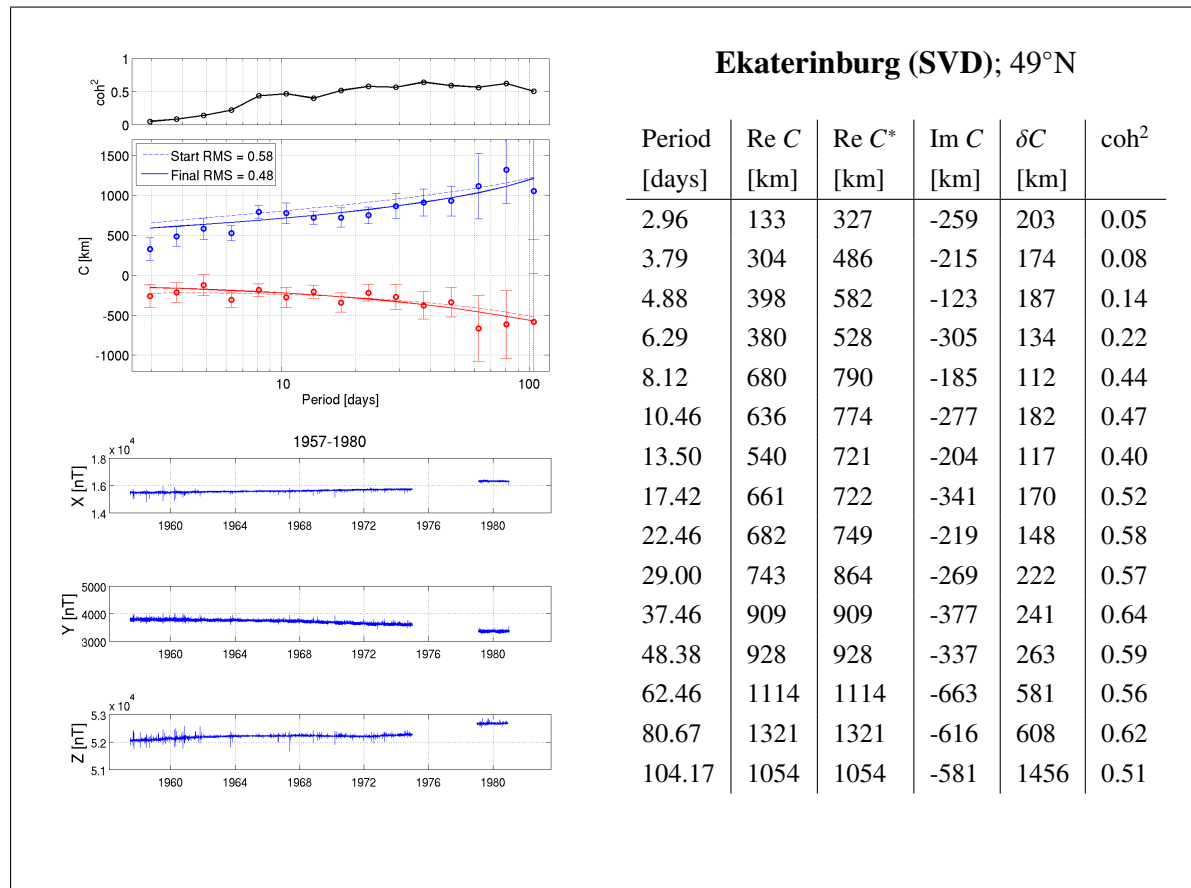


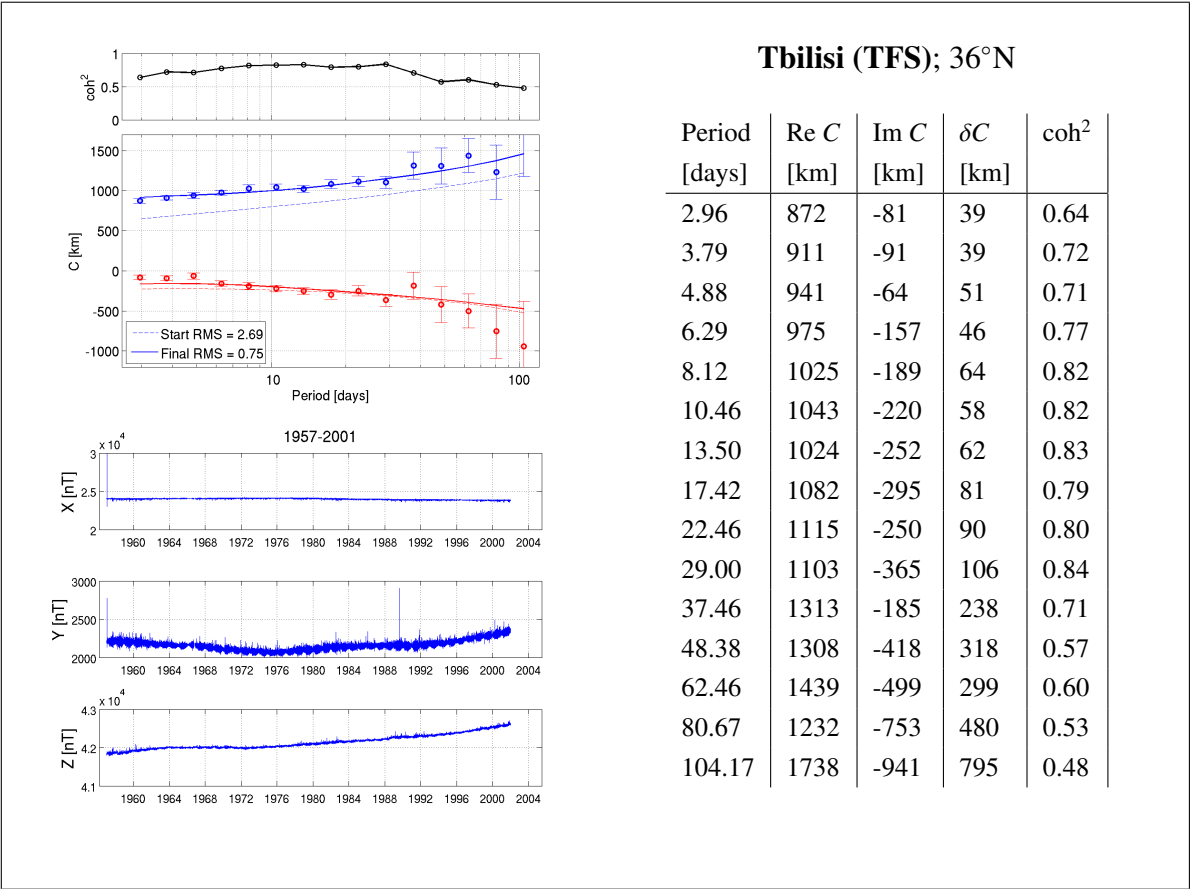
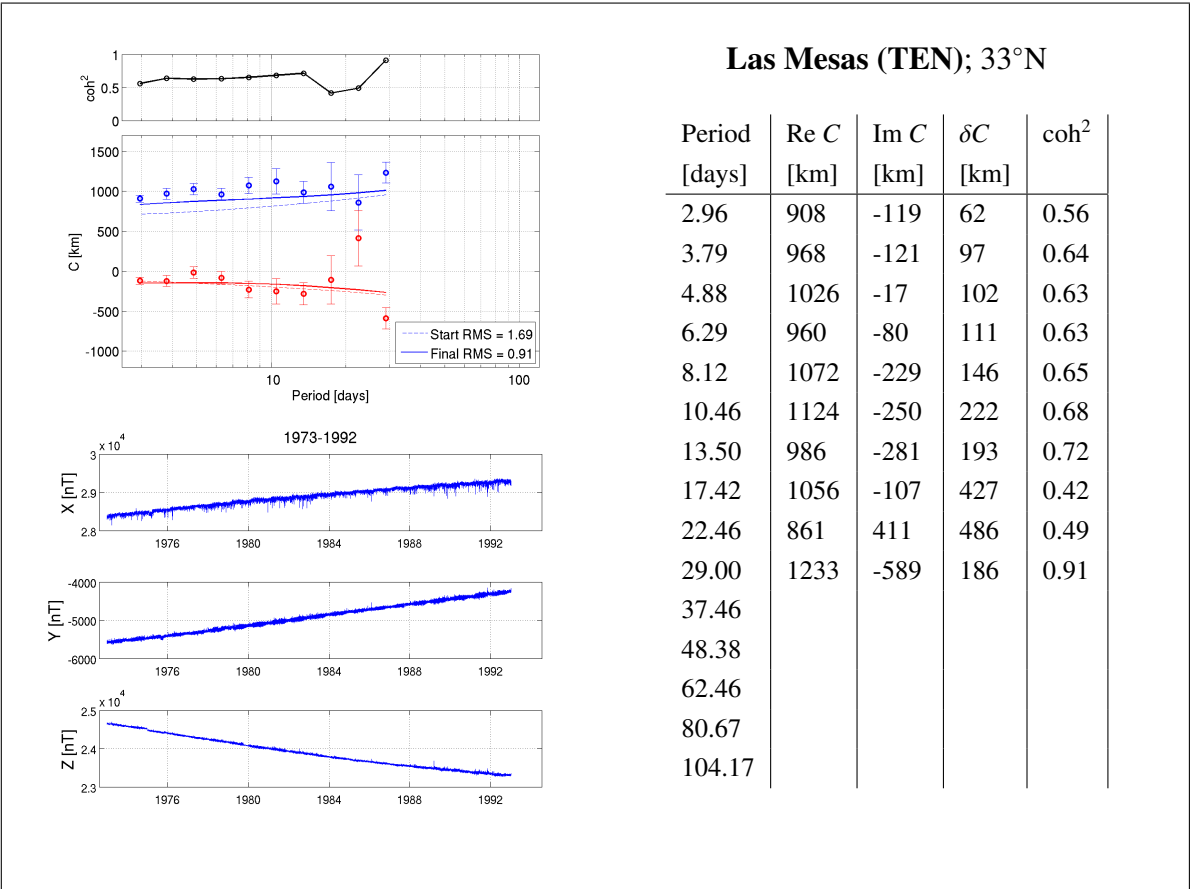


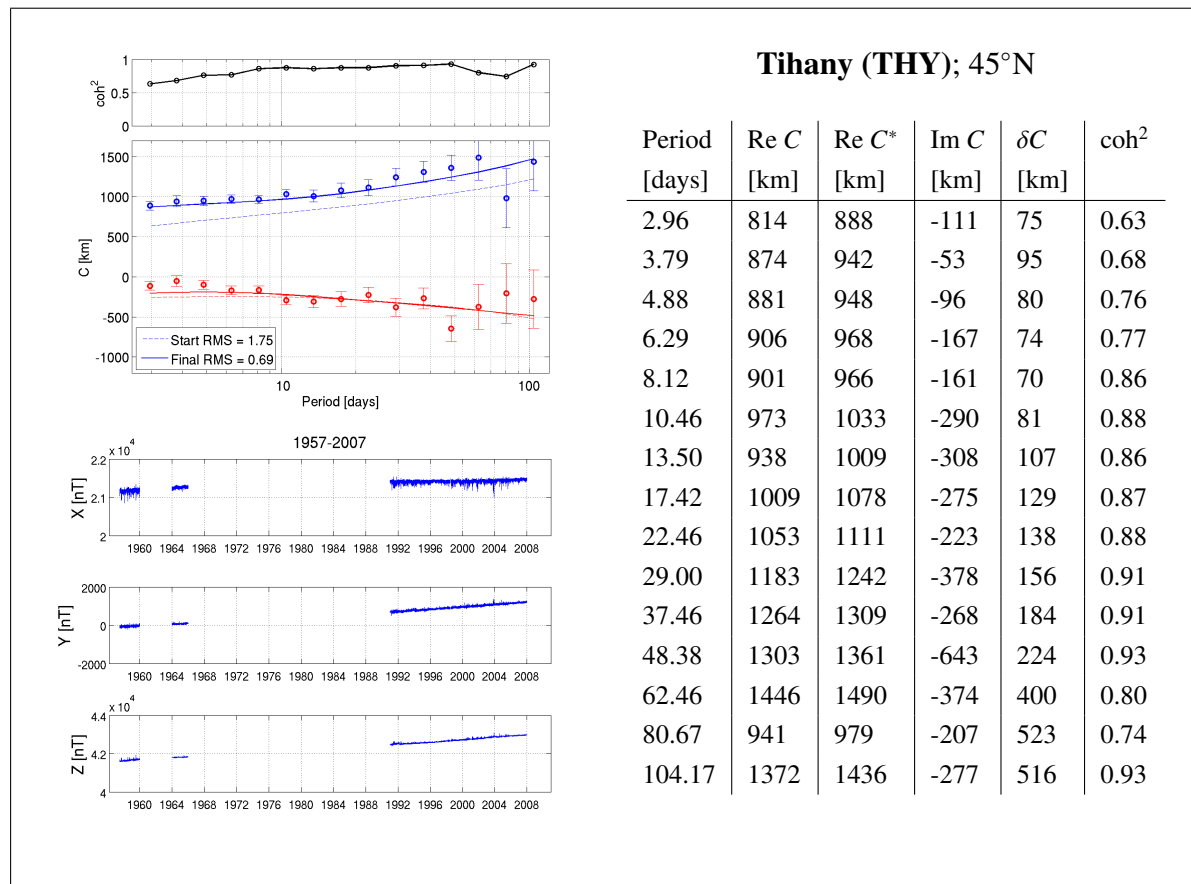
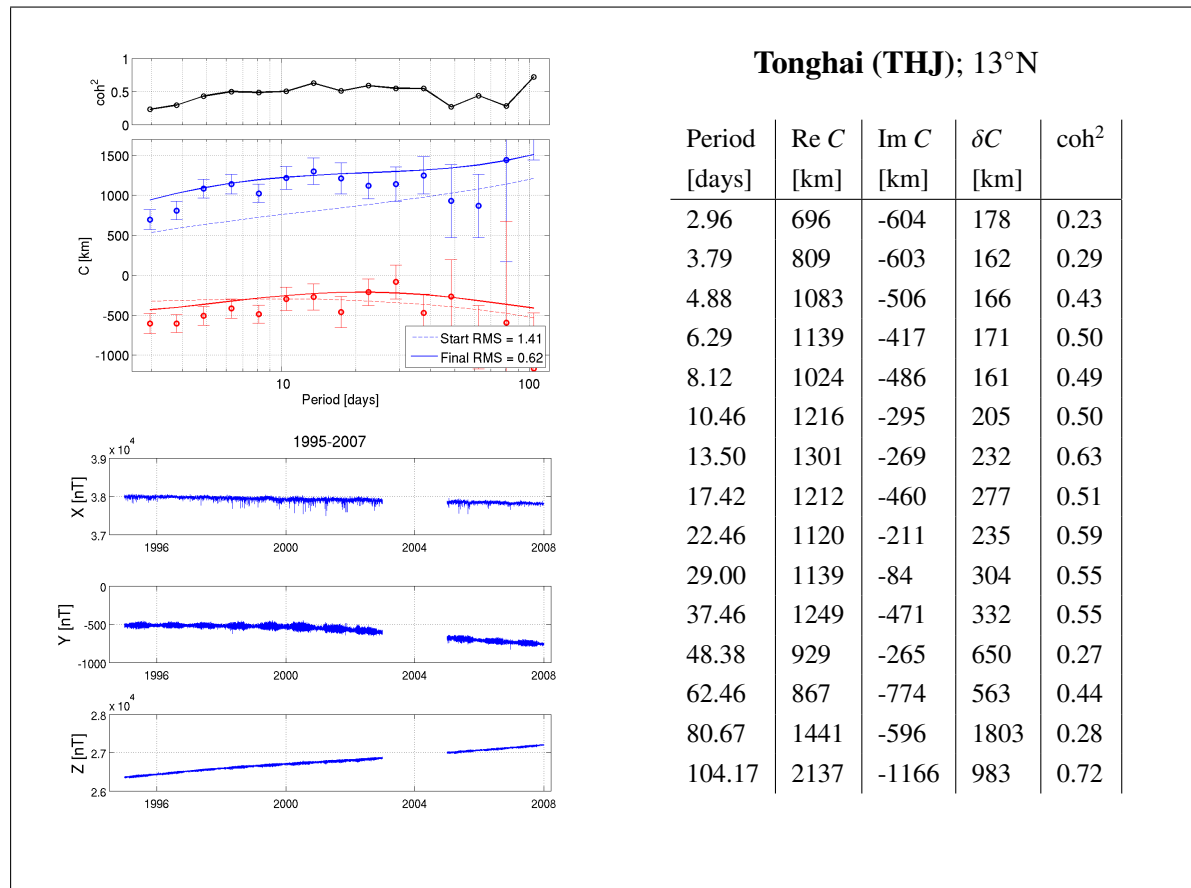


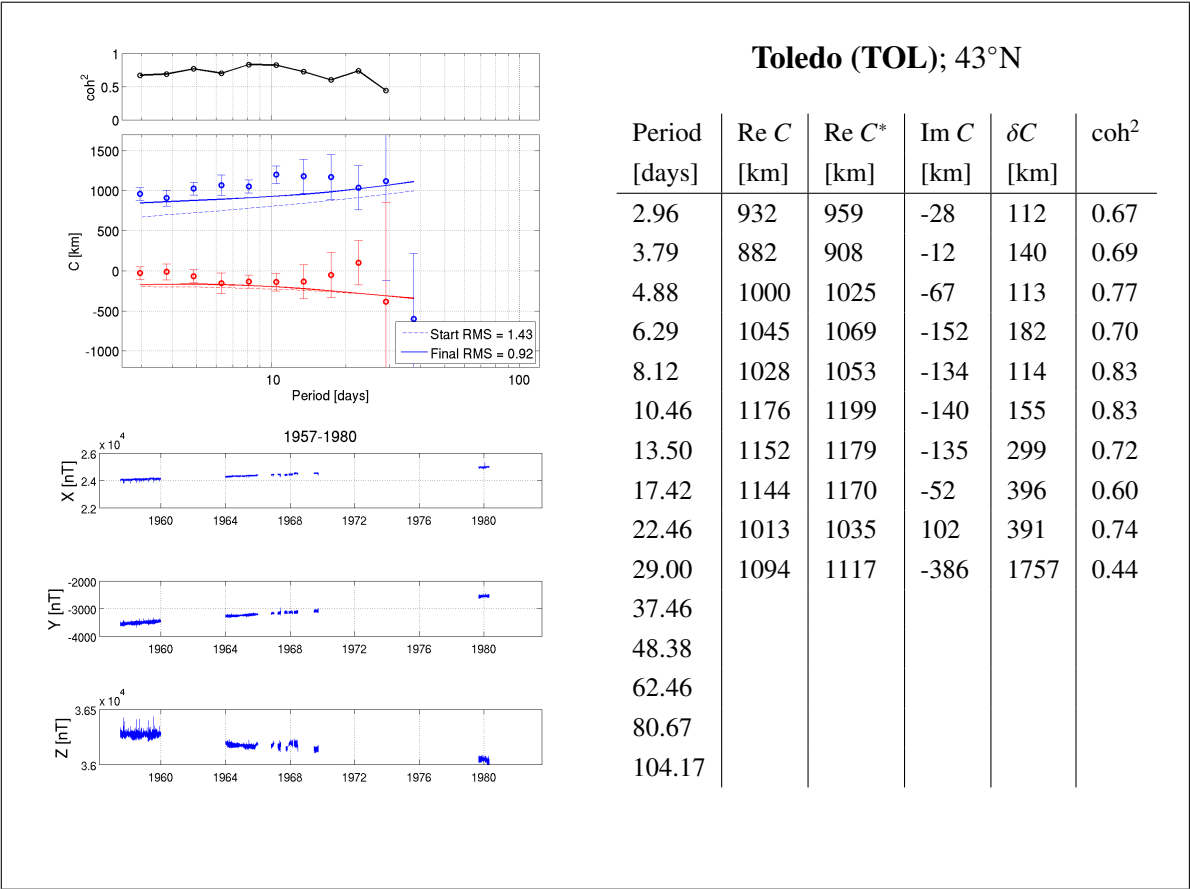
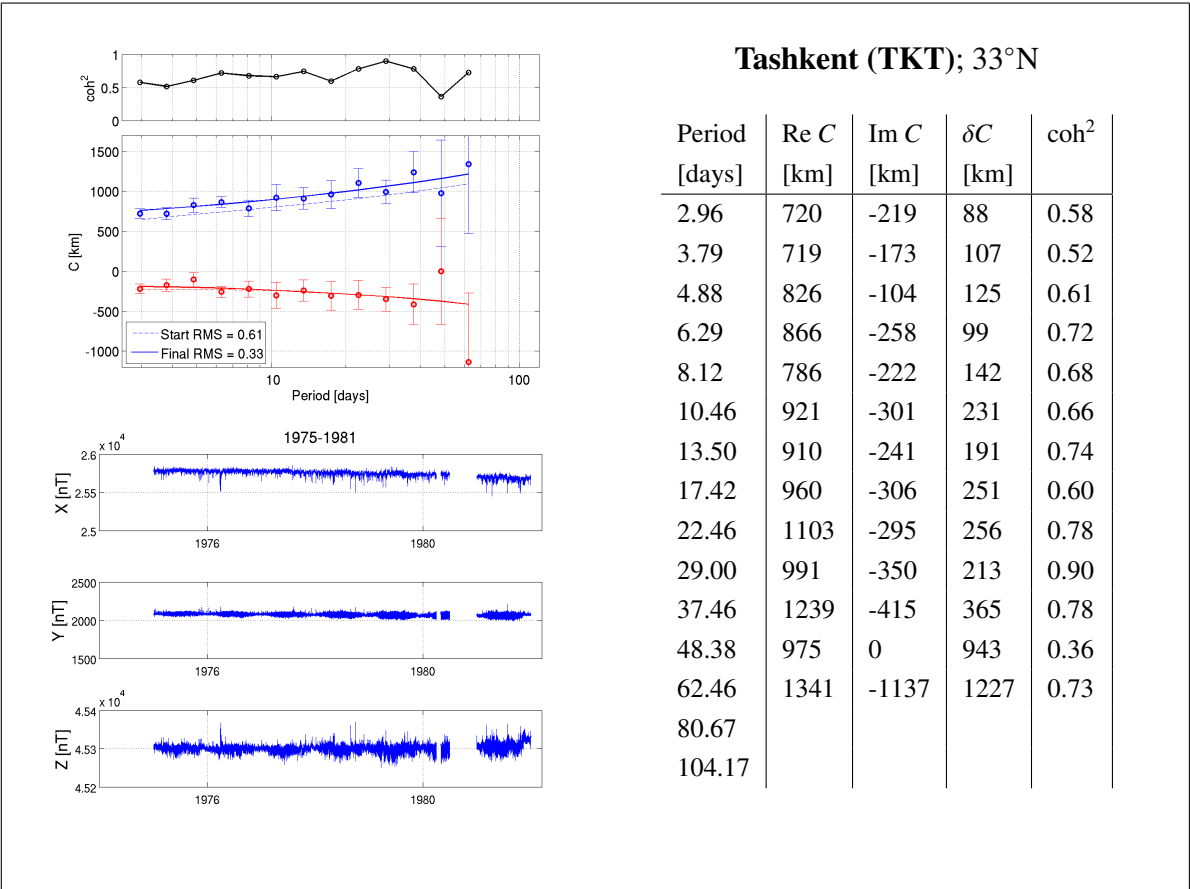


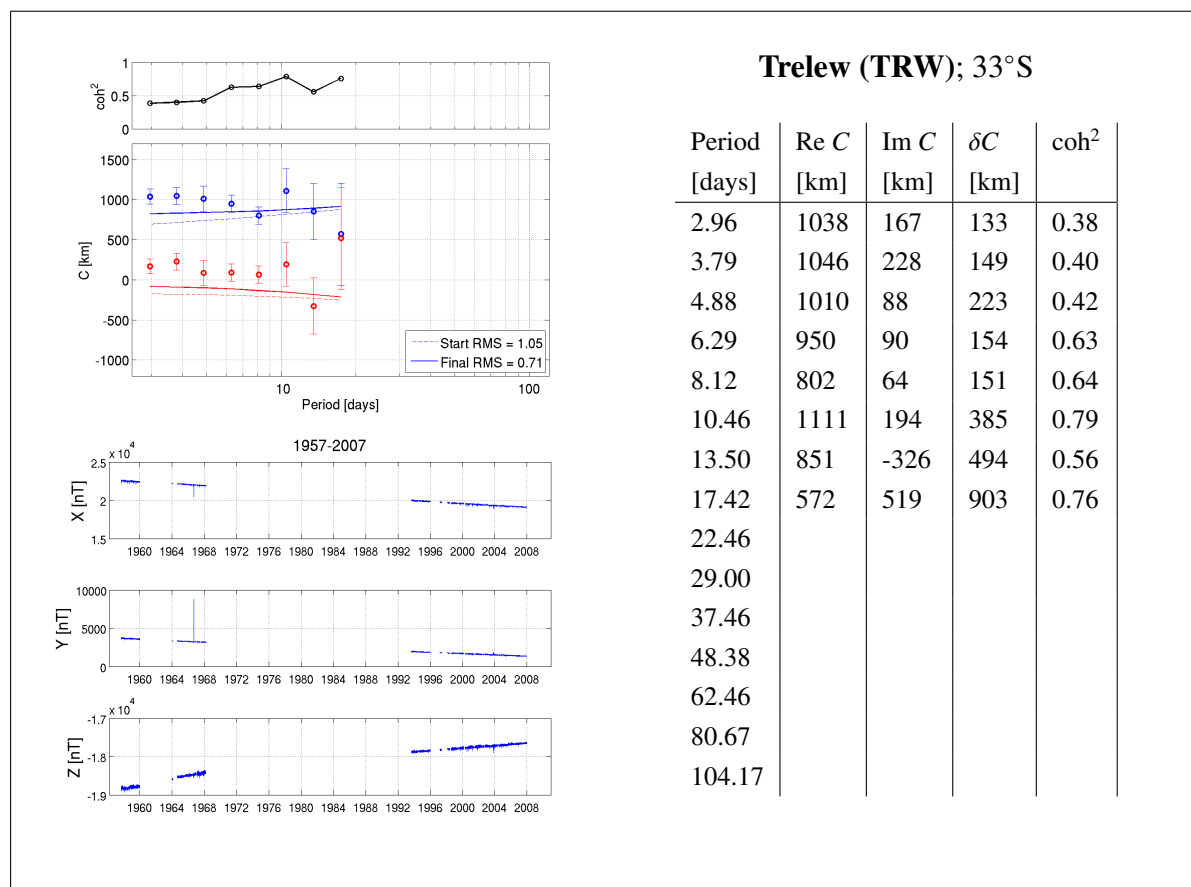
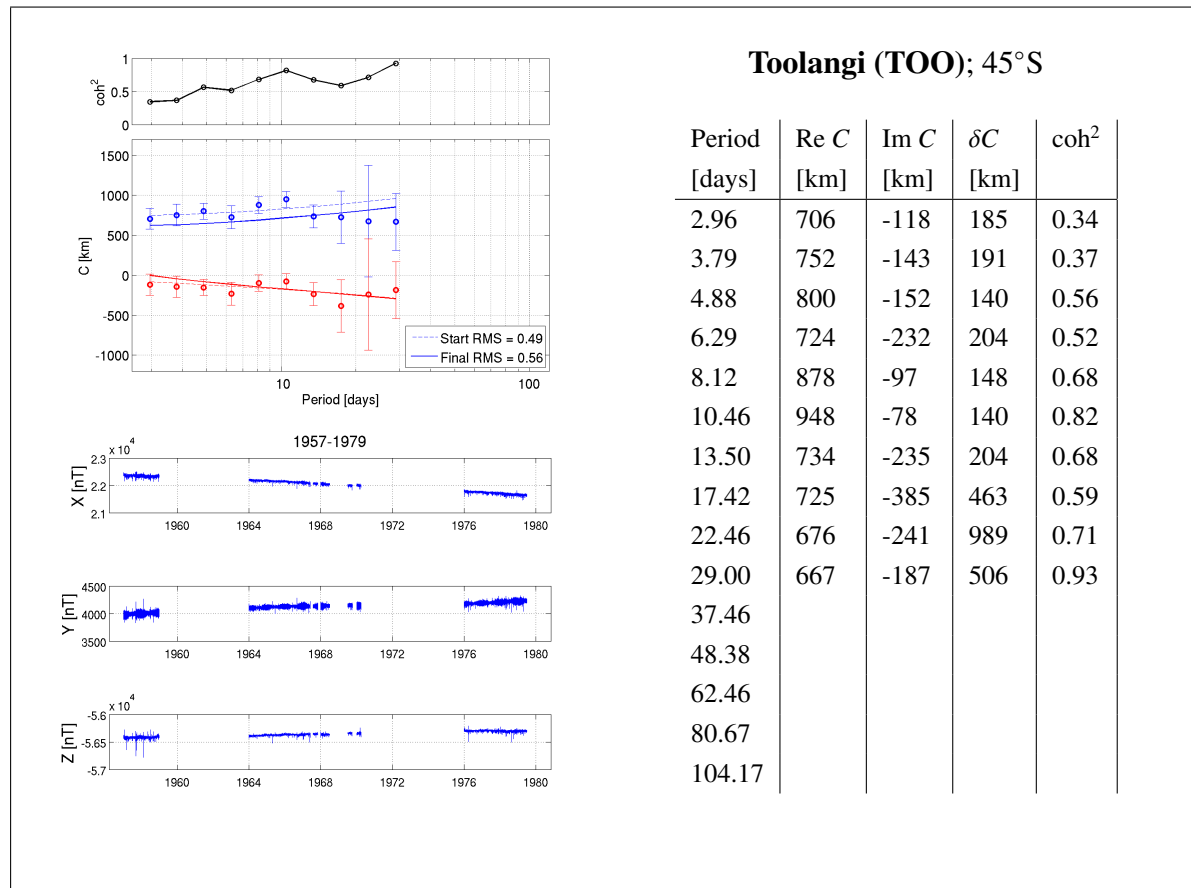


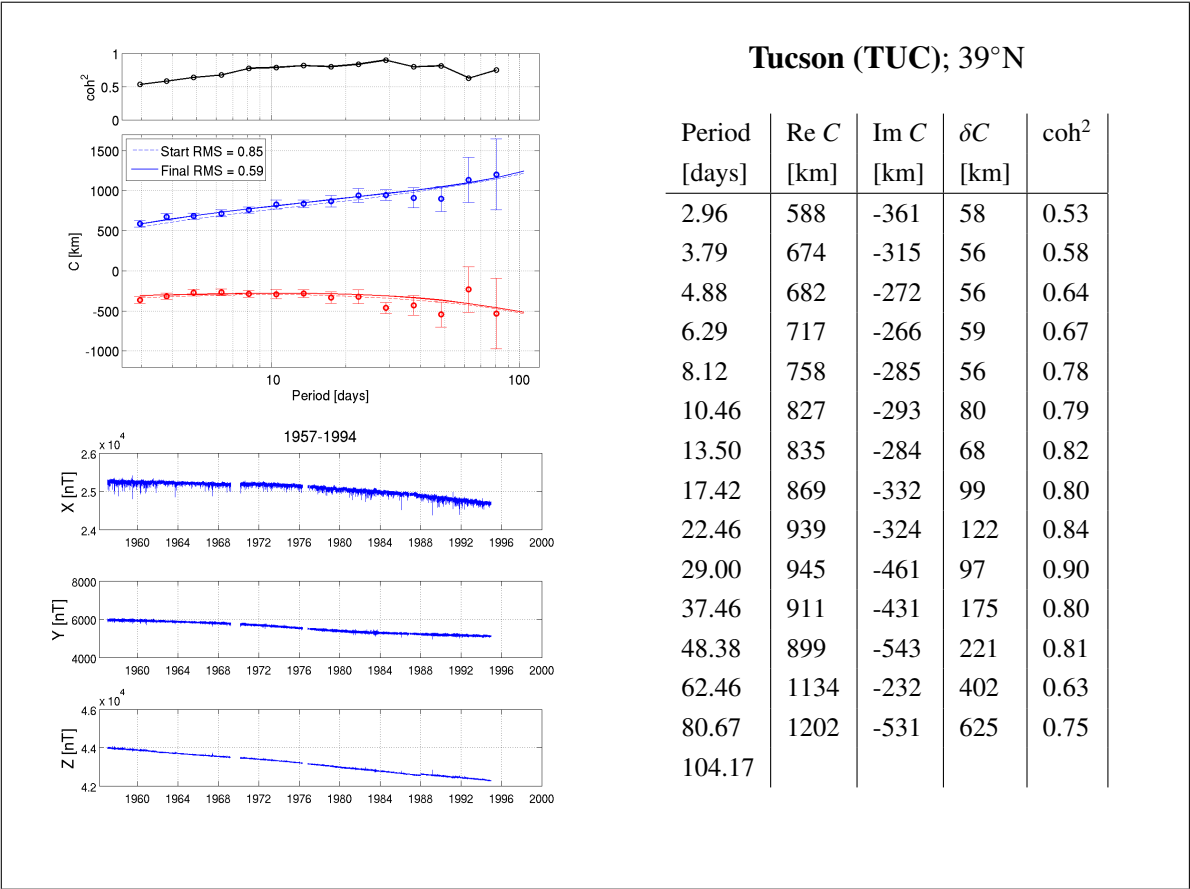
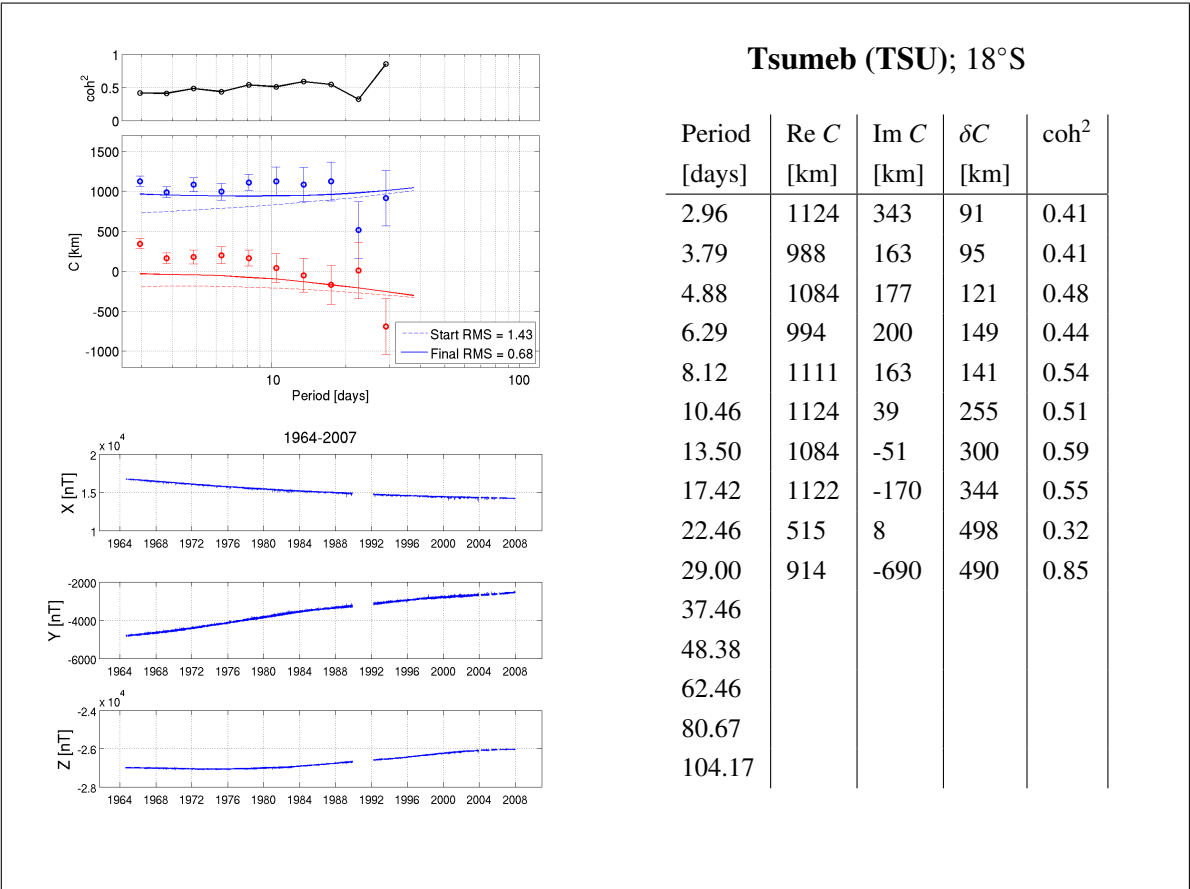


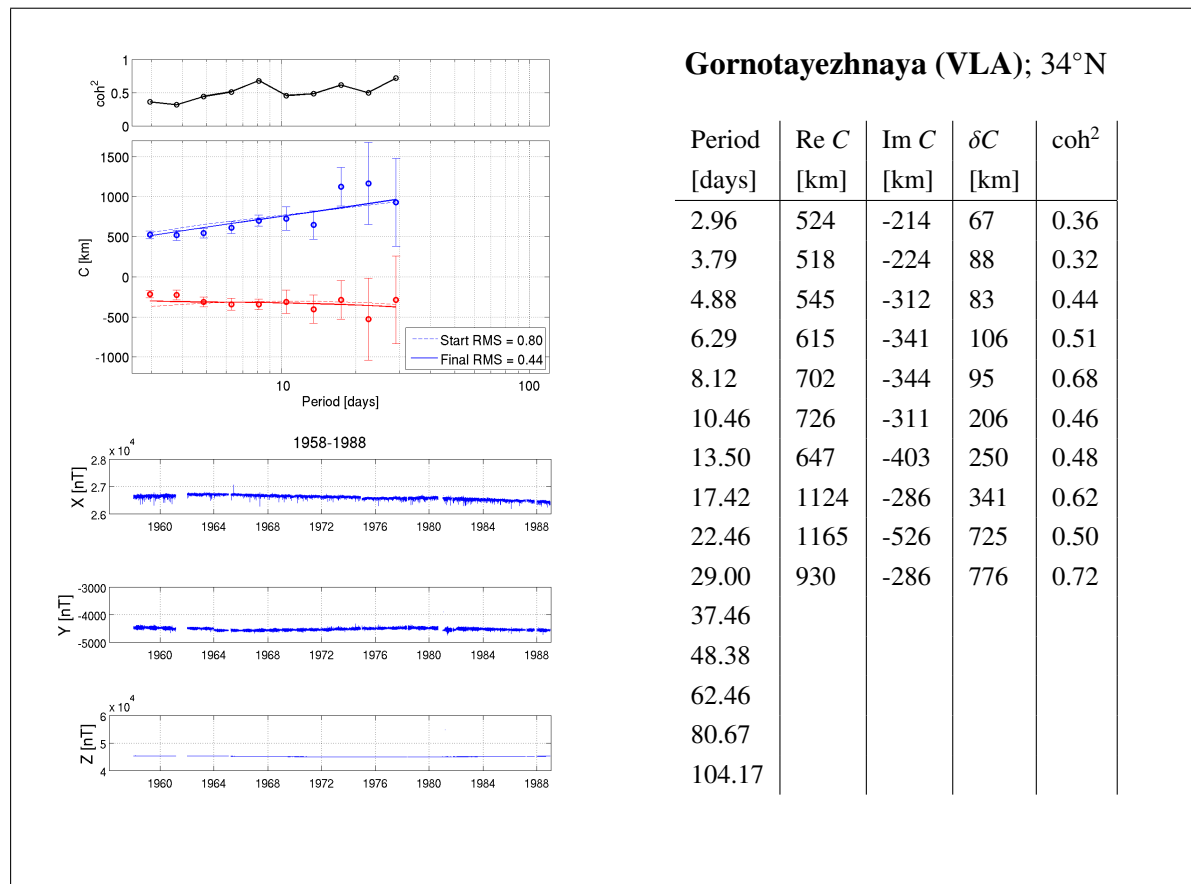
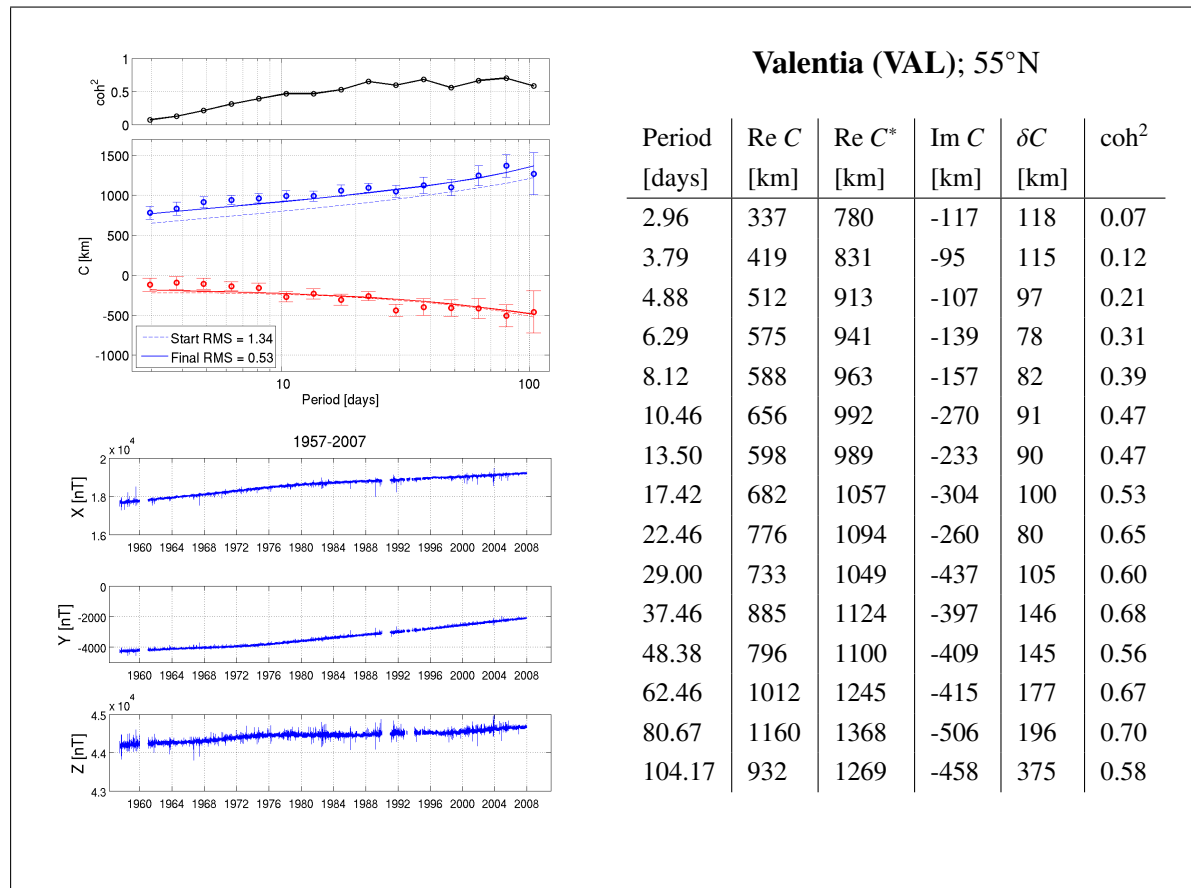


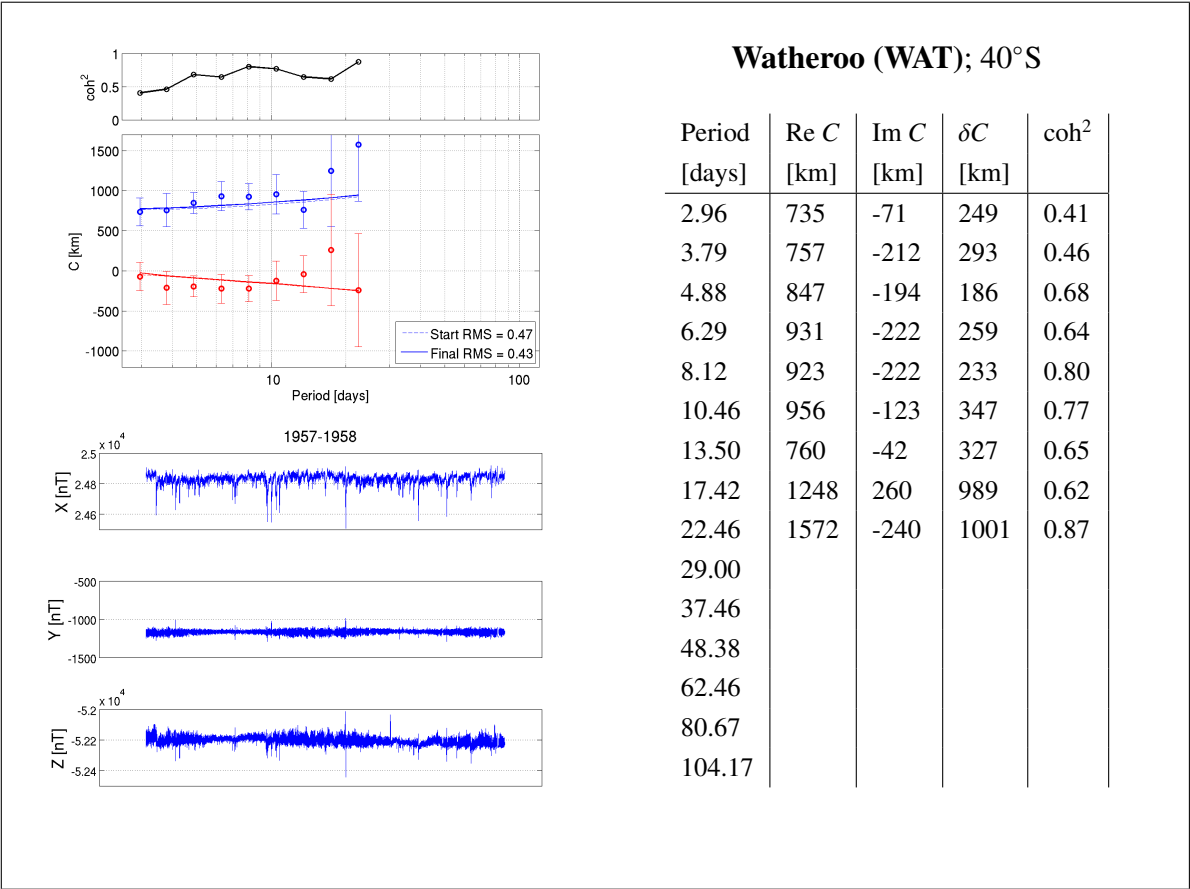
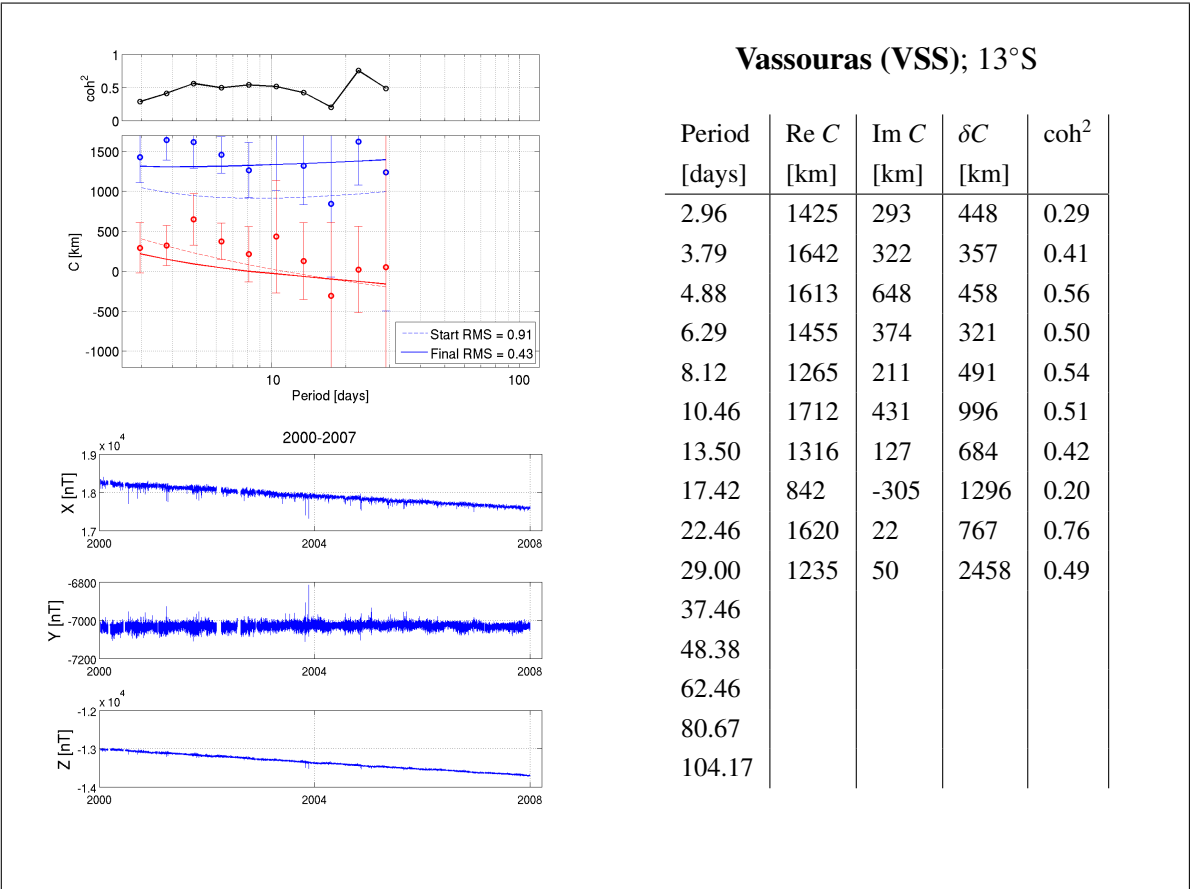


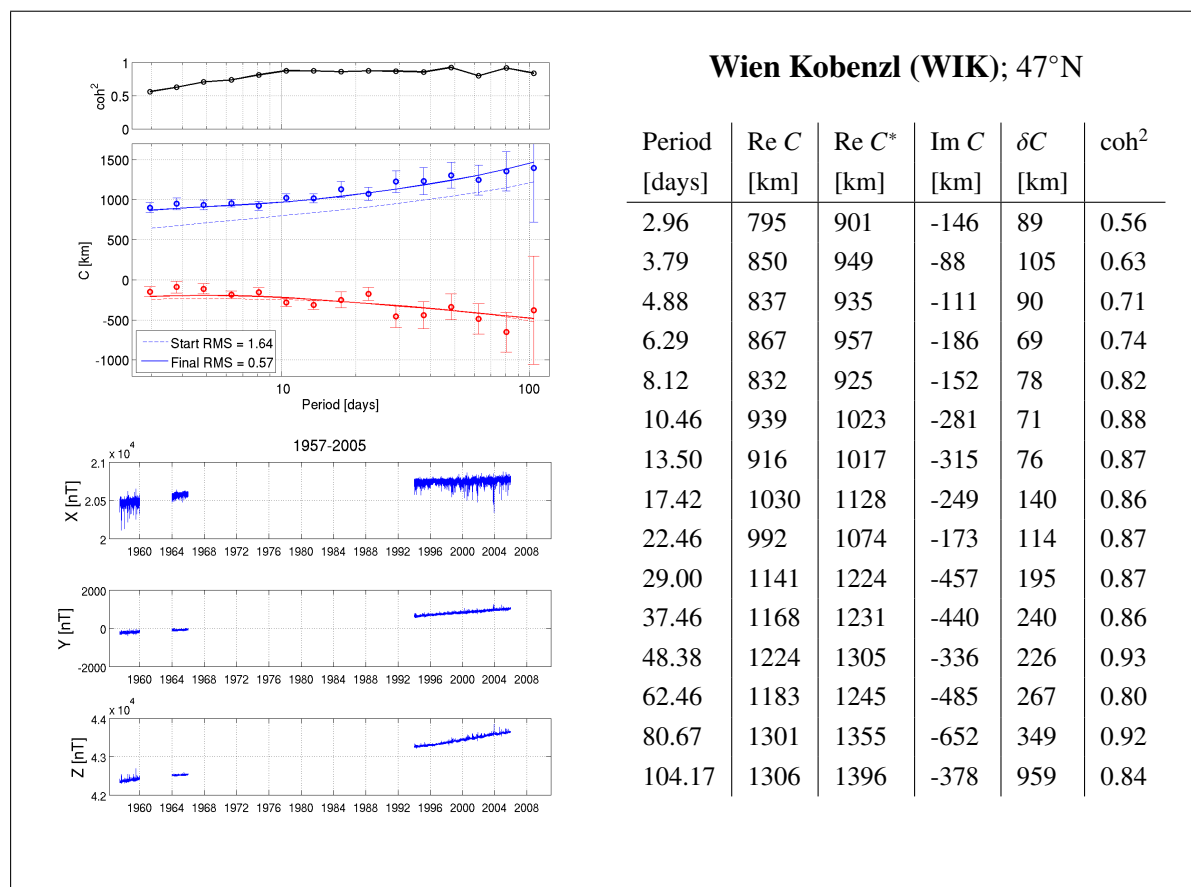
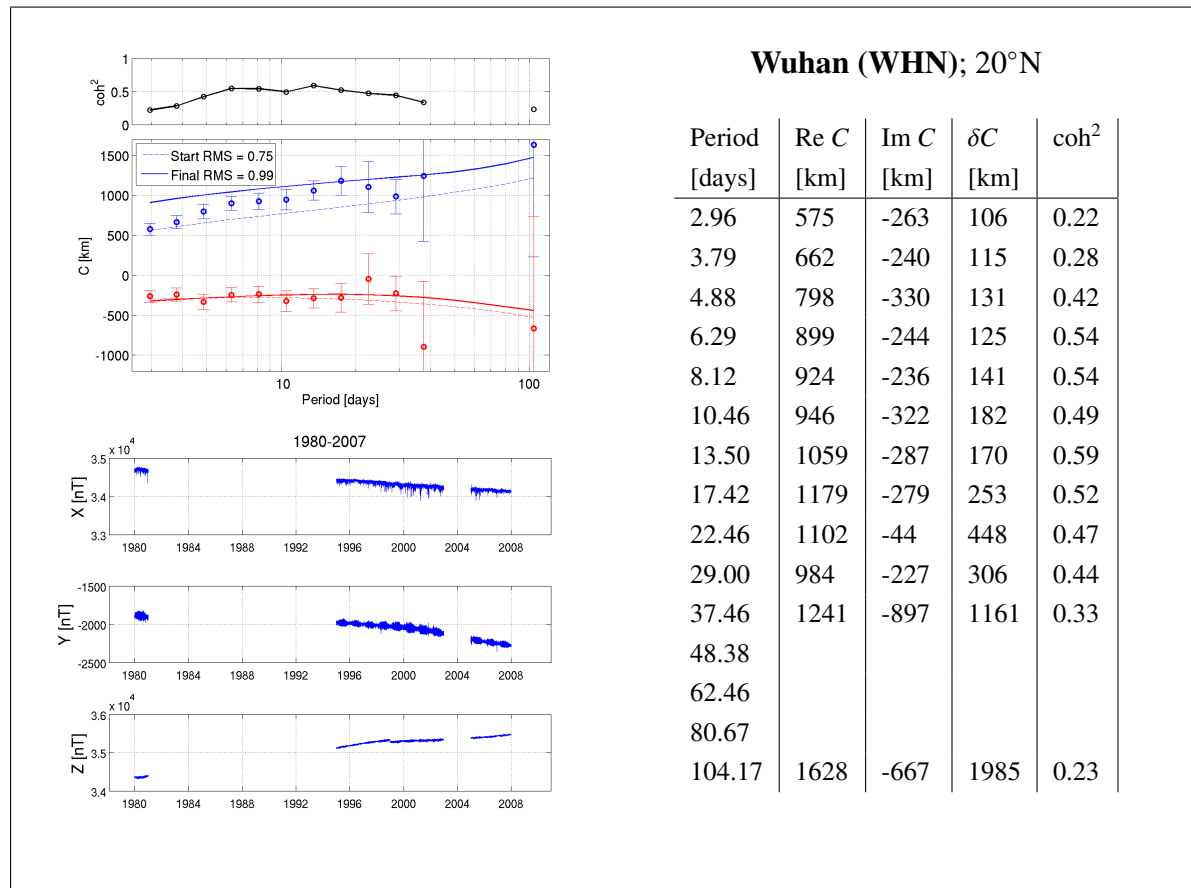


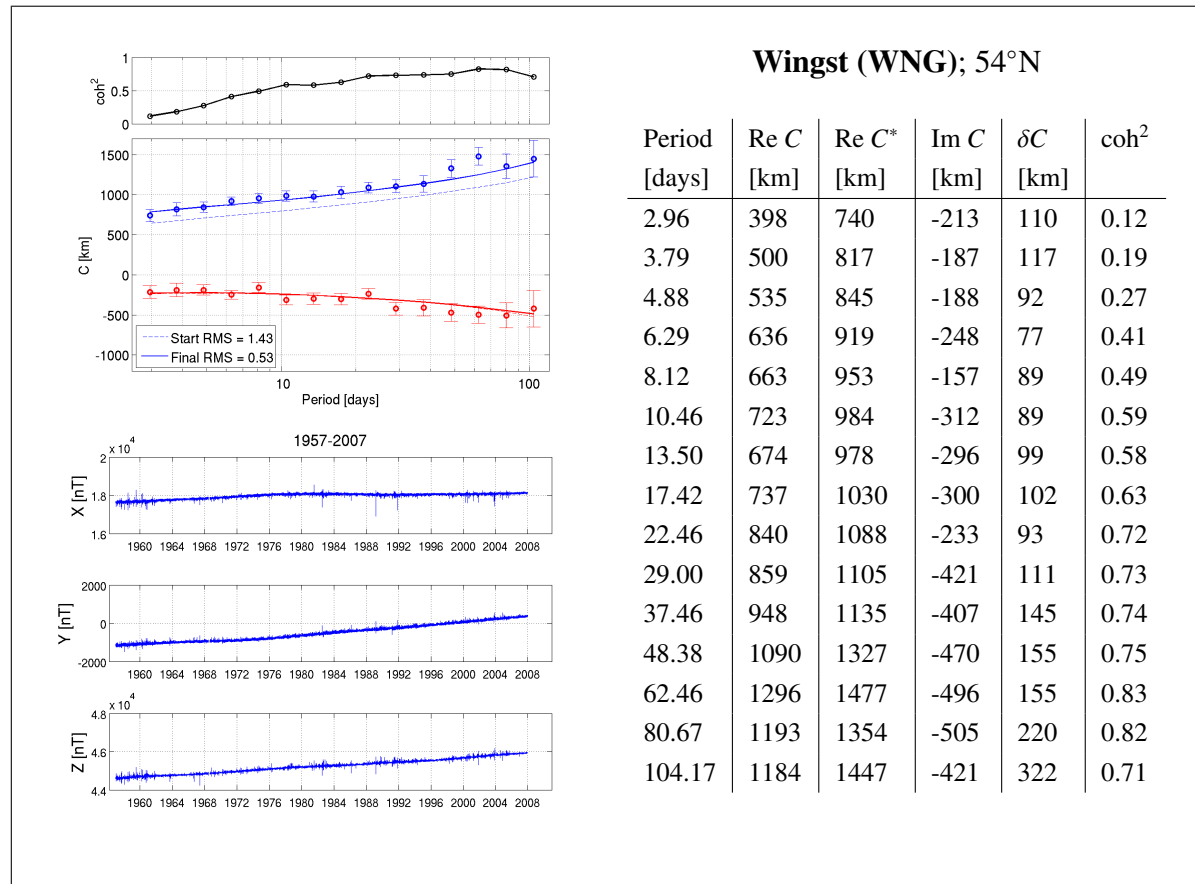
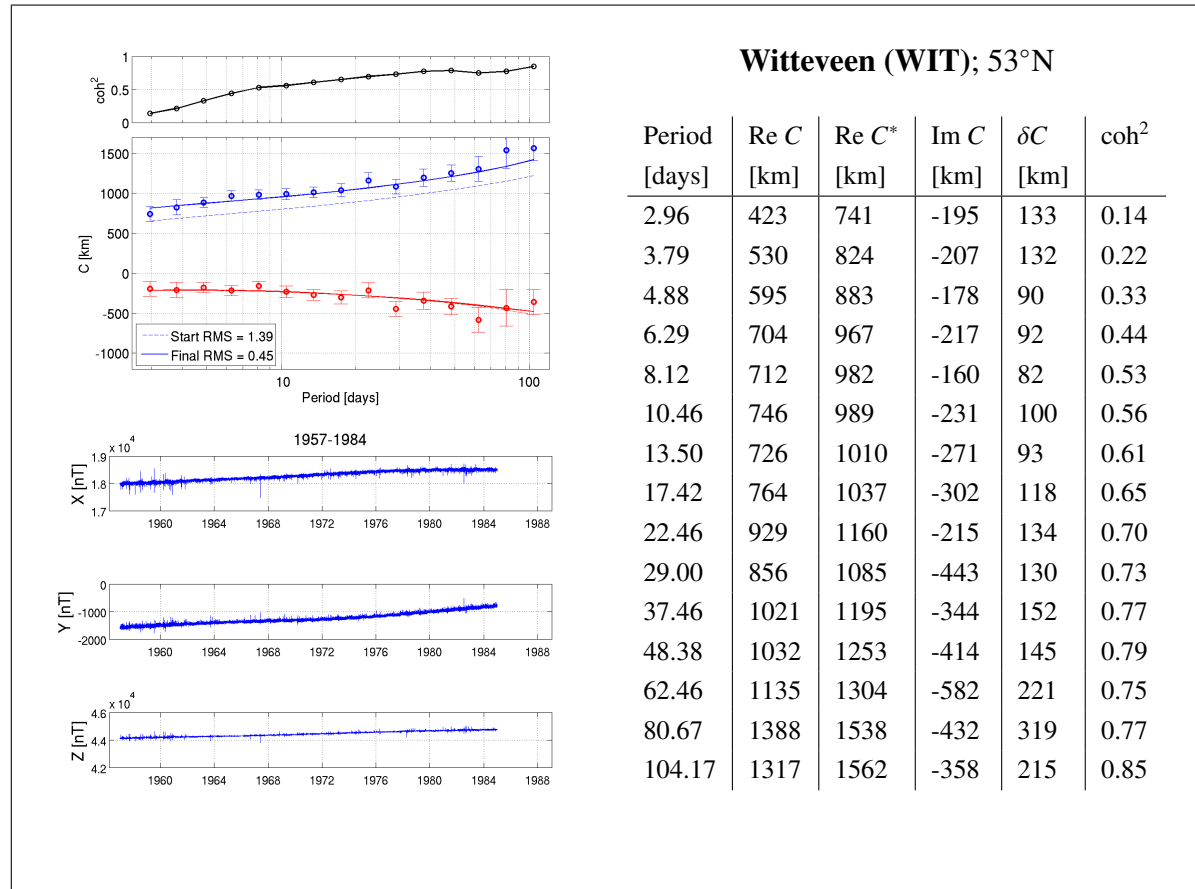


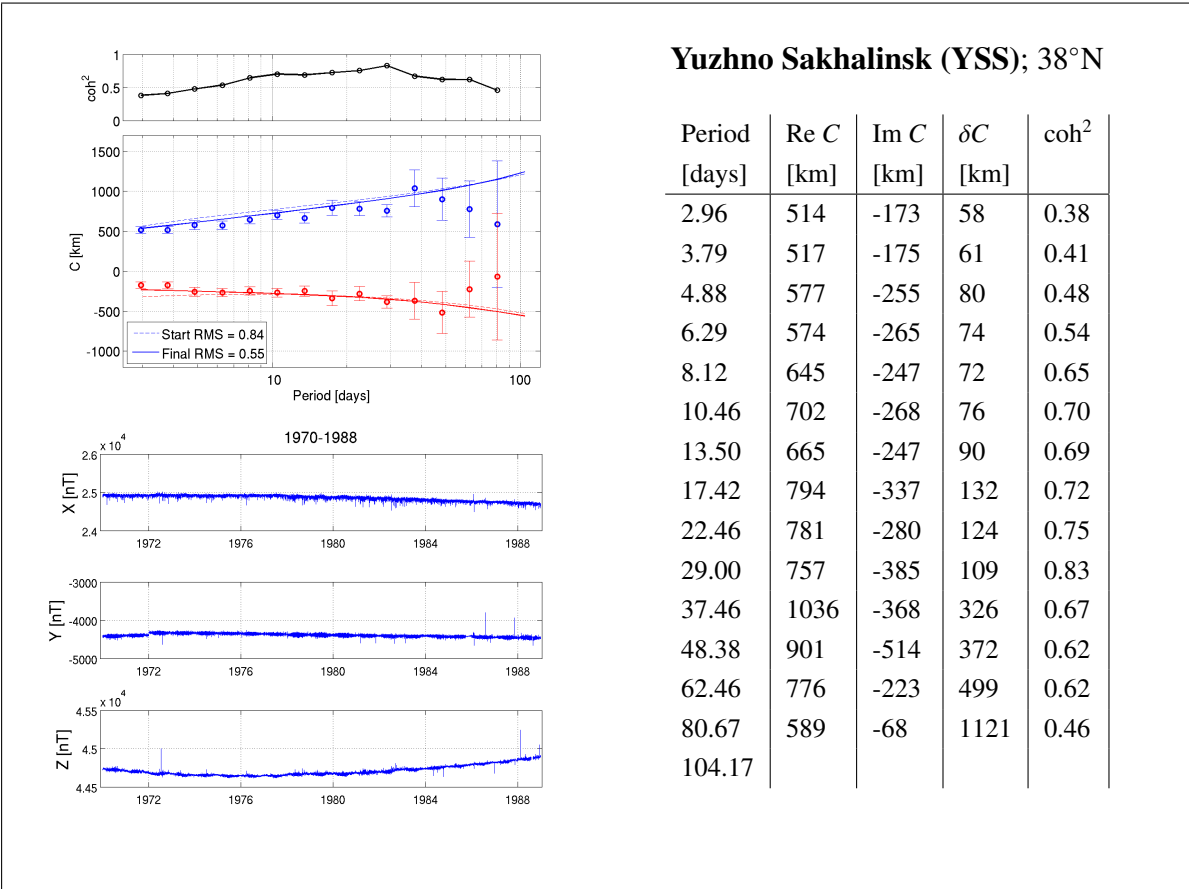












Code	Station	latitude	longitude	gm latitude	gm longitude	Data length
AAA	Alma Ata	43.250	76.920	34.29	152.74	1963-2007
ABG	Alibag	18.638	72.872	10.19	146.16	1957-2007
AIA	Faraday Islands	-65.250	295.730	-55.06	5.49	1957-2007
ALM	Almeria	36.853	357.540	39.83	77.12	1957-1966
AML	Amberley	-43.152	172.722	-46.80	254.13	1961-1977
AMS	Martin de Vivies	-37.796	77.574	-46.39	144.27	1981-2007
AMT	Amatsia	31.550	34.917	28.12	112.26	1979-2000
API	Apia	-13.807	188.225	-15.36	262.65	1957-2007
AQU	L'Aquila	42.383	13.317	42.42	94.50	1960-2007
ARS	Arti	56.433	58.967	49.13	139.91	1973-2007
ASH	Vannovskaya	37.950	58.100	31.01	135.09	1972-1990
ASO	Aso	32.882	131.009	23.35	200.75	1957-1959
ASP	Alice Springs	-23.761	133.883	-32.91	208.18	1992-2007
BDV	Budkov	49.080	14.015	48.97	97.61	1994-2007
BEL	Belsk	51.837	20.792	50.24	105.17	1966-2007
BFE	Brorfelde	55.625	11.672	55.45	98.48	1981-2007
BFO	Black Forest	48.330	8.320	49.06	91.80	2006-2007
BGY	Bar Gyora	31.723	35.088	28.26	112.46	2003-2007
BJI	Beijing	40.040	116.175	29.87	187.02	1960-1980
BMT	Beijing Ming Tombs	40.300	116.200	30.13	187.04	1996-2007
BOU	Boulder	40.130	254.760	48.40	320.59	1967-2007
BOX	Borok	58.070	38.230	53.41	123.52	1980-2007
BSL	Bay St. Louis	30.350	270.370	40.05	339.79	1986-2007
CBI	Chichijima	27.096	142.185	18.47	211.63	1991-2006
CDP	Chengdu	31.000	103.700	20.77	175.86	1995-2007
CLF	Chambon-la-Forêt	48.025	2.261	49.84	85.68	1957-2007
CNB	Canberra	-35.315	149.363	-42.71	226.94	1979-2007
CNH	Changchun	43.827	125.299	33.96	194.80	1979-2007
COI	Coimbra	40.220	351.580	44.14	71.99	1992-1994
CTA	Charters Towers	-20.090	146.264	-28.01	220.97	1990-2007
CZT	Port Alfred	-46.431	51.867	-51.35	113.28	1982-2007
DAL	Dallas	32.980	263.250	42.15	331.47	1964-1974
DLR	Del Rio	29.490	259.080	38.30	327.31	1982-2007
DOU	Dourbes	50.100	4.600	51.43	88.90	1957-2007
EBR	Ebro	40.821	0.493	43.18	81.30	1957-2007
ELT	Eilat	29.670	34.950	26.27	111.89	1998-2007
ESA	Esashi	39.237	141.355	30.46	209.42	2000-2007
ESK	Eskdalemuir	55.317	356.800	57.80	83.75	1957-2007
EYR	Eyrewell	-43.410	172.350	-47.11	253.83	1978-2007
FRD	Fredericksburg	38.200	282.630	48.40	353.38	1957-2007
FRN	Fresno	37.090	240.280	43.52	305.25	1982-2007
FUR	Furstenfeldbruck	48.165	11.277	48.38	94.61	1957-2007

Table 1 Station details: acronyms, names, locations (both in geographic and geomagnetic coordinates), and time interval for estimating C-responses.

Code	Station	latitude	longitude	gm latitude	gm longitude	Data length
GCK	Grocka	44.633	20.767	43.29	102.40	1965-2007
GLM	Golmud	36.400	94.900	26.39	168.06	1995-2006
GNA	Gnangara	-31.780	115.947	-41.93	188.84	1957-2007
GUI	Guimar	28.321	343.559	33.78	60.59	1993-2007
GZH	Guangzhou	23.093	113.343	12.88	184.84	1960-2007
HAD	Hartland	51.000	355.517	53.90	80.17	1957-2007
HBK	Hartebeesthoek	-25.883	27.707	-27.13	94.40	1972-2007
HER	Hermanus	-34.425	19.225	-33.98	84.02	1957-2007
HLP	Hel	54.608	18.817	53.24	104.63	1966-2007
HON	Honolulu	21.320	202.000	21.64	269.74	1961-2007
HRB	Hurbanovo	47.873	18.190	46.87	101.11	1957-2007
HTY	Hatizyo	33.073	139.825	24.20	208.98	1986-2005
IRT	Irkutsk	52.167	104.450	41.93	176.90	1957-2007
ISK	Istanbul Kandilli	41.063	29.062	38.40	109.11	1957-1999
JAI	Jaipur	26.920	78.900	17.92	152.32	1979-1987
KAK	Kakioka	36.232	140.186	27.37	208.95	1957-2007
KDU	Kakadu	-12.686	132.472	-21.99	205.61	1995-2007
KIV	Kiev	50.720	30.300	47.57	113.43	1958-1991
KNY	Kanoya	31.424	130.880	21.89	200.75	1958-2006
KNZ	Kanozan	35.256	139.956	26.38	208.65	1980-2007
KZN	Kazan	55.830	48.850	49.75	131.59	1978-1989
KOU	Kourou	5.210	307.269	14.89	19.66	1996-2007
KSH	Kashi	39.500	76.000	30.64	151.44	1995-2007
LGR	Logrono	42.450	357.500	45.29	78.80	1963-1966
LNP	Lunping	25.000	121.167	14.99	192.14	1965-2007
LRM	Learmonth	-22.222	114.101	-32.42	186.46	1990-2007
LVV	Lviv	49.900	23.750	47.87	107.11	1957-2007
LZH	Lanzhou	36.087	103.845	25.86	176.08	1980-2007
MAB	Manhay	50.300	5.680	51.42	90.05	1995-2007
MBO	Mbour	14.384	343.033	20.11	57.47	1957-2007
MID	Midway	28.210	182.620	25.02	249.50	2000-2002
MIZ	Mizusawa	39.112	141.204	30.32	209.30	2000-2007
MMB	Memambetsu	43.910	144.189	35.35	211.26	1957-2007
MNK	Pleshenitzi(Minsk)	54.500	27.883	51.60	112.82	1961-1994
MOS	Moscow	55.467	37.312	51.04	121.57	1957-2005
MZL	Manzhouli	49.600	117.400	39.45	187.70	1995-2007
NCK	Nagycenk	47.633	16.717	46.90	99.62	1993-2007
NGK	Niemegk	52.072	12.675	51.88	97.64	1957-2007
NVS	Novosibirsk	55.030	82.900	45.57	159.51	1966-2007
ODE	Odessa	46.780	30.880	43.66	112.55	1957-1991
PAG	Panagyurishte	42.520	24.180	40.65	104.95	1964-2007
PEG	Penteli	38.083	23.933	36.37	103.43	1999-2003

Table 1 Station details: acronyms, names, locations (both in geographic and geomagnetic coordinates), and time interval for estimating *C*-responses.

Code	Station	latitude	longitude	gm latitude	gm longitude	Data length
PET	Paratunka	53.100	158.630	45.95	221.73	1969-1995
PMG	Port Moresby	-9.460	147.160	-17.36	220.51	1958-1991
PPT	Pamatai	-17.567	210.426	-15.14	285.14	1968-1994
PST	Port Stanley	-51.703	302.110	-41.69	11.50	1994-2007
QIX	Qianling	34.600	108.200	24.34	179.99	1995-2006
RSV	Rude Skov	55.483	12.457	55.18	99.14	1957-1980
SFS	San Fernando	36.462	353.795	40.09	73.18	1995-2004
SGE	South Georgia	-54.280	323.520	-45.57	28.81	1975-1982
SHL	Shillong	25.550	91.880	15.68	164.72	1976-1987
SJG	San Juan	18.110	293.850	28.31	6.08	1967-1982
SPT	San Pablo	39.547	355.651	42.78	75.98	1997-2007
SSH	Sheshan	31.097	121.187	21.08	191.89	1983-2006
SSO	Simosato	33.575	135.940	24.39	205.19	1957-1965
SUA	Surlari	44.680	26.253	42.39	107.58	1994-2007
SVD	Ekaterinburg	56.730	61.070	49.14	142.07	1957-1980
TAM	Tamanrasset	22.792	5.530	24.66	81.76	1993-2007
TEN	Las Mesas	28.480	343.740	33.91	60.82	1973-1992
TFS	Tbilisi	42.080	44.700	36.91	123.82	1957-2001
THJ	Tonghai	24.000	102.700	13.79	174.81	1995-2007
THY	Tihany	46.900	17.900	45.99	100.47	1957-2007
TKT	Tashkent	41.333	69.617	33.05	146.02	1975-1981
TOL	Toledo	39.880	355.950	43.06	76.39	1957-1980
TOO	Toolangi	-37.530	145.470	-45.38	223.12	1957-1979
TRW	Trelew	-43.248	294.685	-33.05	5.62	1957-2007
TSU	Tsumeb	-19.202	17.584	-18.97	85.83	1964-2007
TUC	Tucson	32.170	249.270	39.88	316.11	1957-1994
VAL	Valentia	51.930	349.750	55.79	74.63	1957-2007
VLA	Gornotayezhnaya	43.683	132.167	34.19	200.79	1958-1988
VSS	Vassouras	-22.400	316.350	-13.29	26.61	2000-2007
WAT	Watheroo	-30.318	115.877	-40.47	188.90	1957-1958
WHN	Wuhan	30.528	114.559	20.33	185.82	2000-2007
WIK	Wien Kobenzl	48.265	16.318	47.58	99.49	1957-1984
WIT	Witteveen	52.813	6.668	53.66	92.20	1957-1984
WNG	Wingst	53.743	9.073	54.12	95.00	1957-2007
YSS	Yuzhno Sakhalinsk	46.950	142.717	38.24	209.49	1970-1988

Table 1 Station details: acronyms, names, locations (both in geographic and geomagnetic coordinates), and time interval for estimating *C*-responses.

Bibliography

- M. Abramowitz and I. Stegun. *Pocketbook of mathematical functions*. Verlah Harri Deutsch, 1984.
- A. Ampere. *Memoir on the Mathematical Theory of Electrodynamic Phenomena, Uniquely Deduced from Experience*. 1826.
- D. Avdeev, A. Kuvshinov, O. Pankratov, and G. Newman. 3-D EM modelling using fast integral equation approach with Krylov subspaces accelerator. *Extended abstracts book, Volume 2, 62nd EAGE Conference & Technical Exhibition*, 2000.
- D. Avdeev, A. Kuvshinov, O. Pankratov, and G. Newman. Three-dimensional induction logging problems, Part I: An integral equation solution and model comparisons. *Geophysics*, 67:413–426, 2002.
- D. B. Avdeev and A. D. Avdeeva. 3D magnetotelluric inversion using a limited-memory quasi-newton optimization. *Geophysics*, 74:45–57, 2009.
- G. Backus, R. Parker, and C. Constable. *Foundations of Geomagnetism*. Cambridge University Press, 1996.
- R. Banks. Geomagnetic variations and the electrical conductivity of the upper mantle. *Geophys. J. R. astr. Soc.*, 17:457–487, 1969.
- W. Barlow. On the spontaneous electrical currents observed in wires of the electric telegraph. *Phil. Trans. R. Soc. London A.*, 139:237–276, 1849.
- T. Becker and L. Boschi. A comparison of tomographic and geodynamic mantle models. *Geochem. Geophys. Geosyst.*, 3:doi:10.129/2001GC000168, 2002.
- S. Chapman. The solar and lunar diurnal variations of terrestrial magnetism. *Phil. Trans. R. Soc. London A.*, 218:1–118, 1919.
- S. Chapman and T. Whitehead. Influence of electrically conducting material within the Earth on various phenomena of terrestrial magnetism. *Trans. Cambridge Philosophical Society*, 22:463–482, 1922.

- D. A. Chave and D. Thomson. Some comments on magnetotelluric response function estimation. *J. Geophys. Res.*, 94:14215–14225, 1989.
- A. Chulliat, X. Lalanne, L. Gaya-Peque, F. Truong, and J. Savary. The new Easter Island magnetic observatory. *Proceedings of the XIIIth IAGA workshop on geomagnetic observatory instruments, data acquisition and processing (Love, J.J.)*; *US Geological Survey Open-File Report 20091*, 20091226, pages 47–53, 2009.
- K. Clement. Das grosse Nordlicht in der Nacht zum 29 August 1959 und die Telegraphenverwirrung in Nord-Amerika und Europe. *Hamburg*, pages 1–21, 1860.
- J. Connolly. Computation of phase equilibria by linear programming: A tool for geodynamic modelling and an application to subduction zone decarbonation. *Earth Planet. Sci. Lett.*, 236:524, 2005.
- S. Constable. SEO3: a new model of olivine electrical conductivity. *Geochem. Geophys. Geosys.*, 5:Q01006, 2006.
- S. Constable. Geomagnetism. In: *Kono, M. (editor) Treatise on Geophysics, Elsevier*, 5: 237–276, 2007.
- S. Constable, T. Shankland, and A. Duba. The electrical conductivity of an isotropic olivine mantle. *J. Geophys. Res.*, 97:3397–3404, 1992.
- C. De Boor. *A Practical Guide To Splines*. Springer, Berlin, 1978.
- S. Della Mora, L. Boschi, P. Tackley, T. Nakagawa, and D. Giardini. Low seismic resolution cannot explain S/P decorrelation in the lower mantle. *Geophys. Res. Lett.*, 2011. doi: 10.1029/2011GL047559, inpress.
- B. Dibner. *Oersted and the Discovery of Electromagnetism*. Blaisdell Publ. Co., 1962.
- P. Dierckx. *Curve and Surface Fitting with Splines*. Clarendon, Oxford, 1993.
- O. Dorn, H. Bertete-Aquirre, J. G. Berryman, and G. C. Papanicolaou. A nonlinear inversion method for 3-D electromagnetic imaging using adjoint fields. *Inverse problems*, 15:1523–1558, 1999.
- W. Du Frane, J. Roberts, D. Toffelmier, and J. Tyburczy. Anisotropy of electrical conductivity in dry olivine. *Geophys. Res. Lett.*, 32:L24315, 2005.
- A. Dziewonski and D. Anderson. Preliminary reference Earth model. *Phys. Earth Planet Inter.*, 25:297–356, 1981.
- B. Efron. *The Jackknife, the Bootstrap, and Other Resampling Plans*. Society for Industrial and Applied Mathematics, Philadelphia, 1982.

- G. Egbert, J. Booker, and A. Schultz. Very long period magneto-tellurics at Tucson observatory: Implications for mantle conductivity. *J. Geophys. Res.*, 97:15099–15112, 1992.
- P. Eilers and B. Marx. Flexible smoothing with B-splines and penalties. *Statistical science*, 11:89–121, 1996.
- M. Everett, S. Constable, and C. Constable. Effects of near-surface conductance on global satellite induction responses. *Geophys. J. Int.*, 153:277–286, 2003.
- L. Eyges. *The Classical Electromagnetic Field*. Dover Publications, New York, 1972.
- C. Faccena, L. Jolivet, C. Piromallo, and A. Morelli. Subduction and the depth of convection in the Mediterranean mantle. *J. Geophys. Res.*, 108:No.B2,2099,doi:10.1029/2001JB001690, 2003.
- E. Fainberg, A. Kuvshinov, and B. Singer. Electromagnetic induction in a spherical earth with non-uniform oceans and continents in electric contact with the underlying medium - I. theory, method, example. *Geophys. J. Int.*, 102:273–281, 1990.
- M. Faraday. *Experimental Researches in Electricity*. Richard and John Edward Taylor, 1839.
- A. Fichtner and J. Trampert. Hessian kernels of seismic data functionals based upon adjoint techniques. *Geophys. J. Int.*, 185:775–798, 2011.
- C. Finlay, S. Maus, C. Beggan, M. Hamoudi, F. Lowes, N. Olsen, and Thébault. Evaluation of candidate geomagnetic field models for igrf-11. *Earth Planet Space*, xx:1–19, 2010.
- I. Fujii and A. Schultz. The 3-D electromagnetic response of the Earth to the ring current and auroral oval excitation. *Geophys. J. Int.*, 151:689–709, 2002.
- Y. Fukao, S. Widiyantoro, and M. Obayashi. Stagnant slabs in the upper and lower mantle transition region. *Rev. Geophys.*, 39:291–323, 2001.
- Y. Fukao, T. Koyama, M. Obayashi, and H. Utada. Trans-Pacific temperature field in the mantle transition region derived from seismic and electromagnetic tomography. *Earth and Planetary Science Letters*, 217:425–434, 2004.
- T. Gamble, J. Clarke, and W. Goubau. Magnetotellurics with a remote magnetic reference. *Geophysics*, 4:53–68, 1979.
- A. Greenbaum. Iterative methods for solving linear systems. *Society of Industrial and Applied Mathematics*, 1997.
- D. Gubbins. Geomagnetic reversals. *Nature*, 452:165–167, 2008.

- L. Hirsch and T. Shankland. Quantitative olivine-defect chemical model: insights on electrical conduction, diffusion, and the role of Fe content. *Geophys. J. Int.*, 114:21–35, 1993.
- L. Hirsch, T. Shankland, and A. Duba. Electrical conduction and polaron mobility in Fe-bearing olivine. *Geophys. J. Int.*, 114:36–44, 1993.
- P. Huber. *Robust statistics*. Wiley, New York, 1981.
- M. Ichiki, M. Uyeshima, H. Utada, Z. Guoze, T. Ji, and M. Mingzhi. Upper mantle conductivity structure of the back-arc region beneath north-eastern China. *Geophys. Res. Lett.*, 28: 3773–3776, 2001.
- T. Inoue, H. Yurimoto, and Y. Kudoh. Hydrous modified spinel, $\text{Mg}_{1.75}\text{SiH}_{0.5}\text{O}_4$: a new water reservoir in the mantle transition zone. *Geophys. Res. Lett.*, 22:117–120, 1995.
- T. Irifune and A. Ringwood. Phase transformations in subducted oceanic crust and buoyancy relationships at depths of 600–800 km in the mantle. *Earth Planet Sci. Lett.*, 77:101–110, 1993.
- E. Ito and T. Takahashi. Post-spinel transformations in the system $\text{Mg}_2\text{SiO}_4\text{--Fe}_2\text{SiO}_4$ and some geophysical implications. *J. Geophys. Res.*, 94:10637–10646, 1989.
- J. Jackson. *Classical electrodynamics*. John Wiley & Sons, New York, 1975.
- E. Kamke. *Differentialgleichungen, Vol I*. Akad. Verlagsges., Leipzig, 1959.
- S. Karato. The role of hydrogen in the electrical conductivity in the upper mantle. *Nature*, 347:272–273, 1990.
- S. Karato. Remote sensing of hydrogen in Earth’s mantle. *Rev. Miner. Geochem.*, 62:343, 2006.
- T. Katsura and E. Ito. Determination of the partitioning between perovskite and magnetite. *Geophys. Res. Lett.*, 23:2005–2008, 1996.
- T. Katsura, K. Sato, and E. Ito. Electrical conductivity of silicate perovskite at lower-mantle conditions. *Nature*, 395:493–495, 1998.
- T. Katsura, S. Yokoshi, K. Kawabe, A. Shatskiy, M. Okube, H. Fikui, E. Ito, A. Nozawa, and K. Funakoshi. Pressure dependence of electrical conductivity of $(\text{Mg,Fe})\text{SiO}_3$ ilmenite. *Phys. Chem. Mineral*, 34:249–255, 2007.
- A. Kelbert, G. Egbert, and A. Schultz. A nonlinear conjugate 3-D inversion of global induction data. Resolution studies. *Geophys. J. Int.*, 173:365–381, 2008.

- A. Kelbert, A. Schultz, and G. Egbert. Global electromagnetic induction constraints on transition-zone water content variations. *Nature*, 460:1003–1007, 2009.
- A. Khan, J. Connolly, and N. Olsen. Constraining the composition and the thermal state of the mantle beneath Europe from inversion of long-period electromagnetic sounding data. *J. Geophys. Res.*, 111:B10102, 2006. doi: 10.1029/2006JB004270.
- A. Khan, L. Boschi, and J. Connolly. On mantle chemical and thermal heterogeneities and anisotropy as mapped by inversion of global surface wave data. *J. Geophys. Res.*, 111: B09305, 2009. doi: 10.1029/2009JB006399.
- A. Khan, A. Kuvshinov, and A. Semenov. On the heterogeneous electrical conductivity structure of the Earth's mantle with implications for transition zone water content. *J. Geophys. Res.*, 116:doi:10.1029/2010JB007458, 2011.
- M. Korte, M. Manda, H. Linthe, A. Hemshorn, P. Kotze, and E. Ricaldi. New geomagnetic field observations in the South Atlantic anomaly region. *Ann. Geophys.*, 52:65–82, 2009.
- T. Koyama. *A study on the electrical conductivity of the mantle by voltage measurements of submarine cables*. PhD thesis, University of Tokyo, 2001.
- T. Koyama, H. Shimizu, H. Utada, M. Ichiki, E. Ohtani, and R. Hae. Water content in the mantle transition zone beneath the North Pacific derived from the electrical conductivity anomaly. *AGU Geophys. Monogr. Ser.*, 168:171–179, 2006.
- F. Kuo and J. Kaiser. *System analysis by digital computer*. New York, Wiley, 1966.
- A. Kuvshinov. 3-D global induction in the oceans and solid Earth: recent progress in modeling magnetic and electric fields from sources of magnetospheric, ionospheric and oceanic origin. *Surv. in Geophys.*, 2008. doi: 10.1007/s10712-008-9045-z.
- A. Kuvshinov. Deep electromagnetic studies from land, sea, and space: Progress status in the past 10 years. *Surv. Geophys.*, 2011. doi: 10.1007/s10712-011-9118-2.
- A. Kuvshinov and N. Olsen. A global model of mantle conductivity derived from 5 years of CHAMP, Ørsted, and SAC-C magnetic data. *Geophys. Res. Lett.*, 33:L18301, 2006. doi: doi:10.1029/2006GL027083.
- A. Kuvshinov and A. Semenov. 3-D mapping of mid-mantle conductivity based on inversion of ground based C-responses. I, An approach and its validation. *Geophys. J. Int.*, submitted, 2011.
- A. Kuvshinov, D. Avdeev, and O. Pankratov. Global induction by Sq and Dst sources in the presence of oceans: bimodal solutions for non-uniform spherical surface shells above

- radially symmetric earth models in comparison to observations. *Geophys. J. Int.*, 137:630–650, 1999.
- A. Kuvshinov, J. Velimsky, P. Tarits, A. Semenov, O. Pankratov, L. Tøffner-Clausen, Z. Martinec, N. Olsen, T. Sabaka, and A. Jackson. *Level 2 products and performances for mantle studies with Swarm*. Final report on ESA project 2009, 2010. URL http://esamultimedia.esa.int/docs/EarthObservation/Induction_Study_150110.pdf.
- A. V. Kuvshinov, D. B. Avdeev, O. V. Pankratov, S. A. Golyshev, and N. Olsen. Modelling electromagnetic fields in 3D spherical Earth using fast integral equation approach. In M. S. Zhdanov and P. E. Wannamaker, editors, *3D Electromagnetics*, chapter 3, pages 43–54. Elsevier, Holland, 2002a.
- A. V. Kuvshinov, N. Olsen, D. B. Avdeev, and O. V. Pankratov. Electromagnetic induction in the oceans and the anomalous behaviour of coastal *C*-responses for periods up to 20 days. *Geophys. Res. Lett.*, 29:doi:10.1029/2001GL014409, 2002b.
- A. V. Kuvshinov, H. Utada, D. Avdeev, and T. Koyama. 3-D modelling and analysis of Dst *C*-responses in the North Pacific ocean region, revisited. *Geophys. J. Int.*, 160:505–526, 2005. doi: 10.1111/j.1365-246X.2005.02477.x.
- B. Lahiri and A. Price. Electromagnetic induction in non-uniform conductors, and the determination of the conductivity of the Earth from terrestrial magnetic variations. *Phil. Trans. R. Soc. London A.*, 237:509–540, 1939.
- H. Lamb. On the vibrations of a spherical shell. *Proc. London Math. Soc.*, 14:50–56, 1883.
- G. Laske and G. Masters. A global digital map of sediment thickness. *EOS Trans. AGU*, 78:F483, 1997.
- T. Lay, Q. Williams, and E. Garnero. The core-mantle boundary layer and deep mantle dynamics. *Nature*, 392:461–468, 1998.
- X. Li and R. Jeanloz. Laboratory studies of the electrical conductivity of silicate perovskite at high pressures and temperatures. *J. Geophys. Res.*, 95:5067–5078, 1990.
- J. Lin, S. Weir, D. Jackson, W. Evans, Y. Vohra, W. Qiu, and C. Yoo. Electrical conductivity of the lower mantle ferropericlase across the electronic spin transition. *Geophys. Res. Lett.*, 34:L16305, 2007. doi: 10.1029/2007GL030523.
- D. Lizarralde, A. Chave, G. Hirth, and A. Schultz. Long period magnetotelluric study using Hawaii-to-California submarine cable data: implications for mantle conductivity. *J. Geophys. Res.*, 100:17873–17884, 1995.

- C. Manoj, A. Kuvshinov, S. Maus, and H. Lühr. Ocean circulation generated magnetic signals. *Earth, Planets and Space*, 58:429–439, 2006.
- Z. Martinec and J. Velimsky. The adjoint sensitivity method of EM induction for CHAMP magnetic data. *Geophys. J. Int.*, 179:1372–1396, 2009.
- J. Matzka, N. Olsen, C. Fox Maule, L. Pedersen, A. Berarducci, and S. Macmillan. Geomagnetic observations on Tristan da Cunha, South Atlantic ocean. *Ann. Geophys.*, 52:97–105, 2009.
- J. Maxwell. A dynamical theory of the electromagnetic field. *Phil. Trans. R. Soc. London A.*, 155:459–512, 1865.
- K. McDonald. Penetration of the geomagnetic secular field through a mantle with variable conductivity. *J. Geophys. Res.*, 62:117–141, 1957.
- C. Megnin and B. Romanowicz. The three-dimensional shear velocity structure of the mantle from the inversion of body, surface and higher mode waveforms. *Geophys. J. Int.*, 143:709–728, 2000.
- M. Morse and H. Feshbach. *Methods of Theoretical Physics*. New York: MacGraw-Hill, 1953.
- K. Mosegaard. Resolution analysis of general inverse problems through inverse Monte-Carlo sampling. *Inverse Probl.*, 14:405–416, 1998.
- M. Murakami, K. Hirose, K. Kawamura, N. Sata, and Y. Ohishi. Post-perovskite phase transition in MgSiO_3 . *Science*, 304:855–858, 2004.
- S. L. Neal, R. L. Mackie, J. C. Larsen, and A. Schultz. Variations in the electrical conductivity of the upper mantle beneath North America and the Pacific Ocean. *J. Geophys. Res.*, 105:8229–8242, 2000.
- G. A. Newman and D. L. Alumbaugh. Three-dimensional magnetotelluric inversion using non-linear conjugate gradient on induction effects of geomagnetic daily variations from equatorial gradients. *Geophys. J. Int.*, 140:410–424, 2000.
- J. Nocedal and S. J. Wright. *Numerical Optimization*. Springer, 2006.
- M. Obayashi, H. Sugioka, H. Yoshimitsu, and Y. Fukao. High temperature anomalies oceanward of subducting slabs at the 410 km discontinuity. *Earth Planet Sci. Lett.*, 243:149–158, 2006.
- K. Ohta, S. Onoda, K. Hirose, R. Shinmyo, K. Shimizu, K. Sata, Y. Ohishi, and A. Yasuhara. The electrical conductivity of post-perovskite in Earth's D'' layer. *Science*, 320:89–91, 2008.

- N. Olsen. The electrical conductivity of the mantle beneath Europe derived from *C*-responses from 3 to 720 hr. *Geophys. J. Int.*, 133:298–308, 1998.
- N. Olsen. Long-period (30 days–1 year) electromagnetic sounding and the electrical conductivity of the lower mantle beneath Europe. *Geophys. J. Int.*, 138:179–187, 1999.
- O. Pankratov and A. Kuvshinov. General formalism for the efficient calculation of derivatives of EM frequency domain responses and derivatives of the misfit. *Geophys. J. Int.*, 181:229–249, 2010.
- O. Pankratov, D. Avdeev, and A. Kuvshinov. Electromagnetic field scattering in a homogeneous Earth: a solution to the forward problem. *Phys. Solis. Earth*, 31:201–209, 1995.
- O. Pankratov, A. Kuvshinov, and D. Avdeev. High-performance three-dimensional electromagnetic modeling using modified Neumann series. Anisotropic case. *J. Geomagn. Geoelectr.*, 49:1541–1547, 1997.
- J. Peyronneau and J. Poirer. Electrical conductivity of the Earth's lower mantle. *Nature*, 342:537–539, 1989.
- R. Roberts. The long-period electromagnetic response of the Earth. *Geophys. J. R. Astr. Soc.*, 78:547–572, 1984.
- W. Rodi and R. L. Mackie. Nonlinear conjugate gradients algorithm for 2-D magnetotelluric inversion. *Geophysics*, 66:174–187, 2000.
- I. Rokityansky. *Geoelectromagnetic investigation of the Earth's crust and mantle*. Berlin-Heidelberg-New York: Springer, 1982.
- C. Romano, B. Poe, N. Kreidie, and C. McCammon. Electrical conductivities of pyrope-almandine garnets up to 19 GPa and 1700°C. *Mineral Soc. America*, 91:1371–1377, 2006.
- B. Romanowicz. Global mantle tomography: progress status in the past 10 years. *Ann. Rev. Earth Planet*, 31:303–328, 2003.
- U. Schmucker. *Anomalies of geomagnetic variations in the south-western United States*, volume 13. Bull. Scripps Inst. Ocean, Univ. Calif., 1970.
- U. Schmucker. A spherical harmonic analysis of solar daily variations in the years 1964–1965: response estimates and source fields for global induction-II.Results. *Geophys. J. Int.*, 136:455–476, 1999.
- U. Schmucker. Horizontal spatial gradient sounding and geomagnetic depth sounding in the period range of daily variations. In: *Protokoll über das Kolloquium Elektromagnetische Tiefenforschung, Königstein*, pages 228–237, 2003.

- U. Schmucker. Substitute conductors for electromagnetic response estimates. *PAGEOPH*, 125:341–367, 1987.
- A. Schultz. EMScope: a continental scale magnetotelluric observatory and data discovery resource. *Data Sci. J.*, 8:IGY6–IGY20, 2010.
- A. Schultz and J. Larsen. On the electrical conductivity of the mid-mantle: I calculation of equivalent scalar magnetotelluric response functions. *Geophys. J. Int.*, 88(3):733–761, 1987.
- A. Schultz and G. Pritchard. A three-dimensional inversion for large scale structure in a spherical domain. *Three dimensional electromagnetics (Spies, B. and Oristaglio, M.); Geophysical Development Series; Society of Exploration Geophysicists*, 7:451–476, 1999.
- A. Schuster. The diurnal variation of terrestrial magnetism. *Phil. Trans. R. Soc. London A.*, 45:481–486, 1889.
- A. Semenov and A. Kuvshinov. 3-D mapping of mid-mantle conductivity based on inversion of ground based *C*-responses. II, Data analysis and results. *Geophys. J. Int.*, submitted, 2011.
- V. Semenov and W. Jozwiak. Lateral variations of the mid-mantle conductance beneath Europe. *Tectonophysics*, 416:279–288, 2006.
- V. Semenov, J. Pek, A. Adam, W. Jozwiak, B. Ladanyvskyy, I. Logvinov, P. Pushkarev, and J. Vozar. Electrical structure of the upper mantle beneath central Europe: results of the CEMES project. *Acta Geophys.*, 56:957–981, 2008.
- T. Shankland and A. Duba. Standart electrical conductivity of isotropic, homogeneous olivine in the temperature range 1200° – 1500°C. *Geophys. J. Int.*, 103:25–31, 1990.
- T. Shankland, J. Peyronneau, and J. Poirer. Electrical conductivity of the Earth’s lower mantle. *Nature*, 366:453–455, 1993.
- H. Shimizu and H. Utada. Ocean hemisphere geomagnetic network: its instrumental design and perspective for long-term geomagnetic observations in the Pacific. *Earth Planets Space*, 51:917–932, 1999.
- H. Shimizu, T. Koyama, K. Baba, and H. Utada. Revised 1-D mantle electrical conductivity structure beneath the North pacific. *Geophys. J. Int.*, 180:1030–1048, 2010a.
- H. Shimizu, H. Utada, K. Baba, T. Koyama, M. Obayashi, and Y. Fukao. Three-dimensional imaging of electrical conductivity in the mantle transition zone beneath the North Pacific ocean by a semi-global induction study. *Phys. Earth Planet. Int.*, 2010b. doi: 10.1016/j.pepi.

- M. Siebert. Ein Verfahren zur unmittelbaren Bestimmung der vertikalen Leitfähigkeitverteilung im Rahmen der erdmagnetischen Tiefensondierung. *Nachr. Akad. Wiss. Göttingen, math.-phys. Kl.*, 2, 1964.
- B. Singer. Method for solution of Maxwell's equations in non-uniform media. *Geophys. J. Int.*, 120:590–598, 1995.
- T. Takahashi and E. Ito. Mineralogy of mantle periodotite along a model geotherm up to 700 km depth. *High-pressure research in mineral physics (Manghnani, M.H. and Shono, Y.)*; American Geophysical Union, Washington, pages 427–437, 1987.
- P. Tarits and M. Manda. The heterogeneous electrical conductivity structure of the lower mantle. *Phys. Earth Planet. Int.*, 2010. doi: 10.1016/j.physletb.2003.10.071.
- P. Tarits, S. Hautot, and F. Perrier. Water in the mantle: results from electrical conductivity beneath the French Alps. *Geophys. Res. Lett.*, 31:L06612, 2004. doi: 10.1029/2003GL019277.
- E. Titchmarsh. *Eigenfunction expansions associated with second order differential equations (2nd edition)*. Oxford University Press, London, 1962.
- H. Toh, Y. Hamano, M. Ichiki, and H. Utada. Geomagnetic observatory operates at the seafloor in the Northwest Pacific Ocean. *EOS*, 85:467–473, 2004.
- H. Toh, Y. Hamano, and M. Ichiki. Long-term seafloor geomagnetic station in the Northwest Pacific: A possible candidate for a seafloor geomagnetic observatory. *Earth Planets Space*, 58:697–705, 2006.
- H. Toh, Y. Hamano, Y. Goto, and H. Utada. Long-term seafloor electromagnetic observation in the northwest Pacific may detect the vector geomagnetic secular variation. *Data Sci. J.*, 9:IGY100–IGY109, 2010.
- J. Trampert, F. Deschamps, J. Resovsky, and D. Yuen. Chemical heterogeneities throughout the lower mantle. *Science*, 306:853–855, 2004.
- H. Utada, T. Koyama, H. Shimizu, and A. Chave. A semi-global reference model for electrical conductivity in the mid-mantle beneath the North Pacific region. *Geophys. Res. Lett.*, 30: doi:10.1029/2002GL016092, 2003.
- H. Utada, T. Koyama, M. Obayashi, and Y. Fukao. A joint interpretation of electromagnetic and seismic tomography models suggests the mantle transition zone below Europe is dry. *Earth Planet Science Letters*, 281:249–257, 2009.

- M. Uyeshima and A. Schultz. Geoelectromagnetic induction in a heterogeneous sphere: a new 3-D forward solver using a staggered-grid integral formulation. *Geophys. J. Int.*, 140: 636–650, 2000.
- J. Velimsky. Electrical conductivity in the lower mantle: Constraints from CHAMP satellite data by time-domain EM induction modeling. *Phys. Earth Planet. Int.*, 180:111–117, 2010. doi: 10.1016/j.pepi.2010.02.007.
- J. Velimsky, Z. Martinec, and M. Everett. Electrical conductivity in the Earth's mantle inferred from CHAMP satellite measurements. data processing and 1-D inversion. *Geophys. J. Int.*, 166:529–542, 2006.
- O. Verhoeven, P. Vacher, A. Mocquet, A. Rivoldini, M. Menviele, P. Arrial, G. Choblet, P. Tardits, V. Dehant, and T. Van Hoolst. Constraints on thermal state and composition of the Earth's lower mantle from electrical impedances and seismic data. *J. Geophys. Res.*, 114, 2008. doi: 10.1029/2008JB005678.
- B. Wanamaker and A. Duba. Electrical conductivity of San Carlos olivine along [100] under oxygen and pyroxene-buffered conditions and implications for defect equilibria. *J. Geophys. Res.*, 98:489–500, 1993.
- P. Weidelt. The inverse problem of geomagnetic induction. *Z. Geophys.*, 38:257–289, 1972.
- B. Wood and J. Nell. High-temperature electrical conductivity of the lower mantle phase (Mg,Fe)O. *Nature*, 351:309–311, 1991.
- B. Wood and D. Rubie. The effect of alumina on phase transformations at the 660 km discontinuity from Fe-Mg partitioning experiments. *Science*, 273:1522–1524, 1996.
- Y. Xu and T. Shankland. Electrical conductivity of orthopyroxene and its high pressure phases. *Geophys. Res. Lett.*, 22:2645–2648, 1999.
- Y. Xu, C. McCammon, and B. Poe. Effect of alumina on the electrical conductivity of silicate perovskite. *Science*, 282:922–924, 1998a.
- Y. Xu, B. Poe, and T. Shankland. Electrical conductivity of olivine, wadsleyite and ringwoodite under upper-mantle condition. *Science*, 280:1415–1418, 1998b.
- T. Yoshino. Laboratory electrical conductivity measurement of mantle minerals. *Surv. Geophysics*, 31:163–206, 2009.
- T. Yoshino, T. Matsuzaki, S. Yamashita, and T. Katsura. Hydrous olivine unable to account for conductivity anomaly at the top of the asthenosphere. *Nature*, 443:973–976, 2006.

- T. Yoshino, G. Manthilake, T. Matsuzaki, and T. Katsura. Dry mantle transition zone inferred from electrical conductivity of wadsleyite and ringwoodite. *Nature*, 451:326–329, 2008a.
- T. Yoshino, K. Nishi, T. Matsuzaki, D. Yamazaki, and T. Katsura. Electrical conductivity of majorite garnet and its implications for electrical structure and mantle transition zone. *Phys. Earth Planet Int.*, 170:193–200, 2008b.
- T. Yoshino, T. Matsuzaki, A. Shatskiy, and T. Katsura. The effect of water on the electrical conductivity of olivine aggregates and its implications for the electrical structure of the upper mantle. *Earth Planet Sci. Lett.*, 2009. doi: 10.1016/j.epsl.2009.09.032.
- M. Zhdanov. *Geophysical inverse theory and regularization problems*. Elsevier Science B.V., Amsterdam, 2002.

Curriculum vitae

Personal Information

Birth date: 24.05.1986

Citizenship: Russian Federation

Education

September, 2007 - August, 2011:

Ph.D. Candidate, Earth and Planetary Magnetism, ETH Zürich, Switzerland.

September, 2002- June, 2007:

Diploma with honours, Mathematics, Lomonosov's Moscow State University, Russia.

Languages

Russian (native), English (fluent), German (fluent)

List of Publications

Peer reviewed journals

Khan, A., Kuvshinov, A., **Semenov, A.**, 2011. On the heterogeneous electrical conductivity structure of the Earth's mantle with implications for transition zone water content, *J. Geophys. Res.*, **116**, doi:10.1029/2010JB007458.

Kuvshinov, A., **Semenov, A.**, 2011. Global 3-D imaging of mantle electrical conductivity based on inversion of observatory *C*-responses - I. An approach and its verification, *Geophys. J. Int.*, submitted

Semenov, A., Kuvshinov, A., 2011. Global 3-D imaging of mantle electrical conductivity based on inversion of observatory *C*-responses - II. Data analysis and results, *Geophys. J. Int.*, submitted

Science study reports

Kuvshinov, A., Velimsky, J., Tarits, P., **Semenov, A.**, Pankratov, O., Martinec, Z., Olsen, N., Jackson, A., 2008. Mapping 3-D mantle conductivity from *Swarm* constellation data. *Final report on ESA project 2008*.

Kuvshinov, A., Velimsky, J., Tarits, P., **Semenov, A.**, Pankratov, O., Tøffner-Clausen, L., Martinec, Z., Olsen, N., Sabaka, T.J., Jackson, A., 2010. Level 2 products and performances for mantle studies with *Swarm*. *Final report on ESA project 2009*.

http://esamultimedia.esa.int/docs/EarthObservation/Induction_Study_150110.pdf

Conference proceedings

Semenov, A., Kuvshinov, A., 2008. Derivation and numerical calculation of fundamental solutions (Greens tensors) of Maxwell equation in a spherical Earths model with radially-symmetric conductivity distribution excited by two types of sources: magnetic dipoles and gradient-type source, *ETH PhD Assembly*. Zürich, Switzerland; 28 March, 2008

Semenov, A., Kuvshinov, A., Jackson, A., 2008. A comparison of regularization schemes in 1D inversion of global induction data, *19th EM induction workshop*. Beijing, China; 23-29 October, 2008

Kuvshinov, A., **Semenov, A., Pankratov, O., Jackson, A., Olsen, N., 2008.** 3-D imaging of mantle conductivity based on inversion of satellite: Proof of concept, *19th EM induction workshop*. Beijing, China; 23-29 October, 2008

Kuvshinov, A., Olsen, N., Velimsky, J., Martinec, Z., Jackson, A., Tarits, P., Pankratov, O., **Semenov, A., 2008.** Benchmarking of global inverse problem solvers, *19th EM induction workshop*. Beijing, China; 23-29 October, 2008

Semenov, A., 2009. Towards 3-D inversion of global ground-based induction data, *Swiss-Russian seminar*. Zürich, Switzerland; March, 2009

Kuvshinov, A., **Semenov, A., Pankratov, O., Olsen, N., 2009.** 3-D Mapping of Mantle Conductivity From Space. An Approach and its Validation, *2nd Swarm meeting*. Potsdam, Germany; 24-26 June, 2009

Semenov, A., Kuvshinov, A., 2009. 3-D imaging of mid-mantle conductivity based on inversion of ground-based *C*-responses, *IAGA Assembly*. Sopron, Hungary; 23-30 August, 2009

Semenov, A., Kuvshinov, A., 2010. Spatial distribution of the mantle conductivity as seen from the 3-D inversion of ground-based *C*-responses, *Geophysical Research Abstracts; EGU General Assembly*, **12**, EGU2010-12565. Vienna, Austria; 02-07 May, 2010

Semenov, A., Kuvshinov, A., 2010. Spatial distribution of the mantle conductivity as recovered by global 3-D EM inversion of ground-based *C*-responses, *20th EM induction workshop*. Giza, Egypt; 18-24 September, 2010

Semenov, A., Kuvshinov, A., 2011. Global 3-D imaging of mantle electrical conductivity based on inversion of ground-based geomagnetic data. *Joint Annual Meeting of the Swiss Physical Society*. Lausanne, Switzerland; 15-17 June, 2011

Semenov, A., Kuvshinov, A., 2011. Inversion of global induction data. From data analysis to the 3-D model of mantle conductivity. *IUGG General Assembly*. Melbourne, Australia; 28 June - 07 July, 2011

Acknowledgements

Working on this project has been a great experience for me, both academic and personal. But this work would not be possible without generous help and support of a number of people.

First of all I would like to thank Alexey Kuvshinov for his thoughtful supervision and support. I highly appreciate many discussions we had, his questioning my work, to make me sure about correct assumptions and prevent from going to wrong directions. He also encouraged me to participate in several international conferences, which highly broadened my view on and beyond my subject of study. I would also like to thank him for his inestimable help during preparation of this manuscript.

I sincerely thank Prof. Andy Jackson for giving me the opportunity to work in Earth and Planetary Magnetism group at ETH Zürich and for building the unique productive environment within a group. I'm grateful to him for reading and revising my manuscripts, for his comments and corrections.

I would like to thank my working colleagues from the EPM group for interesting discussions and seminars: Prof. William Lowrie, Andrey Sheyko, Jenneke Bakker, Stephan Koch, Zacharias Stelzer, Jessica Kind, Kuan Li, Philippe Marti, Bjarne Almqvist, Håkon Fischer, Elisabeth Canet, Sanja Panovska, Friedemann Samrock, Andrea Biedermann, Michalis Charilaou, Fabio Donadini, Hans-Peter Hächler, Prof. Ann Hirt, Lisa Kapper, Jérôme Noir and Yufeng Lin.

In particular I want to thank Amir Khan and Chris Finlay for overall comments, interesting discussions and ideas as well as very important help with improving the English presentation of this manuscript. I am very grateful to Andreas Gehring for his help writing the "Zusammenfassung" for this work and for giving me the opportunity to make some field work and communicate with students. I am especially thankful to him for his help during my preparation for the job interview, which I had last year. Without his advice and ideas it could have been much more difficult.

I would also like to thank Jakub Velimsky, who participated a lot in discussions about my work during the time he worked in ETH. I also thank him for reviewing this manuscript. I thank Prof. Nils Olsen for interest in my study, for his important comments during our meetings on conferences and also for reviewing my work.

For their help and support in all administrative issues I thank Elisabeth Läderach, André Blanchard and Sabine Schulze. For financial support I thank the ETH Zürich (funds 0-20423-07 and 0-42363-06).

I would like to thank very much Alexey Kuvshinov's family - Anastasia and Ilya, for hosting me the first, may be the most difficult, month after my arriving to Switzerland. My life in Zürich could have been much more difficult without many events organized by a Russian community, including Yar and Masha, Denis and Sasha, Venya and Sveta, Zarina and Séb, Yury and Katya, Kri and Vadik, Alexey and Fanny. Special thanks to Denis, Vasya and Andrey for

our climbing trips, travels to European capitals and other great times. I highly appreciate their friendship and help during my PhD.

During my second year I started to play Ultimate Frisbee. I'm happy to have this unimaginable experience, for which I'm very thankful to Züri Ultimate Flyers (ZUF) team, who introduced me to this community. In particular I would like to thank the coaches Fränzi and Greg, and the ZUF-open team - Henning, Dani, Livia, Luca, Reto, Sam, Pascal, Jonatan, Jeff and Niki. From them I learned really a lot about personal spirit and communication with people from completely different backgrounds.

I would like to acknowledge my friends in Moscow, who, even from Russia, were always present during these 4 years of my PhD.

I wish to make a special acknowledgement to my sister Lena and my brother Leonid, who always supported me emotionally in difficult times.

Last but by no means least, I want to express my deep gratitude to my dear parents, Alexander and Natalia. I thank them for their constant love and believing in me.